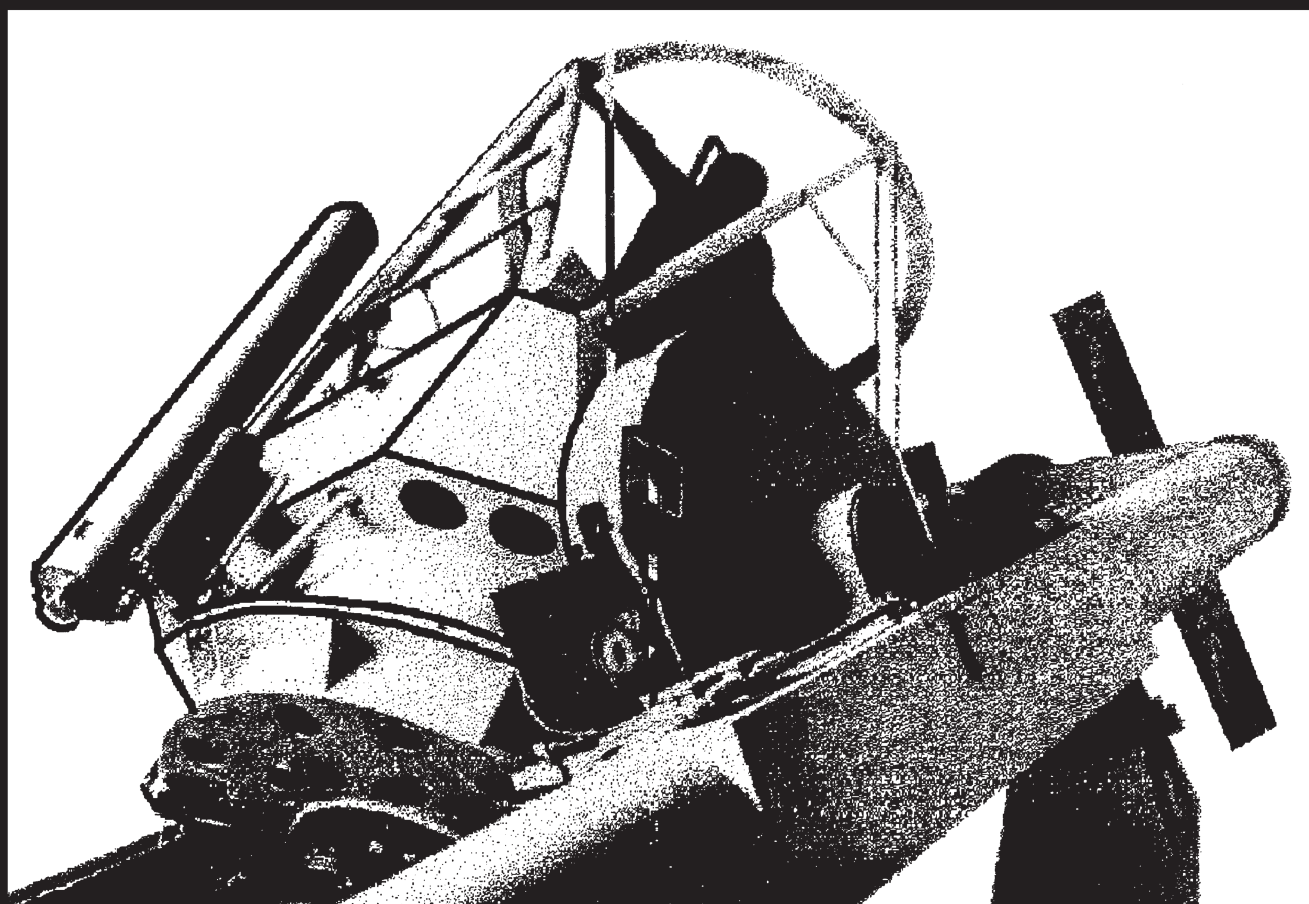




instituto de astronomía

unam

# revista mexicana de astronomía y astrofísica



Instituto de Astronomía  
Universidad Nacional Autónoma de México

## revista mexicana de astronomía y astrofísica

### *Editores fundadores*

Eugenio E. Mendoza V., Paris Pişmiş y Silvia Torres-Peimbert

### *Revista Mexicana de Astronomía y Astrofísica*

*Editora:* Christine Allen

### *Revista Mexicana de Astronomía y Astrofísica. Serie de Conferencias*

*Editora:* Silvia Torres-Peimbert

### *Editores asociados*

William Henney

### *Comité editorial*

Horacio A. Dottori (Universidade Federal Rio Grande do Sul, Brasil)

Guido Garay (Universidad de Chile, Santiago, Chile)

Gloria Koenigsberger (Universidad Nacional Autónoma de México)

Hugo Levato (Complejo Astronómico El Leoncito, Argentina)

Luis F. Rodríguez (Universidad Nacional Autónoma de México)

José-María Torrelles (Institut d'Estudis Espacials de Catalunya, Barcelona, España)

Alan M. Watson (Universidad Nacional Autónoma de México)

### *Asistentes editoriales*

Héctor Miguel Cejudo Camacho

Tulio Lugo Córdova

### *Asesoría en cómputo*

Alfredo Díaz Azuara, Carmelo Guzmán Cerón, Liliana Hernández Cervantes  
y Francisco Ruíz Sala

D.R. © 2024, Universidad Nacional Autónoma de México

Av. Universidad 3000

Col. Universidad Nacional Autónoma de México, C. U.

Alcaldía Coyoacán

04510 Ciudad de México

ISSN: 0185-1101

URL de DOI: <https://doi.org/10.22201/ia.01851101p.2024.60.01>

[rmaa@astro.unam.mx](mailto:rmaa@astro.unam.mx)

<http://www.astroscu.unam.mx/RMxAA/>

La *RMxAA* aparece indexada en Current Contents, Science Citation Index, Astronomy and Astrophysics Abstracts, Physics Briefs, Publicaciones Científicas en América Latina, Astronomy and Astrophysics Monthly Index, PERIODICA, RedALyC, Latindex y SciELO.

---

*Revista Mexicana de Astronomía y Astrofísica*, volumen 60, número 1, abril 2024, es una publicación semestral, editada y distribuida por el Instituto de Astronomía, UNAM, Circuito Exterior, Ciudad Universitaria, 04510, Alcaldía Coyoacán, Ciudad de México, Teléfono: 5556223906, Correo Electrónico: [rmaa@astro.unam.mx](mailto:rmaa@astro.unam.mx), ISSN-0185-1101. Editora responsable: Christine Patricia Allen Armiño. Número de Certificado de Licitud de Título: 10420. Número de Certificado de Licitud de Contenido: 7338. Número de Reserva: 04-2002-090916133200-102. Distribución: Francisco A. Guerra Súchil, Bienes y Servicios del Instituto de Astronomía, UNAM. Impresa por Grupo Edición, S.A. de C.V., Xochicalco 619, Colonia Letrán Valle, 03650, Alcaldía Benito Juárez, Ciudad de México. Fecha de impresión: 27 de marzo de 2024. Número de ejemplares impresos: 500 en papel Couché de 100 gramos los interiores y en cartulina Couché de 250 gramos los forros. Precio de la publicación: gratuito.





# revista mexicana de astronomía y astrofísica

volumen 60  
número 1  
abril 2024

COMPUTING POLYTROPIC AND ISOTHERMAL MODELS USING MONTE CARLO METHOD <i>Mohamed I. Nouh, Essam A. Elkholy, &amp; Samah H. El-Essawy</i>	3
RADIO PROPER MOTIONS OF THE NEARBY ULTRA-COOL DWARF BINARY VHS 1256–1257AB <i>L. F. Rodríguez, S. A. Dzib, L. A. Zapata, &amp; L. Loinard</i>	13
XookSuut: A BAYESIAN TOOL FOR MODELING CIRCULAR AND NON-CIRCULAR FLOWS ON 2D VELOCITY MAPS <i>C. López-Cobá, Lihwai Lin, &amp; Sebastián F. Sánchez</i>	19
THE CALAR ALTO LEGACY INTEGRAL FIELD AREA SURVEY: SPATIAL RESOLVED PROPERTIES <i>S. F. Sánchez, J. K. Barrera-Ballesteros, L. Galbany, R. García-Benito, E. Lacerda, &amp; A. Camps-Fariña</i>	41
INVESTIGATION ON FOUR CONTACT BINARY SYSTEMS AND A SEMIDETACHED ONE AT THE BEGINNING OF THE CONTACT PHASE <i>F. Acerbi, M. Martignoni, R. Michel, C. Barani, H. Aceves, L. Altamirano-Dévora &amp; F. J. Tamayo</i>	69
CCD PHOTOMETRY OF THE GLOBULAR CLUSTER NGC 5897 <i>A. Ruelas-Mayorga, L. J. Sánchez, E. Macías-Estrada, &amp; A. Nigoche-Netro</i>	83
THE FIRST MULTICOLOUR PHOTOMETRY OF THE V840 LYR CONTACT BINARY STAR <i>M. Tanriver, R. Michel, A. Bulut, H. Aceves, &amp; A. Keskin</i>	99
COMPACT RADIO SOURCES IN THE FIELD OF TYCHO'S SUPERNOVA REMNANT <i>Luis F. Rodríguez, Vanessa Yanza, &amp; Sergio A. Dzib</i>	113
ASTRONOMICAL TESTS OF A MEDIUM FORMAT DIGITAL CAMERA ON A LARGE SCHMIDT TELESCOPE <i>F. Della Prugna</i>	121
SN Ia DETECTION ANALYSIS RESULTS FROM REAL AND SIMULATED IMAGES USING SPECIALIZED SOFTWARE <i>Juan Pablo Reyes, Marcela Hernández Hoyos, &amp; Dominique Fouchez</i>	125
TESTING AN ENTROPY ESTIMATOR RELATED TO THE DYNAMICAL STATE OF GALAXY CLUSTERS <i>J. M. Zúñiga, C. A. Caretta, A. P. González, &amp; E. García-Manzanárez</i>	141
ASTRONOMICAL SIGNALS IN BRIGHTEST FIREBALLS FALLEN ON EARTH <i>D. Maravilla, M. Pazos, &amp; G. Cordero</i>	165
CCD PHOTOMETRY OF TRAPEZIA STARS I <i>A. Ruelas-Mayorga, L. J. Sánchez, A. Páez-Amador, O. Segura-Montero, &amp; A. Nigoche-Netro</i>	177
ERRATUM: A PECULIAR GALAXY NEAR M104 (RMxAA, 2023, 59, 323) <i>E. Quiroga</i>	199

Instituto de Astronomía  
Universidad Nacional Autónoma de México

## revista mexicana de astronomía y astrofísica

### *Editores fundadores*

Eugenio E. Mendoza V., Paris Pişmiş y Silvia Torres-Peimbert

### *Revista Mexicana de Astronomía y Astrofísica*

*Editora:* Christine Allen

### *Revista Mexicana de Astronomía y Astrofísica. Serie de Conferencias*

*Editora:* Silvia Torres-Peimbert

### *Editores asociados*

William Henney

### *Comité editorial*

Horacio A. Dottori (Universidade Federal Rio Grande do Sul, Brasil)

Guido Garay (Universidad de Chile, Santiago, Chile)

Gloria Koenigsberger (Universidad Nacional Autónoma de México)

Hugo Levato (Complejo Astronómico El Leoncito, Argentina)

Luis F. Rodríguez (Universidad Nacional Autónoma de México)

José-María Torrelles (Institut d'Estudis Espacials de Catalunya, Barcelona, España)

Alan M. Watson (Universidad Nacional Autónoma de México)

### *Asistentes editoriales*

Héctor Miguel Cejudo Camacho

Tulio Lugo Córdova

### *Asesoría en cómputo*

Alfredo Díaz Azuara, Carmelo Guzmán Cerón, Liliana Hernández Cervantes  
y Francisco Ruíz Sala

D.R. © 2024, Universidad Nacional Autónoma de México

Av. Universidad 3000

Col. Universidad Nacional Autónoma de México, C. U.

Alcaldía Coyoacán

04510 Ciudad de México

ISSN: 0185-1101

URL de DOI: <https://doi.org/10.22201/ia.01851101p.2024.60.01>

[rmaa@astro.unam.mx](mailto:rmaa@astro.unam.mx)

<http://www.astroscu.unam.mx/RMxAA/>

La *RMxAA* aparece indexada en Current Contents, Science Citation Index, Astronomy and Astrophysics Abstracts, Physics Briefs, Publicaciones Científicas en América Latina, Astronomy and Astrophysics Monthly Index, PERIODICA, RedALyC, Latindex y SciELO.

---

*Revista Mexicana de Astronomía y Astrofísica*, volumen 60, número 1, abril 2024, es una publicación semestral, editada y distribuida por el Instituto de Astronomía, UNAM, Circuito Exterior, Ciudad Universitaria, 04510, Alcaldía Coyoacán, Ciudad de México, Teléfono: 5556223906, Correo Electrónico: [rmaa@astro.unam.mx](mailto:rmaa@astro.unam.mx), ISSN-0185-1101. Editora responsable: Christine Patricia Allen Armiño. Número de Certificado de Licitud de Título: 10420. Número de Certificado de Licitud de Contenido: 7338. Número de Reserva: 04-2002-090916133200-102. Distribución: Francisco A. Guerra Súchil, Bienes y Servicios del Instituto de Astronomía, UNAM. Impresa por Grupo Edición, S.A. de C.V., Xochicalco 619, Colonia Letrán Valle, 03650, Alcaldía Benito Juárez, Ciudad de México. Fecha de impresión: 27 de marzo de 2024. Número de ejemplares impresos: 500 en papel Couché de 100 gramos los interiores y en cartulina Couché de 250 gramos los forros. Precio de la publicación: gratuito.

# COMPUTING POLYTROPIC AND ISOTHERMAL MODELS USING MONTE CARLO METHOD

Mohamed I. Nouh<sup>1</sup>, Essam A. Elkholy<sup>2,1</sup>, and Samah H. El-Essawy<sup>1</sup>

*Received March 29 2023; accepted September 7 2023*

## ABSTRACT

Polytropic and isothermal gas spheres are crucial in the theory of stellar structure and evolution, galaxy cluster modeling, thermodynamics, and various other physics, chemistry, and engineering disciplines. Based on two Monte Carlo algorithms (MC<sub>1</sub> and MC<sub>2</sub>), we introduced a numerical approach for solving the Lane-Emden (LE) equations of the polytropic and isothermal gas spheres. We found that the MC<sub>1</sub> and MC<sub>2</sub> models agree with each other and also with numerical and analytical models. We tested the compatibility between the MC and the numerical polytropic models by calculating the mass-radius relation and the pressure profile for the polytrope with  $n = 3$ .

## RESUMEN

Las esferas politrópicas e isotérmicas son importantes para la teoría de la estructura y evolución estelares, para modelar cúmulos de galaxias, en la termodinámica y en diversas disciplinas físicas, químicas e ingenieriles. Con base en dos algoritmos Monte Carlo (MC<sub>1</sub> and MC<sub>2</sub>) presentamos un enfoque numérico para resolver las ecuaciones de Lane-Emden para la esfera politrópica e isotérmica. Encontramos que los modelos MC<sub>1</sub> and MC<sub>2</sub> concuerdan entre sí y también con los modelos numéricos y analíticos. Comprobamos la compatibilidad de MC con los modelos politrópicos numéricos calculando la relación masa-radio y el perfil de presión para el politropo con  $n = 3$ .

*Key Words:* equation of state — methods: numerical — methods: statistical — stars: interiors

## 1. INTRODUCTION

The Lane-Emden equation (LE) is an initial value nonlinear ordinary differential equation describing the equilibrium density distribution of the self-gravitating sphere. LE is often employed to model many problems in physics and astrophysics, like the thermal background of a spherical cloud of gas, stellar structure, and particle currents (Chandrasekhar 1967, Horedt 2004). Polytropic and isothermal gas spheres have been the subject of many studies given their importance as fundamental models for stellar structure, (Chandrasekhar 1967, Shore 2007, Kippenhahn et al. 2012, Maciel 2016). The Lane-Emden equation for a polytropic gas sphere can be written

as (Chandrasekhar 1967)

$$\frac{1}{x^2} \frac{d}{dx} \left( x^2 \frac{d\theta(x)}{dx} \right) = -\theta^n(x), \quad (1)$$

where  $\theta$  is called the Emden function and  $n$  is the polytropic index. The solution of equation (1) holds under the initial conditions

$$\theta'(0) = 0, \quad \theta(0) = 1. \quad (2)$$

For equation (1), there are exact solutions only for the polytropic indexes  $n = 0, 1$ , and  $5$ .

$$\begin{aligned} \theta_0(x) &= 1 - x^2/6, \quad \theta_1(x) = \sin(x)/x, \quad \theta_5(x) \\ &= 1/(1 + x^2/3)^{\frac{1}{2}}. \end{aligned} \quad (3)$$

The LE equation for the isothermal gas sphere is given by (Chandrasekhar 1967)

$$\frac{1}{x^2} \frac{d}{dx} \left( x^2 \frac{d\theta(x)}{dx} \right) = e^{-\theta(x)}, \quad (4)$$

<sup>1</sup>Astronomy Department, National Research Institute of Astronomy and Geophysics(NRIAG), Cairo, Egypt.

<sup>2</sup>Department of Physics, College of Science, Northern Border University, Arar, Saudi Arabia.

subject to the conditions

$$\theta'(0) = 0, \quad \theta(0) = 0. \quad (5)$$

The main application of isothermal gas spheres is in the context of molecular clouds, stellar cluster dynamics, and nonlinear analysis in applied mathematics (Chandrasekhar 1942, Kurth 1957, Davis 1962, Ito et al. 2018). In addition to numerical approaches (i.e., neural networks, Ahmad et al. 2017, Nouh et al. 2021), genetic algorithms (Ahmad et al. 2016), and the pattern search optimization technique (Lewis et al. 2000), various analytical methods exist to solve Lane-Emden-type equations (i.e., Chowdhury 2009, Ibrahim and Darus 2008, Podlubny 1999, Momani and Ibrahim 2008, Nouh 2004, Nouh and Saad 2013).

Monte Carlo (MC) calculations first appeared in astronomy in the late 1960s (Auer 1968, Avery and House 1968, and Magnan 1968, 1970). The Markov Chains method (MCMC) is one of the most powerful Monte Carlo algorithms. The MCMC is used extensively for astrometric orbits (Tuomi & Kotiranta 2009, Otor et al. 2016), visual binary orbits (Mendez et al. 2017), and other problems (see, for instance, Hestroffer 2012, Mede & Brandt 2014).

Compared to traditional approaches to solving differential equations, the MC method has been adopted as an independent method as science, technology, and computers have improved over the last century. MC approaches were implemented to solve the initial value problems of ordinary differential equations by Zhong and Tian (2011) and Akhtar et al. (2015). Akhtar et al. (2015) effectively refined the complexities of Zhong and Tian's algorithm. Uslu and Sari (2020) presented a Monte Carlo-based stochastic technique to solve various Lotka-Volterra equation systems. El-Essawy et al. (2023) introduced a novel numerical solution to LE equations (i.e., positive and negative index polytropes, isothermal gas spheres, and the white dwarf equation) using the MC technique.

In the present paper, we solve the LE equations of the polytropic and isothermal gas spheres using two different MC algorithms (MC<sub>1</sub> and MC<sub>2</sub>). The results from the two MC algorithms are compared to exact and numerical solutions. As an application, we compute the physical parameters of the polytropic and isothermal gas spheres. The structure of the paper is as follows: we introduce the two MC algorithms in § 2, § 3 deals with the results, and § 4 summarises the results.

## 2. THE MC ALGORITHMS

In the following subsections, we shall describe the two algorithms implemented to calculate the Emden

function ( $\theta$ ) of the polytropes and its derivative ( $\theta'$ ). The first algorithm (MC<sub>1</sub>) is proposed by El-Essawy et al. (2023), and the second one is based on the algorithm proposed by Akhtar et al. (2015).

### 2.1. Algorithm 1 (MC<sub>1</sub>)

The LE polytropic equation could be written as

$$\theta''(x) + \frac{2}{x}\theta'(x) + f(x, \theta) = 0. \quad (6)$$

Now, the solutions of  $\theta'(t)$  and  $\theta(t)$  hold under the following steps:

1. Assume  $\theta(t) = \theta_1(t)$  and  $\theta'(t) = \theta_2(t)$ , then, equation (6) can be reduced to a first-order differential equation as

$$\theta'_1(x) = \theta_2(x),$$

$$\theta'_2(x) = -\frac{2}{x}\theta_2(x) - f(x, \theta_1) = g(x, \theta_1, \theta_2). \quad (7)$$

2. Divide the interval  $[0, x_{final}]$  into small, discrete chunks with interval size  $dx = 10^{-3}$ , where  $x_{final}$  is the final limit of the integration.
3. Create a group that has  $10^6$  random variables from a uniform distribution  $[x_i, x_{i+1}]$ .
4. Initialize the iteration with values  $x \rightarrow x_0$ ,  $\theta_1 \rightarrow \theta_0$  and  $\theta_2 \rightarrow \theta'_0$ .
5. Compute  $\theta_2(x_{i+1}) = \theta_2(x_i) + \frac{x_{i+1} - x_i}{M} \sum_{k=1}^M g(\theta_2(x_i), \theta_1(x_i), x_k)$ .
6. The solution of  $\theta_1(x)$  yields  $\theta_1(x_{i+1}) = \theta_1(x_i) + \theta_2(x_{i+1})dx$ .
7. Then set  $x_i = x_i + dx$ .
8. End the iteration process, when  $x_i = x_{final}$ .

### 2.2. Algorithm 2 (MC<sub>2</sub>)

In the second algorithm,  $\theta'(x)$  and  $\theta(x)$  can be integrated according to the strategy below:

1. Firstly, we have to get a solution of  $\theta'(x)$  using the following steps:
  - 1.1. Write the LE equation as  $\theta''(x) = h(x, \theta, \theta')$ .
  - 1.2. Determine the positive upper and negative lower boundaries ( $M_1$  and  $R_1$ ) for  $h(x, \theta, \theta')$  to classify the generated random variables.

- 1.3. Split the specified interval  $[0, x_{final}]$ ,  $x_{final}$  being the final limit of integration, into  $m$  points with a step size  $dx = 0.001$ .
- 1.4. Simulate two groups  $[0, M_1]$  and  $[R_1, 0]$  of random variables from the uniform distribution, each containing  $N = 10^6$ .
- 1.5. Let us consider  $JF_1 = h(x_i, \theta_i, \theta'_i)$  for  $i = 0, 1, \dots, m$ .
- 1.6. Start with initial conditions  $x \rightarrow x_0$ ,  $\theta \rightarrow \theta_0$  and  $\theta' \rightarrow \theta'_0$ .
- 1.7. If  $JF_1 \geq 0$ , evaluate:
  - $S_1 \rightarrow$  count the numbers of random variables from  $[0, M_1]$  which are smaller than or equal to  $JF_1$ .
  - Compute  $\theta'_{i+1}(x) = \theta'_i(x) + M_1 \times \frac{S_1}{N} dx$ .  
Else, if  $JF \leq 0$ :
  - $S_1 \rightarrow$  count the numbers of random variables from  $[R_1, 0]$  which are larger than or equal to  $JF_1$ .
  - Compute  $\theta'_{i+1}(t) = \theta'_i(x) + R_1 \times \frac{S_1}{N} dx$ .
2. Secondly, the solution of  $\theta(x)$  could be obtained using the following steps:
  - 2.1. Classify  $M_2$  and  $R_2$  as positive upper and negative lower boundaries of the solution  $\theta'(x)$ .
  - 2.2. Generate two groups of random variables as  $[R_2, 0]$  and  $[0, M_2]$ .
  - 2.3. Define  $JF_2 = \theta'_{i+1}(x)$ .
  - 2.4. If  $JF_2 \geq 0$ , evaluate:
    - $S_2 \rightarrow$  count the numbers of random variables from  $[0, M_2]$  which are smaller than or equal to  $JF_2$ .
    - Compute  $\theta_{i+1}(x) = \theta_i(x) + M_2 \times \frac{S_2}{N} dx$ .  
Else, if  $JF_2 \leq 0$ :
    - $S_2 \rightarrow$  count the numbers of random variables from  $[R_2, 0]$  which are larger than or equal to  $JF_2$ .
    - Compute  $\theta_{i+1}(x) = \theta_i(x) + R_2 \times \frac{S_2}{N} dx$ .
3. Go to the second iteration with  $x_{i+1} = x_i + \Delta x$ .
4. Repeat the previous steps, until  $x_{i+1} = x_{final}$ .

TABLE 1  
THE MAXIMUM ABSOLUTE ERROR FOR THE EMDEN FUNCTION

$n$	$Max E_1$	$Max E_2$
0	0.0008154	0.0001992
1	0.0004015	0.0001978
1.5	0.0003410	0.0001961
3	0.0002516	0.0002220
5	0.0001984	0.0009020
iso	0.0004567	0.0070129

### 3. RESULTS

To solve the LE differential equations of the polytropic and isothermal gas spheres, we coded  $MC_1$  and  $MC_2$  using R language. A total of 1000000 random samples were used. For the numerical solution, we used the R package function `rkMethod` that implements the Runge-Kutta method (RK). We used an oddly spaced spacing with 0.001 increments. We solved the LE equation (equation 1) for the polytropic indexes  $n = 0, 1, 1.5, 3$ , and 5, and the LE equation of the isothermal gas sphere (equation 4); the results are listed in Tables A1-A6 and plotted in Figure 1. The designations of the columns of Tables A1-A6 are as follows: Column 1 is the dimensionless parameter  $x$ , Column 2 is the Emden function calculated by the exact solutions (using equation (3) for  $n = 0, 1$ , and 5) or from the numerical integration for  $n = 1.5, 3$ , and the isothermal gas sphere; Column 3 is the MC solution using algorithm 1 ( $MC_1$ ); Column 4 is the MC solution using algorithm 2 ( $MC_2$ ); Column 5 is the absolute error such that  $E_1 = (exact/numerical - MC_1)$ ; Column 6 represents the absolute error such that  $E_2 = (exact/numerical - MC_2)$ . The maximum absolute errors between the two MC algorithms and the exact/numerical solutions are listed in Table 1. As shown in Figure 1 and Table 1, the Emden functions ( $\theta$ ) calculated using the second MC algorithm ( $MC_2$ ) have a smaller error than the first MC algorithm ( $MC_1$ ) except in the two situations of the polytrope with  $n = 5$  and the isothermal gas sphere. Similar to the scheme we applied in a previous paper (MC<sub>1</sub>, El-Essawy et al., 2023), we determined the absolute errors between the MC<sub>2</sub> solution and several numerical techniques to assess the effect of the MC calculations on the accuracy of the computed Emden function ( $\theta$ ). For the polytropes with  $n = 1$ , we used the active-set algorithm-based neural networks (AST-NN, Ahmad et al. 2017), Chebyshev neural networks (Ch-NN, Mall and Chakraverty 2014), the



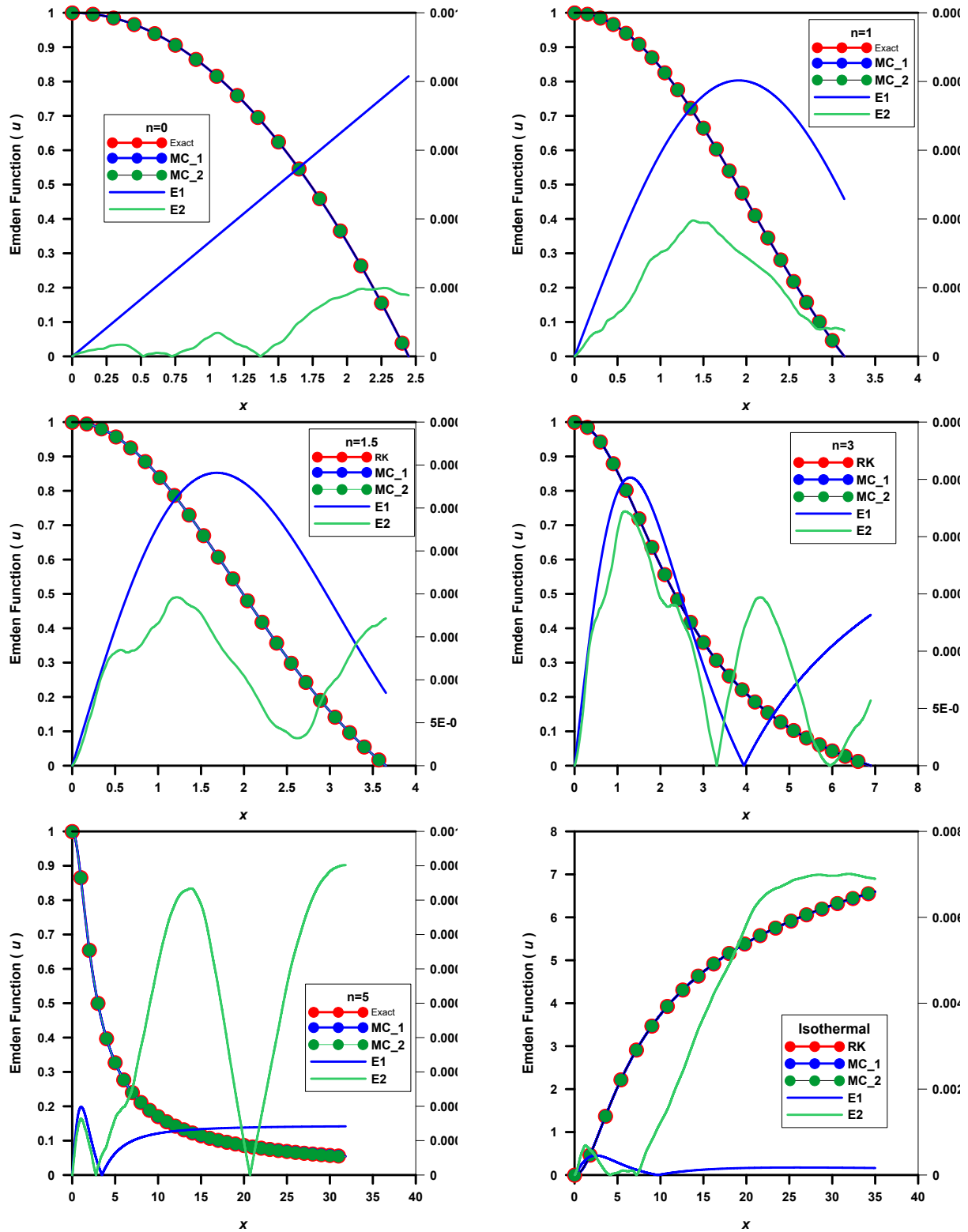


Fig. 1. The distribution of the Emden function for the polytropes with  $n = 0, 1, 1.5, 3, 5$ , and the isothermal gas sphere. The color figure can be viewed online.

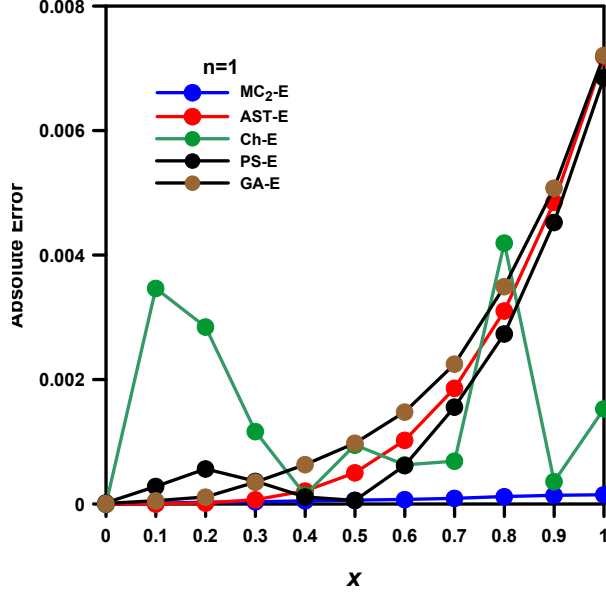


Fig. 2. Comparative study based on values of absolute errors for the polytrope with  $n = 1$ . The color figure can be viewed online.

Pattern Search Optimization Technique (PS, Lewis et al. 2000), and genetic algorithms (GA, Ahmad et al. 2016).

For  $n = 3$ , we compared our results with the Homotopy Analysis Method (HAM), Padé approximants (PA) of an order [4; 4], and the numerical solution with the Simpson rule (SIMP); Al-Hayani et al. (2017). Tables 2 and 3 compare  $\theta$  computed by the  $MC_2$  and by different numerical methods. Figures 2 and 3 plot the absolute errors between the  $MC_2$  values and the above mentioned numerical methods. For the polytrope with  $n = 1$ , the maximum absolute error between the exact solution and  $MC_2$  is the smallest, while for the polytrope with  $n = 3$ , the maximum absolute error between the Simpson rule and  $MC_2$  is the smallest.

Polytropic stellar models may be constructed using the polytropic index  $n = 0-1$  for neutron stars,  $n = 1.5$  for white dwarfs, and  $n = 3$  for solar-type stars. The mass contained in a radius  $R_0$  is given by

$$M_0 = 4\pi \left[ \frac{K(n+1)}{4\pi G} \right]^{\frac{3}{2}} \rho_c^{\frac{3-n}{2n}} \left[ -(x^2 \theta') \right]_{x=x_1}. \quad (8)$$

The radius of the polytrope is given by

$$R_0 = \left[ \frac{K(n+1)}{4\pi G} \right]^{\frac{1}{2}} \rho_c^{\frac{1-n}{2n}} x_1. \quad (9)$$

The pressure is provided by

$$P = P_c \theta^{n+1}. \quad (10)$$

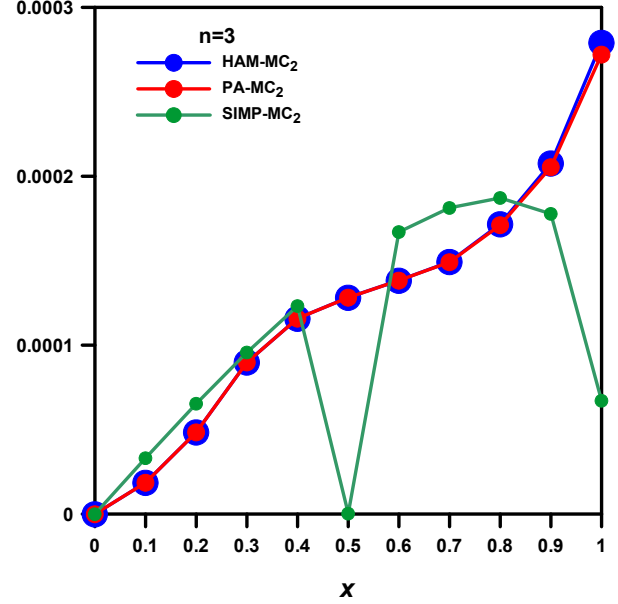


Fig. 3. Comparative study based on values of absolute errors for the polytrope with  $n = 3$ . The color figure can be viewed online.

The central density is computed from the equation

$$\rho_c = -\frac{x_1^2 M_0}{4\pi R_0^3 [\theta']_{x=x_1}}, \quad (11)$$

and finally, the ratio of central density to mean density is

$$\frac{\rho_c}{\rho_m} = \frac{x_1^3}{3[-x^2 \theta']_{x=x_1}}. \quad (12)$$

Table 4 compares the density ratio  $\rho_c/\rho_m$  (equation 12) computed from the three methods ( $ex/num, MC_1, MC_2$ ). The table shows that the ratio calculated from the two MC algorithms agrees with the exact/numerical values.

We construct mass-radius relation and pressure profiles for the model with a polytropic index  $n = 3$ ; the zero of the Emden function ( $x_1$ ) and the first derivative of the Emden function ( $\theta'$ ). The results are listed in Tables 5 and 6 for the mass-radius relation and the pressure profile, respectively. Based on the two tables with absolute errors in Columns 5 and 6, one can demonstrate an excellent agreement between the numerical and MC calculations.

#### 4. CONCLUSION

This paper employed two Monte Carlo (MC) approaches to solve Lane-Emden equations of the polytropic and isothermal gas spheres. We wrote R codes to implement the two MC algorithms, where  $10^6$

TABLE 2  
COMPARISON OF  $\theta$  COMPUTED BY DIFFERENT NUMERICAL METHODS AND THE MC<sub>2</sub> ALGORITHM FOR  $n=1$

$x$	The Emden function ( $\theta$ )					
	Exact	MC <sub>2</sub>	AST-NN	Ch-NN	PS	GA
0	1	1	1.000000	1	0.99998	0.99999
0.1	0.998334	0.998319	0.998337	1.00180	0.99805	0.99828
0.2	0.993346	0.993315	0.993364	0.99050	0.99278	0.99346
0.3	0.985067	0.985030	0.985138	0.98390	0.98470	0.98542
0.4	0.973545	0.973492	0.973757	0.97340	0.97343	0.97418
0.5	0.958851	0.958788	0.959355	0.95980	0.95891	0.95983
0.6	0.941070	0.940996	0.942096	0.94170	0.94169	0.94255
0.7	0.920310	0.920217	0.922172	0.92100	0.92187	0.92256
0.8	0.896695	0.896574	0.899800	0.89250	0.89943	0.90019
0.9	0.870363	0.870221	0.875212	0.87000	0.87489	0.87544
1.0	0.841470	0.841319	0.848656	0.84300	0.84832	0.84868

TABLE 3  
COMPARISON OF  $\theta$  COMPUTED BY DIFFERENT NUMERICAL METHODS AND THE MC<sub>2</sub> ALGORITHM  $n=3$

$x$	The Emden function ( $\theta$ )			
	MC <sub>2</sub>	HAM	PA	SIMP
0	1	1	1	1
0.1	0.998317	0.998335	0.998335	0.998335
0.2	0.993324	0.993373	0.993373	0.993373
0.3	0.985109	0.985199	0.985199	0.985199
0.4	0.973842	0.973958	0.973958	0.973958
0.5	0.959710	0.959839	0.959839	0.959839
0.6	0.942935	0.943073	0.943073	0.943073
0.7	0.923775	0.923925	0.923922	0.923924
0.8	0.902508	0.902680	0.902672	0.902679
0.9	0.879436	0.879643	0.879617	0.879641
1.0	0.854852	0.855132	0.855057	0.855125

random samples were used in each integration procedure. The numerical solution of the differential equations is performed using the R package function `rkMethod`, which is based on the Runge-Kutta technique (RK) for solving ordinary differential equations. An oddly spaced interval with 0.001 increments was chosen.

The MC results were compared to the exact and numerical solutions to determine the accuracy and efficiency of the proposed approach. When the MC and numerical/analytical models are compared, they agree well for the polytropic indexes  $n = 0, 1, 1.5$ ,

TABLE 4  
THE MEAN DENSITY FOR THE POLYTROPIC GAS SPHERES

$n$	$\rho_c / \rho_m$		
	ex/num	MC <sub>1</sub>	MC <sub>2</sub>
0	1.0	0.999	0.999
1	2.895	2.896	2.894
1.5	5.735	5.738	5.733
3	54.138	54.165	54.140

3, while there are significant discrepancies from the models with  $n = 5$  and the isothermal gas sphere.

For the polytropic indexes  $n = 1$  and 3, we compared MC solutions and other numerical approaches like active-set algorithm-based neural networks, Chebyshev neural networks, the Pattern Search Optimization Technique, and genetic algorithms. We may infer that the MC algorithms have the advantage of needing no data training like neural network methods. Based on absolute error, the MC solutions are consistent with solutions from different numerical methods. Moreover, we found that the second algorithm (MC<sub>2</sub>) is faster than the first one (MC<sub>1</sub>) and more accurate. We computed the mass-radius relation and the pressure profile for the polytrope with  $n = 3$ , and we found good agreement between the MC models and the numerical one.

The authors extend their appreciation to the Deanship of Scientific Research at Northern Border University, Arar, KSA for funding this research work through the project number NBU-FFR-2024-194-01.

TABLE 5

THE MASS-RADIUS RELATION FOR THE POLYTROPE WITH  $n=3$  CALCULATED BY RK, MC<sub>1</sub>, AND MC<sub>2</sub> METHODS

$R/R_0$	$(M/M_0)_{num}$	$(M/M_0)_{MC1}$	$(M/M_0)_{MC2}$	$E1$	$E2$
0	0	0	0	0	0
0.0581581	0.003345	0.003343	0.003344	1.61E-06	1.23E-07
0.1741842	0.030005	0.029991	0.030004	1.45E-05	1.10E-06
0.2902103	0.083293	0.083253	0.083290	4.02E-05	3.06E-06
0.4062364	0.163208	0.163129	0.163202	7.89E-05	6.01E-06
0.5222625	0.269750	0.269620	0.269741	0.000130	9.93E-06
0.6382886	0.402920	0.402725	0.402905	0.000194	1.48E-05
0.7543147	0.562717	0.562445	0.562696	0.000272	2.07E-05
0.8703408	0.749141	0.748779	0.749114	0.000362	2.75E-05
0.9863669	0.962193	0.961727	0.962157	0.000465	3.54E-05
1	0.988975	0.988496	0.988938	0.000478	3.64E-05

TABLE 6

THE PRESSURE PROFILE FOR THE POLYTROPE WITH  $n=3$  CALCULATED BY RK, MC<sub>1</sub>, AND MC<sub>2</sub> METHODS

$R/R_0$	$(P/P_c)_{ex}$	$(P/P_c)_{MC1}$	$(P/P_c)_{MC2}$	$E1$	$E2$
0	1	1	1	0	0
0.0581581	0.8993613	0.8988963	0.8989328	0.0005170	0.0004763
0.1741842	0.4143745	0.4138576	0.4139165	0.0012472	0.0011053
0.2902103	0.1151991	0.1150371	0.1150835	0.0014060	0.0010027
0.4062364	0.0249381	0.0249105	0.0249141	0.0011037	0.0009609
0.5222625	0.0046797	0.0046777	0.0046843	0.0004266	0.0009684
0.6382886	0.0007399	0.0007405	0.0007425	0.0007568	0.0035407
0.7543147	0.0000825	0.0000827	0.0000827	0.0030840	0.0029091
0.8703408	0.0000036	0.0000036	0.0000036	0.0096212	0.0001153
0.9863669	2.900E-010	3.3E-010	2.8E-010	0.1379310	0.0344827
1	0	0	0	0	0

## APPENDIX

## A. NUMERICAL RESULTS

We list in the following tables the numerical results obtained for the polytropes with  $n = 0, 1, 1.5, 3$ , and 5, and the isothermal gas sphere. The designation of the columns is as follows:

Column 1: The dimensionless distance ( $x$ ).

Column 2: The Emden function calculated by the exact solution ( $\theta_{Ex}$ ), or RK solution  $\theta_{RK}$ .

Column 3: The Emden function calculated by the first MC algorithm solution ( $\theta_{MC1}$ ).

Column 4: The Emden function calculated by the second MC algorithm solution ( $\theta_{MC2}$ ).

Column 5: The absolute error computed for the first MC algorithm and exact/RK solutions ( $E1$ ).

Column 6: The absolute error computed for the second MC algorithm and exact/RK solutions ( $E2$ ).

TABLE A1

EMDEN FUNCTION FOR THE POLYTROPE WITH  $n=0$  CALCULATED BY EXACT, MC<sub>1</sub>, AND MC<sub>2</sub> METHODS

$x$	$\theta_{ex}$	$\theta_{MC_1}$	$\theta_{MC_2}$	$E_1$	$E_2$
0	1	1	1	0	0
0.1	0.9982998	0.9982666	0.9982852	0.0000332	0.0000146
0.3	0.9848998	0.9848000	0.9848676	0.0000998	0.0000322
0.5	0.9581665	0.9580000	0.9581617	0.0001665	0.0000048
0.7	0.9180998	0.9178667	0.9181047	0.0002331	0.0000048
0.9	0.8646998	0.8644000	0.8646706	0.0002998	0.0000291
1.1	0.7979665	0.7976000	0.7979056	0.0003664	0.0000609
1.3	0.7178999	0.7174667	0.717881	0.0004331	0.0000188
1.5	0.6244999	0.6240001	0.6245375	0.0004997	0.0000377
1.7	0.5177665	0.5172001	0.517882	0.0005664	0.0001154
1.9	0.3976998	0.3970667	0.397868	0.0006330	0.0001681
2.1	0.2642998	0.2636001	0.2644961	0.0006997	0.0001963
2.3	0.1175665	0.1168001	0.1177664	0.0007664	0.0001976
2.44	0.0077333	0.0069205	0.0079122	0.0008127	0.0001789

TABLE A2

EMDEN FUNCTION FOR THE POLYTROPE WITH  $n=1$  CALCULATED BY EXACT, MC<sub>1</sub>, AND MC<sub>2</sub> METHODS

$x$	$\theta_{ex}$	$\theta_{MC_1}$	$\theta_{MC_2}$	$E_1$	$E_2$
0	1	1	1	0	0
0.2	0.9932801	0.9932138	0.9932491	0.0000662	0.0000309
0.4	0.9734145	0.9732838	0.9733613	0.0001306	0.0000532
0.6	0.9408777	0.9406862	0.9408034	0.0001915	0.0000743
0.8	0.896445	0.896198	0.8963242	0.0002470	0.0001207
1.0	0.8411697	0.840874	0.8410183	0.0002956	0.0001514
1.2	0.7763538	0.7760176	0.7761794	0.0003362	0.0001744
1.4	0.7035112	0.7031437	0.7033138	0.0003675	0.0001974
1.6	0.6243247	0.6239358	0.6241356	0.0003889	0.0001891
1.8	0.5405996	0.5401996	0.5404353	0.0004000	0.0001643
2.0	0.4542133	0.4538128	0.4540692	0.0004005	0.0001441
2.2	0.3670638	0.3666731	0.3669389	0.0003907	0.0001249
2.4	0.2810185	0.2806475	0.2809185	0.0003710	0.0001000
2.6	0.197864	0.1975216	0.1977996	0.0003423	0.0000644
2.8	0.1192595	0.1189537	0.1192175	0.0003057	0.0000419
3.0	0.0466944	0.0464320	0.0466540	0.0002623	0.0000403
3.14	0.0005072	0.00046958	0.00000003	0.0002290	0.0000376

TABLE A3

EMDEN FUNCTION FOR THE POLYTROPE WITH  $n=1.5$  CALCULATED BY RK, MC<sub>1</sub>, AND MC<sub>2</sub> METHODS

$x$	$\theta_{RK}$	$\theta_{MC_1}$	$\theta_{MC_2}$	$E_1$	$E_2$
0	1	1	1	0	0
0.2	0.9932868	0.9932207	0.9932323	0.0000660	0.0000545
0.4	0.9735202	0.9733907	0.9734014	0.0001294	0.0001187
0.6	0.9413984	0.9412109	0.9412647	0.0001875	0.0001336
0.8	0.898034	0.8977959	0.8978935	0.0002381	0.0001404
1.0	0.8448824	0.8446029	0.8447165	0.0002795	0.000165
1.2	0.7836536	0.7833431	0.7834578	0.0003105	0.0001958
1.4	0.7162136	0.7158829	0.7160285	0.0003307	0.0001851
1.6	0.6444837	0.6441436	0.6443238	0.0003401	0.0001599
1.8	0.5703465	0.5700071	0.5702177	0.0003393	0.0001287
2.0	0.4955639	0.4952345	0.4954593	0.0003294	0.0001045
2.2	0.4217124	0.4214007	0.4216416	0.0003116	0.0000708
2.4	0.3501363	0.3498488	0.3500921	0.0002875	0.0000441
2.6	0.2819211	0.2816624	0.2818889	0.0002587	0.0000322
2.8	0.2178831	0.2176564	0.2178339	0.0002266	0.0000491
3.0	0.1585734	0.1583805	0.1584807	0.0001929	0.0000927
3.2	0.1042928	0.1041342	0.1041704	0.0001586	0.0001223
3.4	0.0551108	0.0549859	0.0549570	0.0001249	0.0001538
3.6	0.0108816	0.0107889	0.0107135	0.0000927	0.0001681
3.65	0.0003567	0.00027	0.0001852	0.00008486	0.0001714



TABLE A4

EMDEN FUNCTION FOR THE POLYTROPE WITH  $n=3$  CALCULATED BY RK, MC<sub>1</sub>, AND MC<sub>2</sub> METHODS

$x$	$\theta_{RK}$	$\theta_{MC_1}$	$\theta_{MC_2}$	$E_1$	$E_2$
0	1	1	1	0	0
0.4	0.9738309	0.973705	0.9737149	0.000125	0.000163
0.8	0.90245	0.9022354	0.9022865	0.000214	0.000221
1.2	0.8023212	0.8020709	0.8020994	0.000250	0.000196
1.6	0.6912652	0.6910239	0.6910683	0.00024	0.0001461
2.0	0.582589	0.5823841	0.5824429	0.000204	0.0001377
2.4	0.4836957	0.4835379	0.4835579	0.000157	0.0000954
2.8	0.397389	0.3972793	0.3972935	0.000109	0.0000190
3.2	0.3237452	0.3236793	0.3237261	0.000065	0.0000632
3.6	0.2615509	0.261523	0.2616142	0.000027	0.0001253
4.0	0.2091615	0.2091657	0.2092868	0.000004	0.0001458
4.4	0.1649313	0.1649625	0.1650771	0.000031	0.0001152
4.8	0.1273938	0.1274478	0.1275091	0.000054	0.0000692
5.2	0.0953137	0.0953871	0.0953829	0.000073	0.0000183
5.6	0.0676807	0.0677708	0.0676991	0.000090	0.0000012
6.0	0.0436819	0.0437866	0.043680	0.000104	0.0000254
6.4	0.0226683	0.0227859	0.022642	0.000117	0.0000480
6.8	0.0041241	0.00425330	0.0040761	0.000129	0.0001159
6.89	0.0000784	0.0002101	0.0000214	0.000131	0.0000569

TABLE A5

EMDEN FUNCTION FOR THE POLYTROPE WITH  $n=5$  CALCULATED BY EXACT, MC<sub>1</sub>, AND MC<sub>2</sub> METHODS

$x$	$\theta_{ex}$	$\theta_{MC_1}$	$\theta_{MC_2}$	$E_1$	$E_2$
0	1	1	1	0	0
0.4	0.9742312	0.9741098	0.9742616	0.0001214	0.00009308
0.8	0.9076417	0.9074531	0.9076896	0.0001885	0.00015167
1.2	0.8217728	0.8215775	0.82183608	0.0001951	0.00015884
1.6	0.7343418	0.7341757	0.73442448	0.0001660	0.00012867
2.0	0.6544667	0.6543421	0.65456681	0.0001245	0.00008685
2.4	0.5850455	0.5849621	0.58516507	0.0000833	0.00004065
2.8	0.5259371	0.52589	0.52607689	0.0000471	0.00000392
3.2	0.4758956	0.4758787	0.47604990	0.0000169	0.00003929
3.6	0.4334572	0.4334649	0.43361973	0.0000077	0.00006475
4.0	0.3972761	0.3973038	0.39744423	0.0000277	0.00008453
4.4	0.3662176	0.3662617	0.36640865	0.0000440	0.00011893
4.8	0.3393596	0.339417	0.33957048	0.0000574	0.00014836
5.2	0.3159625	0.3160309	0.31619215	0.0000684	0.00017500
5.6	0.2954359	0.2955135	0.29567122	0.0000775	0.00018717
6.0	0.2773074	0.2773926	0.27754826	0.0000851	0.00019816
6.4	0.2611972	0.2612889	0.26144877	0.0000916	0.00021352
6.8	0.246798	0.2468951	0.24706752	0.0000970	0.00023544
7.2	0.2338594	0.2339612	0.23416162	0.0001017	0.00027148
7.6	0.2221761	0.222282	0.22252748	0.0001058	0.00032355
8.0	0.2115784	0.2116877	0.21197515	0.0001093	0.00037146

TABLE A6

EMDEN FUNCTION FOR THE ISOTHERMAL GAS SPHERE CALCULATED BY RK, MC<sub>1</sub>, AND MC<sub>2</sub> METHODS

$x$	$\theta_{RK}$	$\theta_{MC_1}$	$\theta_{MC_2}$	$E_1$	$E_2$
0	1	1	1	0	0
2.0	0.560384	0.560827	0.560931	0.0004424	0.0005470
4.0	1.572729	1.573106	1.572747	0.0003773	0.0000182
6.0	2.467576	2.467785	2.467481	0.0002089	0.0000952
8.0	3.175668	3.175745	3.176027	0.0000773	0.0003593
10.0	3.736768	3.736756	3.737987	0.0000121	0.0012184
12.0	4.191345	4.191273	4.193481	0.0000717	0.0021360
14.0	4.568391	4.56828	4.571572	0.0001112	0.0031808
16.0	4.887732	4.887594	4.891850	0.0001374	0.0041183
18.0	5.163044	5.162889	5.167944	0.0001544	0.0049003
20.0	5.403978	5.403813	5.409809	0.0001652	0.0058305
22.0	5.617513	5.617342	5.623992	0.0001715	0.0064794
24.0	5.808813	5.808638	5.815527	0.0001746	0.0067146
26.0	5.981783	5.981607	5.988679	0.0001755	0.0068959
28.0	6.139433	6.139258	6.146420	0.0001746	0.0069863
30.0	6.284123	6.283951	6.291093	0.0001726	0.0069699
32.0	6.417731	6.417562	6.424744	0.0001696	0.0070128
34.0	6.541771	6.541605	6.548700	0.0001660	0.0069288
35	6.600541	6.600377	6.607436	0.0001640	0.0068956

## REFERENCES

- Ahmad, I., Raja, M., Bilal, M., & Ashraf, F. 2016, SpringerPlus, 5, 1866, <https://doi.org/10.1186/s40064-016-3517-2>
- Ahmad, I., Raja, M. A., Bilal, M., & Ashraf, F. 2017, Neural Comput & Applic, 28 (Suppl. 1): S929-S944
- Akhtar, M. N., Durad, M. H., & Ahmed, A. 2015, Proc. IAM, 4, 149
- Al-Hayani, W., Alzubaidy, L., & Entesar, A. 2017, Amat, 11, 407, <https://doi.org/10.18576/amis/110208>
- Auer, L. H. 1968, ApJ, 153, 783, <https://doi.org/10.1086/149705>
- Avery, L. W., House, L. L. 1968, ApJ, 152, 493, <https://doi.org/10.1086/149566>
- Chandrasekhar, S. 1942, Principles of stellar dynamics (Chicago, IL: UCP)
- . 1967, An introduction to the study of stellar structure (New York, NY: Dover)
- Chowdhury, M. & Hashim, I. 2009, Nonlinear Analysis Real World Applications, 10, 104, <https://doi.org/10.1016/j.nonrwa.2007.08.017>
- Davis, H. T. 1962, Introduction to Nonlinear Differential and Integral Equations (New York, NY: Dover)
- El-Essawy, S. H., Nouh, M. I., Soliman, A. A., Abdel Rahman, H. I., & Abd-Elmougod, G. A. 2023, A&C, 42, 100665, <https://doi.org/10.1016/j.ascom.2022.100665>
- Hestroffer, D. 2012, In Proceedings of the workshop “Orbital Couples: Pas de deus in the Solay Systems and the Milky Way”, ed. F. Arenou & D. Hestroffer, 113
- Horedt, G. P. 2004, Polytropes-Applications in Astrophysics and Related Fields, Volume 306 (Dordrecht: Kluwer Academic Publishers), <https://doi.org/10.1007/978-1-4020-2351-4>
- Ibrahim, R. W. & Darus, M. 2008, JMAA, 345, 871, <https://doi.org/10.1016/j.jmaa.2008.05.017>
- Ito, Y., Poje, A., & Lancellotti, C. 2018, NewA, 58, 15, <https://doi.org/10.1016/j.newast.2017.07.003>
- Kippenhahn, R., Weigert, A., & Weiss, A. 2013, Stellar Structure and Evolution, (Berlin: Springer), <https://doi.org/10.1007/978-3-642-30304-3>
- Kurth, R. 1957, Introduction to the mechanics of stellar systems (London: Pergamon Press)
- Lewis, R. M. & Torczon, V. 2000, SIAM Journal on Optimization, 10, 917, <https://doi.org/10.1137/S1052623497331373>
- Maciel, J. W. 2016, Introduction to Stellar Structure (Switzerland: Springer Nature Switzerland), <https://doi.org/10.1007/978-3-319-16142-6>
- Magnan, C. 1968, ApL, 2, 213
- . 1970, JQSRT, 10, 1, [https://doi.org/10.1016/0022-4073\(70\)90124-X](https://doi.org/10.1016/0022-4073(70)90124-X)
- Mall, S. & Chakraverty, S. 2014, Applied Mathematics and Computation, 247, 100, <https://doi.org/10.1016/j.amc.2014.08.085>
- Mede, K. & Brandt, T. D. 2014, IAUS 299, Exploring the Formation and Evolution of Planetary Systems, 52, <https://doi.org/10.1017/S1743921313007837>
- Mendez, R. A., Claveria, R. M., Orchard, M. E., & Silva, J. F., 2017, AJ, 154, 187, <https://doi.org/10.3847/1538-3881/aa8d6f>
- Momani, S. & Ibrahim, R. W. 2008, JMAA, 339, 1210, <https://doi.org/10.1016/j.jmaa.2007.08.001>
- Nouh, M. I. 2004, NewA, 9, 467, <https://doi.org/10.1016/j.newast.2004.02.003>
- Nouh, M. I. & Saad, A. S. 2013, International Review of Physics, 7, 1, <https://doi.org/10.48550/arXiv.1406.1455>
- Nouh, M., Azzam, Y. A., & Abdel-Salam, E. A. 2021, Neural Computing and Applications, 33, 4533, <https://doi.org/10.1007/s00521-020-05277-9>
- Otor, O. J., Montet, B. T., Johnson, J. A. et al. 2016, AJ, 152, 165, <https://doi.org/10.3847/0004-6256/152/6/165>
- Podlubny, I. 1998, Fractional Differential Equations (SanDiego, CA: Academic Press)
- Tuomi, M. & Kotiranta, S. 2009, A&A, 496, 13, <https://doi.org/10.1051/0004-6361/200811531>
- Uslu, H., Sari, M., & Cosgun, T. 2020, IJOCTA, 10, 181, <https://doi.org/10.11121/ijocta.01.2020.00829>

Samah. H. El-Essawy, Essam A. Elkholy, and Mohamed I. Nouh: Astronomy Department, National Research Institute of Astronomy and Geophysics(NRIAG), 11421 Helwan, Cairo, Egypt.

Essam A. Elkholy: Department of Physics, College of Science, Northern Border University, Arar, Saudi Arabia.

## RADIO PROPER MOTIONS OF THE NEARBY ULTRA-COOL DWARF BINARY VHS 1256–1257AB

L. F. Rodríguez<sup>1,2</sup>, S. A. Dzib<sup>3</sup>, L. A. Zapata<sup>1</sup>, and L. Loinard<sup>1</sup>

*Received July 26 2023; accepted September 15 2023*

### ABSTRACT

The proper motions of a source obtained at different epochs or in different spectral regions should in principle be consistent. However, in the case of a binary source or a source with associated ejecta, they could be different depending on the epochs when the observations were made and on what emission is traced in each spectral region. In this paper we determine the radio proper motions of the ultra-cool dwarf binary VHS 1256–1257AB from Very Large Array (VLA) observations, that we find are consistent within error ( $\simeq 2 - 3\%$ ) with those reported by Gaia DR3. The comparison of the proper motions and the analysis of the VLA data imply that, as in the optical, the radio emission is coming in comparable amounts from both components of the unresolved binary.

### RESUMEN

Los movimientos propios de una fuente obtenidos en diferentes épocas o en distintas regiones espectrales deben, en principio, ser consistentes. Sin embargo, en el caso de una fuente binaria o una fuente con eyecciones asociadas, pueden ser diferentes dependiendo de en qué época se hicieron las observaciones o qué emisión es trazada en cada región espectral. En este artículo determinamos los movimientos propios en radio de la binaria enana ultrafría VHS 1256–1257AB a partir de observaciones hechas con el Very Large Array (VLA), y encontramos que, dentro del error ( $\simeq 2 - 3\%$ ), son consistentes con los valores reportados por Gaia DR3. La comparación de los movimientos propios y el análisis de los datos del VLA implican que, como en el óptico, la emisión en radio proviene en cantidades comparables de ambas componentes de la binaria no resuelta.

*Key Words:* astrometry — binaries: general — radio continuum: stars — stars: individual: VHS 1256–1257AB

### 1. INTRODUCTION

Highly accurate optical proper motions have been provided by the HIPPARCOS ( $\approx 1.2 \times 10^5$  stars; Perryman et al. 1997; van Leeuwen 2007) and the **Gaia third data release (DR3)**;  $\approx 1.5 \times 10^9$  stars; Gaia collaboration et al. 2022) catalogs. As pointed out by Kervella et al. (2019), discrepancies in the proper motions of a source obtained at different epochs (referred to as a proper motion anomaly) could point to the presence of a perturbing secondary object. It is of historical relevance to remember that this was the

technique used by Bessel (1844) to infer the existence of a companion to Sirius (the white dwarf Sirius B).

Besides searching for proper motion anomalies in time at the same spectral window, as done by Kervella et al. (2019), a different approach is to search for them between different spectral windows. For example, the luminosity ratio of the components of a binary system could be very different in different spectral windows. Also, the presence of ejecta with different brightnesses at different frequencies could produce a proper motion anomaly. An example is the energetic pulsar PSR J1813–1749 for which the X-ray (Chandra) proper motions (Ho et al. 2020) are much larger than the radio (VLA) proper motions (Dzib & Rodríguez 2021). Most likely, this anomaly is due to the presence of ejecta moving with respect

<sup>1</sup>Instituto de Radioastronomía y Astrofísica, UNAM, México.

<sup>2</sup>Mesoamerican Center for Theoretical Physics, UNACH, México.

<sup>3</sup>Max-Planck-Institut für Radioastronomie, Germany.

to the host star and detectable in X-rays but not at radio wavelengths. Then, one can search for proper motion anomalies either between different epochs of time at the same wavelength or between different spectral windows at the same epoch.

In this paper we present VLA proper motions for the nearby ultra-cool dwarf binary VHS 1256–1257AB and compare them with the accurate proper motions reported in the **Gaia DR3** (Gaia collaboration et al. 2022). Our search for proper motion anomalies is restricted to different spectral regions.

## 2. VHS 1256–1257

VHS 1256–1257AB is a nearby ( $21.14 \pm 0.22$  pc, Gaia collaboration et al. 2022) ultracool dwarf binary composed of two equal-magnitude stars with a spectral type  $M7.5 \pm 0.5$  (Gauza et al. 2015; Stone et al. 2016). This binary system has an orbital period of  $7.31 \pm 0.02$  yr and a total mass of  $0.141 \pm 0.008 M_{\odot}$  (Dupuy et al. 2023). This mass is consistent with the system being a pair of brown dwarfs or of very low-mass stars. Its orbit is highly eccentric ( $e = 0.88$ ) with the components reaching a maximum separation of  $\approx 0''.14$  on the plane of the sky (Dupuy et al. 2023). Accurate astrometry of the radio emission could help to better diagnose the spectral and stellar types of the binary dwarfs, although radio emission alone is not a good indicator of spectral type. It will be more relevant to determine the location and nature of the radio emission. The radio emission could be coming from one or both stars and even from the space between them, as has been found in the case of massive binaries (i.e. Ortiz-León et al. 2011). Highly sensitive observations of the spectral index, time variability and polarization of the radio emission could discriminate between thermal (i.e. free-free) or non thermal (i.e. gyrosynchrotron) mechanisms.

In addition, VHS 1256–1257AB hosts a wide-separation planetary-mass companion, VHS 1256–1257b, located at  $\approx 8''$  ( $\approx 170$  au) to the southwest of the ultracool binary. This companion has a spectral type  $L7.0 \pm 1.5$  (Gauza et al. 2015) and a mass of  $19 \pm 5 M_{Jup}$  (Petrus et al. 2023). VHS 1256–1257b is then at the threshold between brown dwarfs and planets and its potentially planetary mass makes it a target of recent and future studies. Indeed, VHS1256-1257b is the primary spectroscopy target for the Exoplanet Early Release Science program of the JWST (Hinkley et al. 2022).

## 3. VLA OBSERVATIONS

Ideally, the search for proper motion anomalies should be made by comparing HIPPARCOS with Gaia data. Unfortunately, VHS 1256–1257AB is not included in the much smaller HIPPARCOS catalog. We then determined the proper motions from less accurate VLA observations. These observations are relevant because this source is not detected at centimeter wavelengths with the European Very-Long-Baseline Interferometry (VLBI) Network, or in the millimeter range with the NOEMA or the Atacama Large Millimetre Array (ALMA; Climent et al. 2022). We searched in the archives of the Karl G. Jansky VLA of NRAO<sup>4</sup> for observation of VHS 1256–1257 of good quality and angular resolution, made using the same gain calibrator (in this case J1305–1033). This last criterion allows us to obtain positions that can be compared reliably among different epochs.

In Table 1 we list the three projects found, indicating the epoch of observation, the configuration of the VLA in that epoch, the frequency and bandwidth observed and the synthesized beam. In this table we also give the radio flux density and position of the unresolved binary VHS 1256–1257AB. In no epoch was VHS 1256–1257AB detected in circular polarization. Also, in no epoch was the planetary-mass companion VHS 1256–1257b detected, either in the I or V Stokes parameters. These radio data have been analyzed previously by Guirado et al. (2018) and Climent et al. (2022). Here we present a combined analysis of the observations that allows a determination of the radio proper motions of the source.

The data were calibrated in the standard manner using the CASA (Common Astronomy Software Applications; McMullin et al. 2007) package of NRAO and the pipeline provided for VLA<sup>5</sup> observations. The images were made using a robust weighting of 0 (Briggs 1995), seeking to optimize the compromise between angular resolution and sensitivity. The positions of VHS 1256–1257AB are given in Table 1 and plotted in Figure 1. These positions have been corrected for the effect of parallax (e.g., Launhardt et al. 2022). The resulting proper motions are given in Table 2.

<sup>4</sup>The National Radio Astronomy Observatory is a facility of the National Science Foundation operated under cooperative agreement by Associated Universities, Inc.

<sup>5</sup><https://science.nrao.edu/facilities/vla/data-processing/pipeline>

TABLE 1  
PARAMETERS OF THE VLA OBSERVATIONS OF VHS 1256–1257AB

Project	Epoch	VLA Configuration	Frequency (GHz)	Bandwidth (GHz)	Synthesized Beam	Peak Flux Density <sup>a</sup>	Position <sup>b</sup>	
							RA(J2000) <sup>c</sup>	DEC(J2000) <sup>d</sup>
15A-487	2015 May 15	B⇒BnA	10.0	3.9	0''53×0''28; +74°3	69.9±4.8	01 <sup>s</sup> 8478±0 <sup>s</sup> 0016	24''8723±0''0064
18A-430	2018 Apr 13	A	6.0	3.9	0''39×0''22; −24°5	69.6±2.6	01 <sup>s</sup> 7947±0 <sup>s</sup> 0003	25''4349±0''0082
18B-143	2018 Nov 17+26	C	33.1	7.8	0''72×0''46; +6°4	65.7±9.2	01 <sup>s</sup> 7824±0 <sup>s</sup> 0022	25''5549±0''0394

<sup>a</sup>In  $\mu\text{Jy}$ .

<sup>b</sup>Corrected for parallax.

<sup>c</sup>Offset from RA(J2000) = 12<sup>h</sup>56<sup>m</sup>00<sup>s</sup>.

<sup>d</sup>Offset from DEC(J2000) = −12°57'00''.

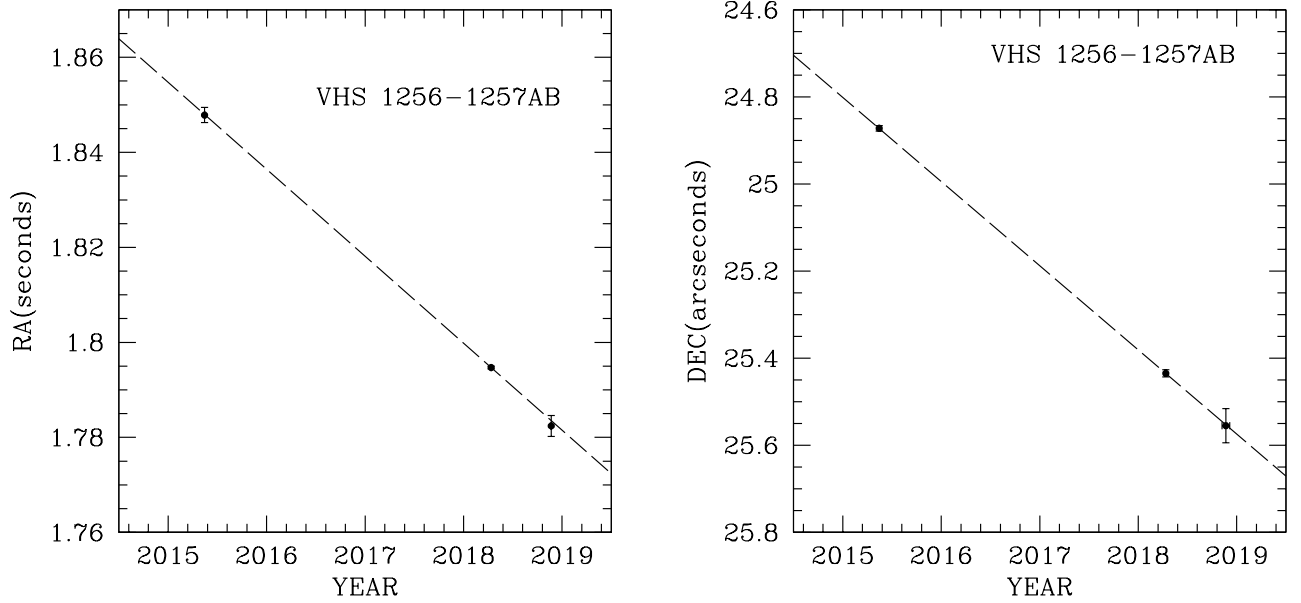


Fig. 1. Left panel: right ascension; right panel: declination of VHS 1256–1257AB as a function of time for the three epochs analyzed. The dashed lines indicate the least squares fit for each parameter. The resulting proper motions are given in Table 2. The positions are given as offsets from RA(J2000) = 12<sup>h</sup>56<sup>m</sup>00<sup>s</sup> and DEC(J2000) = −12°57'00''.

TABLE 2  
POSITION AND PROPER MOTIONS OF VHS 1256–1257AB

Telescope	Epoch Interval	Position <sup>a</sup>		Proper Motions <sup>d</sup>	
		RA(J2000) <sup>b</sup>	DEC(J2000) <sup>c</sup>	cos(DEC) $\mu_{RA}$	$\mu_{DEC}$
Red Digital Sky Survey	1956-1997	02 <sup>s</sup> 035±0 <sup>s</sup> 075	21''828±1''113	−265.0±47.2	−195.0±48.1
Gaia DR3	2014-2019	02 <sup>s</sup> 133705±0 <sup>s</sup> 000029	21''92431±0''00033	−272.46±0.57	−190.24±0.50
Very Large Array	2015-2018	02 <sup>s</sup> 1292±0 <sup>s</sup> 0100	21''900±0''058	−267.6±8.1	−193.4±3.5

<sup>a</sup>For epoch 2000.0.

<sup>b</sup>Offset from RA(J2000) = 12<sup>h</sup>56<sup>m</sup>00<sup>s</sup>.

<sup>c</sup>Offset from DEC(J2000) = −12°57'00''.

<sup>d</sup>In mas yr<sup>−1</sup>.

#### 4. COMPARISON BETWEEN VLA AND GAIA DR3 POSITIONS AND PROPER MOTIONS

In Table 2 we show the J2000 epoch positions and the proper motions of VHS 1256–1257AB from Gaia DR3 (Gaia collaboration et al. 2022) and the VLA (this paper). For completeness, we also include these parameters as determined from two images of the Red Digital Sky Survey taken on 1956 April 07

and 1997 June 02 (Minkowski & Abell 1968; Djorgovski et al. 1998). The parameters from the three observations are all consistent at the  $\approx 1\sigma$  level and we can rule out the existence of large proper motion anomalies.

Although the proper motions determined with the VLA have a good precision of  $\approx 2\text{--}3\%$ , they are not accurate enough to apply criteria similar to those



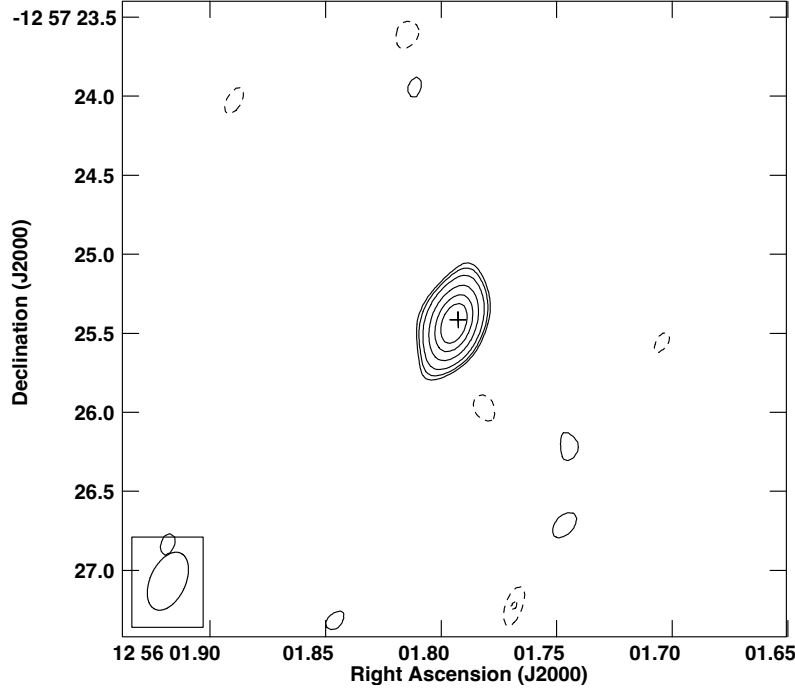


Fig. 2. Very Large Array contour image of VHS 1256–1257AB at 6.0 GHz for epoch 2018.28 corrected for parallax. Contours are -4, -3, 3, 4, 6, 10, 15 and 20 times  $2.6 \mu\text{Jy beam}^{-1}$ , the rms noise in this region of the image. The synthesized beam ( $0''.39 \times 0''.22$ ;  $-24^\circ 6'$ ) is shown in the bottom left corner of the image. The cross marks the Gaia DR3 position of VHS 1256–1257AB corrected for proper motion and parallax to epoch 2018.28.

used by Kervella et al. (2019) in their comparison of HIPPARCOS and Gaia proper motions. We then analyze in more detail the optical and radio data with the purpose of comparing the origin of both emissions.

VHS 1256–1257AB is composed of two equal-magnitude stars with spectral type  $M7.5 \pm 0.5$  (Gauza et al. 2015; Stone et al. 2016; Dupuy et al. 2023). We then expect the barycenter and the photocenter of this binary to practically coincide and this explains the lack of obvious proper motion anomalies in the optical observations. However, if the radio emission is coming preferentially from one of the stars we expect different positions and different proper motions in the optical and in the radio. The fact that the optical and radio proper motions are consistent suggests that, as in the optical, the radio emission is coming from both stars in comparable amounts.

We now compare the radio and optical positions of VHS 1256–1257AB for the epoch 2018 April 13 (=2018.28). We used this epoch because it is when the radio data have the highest angular resolution (see Table 1). The radio position is given in Table 1 and the optical Gaia DR3 position after correcting for proper motions and parallax for

the same epoch is  $RA(J2000) = 12^h 56^m 01^s.7927 \pm 00^s.0007$ ;  $DEC(J2000) = -12^\circ 57' 25''.4148 \pm 00''.0094$ . Most of the error in this position comes from the propagation of the error in the proper motions. In Figure 2 we show the contour image of the radio emission and the Gaia DR3 position for this epoch. The differences in the optical and radio positions are  $\Delta RA(\text{radio} - \text{optical}) = 0^s.0020 \pm 0^s.0008$ ;  $\Delta DEC(\text{radio} - \text{optical}) = -0''.0201 \pm 0''.0125$ .

At epoch 2018.28 the components of VHS 1256–1257AB were separated by  $\approx 0''.13$  at a position angle of  $\approx 156^\circ$ ; (Dupuy et al. 2022). If the radio emission was coming only from one of the components we expected a difference in the radio and optical declinations of one half of the separation,  $\Delta DEC(\text{radio} - \text{optical}) = \pm 0''.065$ , with the sign of the uncertainty depending on which of the two stellar components was the radio source. The small difference we found ( $\Delta DEC(\text{radio} - \text{optical}) = -0''.0201 \pm 0''.0125$ ) suggests that both stars are emitting radio waves in similar amounts, perhaps with the southern component VHS 1256–1257 B being a slightly brighter radio source. This is an interesting result because there is no *a priori* reason to expect

that stars that are similar in the optical are also similar in the radio.

We now discuss the deconvolved angular size of the 6.0 GHz source associated with VHS 1256–1257AB. In the image plane we used the CASA task IMFIT to find that the emission can be modeled with a deconvolved Gaussian ellipsoid with dimensions of  $0''.16 \pm 0''.07 \times 0''.05 \pm 0''.04$  at a position angle of  $178^\circ \pm 35^\circ$ . A direct fit to the  $(u, v)$  data with the CASA task UVMODELFIT gives a Gaussian ellipsoid with dimensions of  $0''.15 \pm 0''.02 \times 0''.05 \pm 0''.03$  at a position angle of  $178^\circ \pm 9^\circ$ . As expected, the fits are consistent, and again support the conclusion that the radio emission is coming from both stellar components of VHS 1256–1257AB. New VLA observations with very high angular resolution and sensitivity will be needed to confirm or refute that the radio emission is coming from both stars and to investigate the spectral index, variability and polarization of this radio source. Eventually, the Next Generation VLA will be the ideal instrument for the study of compact radio emission from stars, either single or multiple.

Finally, we note that there is also evidence of binarity from the RUWE (Renormalized Unit Weight Error) value for VHS 1256–1257AB in the Gaia DR3 data. The RUWE is a quality metric provided by the Gaia mission that measures the goodness of fit between the astrometric observations and the astrometric model. The RUWE is expected to be around 1.0 for sources where the single-star model provides a good fit to the astrometric observations. A value significantly larger than 1.0 could indicate that the source is non-single or otherwise problematic for the astrometric solution. For VHS 1256–1257AB we have  $\text{RUWE} = 7.3$ , consistent with the binary nature of the source.

## 5. CONCLUSIONS

1) We analyzed VLA observations of the ultra-cool dwarf binary VHS 1256–1257AB to obtain its radio proper motions and position. These parameters are consistent within the noise with the ultra-accurate values of Gaia DR3.

2) In combination with the proper motions, the position and angular size of the radio emission from VHS 1256–1257AB are consistent with both stars of the binary emitting comparable amounts of radio waves, but with the southern component VHS 1256–1257 B being somewhat more important. The radio emission alone is not a good discriminator of spectral type but future sensitive radio observations of the spectral index, time variability and polarization will help to better understand this dwarf binary.

3) Future very high angular resolution, high sensitivity observations with the VLA can be used to test these conclusions and improve our understanding of stellar radio binaries. Eventually, the Next Generation VLA will be the ideal instrument for the study of compact radio emission from stars, either single or multiple.

We are thankful to an anonymous referee for valuable comments that improved the manuscript. This work has made use of data from the European Space Agency (ESA) mission *Gaia* (<https://www.cosmos.esa.int/gaia>), processed by the *Gaia* Data Processing and Analysis Consortium (DPAC, <https://www.cosmos.esa.int/web/gaia/dpac/consortium>). Funding for the DPAC has been provided by national institutions, in particular the institutions participating in the *Gaia* Multilateral Agreement. This work also made use of the Digitized Sky Surveys that were produced at the Space Telescope Science Institute under U.S. Government grant NAG W-2166. The images of these surveys are based on photographic data obtained using the Oschin Schmidt Telescope on Palomar Mountain and the UK Schmidt Telescope. L.A.Z. acknowledges financial support from CONACyT-280775 and UNAM-PAPIIT IN110618, and IN112323 grants, México. L.L. acknowledges the support of DGAPA PAPIIT grant IN112820 and CONACyT-CF grant 263356. L.F.R. acknowledges the financial support of DGAPA (UNAM) IN105617, IN101418, IN110618 and IN112417 and CONACyT 238631 and 280775-CF grant 263356.

## REFERENCES

- Bessel, F. W. 1844, MNRAS, 6, 136, <https://doi.org/10.1093/mnras/6.11.136>
- Briggs, D. S. 1995, High Fidelity Deconvolution of Moderate Resolved Sources, Ph.D. Thesis, The New Mexico Institute of Mining and Technology
- Climent, J. B., Guirado, J. C., Zapatero Osorio, M. R., et al. 2022, A&A, 660, 65, <https://doi.org/10.1051/0004-6361/202142260>
- Djorgovski, S. G., Gal, R. R., Odewahn, S. C., et al. 1998, wfsd.conf, 14, 89, <https://doi.org/10.48550/arXiv.astro-ph/9809187>
- Dupuy, T. J., Liu, M. C., Evans, E. L., et al. 2023, MNRAS, 519, 1688, <https://doi.org/10.1093/mnras/stac3557>
- Dzib, S. A. & Rodríguez, L. F. 2021, ApJ, 923, 228, <https://doi.org/10.3847/1538-4357/ac312f>
- Gaia Collaboration, Vallenari, A., Brown, A. G. A., et al. 2022, arXiv:2208.00211, <https://doi.org/10.48550/arXiv.2208.00211>

- Gauza, B., Béjar, V. J. S., Pérez-Garrido, A., et al. 2015, *ApJ*, 804, 96, <https://doi.org/10.1088/0004-637X/804/2/96>
- Guirado, J. C., Azulay, R., Gauza, B., et al. 2018, *A&A*, 610, 23, <https://doi.org/10.1051/0004-6361/201732130>
- Hinkley, S., Carter, A. L., Ray, S., et al. 2022, *PASP*, 134, 095003, <https://doi.org/10.1088/1538-3873/ac77bd>
- Ho, W. C. G., Guillot, S., Saz Parkinson, P. M., et al. 2020, *MNRAS*, 498, 4396, <https://doi.org/10.1093/mnras/staa2653>
- Kervella, P., Arenou, F., Mignard, F., et al. 2019, *A&A*, 623, 72, <https://doi.org/10.1051/0004-6361/201834371>
- Launhardt, R., Loinard, L., Dzib, S. A., et al. 2022, *ApJ*, 931, 43, <https://doi.org/10.3847/1538-4357/ac5b09>
- McMullin, J. P., Waters, B., Schiebel, D., Young, W., & Golap, K. 2007, *Astronomical Data Analysis Software and Systems XVI ASP Conference Series*, 376, 127
- Minkowski R. L. & Abell G. O. 1968, in *Basic Astronomical Data: Stars and stellar systems*, The National Geographic Society-Palomar Observatory Sky Survey, ed. K. A. Strand (Chicago, IL: UCP), 481
- Ortiz-León, G. N., Loinard, L., Rodríguez, L. F., et al. 2011, *ApJ*, 737, 30, <https://doi.org/10.1088/0004-637X/737/1/30>
- Perryman, M. A. C., Lindegren, L., Kovalevsky, J., et al. 1997, *A&A*, 323, 49
- Petrus, S., Chauvin, G., Bonnefoy, M., et al. 2023, *A&A*, 670, 9, <https://doi.org/10.1051/0004-6361/202244494>
- Stone, J. M., Skemer, A. J., Kratter, K. M., et al. 2016, *ApJ*, 818, 12, <https://doi.org/10.3847/2041-8205/818/1/L12>
- van Leeuwen, F. 2007, *A&A*, 474, 653, <https://doi.org/10.1051/0004-6361:20078357>

Sergio A. Dzib: Max-Planck-Institut für Radioastronomie, Auf dem Hügel 69, D-53121 Bonn, Germany.  
 Laurent Loinard, Luis F. Rodríguez, & Luis A. Zapata: Instituto de Radioastronomía y Astrofísica, Universidad Nacional Autónoma de México, Apartado Postal 3-72, 58090 Morelia, Michoacán, México (l.rodriguez@irya.unam.mx).

## XookSuut: A BAYESIAN TOOL FOR MODELING CIRCULAR AND NON-CIRCULAR FLOWS ON 2D VELOCITY MAPS

C. López-Cobá<sup>1</sup>, Lihwai Lin<sup>1</sup>, and Sebastián F. Sánchez<sup>2</sup>

*Received February 7 2022; accepted September 20 2023*

### ABSTRACT

We present **XookSuut**, a Python implementation of the **DiskFit** algorithm, optimized to perform robust Bayesian inference on parameters describing models of circular and noncircular rotation in galaxies. **XookSuut** surges as a Bayesian alternative for kinematic modeling of 2D velocity maps; it implements efficient sampling methods, specifically Markov Chain Monte Carlo (MCMC) and Nested Sampling (NS), to obtain the posteriors and marginalized distributions of kinematic models including circular motions, axisymmetric radial flows, bisymmetric flows, and harmonic decomposition of the LoS velocity. In this way, kinematic models are obtained by pure sampling methods, rather than standard minimization techniques based on the  $\chi^2$ . All together, **XookSuut** represents a sophisticated tool for deriving rotational curves and to explore the error distribution and covariance between parameters.

### RESUMEN

Presentamos **XookSuut**, una implementación en Python del algoritmo **DiskFit**, optimizado para realizar inferencia Bayesiana robusta sobre parámetros que describen modelos cinemáticos de rotación circular y no circular en galaxias. **XookSuut** es una alternativa Bayesiana para el modelado cinemático de mapas dos dimensionales; el código implementa métodos de muestreo eficientes, específicamente Markov Chain Monte Carlo y Nested Sampling, para obtener las distribuciones posteriores de modelos cinemáticos entre ellos: movimientos circulares, flujos axisimétricos, flujos bisimétricos y una descomposición en armónicos del campo de velocidad. Así, los modelos cinemáticos son derivados por métodos de muestreo en vez de adoptar técnicas de minimización basadas en la  $\chi^2$ . **XookSuut** es ideal para derivar curvas de rotación y explorar la distribución de errores y covarianza entre parámetros.

*Key Words:* galaxies: kinematics and dynamics — software: data analysis

### 1. INTRODUCTION

The rotation pattern observed on two-dimensional velocity maps is the result of the gravitational potential and the mass distribution in a galaxy, together with environmental factors and projection effects (e.g., Rubin & Ford 1970; Binney 2008). In disk-like systems the rotation, or azimuthal velocity, is the dominant velocity component. When this velocity is plotted against the

galactocentric distance it describes the rotational curve of a galaxy (e.g. Rubin & Ford 1970; Rubin et al. 1980).

Since early studies of the neutral hydrogen distribution in nearby galaxies, it was possible to obtain resolved velocity fields (e.g., Warner et al. 1973); these HI velocity maps showed ordered kinematic patterns that, in most cases, could be described by pure circular rotation (e.g., Wright 1971; Begeman 1989; de Blok et al. 2008). Since then, many efforts have been done for recovering rotation curves of galaxies, not only with HI data, but also with molecular and ionized gas observations. Begeman (1987, 1989) introduced a methodology to extract the rota-

<sup>1</sup>Institute of Astronomy & Astrophysics, Academia Sinica, 106, Taipei, Taiwan.

<sup>2</sup>Instituto de Astronomía, Universidad Nacional Autónoma de México  
 Circuito Exterior, Ciudad Universitaria, Ciudad de México 04510, Mexico.

tional velocity curve from two-dimensional (2D) velocity maps based on the so-called tilted rings. This idea became the core of most of the algorithms focused on the determination of the rotation curves of galaxies, for instance the GIPSY task ROTCUR (e.g., Begeman 1987). The tilted ring model assumes that the observed velocity field can be described by pure circular motions with possible variations in the projection angles. From it, several algorithms have been developed to study the kinematic structures of galaxies. On one side are those who use 3D data-cubes, for instance 3DBarolo (e.g., Di Teodoro & Fraternali 2015), TiRiFiC (e.g., Józsa et al. 2007), GalPak<sup>3D</sup> (e.g., Bouché et al. 2015), KinMSpy (Davis et al. 2013). In a second category are those which work on velocity fields, such as RESWRI (e.g., Schoenmakers 1999), DiskFit (e.g., Sellwood & Spekkens 2015), 2DBAT (e.g., Oh et al. 2018), and KINEMETRY (e.g., Krajnović et al. 2006) among others.

3D algorithms have the advantages of extracting all the information from the datacubes. These methods model the entire datacube, which allows them to correct for beam smearing effects and also to handle projection effects. However, the inclusion of datacubes usually involves the addition of extra parameters during the fitting process, which in most cases involves longer computing times depending on the dimensions of the datacube and the fitting routine. On the other hand, 2D algorithms work on the projected line of sight velocity (LOS<sub>V</sub>); for this reason they tend to be faster than 3D methods. If galaxies are not severely affected by spatial resolution effects, (i.e., the observational point spread function, PSF), both methods show consistent results for rotational velocities (e.g., Kamphuis et al. 2015).

Nevertheless, non-circular motions driven by structural components of galaxies (such as spiral arms, bars, bulge), or by angular momentum loss, are not included within the circular rotation assumption (e.g., Kormendy 1983; Lacey & Fall 1985; Wong et al. 2004); nor are those motions induced by internal processes (stellar winds, H II regions, shocks, outflows). Altogether, and taking into account projection effects, the modeling of non-circular motions is a big challenge. Only a few algorithms take into account deviations of circular motions, among which are: TiRiFiC, ideal for modeling warped disks; DiskFit, suitable to model bar-like and radial flows; and KINEMETRY to model non-circular motions of any order through harmonic decomposition.

For deriving rotational curves, most algorithms adopt frequentist methods that minimize the residuals from a model function and the data, and those pa-

rameters that minimize the residuals are chosen for creating the kinematic model that better describes the data. This means that from a frequentist perspective, there is a single set of true parameters that describes the data. Conversely, Bayesian methods assume that model parameters are totally random variables, and each parameter has associated a probability density function. In this way solutions are based on the likelihood of a parameter given the data; that is, on the posterior distribution of the parameters.

These are two different perspectives to estimate the parameters from a model. Rotational curves are often described by several parameters, which makes it a high-dimensional problem, and therefore susceptible to find local solutions. Therefore, it is worth exploring methods that survey the parameter space of kinematic models to derive the best representation of the observed rotation patterns of disk galaxies.

In this paper we introduce **XookSuut**<sup>3</sup> (or **XS** for short). This is a Python tool that implements Bayesian methods for modeling circular and non-circular motions on 2D velocity maps. The name of this tool is a combination of two Mayan words: **Xook** which means “study” and **Suut** which means “rotation”.

This paper is organized as follows. In § 2 we describe the different kinematic models included in **XookSuut**. In § 3 we describe the algorithm, the fitting procedure, and the error estimations. In § 4 we show the performance of this code when it is applied on simulated velocity fields of galaxies with oval distortions, as well as on real velocity maps. In § 5 we discuss our results. Finally, in § 6 we present our conclusions.

## 2. KINEMATIC MODELS

In this section we describe the kinematic models included in **XookSuut**. We start with the simplest model, which is the circular rotation model, then we add a radial term for modeling radial flows. A bisymmetric model is included for describing oval distortions (i.e., bar-driven flows); finally, **XookSuut** includes a more general harmonic decomposition of the line of sight velocity, for a total of three non-circular rotation models. For constructing these models, **XookSuut** assumes that galaxies are flat and circular systems and that they are viewed in projection, with a constant position angle ( $\phi'_{\text{disk}}$ )<sup>4</sup>, fixed inclina-

<sup>3</sup><https://github.com/CarlosCoba/XookSuut-code>

<sup>4</sup>Angles measured in the sky plane are marked with a prime symbol ('), otherwise they are measured in the galaxy plane. The disk position angle is measured from the north to east for the receding side of the galaxy.



tion ( $i$ ), fixed kinematic center ( $x_0, y_0$ ) and constant systemic velocity throughout the disk. The flat disk approximation represents the more suitable assumption whenever the spatial resolution of the data, i.e., the point spread function, dominates over the typical thickness of disks. With these assumptions, galaxies with strong warped disks are excluded. In addition, systems where the inclination or position angle varies as a function of the galactocentric distance are also excluded, since radial variations in these angles induce artificial non-circular motions when observed in projection, and such contributions to the line-of-sight velocities would be difficult to discern from true non-circular motions (e.g., Schoenmakers et al. 1997).

**XookSuut** adopts the methodology introduced by **DiskFit** (e.g., Sellwood & Spekkens 2015) for creating a two dimensional interpolated map of the referred kinematic models and described in the following sections.

### 2.1. Circular Model

The simplest model included in **XookSuut** is the circular rotation model, which is the most frequently adopted for describing the rotation of galaxies. It assumes no other movements than pure circular motions in the plane of the disk and describes the rotation curve of disk galaxies.

Assuming that particles follow circular orbits on the disk, the circular model is given by the projection of the velocity vector  $\vec{V}$  along the line-of-sight direction:

$$V_{\text{circ,model}} = V_{\text{sys}} + V_t(r) \sin i \cos \theta . \quad (1)$$

$V_t$  is the circular rotation or azimuthal velocity and is a function of the galactocentric distance;  $V_{\text{sys}}$  is the systemic velocity and is assumed constant for all points in the galaxy. In this equation and in the following,  $r$  is the radius of a circle in the disk plane, which projects into an ellipse in the sky plane. The angle  $\theta$  is the azimuthal angle relative to the disk major axis, and  $i$  is the disk inclination angle.

### 2.2. Radial Model

When radial motions are not negligible, the disk circular velocity is described by two components of the velocity vector: the tangential velocity ( $V_t$ ) and the radial one ( $V_r$ ). In this way, the model including radial velocities is described by the following expression:

$$V_{\text{rad,model}} = V_{\text{sys}} + \sin i (V_t(r) \cos \theta + V_r(r) \sin \theta). \quad (2)$$

Comparing with equation 1, the only difference is the addition of the  $V_r \sin \theta$  term. This term accounts for axisymmetric radial flows (inflow or outflow) on the disk plane.

### 2.3. Bisymmetric Model

The bisymmetric model describes an oval distortion on the velocity field, such as that produced by stellar bars (e.g., Spekkens & Sellwood 2007; Sellwood & Spekkens 2015), or by a triaxial halo potential. In the presence of an oval distortion particles follow elliptical orbits elongated towards an angle that in general differs from that of the disk position angle (e.g., Spekkens & Sellwood 2007). This kinematic distortion shows a characteristic “S” shape in the projected velocity field that makes the minor and major axes not orthogonal (e.g., Kormendy 1983). Given that this pattern has been mostly observed in the velocity field of barred galaxies, we will refer to the origin of the oval distortion to stellar bars, although it is not necessarily the case, as mentioned before. The model that intends to describe this pattern is called bisymmetric model (e.g., Spekkens & Sellwood 2007) since most of the perturbation is kept in the second order of an harmonic decomposition on the disk plane. The bisymmetric model is described by following the expression:

$$V_{\text{bis,model}} = V_{\text{sys}} + \sin i \left( V_t(r) \cos \theta - V_{2,t}(r) \cos 2\theta_{\text{bar}} \cos \theta - V_{2,r}(r) \sin 2\theta_{\text{bar}} \sin \theta \right) . \quad (3)$$

$V_{2,t}$  and  $V_{2,r}$  are the nonaxisymmetric velocities induced by the oval distortion and represent, respectively, the tangential and radial deviations from  $V_t$ , where the latter describes the disk circular rotation. The angular variable  $\theta_{\text{bar}}$  is the location relative to the position angle of the bar ( $\phi_{\text{bar}}$ ), in this way<sup>5</sup>:

$$\theta_{\text{bar}} = \theta - \phi_{\text{bar}} . \quad (4)$$

Note that in this expression both angles are measured on the disk plane. If  $\phi_{\text{bar}}$  represents the major (minor)-axis position angle of a bar, then both  $V_{2,t}(r)$  and  $V_{2,r}(r)$  have positive (negative) values. Unlike the disk position angle  $\phi'_{\text{disk}}$ ,  $\phi_{\text{bar}}$  is not a

<sup>5</sup>Note that the problem becomes degenerate when the bar position angle is aligned to the galaxy major axis. When  $\phi_{\text{bar}} = 0^\circ$ , the terms  $\cos 2(\theta - \phi_{\text{bar}}) \cos \theta$  and  $\sin 2(\theta - \phi_{\text{bar}}) \sin \theta$  can be expressed as  $\frac{1}{2}(\cos \theta + \cos 3\theta)$  and  $\frac{1}{2}(\cos \theta - \cos 3\theta)$ , respectively. A similar relation occurs when the bar is oriented along the minor axis,  $\phi_{\text{bar}} = 90^\circ$ .

variable than can be easily recognized from the velocity field of barred galaxies; however, its projection on the sky plane is related to  $\phi'_{\text{disk}}$  and the disk inclination angle, as follows:

$$\phi'_{\text{bar}} = \phi'_{\text{disk}} + \arctan(\tan \phi_{\text{bar}} \cos i), \quad (5)$$

where  $\phi'_{\text{bar}}$  is the position angle of the bar on the sky plane. Computationally, it is more practical to estimate  $\phi_{\text{bar}}$  instead of  $\phi'_{\text{bar}}$ . When the oval distortion is produced by a stellar bar,  $\phi'_{\text{bar}}$  is expected to be aligned with the photometric position angle of the bar, while the radial profile of  $V_{2r}(r)$  and  $V_{2t}(r)$  should extend to the length of the bar.

#### 2.4. Harmonic Decomposition

Similar to the photometric decomposition of galaxy images into light profiles via Fourier expansions, the line of sight (LoS) velocity field of a galaxy can be expressed as a sum of harmonic terms as follows:

$$V_{\text{hrm,model}} = V_{\text{sys}} + \sum_{m=1}^M (c_m(r) \cos m\theta + s_m(r) \sin m\theta) \sin i, \quad (6)$$

where  $c_m$  and  $s_m$  are the harmonic velocities,  $m$  is the harmonic number, and  $\theta$  and  $r$  have the same meaning as before. For convenience we have taken the inclination angle out of the Fourier expansion; also note that the 0<sup>th</sup> order of the expansion  $c_0(r)$  is assumed a constant equal to the systemic velocity. However, in addition to the expansion up to  $M = 1$ , where we recover the radial model, note that  $c_1 \approx V_t$  and  $s_1 \approx V_r$ ; the expansion to higher orders does not offer a direct interpretation of  $c_m$  and  $s_m$  since these terms represent a mere decomposition of the LoS velocities, although it is possible to assign to these velocities a physical meaning. The harmonic number is closely related to perturbations of the gravitational potential; under the epicycle theory, such perturbations will induce the appearance of harmonic sectors in the LoS velocities in such a way that if the gravitational potential contains a perturbation of order  $m$ , the LoS velocities contain the  $m + 1$  and  $m - 1$  harmonic terms of the Fourier expansion (see Schoenmakers et al. 1997, for a detailed description). For instance, a bar-potential can be described by a 2<sup>nd</sup> order perturbation, which means that the LoS velocity field will contain the 1<sup>st</sup> and 3<sup>rd</sup> harmonic terms of equation 6 (e.g., Wong et al. 2004; Fathi et al. 2005). Similarly, this analysis can be extended for the case of spiral arms (e.g., van de Ven & Fathi 2010).

In **XookSuut** the harmonic model, (equation 6), can be expanded to any harmonic order, although, most of the non-circular motions induced by spiral arms or bars are captured by a third order expansion (e.g., Trachternach et al. 2008).

The harmonic model was first included in the GIPSY task **RESWRI** (e.g., Schoenmakers 1999) under the assumption of a thin disk. Afterwards the harmonic decomposition was generalized in **KINEMETRY** (e.g., Krajnović et al. 2006) including not only disks but also triaxial structures. The major difference between **RESWRI** and **XookSuut** is the assumption of a flat disk. While **RESWRI** and **KINEMETRY** allow varying the disk position angle and inclination during the fitting analysis, **XookSuut** keeps these angles fixed to allow the residual velocities of a circular model to be adjusted with non-circular motions and not absorbed by the variations of these angles, as explained before. However, when large variations of  $\phi'_{\text{disk}}$  or  $i$  are present throughout the disk, **XookSuut** will fail in the interpretation of the harmonic velocities, even when the fit is successful.

### 3. THE ALGORITHM

**XookSuut** works on 2D velocity maps, such as those extracted from first moment maps from data-cubes. As others codes that rely on 2D maps for kinematic modelling, **XookSuut** assumes that the velocity recorded in each pixel is representative of the disk velocity. In this sense, there are a wide variety of methods for representing the velocity field of a galaxy, and many of these depend on the spectral resolution and the signal-to-noise of the data; going from simple first moment maps, to modeling Gaussian profiles in combination with Hermite polynomials to better reproduce the shape of the emission lines (see de Blok et al. 2008; Sellwood et al. 2021, for a revision of different methods).

For **XookSuut** to obtain confident estimations of the kinematic models, the data should not be strongly affected by the point-spread-function. The PSF contributes to increase the velocity dispersion of the emission-lines and consequently to underestimate the rotation velocities, particularly in the inner gradient of the rotation curve. In such a case, a 3D modeling of the data-cubes should be a better approach (e.g., Di Teodoro et al. 2016). Under the previous assumptions the algorithm proceeds in the following way.

Let  $(x_n, y_n)$  be the position of a data point in the sky plane. The corresponding ellipse passing through this point, with center  $(x_0, y_0)$  and rotated

by an angle  $\phi'_{\text{disk}}$  is described by:

$$x_e = -(-x_n - x_0) \sin \phi'_{\text{disk}} + (y_n - y_0) \cos \phi'_{\text{disk}}, \quad (7)$$

$$y_e = -(x_n - x_0) \cos \phi'_{\text{disk}} - (y_n - y_0) \sin \phi'_{\text{disk}}. \quad (8)$$

The radius of the circle on the disk plane passing through this point is then:

$$r_n^2 = x_e^2 + \left( \frac{y_e}{\cos i} \right)^2. \quad (9)$$

The azimuthal angle on the disk plane  $\theta$ , is related to the sky coordinates as follows:

$$\cos \theta = \frac{-(-x_n - x_0) \sin \phi'_{\text{disk}} + (y_n - y_0) \cos \phi'_{\text{disk}}}{r_n}, \quad (10)$$

$$\sin \theta = \frac{-(x_n - x_0) \cos \phi'_{\text{disk}} - (y_n - y_0) \sin \phi'_{\text{disk}}}{r_n \cos i}. \quad (11)$$

Therefore,  $\theta$  comprises both projection angles  $\phi'_{\text{disk}}$  and  $i$ , as well as the kinematic center, thus contributing with four more free variables in each kinematic model (although it is represented by a single variable for simplicity). Henceforth, we define “constant parameters” as those variables that do not change with radius; they are:  $\langle \phi'_{\text{disk}}, i, x_0, y_0, V_{\text{sys}}, \phi_{\text{bar}} \rangle$ . We will also refer as “geometric parameters” to those variables that describe the orientation of the projected ellipse on the sky plane, namely  $\phi'_{\text{disk}}, i, x_0, y_0$ .

### 3.1. $\chi^2$ Minimization Technique

As we will see in further sections, Bayesian methods like MCMC require to start sampling around the *maximum a posteriori*, or maximum likelihood, to generate new samples also known as chains; this requires necessarily to find those parameters that minimize the residuals from a given kinematic model and the data. Therefore, in the following we describe the method to solve for each of the different kinematic components of the models, and the constant parameters. The first part corresponds to the analysis adopted in *DiskFit* (e.g., Spekkens & Sellwood 2007; Sellwood & Spekkens 2015), with minimum changes.

A given set of initial conditions for the geometric parameters defines the projected disk with an elliptical shape on the sky plane. Ideally, the initial conditions for the gaseous disk geometry should be close to that of the stellar disk. This geometry will be the starting configuration for the minimization analysis; then, the field of view is divided into  $K$  concentric rings of fixed width that follow the same

orientation as before. The maximum length of the ellipse semi-major axis can be easily set-up as described in Appendix A; this will create a 2D mask and only those pixels inside this maximum ellipse will be considered for the analysis. The geometry of this mask will be adapted in subsequent iterations until reaching the orientation that better describes the observed velocity field.

The algorithm will solve for each ring a set of velocities that will depend on the kinematic model considered, namely equations 1–3 or equation 6. Thus, the number of different velocity components to derive will be  $K$  velocities in the circular model ( $V_{t,K}$ );  $2K$  in the radial model ( $V_{t,K}, V_{r,K}$ );  $3K$  in the bisymmetric model ( $V_{t,K}, V_{2r,K}, V_{2t,K}$ ) and  $2MK$  in the harmonic model ( $c_{1,K}, \dots, c_{M,K}, s_{1,K}, \dots, s_{M,K}$ ).

The velocity map consists of a two-dimensional image of size  $n_x \times n_y$ , with  $N$  observed data points  $\mathcal{D}_n$  with individual errors  $\sigma_n$ . Let  $\vec{V}$  be the set of velocities that describe the corresponding kinematic model (namely,  $\vec{V} = \langle \vec{V}_t, \vec{V}_{2,t}, \vec{V}_{2,r} \rangle$  for the bisymmetric model and similarly for other models). Frequentist methods adopt the chi-square  $\chi^2$ , to derive from a model the set of parameters that describes the data. In this case, the reduced  $\chi_r^2$  for the different kinematic models is given by:

$$\chi_r^2 = \frac{1}{\nu} \sum_{n=1}^N \left( \frac{\mathcal{D}_n - \sum_{k=1}^K W_{k,n} \vec{V}_k}{\sigma_n} \right)^2. \quad (12)$$

Here  $\nu$  is the total number of degrees of freedom (i.e.,  $\nu = N - N_{\text{vars}}$ , and  $N_{\text{vars}}$  is the number of parameters to estimate from the model);  $W_{k,n}$  are a set of weights that depend on the pixel position, and will serve to define an interpolated model; and  $\vec{V}_k$  is the set of velocities in the  $k$ -th ring that describes the considered kinematic model.

Each kinematic component from  $\vec{V}_k$  would require different weights. For instance, for the circular model the weights adopt the following expression:

$$W_{k,n}^t = \sin i \cos \theta * w_{k,n}, \quad (13)$$

where the super-index  $t$  makes reference to the circular rotation component. The radial model requires two different weights for the different kinematic components:

$$W_{k,n}^t = \sin i \cos \theta * w_{k,n}, \quad (14)$$

$$W_{k,n}^r = \sin i \sin \theta * w_{k,n}. \quad (15)$$

Similarly, the bisymmetric model would require three different weights:

$$W_{k,n}^t = \sin i \cos \theta * w_{k,n}, \quad (16)$$

$$W_{k,n}^{2r} = \sin i \cos \theta \cos 2\theta_{\text{bar}} * w_{k,n}, \quad (17)$$

$$W_{k,n}^{2t} = \sin i \sin \theta \sin 2\theta_{\text{bar}} * w_{k,n}. \quad (18)$$

Finally, the harmonic decomposition model will have  $2M$  weights given by:

$$W_{k,n}^c = \sum_{m=1}^M \sin i \cos m\theta * w_{k,n}, \quad (19)$$

$$W_{k,n}^s = \sum_{m=1}^M \sin i \sin m\theta * w_{k,n}. \quad (20)$$

Note that for  $M = 1$  it reduces to the radial model.

The  $w_{k,n}$  terms define the interpolation method to be performed between the  $K$ -rings. As in **DiskFit**, these weights adopt the form of a simple linear interpolation given by the usual expression:

$$w_{k,n} = \left( \frac{r_{k+1} - r_n}{\delta r_k} \right), \quad (21)$$

$$w_{k+1,n} = \left( \frac{r_n - r_k}{\delta r_k} \right), \quad (22)$$

where  $r_k$  and  $r_{k+1}$  are the position of the  $k^{\text{th}}$  and  $(k+1)^{\text{th}}$  rings respectively, and  $\delta r_k = r_{k+1} - r_k$  is the spacing between rings. As the first ring ( $k = 1$ ) cannot be placed at the kinematic centre, **XookSuut** implements different strategies for assigning velocities to pixels down the first ring. Depending on the spatial resolution of the data or the signal-to-noise ratio (S/N), one may opt for one of the following extrapolation options.

The first method is to assume that velocities grow linearly from zero to the velocities derived in the first ring ( $\vec{V}_1$ ). This implies that  $\vec{V}_0 = 0$  at  $r = 0$ ; therefore, the kinematic center does not rotate. In the second approach, the set of velocities and positions ( $\vec{V}_1, r_1$ ) and ( $\vec{V}_2, r_2$ ) are used to extrapolate velocities to pixels down  $r_1$ ; in this way  $\vec{V}_0 \neq 0$  at  $r = 0$ . The third option allows the user to fix the velocity at the origin to some value. Then  $\vec{V}_0$  and  $\vec{V}_1$  are linearly interpolated for sampling pixels down  $r_1$ .

As  $\vec{V}_k$  is linear in equations 1–3 and equation 6, we can set the derivative with respect to  $\vec{V}_j$  in equation 12, giving as result:

$$\frac{\partial \chi_r^2}{\partial \vec{V}_j} = \frac{2}{\nu} \sum_{n=1}^N \left( \frac{\mathcal{D}_n - \sum_{k=1}^K W_{k,n} \vec{V}_k}{\sigma_n} \right) \frac{W_{j,n}}{\sigma_n} = 0. \quad (23)$$

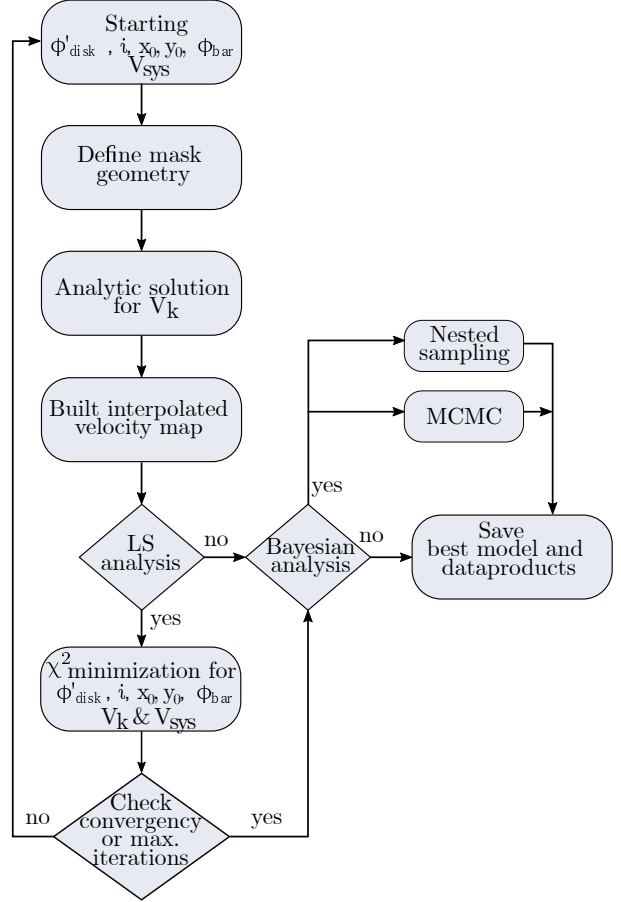


Fig. 1. Flowchart of the fitting procedure to derive the best kinematic model.

Rearranging this expression we obtain:

$$\sum_{k=1}^K \left( \sum_{n=1}^N \frac{W_{k,n}}{\sigma_n} \frac{W_{j,n}}{\sigma_n} \right) \vec{V}_k = \sum_{n=1}^N \frac{W_{j,n}}{\sigma_n^2} \mathcal{D}_n. \quad (24)$$

The minimization technique from equation 24 was first introduced by Barnes & Sellwood (2003), and subsequently incorporated into **DiskFit** (Sellwood & Spekkens 2015). Here, equation 24 is generalized for the harmonic decomposition model. The latter expression is a system of linear equations for the  $\vec{V}_k$  unknowns; thus  $\vec{V}_k$  values are solved arithmetically. As mentioned before, the number of velocity components  $\vec{V}_k$  depends on the number of rings and the adopted kinematic model; therefore the dimensions of the matrix to solve will increase as more rings are included in the analysis, and as the kinematic model becomes more complex.

Given a set values for the constant parameters and  $K$  rings positioned at  $r_k$  on the disk plane, we can solve for  $\vec{V}_k$  in equation 24 by assigning uni-

form weighting factors ( $w_{k,n} = 1$ ). This way we are obtaining a row-stacked velocities ( $r_k$  vs.  $V_k$ ). In essence the row-stacked velocities represent the average velocity of each ring; then, we use these velocities as initial conditions to perform an iteratively least squares analysis (LS) through equation 12, but now with the proper weighting factors (namely equations 13–19). Note that if the initial geometric parameters passed to the algorithm are close the true ones, then the arithmetic solutions to  $\vec{V}_k$  should be close the true velocities. This can speedup the MCMC sampling as we will see in further sections.

The minimization procedure in equation 12 is performed by constructing a 2D model from the interpolation weights of equation 21. In each  $\chi^2$  iteration a new set of velocities  $\vec{V}'_k$  are obtained, together with a new set of constant parameters. The latter will define a new geometry for the mask, and new row-stacked velocities will be obtained for the next iteration. Multiple rounds of  $\chi^2$  minimization will be performed up to some maximum iteration defined by the user, or until the difference in  $\chi^2$  evaluations varies less than 10%. Commonly after three iterations the disk geometry becomes stable and simultaneously  $\vec{V}_K$ . Figure 1 summarizes all the fitting procedure in a flowchart.

Rings not properly sampled with data may give absurd values of  $\vec{V}_k$  when solving equation 24. To avoid this problem, we define a covering factor to guarantee a minimum number of data per ring. If the covering factor is 1, it means that rings must be 100% occupied by data to estimate  $\vec{V}_k$ , as described in Appendix A. In addition, isolated pixels in the image due to low S/N may not be desired during the analysis; **XookSuut** allows to remove these pixels by excluding those with velocity errors greater than a certain threshold defined by the user.

To perform the LS analysis in equation 12, **XookSuut** adopts the Levenberg–Marquardt (LM) algorithm included in the **lmfit** package (e.g., Newville et al. 2014). This algorithm has the advantage that it is fast, although it is widely known to be susceptible to getting trapped at a local minimum. Note that **DiskFit** adopts the Powell method since this method only performs evaluation of functions with no derivatives performed.

So far the algorithm adopts an LS method for deriving the best parameters defined by the kinematic models. In the following we use sampling methods to infer the posterior distributions of the parameters.

### 3.2. Bayesian Analysis

The novelty of **XookSuut** resides in the estimation of the posterior distribution of the non-circular motions and the model parameters. Given the high-dimension of the models, it is desired to perform a thorough analysis of the prior space to obtain the most likely solutions to the problem for each kinematic model regardless of its complexity. For this purpose we adopt Bayesian inference methods for sampling their posterior distributions. Other packages like 2DBAT and KINMSPY (i.e., Oh et al. 2018; Davis et al. 2013) also use Bayesian approaches for extracting rotational curves of galaxies. The difference is that KINMSPY is able to fit non-circular motions (radial and bisymmetric).

According to Bayes' theorem, given a set of data  $\mathcal{D}$  described by a model function  $\mathcal{M}$  with parameters  $\vec{\alpha} = \alpha_1, \alpha_2, \dots, \alpha_n$ , the posterior distribution of  $\vec{\alpha}$  given  $\mathcal{D}$  follows the expression:

$$p(\vec{\alpha}|\mathcal{D}, \mathcal{M}) = \frac{p(\mathcal{D}|\vec{\alpha}, \mathcal{M})p(\vec{\alpha})}{p(\mathcal{D}, \mathcal{M})}, \quad (25)$$

where  $p(\vec{\alpha}|\mathcal{D}, \mathcal{M})$  is the joint posterior distribution of the whole set of parameters;  $p(\mathcal{D}|\vec{\alpha}, \mathcal{M})$  is the probability density of the data given the parameters and the assumed model;  $p(\vec{\alpha})$  is the prior probability distribution of the parameters and  $p(\mathcal{D}, \mathcal{M})$  is a normalization constant also known as *marginal evidence* or *evidence*. It is common to find equation 25 expressed in terms of the likelihood function  $\mathcal{L}$ , as follows:

$$p(\vec{\alpha}|\mathcal{D}, \mathcal{M}) = \frac{\mathcal{L}(\vec{\alpha})p(\vec{\alpha})}{\mathcal{Z}}, \quad (26)$$

with the evidence defined as:

$$\mathcal{Z} = \int_{\Omega_{\alpha}} \mathcal{L}(\vec{\alpha})p(\vec{\alpha})d\vec{\alpha}, \quad (27)$$

where the integral is computed over all the parameter space defined by the priors,  $\Omega_{\alpha}$ . The evidence can be interpreted as the likelihood of the observed data under the model assumptions; in other words, it is the average of the likelihood over the priors.

The final goal of Bayesian inference is to obtain the posterior distribution  $p(\vec{\alpha}|\mathcal{D}, \mathcal{M})$  of all parameters  $\vec{\alpha}$  describing the model function  $\mathcal{M}$ . Multiple methods have been developed for this purpose. For instance, Markov-Chain Monte Carlo (MCMC) methods evaluate the unnormalized posterior distribution (i.e.,  $p(\vec{\alpha}|\mathcal{D}, \mathcal{M}) \propto \mathcal{L}(\vec{\alpha})p(\vec{\alpha})$ ), by generating samples or chains from the likelihood function. One of the main characteristics of Markov chains is that the position of a point in the chain depends only

on the position of the previous step. Different algorithms with automating chain tuning have been developed to efficiently sample the posterior distribution. Among the most popular MCMC samplers are those who implement *affine-invariant ensemble sampling* and *ensemble slice sampling* (e.g., Foreman-Mackey et al. 2013; Karamanis et al. 2021).

Other methods, such as nested sampling (NS, Skilling 2006), are designed to compute the evidence by numerical integration of equation 27, which often makes them computationally more expensive than MCMC methods. This integral is performed from the priors space (or prior volume), and unlike MCMC, does not require an initialization point. Nevertheless, computing the evidence is crucial for model comparison as it represents the degree to which the data are in agreement with the model. Although the main goal of NS is to compute the evidence, the posterior distribution is obtained as a by-product; because of that, NS methods are becoming popular for the inference of parameters in astronomy (see Ashton et al. 2022, for a thorough description of the method).

One of the advantages of nested sampling with respect to MCMC methods is regarding the convergence criteria. There is no defined convergence criteria among MCMC algorithms, although some of them are based on the number of independent samples in the chains, the so-called *integrated autocorrelation time (IAT)*; however this is often evaluated a posteriori. If the whole chain contains between 10-50 times the IAT, then it is a good indicator that chains are converging (Foreman-Mackey et al. 2013; Karamanis et al. 2021). In contrast, in nested sampling the stopping evaluation criterion is well defined, since sampling stops after the whole prior space has been integrated.

A detailed discussion of these two sampling methods is, however, beyond the scope of this paper. Following we show the implementation of MCMC and nested sampling methods for the parameter extraction of the kinematic models presented in Sec. 2.

### 3.2.1. Likelihood and Priors

Let  $\vec{\alpha}$  be all the parameters that describe any of the kinematic models. Then, the log posterior distribution of the parameters is given by:

$$\ln p(\vec{\alpha}|\mathcal{D}, \mathcal{M}) = \ln \mathcal{L}(\vec{\alpha}) + \ln p(\vec{\alpha}) - \ln \mathcal{Z}. \quad (28)$$

The likelihood function is a key term in Bayesian inference, since it will define the shape of the posterior distributions. The most common distribution

for the likelihood is Gaussian, but other distributions like Cauchy, T-student, or the absolute value of the residuals are also adopted in the literature (e.g., Di Teodoro & Fraternali 2015; Bouché et al. 2015; Oh et al. 2018). **XookSuut** adopts the Gaussian distribution as the main likelihood function, although the Cauchy distribution is also included (see Appendix B). The individual likelihood for each data point  $\mathcal{D}_n$  with error  $\sigma_n$  is expressed as:

$$\mathcal{L}(\alpha_n) = (2\pi\sigma_n)^{-1/2} \exp\left(-\frac{(\mathcal{D}_n - \mathcal{M}_n)^2}{2\sigma_n^2}\right), \quad (29)$$

and the joint likelihood for the data set is the product of individual likelihoods, in this way

$$\mathcal{L} = (2\pi)^{-N/2} \left(\prod_{n=1}^N \sigma_n\right) \exp\left(-\sum_{n=1}^N \frac{(\mathcal{D}_n - \mathcal{M}_n)^2}{2\sigma_n^2}\right). \quad (30)$$

It is easy to recognize from this expression that the summation is the  $\chi^2$  from Eq 12, with  $\mathcal{M}_n$  being the kinematic model function,  $\mathcal{V}_{\text{model}}$ . In this way the log posterior distribution of the parameters is expressed as:

$$\begin{aligned} \ln p(\vec{\alpha}|\mathcal{D}, \mathcal{V}_{\text{model}}) = & -\frac{1}{2} \sum_{n=1}^N \frac{(\mathcal{D}_n - \sum_{k=1}^K W_{k,n} \vec{V}_k)^2}{\sigma_n^2} \\ & - \ln \sigma_n - \frac{N}{2} \ln(2\pi) + \ln p(\alpha) - \ln \mathcal{Z}, \quad (31) \end{aligned}$$

with  $N$  being the number of data points, or pixels, to be considered in the model. We can redefine  $\sigma$  to include the intrinsic dispersion of the data, which we assume constant for all pixels; namely,  $\sigma_n^2 = \sigma_n^2 + \sigma_{\text{int}}^2$ .

The priors are the constrain of our model function and enclose all we know about the data. Uniform or non-informative priors give the same probability to any point within the considered boundaries. This allows the likelihood function to survey the prior space without any preferred direction. **XookSuut** adopts either uniform or truncated Gaussians (TG), with values shown in Table 1. TG priors are of the form  $\text{TG}(\mu, \sigma, \mu_{\min}, \mu_{\max})$ , with  $\mu$  and  $\sigma$  being the mean and standard deviation of the Gaussian, and  $\mu_{\min}$  and  $\mu_{\max}$  represent the lower and upper boundaries, respectively. The mean values can be chosen arbitrary, although good values are those that maximize the likelihood function (i.e., equation 12). In most cases, choosing uniform or TG priors does not affect the posterior distributions. The difference resides in the computational cost needed to explore the prior space; narrow distributions like

TABLE 1  
TYPE OF PRIORS ADOPTED IN XookSuut

Parameter	Uniform prior	Truncated Gaussians <sup>a</sup>
$\phi_{\text{disk}}$	0 if $-2\pi < \phi_{\text{disk}} < 2\pi$	TG( $\hat{\phi}_{\text{disk}}, 15^\circ, \mp 45$ )
$i$	0 if $30 < i < 75$	TG( $\hat{i}, 10^\circ, 30, 75$ )
$\phi_{\text{bar}}$	0 if $-\pi < \phi_{\text{bar}} < \pi$	TG( $\hat{\phi}_{\text{bar}}, 20^\circ, \hat{\phi}_{\text{bar}} \mp 45$ )
$x_0$	0 if $0 < x_0 < nx$	TG( $\hat{x}_0, 2'', \hat{x}_0 \mp 10''$ )
$y_0$	0 if $0 < y_0 < ny$	TG( $\hat{y}_0, 2'', \hat{y}_0 \mp 10''$ )
$V_{\text{sys}}$	0	TG( $\hat{V}_{\text{sys}}, 50 \text{ km s}^{-1}$ )
$V_k$	0 if $-400 < V_k < 400$	TG( $\hat{V}_k, 150 \text{ km s}^{-1}, -250, 250$ )
$\ln \sigma_{\text{int}}^2$	0 if $-10 < \ln \sigma_{\text{int}}^2 < 10$	TG(0.1, 1, -10, 10)

<sup>a</sup>Values with hat represent LS results.  $V_k$  refers to any of the different radial dependent velocities.

TG are sampled more efficiently than uniform distributions.

In order to infer the posterior distribution of the parameters, **XookSuut** adopts two well known Python packages for Bayesian analysis; these are the EMCEE package (e.g., Foreman-Mackey et al. 2013), and DYNESTY (e.g., Speagle 2020). EMCEE is a Python implementation of the affine-invariant method for MCMC with automatic chain tuning; while DYNESTY is a Python implementation of dynamic nested sampling methods. MCMC and NS are two robust sampling techniques to derive posterior distributions in high dimensional likelihood functions, such as the kinematic models described before. Both packages have been extensively applied in astronomy for making Bayesian inference, with particular implementations in cosmology. For a detailed description of these codes we suggest reading their corresponding documentation. Both packages require a set of configurations whose purpose is to guarantee convergence of the sampling procedure. **XookSuut** is optimized to pass a configuration file to set up EMCEE and DYNESTY. The main setups in these codes are the length of the join-chains and the discarding fraction (burning period) in the case of MCMC, and the integration limit for NS. For both packages, **XookSuut** adapts the likelihood functions and priors to make it compatible with MCMC or NS methods.

As mentioned before, MCMC samplers like EMCEE sample from the likelihood; therefore the chains need to be initialized at some position, for which **XookSuut** chooses a random region around the maximum likelihood. For MCMC samplers the joint posterior distribution is estimated up to a normalization constant, here adopted equal to 1 (or zero in ln). For running DYNESTY **XookSuut** transform the priors from Table 1 into a unit cube, in such a way that all

parameters vary from 0 to 1 and they are re-scaled at the end of the sampling process.

Finally, representative values of the parameters are taken as the 50% percentile of the marginalized distributions. The uncertainty in the parameters is addressed in the following section.

Although EMCEE makes use of frequentist methods for starting the sampling process, this could be suppressed if relatively good initial positions of the disk geometry are given. On the other hand, DYNESTY does not require at all the LS initialization as the numerical integration is performed over the prior space.

### 3.2.2. Error Estimation

The true uncertainty in rotational velocities is known to be underestimated with standard least squares minimization techniques and even with MCMC methods (e.g., de Blok et al. 2008; Oh et al. 2018). Errors estimated with these methods are usually of the order of the turbulence of the ISM (a few  $\text{km s}^{-1}$ ) and do not represent the systematic errors. Some works adopt the mean dispersion per ring as a measure of the uncertainty in the rotation curve. However, when non-circular components are added to the model, this assumption is no longer valid since each ring may contain multiple kinematic components.

**XookSuut** provides different error estimates for the derived parameters. The Levenberg–Marquardt least-squares minimization automatically computes errors from the covariance matrix; these represent statistical errors and may be used for a quick analysis. However, the power of Bayesian inference relies on the estimation of posterior distributions, from which we can obtain uncertainties of the parameters. **XookSuut** adopts the marginalized distributions to quote the uncertainties in each parameter, including the velocities. These uncertainties are in gen-

eral smaller than simple Monte-Carlo errors since marginalized distributions are not expected to contain unstable (*burn-in*) chains. This necessarily requires dropping an important fraction of the total samples during a run, which is customized within **XookSuut**. Therefore, it is common to report  $2\sigma$  credible intervals in Bayesian analysis. In fact, finding “large” uncertainties in MCMC methods would be an indication that chains are not fully converging; either because a large fraction of samples are being rejected, or chains are surveying complicated likelihood functions, often multi-modal distributions, for which NS would be a better solution.

Additionally, **XookSuut** also implements a bootstrap analysis for error estimation. Our procedure differs from the one described by Sellwood & Sánchez (2010), as explained below. The residuals from the best 2D interpolated model are used to generate new samples. Instead of shuffling residuals at random locations on the disk,  $K$  rings of width  $\delta_r$  are constructed with projection angles given by the best values. Then, residuals in each ring are chosen to resample the best 2D model in the same ring locations. In this way any residual pattern associated to a bar or spiral arms remains around the same galactocentric distance but not in the same pixel location. The new re-sampled velocity map is used in a least squares analysis for deriving a new set of velocities and constant parameters. This procedure is performed iteratively; finally the root mean square deviation is taken as  $1\sigma$  error; however, for consistency with the Bayesian methods, we report  $2\sigma$  errors throughout the paper.

In general, we find that the estimated uncertainties of the parameters increase in the following order: Bayesian methods > bootstraps > LS, with computational cost increasing in the same direction.

#### 4. TESTING **XookSuut**

We now proceed to evaluate **XookSuut** in a series of simulated velocity maps and real velocity fields.

##### 4.1. Toy Model Example

As an example of its use, we run **XookSuut** on a simulated velocity map. This is the velocity field of a galaxy at 31.4 Mpc with a  $32''$  optical radius. We model a velocity field with an oval distortion described by equation 3. For the rotation curve we adopt the parameterization from Bertola et al. (1991). The non-circular motions were modeled using the Gamma probability density function; Gamma(2,3.5) for describing the  $V_{2,t}$  component and Gamma(2,3) for  $V_{2,r}$ . The constant parameters were

set to  $\phi'_{\text{disk}} = 77^\circ$ ,  $\phi_{\text{bar}} = 35^\circ$ ,  $i = 55^\circ$ ,  $x_0 = 76.5$ ,  $y_0 = 75.2$  and  $V_{\text{sys}} = 2142 \text{ km s}^{-1}$ . The field of view (FoV) is defined as  $64'' \times 74''$  and the pixel scale was set to  $0.5''$ . Finally we convolved the image for decreasing its spatial resolution. We simulate a circular PSF with a 2D Gaussian function with a  $1''$  full width at half maximum (FWHM). We perturb the velocity profiles by adding Gaussian noise centered at zero and with a standard deviation of  $5 \text{ km s}^{-1}$ .

We started **XookSuut** by assigning random values to each of the constant parameters, except for  $\phi_{\text{bar}}$  which is initialized around its maximum (i.e.,  $\phi_{\text{bar}} = 45^\circ$ ). We set the initial and last ring exploration at  $2.5''$  and  $40''$  respectively; we also estimate the radial velocities each  $2.5''$ . A LS analysis was performed with 3 round iterations before starting the MCMC run. For comparison with Bayesian methods we adopt 1000 bootstraps during the LS analysis. For MCMC sampling, we run a total of 4000 iterations with 60 different chains, which represent twice the number of free variables for this case. We discarded 50% of the joint chain, for a total of 120k posterior samples on each parameter. The IAT for this run resulted in 127 which is superior to 50.

On the other hand, nested sampling only requires the prior information, for which we adopted the uniform priors from Table 1. No initial LS was performed for this case. We stopped the sampling procedure only when the remaining evidence to be integrated was  $\leq 0.1$ .

We test all the different kinematic models, i.e., circular, radial, bisymmetric models and we arbitrarily expand the harmonic series up to  $M = 3$ . MCMC and NS derive the posterior distribution for each variable of the kinematic model; thus, we can take advantage of corner plots to represent their marginalized distributions and explore possible correlations between parameters. The median values and  $2\sigma$  errors for each parameter are shown in Table 2, while in Figure 2 we show the marginalized posteriors; for simplicity we only show the constant parameters for the bisymmetric model, although note this should be a  $30 \times 30$  dimensions plot.

MCMC and nested sampling methods converge to the same solutions found by the LS method; this represents a great success for Bayesian methods to derive kinematic parameters from an input velocity map given the large dimension of the likelihood function. We note that the input parameters are recovered in the bisymmetric model, which is not the case for the circular, radial and harmonic, as expected; this is better appreciated in the corner plot from Figure 2. MCMC and nested sampling recover the input



TABLE 2  
BEST FIT PARAMETERS FOR THE TOY MODEL EXAMPLE

Model	Method	$\Delta\phi'_{\text{disk}}$ ( $^{\circ}$ )	$\Delta i$ ( $^{\circ}$ )	$\Delta x_0$ ( $\text{pix}$ )	$\Delta y_0$ ( $\text{pix}$ )	$\Delta V_{\text{sys}}$ ( $\text{km s}^{-1}$ )	$\Delta\phi_{\text{bar}}$ ( $^{\circ}$ )	RMS ( $\text{km s}^{-1}$ )	BIC
circular	LM	$-1.1 \pm 0.1$	$-0.4 \pm 0.1$	$0.0 \pm 0.0$	$0.1 \pm 0.0$	$-0.0 \pm 0.2$	$\dots$	8.5	4.5
	MCMC	$-1.1 \pm 0.1$	$-0.1 \pm 0.3$	$0.0 \pm 0.1$	$0.1 \pm 0.1$	$-0.0 \pm 0.2$	$\dots$	9.3	4.5
	NS	$-1.1 \pm 0.1$	$-0.1 \pm 0.3$	$0.0 \pm 0.1$	$0.1 \pm 0.1$	$-0.0 \pm 0.2$	$\dots$	9.3	4.5
radial	LM	$-0.1 \pm 0.1$	$-0.2 \pm 0.2$	$0.0 \pm 0.0$	$0.1 \pm 0.0$	$0.0 \pm 0.2$	$\dots$	9.3	4.4
	MCMC	$-0.1 \pm 0.1$	$0.1 \pm 0.3$	$0.0 \pm 0.1$	$0.1 \pm 0.1$	$-0.0 \pm 0.2$	$\dots$	8.5	4.4
	NS	$-0.1 \pm 0.1$	$0.0 \pm 0.3$	$0.0 \pm 0.1$	$0.1 \pm 0.1$	$-0.0 \pm 0.2$	$\dots$	8.5	4.4
bisymmetric	LM	$0.0 \pm 0.1$	$0.1 \pm 0.2$	$0.0 \pm 0.0$	$0.1 \pm 0.0$	$-0.0 \pm 0.2$	$3.8 \pm 8.0$	8.5	4.4
	MCMC	$0.0 \pm 0.2$	$0.1 \pm 0.3$	$0.0 \pm 0.1$	$0.1 \pm 0.1$	$-0.0 \pm 0.2$	$3.7 \pm 7.8$	8.5	4.4
	NS	$0.0 \pm 0.2$	$0.1 \pm 0.3$	$0.0 \pm 0.1$	$0.1 \pm 0.1$	$-0.0 \pm 0.2$	$3.6 \pm 8.2$	8.5	4.4
harmonic	LM	$-0.1 \pm 0.1$	$-0.0 \pm 0.3$	$0.0 \pm 0.0$	$0.1 \pm 0.0$	$-0.0 \pm 0.2$	$\dots$	8.5	4.4
	MCMC	$-0.1 \pm 0.1$	$0.0 \pm 0.3$	$0.0 \pm 0.1$	$0.1 \pm 0.1$	$-0.0 \pm 0.2$	$\dots$	8.5	4.4
	NS	$-0.1 \pm 0.1$	$0.0 \pm 0.3$	$0.0 \pm 0.1$	$0.1 \pm 0.1$	$-0.0 \pm 0.2$	$\dots$	8.5	4.4

$\Delta \equiv \alpha_{\text{recovered}} - \alpha_{\text{true}}$ .

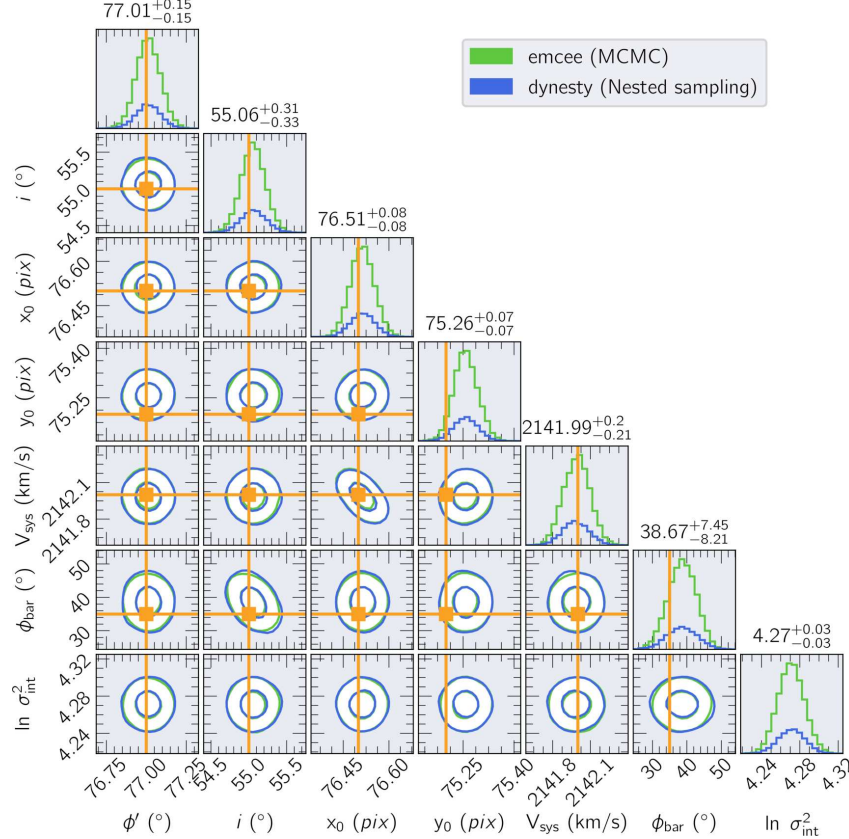


Fig. 2. Marginalized distributions of the parameters describing the bisymmetric model for our toy model described in § 4.1. This corner plot shows only the parameters describing the disk geometry. Contours enclose 68% and 95% of the data. Histograms of individual distributions are shown on top, together with the median values and  $2\sigma$  credible intervals for each parameter. The orange straight lines represent the true values. As observed, all parameters but  $y_0$ , are recovered within the  $\pm 1\sigma$  region. The color figure can be viewed online.

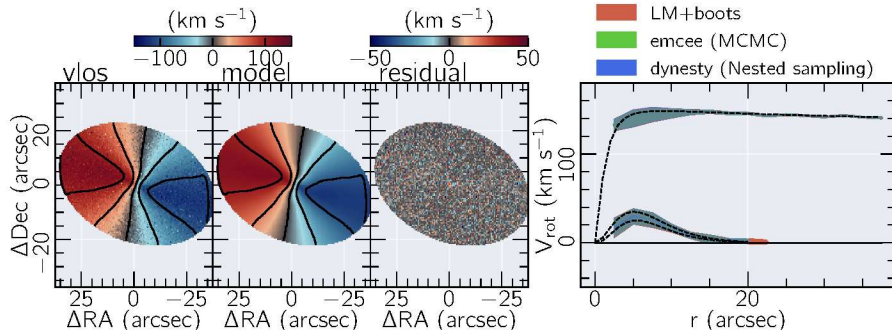


Fig. 3. **XookSuut** results for the toy model example, for the bisymmetric model case. Figures from left to right: simulated velocity field; best two dimensional interpolated model from MCMC; residual map (input minus output). Overlaid on these maps are iso-velocity contours starting at  $0 \text{ km s}^{-1}$  with steps of  $\pm 50 \text{ km s}^{-1}$ . The fourth column shows the radial variation of the different kinematic components included in the model. Here the input velocities are shown with discontinuous lines while continuous lines represent the velocities derived by **XookSuut** using MCMC (green), nested sampling (blue) and LM + bootstrap (red). The shadowed regions represent  $2\sigma$  errors. The color figure can be viewed online.

parameters within the  $1\sigma$  credible interval, except for  $y_0$  which lies within  $2\sigma$ ; among the constant parameters, the position angle of the oval distortion shows the largest uncertainty. From Table 2, we notice that the uncertainties derived with Bayesian methods and bootstraps are of the same order.

The different velocities,  $V_t(r)$ ,  $V_{2,r}(r)$  and  $V_{2,t}(r)$ , are also recovered within the  $2\sigma$  errors as observed from the rightmost panel of Figure 3. For consistence, in Appendix C we include the results using **DiskFit**; we notice that the **XookSuut** results are in total agreement with those obtained with **DiskFit**.

Table 2 also shows the root mean square (RMS) for each kinematic model; models including non-circular rotation show a RMS value around  $8.5 \text{ km s}^{-1}$ . This leads to the question of which model is the preferred one for describing a particular velocity field. In a statistical sense, when comparing different models one should choose the one with fewer parameters, since more variables in a model often reduce further the RMS, which does not necessarily provide the best physical interpretation of the data. Statistical tests such as the Bayesian information criterion (BIC) penalizes over the variables from the model; BIC is defined in terms of the likelihood (or the chi-square) as,  $\text{BIC} = -2 \ln \mathcal{L}(\hat{\alpha}) + N_{\text{vars}} \ln(N)$ , where  $\hat{\alpha}$  represents the parameters that maximize the likelihood function and  $N$  is the number of data; thus, the model with the lowest BIC should be preferred. Additionally, the evidence  $\mathcal{Z}$  computed from NS, is a measure of the agreement of the data with the priors; in this way large (small)  $\mathcal{Z}$  values are more (less) compatible with the priors.

However, when there is little information about the data, or only the data itself, it is difficult to select a model description of the data based on any information other than statistical tests. Regardless of the statistical method adopted, it is important to have a physical motivation for accepting or rejecting a model; otherwise, erroneous interpretations of the velocity field could arise.

For the toy model example, Table 2 shows that non-circular models have similar BIC values. Even when the harmonic decomposition model seems to perform a good fitting based on the residuals, the physical interpretation of the  $m = 2$  components are meaningless for this example. Thus in a real scenario the radial and bisymmetric model should be compared. The Bayesian evidence for the radial and bisymmetric models results in  $\ln \mathcal{Z} = -36136$  and  $-36135$ , respectively. In a statistically sense both solutions are equally probable; in other words, the data are insufficient for making an informed judgment. This is not surprising given the simplicity of our velocity field model.

#### 4.2. Simulations

We carried out a set of 1000 simulations with different inclination angles ranging from  $30^\circ < i < 70^\circ$ , disk position angle  $0^\circ < \phi'_{\text{disk}} < 360^\circ$ , and to avoid degeneracy, the bar position angle varies from  $5^\circ < \phi_{\text{bar}} < 85^\circ$ ; velocity profiles and kinematic center have the same values as in the toy example. We also adopt the same sampling configurations as before. We notice that sometimes **XookSuut** detects the minor-axis bar position angle instead of the major one; in such cases,  $\phi_{\text{bar}}$  is found  $90^\circ$  away from

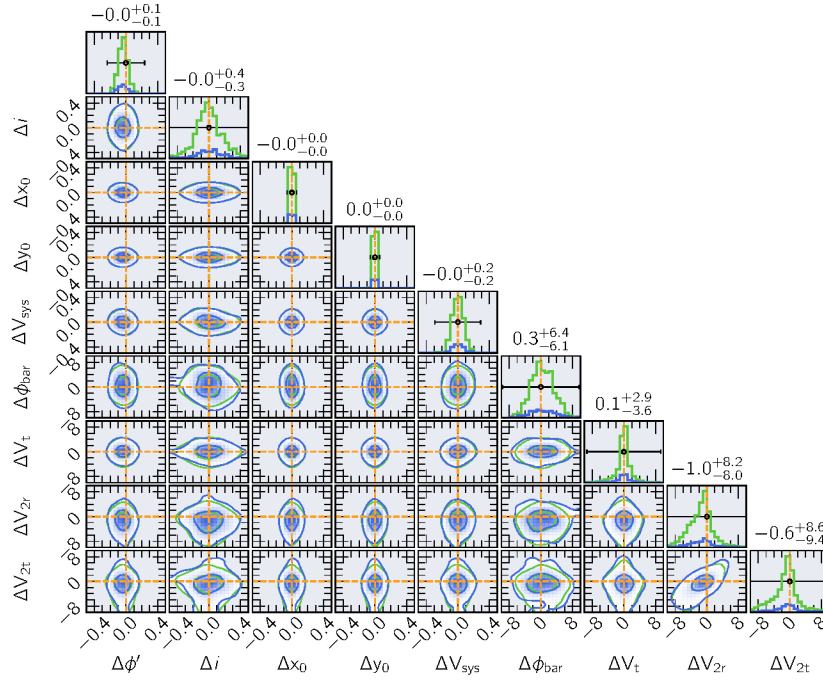


Fig. 4. **XookSuut** results for the bisymmetric model on 1000 synthetic velocity maps with oval distortions. Values are reported with respect their true value, namely  $\Delta\alpha = \alpha_{\text{recovered}} - \alpha_{\text{true}}$ , where  $\alpha$  is any of the parameters considered in this example. Straight orange lines represent the true values (i.e.,  $\Delta\alpha = 0$ ). Blue and lime colors show the results for NS and MCMC methods, respectively. The inner and outer density contours contain 68% and 95% of the data, respectively. The upper histograms represent the 1D distributions of the parameters on the x-axis, while the size of the error bars represents the average value of the  $2\sigma$  credible interval for each parameter. Note that all parameters are recovered within the reported error bars. Values on-top the histograms represent the 50% percentile of  $\Delta\alpha$ , together with the  $\pm 2\sigma$  dispersion. The color figure can be viewed online.

TABLE 3

**XookSuut** BISYMMETRIC RESULTS FOR NGC 7321

Method	$\phi'_{\text{disk}}$ ( $^{\circ}$ )	$i$ ( $^{\circ}$ )	$x_0$ (pixels)	$y_0$ (pixels)	$V_{\text{sys}}$ ( $\text{km s}^{-1}$ )	$\phi_{\text{bar}}$ ( $^{\circ}$ )
LS+bootstraps	$11 \pm 1$	$46 \pm 1$	$35.5 \pm 0.0$	$33.6 \pm 0.0$	$7123 \pm 1$	$46 \pm 4$
NS	$11 \pm 0$	$46 \pm 1$	$35.5 \pm 0.1$	$33.6 \pm 0.1$	$7123 \pm 1$	$46 \pm 6$
MCMC	$11 \pm 0$	$46 \pm 1$	$35.5 \pm 0.1$	$33.6 \pm 0.1$	$7123 \pm 1$	$46 \pm 7$
<b>DiskFit</b> *	$12 \pm 1$	$46 \pm 2$	...	...	$7123 \pm 3$	$47 \pm 6$

\*Results from Holmes et al. (2015). Errors in Holmes et al. (2015) represent  $1\sigma$ , so a factor of 2 should be considered for comparison.

the minor axis. This result is also a totally acceptable model since the difference resides only in the sign of the bisymmetric components,  $V_{2,r}$  and  $V_{2,t}$ , which for these cases both have negative values. **XookSuut** computes the projected major axis position angle of the bar via equation 5, while the

projected minor axis position angle is computed by shifting  $\phi_{\text{bar}}$  by  $90^{\circ}$ .

In Figure 4 we show the results of the analysis in corner plots; the derived values are shown relative to the true ones, namely  $\Delta\alpha = \alpha_{\text{recovered}} - \alpha_{\text{true}}$ ; for the radial dependent velocities, we subtract the velocity

profile of each component from the derived velocities. These results show that the median values of  $\Delta\alpha$  lie around zero for all parameters describing the bisymmetric model; furthermore, the scatter of the differences is contained within the average value of the  $2\sigma$  credible interval for each parameter. Results from this analysis demonstrate that MCMC and NS methods are able to recover the true parameters of our simulated velocity maps, even when each model is described by +30 free variables.

The final accuracy of the recovered parameters would depend on the details of data themselves (resolution, S/N, spatial coverage etc.). Therefore, ad-hoc simulations are encouraged.

#### 4.3. NGC 7321

We proceed to evaluate **XookSuut** over the velocity field of a galaxy hosting a stellar bar. For this purpose we adopt the galaxy NGC 7321 observed as part of the CALIFA galaxy survey (e.g., Sánchez et al. 2012). This object has been previously analyzed by Holmes et al. (2015) using **DiskFit**. The H $\alpha$  velocity field of this object represents a good example of a galaxy with a strong kinematic distortion, most probably caused by the stellar bar. Holmes et al. (2015) found the bisymmetric model as the best model for reproducing the inner distortion observed in this object; they found best fit values and  $1\sigma$  errors for the constant parameters given by  $\phi'_{\text{disk}} = 12 \pm 1^\circ$ ,  $i = 46 \pm 2^\circ$ ,  $V_{\text{sys}} = 7123 \pm 3 \text{ km s}^{-1}$  and a bar position angle oriented at  $\phi_{\text{bar}} = 47 \pm 6^\circ$ . We implemented **XookSuut** on the H $\alpha$  velocity map taken from the CALIFA data products (e.g., Sánchez et al. 2016). We adopted the same ring configurations as before, excluding pixels from the error map with values larger than  $25 \text{ km s}^{-1}$ ; we proceed to explore the non-circular motions up to  $r = 18''$ , and set the maximum radius for the circular velocities up to  $40''$ ; this leads to a total of 36 free variables that will be estimated with Bayesian inference. We adopt 3 rounds of iterations for the LS method, and also compute the errors on the parameters with 1000 bootstraps. For MCMC, we adopt 5000 steps and drop half of the total samples to let the joint chain stabilize. For NS we stop the sampling when the remaining evidence to be integrated is 0.1.

Figure 5 shows the marginalized distributions of the constant parameters. From the 1D histograms we obtain  $\phi'_{\text{disk}} = 11 \pm 0^\circ$ ,  $i = 46 \pm 1^\circ$ ,  $V_{\text{sys}} = 7123 \pm 1 \text{ km s}^{-1}$  and  $\phi_{\text{bar}} = 46 \pm 6^\circ$ ; additionally we compute the intrinsic scatter of the data as  $\approx 16 \text{ km s}^{-1}$ . Table 3 shows a summary of these results. As can be read from this table, the con-

stant parameters derived by **XookSuut** are in concordance with those previously reported by Holmes et al. (2015), although our uncertainties are smaller when comparing the errors at  $2\sigma$ , probably due to differences in methods. The bottom figure shows the best model and residual map obtained from nested sampling. The kinematic distortion observed in the central region is well reproduced with the bisymmetric model. The bisymmetric motions, i.e., the bar-like flows, are oriented at  $46 \pm 8^\circ$  on the sky plane. The rightmost panel shows the radial profile of the different velocity components derived from NS, MCMC and LS+bootstrap methods. Again, the uncertainties reported from NS and MCMC are of similar magnitude, and these are larger than those obtained with bootstrap methods.

In Appendix D we show the implementation of **XookSuut** on other data with different instrumental configurations.

## 5. DISCUSSION

Our simulations and toy example show that sampling methods are able to produce results similar to those obtained with frequentist methods based on the  $\chi^2$  minimization. The widely used Levenberg-Marquardt algorithm is able to obtain solutions to the kinematic models in a fast way, although errors from the covariance matrix are always small. On the other hand, our resampling implementation produces larger uncertainties compared with the covariance matrix. We notice that the magnitude of the errors increases with the number of bootstrap iterations; however, increasing the number of bootstrap samples increases the total execution time, since at each iteration a new LS analysis is performed.

Bayesian methods, i.e., MCMC and NS, provide the largest uncertainties on the parameters compared to the two other techniques. The major disadvantage is the computational cost needed to sample the posterior distributions. For the toy model example presented, the execution times on an 8 core machine are  $\approx 1$  hour for LM+1k bootstraps,  $\approx 1$  hour for MCMC with 4k steps and  $\approx 2.5$  hours with NS.

If Bayesian methods and LS+bootstrap provide similar solutions for the parameters, then in principle one could choose either of the two methods to quote the uncertainties. However, the most interesting cases are when Bayesian methods differ from the frequentist ones. **XookSuut** has the advantage that both bootstrap and Bayesian methods can be executed in parallel. This can drastically reduce the execution times depending on the number of CPUs available during the running.

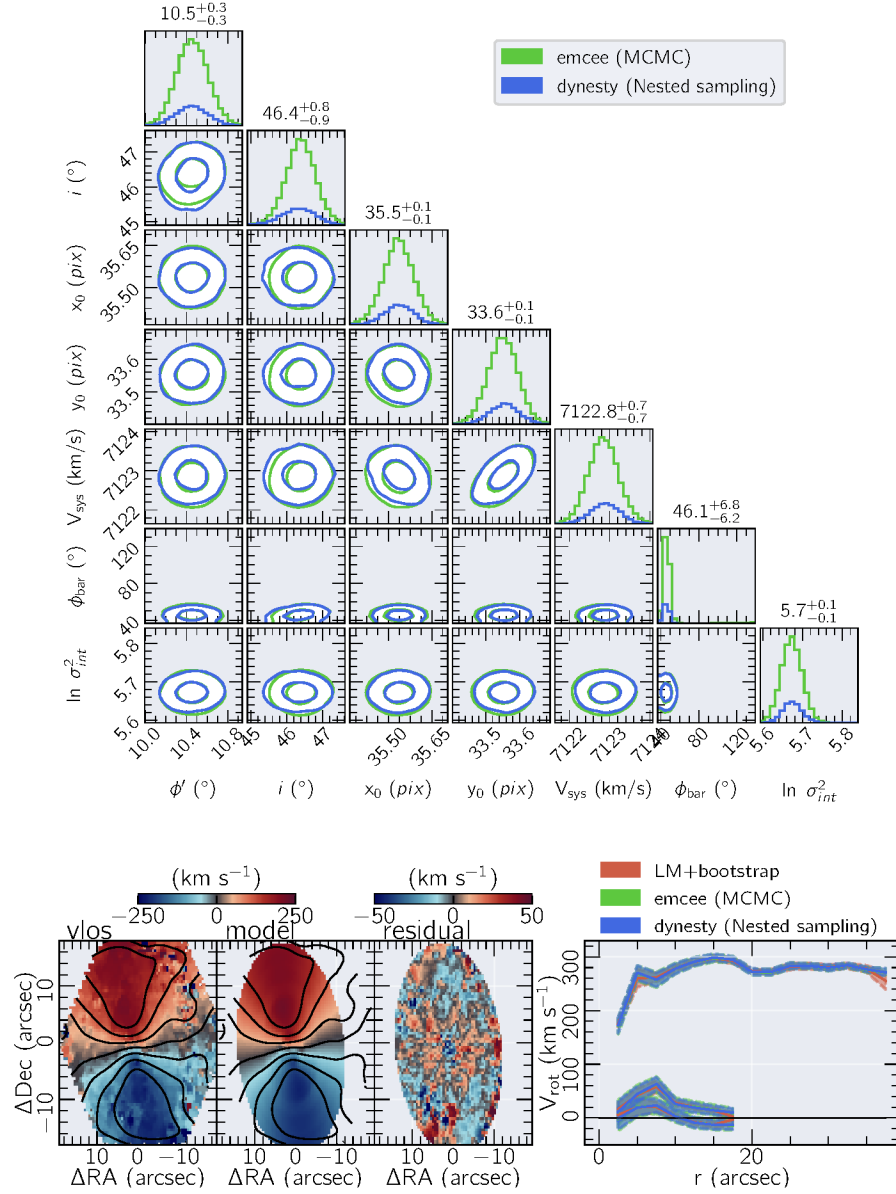


Fig. 5. **XookSuut** results for NGC 7321 for the bisymmetric model. Top figure shows the marginalized distribution for the constant parameters with MCMC methods in green colors and NS in blue. As in Figure 2, the quoted values on top the histograms represent the median and  $2\sigma$  errors obtained from the posterior distributions. Bottom figure shows from left to right the  $\text{H}\alpha$  velocity map; the two-dimensional model from NS; the residual map; and the radial profile of the different velocities. Shadow regions represent the  $2\sigma$  credible intervals obtained from each method (bootstrap in red colors). The color figure can be viewed online.

## 6. CONCLUSIONS

We have presented a tool for the kinematic study of circular and non-circular motions of galaxies with resolved velocity maps. This tool named **XookSuut** (or **XS** for short), is an adaptation of the **DiskFit** algorithm, designed to perform Bayesian inference on parameters describing circular rotation, radial flows, bisymmetric motions and an ar-

bitrary harmonic decomposition of the LoS velocities. **XookSuut** implements robust Bayesian sampling methods to obtain the posterior distribution of the kinematic parameters. In this way, the “best-fit” values, and their uncertainties are obtained from the marginalized distributions, unlike frequentist methods where best values are obtained at a single point from the likelihood function. **XookSuut** adopts



Markov Chain Monte Carlo methods and dynamic nested sampling to sample the posterior distributions. In particular, **XookSuut** makes use of the EMCEE and DYNESTY packages developed to perform Bayesian inference.

**XookSuut** is a free access code written in Python language. The details about running the code, as well as the required inputs and the outputs are described in Appendix A.

**XookSuut** is suitable to use on velocity maps not strongly affected by spatial resolution effects, i.e., when the PSF FWHM is smaller than the size of structural components of disk galaxies, such as stellar bars. In addition, disk inclination should range from  $30^\circ < i < 70^\circ$ . The fundamental assumption of the code is that galaxies are flat systems observed in projection on the sky with a constant inclination angle, constant disk position angle and fixed kinematic center. This makes **XookSuut** suitable for studying the kinematics of galaxies within dynamical equilibrium, but not for highly perturbed disks.

Applying **XookSuut** over a set of simulated maps with oval distortions we showed that Bayesian methods are able to recover the input parameters despite the high dimension of the likelihood function. True parameters are recovered within  $1\sigma$  credible interval, with the position angle of the oval distortion being the parameter with the larger scatter. We tested **XookSuut** over a well known galaxy with an oval distortion in the velocity field, NGC 7321, and found results similar to those obtained with **DiskFit**.

Regarding the uncertainty of the parameters, Bayesian methods provide the largest uncertainties compared with resampling methods like bootstrap. However, the computational cost for sampling the joint posterior distribution is in general more expensive than, for instance 1k bootstraps. Fortunately, a fraction of time can be saved when these methods are run in parallel.

We also tested **XookSuut** on velocity maps from different galaxy surveys. Despite the instrumental differences in these data, **XookSuut** is able to build kinematic models of circular and non-circular motions.

Finally, **XookSuut** is ideal for running on individual objects, or in galaxy samples since it is easy to systematize for use in large data sets. **XookSuut** is a free access code available at the following link <https://github.com/CarlosCoba/XookSuut-code>.

We thank K. Spekkens, J. A. Sellwood, and anonymous peer reviewers for providing helpful suggestions to improve this manuscript.

C. L. C. thanks support from the IAA of Academia Sinica. L. L. thank supports from the Academia Sinica under the Career Development Award CDA107-M03, the Ministry of Science & Technology of Taiwan under the grant MOST 108-2628-M-001-001-MY3, and National Science and Technology Council under the grant NSTC 111-2112-M-001-044.

## APPENDIX

### A. RUNNING XOOKSUUT

**XookSuut** is designed to run directly from the command line by passing a number of parameters whose purpose is to guide the user through a successful fit.

After a successful installation and typing **XookSuut** on a terminal the code will display the entrance required for starting the analysis. The meaning of each parameter is described in Table 4, while the output files are described in Table 5.

### B. CAUCHY DISTRIBUTION

Although a Gaussian distribution is mostly assumed for the likelihood function, there is no restriction to use other distributions. In fact, multiple algorithms adopt arbitrary parameterization of the residual function (e.g., Di Teodoro & Fraternali 2015). In addition to a Gaussian distribution, **XookSuut** also includes the Cauchy distribution in the likelihood function. It assumes a unique form of the errors parameterized with  $\gamma$ . The Cauchy log-posterior distribution for our models adopts the following form:

$$\ln p(\vec{\alpha}|\mathcal{D}, \mathcal{V}_{\text{model}}) = -N \ln \pi \gamma - \sum_{n=1}^N \ln \left( 1 + \frac{\left( \mathcal{D}_n - \sum_{k=1}^K W_{k,n} \vec{V}_k \right)^2}{\gamma^2} \right) + \ln p(\alpha) - \ln \mathcal{Z}. \quad (\text{B32})$$

An example using the Cauchy distribution is shown in Figure 6. As noted, there can be differences in the results depending on the election of the likelihood function. There is no a general rule on when to use the Cauchy distribution; often, it is used when the data contain many outliers.

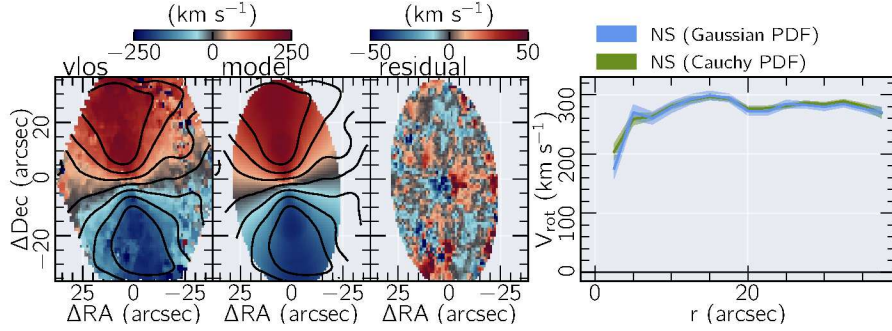


Fig. 6. Results for Gaussian and Cauchy likelihood functions for the circular model of NGC 7321. In this example we used nested sampling for the Bayesian analysis. We found the width of the Cauchy distribution at  $\gamma = 7.6 \pm 0.3 \text{ km s}^{-1}$ . The color figure can be viewed online.

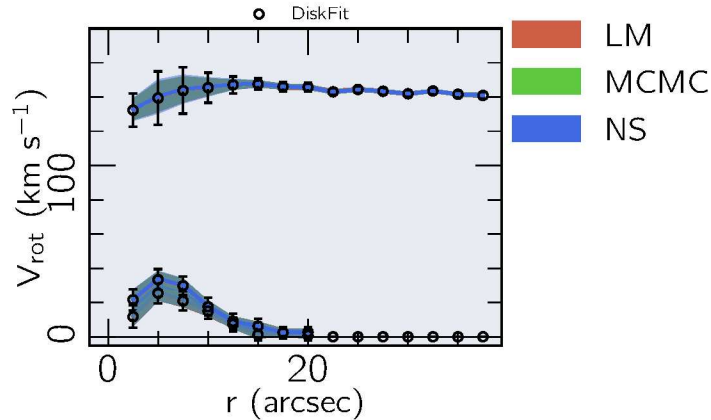


Fig. 7. Results of the fitting analysis using **DiskFit** for the simulated velocity map described in Sec 4.1. Black empty circles and error bars show velocities and uncertainties derived by **DiskFit**; 1000 bootstraps were adopted in **DiskFit** for this purpose. Colored lines represent results from **XookSuut** using LM+bootstrap in red, MCMC in green and NS in blue. Results for the constant parameters using **DiskFit** are the following,  $\phi'_{\text{disk}} = 77.02 \pm 0.13^\circ$ ,  $i = 55.06 \pm 0.48^\circ$ ,  $(x_0, y_0) = (77.51 \pm 0.09, 76.26 \pm 0.09)$  pixels,  $V_{\text{sys}} = 2141.98 \pm 0.20 \text{ km s}^{-1}$  and  $\phi_{\text{bar}} = 39.47 \pm 15.60^\circ$ ,  $\chi^2 = 72.5$ . In all cases error bars represent  $2\sigma$  errors. The color figure can be viewed online.

### C. **DiskFit** RESULTS

Figure 7 shows the results of the bisymmetric model using **DiskFit** applied on the simulated velocity map described in Section 4.1; 1000 bootstraps were adopted in **DiskFit** to quote the uncertainties of the parameters. The median values estimated with Bayesian methods and LM+bootstraps are in concordance with those obtained with **DiskFit**. In addition, the uncertainties of the velocities reported by **DiskFit** are comparable to or lower than those obtained with Bayesian methods. This figure shows that **XookSuut** produces results similar to **DiskFit**.

### D. IMPLEMENTATION ON DATA WITH DIFFERENT CONFIGURATIONS

We apply **XookSuut** to a sample of galaxies observed with different instrumental configurations and

different redshifts. We obtain  $\text{H}\alpha$  velocity maps from different integral field spectroscopy (IFS) galaxy surveys, namely MaNGA (e.g., Bundy et al. 2015), AMUSING++ (e.g., López-Cobá et al. 2020), SAMI (e.g., Allen et al. 2015); these objects correspond to manga-9894-6104, IC 1320 and SAMI511867, respectively. These objects were chosen for showing rich emission in  $\text{H}\alpha$ . The velocity maps were obtained from the public dataproducs.

For each galaxy we run circular, radial, bisymmetric and harmonic decomposition models up to  $M = 3$ . However we only report the model with the lowest BIC value. The initial position angle and inclination angles were adopted from those reported in Hyperleda or by our own previous analysis (e.g., Walcher et al. 2014; López-Cobá et al. 2020). The

TABLE 4  
XookSuut INPUT PARAMETERS

Input	Type	Description
name	str	Name of the object.
vel_map.fits	fits	Fits file containing the 2D velocity map in $\text{km s}^{-1}$ .
error_map.fits	fits	Fits file containing the 2D error map in $\text{km s}^{-1}$ .
SN	float	Pixels in the error map above this value are excluded.
pixel_scale	float	Pixel scale of the image ( $''$ / pixel).
PA	float	Kinematic position angle guess ( $^\circ$ ).
INC	float	Disk inclination guess ( $^\circ$ ).
X0	float	X-coordinate of the kinematic centre ( $pix$ ).
Y0	float	Y-coordinate of the kinematic centre ( $pix$ ).
VSYS	float	Initial guess for the systemic velocity in $\text{km s}^{-1}$ . If no argument is passed, it will take the weighted mean value within a $5''$ aperture centered in (X0, Y0).
vary_PA	bool	Whether $\phi'_{\text{disk}}$ varies in the fit or not.
vary_INC	bool	Whether $i$ varies in the fit or not.
vary_X0	bool	Whether $x_0$ varies in the fit or not.
vary_Y0	bool	Whether $y_0$ varies in the fit or not.
vary_VSYS	bool	Whether $V_{\text{sys}}$ varies in the fit or not.
ring_space	float	Spacing between rings in arcsec. The user may want to use FWHM spatial resolution.
delta	float	The width of the ring is defined as 2delta. The user may want to use 0.5 ring_space if independent rings are desired.
Rstart,Rfinal	float	Starting and initial position of the rings on disk plane. (arcsec)
cover	float	Fraction of pixels in a ring needed to compute the row stacked velocities. If 1 the ring area must be 100% sampled.
kin_model	str	Choose between: “circular”, “radial” flows, “bisymmetric” (oval distortion) or “hrm_M”, where M is the harmonic number.
fit_method	str	Minimization technique used in the least-squares analysis. Options are “Powell” or “LM” (Levenberg–Marquardt).
N_it	float	Number of round iterations for the least-squares analysis.
Rbar_min,max	float	Minimum and maximum radius for modeling the non-circular flows. If only one value is passed, it will be considered as the maximum radius to fit.
config_file	file	Configuration file to access high configuration settings including the Bayesian sampling methods, bootstrap errors, and other general model configurations. See the documentation for a detailed description of this file.
prefix	str	Extra string passed to the object’s name. This prevents overwriting the outputs in case multiple analyses of the same object are performed.

coordinates of the kinematic center were set by eye from the velocity maps. When available we used the error maps to exclude pixels with large uncertainties (namely  $> 25 \text{ km s}^{-1}$ ). The width of the rings was set to the size of the PSF for each dataset (ranging from  $1'' - 2.5''$ ). For these objects we only adopt

NS methods. To speed up the analysis we adopted truncated Gaussian priors, for which we performed an LS analysis to set the mean values of the Gaussian priors.

The best fit models are shown in Figure 8, while results of the constant parameters are shown in Ta-



TABLE 5

## XookSuut DATA PRODUCTS

Output	Description
name.model.vlos_model.fits.gz	Two dimensional representation of the adopted kinematic model (equations 1,2,3 or 6).
name.model.chisq.fits.gz	Fits file containing the chi-square map defined as $(\text{obs}-\text{model})^2/\text{error}^2$ .
name.model.chain.fits.gz	Fits file containing the marginalized samples (i.e., the joint chain), explored in the Bayesian analysis.
name.model.2D_Vmodel.fits.gz	Two dimensional representation of each velocity component from the model.
name.model.marginal_dist.fits.gz	Fits file containing the 50 percentile distribution for each parameter, together with the $\pm 1\sigma$ and $\pm 2\sigma$ credible intervals.
name.model.residual.fits.gz	Map containing the residuals of the model, i.e., $\text{obs} - \text{model}$ .
name.model.2D_R.fits.gz	Deprojected distance map in arcsec, obtained from the best fit disk geometry.
name.model.1D_model.fits.gz	Values for the best fit parameters together with the $2\sigma$ errors.
name.model.2D_theta.fits.gz	Two dimensional representation of the azimuthal angle $\theta$ .

TABLE 6

## XookSuut APPLIED TO DIFFERENT DATA WITH DIFFERENT INSTRUMENTAL CONFIGURATIONS

Object	Survey	Model	$\phi'_{\text{disk}}$ ( $^{\circ}$ )	$i$ ( $^{\circ}$ )	$x_0$ (pixels)	$y_0$ (pixels)	$V_{\text{sys}}$ ( $\text{km s}^{-1}$ )
9894-6104	MaNGA	Eq 1	$296 \pm 0$	$35 \pm 1$	$27.2 \pm 0.1$	$26.7 \pm 0.1$	$10696 \pm 1$
511867	SAMI	Eq 2	$206.0 \pm 2$	$46 \pm 1$	$24.9 \pm 0.1$	$24.5 \pm 0.2$	$16493 \pm 1$
IC 1320	AMUSING++	Eq 6	$85 \pm 0$	$57 \pm 3$	$165.4 \pm 0.1$	$168.7 \pm 0.0$	$4950 \pm 0$

ble 6 for each object. Figure 8 shows the observed velocity, the best model from NS methods, the residual maps and the radial profiles of the different kinematic components for each considered model. Each row in this figure represents the outputs for a different galaxy.

The manga-9894-6104 galaxy is well described by the circular model. It shows a symmetric velocity field with orthogonal major and minor axes. The circular model describes well the observed velocities and produces small residuals of the order of  $\pm 10 \text{ km s}^{-1}$ . The rotation curve is flat within the FoV, with  $V_{\text{max}} \approx 248 \text{ km s}^{-1}$ .

The velocity field of SAMI511867 shows a slight twist along the minor axis, which is well reproduced by the radial flow model. Significant contributions of radial motions of the order of  $40 \text{ km s}^{-1}$  are observed across the SAMI FoV. However, because of its

small FoV, large PSF  $\approx 2''$  and the physical spatial resolution (FWHM  $\approx 2 \text{ kpc}$ ), parameters derived in Table 6 could be affected by these effects.

Finally, IC 1320 is part of the AMUSING++ galaxy compilation. This object was observed with the modern instrument MUSE (e.g., Bacon et al. 2010). The IFU of this instrument has the smallest spaxel size ( $0.2''$ ) and the best spatial resolution (seeing limited) of the data analyzed here; as a consequence, IC 1320 shows a velocity field rich in details. Among the different kinematic models, the harmonic model showed the lowest BIC value. The  $c_1$  component, which is a proxy of the circular rotation, is mostly flat across its optical extension with  $v_{\text{max}} \approx 200 \text{ km s}^{-1}$ . Non-circular terms are dominant within the inner  $10''$ . The  $c_3$  and  $s_3$  coefficients may indicate the presence of stream flows associated with spiral arms or a stellar bar.

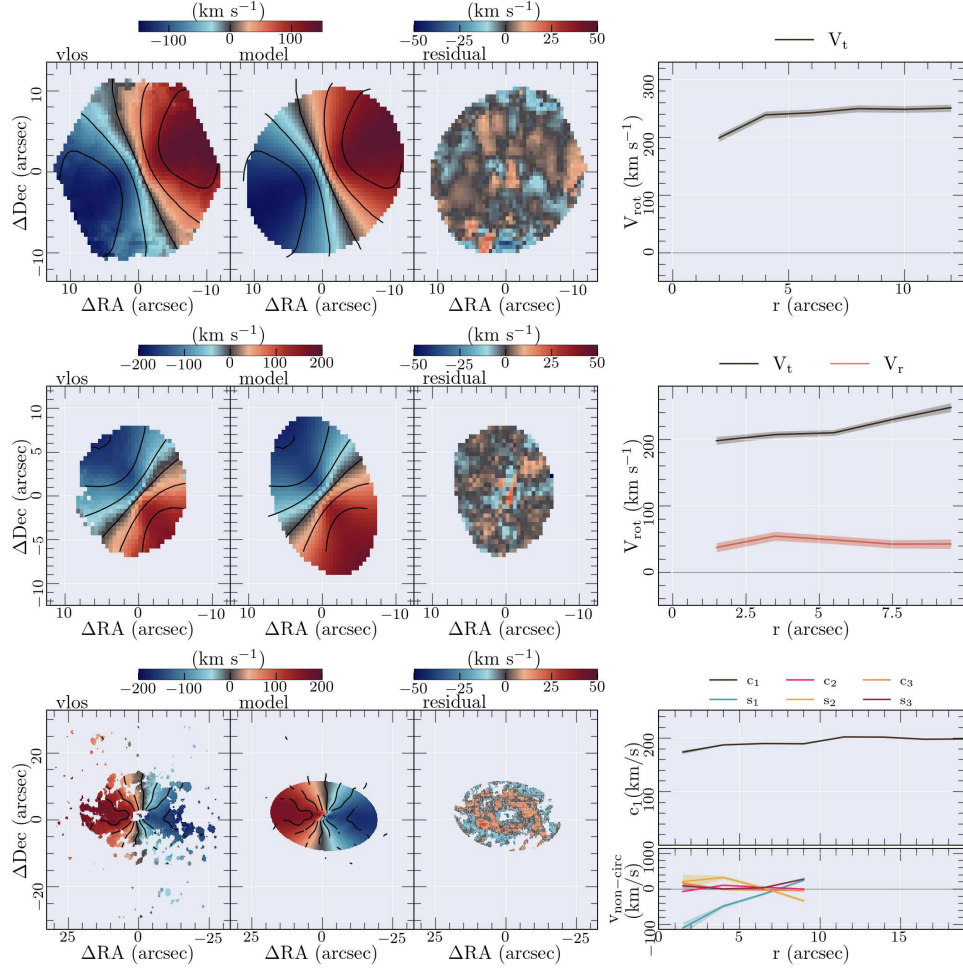


Fig. 8. Implementation of XookSuut on different velocity maps. Each set of panels, from top to bottom, corresponds to a different galaxy taken from different IFS galaxy surveys (i.e., MaNGA, SAMI and AMUSING++ from top to bottom). In each row, from left to right: (i) the  $H\alpha$  velocity field; (ii) best two-dimensional model from NS; (iii) residual map of the fitting; (iv) radial variation of the different velocities in the considered model. Shadow regions in this plot represent the  $1\sigma$  credible interval obtained from NS. Note that each map has different instrumental configurations and FoVs. Iso-velocity contours spaced by  $\pm 50 \text{ km s}^{-1}$  are overlayed on each velocity map. The color figure can be viewed online.

## REFERENCES

- Allen, J. T., Croom, S. M., Konstantopoulos, I. S., et al. 2015, *MNRAS*, 446, 1567, <https://doi.org/10.1093/mnras/stu2057>
- Ashton, G., Bernstein, N., Buchner, J., et al. 2022, *NRvMP*, 2, 39, <https://doi.org/10.1038/s43586-022-00121-x>
- Bacon, R., Accardo, M., Adjali, L., et al. 2010, *SPIE* 7735, 773508, <https://doi.org/10.1117/12.856027>
- Barnes, E. I. & Sellwood, J. A. 2003, *AJ*, 125, 1164, <https://doi.org/10.1086/346142>
- Begeman, K. G. 1987, *HI rotation curves of spiral galaxies*, PhD Thesis, Kapteyn Institute, University of Groningen
- \_\_\_\_\_. 1989, *A&A*, 223, 47
- Bertola, F., Bettoni, D., Danziger, J., et al. 1991, *ApJ*, 373, 369, <https://doi.org/10.1086/170058>
- Binney, J. 2008, *Galactic Dynamics: Second Edition* (Princeton, NJ: PUP)
- Bouché, N., Carfantan, H., Schroetter, I., Michel-Dansac, L., & Contini, T. 2015, *AJ*, 150, 92, <https://doi.org/10.1088/0004-6256/150/3/92>
- Bundy, K., Bershady, M. A., Law, D. R., et al. 2015, *ApJ*, 798, 7, <https://doi.org/10.1088/0004-637X/798/1/7>
- Davis, T. A., Alatalo, K., Bureau, M., et al. 2013, *MNRAS*, 429, 534, <https://doi.org/10.1093/mnras/sts353>
- de Blok, W. J. G., Walter, F., Brinks, E., et al. 2008, *AJ*, 136, 2648, <https://doi.org/10.1088/>

- 0004-6256/136/6/2648
- Di Teodoro, E. M. & Fraternali, F. 2015, MNRAS, 451, 3021, <https://doi.org/10.1093/mnras/stv1213>
- Di Teodoro, E. M., Fraternali, F., & Miller, S. H. 2016, A&A, 594, 77, <https://doi.org/10.1051/0004-6361/201628315>
- Fathi, K., van de Ven, G., Peletier, R. F., et al. 2005, MNRAS, 364, 773, <https://doi.org/10.1111/j.1365-2966.2005.09648.x>
- Foreman-Mackey, D., Hogg, D. W., Lang, D., & Goodman, J. 2013, PASP, 125, 306, <https://doi.org/10.1086/670067>
- Holmes, L., Spekkens, K., Sánchez, S. F., et al. 2015, MNRAS, 451, 4397, <https://doi.org/10.1093/mnras/stv1254>
- Józsa, G. I. G., Kenn, F., Klein, U., & Oosterloo, T. A. 2007, A&A, 468, 731, <https://doi.org/10.1051/0004-6361/20066164>
- Kamphuis, P., Józsa, G. I. G., Oh, S.-H., et al. 2015, MNRAS, 452, 3139, <https://doi.org/10.1093/mnras/stv1480>
- Karamanis, M., Beutler, F., & Peacock, J. A. 2021, MNRAS, 508, 3589, <https://doi.org/10.1093/mnras/stab2867>
- Kormendy, J. 1983, ApJ, 275, 529, <https://doi.org/10.1086/161552>
- Krajnović, D., Cappellari, M., de Zeeuw, P. T., & Copin, Y. 2006, MNRAS, 366, 787, <https://doi.org/10.1111/j.1365-2966.2005.09902.x>
- Lacey, C. G. & Fall, S. M. 1985, ApJ, 290, 154, <https://doi.org/10.1086/162970>
- López-Cobá, C., Sánchez, S. F., Anderson, J. P., et al. 2020, AJ, 159, 167, <https://doi.org/10.3847/1538-3881/ab7848>
- Newville, M., Stensitzki, T., Allen, D. B., & Ingargiola, A. 2014, Zenodo, <https://doi.org/10.5281/zenodo.11813>
- Oh, S.-H., Staveley-Smith, L., Spekkens, K., Kamphuis, P., & Koribalski, B. S. 2018, MNRAS, 473, 3256, <https://doi.org/10.1093/mnras/stx2304>
- Rubin, V. C., Ford, W. K., J., & Thonnard, N. 1980, ApJ, 238, 471, <https://doi.org/10.1086/158003>
- Rubin, V. C. & Ford, W. Kent, J. 1970, ApJ, 159, 379, <https://doi.org/10.1086/150317>
- Sánchez, S. F., Kennicutt, R. C., Gil de Paz, A., et al. 2012, A&A, 538, 8, <https://doi.org/10.1051/0004-6361/201117353>
- Sánchez, S. F., Pérez, E., Sánchez-Blázquez, P., et al. 2016, RMxAA, 52, 21
- Schoenmakers, R. H. M. 1999, Asymmetries in spiral galaxies, PhD Thesis, University of Groningen, Netherlands
- Schoenmakers, R. H. M., Franx, M., & de Zeeuw, P. T. 1997, MNRAS, 292, 349, <https://doi.org/10.1093/mnras/292.2.349>
- Sellwood, J. A. & Sánchez, R. Z. 2010, MNRAS, 404, 1733, <https://doi.org/10.1111/j.1365-2966.2010.16430.x>
- Sellwood, J. A. & Spekkens, K. 2015, arXiv:1509.07120, <https://doi.org/10.48550/arXiv.1509.07120>
- Sellwood, J. A., Spekkens, K., & Eckel, C. S. 2021, MNRAS, 502, 3843, <https://doi.org/10.1093/mnras/stab009>
- Skilling, J. 2006, Bayesian Analysis, 1, 833, <https://doi.org/10.1214/06-BA127>
- Speagle, J. S. 2020, MNRAS, 493, 3132, <https://doi.org/10.1093/mnras/staa278>
- Spekkens, K. & Sellwood, J. A. 2007, ApJ, 664, 204, <https://doi.org/10.1086/518471>
- Trachternach, C., de Blok, W. J. G., Walter, F., Brinks, E., & Kennicutt, R. C., J. 2008, AJ, 136, 2720, <https://doi.org/10.1088/0004-6256/136/6/2720>
- van de Ven, G. & Fathi, K. 2010, ApJ, 723, 767, <https://doi.org/10.1088/0004-637X/723/1/767>
- Walcher, C. J., Wisotzki, L., Bekeraité, S., et al. 2014, A&A, 569, 1, <https://doi.org/10.1051/0004-6361/201424198>
- Warner, P. J., Wright, M. C. H., & Baldwin, J. E. 1973, MNRAS, 163, 163, <https://doi.org/10.1093/mnras/163.2.163>
- Wong, T., Blitz, L., & Bosma, A. 2004, ApJ, 605, 183, <https://doi.org/10.1086/382215>
- Wright, M. C. H. 1971, ApJ, 166, 455, <https://doi.org/10.1086/150975>

Carlos López-Cobá: Institute of Astronomy & Astrophysics, Academia Sinica, 106, Taipei, Taiwan (calopez@asiaa.sinica.edu.tw).

Lihwai Lin : Institute of Astronomy & Astrophysics, Academia Sinica, 106, Taipei, Taiwan (lihwailin@asiaa.sinica.edu.tw)

Sebastián F. Sánchez : Instituto de Astronomía, Universidad Nacional Autónoma de México. Circuito Exterior, Ciudad Universitaria, Ciudad de México 04510, Mexico (sfsanchez@astro.unam.mx)



# THE CALAR ALTO LEGACY INTEGRAL FIELD AREA SURVEY: SPATIAL RESOLVED PROPERTIES

S. F. Sánchez<sup>1</sup>, J. K. Barrera-Ballesteros<sup>1</sup>, L. Galbany<sup>2,3</sup>, R. García-Benito<sup>4</sup>, E. Lacerda<sup>1</sup>, and A. Camps-Fariña<sup>5</sup>

*Received April 12 2023; accepted September 22 2023*

## ABSTRACT

We present the analysis using the pyPipe3D pipeline for the 895 galaxies that comprise the eCALIFA data release (Sanchez et al. 2023), data with a significantly improved spatial resolution (1.0-1.5''/FWHM). We include a description of (i) the analysis performed by the pipeline, (ii) the adopted data model for the derived spatially resolved properties and (iii) the catalog of integrated, characteristics and slope of the radial gradients for a set of observational and physical parameters derived for each galaxy. We illustrate the results of the analysis (i) using the NGC 2906 galaxy, showing the spatial distribution of the different derived parameters, and (ii) showing the distribution of the spatial resolved ionized gas across the [O<sub>III</sub>]/H $\beta$  vs. [N<sub>II</sub>]/H $\alpha$  diagram for the whole galaxy sample. A general agreement is found with published results, with a clear improvement in the tracing of radial patterns and the segregation of individual ionized structures. Access to all the discussed data products: [http://ifs.astroscu.unam.mx/CALIFA\\_WEB/public\\_html/](http://ifs.astroscu.unam.mx/CALIFA_WEB/public_html/).

## RESUMEN

Presentamos el análisis utilizando pyPipe3D en las 985 galaxias de la distribución de datos eCALIFA (Sanchez et al. 2023), los cuales presentan una mejora significativa en la resolución espacial (1.0-1.5''/FWHM); incluimos una descripción de (i) el análisis realizado por el dataducto, (ii) el modelo de datos adoptado para las propiedades espacialmente resueltas obtenidas, y (iii) el catálogo de propiedades físicas y observacionales, integradas, características y las pendientes de sus gradientes radiales. Ilustramos los resultados del análisis (i) con la galaxia NGC 2906, mostramos la distribución espacial de los diferentes parámetros obtenida, y (ii) exploramos la distribución del gas ionizado espacialmente resuelto a lo largo del diagrama [O<sub>III</sub>]/H $\beta$  vs. [N<sub>II</sub>]/H $\alpha$  para la muestra completa de galaxias. Se reporta un acuerdo general con resultados anteriores, mejorando la determinación de patrones radiales y la segregación de estructuras ionizadas. Acceso a los productos del análisis: [http://ifs.astroscu.unam.mx/CALIFA\\_WEB/public\\_html/](http://ifs.astroscu.unam.mx/CALIFA_WEB/public_html/).

*Key Words:* galaxies: evolution — galaxies: star formation — galaxies: stellar content — galaxies: ISM — techniques: imaging spectroscopy

## 1. INTRODUCTION

The Calar Alto Legacy Integral Field Area (CALIFA) project is an integral field spectroscopic (IFS) galaxy survey focused on the exploration of the spatial resolved spectroscopic properties of a statistical well defined and significant sample of galaxies in the nearby survey (Sánchez et al. 2012). It selected galaxies using their optical extension (diameter) as the primary crite-

rion ( $D_{iso} \approx 60''$ ), in order to fit them within the field-of-view of the adopted integral-field unit (PPAK; Kelz et al. 2006). Besides that, the sample was restricted to a redshift range around  $z \approx 0.015$ , and a lower-limit to the apparent magnitude was imposed to limit the contribution of dwarf galaxies that would in other case dominate the statistics (Walcher et al. 2014). This survey gathered data for a time period between 2010 and 2016, and presented its last formal data release in Sánchez et al. (2016a). Afterwards, a set of programs continue using similar selection criteria and the same instrumental and observational setup to explore galaxies under-represented in the original sample, like companion galaxies in interacting

<sup>1</sup>Instituto de Astronomía, Universidad Nacional Autónoma de México, México.

<sup>2</sup>Institute of Space Sciences (ICE, CSIC), Campus UAB, Spain.

<sup>3</sup>Institut d'Estudis Espacials de Catalunya (IEEC), Spain.

<sup>4</sup>Instituto de Astrofísica de Andalucía (IAA/CSIC), Spain.

<sup>5</sup>Universidad Complutense de Madrid (UCM), Spain.

systems, cluster members, and in particular supernovae hosts (e.g. Galbany et al. 2018). All those additional subsamples of galaxies can be considered as extensions of the original sample, comprising the so-called extended CALIFA compilation (e.g. Sánchez et al. 2016a; Lacerda et al. 2020; Espinosa-Ponce et al. 2020).

In a recent companion article Sanchez et al. (2023) presented the final compilation of the extended CALIFA data set (eCALIFA), releasing the data cubes using an improved version of the data-reduction that significantly improves the spatial resolution and image quality. This data release (DR) comprises the data cubes corresponding to the V500 setup (e.g., low-resolution Sánchez et al. 2012) of 895 individual galaxies, together with a set of integrated and central aperture observational and physical parameters included in a single table <sup>6</sup>.

Following an approach similar to that adopted in previous DRs of IFS galaxy surveys (e.g. Sánchez et al. 2022), we distribute in this paper the data products of the analysis for this data set using the `pyPipe3D` pipeline (Lacerda et al. 2022). `pyPipe3D` is a recently updated version of `Pipe3D` fully coded in `python`. The `Pipe3D` pipeline makes use of the routines and algorithms included in the `FIT3D` package (Sánchez et al. 2016c), whose main goal is to extract the properties of the ionized gas and the stellar component from IFS data in the optical range. `Pipe3D` has been frequently used to explore the data from different surveys: e.g., CALIFA (Sánchez-Menguiano et al. 2016; Espinosa-Ponce et al. 2020), SAMI (Sánchez et al. 2019b), AMUSING++ (Sánchez-Menguiano et al. 2018; López-Cobá et al. 2020) and MaNGA (Sánchez et al. 2018, 2022).

The structure of this article is as follows: (i) §2 includes a description of the explored data, with a brief summary of the data reduction; (ii) the analysis performed on the data is included in §3, comprising (iii) a summary of the main properties of `pyPipe3D` (§3.1), that includes (iii.1) a description of the adopted spatial binning (§3.1.1), (iii.2) details on the stellar population fitting (§3.1.2), (iii.3) how the emission line properties are derived (§3.1.3), (iii.4) a description of the derivation of stellar indices (§3.1.4), and finally (iii.5) how the errors of the different parameters are derived (§3.1.5) and (iii.6) the final masks generated to exclude field stars and low signal-to-noise (S/N) regions (§3.2); (iv) a description of the physical quantities derived from `pyPipe3D` data products (such as the stellar mass,  $M_\star$  and the star-formation rate, SFR) is included in §3.3, with a particular description of the derivation of some kinematics parameters, such as the specific angular momentum ( $\lambda_R$ ) included in §3.3.1; (v) Finally, we describe how we derive

the integrated, characteristics and slope of radial gradients of different properties in §3.4; (vi) The results of all these analyses is included in §4, comprising a description of the adopted data format (§4.1), and each of its extensions (§4.1.1 to §4.1.6); (vii) §4.3 illustrates the content of the derived data products using NGC 2906 as an archetype galaxy, with (vii.1) a detailed exploration of the properties of the ionized gas (§4.3.1) and (vii.2) a comparison of the detectability of H II regions among the current data, the former reduced data set, and data of a much better spatial resolution (§4.3.2; (viii) an exploration of the different ionizing sources across the extension of galaxies is included in §4.4; (ix) the conclusions of the current study are included in §5.

When required along the current study, we adopted an standard  $\Lambda$  Cold Dark Matter cosmology with the parameters:  $H_0=71$  km/s/Mpc,  $\Omega_M=0.27$ ,  $\Omega_\Lambda=0.73$ .

## 2. DATA

As described previously the data analyzed in this article comprise the IFS data cubes included in the eCALIFA data release (Sanchez et al. 2023). These data were acquired using the 3.5m telescope at the Calar Alto observatory using the PPAK integral field unit (Kelz et al. 2006) of the PMAS spectrograph (Roth et al. 2005). All observations were performed with the V500 grating, set up at the same goniometer angle, using a similar exposure time and the same dithering scheme (to cover completely the FoV) as the one designed and adopted by the CALIFA survey (Sánchez et al. 2012, 2016a, for more details). This setup allows to cover a wavelength range between 3745-7500Å, with a spectral resolution of  $R \approx 850$  (FWHM  $\approx 6.5\text{\AA}$ ), covering an hexagonal area of  $74'' \times 64''$ .

The data were reduced using version 2.3 of the CALIFA pipeline, described in detail in Sanchez et al. (2023), and previous studies (Sánchez 2006; García-Benito et al. 2015; Sánchez et al. 2016a). We present here a brief summary of the most relevant steps: (i) pre-processing the raw data to join in a single frame the data read by different amplifiers, removing the bias, normalizing by the GAIN, and cleaning for cosmic-rays, (ii) identifying and tracing the spectra corresponding to different fibers in the CCD, obtaining the width of the light projected along the dispersion and cross-dispersion axis, (iii) extraction of the spectra using the trace and widths estimated during the previous setup, removing the effects of the stray-light, (iv) performing a wavelength calibration and re-sampling of the data to follow a linear wavelength solution ( $2\text{\AA}/\text{spectral pixel}$ ), (v) homogenization of the spectral resolution along the wavelength range fixing the final resolution to FWHM =  $6.5\text{\AA}$ , (vi) correcting for the differential fiber-to-fiber transmission, (vii) flux-calibrating

<sup>6</sup>[http://ifs.astroscu.unam.mx/CALIFA\\_WEB/public\\_html/](http://ifs.astroscu.unam.mx/CALIFA_WEB/public_html/).

the spectra, (viii) separating the science fibers, covering the central hexagonal region, from those fibers that sample the sky (and those coupled to the calibration), generating and subtracting a night-sky spectrum for each dither pointing, (ix) glueing the three dithering pointings into a single spectral frame with its corresponding position table, (x) derivation of the astrometric solution for each dithering pointing using the data from the PanStarrs survey as astrometry reference (PS; Chambers et al. 2016; Flewelling et al. 2020), correcting the nominal position table based on this registration, (xi) correcting of the broken fibers and vignetted regions of the spectra using the information of adjacent fibers, and finally (xii) implementing a new image reconstruction procedure that modifies the previously adopted interpolation kernel (Sánchez et al. 2016a), introduces a low-order deconvolution procedure, and a final monochromatic flat-fielding.

The major differences of this new reduction procedure with respect to previous versions are introduced in the last three steps. As a result a considerable improvement in the image quality and the final spatial resolution is obtained, that approaches that provided by the natural seeing ( $\text{FWHM}_{psf} \approx 1.5''$ , on average). This improved spatial resolution requires that the new data cube have a smaller spaxel size ( $0.5''/\text{spaxel}$ ) for a proper sampling of the point-spread-function (PSF). This is half of the size of the CALIFA data cubes delivered in previous DR (Husemann et al. 2013; García-Benito et al. 2015; Sánchez et al. 2016a). Finally, the absolute photometry is anchored to that of the PS survey, in contrast to previous reductions in which the Sloan Digital Sky Survey (SDSS York et al. 2000) photometry was adopted.

The final data set, once a set of quality control criteria is established, comprises 895 cubes, each one corresponding to an individual galaxy. Sanchez et al. (2023) demonstrate that this compilation, covering a wide range of galaxy morphologies and masses ( $\approx 10^7 - 10^{12} M_{\odot}$ ), behaves as a diameter selected sample, being roughly representative of the population of galaxies in the nearby universe ( $z \approx 0.015$ ). For more details on the data reduction, its quality and the properties of the sample we refer the reader to Sanchez et al. (2023).

### 3. ANALYSIS

As indicated before, the analysis performed on the described dataset follows Sánchez et al. (2022). We estimate the main spatial resolved, characteristics and integrated properties of each galaxy by applying `pyPipe3D` to each data cube. Then, the data products provided by this pipeline were processed to obtain a set of physical quantities. We integrated them galaxy-wide, and explored their radial distributions to derive their value at the effective radius ( $Re$ ), i.e., the characteristic value, and the

radial gradient. We present here a brief summary of the analysis and the derived quantities, referring to previous publications for more details to avoid repetition (in particular to Sánchez et al. 2016a, 2021, 2022).

#### 3.1. `pyPipe3D` Analysis

We use `pyPipe3D` (Lacerda et al. 2022), the new version of the `Pipe3D` pipeline (Sánchez et al. 2016b). This version adapts to python the algorithms and analysis sequence of the precedent one, improving its performance thanks to the computational capabilities of this coding language, and correcting some bugs when necessary. `Pipe3D` is a well-proved pipeline, that has been used to study IFS data from different data sets, including the massive exploration of CALIFA (e.g. Cano-Díaz et al. 2016; Espinosa-Ponce et al. 2020), MaNGA (e.g. Ibarra-Medel et al. 2016; Barrera-Ballesteros et al. 2018; Sánchez et al. 2019a; Bluck et al. 2019; Sánchez-Menguiano et al. 2019), SAMI (e.g. Sánchez et al. 2019b), and AMUS-ING++ data sets (Sánchez-Menguiano et al. 2018; López-Cobá et al. 2020). Besides that, it has been tested using mock data sets and ad-hoc simulations based on hydrodynamical simulations (Guidi et al. 2018; Ibarra-Medel et al. 2019; Sarmiento et al. 2022). We present here just a brief description of the code to avoid unnecessary repetitions.

##### 3.1.1. *Spatial Binning/Tessellation*

`pyPipe3D` pipeline uses the algorithms included in the `pyFIT3D` package to analyze automatically each data cube. However, to provide a reliable result in the analysis of the stellar population (that we will describe below) it is required to perform a spatial binning to increase the signal-to-noise (S/N) above a minimum value (see Sánchez et al. 2016c; Lacerda et al. 2022, for details). The binning procedure adopted by `pyPipe3D` preserves the shape of the original light distribution to a larger extent than other methods frequently implemented in the literature (see Sánchez et al. 2016c, for detailed discussion on the topic). Then the fitting procedure is applied to each binned spectrum, recovering the parameters of the stellar population and emission lines in each tessella/spatial-bin.

We need to recall that the new reduced data (Sanchez et al. 2023), have a spaxel scale 4-times smaller than the original ones. Besides, the whole image reconstruction algorithm has changed considerably. This means that the covariance pattern between adjacent spaxels has changed too. Thus, a new covariance correction has to be introduced during the binning/tessellation process, as discussed in §5.4 of Sanchez et al. (2023), shown in Figure 26. The code has been modified to take into account this modification.

### 3.1.2. Stellar Population Analysis

As already mentioned, each binned spectrum is analyzed using `pyFIT3D`. This code separates the stellar and ionized-gas emission in each spectrum by creating a model of the former one using a linear combination of a set of pre-defined single stellar populations (SSP) spectra ( $S_{ssp}$ ). Following Sánchez et al. (2022) and Sanchez et al. (2023), we use the `MASTAR_sLOG` SSP library for the current analysis. This library comprises 273 SSP templates with 39 ages,  $\mathcal{A}_\star/\text{Gyr} = (0.001, 0.0023, 0.0038, 0.0057, 0.008, 0.0115, 0.015, 0.02, 0.026, 0.033, 0.0425, 0.0535, 0.07, 0.09, 0.11, 0.14, 0.18, 0.225, 0.275, 0.35, 0.45, 0.55, 0.65, 0.85, 1.1, 1.3, 1.6, 2, 2.5, 3, 3.75, 4.5, 5.25, 6.25, 7.5, 8.5, 10.25, 12, 13.5)$ , and 7 metallicities,  $Z_\star = (0.0001, 0.0005, 0.002, 0.008, 0.017, 0.03, 0.04)$ . Details on the library and its ingredients are included in Appendix A of Sánchez et al. (2022). Before doing this modelling, the SSP templates are shifted and broadened to take into account the systemic velocity ( $v_\star$ ) and the velocity dispersion ( $\sigma_\star$ ), assuming that the line-of-sight velocity distribution follows a Gaussian distribution  $G(v_\star, \sigma_\star)$ . In addition, the dust attenuation affecting the stellar populations ( $A_{V,\star}$ ) is modelled using the Cardelli et al. (1989) extinction law ( $E(\lambda)$ ). The derivation of these three parameters is performed by selecting a limited sub-set of the SSP spectra that limits the range of ages and metallicities, avoiding possible degeneracies.

Then, the shifted, broadened and dust attenuated SSP templates are fitted to the data by an iterative set of linear decompositions that includes or removes templates into the library forcing the procedure to provide only positive coefficients ( $w_{ssp,\star,L}$ ) in the linear decomposition as explained in Sánchez et al. (2016c) and Lacerda et al. (2022). Finally, the observed spectrum ( $S_{obs}$ ) is fitted by a stellar model ( $S_{mod}$ ) that follows the expression

$$S_{obs}(\lambda) \approx S_{mod}(\lambda) = \left[ \sum_{ssp} w_{ssp,\star,L} S_{ssp}(\lambda) \right] 10^{-0.4 A_{V,\star} E(\lambda)} * G(v_\star, \sigma_\star). \quad (1)$$

In the particular implementation for the current analysis the light-fractions or weights of the stellar population decomposition (i.e.,  $w_{\star,L}$ ), are normalized to the 5450–5550 Å spectral range (approximately the *V*-band central wavelength).

`pyFIT3D` derives the luminosity- and mass-weighted parameters of the stellar population ( $P_{LW}$  and  $P_{MW}$ ) with the coefficients of the stellar decomposition described before, using the equation:

$$\begin{aligned} \log P_{LW} &= \sum_{ssp} w_{ssp,\star,L} \log P_{ssp}, \\ \log P_{MW} &= \frac{\sum_{ssp} w_{ssp,\star,L} Y_{ssp,\star} \log P_{ssp}}{\sum_{ssp} w_{ssp,\star,L} Y_{ssp,\star}}, \end{aligned} \quad (2)$$

where  $P_{ssp}$  is the value of a particular parameter for each SSP (for instance, age,  $\mathcal{A}_\star$ , or metallicity,  $Z_\star$ ), and  $Y_{ssp,\star}$  is the stellar mass-to-light ratio. It also estimates the stellar mass across the considered aperture, using the equation:

$$M_\star = L_V \sum_{ssp} w_{ssp,\star,L} Y_{ssp,\star}, \quad (3)$$

where  $L_V$  is the dust-corrected *V*-band luminosity.

### 3.1.3. Emission Line Analysis

To derive the properties of the ionized gas emission the code subtracts the best stellar population model from the observed one. Then, it fits each emission line (*el*) extracted from a pre-defined list<sup>7</sup> with a Gaussian function ( $G(v_{el}, \sigma_{el})$ ), where  $v_{el}$  and  $\sigma_{el}$  are the *el* velocity and velocity dispersion, respectively, scaled by the integrated flux intensity ( $F_{el}$ ). The bulk procedure (analysis of stellar population and emission lines) is repeated iteratively, using the best emission line model to decontaminate the original spectrum that then is modelled by the combination of SSPs. In each iteration the  $\chi^2$ , considering both the stellar population and emission line model, is adopted as the figure of merit of the quality of the fitting.

The described procedure provides the properties of the emission lines for each tessella/spatial-bin. In order to recover the properties of the emission lines spaxel-wise, an additional procedure is implemented. First, the best fitted stellar population model derived for each tessella is scaled to each spaxel within the bin using the so-called dezonification parameter (DZ, Cid Fernandes et al. 2013). Then this spaxel-wise stellar population model is subtracted from the original data cube to create the so-called pure-GAS cube, which comprises the emission from the ionized gas, plus noise and residuals of the stellar population fitting. Finally, two different procedures are implemented to extract the parameters of the ionized gas emission lines from this cube: (i) a Gaussian model similar to the one described before is applied to the strongest emission lines in the wavelength range (listed before); and (ii) a weighted-moment analysis is performed for a large set of emission lines, including both the strong and weak emission lines. Both methods provide the same three parameters ( $F_{el}$ ,  $v_{el}$  and  $\sigma_{el}$ ). However, the second one determines also the equivalent width of each analyzed emission line ( $EW_{el}$ ). The complete list of emission lines analyzed using this latter method will be described later (§ 4.1.5).

### 3.1.4. Stellar Indices

In addition, `pyPipe3D` estimates a set of the stellar indices for each voxel/tessella. For doing so, a stellar

<sup>7</sup>In this analysis, [O II]  $\lambda 3727$ , H $\delta$ , H $\gamma$ , H $\beta$ , [O III]  $\lambda 4959, 5007$ , H $\alpha$ , [N II]  $\lambda 6548, 84$  and [S II]  $\lambda 6717, 31$



spectrum is first generated, decontaminated by the ionized gas contribution by removing the best emission line model derived along the fitting procedure described before. Afterwards, the equivalent width is derived for each stellar index defining three wavelength ranges: (i) a central one at which the stellar index is defined, and (ii) two adjacent ones at which the density flux of the continuum is estimated. The particular list of stellar indices included in the current analysis is described in §4.1.3.

### 3.1.5. Error Estimation

The errors of all the derived parameters are estimated by performing a Monte Carlo (MC) procedure. Each original spectrum (spaxel-wise or binned) is perturbed by co-adding a random value using the errors provided by the data reduction. Then, the full procedure is repeated for each perturbed spectrum, defining the errors as the standard deviation of the individual values derived for each set of modified spectra. We should note that when an ionized-gas or stellar population model is subtracted from the original spectrum the errors are updated, considering the uncertainties of the model. For more details on the estimation of the errors we refer the reader to Lacerda et al. (2022).

Once more we remind the reader that the new data reduction introduces a new image reconstruction scheme that improves the spatial resolution, and therefore the data cubes have a spaxel size two times smaller than the one adopted in previous reductions:  $0.5''/\text{spaxel}$  Sanchez et al. (2023), rather than  $1.0''/\text{spaxel}$  (Sánchez et al. 2016a). Thus, the flux per spaxel at any wavelength is now four times smaller than in the previous versions of the data reduction. On the other hand, the S/N per arcsec<sup>2</sup> is roughly the same in the two versions of the data reduction, as seen when comparing Figure 5 of Sanchez et al. (2023) with Figure 14 of Sánchez et al. (2016a). Therefore, the S/N per spaxel is  $\approx 4$  times lower at any wavelength in the new data set, what affects equally the continuum and emission lines. This has to be taken into account in any spatial resolved analysis performed with the new data products.

### 3.2. Data Masks

The errors of each parameter, and in particular the error of the flux intensity, are used to define different masks. In the case of the continuum, we select those regions above a signal-to-noise ratio of one prior to the spatial binning described in §3.1.1. This defines a selection mask that is applied prior to any analysis of the stellar population properties. In addition to this mask, regions strongly affected by foreground field stars should be masked too. As we describe in Sanchez et al. (2023) we follow the procedure included in Sánchez et al. (2022),

searching for possible foreground field stars in the FoV of the analyzed datacubes, using the Gaia DR3 catalog<sup>8</sup> (Gaia Collaboration et al. 2016, 2021). This catalog comprises the most accurate and complete list of stars with good quality astrometry covering the full sky. Only those sources with an accurate parallax (five times larger than the uncertainty) are selected, and we generate a circular mask of  $2.5''$  around each of them. This mask is then used ignoring the values reported by the analysis in those regions and replacing them by an interpolated version of the values in the adjacent spaxels.

### 3.3. Physical Quantities

The observational properties estimated by pyPipe3D for each spaxel or tessella within the data cubes for both the stellar populations and ionized gas emission lines are used to estimate further physical parameters. Details of the derivation of all them have been extensively discussed in previous articles, in particular in Sánchez et al. (2021) and Sánchez et al. (2022). We provide here with a brief summary to avoid repetition:

**Stellar Masses:** The stellar mass is derived directly by pyFIT3D as one of the quantities directly estimated from the stellar decomposition analysis, as indicated in §3.1.2. From this estimation is derived the stellar mass density ( $\Sigma_\star$ ), and the corresponding values in different apertures. Based on this value it is possible to derive the integrated  $\Upsilon_\star$  (i.e.,  $M_\star/L_\star$  for each spaxel), that is different than the LW or MW average value that would be provided by equation 2.

**Star-formation and chemical enrichment histories:** Equations 2 and 3 can be integrated up to a certain look-back time, correcting for the mass loss when needed (e.g. Courteau et al. 1996), obtaining the mass-assembly (MAH, Pérez et al. 2013; Ibarra-Medel et al. 2016, 2019), star-formation (SFH, Panter et al. 2007; González Delgado et al. 2017; López Fernández et al. 2018; Sánchez et al. 2019a), and chemical-enrichment histories (ChEH, Vale Asari et al. 2009; Camps-Fariña et al. 2021, 2022). From those distributions we estimate (i) the current SFR ( $\text{SFR}_{\text{ssp,t}}$ ), by restricting the SFH to the most recent (short) time scales (e.g.,  $\text{SFR}_{\text{ssp,10Myr}}$ , average SFR in the last 10 Myr), (ii) a set of time-scales that characterize the SFHs, defined as the time in which a fraction of the stellar mass is formed ( $T\%$ , e.g.,  $T80$ , time in which 80% of the stellar mass was formed); and (iii) the metallicity at those time scales ( $a_{\text{ZH}}T\%$ ).

**Emission line ratios:** line ratios are frequently used to estimate the nature of the ionizing source and the physical properties of the ionized gas itself. From the emission line fluxes derived using the moment analysis we estimate a set of line ratios including the most popular

<sup>8</sup><https://www.cosmos.esa.int/web/gaia/dr3>

ones, namely  $[\text{O II}]/\text{H}\beta$ ,  $[\text{O III}]/\text{H}\beta$ ,  $[\text{O I}]/\text{H}\alpha$ ,  $[\text{N II}]/\text{H}\alpha$ ,  $[\text{S II}]/\text{H}\alpha$  and  $\text{H}\alpha/\text{H}\beta$ .

**Ionized gas dust extinction:** The  $\text{H}\alpha/\text{H}\beta$  line ratio is used to estimate the dust extinction ( $A_{\text{V,gas}}$ ). To do so we adopt a nominal ratio for  $\text{H}\alpha/\text{H}\beta$  of 2.86, that corresponds to case-B recombination with an electron density of  $n_e=100 \text{ cm}^{-3}$  and a temperature of  $T_e=10^4 \text{ K}$  (Osterbrock 1989). The Cardelli et al. (1989) dust attenuation law was applied, with a total-to-selective extinction value of  $R_V=3.1$ .

**Oxygen and nitrogen abundances and ionization parameter:** the line ratios described before are frequently used to estimate the oxygen and nitrogen abundances and the ionization parameter using strong-line calibrators. These calibrators are only valid for those ionization sources for which they are derived (i.e., regions ionized by OB stars related with recent SF events). We classify the ionizing source following Sánchez et al. (2021), selecting as SF regions those located below the demarcation line defined by Kewley et al. (2001) in the  $[\text{O III}]/\text{H}\beta$  vs  $[\text{N II}]/\text{H}\alpha$  diagnostic diagram with an  $\text{EW}(\text{H}\alpha) > 3\text{\AA}$ . Then, for those regions we estimate the oxygen (O/H) and nitrogen (N/H and/or N/O) abundance and the ionization parameter ( $U$ ) using a set of strong-line calibrators. In total we use 28 calibrators for the oxygen abundances, 3 calibrators for the nitrogen abundance and 4 for the ionization parameter. The complete list of calibrators, the line ratios that are used to derive them, and a detailed description of their nature is included in Sánchez et al. (2022, in particular in Appendix D and Table 15). We refer the reader to that reference to avoid repetition.

**$\text{H}\alpha$  based star-formation rate:** The SFR is derived spaxel-wise using the Kennicutt (1998) relation between this quantity and the dust-corrected  $\text{H}\alpha$  luminosity:

$$\text{SFR} (M_{\odot} \text{ yr}^{-1}) = 0.79 \cdot 10^{-41} L_{\text{H}\alpha} (\text{erg/s}). \quad (4)$$

This relation corresponds to a Salpeter (1955) IMF. Like in the case of other extensive quantities (e.g.  $M_{\star}$ ), from the SFR estimated at each spaxel it is possible to derive the SFR surface density ( $\Sigma_{\text{SFR}}$ ), and the corresponding quantities at different apertures. Following Sánchez et al. (2021) we derive the SFR for all spaxels, irrespective of its ionizing source. However, it is possible to select only those regions compatible with being ionized by young massive OB-stars (as indicated in the previous section) in the derivation of the integrated or aperture limited SFR. A correction to the possible contribution of other ionizing sources can also be applied, either applying a mask that exclude the contaminating regions or estimating its contribution. Following Sánchez et al. (2022) we also estimate the SFR decontaminated from the contribution of

the diffuse ionization due to old/evolved post-AGB stars (e.g. Singh et al. 2013).

**Molecular gas estimation:** we use the recent calibrators proposed by Barrera-Ballesteros et al. (2020) and Barrera-Ballesteros et al. (2021) to estimate the molecular gas mass density from the dust attenuation:

$$\begin{aligned} \Sigma_{\text{mol}} (M_{\odot} \text{ pc}^{-2}) &= 23 A_{\text{V,gas}} (\text{mag}), \\ \Sigma_{\text{mol}} (M_{\odot} \text{ pc}^{-2}) &= 1.06 A_{\text{V,gas}}^{2.58} (\text{mag}). \end{aligned} \quad (5)$$

Different variations of this calibrator have been applied, including possible corrections taking into account the  $\text{EW}(\text{H}\alpha)$ , the oxygen abundance, and using as tracer of the gas the dust attenuation derived for the stellar populations ( $A_{\text{V},\star}$ ) and the ionized gas ( $A_{\text{V,gas}}$ ).

**Electron density:** The electron density is derived spaxel-wise using the  $[\text{S II}]\lambda 6717,31$  line ratio solving the equation:

$$\frac{[\text{S II}]\lambda 6717}{[\text{S II}]\lambda 6731} = 1.49 \frac{1 + 3.77x}{1 + 12.8x}, \quad (6)$$

where  $x = 10^{-4} n_e t^{-1/2}$ , with  $t$  being the electron temperature in units of  $10^4 \text{ K}$  (McCall et al. 1985), and  $n_e$  being the electron density in units of  $\text{cm}^{-3}$ . We solve this equation assuming a temperature of  $T_e = 10^4 \text{ K}$  (i.e.,  $t = 1$ ). As the dependence of the electron density with  $T_e$  is rather weak this assumption does not affect significantly the derivation of this parameter.

### 3.3.1. Kinematics Parameters

**pyPipe3D** provides the spatial distribution of the stellar and gas velocity and velocity dispersion. From these distributions we estimate (i) the velocity to velocity dispersion ratio ( $\frac{v}{\sigma_R}$ ) for both the stellar and ionized gas components, and (ii) the apparent stellar angular momentum parameter ( $\lambda_R$ ) at different deprojected galactocentric distances ( $R$ ). For  $\frac{v}{\sigma_R}$  we adopt the formula:

$$\frac{v}{\sigma} = \sqrt{\frac{\sum_{r < 1.15R} f_{\star} v_{\star}^2}{\sum_{r < 1.15R} f_{\star} \sigma_{\star}^2}}, \quad (7)$$

where  $f_{\star}$  is the stellar flux intensity in the  $V$ -band, and  $v_{\star}$  and  $\sigma_{\star}$  are the the velocity and velocity dispersions. A similar formula is adopted for the ionized gas, changing each parameter in eq. 7 by the corresponding values derived for the  $\text{H}\alpha$  emission lines. Finally, for  $\lambda_R$  we followed Emsellem et al. (2007), using the formula:

$$\lambda_R = \frac{\sum_{r < 1.15R} f_{\star} r |v_{\star}|}{\sum_{r < 1.15R} f_{\star} R \sqrt{v_{\star}^2 + \sigma_{\star}^2}}, \quad (8)$$

where  $f_{\star}$ ,  $v_{\star}$  and  $\sigma_{\star}$  are the same parameters adopted in Eq. 7. An inclination correction was applied, following

the prescriptions included in the Appendix of Emsellem et al. (2011).

We should note that the spectral resolution of the current data, that corresponds to  $\sigma_{inst} \approx 150 \text{ km s}^{-1}$ , is not optimal to derive these kinematics parameters, in particular in the regime of low velocity dispersion.

### 3.4. Integrated, Aperture Limited and Characteristic Properties

The analysis described so far provides a set of parameters for each individual spaxel, tessella, or as a function of the galactocentric distance. Based on those distributions we estimate for the extensive quantities (e.g.,  $M_*$  or SFR) the values at different apertures: integrated galaxy wide, the value within  $1 Re$ , or in the central aperture ( $1.5''/\text{diameter}$ ). For the intensive quantities (e.g.,  $\Sigma_*$ , the oxygen abundance or any of the analyzed stellar indices), we estimate the azimuthal average radial distribution as described in Sánchez et al. (2021) and Barrera-Ballesteros et al. (2022). Essentially, we use the coordinates of the galaxy, the position angle and ellipticity to trace a set of elliptical apertures of  $0.15 Re$  width, from 0 to  $3.5 Re$  (or the edge of the FoV). Then, for each aperture we estimate the average value of the corresponding parameter ( $P_R$ ) and its standard deviation ( $e_{P_R}$ ). Then, for each of those radial distributions we perform a linear regression to estimate the value at the effective radius ( $P_{Re}$ ) and the slope of the gradient ( $slope_P$ ). As already discussed in previous studies, for many parameters the value at the effective radius can be considered a good characterization of the average value galaxy-wide (e.g. Sánchez et al. 2021, and references therein). For completeness, for some intensive parameters we derive the value in the central aperture and the average value galaxy-wide.

## 4. RESULTS

Along this section we describe the results from the analysis outlined in the previous section, including a description of the delivered data products, together with some examples that illustrate their possible scientific use, highlighting the improvements introduced by the new distributed data set.

### 4.1. Pipe3D Data Model

The analysis described in §3.1 provides a list of parameters estimated at each individual spaxel or within a tessella with their corresponding errors. Thus, for each data cube the analysis provides a set of maps or 2D arrays for each parameter, whose astrometry and dimensions correspond to that of the analyzed data cube. Following Sánchez et al. (2016b, 2018, 2022) we group those maps depending on the analysis that produced them and pack them in a set of 3D arrays or cubes of data products. This

way, each channel in the z-axis of each cube corresponds to the spatial distribution of one particular parameter. Finally, each of those `pyPipe3D` data cubes is stored as an extension of the same FITS file for its distribution.

For the data analyzed along this study the Pipe3D files comprise nine extensions for each derived FITS file: (i) `ORG_HDR`, an initial extension without data, containing all the metadata of the analyzed datacube, in particular the astrometric solution (world coordinate system); (ii) `SSP`, comprises the spatial distributions of the average stellar properties derived by the stellar population fitting (§3.1.2); (iii) `SFH`, includes the spatial distribution of the coefficients  $w_{*,L}$  of the fitting of the stellar population with the templates adopted SSP library (i.e., Eq. 1); (iv) `INDICES`, includes the spatial distribution of the stellar indices (§3.1.4); (v) `ELINES`, comprises the properties of the strong emission lines derived by fitting them with a set of Gaussian functions (§3.1.3); (vi) `FLUX_ELINES` and (vii) `FLUX_ELINES_LONG` include the parameters of the emission lines derived using a weighted-moment analysis (§3.1.3), for a two subsets of emission lines. In the first case we use the list of 54 emission lines adopted in a previous analysis of the CALIFA data using Pipe3D (Sánchez et al. 2016b). In the second case we adopt a larger list of emission lines, with an updated value for the rest-frame wavelength, included in Sánchez et al. (2022), adapted for the more limited wavelength range of the current data (with a total of 130 emission lines); (viii) `GAIA_MASK`, mask of the field stars derived from the Gaia catalog described in §3.2, and finally (ix) `SELECT_REG`, mask of the regions with signal-to-noise larger than 3 in the stellar continuum (V-band), i.e., those regions where the analysis of the stellar population is reliable. A summary of the format of the FITS file is presented in Table 1. For each analyzed galaxy (`CUBENAME.V500.drscube.fits.gz`) we provide one of those files, adopting the nomenclature `CUBENAME.Pipe3D.cube.fits.gz`. The entire list of data products files is distributed in the eCALIFA data release webpage<sup>9</sup>

#### 4.1.1. SSP Extension

This extension comprises the datacube in which are stored: (i) the average properties of the stellar populations derived by `pyPipe3D` based on the decomposition of the stellar population on a set of SSP templates ( $\mathcal{A}_{*,L}$ ,  $\mathcal{A}_{*,M}$ ,  $\mathcal{Z}_{*,L}$  and  $\mathcal{Z}_{*,M}$ ), (ii) parameters such as the stellar mass and the  $\Upsilon_*$ , (iii) the non-linear parameters ( $\nu_*$ ,  $\sigma_*$  and  $A_{V,*}$ ), and (iv) additional parameters describing the light distribution, the binning pattern, and the dezonification scaling applied during the fitting procedure. As the

<sup>9</sup><http://ifs.astroscu.unam.mx/CALIFA/V500/v2.3/pyPipe3D/>

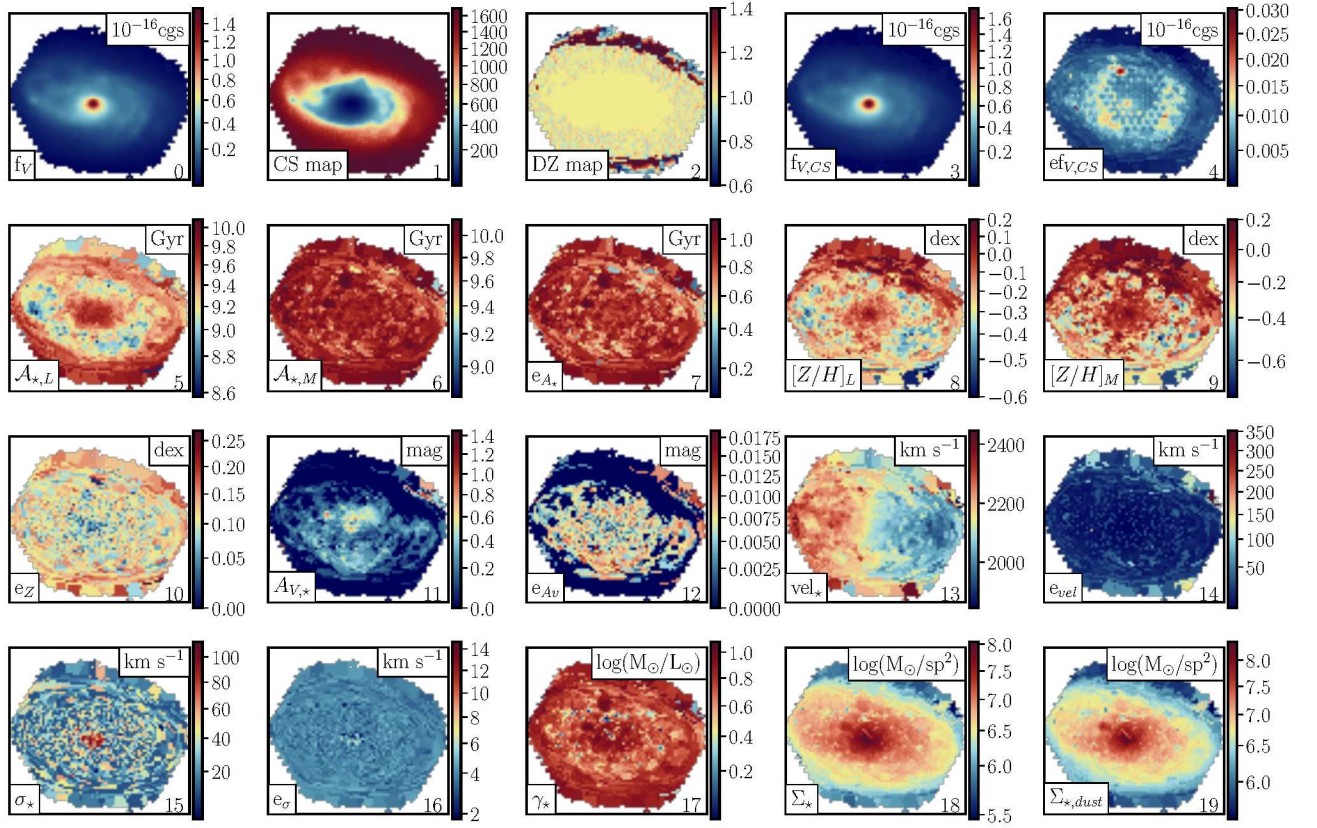


Fig. 1. Example of the content of the SSP extension in the Pipe3D fitsfile, corresponding to the galaxy NGC2906. Each panel shows a color image with the property stored in the corresponding channel of the data cube, as listed in Table 2. The index, corresponding property, and units, are indicated in each panel as a label at bottom-right, bottom-left and top-right of the figure. The color figure can be viewed online.

TABLE 1  
DESCRIPTION OF THE PIPE3D FILE

HDU	EXTENSION	Dimensions
0	ORG_HDR	()
1	SSP	(NX, NY, 21)
2	SFH	(NX, NY, 319)
3	INDICES	(NX, NY, 70)
4	ELINES	(NX, NY, 11)
5	FLUX_ELINES	(NX, NY, 432)
6	FLUX_ELINES_LONG	(NX, NY, 1040)
7	GAIA_MASK	(NX, NY)
8	SELECT_REG	(NX, NY)

NX and NY may change from galaxy to galaxy, being  $\approx 160$  and  $\approx 150$  respectively.

stellar population analysis is performed on the spatial-binned data cube, the parameters stored in this extension reflect this binning. Thus, apart from the original light

distribution and the dezonication scale, all parameters are equal within each considered tessella.

Table 2 describes the parameter delivered in each channel (starting with 0), and its corresponding units (when required). This information is included in a set of header keywords labelled DESC\_N, with N corresponding to each channel in the z-axis. Figure 1 illustrates the content of this extension, showing for each channel the spatial distribution of the stored parameter corresponding to the galaxy NGC 2906, an archetypal spiral galaxy included in the analyzed sample. Some patterns known for this kind of galaxies, like radial gradients in the  $\mathcal{A}_{*,L}$  and  $\mathcal{Z}_{*,L}$ , the drop  $\sigma_*$  from the bulge outwards, and the clear rotational pattern seen in the  $v_*$  map, are evident in this figure. Like in previous sections, for more details on each parameter we refer the reader to Sánchez et al. (2022).



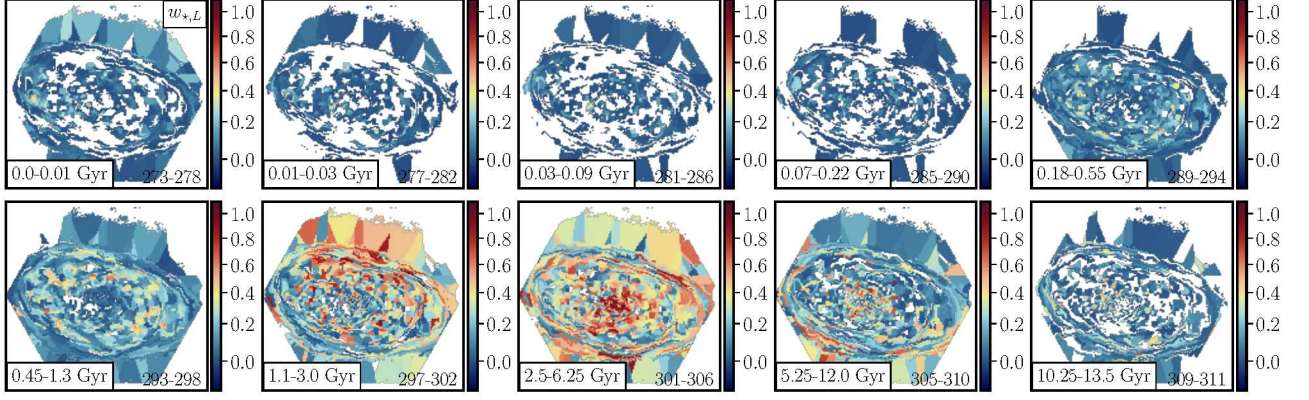


Fig. 2. Example of the content of the SFH extension in the Pipe3D fitsfile, corresponding to the galaxy NGC2906. Each panel shows a color image with the fraction of light at the normalization wavelength ( $w_{*,L}$ ) for different ranges of age included in the SSP library. The range of ages is indicated in the bottom-left inbox, and the corresponding indices of the co-added channels in the SFH extension are shown in the bottom-right legend. For instance, the top-left panel corresponds to the co-adding of all the maps in the SFH\_CUBE from the 273 to the 278, covering the age range between zero and 0.01 Gyr. As described in §4.1.2 and shown in Table 3, these channels run for the indices from 273 to 311, and they corresponds to light-weight maps at a fixed age (each channel) derived by co-adding all the light-weighted maps for the seven different metallicities at that particular age. . For clarity we do not show the individual  $w_{*,L}$  maps included in the SFH extension, as this would require a plot with a total of 318 panels, that would not add any relevant information. The color figure can be viewed online.

#### 4.1.2. SFH Extension

The data cube stored in this extension includes the spatial distribution of the coefficients of stellar decomposition for each SSP template in the adopted library, i.e.,  $w_{*,L}(\mathcal{A}_*, \mathcal{Z}_*)$  in Eq. 1. Thus, the first 273 channels cover the total range of ages (39) and metallicities (7) included in the adopted SSP template (MaStar\_sLOG). In addition 39 additional channels are included comprising the weights corresponding to each age, i.e.,  $w_{*,L}(\mathcal{A}_*)$ , obtained by co-adding all  $w_{*,L}$  corresponding to the same age covering the seven different metallicities (channels from 273 to 311). Finally, 7 additional channels are also included with the weights corresponding to each metallicity, i.e.,  $w_{*,L}(\mathcal{Z}_*)$ , obtained by co-adding all  $w_{*,L}$  corresponding to the same metallicity and covering the 39 different ages (channels from 311 to 318). Table 3 lists the content of each channel in this extension, information included in a set headers keywords named DESC\_N, with N indicating the actual channel (running from 0 to 318)

Figure 2 illustrates the content of this extension, showing the spatial distribution of the weights for each age,  $w_{*,L}(\mathcal{A}_*)$ , re-binned in a set of 10 age ranges. This figure illustrates how the age distribution of the stellar population changes with the galactocentric distance, with a larger (smaller) fraction of light corresponding to older (younger) stellar populations, e.g.,  $\mathcal{A}_* > 2.5\text{Gyr}$  ( $< 300\text{ Myr}$ ) is more concentrated in the inner (outer) regions.

As described in Lacerda et al. (2022) and summarized in §3.1.5, pyPipe3D includes a procedure to estimate the errors of any derived quantity based on a MC procedure. However, for the current extension we decided not to distribute the errors as it would unnecessarily increase the size of this extension beyond the reasonable (due to the number of channels involved). Instead, we recommend the user to estimate the errors from the data themselves. The procedure to do so uses the covariance between adjacent spaxels, estimating the error as the standard deviation within in a box of the size of the PSF FWHM ( $\approx 1.5''$  on average Sanchez et al. 2023) of the residuals once subtracted from the map corresponding to each channel a smoothed version with a Gaussian function of the size of the PSF. This calculation relies on the fact that no parameter should change significantly within the size a resolution element (i.e., the PSF), and therefore, the observed variations spaxel by spaxel should be representative of the error. On average, the typical error of  $w_{*,L}(\mathcal{A}_*, \mathcal{Z}_*)$  for the average S/N of our spectra is of the order of 30-50%, which corresponds to  $\approx 20\%$  ( $\approx 10\%$ ) error for  $w_{\mathcal{A}_*}$  ( $w_{\mathcal{Z}_*}$ )<sup>10</sup>.

#### 4.1.3. INDICES Extension

As described in §3.1.4, pyPipe3D estimates the spatial distribution of a set of stellar indices, using the

<sup>10</sup>The procedure is included in the following notebook [https://github.com/sfsanchez72/califa\\_v2.3/blob/main/CALIFA\\_eDR\\_pyPipe3d.ipynb](https://github.com/sfsanchez72/califa_v2.3/blob/main/CALIFA_eDR_pyPipe3d.ipynb), used to create figures in §4.1.



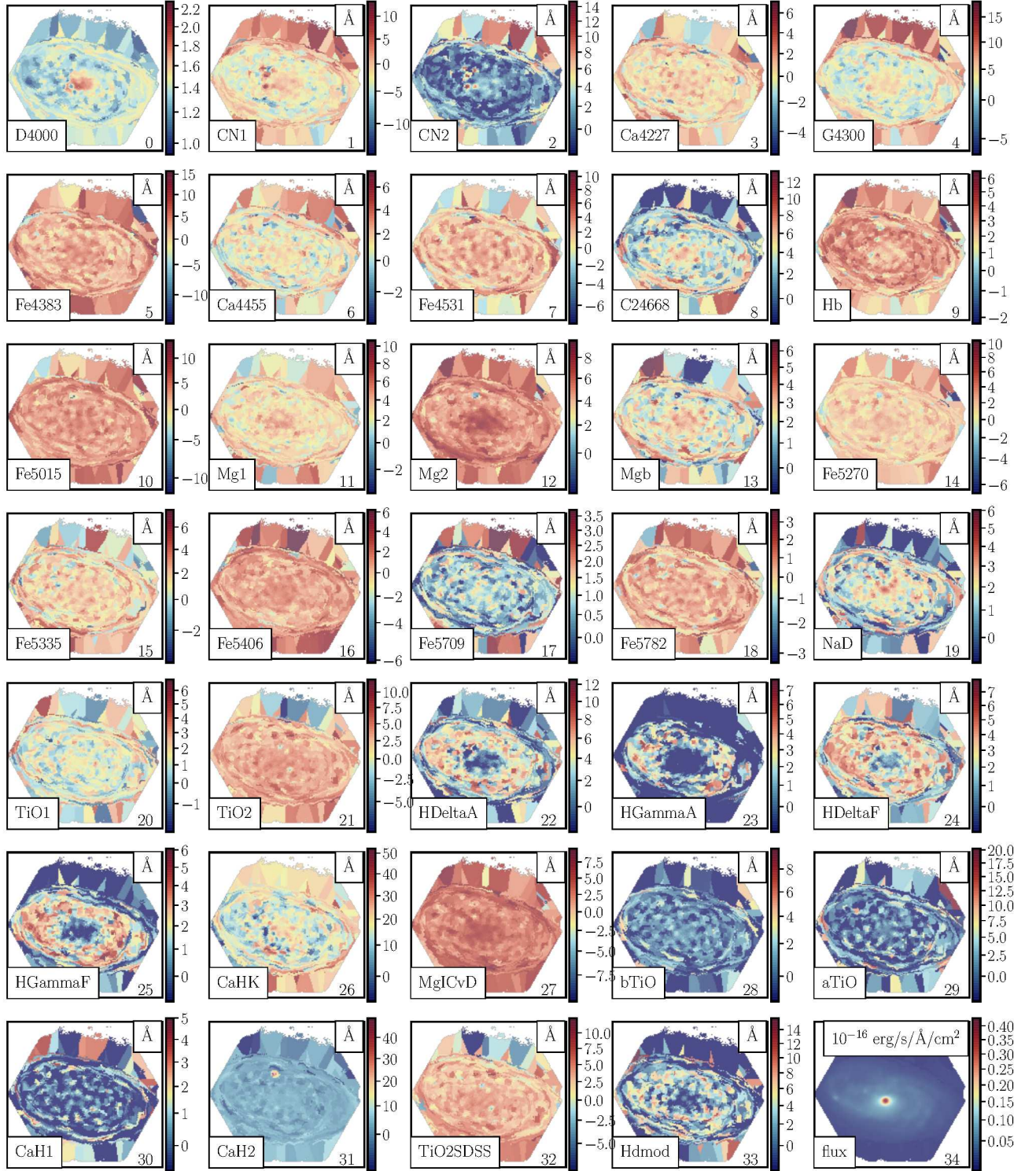


Fig. 3. Example of the content of the INDICES extension in the Pipe3D file, corresponding to the galaxy NGC2906. Each panel shows a color image with the content of a channel in this datacube. The actual content is indicated for each panel in the lower-left, the channel in the lower-right and the units of the represented quantity in the upper-right legend. For the flux and flux error the units are  $10^{-16} \text{ erg/s/Å/cm}^2$ . The colour figure can be viewed online.

TABLE 2

## DESCRIPTION OF THE SSP EXTENSION

Channel	Units	Stellar index map
0	$10^{-16} \text{ erg s}^{-1} \text{ cm}^{-2}$	Unbinned flux intensity at $\approx 5500\text{\AA}$ , $f_V$
1	none	Continuum segmentation index, $CS$
2	none	Dezonification parameter, $DZ$
3	$10^{-16} \text{ erg s}^{-1} \text{ cm}^{-2}$	Binned flux intensity at $\approx 5500\text{\AA}$ , $f_{V,CS}$
4	$10^{-16} \text{ erg s}^{-1} \text{ cm}^{-2}$	StdDev of the flux at $\approx 5500\text{\AA}$ , $ef_{V,CS}$
5	$\log_{10}(\text{yr})$	Lum. weighted age, $\mathcal{A}_{\star,L}$ , (log scale)
6	$\log_{10}(\text{yr})$	Mass weighted age, $\mathcal{A}_{\star,M}$ , (log scale)
7	$\log_{10}(\text{yr})$	Error of both $\mathcal{A}_{\star}$ , (log scale)
8	dex	Lum. weighted metallicity, $Z_{\star,L}$ in logarithmic scale, normalized to the solar value ( $Z_{\odot}=0.017$ )
9	dex	Lum. weighted metallicity, $Z_{\star,M}$ in logarithmic scale, normalized to the solar value ( $Z_{\odot}=0.017$ )
10	dex	Error of both $Z_{\star}$
11	mag	Dust extinction of the stellar pop., $A_{V,\star}$
12	mag	Error of $A_{V,\star}$ , $e_{A_V}$
13	km/s	Velocity of the stellar pop., $vel_{\star}$
14	km/s	Error of the velocity, $e_{vel}$
15	km/s	Velocity dispersion of the stellar pop., $\sigma_{\star}$
16	km/s	Error of $\sigma_{\star}$ , $e_{\sigma}$
17	$\log_{10}(M_{\odot}/L_{\odot})$	Stellar mass-to-light ratio, $\Upsilon_{\star}$
18	$\log_{10}(M_{\odot}/\text{sp}^2)$	Stellar mass density per spaxel., $\Sigma_{\star}$
19	$\log_{10}(M_{\odot}/\text{sp}^2)$	Dust corrected $\Sigma_{\star}$ , defined as $\Sigma_{\star,dust}$
20	$\log_{10}(M_{\odot}/\text{sp}^2)$	Error of $\Sigma_{\star}$

Channel indicates the Z-axis of the datacube starting from 0. (1) measured along the entire wavelength range covered by the spectroscopic data.

emission-line decontaminated spectra obtained as a by product of the analysis described in §3.1.2. This exten-

TABLE 3

## DESCRIPTION OF THE SFH EXTENSION

Channel	Description of the map
0	$w_{\star,L}$ for $(\mathcal{A}_{\star}, Z_{\star}) = (0.001 \text{ Gyr}, 0.0001)$
...	...
272	$w_{\star,L}$ for $(\mathcal{A}_{\star}, Z_{\star}) = (13.5 \text{ Gyr}, 0.04)$
273	$w_{\star,L}$ for $\mathcal{A}_{\star} = 0.001 \text{ Gyr}$
...	...
311	$w_{\star,L}$ for $\mathcal{A}_{\star} = 13.5 \text{ Gyr}$
312	$w_{\star,L}$ for $Z_{\star} = 0.0001$
...	...
318	$w_{\star,L}$ for $Z_{\star} = 0.04$

Channel indicates the Z-axis of the datacube starting from 0, and  $w_{\star,L}$  indicates the fraction (weight) of light at  $5500\text{\AA}$  corresponding to: (i) an SSP of a certain age ( $\mathcal{A}_{\star}$ ) and metallicity ( $Z$ ) (channels 0 to 272), (ii) a certain age, i.e., co-adding all  $w_{\star,L}$  corresponding to SSPs with the same age but different metallicity (channels 273 to 311), and (iii) a certain metallicity, i.e., co-adding all  $w_{\star,L}$  corresponding to SSPs with the same metallicity but different age (channels 312 to 318).

sion comprises the results from this analysis, including in each channel the values derived for each stellar index and the corresponding error. In this particular analysis we have updated the list of stellar indices previously included in the analysis by Pipe3D, comprising a total of 33 indices, whose actual definition and wavelength range were obtained from the compilation incorporated in the MaNGA Data Analysis Pipeline (Westfall et al. 2019)<sup>11</sup>. In addition we include the D4000 parameter as defined by Gorgas et al. (1999, their Eq. 2). We depart in this definition from the more usual one derived using the flux intensity in units of frequency (i.e.,  $F_{\nu}$  Bruzual A. 1983), as we find this former definition more convenient to work with. Table 4 describes the content of this extension, indicating the channel in which each stellar index and its corresponding error are stored. In addition, it includes the wavelength range defining the stellar index together with the blue and red wavelength ranges used to estimate the adjacent continuum. Finally, we illustrate the content of this extension in Figure 3, showing the stellar indices derived for the galaxy NGC 2906. Note how some stellar indices sensitive to the  $\mathcal{A}_{\star}$  ( $Z_{\star}$ ) like D4000 (Mg2 or Mgb) present a negative gradient from the inside-out, while other indices more sensitive to the presence of young stellar populations (e.g., HdeltaA or Hb) present a clear increase near the location of the spiral arms (i.e., where the younger stellar populations are found).

<sup>11</sup><https://www.sdss4.org/dr17/manga/manga-analysis-pipeline/>

TABLE 4  
DESCRIPTION OF THE INDICES EXTENSION

ID	Channel	Units	Index $\lambda$ range (Å)	Blue $\lambda$ range (Å)	Red $\lambda$ range (Å)
D4000	0/35	Å	4050.000-4250.000	3750.000-3950.000	
CN1	1/36	Å	4142.125-4177.125	4080.125-4117.625	4244.125-4284.125
CN2	2/37	Å	4142.125-4177.125	4083.875-4096.375	4244.125-4284.125
Ca4227	3/38	Å	4222.250-4234.750	4211.000-4219.750	4241.000-4251.000
G4300	4/39	Å	4281.375-4316.375	4266.375-4282.625	4318.875-4335.125
Fe4383	5/40	Å	4369.125-4420.375	4359.125-4370.375	4442.875-4455.375
Ca4455	6/41	Å	4452.125-4474.625	4445.875-4454.625	4477.125-4492.125
Fe4531	7/42	Å	4514.250-4559.250	4504.250-4514.250	4560.500-4579.250
C24668	8/43	Å	4634.000-4720.250	4611.500-4630.250	4742.750-4756.500
Hb	9/44	Å	4847.875-4876.625	4827.875-4847.875	4876.625-4891.625
Fe5015	10/45	Å	4977.750-5054.000	4946.500-4977.750	5054.000-5065.250
Mg1	11/46	Å	5069.125-5134.125	4895.125-4957.625	5301.125-5366.125
Mg2	12/47	Å	5154.125-5196.625	4895.125-4957.625	5301.125-5366.125
Mgb	13/48	Å	5160.125-5192.625	5142.625-5161.375	5191.375-5206.375
Fe5270	14/49	Å	5245.650-5285.650	5233.150-5248.150	5285.650-5318.150
Fe5335	15/50	Å	5312.125-5352.125	5304.625-5315.875	5353.375-5363.375
Fe5406	16/51	Å	5387.500-5415.000	5376.250-5387.500	5415.000-5425.000
Fe5709	17/52	Å	5696.625-5720.375	5672.875-5696.625	5722.875-5736.625
Fe5782	18/53	Å	5776.625-5796.625	5765.375-5775.375	5797.875-5811.625
NaD	19/54	Å	5876.875-5909.375	5860.625-5875.625	5922.125-5948.125
TiO	20/55	Å	5936.625-5994.125	5816.625-5849.125	6038.625-6103.625
TiO2	21/56	Å	6189.625-6272.125	6066.625-6141.625	6372.625-6415.125
HDeltaA	22/57	Å	4083.500-4122.250	4041.600-4079.750	4128.500-4161.000
HGammaA	23/58	Å	4319.750-4363.500	4283.500-4319.750	4367.250-4419.750
HDeltaF	34/59	Å	4091.000-4112.250	4057.250-4088.500	4114.750-4137.250
HGammaF	25/60	Å	4331.250-4352.250	4283.500-4319.750	4354.750-4384.750
CaHK	26/61	Å	3899.500-4003.500	3806.500-3833.800	4020.700-4052.400
MgICvD	27/62	Å	5165.000-5220.000	5125.000-5165.000	5220.000-5260.000
bTiO	28/63	Å	4758.500-4800.000	4742.750-4756.500	4827.875-4847.875
aTiO	29/64	Å	5445.000-5600.000	5420.000-5442.000	5630.000-5655.000
CaH1	30/65	Å	6357.500-6401.750	6342.125-6356.500	6408.500-6429.750
CaH2	31/66	Å	6775.000-6900.000	6510.000-6539.250	7017.000-7064.000
TiO2SDSS	32/67	Å	6189.625-6272.125	6066.625-6141.625	6422.000-6455.000
Hdmod	33/68	Å	4083.500-4122.250	4079.000-4083.000	4128.500-4161.000
SN	34/69	$10^{-16}$ cgs	Signal/Error across the entire wavelength range		

Channel indicates the Z-axis of the datacube starting from 0.

#### 4.1.4. *ELINES* extension

As described in §3.1.3 the emission lines were analyzed using two different methods. In the first one a set of strong emission lines were modelled with a Gaussian function. The spatial results of this analysis are included in the *ELINES* extension, whose content is described in Table 5. The information provided in this table is stored in a set of header keywords, *DESC\_N*, with *N*

being the channel number. Figure 4 shows an example of the content included in this extension corresponding to the analysis on the galaxy NGC 2906. The first channel, that comprises the  $H\alpha$  velocity map, shows a typical rotational pattern for a spiral galaxy. The pattern is visible for those regions with clear detection of the ionized gas (e.g., in  $H\alpha$ , 7th channel). For all emission lines the ionized gas intensity maps present a clumpy structure tracing the lo-



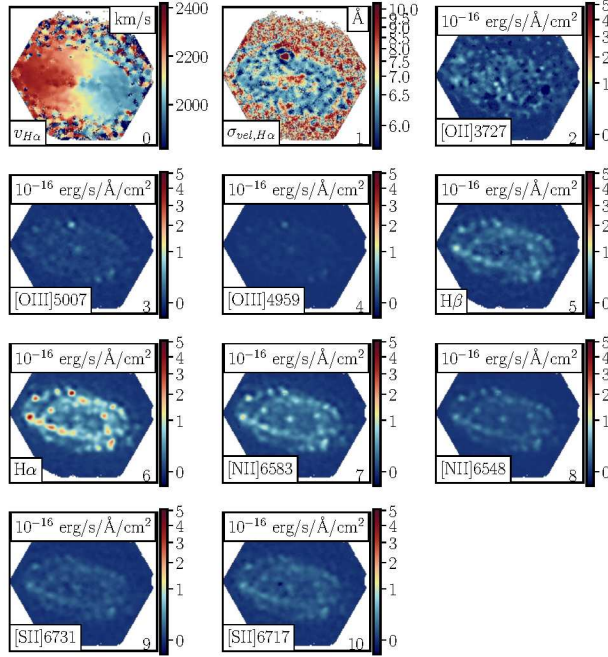


Fig. 4. Example of the content of the ELINES extension in the Pipe3D file, corresponding to the galaxy NGC2906. Each panel shows a color image with the content of a channel in this data cube. The first panel corresponds to the velocity, in km/s, and the 2nd panel to EW( $H\alpha$ ), in Å. The remaining panels represent the distribution of the flux intensities for the different analyzed emission lines (lower-left legend), in units of  $10^{-16}$  erg/s/Å/cm<sup>2</sup>. The color figure can be viewed online.

TABLE 5

DESCRIPTION OF THE ELINES EXTENSIONS

Channel	Units	Description of the map
0	km/s	$H\alpha$ velocity
1	Å	$H\alpha$ velocity dispersion <sup>a</sup>
2	$10^{-16}$ erg s <sup>-1</sup> cm <sup>-2</sup>	[OII]3727 flux intensity
3	$10^{-16}$ erg s <sup>-1</sup> cm <sup>-2</sup>	[OIII]5007 flux intensity
4	$10^{-16}$ erg s <sup>-1</sup> cm <sup>-2</sup>	[OIII]4959 flux intensity
5	$10^{-16}$ erg s <sup>-1</sup> cm <sup>-2</sup>	$H\beta$ flux intensity
6	$10^{-16}$ erg s <sup>-1</sup> cm <sup>-2</sup>	$H\alpha$ flux intensity
7	$10^{-16}$ erg s <sup>-1</sup> cm <sup>-2</sup>	[NII]6583 flux intensity
8	$10^{-16}$ erg s <sup>-1</sup> cm <sup>-2</sup>	[NII]6548 flux intensity
9	$10^{-16}$ erg s <sup>-1</sup> cm <sup>-2</sup>	[SII]6731 flux intensity
10	$10^{-16}$ erg s <sup>-1</sup> cm <sup>-2</sup>	[SII]6717 flux intensity

Channel indicates the Z-axis of the data cube starting from 0.  
<sup>a</sup> FWHM, i.e.,  $2.354\sigma$ . The instrumental velocity dispersion has not been removed.

TABLE 6

DESCRIPTION OF THE FLUX\_ELINES EXTENSIONS

Channel	Units	Description of the map
I	$10^{-16}$ erg s <sup>-1</sup> cm <sup>-2</sup>	Flux intensity
I+N	km/s	Velocity
I+2N	Å	Velocity dispersion FWHM
I+3N	Å	Equivalent width
I+4N	$10^{-16}$ erg s <sup>-1</sup> cm <sup>-2</sup>	Flux error
I+5N	km/s	Velocity error
I+6N	Å	Velocity dispersion error
I+7N	Å	Equivalent width error

I is the index that identifies each of the analyzed emission lines, running from 0 to N, where N is the total number of analyzed emission lines: (i) 53 for the FLUX\_ELINES extension and (ii) 130 for the FLUX\_ELINES\_LONG one.

cation of the  $H\alpha$  regions and clusters, which is the typical distribution for this kind of galaxies (e.g., Sánchez 2020; Sánchez et al. 2021).

#### 4.1.5. FLUX\_ELINES and FLUX\_ELINES\_LONG Extensions

In addition to the Gaussian modelling the emission parameters are estimated using a moment analysis, as described in §3.1.3. This second analysis is performed twice, using two different list of emission lines, and the results are stored in two different extensions of the pyPipe3D data file: (i) the 53 emission lines included in original version of the Pipe3D pipeline (Sánchez et al. 2016b, Table 1, limited to  $\lambda < 7400\text{Å}$ ), included in the FLUX\_ELINES extension, and (ii) a new set of 130 emission lines extracted from the list published by Fesen & Hurford (1996), covering the wavelength range between 3700Å and 7200Å, in the rest-frame, included in the FLUX\_ELINES\_LONG extension. Details about this new list of emission lines are included in Appendix A.

Table 6 describes the format of both extensions. For each analyzed emission line (defined by the running index I), the extension comprises four different parameters (flux intensity, velocity, velocity dispersion and equivalent width) and their corresponding errors. Thus, a total of eight channels, from I to I+7N, correspond to the N different parameters derived for the same I emission line, with  $0 \leq N < 8$  and I running from 0 to 53 (130) for the FLUX\_ELINES (FLUX\_ELINES\_LONG) extension.

Figure 5 shows an example of the content of these extensions, corresponding to the four parameters derived for the  $H\alpha$  emission line, and their associated errors, stored in the FLUX\_ELINES extension of the galaxy

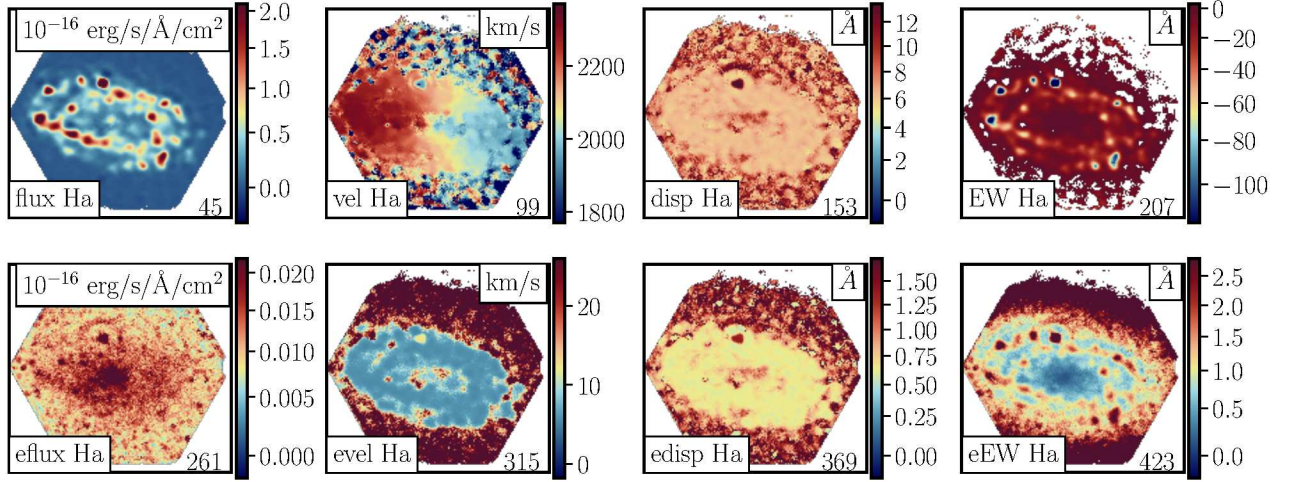


Fig. 5. Example of the content of the FLUX\_ELINES extension in the Pipe3D file, corresponding to the galaxy NGC2906. Each panel shows a color image with the content of a channel in this datacube. For each panel, the actual content is indicated in the lower-left, the channel number in the lower-right, and the units of the represented quantity in the upper-right legend. For the flux and flux error the units are  $10^{-16}$  erg/s/Å/cm<sup>2</sup>. The color figure can be viewed online.

NGC 2906. As expected the distributions observed in the flux intensity, velocity and velocity dispersion maps are very similar to those already seen in Figure 4, corresponding to the same emission line derived adopting a Gaussian model. Finally, the EW(H $\alpha$ ) map presents a clumpy pattern that follows the intensity distribution, with clear negative values at the location of the H II regions. Much lower values, near to 3 Å or below (in absolute values) are found at the locations where the ionized gas presents a more smooth distribution, being compatible with a diffuse ionized gas dominated by hot evolved/post-AGB stars (see §4 of Sánchez et al. 2021, for a more clear description of this distribution).

As a final remark, we should highlight that in both the ELINES and FLUX\_ELINES extensions the distributed velocity dispersion corresponds to the FWHM of the emission lines measured in units of Å. Furthermore, the instrumental dispersion is not subtracted. As described in Sánchez et al. (2022) it is needed to apply the following formula to estimate the velocity dispersion in km s<sup>-1</sup>:

$$\sigma_{\text{Å}} = \text{FWHM}/2.354, \quad \sigma_{\text{km s}^{-1}} = \frac{c}{\lambda} \sqrt{\sigma_{\text{Å}}^2 - \sigma_{\text{inst}}^2}, \quad (9)$$

where  $c$  is the speed of light in km s<sup>-1</sup>,  $\lambda$  is the wavelength of the emission line and  $\sigma_{\text{inst}}$  is the instrumental resolution ( $\approx 2.6$  Å).

#### 4.1.6. GAIA\_MASK Extension SELECT\_REG Extension

These two extensions comprise the results of the two masking processes described in §3.2: GAIA\_MASK includes the mask of the foreground stars identified using

the Gaia DR3 catalog, while SELECT\_REG includes the mask generated using the signal-to-noise distribution for the continuum, by selecting a minimum value of S/N > 1. The S/N ratio was derived by estimating the flux intensity and standard deviation for each individual spectrum within the wavelength range between 5589 and 5680 Å. Although the main shape of the continuum is removed, the absorption features remain. Therefore, this S/N is an lower limit to the real one.

#### 4.2. Catalog of Individual Parameters

As described in §3.4, following Sánchez et al. (2022), we derive a set of individual parameters for each galaxy, comprising both integrated, aperture limited and characteristics parameters (i.e., values at the effective radius), and, for a subset of them, the slopes of their radial gradients. For doing so we use the information included in each individual pyPipe3D file described in §4.1, and the calculations described in §3.3. The final parameter set is distributed as a catalog and described in Appendix B.

#### 4.3. NGC 2906: A Show-Case Galaxy

Along the previous sections we have used the galaxy NGC 2906 as a show case to illustrate the content of each of the extensions in the distributed pyPipe3D files. NGC 2906 is a rotational supported Sbc galaxy with a stellar mass similar to that of the Milky-Way ( $\approx 10^{10} M_{\odot}$ ), being a star-forming galaxy located within  $1\sigma$  of the star-formation main sequence, and possibly hosting a weak AGN (e.g. Anghopo et al. 2022). Furthermore, it



presents a well defined bulge and two clearly distinguishable spiral arms. With these properties it can be considered an archetype late-type galaxy, suitable to illustrate the content of the distributed data products. NGC 2906 was observed by the CALIFA survey on 17th December 2012. Later on, it was observed during the science verification of the MUSE instrument, being included in the AMUSING++ compilation (López-Cobá et al. 2020). Therefore, it is also a suitable target to explore the improvement of spatial resolution introduced by the new reduction.

#### 4.3.1. NGC 2906: Resolved Properties of the Ionized Gas

We already mentioned that one of the major improvements of the new analyzed and distributed data set is the increased spatial resolution. The previous reduction provides a spatial resolution that on average is of the order of  $\approx 2.5''/\text{FWHM}$  (version 2.2; Sánchez et al. 2016a). For the particular case of NGC 2906, this FWHM was estimated as  $2.37''$ , according to the information provided by the data reduction stored in the datacube header. The new reduction improves the spatial resolution with a final PSF FWHM near to the one provided by the natural seeing (Sanchez et al. 2023). In the particular case of NGC 2906 is estimated as  $1.1''/\text{FWHM}$ . When considering the offset between the PSF FWHM estimated by the data-reduction itself and the real FWHM of the natural seeing (Sanchez et al. 2023), a more realistic estimation would be  $\approx 1.5''$ . This is, in any case, a very significant improvement in the spatial resolution with respect to the previous data reduction.

A clear advantage of an improved spatial resolution is the ability to distinguish between different structures within a galaxy. This is particularly important, for instance, in the exploration of the different ionizing sources and the understanding of the changes in the physical conditions of the inter-stellar medium (ISM) across the optical extension of galaxies. This has been highlighted in recent reviews on the topic (Sánchez 2020; Sánchez et al. 2021), and the results by recent projects aimed to explore the ionizing conditions using IFS with unprecedented spatial resolutions (e.g., PHANGS-MUSE; Emsellem et al. 2022).

Figure 6 shows a comparison between the spatial distribution of the continuum emission, created using the  $u$ -,  $g$ - and  $r$ -band images synthesized from the reduced eCALIFA data cube, dominated by the stellar population (panel a), and the ionized gas emission lines, created using the  $[\text{O III}]$  (blue),  $\text{H}\alpha$  (green) and  $[\text{N II}]$  (red) emission maps (panel b). The different morphological structures within this galaxy are clearly appreciated in the contin-

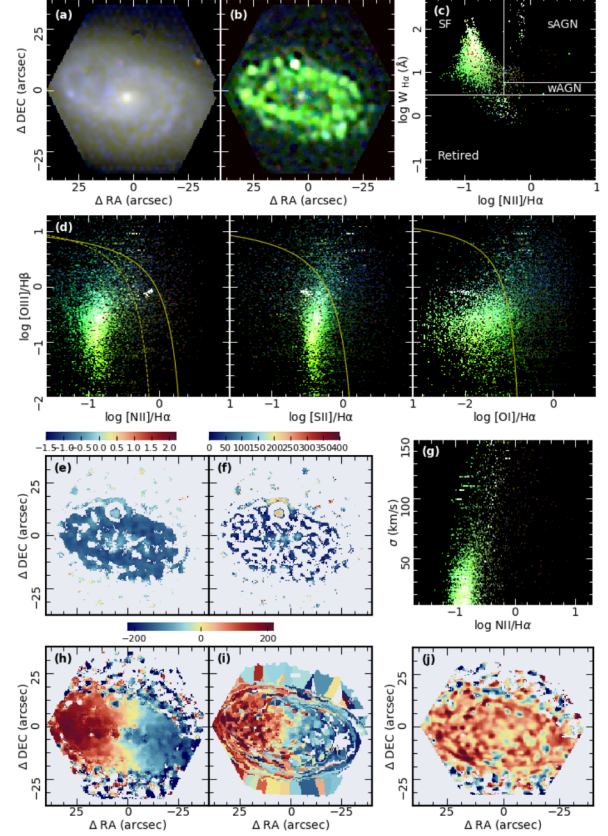


Fig. 6. Example of the information explored in the quality control process for the galaxy/cube NGC2906, extracted from the analysis presented by López-Cobá et al. (2020). Each panel comprises the following information: (a) RGB three-color image created using the  $u$ -,  $g$ - and  $r$ -band images synthesized from the reduced eCALIFA data cubes; (b) RGB color image created using the  $[\text{O III}]$  (blue),  $\text{H}\alpha$  (green), and  $[\text{N II}]$  (red) intensity maps estimated by pyPipe3D; (c) spatially resolved WHAN diagnostic diagram, with each spaxel color-coded using the color-scheme shown in panel (b). The white solid lines indicate the boundaries proposed by Cid Fernandes et al. (2011), with the dominant ionizing source in each region included as labels; (d) spatially resolved diagnostic diagrams showing the distribution of  $[\text{O III}]/\text{H}\beta$  as a function of  $[\text{N II}]/\text{H}\alpha$ ,  $[\text{S II}]/\text{H}\alpha$  and  $[\text{O I}]/\text{H}\alpha$ , using a similar color scheme as panel (c) (Baldwin et al. 1981; Veilleux et al. 2001). The yellow solid and dashed lines in each panel correspond to the demarcation line proposed to separate between SF and non-SF dominated ionization by Kewley et al. (2001) and Kauffmann et al. (2003), respectively; (e) spatial distribution of the  $[\text{N II}]/\text{H}\alpha$  line ratio; (f) spatial distribution of the  $\text{H}\alpha$  velocity dispersion; (g) distribution of the  $[\text{N II}]/\text{H}\alpha$  line ratio as a function of the  $\text{H}\alpha$  velocity dispersion across the extension of the galaxy; (h)  $\text{H}\alpha$  velocity map (spaxel-wise); (i) stellar population velocity map (following the spatial-binning/tessellation); (j) difference between velocity maps shown in panels (h) and (i). Note that the scale of this later panel is not the same as those in panel (h) and (i). The color figure can be viewed online.

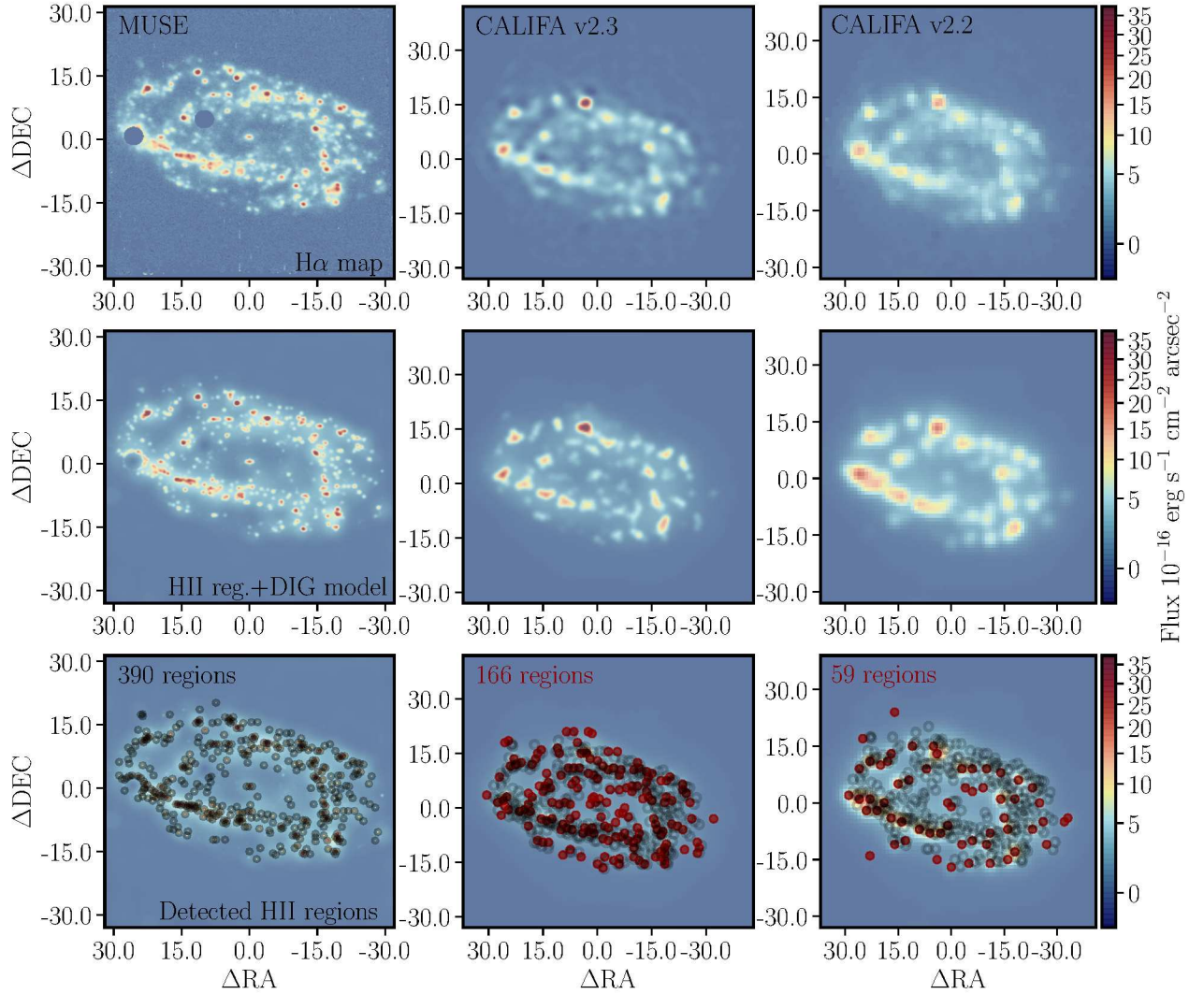


Fig. 7.  $H\alpha$  intensity maps of NGC 2906 extracted using pyPipe3D from (i) the MUSE data cube included in the AMUSING++ compilation (López-Cobá et al. 2020) (top-left panel), (ii) the eCALIFA data cube corresponding to version 2.3 of the data reduction Sanchez et al. (2023) (top-central panel), and (iii) the CALIFA data cube corresponding to version 2.2 of the data reduction (top-right panel). The best models for the  $HII$  regions and diffuse ionized gas recovered by pyHIIExtractor (Lugo-Aranda et al. 2022) for each of those maps shown in the top panels are included in the middle panels, following the same sequence from left-to-right (MUSE, eCALIFA v2.3 and v2.2). Finally, the bottom panels show each of these models together with the distribution of good-quality  $HII$  regions detected using the MUSE data (black open-circles, included in all the bottom panels), and the regions detected using each of the eCALIFA data (solid red-circles). The number of  $HII$  regions detected using each dataset is included in a label in each of the bottom panels. The figure illustrates the effects of the degradation of the spatial resolution in the detectability of individual structures (e.g.,  $HII$  regions) in galaxies using this kind of data. The color figure can be viewed online.

uum image: (i) an evident (but small) bulge is observed in the center of the galaxy, clearly dominated by a red/old stellar population; (ii) two spiral arms, with some additional sub-arms, are traced by a blue/young stellar component; in addition, (iii), a diffuse component dominated by reddish/oldish stellar populations is appreciated be-

yond and in between the spiral arms. The ionized gas map is dominated by a clumpy structure, mostly green (i.e., with a dominant  $H\alpha$  flux over the other two emission lines), that traces the location of the spiral arms seen in the continuum image (i.e., associated with the presence of a blue/young stellar population).

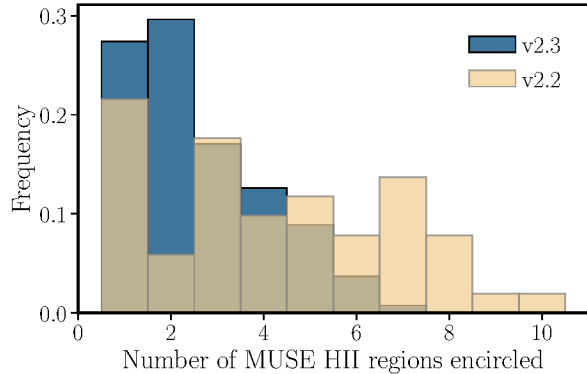


Fig. 8. Distribution of the frequency in which a certain number of H II regions detected using the MUSE data shown in Figure 7 is encircled within the radius of an H II region detected using the eCALIFA v2.3 dataset (blue histogram) or the v2.2 one (yellow histogram). Figure illustrates the effect of the degradation of the spatial resolution in the clustering of H II regions into a single blended structure. The color figure can be viewed online.

These clumps are most probably tracing H II regions/clusters. This is evident when explored their distribution in the different diagnostics diagrams included in Figure 6, panels (c) and (d). The vast majority of them are found in regions within the diagnostic diagrams usually associated with classical H II regions (e.g. Osterbrock 1989; Kewley et al. 2001; Kauffmann et al. 2003) or regions in which ionization is associated with recent star-formation activity (e.g. Cid Fernandes et al. 2011), in agreement with the prescriptions outlined by Sánchez et al. (2021). Besides those clumps there is a smooth/diffuse component that is observed at any location within the galaxy, including the central regions and inter-arms, that most probably is due to a combination of different ionizing sources, such as photons leaked from H II regions and ionization due to the presence of hot evolved/post-AGB stars (e.g. Binette et al. 1994; Relaño et al. 2012; Singh et al. 2013; Weilbacher et al. 2018; Sánchez et al. 2021; Belfiore et al. 2022). Finally, this object is a known host of a supernova remnant (SNR; Martínez-Rodríguez in prep.) located at  $\approx 10''$  north and  $\approx 2''$  east from the center of the galaxy. This SNR is observed as a white-roundish ionized structure in panel (b), and as a cluster of white points in the intermediate region<sup>12</sup> in the [O III]/H $\beta$  vs [N II]/H $\alpha$  diagram (BPT diagram; Baldwin et al. 1981), included in panel (b).

Figure 6, panel (e) shows the spatial distribution of the N2 parameter, defined as  $\log([N II]/H\alpha)$ . This parameter is sensitive to oxygen abundance when the ionization is due to young OB-stars (e.g. Pettini & Pagel 2004;

Marino et al. 2013). A mild negative gradient is observed, with values of N2 slightly larger in the central regions than in the outskirts, compatible with the known decline of the oxygen abundance described for galaxies of this stellar mass and morphology (e.g., Sánchez et al. 2014; Belfiore et al. 2017b; Sánchez et al. 2021; Boardman et al. 2023). Those regions ionized by other sources, different than young massive stars, usually present larger values of N2. This is the reason why this parameter is used to discriminate the ionizing source in the WHAN diagram (panel c). In this particular galaxy we find anomalous large values of the N2 ratio compared to those at the same galactocentric distances at the location of the reported SNR (e.g., Cid Fernandes et al. 2021). We stress that this N2-enhancement is a direct consequence of an extra ionizing source, and should never be considered as an increase of the oxygen abundance.

If we compare the N2 distribution with the one shown in panel (f), the H $\alpha$  velocity dispersion, we can appreciate that there is an increase of this parameter at the location of the SNR too. As we indicated before the spectral resolution of these data is not optimal to measure the velocity dispersion, in particular in the disk of late-type spirals, where this parameter is expected to be well below the instrumental resolution. This is the reason why in many locations across the extension of this galaxy the velocity dispersion is masked. For those regions for which a reliable estimation is obtained we appreciate that a decline in the velocity dispersion from a value near  $\approx 150 \text{ km s}^{-1}$  in the central regions to values as low as  $\approx 30 \text{ km s}^{-1}$ , in the outer disk. However, at the location of the SNR the velocity dispersion rises up to  $\approx 200 \text{ km s}^{-1}$ . Recent explorations have proposed that the velocity dispersion should be considered as an extra parameter to discriminate between different ionizing sources (D’Agostino et al. 2019; López-Cobá et al. 2020; Law et al. 2021). Indeed, the N2 parameter usually follows the velocity dispersion, as appreciated in panel (g) of Figure 6. Due to their association with the gas disk and their relatively low internal pressure H II/SF regions are usually associated with regions of low velocity dispersion (e.g. Law et al. 2021). On the contrary, regions ionized by shocks present larger velocity dispersions (e.g. D’Agostino et al. 2019; López-Cobá et al. 2020).

The last three panels of Figure 6 show the H $\alpha$  and stellar velocity maps (panels h and i), and finally the difference between both of them (panel j). The well defined rotational pattern appreciated in both velocity maps, together with the low velocity dispersion seen in panel (f), suggests that this is a rotationally supported galaxy. A possible perturbation on the rotational pattern is appreciated in the inner regions of the H $\alpha$  velocity map, although a more detailed analysis would be required to

<sup>12</sup>In between the Kewley et al. (2001) and Kauffmann et al. (2003) demarcation lines in the diagnostic diagram

drawn any conclusion in this regards, which is beyond the scope of the current analysis. Apart from a general offset, there is no discernible pattern in the difference between both velocity maps. The nature of the offset is a known effect in the calibration of the zero-velocity associated with the measurements using an SSP template, a mismatch that we have already reported in previous articles (e.g. Sánchez et al. 2022), that it is associated with the definition of the central wavelength at the edge or at center of the spectral pixel. It produces an offset of half of the spectral pixel (in velocities), times the expansion factor introduced by the redshift, i.e.,  $1+z$ . This offset should be corrected prior to any detailed comparison between the two velocity maps (for all the delivered data sets). A more detailed exploration, matching the offset in velocity in the central regions, is required to explore possible patterns associated with known effects, such as the asymmetric drift or the possible presence of non-radial motions that may affect differently the gas and the stellar populations. Like in the case of the N2 and velocity dispersion maps the strongest deviation appreciated in the gas velocity maps is at the location of the SNR, where a clear blue-shift is observed. These asymmetries or multiple kinematic components are frequent in the presence of shock ionization (e.g. Veilleux et al. 2001; López-Cobá et al. 2017).

#### 4.3.2. NGC 2906: Ability to Segregate H II Regions

The content of Figure 6, together with the distributions shown in Figures 1 to 5 clearly illustrate the kind of information extracted by `pyPipe3D` from the new reduced data cubes. It also shows in a qualitative way how the new spatial resolution allows to distinguish between different structures within the galaxy. In this section we present a more quantitative statement of this improvement, by comparing the ability to detect and segregate H II regions (and associations) using three IFS data sets on the galaxy NGC 2906: (i) the MUSE data analyzed by `Pipe3D` as part of the AMUSING++ compilation (López-Cobá et al. 2020); (ii) the eCALIFA v2.3 data analyzed by `pyPipe3D` discussed in this article and (iii) the CALIFA v2.2 data analyzed by `pyPipe3D` distributed as part of the DR3 (Sánchez et al. 2016a).

Figure 7, top panels, show the H $\alpha$  intensity map extracted from the three data sets. As expected the MUSE data present the richest content of sub-structures/clumpy regions (i.e., H II regions), due to its better spatial resolution (FWHM $\approx 0.6''$ ). In comparison, the eCALIFA v2.3 data (FWHM $\approx 1.1$ - $1.5''$ ) still traces the brightest clumpy structures seen in the MUSE data. However, they present a clear degradation of the image quality, blurring and/or grouping into a single structure several clumps clearly visible and/or segregated in the MUSE data. Finally,

the lowest number of substructures is appreciated in the CALIFA v2.2 data (FWHM $\approx 2.37''$ ), with the largest degree of clumpy regions lost or grouped into a single unresolved or barely resolved structure.

To quantify these differences we apply the recently developed `pyHIIEExtractor` code (Lugo-Aranda et al. 2022) to the three data sets. This code comprises an algorithm that detects clumpy regions in emission line maps, deriving both their flux intensities and sizes. It also segregates the detected regions from the diffuse ionized gas (DIG), generating a model for both components. Being developed to explore the H II regions of the galaxies within the AMUSING++ compilation (Lugo Aranda et al., in prep.), its capabilities have been tested with a wide range of simulations. Figure 7, middle-column panels, show the combined models (H II regions+DIG) generated by this code when applied to the H $\alpha$  maps shown in the upper panels, using the same input parameters: (i) a minimum size of 30 pc ( $\approx 0.6''$  at the redshift of the object), (ii) a maximum size of 300 pc, (iii) a overall detection limit of  $3\sigma$ , and (iv) a minimum contrast of a 50% with respect to the DIG in the detection of a clumpy structure. A direct comparison between the upper and middle-column panels illustrates how well the code recovers the original light distribution. It also highlights its limits: it is unable to recover some of the faintest/smaller clumpy regions in the MUSE data. We should note that the most limiting factor is the contrast with respect to the level of the adjacent DIG, followed by the imposed minimum size.

The three bottom panels in Figure 7 show again the same H $\alpha$  models, together with the distribution of clumpy structures detected by `pyHIIEExtractor` using the MUSE data, that is repeated in the three panels for comparison purposes. In addition, it is shown the distribution of regions detected by this code using the eCALIFA v2.3 (central panel), and CALIFA v2.2 (right panel), respectively. In the case of the MUSE data a total of 390 clumpy regions is detected, a number that decreases to 166 for the eCALIFA v2.3 data and to just 59 for the CALIFA v2.2 data, respectively. Thus, the resolution clearly affects the ability to detect individual structures such as H II regions. Furthermore the new reduced and analyzed data set presents a clear improvement with respect to the previous data set.

As discussed previously, H II regions are lost due to the blurring effect introduced by the degradation of the resolution (i.e., they are not distinguished from the background), but also due to an aggregation with nearby clumps. To quantify both effects we determine how many of the detected regions in the MUSE data are not included within the radius of the clumpy structures detected in the other two data sets. This will tell us the number of regions



that are totally lost. Finally, we determine the number of regions detected in the MUSE encircled within the radius of the regions detected using the other two data sets. This will quantify the frequency with which an original region is aggregated to form a new structure in the lower resolution datasets. To do so we make use of the `cKDtree` algorithm included in the `scipy.spatial` python package to look for the nearest neighbours of each of the regions detected in the MUSE data in the catalog of regions derived using the other two data sets. Then, we determine whether a region is included within any nearest neighbor by comparing their radii with the distance.

Of the 390 regions detected in the MUSE data, 351 are included within one of the 166 regions detected in the eCALIFA data. Thus, most of the regions are not really lost ( $\approx 90\%$ ), but they are rather aggregated into larger clumps, that on average comprise  $\approx 2$  of the former regions. On the contrary, in the case of the CALIFA v2.2 data, only 218 of the original 390 regions are included within one of the detected 59 regions. Therefore, the “recovery” rate is much lower ( $\approx 55\%$ ). Furthermore, the new clumps comprise a larger number of the original regions ( $\approx 3-4$ ). Therefore, the improved resolution achieved by the new reduction increases the recovery rate of H II regions and decreases the number of aggregated/grouped regions by a factor of two. A more detailed exploration on how the original H II regions are aggregated into larger structures is presented in Figure 8, where is shown the frequency at which a certain number of the former regions is aggregated to a region detected in the other data sets. In the case of the eCALIFA v2.3 data set most of the detected regions comprise one or two MUSE-detected regions ( $\approx 60\%$ ), with less than  $\approx 20\%$  encircling more than four of those regions. On the contrary, in the case of the CALIFA v2.2 data, only  $\approx 25\%$  of the regions comprise one or two MUSE-detected regions, while more than  $\approx 50\%$  aggregates more than four of those regions.

In summary, this exploration clearly indicates that the new reduced and analyzed data have significantly improved out the ability to detect and study sub-structures in the observed galaxies.

#### 4.4. Ionization Conditions Across the Optical Extension of Galaxies

In previous sections we have illustrated the impact of the intrinsic properties of the data (i.e., spatial coverage and sampling) and the improved spatial resolution of the new reduced data set, on the exploration of the ionizing conditions and ISM properties in one particular galaxy NGC 2906. In this section we illustrate their impact on the exploration of the general patterns of those properties described for the full population of galaxies. To do

so we replicate the explorations presented by Sánchez (2020) and Sánchez et al. (2022), shown in their Figure 5 and Figure 10, respectively. There it was presented the spaxel-wise spatial resolved distribution of values across the classical BPT diagnostic diagram,  $[\text{OIII}]/\text{H}\beta$  vs.  $[\text{NII}]/\text{H}\alpha$  (BPT; Baldwin et al. 1981) for two different samples of galaxies, segregated by stellar mass and morphology. In both cases it was claimed that the selected samples were representative of the galaxy population in the nearby Universe: (i) Sánchez (2020) explored an heterogeneous compilation of galaxies observed using different IFS instruments by different surveys, and (ii) Sánchez et al. (2022) used the final DR of the MaNGA IFS galaxy survey.

Following both studies we select a refined sub-sample of 660 galaxies from the original data set, excluding edge-on galaxies ( $a/b > 0.85$ ), galaxies poorly resolved ( $\text{Re} < 2''$ ), and limiting the redshift range ( $0.005 < z < 0.05$ ). This way we (i) avoid projection issues, providing a cleaner interpretation of the galactocentric distances, (ii) exclude galaxies that are not resolved by the data, and (iii) limit the effects of the wide range of physical resolutions ( $\approx 500$  pc, on average, ranging from 150 pc to 1 kpc) in the interpretation of the results. We should highlight that this selection biases the sample excluding (i) the most prominent/evident galactic outflows, shock ionized and frequently observed as biconical, conical or filamentary structures of gas extending along the vertical axis in edge-on galaxies (e.g. Bland-Hawthorn 1995; Heckman et al. 1990; López-Cobá et al. 2020); and (ii) the weak extra-planar diffuse ionized gas that is observed as part of the thick disk in some edge-on galaxies too (e.g. Flores-Fajardo et al. 2011; Levy et al. 2018).

For each galaxy we obtain the distribution of the average EW( $\text{H}\alpha$ ) and the density of spaxels across the considered BPT diagram. Then, for the full sample and for any sub-sample selected by stellar mass and/or morphology, we average both distributions. This way each ionized spaxel and each galaxy weighs the same, irrespectively of the flux intensity of the emission lines. Therefore, by construction the possible contribution of strong but spatially concentrated ionizing sources, like AGNs, is somehow diluted. Together with the bias against strong shock ionized structures, we acknowledge that most of the patterns that emerge from this exploration are related to the dominant (in terms of spatial extent) ionizing sources in galaxies: i.e., stars.

Figure 9 shows, for each panel, the average distributions along the BPT diagram for a different subset of galaxies. Top-left panel includes the diagram for the full sub-sample. Then, each column corresponds to galaxies of different morphologies: (i) early-type galaxies (E/S0), (ii) early-spirals or spirals with prominent bulge (Sa/Sb),

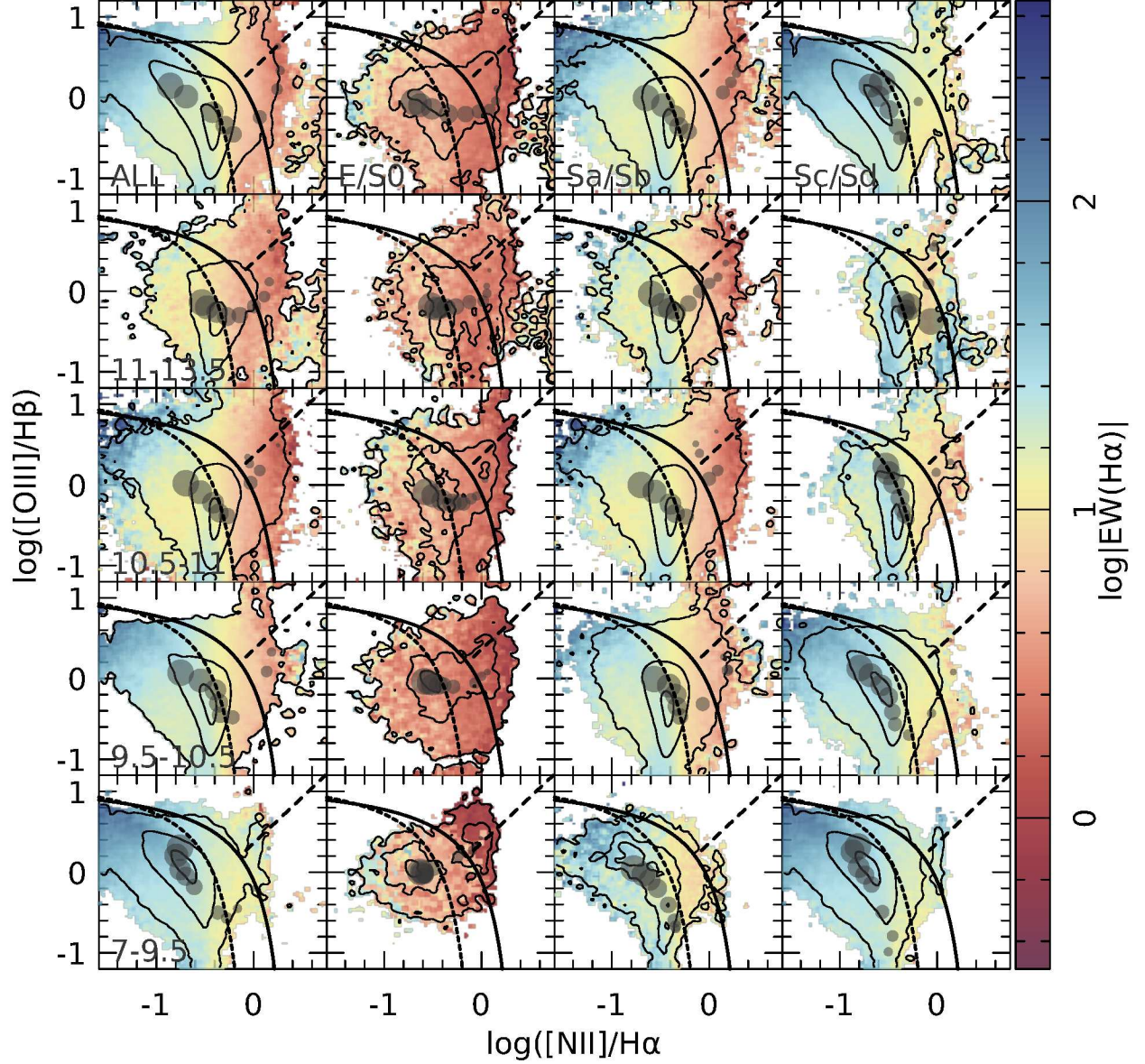


Fig. 9.  $EW(H\alpha)$  across the classical  $[OIII]/H\beta$  vs.  $[NII]/H\alpha$  BPT diagram (Baldwin et al. 1981) for  $\approx 9$  million individual spaxels extracted from a sub-sample of 660 face-on ( $a/b < 0.85$ ), well resolved ( $Re > 2''$ ) and redshift limited ( $0.005 < z < 0.05$ ) galaxies. Each panel shows the distribution for a sub-set of galaxies with different morphologies (columns) and stellar masses (rows), and the top-left panel includes the complete sub-sample, using the same symbols and color schemes: (i) the density of spaxels is traced by the successive contours encircling 90, 50 and 10% of the individual points; (ii) the average values at different galactocentric distances, ranging from 0.1 to 2.1  $Re$  ( $\Delta Re = 0.2$ ), are represented by the grey circles, whose size increases with the distance; (iii) the classical demarcation lines defined by Kewley et al. (2001) and Kauffmann et al. (2003) are represented by solid and short-dashed lines, respectively; finally (iv) the demarcation line segregating between Seyferts and LINES defined by Kewley et al. (2001) is shown as a long-dashed line. The color figure can be viewed online.

and (iii) late-spirals, or spirals with weak or no bulge (Sc/Sd). Finally, each row corresponds to galaxies with a different stellar mass, from high-mass ( $10^{11-13.5} M_{\odot}$ ) to

low-mass ( $10^{7-9.5} M_{\odot}$ ). This way, any panel at a certain column and row represents the BPT diagram for galaxies with a particular morphology and stellar mass. In



addition in each panel is included the location of the azimuthal average  $[OIII]/H\beta$  and  $[NII]/H\alpha$  value at different galactocentric distances.

Figure 9 shows very similar patterns and distributions as those already reported by Sánchez (2020) and Sánchez et al. (2022). For the full sub-sample (top-left panel) the three studies show the highest densities along the known location of either classical H II regions (e.g. Osterbrock 1989) or SF galaxies (e.g. Kauffmann et al. 2003). The highest values of  $EW(H\alpha)$  ( $>10\text{\AA}$ ) are found at these locations too, corresponding to galactocentric distances  $>0.7\text{ }Re$  (i.e., to the disk of galaxies). The distribution presents an extension of much lower density towards the right-side of the diagram, where the  $EW(H\alpha)$  presents the lowest average values ( $\approx 1\text{\AA}$ ), corresponding to the inner regions of galaxies ( $<0.5\text{ }Re$ , i.e., the bulges). This pattern agrees with our current understanding of the dominant ionizing processes in galaxies (e.g. Sánchez et al. 2021). While the ionization in the disk is dominated by the contribution of OB young massive stars, tracers of recent SF processes, the inner region is dominated by a LINER-like ionization (Heckman 1987) produced most probably by Hot-Evoled Low-Mass/post-AGB stars (HOLMES; Binette et al. 1994; Flores-Fajardo et al. 2011; Singh et al. 2013; Belfiore et al. 2017a; Lacerda et al. 2018). Thus, the radial pattern of line ratios is primarily dominated by a change in the dominant ionizing source. Besides that, there is an additional change in the line ratios from the inside-out within the disk regions of galaxies, spanning from the bottom-right (for  $R\approx 0.6\text{ }Re$ ) towards the upper-left (for  $R\approx 2\text{ }Re$ ) regions of higher density. This additional pattern is induced by a general decline of the metal abundances from the inside-out that it observed in the average population of spiral galaxies (e.g. Sánchez et al. 2014; Sánchez 2020).

The main result from this exploration is that the dominant ionizing source is traced by the dominant stellar population. Therefore, as the star-formation history, final stellar composition, and inside-out distribution within galaxies depend on the current morphology and accumulated stellar mass (e.g. González Delgado et al. 2014; García-Benito et al. 2017; Sánchez 2020), and thus the described patterns will be strongly modulated by those two parameters. This is evident in Figure 9. Massive and early-type galaxies (E/S0 and  $M_\star \approx 10^{11-13.5}\text{ }M_\odot$ ), those presenting the older and less diverse stellar population, present the lowest and more homogeneous distribution of  $EW(H\alpha)$ , with most of the ionized regions covering a regime between the center and the right-side of the BPT diagram. We should stress that, contrary to the usual perception their ionized regions are not all restricted to the regime above the classical demarcation lines adopted to separate between SF and non-SF ionization (e.g. Kewley

et al. 2001; Kauffmann et al. 2003), despite the fact that no star formation (and therefore, no young OB-stars) are present in these galaxies. As indicated before, their ionization is dominated by either HOLMES/post-AGB stars (the presence of a significant contribution of low-/mid-velocity shocks also cannot be excluded; and see Dopita et al. 1996). Early-type of lower stellar masses present a larger fraction of ionization in the H II/SF regime of the diagram, although the presence of LINER-like ionization is observed at any stellar mass. Rejuvenation induced by the capture of less massive, gas rich, galaxies or the effect of the slow dimming of a disk remnant could explain this ionization (Gomes et al. 2016; Oyarzun et al. 2019).

On the other hand, low massive and late-type galaxies (Sc/Sd and  $M_\star \approx 10^{7-9.5}\text{ }M_\odot$ ), those presenting the youngest stellar populations, present the highest  $EW(H\alpha)$  values, with a significant variation from the inside-out (from  $10\text{\AA}$  to  $100\text{\AA}$ ). Their ionized regions are essentially restricted to the classical location of H II regions, well below the Kewley et al. (2001) demarcation line, and in most of the cases even below the more restrictive Kauffmann et al. (2003) one. We discussed before that their line ratios change from the inside-out following a negative galactocentric abundance gradient. Following the same trend described for early-type galaxies (E/S0) discussed before, late-type galaxies of higher stellar mass, being still dominated by the presence of young massive stars, present a clear increase of harder ionizations, with the distribution steadily shifting towards the so-called intermediate and LINER-like region of the diagram (i.e., they present an increase in the  $[NII]/H\alpha$  line ratio).

Finally, early-spirals with MW-like stellar masses (Sa/Sb  $M_\star \approx 10^{10.5-11}\text{ }M_\odot$ ), those with the strongest gradient in the stellar populations from the inside-out, present the highest range of  $EW(H\alpha)$  too (from  $\approx 1\text{\AA}$  to  $\approx 100\text{\AA}$ ). Their ionized regions cover the widest range of possible line ratios, with a location similar to those of massive/early-type galaxies (for their central regions), and similar to those of less-massive/late-type galaxies (for the outer regions). This highlights again the strong connection between the dominant stellar population and the observed properties of the ionized gas (i.e., line ratios). Like in the two previous cases (E/S0 and Sc/Sb), the low mass early-type spirals present an ionization more dominated by young massive stars, while the high mass ones present a stronger component of intermediate/LINER-like ionization.

As indicated before, all these patterns are very similar to those described in Sánchez (2020) and Sánchez et al. (2022). However, there are subtle but relevant differences, most of them related to the average radial distribution (traced by the grey solid circles in Figure 9).

In the two previous explorations the radial trends were well defined for all morphological subsamples for stellar masses above  $10^{10.5} M_{\odot}$ . These trends are very similar to the one reported here, describing a shift from the right-side in the central regions (more to the LINER-like in the presense of a bulge or for early-type galaxies) towards the left-side in the outer ones (more prominent and following the loci of classical H II regions for disk dominated galaxies). However, below that mass in both previous studies the trends are less clear, or they directly bend or reverse from this average one observed in the current dataset. This is more evident for late-type/low-mass galaxies (bottom-right panel, Figure 9). As this radial trend, for this particular sub-sample, is determined by a decrease (increase) in the oxygen abundance (ionization strength) from the inside-out, we consider that the distributions observed when using the current dataset fit better with our current understanding of the chemical structure of disk galaxies than the previously reported ones.

We consider that most probably the source of the discrepancy is in the analyzed data themselves. In the case of Sánchez (2020) an heterogeneous compilation of IFS data from different surveys was used, including data of high spatial resolution (AMUSING++; López-Cobá et al. 2020), but also data from CALIFA v2.2, MaNGA (Bundy et al. 2015) and SAMI (Croom et al. 2012), that indeed dominate the statistics. Despite the effort in that review to homogenize the dataset and select only the well resolved data, as we show in §4.3.2, the improved spatial resolution resolution has a clear effect in the exploration of the properties of the ionized gas. The fact that the results presented in Sánchez et al. (2022), using the MaNGA data with lower spatial resolution (even lower in physical terms, due to the average redshift of that sample), present the same discrepancies, reinforces that suspicion.

## 5. SUMMARY AND CONCLUSIONS

Along this article we present one of the largest and better quality distributions of spatial resolved spectroscopic properties of galaxies obtained using IFS data. Comparing with the most recent distributions of similar products, like the results from the analysis using pyPipe3D on the final DR of the MaNGA IFS galaxy survey (Sánchez et al. 2022), we acknowledge that this latter distribution covers a much larger number of galaxies ( $\approx 10,000$ ). However, the number of independent spectra provided by that survey ( $\approx 2$  millions) is only a factor of two larger than the one provided here. This implies that, on average, eCALIFA provides with nearly five times more sampled spatial elements per galaxy. In addition, the MaNGA covers up to  $1.5 R_e$  for  $\approx 2/3$  of the sample, while eCALIFA covers more than  $2 R_e$

for  $\approx 85\%$  of the galaxies (Sánchez 2020, Sanchez et al. 2023). Finally, the new reduction introduced by Sanchez et al. (2023) improved the spatial resolution of the original CALIFA data from  $2.4''/\text{FWHM}$  ( $\approx 700$  pc) to  $\approx 1.0-1.5''/\text{FWHM}$  ( $\approx 300$  pc). In summary, despite the more limited number of galaxies, the spatial sampling and coverage of the optical extension of galaxies is significantly better, in comparison to other IFS surveys with larger galaxy samples.

We describe along this article the analysis performed on this data set, particularly emphasizing the description of the changes introduced in the analysis with respect to previous similar explorations. For each galaxy we deliver a single FITS file comprising different extensions in which each of them includes the spatial distributions of the different physical and observational quantities derived by the analysis. We present a detailed description of each of these extensions, illustrating their content using the results for the galaxy NGC 2906 as a showcase. Finally, we extract for each galaxy a set of integrated and/or characteristic parameters and, when required, the slopes of their radial gradients. We provide an additional catalog containing over 550 derived quantities for each object in the data set.

We illustrate the content of this new set of dataproducs by exploring (i) the properties of the ionized gas in the archetypal galaxy NGC 2906, and (ii) the distribution across the classical BPT diagnostic diagram of the spatial resolved ionized gas for the full sample, segregated by morphology and stellar mass. In both cases, the effects of the improved spatial resolution are appreciated, in particular the ability to detect H II regions and to recover radial trends that were less evident or not directly observed when using data of coarser resolution.

The complete set of data products and the catalog of invidual quantities is freely distributed for its use by the community as part of the eCALIFA data release <sup>13</sup>.

We thank the referee for his/her suggestions that have improved the content of the current manuscript.

S.F.S. thanks the PAPIIT-DGAPA AG100622 project. J.K.B.B. and S.F.S. acknowledge support from the CONACYT grant CF19-39578. R.G.B. acknowledges financial support from the grants CEX2021-001131-S funded by MCIN/AEI/10.13039/501100011033, SEV-2017-0709, and to PID2019-109067-GB100. L.G. acknowledges financial support from the Spanish Ministerio de Ciencia e Innovación (MCIN), the Agencia Estatal de Investigación (AEI) 10.13039/501100011033, and the European Social Fund (ESF) "Investing in your future" under the 2019 Ramón y Cajal program

<sup>13</sup>[http://ifs.astroscu.unam.mx/CALIFA\\_WEB/public\\_html/](http://ifs.astroscu.unam.mx/CALIFA_WEB/public_html/)

TABLE 7  
FLUX\_ELINES\_LONG EXTENSION: ANALYZED EMISSION LINES

#I	$\lambda$ (Å)	Id	#I	$\lambda$ (Å)	Id	#I	$\lambda$ (Å)	Id	#I	$\lambda$ (Å)	Id	#I	$\lambda$ (Å)	Id
0	3726.03	[OII] *	26	4287.4	[FeII]	52	4754.83	[FeIII]	78	5158.0	[FeII]	104	5577.34	[OI]
1	3728.82	[OII] *	27	4340.49	H $\gamma$ *	53	4769.6	[FeIII]	79	5158.9	[FeVII]	105	5631.1	[FeVI]
2	3734.37	HI*	28	4358.1	[FeII]	54	4774.74	[FeII]	80	5176.0	[FeVI]	106	5677.0	[FeVI]
3	3750.15	HI	29	4358.37	[FeII]	55	4777.88	[FeIII]	81	5184.8	[FeII]	107	5720.7	[FeVII]
4	3758.9	[FeVII]	30	4359.34	[FeII]	56	4813.9	[FeIII]	82	5191.82	[ArIII]	108	5754.59	[NII]
5	3770.63	HI	31	4363.21	[OIII]	57	4814.55	[FeII]	83	5197.9	[NI]*	109	5876.0	HeI*
6	3797.9	HI*	32	4413.78	[FeII]	58	4861.36	H $\beta$ *	84	5200.26	[NI]*	110	5889.95	NaI*
7	3819.61	HeI	33	4414.45	[FeII]	59	4881.11	[FeIII]	85	5220.06	[FeII]	111	5895.92	NaI*
8	3835.38	HI	34	4416.27	[FeII]	60	4889.63	[FeII]	86	5261.61	[FeII]	112	6087.0	[FeVII]
9	3868.75	[NeIII]	35	4452.11	[FeII]	61	4893.4	[FeVII]	87	5268.88	[FeII]	113	6300.3	[OI]*
10	3888.65	HeI*	36	4457.95	[FeII]	62	4905.35	[FeII]	88	5270.3	[FeIII]	114	6312.06	[SIII]
11	3889.05	HI*	37	4470.29	[FeII]	63	4921.93	HeI	89	5273.38	[FeII]	115	6363.78	[OI]
12	3933.66	CaII	38	4471.48	HeI	64	4924.5	[FeIII]	90	5277.8	[FeVI]	116	6374.51	[FeX]
13	3964.73	HeI*	39	4474.91	[FeII]	65	4930.5	[FeIII]	91	5296.84	[FeII]	117	6435.1	[ArV]
14	3967.46	[NeIII]*	40	4485.21	[NiII]	66	4942.5	[FeVII]	92	5302.86	[FeXIV]	118	6548.05	[NII]*
15	3968.47	CaII *	41	4562.48	[MgI]	67	4958.91	[OIII]*	93	5309.18	[CaV]	119	6562.85	H $\alpha$ *
16	3970.07	H $\epsilon$ *	42	4571.1	[MgI]	68	4972.5	[FeVI]	94	5333.65	[FeII]	120	6583.45	[NII]*
17	4026.19	HeI	43	4632.27	[FeII]	69	4973.39	[FeII]	95	5335.2	[FeVI]	121	6678.15	HeI
18	4068.6	[SII]	44	4658.1	[FeIII]	70	4985.9	[FeIII]	96	5376.47	[FeII]	122	6716.44	[SII]*
19	4076.35	[SII]	45	4685.68	HeII	71	5006.84	[OIII]*	97	5411.52	HeII	123	6730.82	[SII]*
20	4101.77	H $\delta$ *	46	4701.62	[FeIII]	72	5015.68	HeI*	98	5412.64	[FeII]	124	6855.18	FeI
21	4120.81	HeI	47	4711.33	[ArIV]	73	5039.1	[FeII]	99	5424.2	[FeVI]	125	7005.67	[ArV]
22	4177.21	[FeII]	48	4713.14	HeI	74	5072.4	[FeII]	100	5426.6	[FeVI]	126	7065.19	HeI
23	4227.2	[FeV]	49	4724.17	[NeIV]	75	5107.95	[FeII]	101	5484.8	[FeVI]	127	7135.8	[ArIII]*
24	4243.98	[FeII]	50	4733.93	[FeIII]	76	5111.63	[FeII]	102	5517.71	[ClIII]	128	7155.14	[FeII]
25	4267.0	CII	51	4740.2	[ArIV]	77	5145.8	[FeVI]	103	5527.33	[FeII]	129	7171.98	[FeII]

#I is the running index described in Tab. 6, and Id is a label to identify the emission lines the is the label to each emission line included in the FLUX\_ELINES\_LONG extension. \* emission lines most frequently detected in galaxies, according to Sánchez et al. (2022), for which we distribute the characteristic value (value at the effective radius) and the slope of its radial gradient (§3.4).

RYC2019-027683-I and the PID2020-115253GA-I00 HOSTFLOWS project, from Centro Superior de Investigaciones Científicas (CSIC) under the PIE project 20215AT016, and the program Unidad de Excelencia María de Maeztu CEX2020-001058-M.

This study uses data provided by the Calar Alto Legacy Integral Field Area (CALIFA) survey (<http://califa.caha.es/>). Based on observations collected at the Centro Astronómico Hispano Alemán (CAHA) at Calar Alto, operated jointly by the Max-Planck-Institut für Astronomie and the Instituto de Astrofísica de Andalucía (CSIC).

This research made use of Astropy,<sup>14</sup> a community-developed core Python package for Astronomy (Astropy Collaboration et al. 2013, 2018).

<sup>14</sup><http://www.astropy.org>

## APPENDIX

### A. LIST OF EMISSION LINES USING THE MOMENT ANALYSIS

As indicated before, we perform the moment analysis described in Sec 3.1.3 over two different list of emission lines, whose results are distributed in the FLUX\_ELINES and FLUX\_ELINES\_LONG extensions (§4.1). In the case of the FLUX\_ELINES extension we use the list of emission lines distributed in Sánchez et al. (2016b), Table 1 of that article. For the FLUX\_ELINES\_LONG extension the list of emission lines included in Table 7 was analyzed. For each emission line we include in this table a running index I that defines the channel in which each parameter is included (as described in Tab. 6), together with its rest-frame wavelength and an Id to identify each line. The reported wavelegnth of these emission lines were extracted from Fesen & Hurford (1996).

## B. LIST OF INTEGRATED AND CHARACTERISTIC PARAMETERS

Table 8 lists the complete set of integrated, characteristic parameters and radial gradient slopes distributed for each analyzed data cube, described in §3.4 and included in the `eCALIFA.pyPipe3D.fits` FITs file<sup>15</sup>. For each parameter we include the column in which the information in the FITs file table is stored, the name of the parameter, its units (when required) and a brief description.

TABLE 8

INTEGRATED AND CHARACTERISTIC PARAMETERS DELIVERED FOR EACH ANALYZED DATA CUBE\*

#	parameter name	units	Description
0	ID	–	None
1	cubename	–	eCALIFA name of the data cube
2	galaxy	–	eCALIFA name of the galaxy
3	Re_arc	arcsec	Adopted effective radius in arcsec
4	FoV	–	Ratio between the diagonal radius of the cube and Re
5	redshift	–	Redshift of the galaxy derived by pyPipe3D
6	DL	Mpc	Adopted luminosity distance
7	DA	Mpc	Adopted angular-diameter distance
8	PA	degrees	Adopted position angle in degrees
9	ellip	–	Adopted ellipticity
10	Re_kpc	kpc	Effective radius in kpc
11	log_Mass	log( $M_{\odot}$ )	Integrated stellar mass in units of the solar mass in logarithm scale
12	e_log_Mass	log( $M_{\odot}$ )	Error of the integrated stellar mass in logarithm-scale
13	log_SFR_Ha	–	–
14	e_log_SFR_Ha	–	–
15	log_SFR_ssp	log( $M_{\odot} \text{ yr}^{-1}$ )	Integrated SFR derived from the SSP analysis $t < 32 \text{ Myr}$
16	e_log_SFR_ssp	–	–
17	log_NII_Ha_cen	–	Logarithm of the [NII]6583/H $\alpha$ line ratio in the central aperture
18	e_log_NII_Ha_cen	–	Error in the logarithm of the [NII]6583/H $\alpha$ line ratio
19	log_OIII_Hb_cen	–	Logarithm of the [OIII]5007/H $\beta$ line ratio in the central aperture
20	e_log_OIII_Hb_cen	–	Error in the logarithm of the [OIII]5007/H $\beta$ line ratio
21	log_SII_Ha_cen	–	Logarithm of the [SII]6717+6731/H $\alpha$ line ratio in the central aperture
22	e_log_SII_Ha_cen	–	Error in the logarithm of the [SII]6717/H $\alpha$ line ratio
23	log_OII_Hb_cen	–	Logarithm of the [OII]3727/H $\beta$ line ratio in the central aperture
24	e_log_OII_Hb_cen	–	Error in the logarithm of the [OII]3727/H $\beta$ line ratio
25	EW_Ha_cen	Å	EW of H $\alpha$ in the central aperture
26	e_EW_Ha_cen	Å	Error of the EW of H $\alpha$ in the central aperture
27	ZH_LW_Re_fit	dex	LW metallicity of the stellar population at Re, normalized to the solar value, in logarithm scales
28	e_ZH_LW_Re_fit	dex	Error in the luminosity weighted metallicity of the stellar population
29	alpha_ZH_LW_Re_fit	dex/Re	Slope of the gradient of the LW metallicity of the stellar population
30	e_alpha_ZH_LW_Re_fit	dex/Re	Error of the slope of the gradient of the LW log-metallicity
31	ZH_MW_Re_fit	dex	MW metallicity of the stellar population at Re, normalized to the solar value, in logarithm scales
32	e_ZH_MW_Re_fit	dex	Error in the mass weighted metallicity of the stellar population
33	alpha_ZH_MW_Re_fit	dex/Re	Slope of the gradient of the MW log-metallicity of the stellar population

\*The full table can be viewed online in [https://www.astroscu.unam.mx/rmaa/RMxAA..60-1/PDF/RMxAA..60-1\\_ssanchez-IV-Table8.pdf](https://www.astroscu.unam.mx/rmaa/RMxAA..60-1/PDF/RMxAA..60-1_ssanchez-IV-Table8.pdf).

<sup>15</sup><http://ifs.astroscu.unam.mx/CALIFA/V500/v2.3/tables/>

## REFERENCES

- Anghopo, J., del Moral-Castro, I., Ferreras, I., García-Lorenzo, B., & Ramos Almeida, C. 2022, *MNRAS*, 515, 378, <https://doi.org/10.1093/mnras/stac1655>
- Astropy Collaboration, Price-Whelan, A. M., SipHocz, B. M., et al. 2018, *AJ*, 156, 123, <https://doi.org/10.3847/1538-3881/aabc4f>
- Astropy Collaboration, Robitaille, T. P., Tollerud, E. J., et al. 2014, *A&A*, 558, 33, <https://doi.org/10.1051/0004-6361/201322068>
- Baldwin, J. A., Phillips, M. M., & Terlevich, R. 1981, *PASP*, 93, 5, <https://doi.org/10.1086/130766>
- Barrera-Ballesteros, J. K., Heckman, T., Sánchez, S. F., et al. 2018, *ApJ*, 852, 74, <https://doi.org/10.3847/1538-4357/aa9b31>
- Barrera-Ballesteros, J. K., Sánchez, S. F., Espinosa-Ponce, C., et al. 2022, *arXiv:2206.07058*, <https://doi.org/10.48550/arXiv.2206.07058>
- Barrera-Ballesteros, J. K., Sánchez, S. F., Heckman, T., et al. 2021, *arXiv:2101.04683*, <https://doi.org/10.48550/arXiv.2101.04683>
- Barrera-Ballesteros, J. K., Utomo, D., Bolatto, A. D., et al. 2020, *MNRAS*, 492, 2651, <https://doi.org/10.1093/mnras/stz3553>
- Belfiore, F., Maiolino, R., Maraston, C., et al. 2017a, *MNRAS*, 466, 2570, <https://doi.org/10.1093/mnras/stw3211>
- Belfiore, F., Maiolino, R., Tremonti, C., et al. 2017b, *MNRAS*, 469, 151, <https://doi.org/10.1093/mnras/stx789>
- Belfiore, F., Santoro, F., Groves, B., et al. 2022, *A&A*, 659, 26, <https://doi.org/10.1051/0004-6361/202141859>
- Binette, L., Magris, C. G., Stasińska, G., & Bruzual, A. G. 1994, *A&A*, 292, 13
- Bland-Hawthorn, J. 1995, *PASA*, 12, 190, <https://doi.org/10.1017/S132335800020269>
- Bluck, A. F. L., Maiolino, R., Sánchez, S., et al. 2020, *MNRAS*, 492, 96, <https://doi.org/10.1093/mnras/stz3264>
- Boardman, N., Wild, V., Heckman, T., et al. 2012, *MNRAS*, 520, 4301, <https://doi.org/10.1093/mnras/stad277>
- Bruzual A., G. 1983, *ApJ*, 273, 105, <https://doi.org/10.1086/161352>
- Bundy, K., Bershad, M. A., Law, D. R., et al. 2015, *ApJ*, 798, 7, <https://doi.org/10.1088/0004-637X/798/1/7>
- Camps-Fariña, A., Sánchez, S. F., Lacerda, E. A. D., et al. 2021, *MNRAS*, 504, 3478, <https://doi.org/10.1093/mnras/stab1018>
- Camps-Fariña, A., Sánchez, S. F., Mejía-Narváez, A., et al. 2022, *arXiv:2203.01159*, <https://doi.org/10.48550/arXiv.2203.01159>
- Cano-Díaz, M., Sánchez, S. F., Zibetti, S., et al. 2016, *ApJ*, 821, 26, <https://doi.org/10.3847/2041-8205/821/2/L26>
- Cardelli, J. A., Clayton, G. C., & Mathis, J. S. 1989, *ApJ*, 345, 245, <https://doi.org/10.1086/167900>
- Chambers, K. C., Magnier, E. A., Metcalfe, N., et al. 2016, *arXiv:1612.05560*, <https://doi.org/10.48550/arXiv.1612.05560>
- Cid Fernandes, R., Carvalho, M. S., Sánchez, S. F., de Amorim, A., & Ruschel-Dutra, D. 2021, *MNRAS*, 502, 1386, <https://doi.org/10.1093/mnras/stab059>
- Cid Fernandes, R., Pérez, E., García Benito, R., et al. 2013, *A&A*, 557, 86, <https://doi.org/10.1051/0004-6361/201220616>
- Cid Fernandes, R., Stasińska, G., Mateus, A., & Vale Asari, N. 2011, *MNRAS*, 413, 1687, <https://doi.org/10.1111/j.1365-2966.2011.18244.x>
- Courteau, S., de Jong, R. S., & Broeils, A. H. 1996, *ApJ*, 457, 73, <https://doi.org/10.1086/309906>
- Croom, S. M., Lawrence, J. S., Bland-Hawthorn, J., et al. <https://doi.org/10.1111/j.1365-2966.2011.20365.x>
- D'Agostino, J. J., Kewley, L. J., Groves, B. A., et al. 2019, *MNRAS*, 487, 4153, <https://doi.org/10.1093/mnras/mnras/stz1611>
- Dopita, M. A., Koratkar, A. P., Evans, I. N., 1996, *ASPC* 103, *The Physics of Liners in view of recent observations*, ed. M. Eracleous, A. Koratkar, and L. Ho, 44
- Emsellem, E., Cappellari, M., Krajnović, D., et al. 2011, *MNRAS*, 414, 888, <https://doi.org/10.1111/j.1365-2966.2011.18496.x>
- Emsellem, E., Cappellari, M., Krajnović, D., et al. 2007, *MNRAS*, 379, 401, <https://doi.org/10.1111/j.1365-2966.2007.11752.x>
- Emsellem, E., Schinnerer, E., Santoro, F., et al. 2022, *A&A*, 659, 191, <https://doi.org/10.1051/0004-6361/202141727>
- Espinosa-Ponce, C., Sánchez, S. F., Morisset, C., et al. 2020, *MNRAS*, 494, 1622, <https://doi.org/10.1093/mnras/staa782>
- Fesen, R. A. & Hurford, A. P. 1996, *ApJS*, 106, 563, <https://doi.org/10.1086/192348>
- Flewelling, H. A., Magnier, E. A., Chambers, K. C., <https://doi.org/10.3847/1538-4365/abb82d>
- Flores-Fajardo, N., Morisset, C., Stasińska, G., & Binette, L. 2011, *MNRAS*, 415, 2182, <https://doi.org/10.1111/j.1365-2966.2011.18848.x>
- Gaia Collaboration, Brown, A. G. A., Vallenari, A., et al. 2021, *A&A*, 649, 1, <https://doi.org/10.1051/0004-6361/202039657>
- Gaia Collaboration, Prusti, T., de Bruijne, J. H. J., et al. 2016, *A&A*, 595, 1, <https://doi.org/10.1051/0004-6361/201629272>
- Galbany, L., Anderson, J. P., Sánchez, S. F., et al. 2018, *ApJ*, 855, 107, <https://doi.org/10.3847/1538-4357/aaaf20>
- García-Benito, R., González Delgado, R. M., Pérez, E., et al. 2017, *A&A*, 608, 27, <https://doi.org/10.1051/0004-6361/201731357>
- García-Benito, R., Zibetti, S., Sánchez, S. F., et al. 2015, *A&A*, 576, 135, <https://doi.org/10.1051/0004-6361/201425080>
- Gomes, J. M., Papaderos, P., Vílchez, J. M., et al. 2016, *A&A*, 585, 92, <https://doi.org/10.1051/0004-6361/201525974>
- González Delgado, R. M., Pérez, E., Cid Fernandes, R., et

- al. 2014, *A&A*, 562, 47, <https://doi.org/10.1051/0004-6361/201322011>
- González Delgado, R. M., Pérez, E., Cid Fernandes, R., et al. 2017, *A&A*, 607, 128, <https://doi.org/10.1051/0004-6361/201730883>
- Gorgas, J., Cardiel, N., Pedraz, S., & González, J. J. 1999, *A&AS*, 139, 29, <https://doi.org/10.1051/aas:1999375>
- Guidi, G., Casado, J., Ascasibar, Y., et al. 2018, *MNRAS*, 479, 917, <https://doi.org/10.1093/mnras/sty1480>
- Heckman, T. M. 1987, *IAUS* 121, *Observational Evidence of Activity in Galaxies*, ed. E.E. Khachikian, K. J. Fricke and J. Melnick (Kluwer Academic Publishers, Dordrecht) 421
- Heckman, T. M., Armus, L., & Miley, G. K. 1990, *ApJS*, 74, 833, <https://doi.org/10.1086/191522>
- Husemann, B., Jahnke, K., Sánchez, S. F., et al. 2013, *A&A*, 549, 87, <https://doi.org/10.1051/0004-6361/201220582>
- Ibarra-Medel, H. J., Avila-Reese, V., Sánchez, S. F., González-Samaniego, A., & Rodríguez-Puebla, A. 2019, *MNRAS*, 483, 4525, <https://doi.org/10.1093/mnras/sty3256>
- Ibarra-Medel, H. J., Sánchez, S. F., Avila-Reese, V., et al. 2016, *MNRAS*, 463, 2799, <https://doi.org/10.1093/mnras/stw2126>
- Kauffmann, G., Heckman, T. M., Tremonti, C., et al. 2003, *MNRAS*, 346, 1055, <https://doi.org/10.1111/j.1365-2966.2003.07154.x>
- Kelz, A., Verheijen, M. A. W., Roth, M. M., et al. 2006, *PASP*, 118, 129, <https://doi.org/10.1086/497455>
- Kennicutt, Jr., R. C. 1998, *ARA&A*, 36, 189, <https://doi.org/10.1146/annurev.astro.36.1.189>
- Kewley, L. J., Dopita, M. A., Sutherland, R. S., Heisler, C. A., & Trevena, J. 2001, *ApJ*, 556, 121, <https://doi.org/10.1086/321545>
- Lacerda, E. A. D., Cid Fernandes, R., Couto, G. S., et al. 2018, *MNRAS*, 474, 3727, <https://doi.org/10.1093/mnras/stx3022>
- Lacerda, E. A. D., Sánchez, S. F., Cid Fernandes, R., et al. 2020, *MNRAS*, 492, 3073, <https://doi.org/10.1093/mnras/staa008>
- Lacerda, E. A. D., Sánchez, S. F., Mejía-Narváez, A., et al. 2022, *arXiv:2202.08027*, <https://doi.org/10.48550/arXiv.2202.08027>
- Law, D. R., Belfiore, F., Bershad, M. A., et al. 2022, *arXiv:2112.11281*, <https://doi.org/10.48550/arXiv.2112.11281>
- Levy, R. C., Bolatto, A. D., Teuben, P., et al. 2018, *ApJ*, 860, 92, <https://doi.org/10.3847/1538-4357/aac2e5>
- López-Cobá, C., Sánchez, S. F., Anderson, J. P., et al. 2020, *AJ*, 159, 167, <https://doi.org/10.3847/1538-3881/ab7848>
- López-Cobá, C., Sánchez, S. F., Moiseev, A. V., et al. 2017, *MNRAS*, 467, 4951, <https://doi.org/10.1093/mnras/stw3355>
- López Fernández, R., González Delgado, R. M., Pérez, E., et al. 2018, *A&A*, 615, 27, <https://doi.org/10.1051/0004-6361/201732358>
- Lugo-Aranda, A. Z., Sánchez, S. F., Espinosa-Ponce, C., et al. *RASTI*, 1, 3, <https://doi.org/10.1093/rasti/rzac001>
- Marino, R. A., Rosales-Ortega, F. F., Sánchez, S. F., et al. 2013, *A&A*, 559, 114, <https://doi.org/10.1051/0004-6361/201321956>
- McCall, M. L., Rybski, P. M., & Shields, G. A. 1985, *ApJS*, 57, 1, <https://doi.org/10.1086/190994>
- Osterbrock, D. E. 1989, *Astrophysics of gaseous nebulae and active galactic nuclei* (University Science Books)
- Oyarzun, G. A., Bundy, K., Westfall, K. B., et al. 2019, *ApJ*, 880, 111, <https://doi.org/10.48550/arXiv.1906.05298>
- Panther, B., Jimenez, R., Heavens, A. F., & Charlot, S. 2007, *MNRAS*, 378, 1550, <https://doi.org/10.1111/j.1365-2966.2007.11909.x>
- Pérez, E., Cid Fernandes, R., González Delgado, R. M., <https://doi.org/10.1088/2041-8205/764/1/L1>
- Pettini, M. & Pagel, B. E. J. 2004, *MNRAS*, 348, 59, <https://doi.org/10.1111/j.1365-2966.2004.07591.x>
- Relaño, M., Kennicutt, Jr., R. C., Eldridge, J. J., Lee, J. C., & Verley, S. 2012, *MNRAS*, 423, 2933, <https://doi.org/10.1111/j.1365-2966.2012.21107>
- Roth, M. M., Kelz, A., Fechner, T., et al. 2005, *PASP*, 117, 620, <https://doi.org/10.1086/429877>
- Salpeter, E. E. 1955, *ApJ*, 121, 161, <https://doi.org/10.1086/145971>
- Sánchez, S. F. 2006, *AN*, 327, 850, <https://doi.org/10.1002/asna.200610643>
- . 2020, *ARA&A*, 58, 99, <https://doi.org/10.1146/annurev-astro-012120-013326>
- Sánchez, S. F., Avila-Reese, V., Hernandez-Toledo, H., et al. 2018, *RMxAA*, 54, 217
- Sánchez, S. F., Avila-Reese, V., Rodríguez-Puebla, A., et al. 2019, *MNRAS*, 482, 1557, <https://doi.org/10.1093/mnras/sty2730>
- Sánchez, S. F., Barrera-Ballesteros, J. K., Lacerda, E., et al. 2022, *ApJS*, 262, 36, <https://doi.org/10.3847/1538-4365/ac7b8f>
- Sánchez, S. F., Barrera-Ballesteros, J. K., López-Cobá, C., et al. 2019b, *MNRAS*, 484, 3042, <https://doi.org/10.1093/mnras/stz019>
- Sanchez, S. F., Galbany, L., Walcher, C. J., Garcia-Benito, R., & Barrera-Ballesteros, J. K. 2023, *arXiv:2304.13022*, <https://doi.org/10.48550/arXiv.2304.13022>
- Sánchez, S. F., García-Benito, R., Zibetti, S., et al. 2016a, *A&A*, 594, 36, <https://doi.org/10.1051/0004-6361/201628661>
- Sánchez, S. F., Kennicutt, R. C., Gil de Paz, A., et al. 2012, *A&A*, 538, 8, <https://doi.org/10.1051/0004-6361/201117353>
- Sánchez, S. F., Pérez, E., Sánchez-Blázquez, P., et al. 2016b, *RMxAA*, 52, 171
- Sánchez, S. F., Pérez, E., Sánchez-Blázquez, P., et al. 2016c, *RMxAA*, 52, 21
- Sánchez, S. F., Rosales-Ortega, F. F., Iglesias-Páramo, J., et al. 2014, *A&A*, 563, 49, <https://doi.org/10.1051/0004-6361/201322343>

- Sánchez, S. F., Walcher, C. J., Lopez-Cobá, C., et al. 2021, *RMxAA*, 57, 3, <https://doi.org/10.22201/ia.01851101p.2021.57.01.01>
- Sánchez-Menguiano, L., Sánchez, S. F., Pérez, I., et al. 2016, *A&A*, 587, 70, <https://doi.org/10.1051/0004-6361/201527450>
- Sánchez-Menguiano, L., Sánchez, S. F., Pérez, I., Ruiz-Lara, T., Galbany, L., Anderson, J. P., Krühler, T., Kuncarayakti, H., & Lyman, J. D. 2018, *A&A*, 609, A119
- Sánchez-Menguiano, L., Sánchez Almeida, J., Muñoz-Tuñón, C., et al. 2019, *ApJ*, 882, 9, <https://doi.org/10.3847/1538-4357/ab3044>
- Sarmiento, R., Huertas-Company, M., Knapen, J. H., et al. 2023, *arXiv:2211.11790*, <https://doi.org/10.48550/arXiv:2211.11790>
- Singh, R., van de Ven, G., Jahnke, K., et al. 2013, *A&A*, 558, 43, <https://doi.org/10.1051/0004-6361/201322062>
- Vale Asari, N., Stasińska, G., Cid Fernandes, R., et al. 2009, *MNRAS*, 396, 71, <https://doi.org/10.1111/j.1745-3933.2009.00664.x>
- Veilleux, S., Shopbell, P. L., & Miller, S. T. 2001, *AJ*, 121, 198, <https://doi.org/10.1086/318046>
- Walcher, C. J., Wisotzki, L., Bekeraité, S., et al. 2014, *A&A*, 569, 1, <https://doi.org/10.1051/0004-6361/201424198>
- Weilbacher, P. M., Monreal-Ibero, A., Verhamme, A., et al. 2018, *A&A*, 611, 95, <https://doi.org/10.1051/0004-6361/201731669>
- Westfall, K. B., Cappellari, M., Bershad, M. A., et al. 2019, *AJ*, 158, 231, <https://doi.org/10.3847/1538-3881/ab44a2>
- York, D. G., Adelman, J., Anderson, Jr., J. E., et al. 2000, *AJ*, 120, 1579, <https://doi.org/10.1086/301513>

- J. K. Barrera-Ballesteros, E. Lacerda, and S. F. Sánchez: Instituto de Astronomía, Universidad Nacional Autónoma de México, A.P. 70-264, 04510 CDMX, México ([sfsanchez@astro.unam.mx](mailto:sfsanchez@astro.unam.mx)).
- A. Camps-Fariña: Departamento de Física de la Tierra y Astrofísica, Universidad Complutense de Madrid, Pl. Ciencias, 1, Madrid, 28040, Madrid.
- L. Galbany: Institute of Space Sciences (ICE, CSIC), Campus UAB, Carrer de Can Magrans, s/n, E-08193 Barcelona, Spain.
- L. Galbany: Institut d'Estudis Espacials de Catalunya (IEEC), E-08034 Barcelona, Spain.
- R. García-Benito: Instituto de Astrofísica de Andalucía (IAA/CSIC), Glorieta de la Astronomía s/n Aptdo. 3004, E-18080 Granada, Spain.





# INVESTIGATION ON FOUR CONTACT BINARY SYSTEMS AND A SEMI-DETACHED ONE AT THE BEGINNING OF THE CONTACT PHASE

F. Acerbi<sup>1</sup>, M. Martignoni<sup>1</sup>, R. Michel<sup>2</sup>, C. Barani<sup>1</sup>, H. Aceves<sup>2</sup>, L. Altamirano-Dévora<sup>2</sup>, and F. J. Tamayo<sup>3</sup>

*Received July 3 2023; accepted September 25 2023*

## ABSTRACT

We present  $B$ ,  $V$ ,  $R_c$  and  $I_c$  light curves of four contact binary systems and one semi-detached system. New observations confirm and revise the short-period (0.22–0.25d) of the systems and that all stars belong to the spectral type K. In J105924 and J164349 a third light was found while the shape of the light curves of four systems (excluding J105924) suggests the presence of inhomogeneities on the surface of one component which confirms that the systems are active. Also they are observed at low orbital inclination  $i \in (41^\circ, 62^\circ)$ . The temperature difference range is  $\Delta T \in (4, 640)\text{K}$  and the mass ratios  $q \in (0.20, 0.75)$ . Absolute parameters are estimated using statistical diagrams. The systems follow the general pattern of the relative subtype of W Ursae Majoris systems. The sum of the component masses of four systems is below the mass limit of  $1.0 - 1.2M_\odot$  assumed for the known contact binary stars; this tells us that they belong to the class of low mass contact binaries.

## RESUMEN

Se presentan curvas de luz en  $B, V, R_c$  e  $I_c$  de cuatro binarias en contacto y un sistema semi-ligado. Nuevas observaciones confirman y actualizan los cortos períodos (0.22-0.25d) de los sistemas y que todas las estrellas son del tipo espectral K. En J105924 y J164349 se encontró una tercera luz, mientras que en cuatro sistemas (excluyendo J105924) se sugiere la presencia de inhomogeneidad en la superficie de un componente, confirmando que los sistemas están activos. También tienen una inclinación orbital baja  $i \in (41^\circ, 62^\circ)$ , diferencias en temperatura  $\Delta T \in (4, 640)\text{K}$ , y cocientes de masa  $q \in (0.20, 0.75)$ . Los parámetros absolutos se estiman utilizando diagramas estadísticos. Los sistemas siguen el patrón general del subtipo W Ursae Majoris. La suma de las masas en cuatro sistemas está por debajo del límite de masa de  $1.0-1.2M_\odot$ , asumido para las estrellas binarias de contacto conocidas; esto nos dice que pertenecen a la clase de binarias de contacto de baja masa.

*Key Words:* stars: individual: 1SWASP J105924.30+220458.0, 1SWASP J123609.78+341159.5, 1SWASP J161858.05+261303.5 (V1458 Her), 1SWASP J164349.61+325637.8 (V1475 Her), 1SWASP J132308.74+424613.3 (HW CVn) — techniques: photometric

## 1. INTRODUCTION

Our knowledge of binary systems allows us to divide them in three large groups. (1) The detached systems, in which both the stars are inside their respective Roche lobes without interactions between the components. (2) The semi-detached systems, with mass transfer from a component that fills its Roche lobe to the other one. And (3) contact, or

over-contact, binaries that share the same outer atmosphere, the common convective envelope (CCE), and generally are in thermal and physical contact.

The transition between semidetached to contact phase, and viceversa, is predicted by the thermal relaxation oscillation theory (TRO theory) (Lucy 1976; Flannery 1976; Robertson & Eggleton 1977; Yakut & Eggleton 2005; Li et al. 2008). TRO considers that the mass transfer between the components causes them to evolve oscillating in a cycle, where the flow of mass is reversed and the contact binary evolves

<sup>1</sup>Stazione Astronomica Betelgeuse, Magnago, Italy.

<sup>2</sup>Instituto de Astronomía, UNAM. Ensenada, México.

<sup>3</sup>Facultad de Ciencias Físico-Matemáticas, UANL, Nuevo León, México.

TABLE 1  
PARAMETERS OF THE TARGETS FROM THE VSX DATABASE

Target	RA(2000)	Dec(2000)	Period, d	Ampl.	Reference
J105924	10 59 24.30	+22.04.58.5	0.231092	0.12	Drake et al. (2014)
J123609	12 36 09.75	+34.11.59.7	0.248408	0.19	Drake et al. (2014)
J132308	13 23 08.74	+42 46 13.0	0.225133	0.16	Butters et al.(2010)
J161858	16 18 57.85	+26 13 38.5	0.228779	0.17	Butters et al.(2010)
J164349	16 43 49.61	+32 56 37.8	0.2250909	0.11	Akerlof et al. (2000)

toward small mass ratios  $q$ . Upon reaching the  $q_{min}$  the contact binary becomes unstable and may coalesce as progenitor of a single rapidly rotating star (Stępień (2011); Tylenda et al. (2011); Zhu et al. (2016); Liao et al. (2017); Li et al. (2021); Li et al. (2022) .

All the systems analyzed in this work belong to the spectral type K. The contact K-type systems here presented are of particular interest because only a few of them are well studied, especially systems with periods shorter than 0.25 days that are important objects for explaining the period cut-off phenomenon (Paczynski et al. (2006); Ruciński & Pribulla (2008); Liu et al. (2014); Li et al. (2019)).

It is clear that the study of binary systems is fundamental to acquire information about their formation and evolutionary status. The objective of this work is to acquire and estimate properties of a set of CBs using high quality photometric data and empirical relations.

## 2. INFORMATION ABOUT THE SYSTEMS

1SWASP J105924.30+220458.0 (J105924) and 1SWASP J123609.78+341159.5 (J123609) were found to be variable stars in the region covered by the Catalina Surveys Data Release-1 (CSDR1) (Drake et al. 2014). The type of variation was given for both systems (W UMa type), the amplitude as 0.12 mag. and the period as 0.231092 days for J105924; and the amplitude as 0.19 mag. and the period as 0.248408 days for J123609.

1SWASP J132308.74+424613.3 (J132308 = HW CVn): the type of variability was reported by Butters et al. (2010) as a generical EA/EB in the first WASP public data release. The period was identified by Lohr et al. (2013) as 19451.249s or 0.225130 days while the 5<sup>th</sup> edition of the General Catalogue of Variable Stars (GCVS) by Samus' et al. (2017) report the first complete ephemerides:

$$HJD = 2456311.0270 + 0.225133 E. \quad (1)$$

The type of variability is EW and the amplitude of the light variation is 0.35 mag.

The first period for 1SWASP J161858.05+261303.5 (J161858 = V1458 Her) was found by Lohr et al. (2013) as 19766.679s or 0.228781 days, and Samus' et al. (2017) in the GCVS report the complete ephemeris

$$HJD = 2456395.9480 + 0.228779 E. \quad (2)$$

suggesting the type of variation and a low amplitude of 0.17 mag. The system was analysed in a 2020 article (Li et al. 2020) together with other eight contact binaries around the short-period cutoff; a comparison of the results will be discussed later.

1SWASP J164349.61+325637.8 (J164349 = V1475 Her) was first reported as a Delta Scuti star in the Robotic Optical Transient Search Experiment I (ROTSE-I) surveys (Akerlof et al. 2000) with the half period of 0.11255 days. The correct period (19447.858s or 0.225091 days) and the nature of the eclipsing system was reported again by Lohr et al. (2013). The complete ephemerides was published in the GCVS (Samus' et al. 2017):

$$HJD = 2456459.8550 + 0.225091 E. \quad (3)$$

The amplitude of the EW light variation was found to be 0.21 mag.

J123609 and J164349, with a mass ratio  $q > 0.72$  are considered high mass ratio systems, or H-type systems, as suggested by Csizmadia & Klagyivik (2004).

## 3. OBSERVATIONS AND NEW EPHEMERIDES

The preliminary available information about the targets was taken from the AAVSO Variable Star Index database (VSX) and is presented in Table 1.

All the observations were carried out at the San Pedro Mártir National Observatory (SPM, México) with the 0.84-m telescope (an f/15 Ritchey-Chretien), the Mexman filter-wheel and the *Marconi 5* CCD detector (an e2v CCD231-42 chip with  $15 \times 15 \mu^2$  pixels, gain of 2.38 e<sup>-</sup>/ADU and read-out noise of 4.02 e<sup>-</sup>). The field of view was  $9' \times 9'$

TABLE 2  
LOG OF THE OBSERVATIONS

Object	UTObsDate	Hours	ExpTime <i>B</i>	ExpTime <i>V</i>	ExpTime <i>R</i>	ExpTime <i>I</i>
J105924	2022-03-27	5.75	40	20	15	15
J123609	2022-03-26	7.53	40	20	15	15
	2022-04-27	2.63	80	40	30	30
	2023-03-29	6.54	60	40	25	25
J132308	2022-03-23	5.47	40	20	15	15
	2022-03-25	1.88	40	20	15	15
J161858	2022-04-23	4.44	-	40	20	15
	2022-04-25	5.71	40	20	15	15
J164349	2022-04-14	5.81	40	20	15	15

TABLE 3  
TIMES OF MINIMUM AND NEW EPHEMERIDES FROM OUR OBSERVATIONS

Object	HJD	Epoch	O-C	Error	Source	New Ephemerides	
J105924	2459665.6977	-0.5	0	0.0027	[1]	HJD 2459665.8122(10)	0.d2290620(5)
	2459665.8122	0	0	0.0032	[1]		
J123609	2459664.7260	0	0.0002	0.0057	[1]	HJD 2459664.7258(11)	0.d2484199(171)
	2459664.8480	0.5	-0.002	0.0047	[1]		
	2459664.9760	1	0.0018	0.0044	[1]		
	2459696.6477	128.5	0	0.0028	[1]		
J132308	2456311.0270	0	0	-	[2]	HJD 2456311.0270(14)	0.d2251345(1)
	2459661.8169	14883.5	0.001	0.0016	[1]		
	2459663.9537	14893	-0.001	0.002	[1]		
J161858	2456395.9480	0	0	-	[2]	HJD 2456395.9480(20)	0.d2287771(2)
	2459694.8008	14419.5	0.0014	0.0024	[1]		
	2459694.9124	14420	-0.0014	0.0019	[1]		
J164349	2456459.8550	0	0	-	[2]	HJD 2456459.8550(13)	0.d2250909(1)
	2459683.8340	14323	0.0014	0.0016	[1]		
	2459683.9439	14323.5	-0.0012	0.0018	[1]		
	2459711.8561	14447.5	-0.0002	0.0018	[1]		

[1] This paper. [2] AAVSO VSX.

and a binning of  $2 \times 2$  was employed during all the observations.

Alternated exposures in filters *B*, *V*, *R<sub>c</sub>* and *I<sub>c</sub>* were taken during the observing runs. The details of the observations are shown in Table 2.

All the images were processed using IRAF<sup>4</sup> routines. Images were bias subtracted and flat field corrected before the instrumental magnitudes were computed with the standard aperture photometry method.

<sup>4</sup>IRAF is distributed by the National Optical Observatories, operated by the Association of Universities for Research in Astronomy, Inc., under cooperative agreement with the National Science Foundation.

In Table 3 are reported the ToMs and the new ephemerides derived from our observations.

The Transiting Exoplanet Survey Satellite (TESS; Prša et al. (2022)) provides some photometric data for our binary systems expressed in what are called T-magnitudes. These magnitudes are derived under some assumptions from the properties of the binary stars and their magnitudes at different wavelengths (Stassun et al. 2018). Here we abstain from using T-magnitude data and prefer to use our four clear-cut photometric bands data from SPM, and leave for future work a possible comparison on how the derived parameters here are affected when using the TESS data. Given the excellent quality and multi-wavelength data of our terrestrial obser-

TABLE 4  
TARGET TEMPERATURE

Target	[1]	[2]	[3]	[4]	[5]	[6]	[7]	[8]	[9]	[10]
J105924	5022									5022
J123609		4996	4890	4890	4731	4844	4814			4860
J132308			4447	4447	4377	4638	4452		4542	4480
J161858				4580						4580
J164349			4457	4324				4361		4380

[1] LAMOST DR7, (Qian et al. 2020), [2] CRTS VSC, (Marsh et al. 2017), [3] ATLAS Refecat2, (Tonry et al. 2018), [4] Gaia DR2, (Brown et al. 2018), [5] Regression in GaiaDR2, (Bai et al. 2019), [6] Gaia EDR3, (Anders et al. 2022), [7] TESS Input Catalog - v8.0, (Stassun et al. 2019), [8] TESS Input Catalog - v8.2, (Paegert et al. 2021), [9] SDSS, (Miller 2015), [10] Average.

variations we conjecture that differences might be in the last one or two digits of our derived values reported below.

#### 4. PHOTOMETRIC SOLUTION WITH THE W-D METHOD

The light curves of the systems were analyzed using the latest version of the Wilson-Devinney (W-D) code (Wilson & Devinney (1971); Wilson (1990); Wilson & van Hamme. (2016)).

Before starting the analysis some input parameters must be fixed, one of the most important being the temperature of the primary component ( $T_1$ ). For this purpose, we have averaged the temperatures published in different stellar surveys (Table 4) and used this value in our set of parameters.

The temperature of the primary component of the systems suggests a convective envelope. Hence, we fixed in the W-D code the following atmospheric parameters to their theoretical values: the gravity-darkening coefficients  $g_1 = g_2 = 0.32$  (Lucy 1967) and the bolometric albedos  $A_1 = A_2 = 0.5$  (Ruciński 1973); the limb-darkening values originate from van Hamme (1993) for  $\log g = 4.0$  and solar abundances.

The other parameters left as adjustable during the calculation were those suggested by the operation Mode 3 of the code; Mode 3 is used for the analysis of binary systems in contact and the free parameters are the orbital inclination  $i$ , the mean surface effective temperature of the secondary component  $T_2$ , the dimensionless surface potentials of the primary and secondary stars  $\Omega_1 = \Omega_2$ , the monochromatic luminosity of the primary component  $L_1$  and the third light  $L_3$ .

The well-known  $q$ -search method was used to find the best initial mass ratio value fixed at each iteration and increased by 0.05 from  $q = 0.05$  to 1 and by 0.1 beyond  $q = 1$ , since the mean residual showed a minimum.

For the systems J105924 and J164349, the results indicated the presence of a third light while for the other three systems the values for third light were negligible (smaller than the uncertainties).

The well know O’Connell effect, i.e. the different height of the maxima, (O’Connell 1951) is visible in the light curves of four of the systems (Figure 2). For this reason the spot parameters, co-latitude  $\theta$ , longitude  $\phi$ , angular radius  $\gamma$ , and the temperature factor  $T_s/T_*$  were treated as free.

For system J132308 we were not able to find a good fit to its light curves using Mode 3, so we switched to Mode 2, a detached configuration with no constraint on the potentials (Leung & Wilson 1977) to test the semi-detached configuration. After few iterations, the solution converged to Mode 5 – a semi-detached configuration with star 2 filling its Roche lobe. Using this Mode, the fixed parameters are the same of Mode 3 while among the free parameters  $\Omega_1$  is adjustable and  $\Omega_2$  is fixed by the code to the respective value of the mass ratio, so that the secondary component accurately fills its Roche lobe.

In Figure 1 the behavior of the  $q$  search procedure is visible, where the mean residual for the input data ( $\Sigma$ ) is plotted against the value of the mass ratio  $q$ .

The value of  $q$  corresponding to the minimum value of  $\Sigma$  was subsequently included in the list of the adjustable parameters and a more detailed analysis was performed simultaneously for all the available light curves.

The final results obtained are listed in Table 5 where, for systems with mass ratio  $q > 1$  the use of the reciprocal value of  $q$  ( $q_{inv}$ ), as accepted in the general meaning, was used, while the obtained fits are shown in Figure 2.

Graphic representations of the systems are shown in Figure 3, using the **Binary Maker 3.0** software (Bradstreet & Steelman 2002).

TABLE 5  
VALUES OF THE FIXED AND CALCULATED PARAMETERS

Parameter	J105924	J123609	J132308	J161858	J164349
Spectral type	K2 + K2	K3 + K6/K7	K4 + K6/K7	K4 + K7	K5 + K9
$i$	55°.028(0.129)	40°.980(0.710)	62°.070(0.392)	46°.040(0.289)	59°.368(0.055)
$T_1$	5022K Fixed	4860K Fixed	4480K Fixed	4580K Fixed	4380K Fixed
$T_2$	5018K(71)	4216K(42)	4209K(24)	4065K(18)	3909K(10)
$\Omega_{1,2}$	2.5898(0.0017)	3.9074(0.0042)	8.6765(0.0472)	2.7618(0.0039)	2.9562(0.0018)
$\Omega_2$			9.03996 Fixed		
mass ratio $q$ or $q_{inv}$	0.5017(0.0091)	0.7470(0.0261)	0.2020(0.0524)	0.5486(0.0048)	0.7499(0.0010)
$\Delta T$	4K	644K	271K	515K	471K
$f$	93.30%	54.80%	6.70%	63.60%	78.90%
$f_2$			0%		
$L_{1B}$	0.2189(0.0214)	0.5601(0.0192)	0.2755(0.0076)	0.6711(0.0060)	0.2908(0.0026)
$L_{1V}$	0.2227(0.0186)	0.5283(0.0172)	0.2623(0.0060)	0.6510(0.0054)	0.2802(0.0024)
$L_{1R}$	0.2233(0.01869)	0.5083(0.0153)	0.2509(0.0048)	0.6411(0.0050)	0.2674(0.0021)
$L_{1I}$	0.2225(0.0175)	0.4909(0.0136)	0.2453(0.0039)	0.6286(0.0045)	0.2405(0.0018)
$L_{2B}$	0.1304(0.0099)	0.2423(0.0101)	0.6060(0.0020)	0.1664(0.0008)	0.0976(0.0010)
$L_{2V}$	0.1327(0.0092)	0.2807(0.0081)	0.6304(0.0018)	0.1910(0.0009)	0.1107(0.0008)
$L_{2R}$	0.1331(0.0088)	0.3185(0.0085)	0.6484(0.0027)	0.2162(0.0011)	0.1211(0.0011)
$L_{2I}$	0.1329(0.0086)	0.3525(0.0094)	0.6726(0.0031)	0.2375(0.0008)	0.1218(0.0012)
$L_{3B}$	0.5809(0.0193)	0	0	0	0.5485(0.0003)
$L_{3V}$	0.5755(0.0189)	0	0	0	0.5510(0.0003)
$L_{3R}$	0.5844(0.0186)	0	0	0	0.5556(0.0005)
$L_{3I}$	0.5914(0.0182)	0	0	0	0.5844(0.0004)
$R_{1pole}$	0.4679(0.0018)	0.3745(0.0035)	0.2572(0.0043)	0.4421(0.0011)	0.4408(0.0002)
$R_{1side}$	0.5134(0.0030)	0.4008(0.0049)	0.2712(0.0053)	0.4780(0.0016)	0.4817(0.0003)
$R_{1back}$	0.5760(0.0069)	0.4679(0.0123)	0.3339(0.0157)	0.5255(0.0030)	0.5635(0.0008)
$R_{2pole}$	0.3575(0.0041)	0.4192(0.0026)	0.4856(0.0008)	0.3436(0.0019)	0.3948(0.0002)
$R_{2side}$	0.3859(0.0060)	0.4516(0.0039)	0.5278(0.0010)	0.3659(0.0025)	0.4286(0.0003)
$R_{2back}$	0.5240(0.0520)	0.5078(0.0082)	0.5505(0.0010)	0.4342(0.0067)	0.5436(0.0017)
$\Sigma$	0.00075351	0.00237069	0.00207468	0.00155913	0.00058782
$Lat_{spot}$		89°.4(0.9)	41°.7(1.2)	121°.1(1.9)	99°.5(1.7)
$Long_{spot}$		110°.6(1.3)	285°.2(1.9)	79°.2(1.4)	85°.2(1.2)
Radius		28°.7(0.56)	35°.5(0.89)	36°.7(0.63)	48°.5(1.11)
T/F		1.035(0.04)	0.945(0.08)	0.750(0.08)	1.03(0.06)
Component		1	2	1	1

## 5. EVOLUTIONARY STATUS OF THE SYSTEMS

For the determination of the absolute parameters of the systems under study, we used the relationship  $P - a$  (period–semi-major axis) developed by Dim-

itrov & Kjurkchieva (2015). This relationship was developed based on 14 binary stars having  $P < 0.27$ d as follows:

$$a = -1.154 + 14.633 P - 10.319 P^2 \quad (4)$$

where  $P$  is given in days and  $a$  in solar radii.

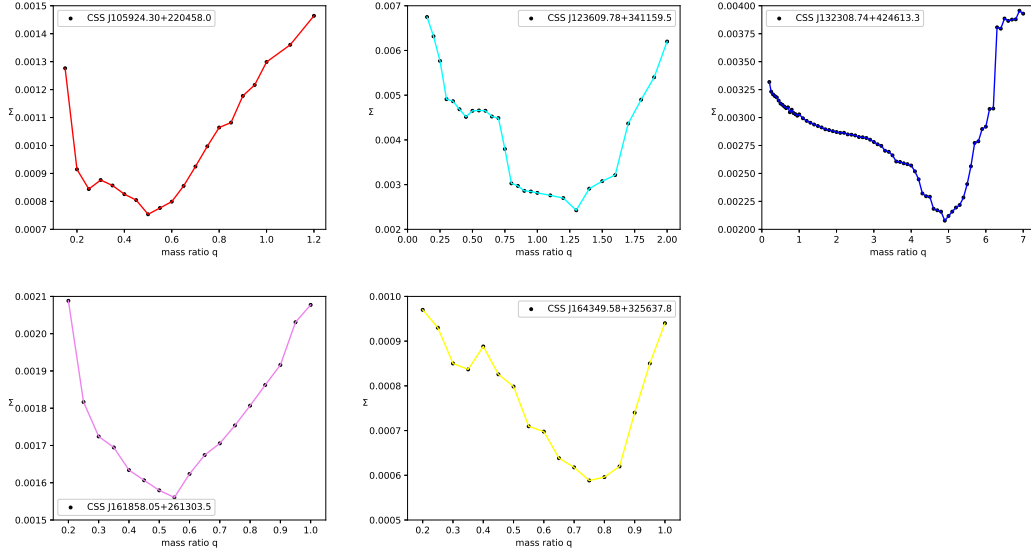


Fig. 1. The relation  $\Sigma$  (the mean residuals for input data) versus mass-ratio  $q$ . The color figure can be viewed online.

TABLE 6  
ESTIMATED ABSOLUTE ELEMENTS

Target	J105924	J123609	J132308	J161858	J164349
Sub-type	A	W	Semidetached	A	A
$L_{1\odot}$	0.423(0.033)	0.361(0.024)	0.201(0.017)	0.252(0.021)	0.212(0.013)
$L_{2\odot}$	0.280(0.035)	0.166(0.019)	0.078(0.009)	0.098(0.011)	0.114(0.008)
$R_{1\odot}$	0.860(0.033)	0.848(0.028)	0.843(0.025)	0.797(0.027)	0.801(0.025)
$R_{2\odot}$	0.700(0.030)	0.764(0.029)	0.464(0.025)	0.630(0.030)	0.737(0.024)
$a$	1.65(0.05)	1.84(0.05)	1.61(0.05)	1.65(0.05)	1.61(0.05)
$M_{1\odot}$	0.773(0.078)	0.780(0.050)	0.931(0.077)	0.748(0.073)	0.639(0.058)
$M_{2\odot}$	0.388(0.046)	0.582(0.096)	0.188(0.020)	0.410(0.044)	0.479(0.044)
$\log g_1$	4.40	4.41	4.50	4.45	4.38
$\log g_2$	4.28	4.38	4.32	4.39	4.33
$J_0$	$2.15^{51}$	$3.19^{51}$	$1.27^{51}$	$2.21^{51}$	$2.22^{51}$
$\log J_0$	51.34	51.50	51.10	51.35	51.35
$J_{lim}$	$2.66^{51}$	$3.53^{51}$	$2.50^{51}$	$2.65^{51}$	$2.49^{51}$
$\log J_{lim}$	51.42	51.55	51.40	51.42	51.40

Knowing the semi-major axis  $a$  the total mass was determined and, with the fractional radii of the systems  $r_{1,2}$ , we calculated the absolute radii  $R_{1,2}$  and therefore the absolute luminosities  $L_{1,2}$ .

Finally, following Wilson (1978), we may make a comparison between the absolute separation  $a_k$  from Kepler's law:

$$a_k = 4.2088 P^{2/3} (1+q)^{1/3} M_1^{1/3} \quad (5)$$

and the separation that the system would have in contact  $a_z$

$$a_z = (1+q)^{0.6} \frac{M_1^{0.61}}{r_h + r_g}. \quad (6)$$

For the value of  $M_1$  as given in Table 6 all the systems turns out to be not a zero-age contact systems, because we have always  $a_k > a_z$ .

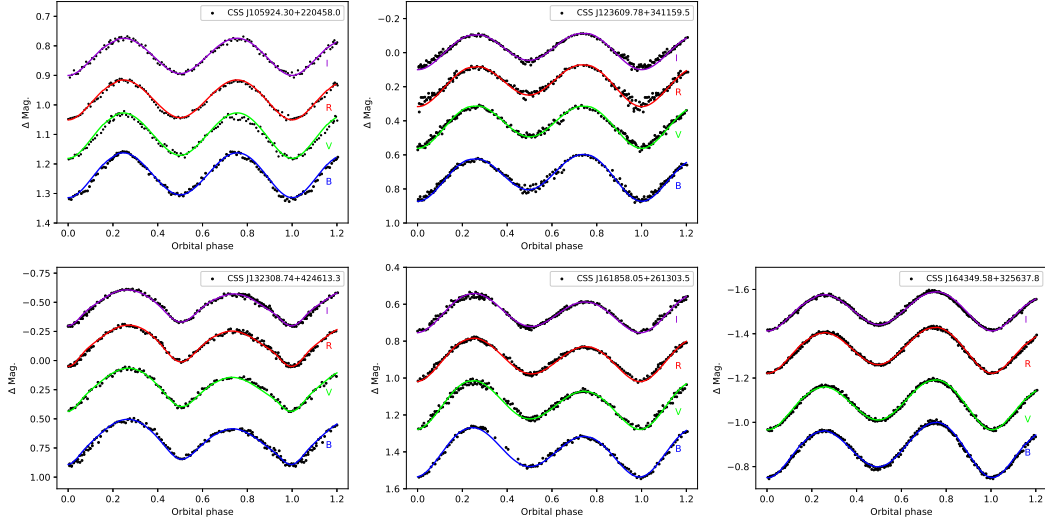


Fig. 2. CCD light curves of the systems. The points are the original CCD observations and the full lines are the theoretical fits with the surface spot contribution and third light. The color figure can be viewed online.

To investigate the current evolutionary status of our systems, the physical parameters listed in Table 6 are used.

In Figure 4, we plotted the primary, more massive (circles) and secondary, less massive (diamonds) components together with other W- and A-type W UMa systems collected by Latković et al. (2021) in the logarithmic mass-luminosity ( $M-L$ ) relations along with the ZAMS and TAMS computed by Girardi et al. (2000).

As it is clear from the Figure 4, both components of the systems seem to be in good agreement with the well-known W UMa binaries on the  $\log M - \log L$  plane. The location of the primary components is between the ZAMS and TAMS lines; that means that they are slightly evolved. Only the primary component of J132308 is located under the ZAMS as an unevolved star.

On the other hand, the secondary components deviate significantly from ZAMS like most of the secondaries of other W UMa systems.

Also, the secondary component of J132308 is located far from the other secondaries, overluminous and oversized with respect to its present mass.

For all the systems we calculated the orbital angular momentum  $J_0$  (Eker et al. 2006) and its position in the logarithmic  $J_0 - M$  diagram (Figure 5). The value of  $\log J_0$  as reported in Table 6, indicates that the systems are beyond the curved limit (separating the detached and contact systems) in the region of contact.

The physical significance of this limit is that it marks the maximum orbital angular momentum (OAM) for a contact system to survive. If the OAM of a contact system is more than  $J_{lim}$ , the contact configuration breaks.

Our semi-detached system J132308 is located in the contact region endorsing the hypothesis that the system is only formally semi-detached, and we can consider it as a contact system at a key turn-off as predicted by the TRO theory.

Finally, following the work of Qian et al. (2020), who investigated the period-temperature relation of contact binary systems using the LAMOST stellar atmospheric parameters, and constructed the heat map for this relation as shown in our Figure 6, we can see that our systems are located inside the red and blue lines that are the boundaries of the normal EW systems.

The position of J132308 suggests again that it could be a system at the beginning of the contact phase.

## 6. DETAILS OF THE SYSTEMS AND FINAL REMARKS

### 6.1. Common Features

#### 6.1.1. Short Period

Our systems possess a short period, four with  $P \in (0.225, 0.229)$ d and one with  $P = 0.248$ d.

It is known that W UMa-type eclipsing binaries show a period cut-off around 0.22 day (Ruciński (1992); Ruciński (2007)). Despite several theories

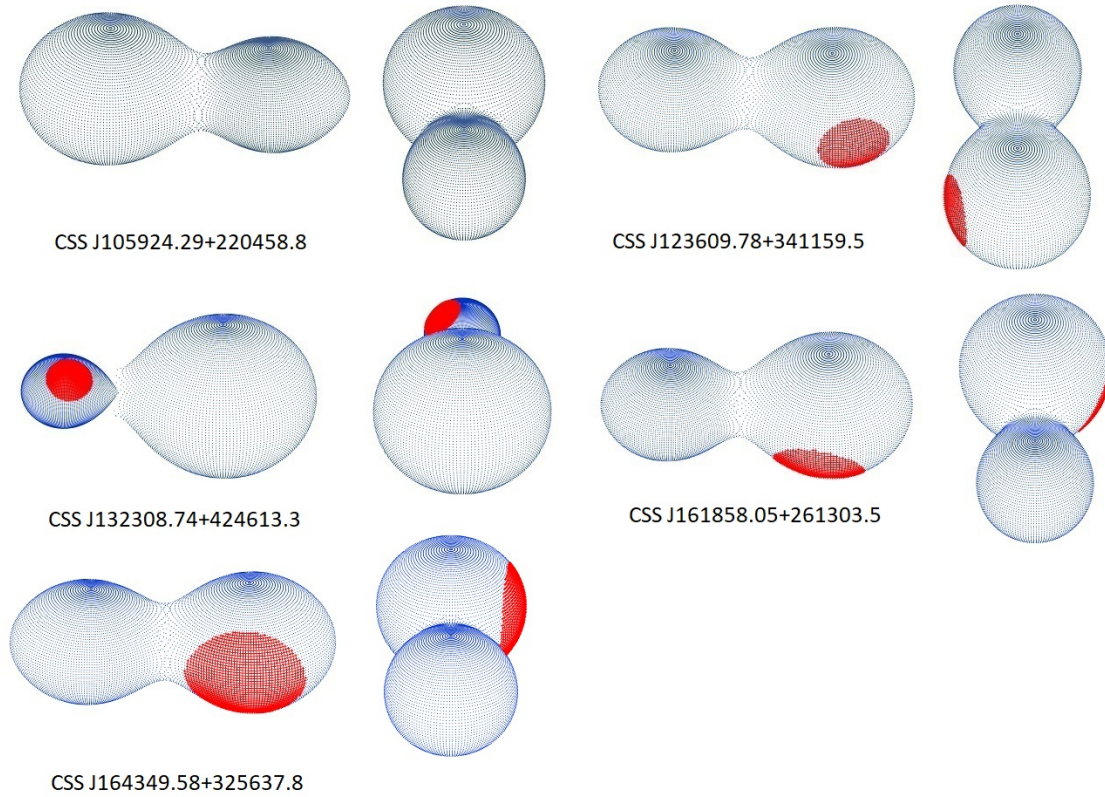


Fig. 3. Graphic images of the systems at quadrature (left) and at the primary minimum (right) according to our solution. The color figure can be viewed online.

(Stępień 2006; Jiang et al. 2012; Li et al. 2019) tried to explain this abrupt short period limit, the question is still open.

Thanks to the increase of survey missions newer EWs were found in the last years, so that it was possible to fix now this limit at the new value of  $P \approx 0.15$  day determined by Zhang & Qian (2020); Qian et al. (2020); however, the 0.22-day period cut-off remains (Li et al. 2019).

The systems near the short-period end, according to the period–color relation for contact binaries, are expected to be composed of two K or later-type components (Zhu et al. 2015) with short periods ( $P < 0.3$ d) and to be very close to the short period limit.

#### 6.1.2. *K Spectral Type*

K-type contact systems are rare objects and of great interest to investigate the cause of the period cut-off, and to study the structure and evolution of eclipsing binaries (TRO theory).

It is expected that K-type contact binaries, due to the presence of deep convective envelopes and fast rotation, would present magnetic activity, and

dark/hot spots should be observed on one or both of the components.

Both components of the five systems studied here belong to the K spectral type and four are found to be spotted.

#### 6.1.3. *Low Inclination*

The low inclination, between  $41^\circ$  and  $62^\circ$ , is another common characteristic of the systems here presented; values like this are often seen in other contact binaries.

Without spectroscopic data available, the WD solution may not give the correct solution for such partially eclipsing binaries and hence the corresponding results are preliminary solutions to unveil the nature of the variables. To improve the determination of the mass ratios we applied the  $q$ -search procedure.

#### 6.1.4. *Low Mass Contact Binaries*

Except for J123609, the other four systems possess the typical characteristics of the low mass contact binaries (LMCBs) as proposed by Stępień & Gazeas (2012), that is, systems where the total mass is under  $1.0 - 1.2 M_\odot$ .



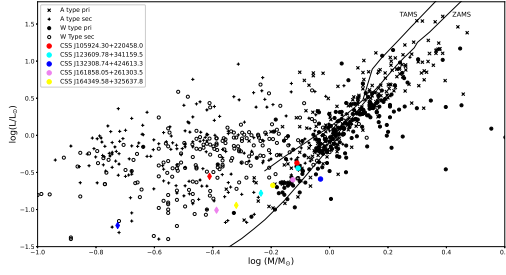


Fig. 4. Location of the components of our systems on the  $\log M - \log L$  diagram. The primaries are marked with circles and the secondaries with diamonds. The sample of W UMa type systems was obtained from a compilation of Latković et al. (2021). zero age main sequence (ZAMS) and terminal age main sequence (TAMS) are taken from Girardi et al. (2000) for the solar chemical composition. The color figure can be viewed online.

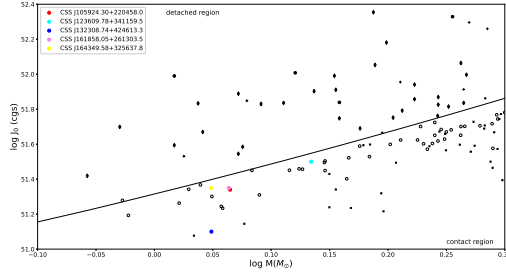


Fig. 5. The position of the five systems in the  $\log J_0 - \log M$  diagram is under the  $J_{lim}$  borderline, which justifies the geometrical contact situation. The color figure can be viewed online.

## 6.2. CSS J105924.29+220458.8 and CSS J161858.05+261303

J105924 and J161858 are short period ( $P \approx 0.23$  d) A sub-type systems with an unusual mass ratio ( $q = 0.5 - 0.55$ ), in relation to its overcontact factor ( $f \approx 93.3\%$  and  $f \approx 63.6\%$  respectively); the former is in thermal equilibrium ( $\Delta T = 4$  K), while the latter is not ( $\Delta T = 515$  K).

Generally, deep, low mass ratio contact binaries (DLMR) have high fill-out factors ( $f > 50\%$ ) and mass ratios  $q$  less than 0.25 (Qian et al. 2006). It is believed that they could be pre-merger systems, progenitors of single rapid rotating stars as FK com-type stars, blue straggler and luminous red novae such as V1309 Sco (Stępień (2011); Tylenda et al. (2011); Zhu et al. (2016); Liao et al. (2017)).

The existence of a value of the mass ratio  $q_{min}$ , defined as the value of  $q$  under which a binary system quickly merges into a single rapidly rotating star, was investigated by many authors. Its value ranges

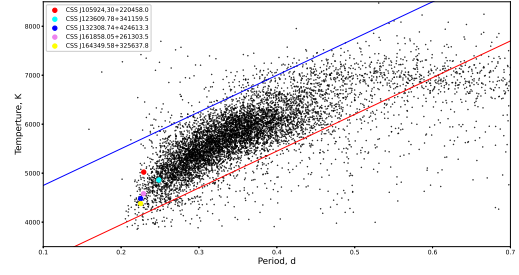


Fig. 6. Correlation between orbital period and temperature based on parameters of 8510 contact binaries from Qian et al. (2020). The red and blue lines are the boundaries of normal EWs. The color figure can be viewed online.

from  $q_{min} \approx 0.109$  (Arbutina 2007) to  $q_{min} \approx 0.044$  (Yang & Qian 2015).

J105429 and J161858 seem to be in contradiction, but they are not alone, other targets were found with those characteristics and they are summarized in Table 7.

From Table 7 is easy to see that among the nine systems, eight belong to the subtype A of the W UMa group, all have late spectral types (from K to M), for four of them a third light was found during the analysis of the light curves, for another one the third light cannot be excluded, while for four the third light has not a relevant value.

The presence of a third body is, according to different authors, one of most probable causes of this contradiction. In fact, it justifies the deep fill-out factor, and the angular momentum loss (AML) extracted by the stellar companion can be the cause of this rapid orbit shrinking (Stępień (2006); Stępień (2011)).

The light curves of J105924 are symmetrical and no significant evidence of inhomogeneities on the surfaces of the two components, i.e. the O'Connell effect, is noticeable. On the contrary, to obtain a good fit of its light curves it was necessary to invoke a cool spot on the primary component of J161858.

Li et al. (2020) analyzed the 2018 observations of J161858 done at the Ningbo Bureau of Education and Xinjiang Observatory Telescope and obtained values of the parameters sometimes similar to ours (the mass ratio, the inclination, the fractional radii) and sometimes very different.

The main differences are  $T_2$ ,  $T_1$ , the presence of a third light, the low fill-out value (3.8%, Li et al. (2020), 63.6% here), the presence of a hot spot on the secondary component, while our analysis returns a cold spot on the primary component. The absolute

TABLE 7  
CHARACTERISTICS OF SOME OVERCONTACT SYSTEMS  
WITH HIGH FILL-OUT AND HIGH MASS RATIO Q

Target	Period(days)	mass ratio	fill-out(%)	Sub-type	Spectral type	delta T(K)	3d light	Source
NSVS 925605	0.217629	0.678	70.2	A	M + M	678	Yes	[1]
1SWASP J161858.05+261303.5	0.2287771	0.549	63.6	A	K5 + K7	515	No	[2]
1SWASP J200059.78+054408.9	0.20569054	0.535	58.4	A	K3 + K4	272	not excluded	[3]
ER Cep	0.28573901	0.45	62	A	K0 + K2	232K	No	[4]
GSC 1387-0475	0.21781128	0.474	76.3	A	K3 + K4	166	Yes	[5]
EQ Cep	0.30696328	0.526	62.1	A	K2 + K3	111	No	[6]
1SWASP J075102.16+342405.3	0.20917273	0.78	95.4 - 98.4	A	M3.5 + M4	76 - 83	Yes	[7]
1SWASP J105924.29+220458.8	0.229062	0.502	93.3	A	K2+K2	4K	Yes	[8]
OGLE-BLG-ECL 000104	0.2007504	0.42	80	W	K3+K3	-6K	No	[9]

[1] Dimitrov & Kjurkchieva (2015), [2] this paper, [3] Liu et al. (2018), [4] Liu et al. (2011), [5] Yang et al. (2010), [6] Liu et al. (2011), [7] Jiang et al. (2015), [8] This paper, [9] Papageorgiou et al. (2023).

estimated parameters, except for the value of the radius of the primary component, are comparable.

The sometimes strong differences in the parameters that come out of the W-D analysis can be surely justified by the low inclination of the system. It is well established that low inclination values can bring a W-D solution that may not give the correct solution for partially eclipsing binaries (Ruciński 2001). Moreover, the low inclination of the system influences also the correct determination of the spot parameters; the appearance (or disappearance) of a spot on one component of the system could even produce minimum depths reversal and thus the classification of the system could fluctuate between the A and W subtype, or vice versa, a classification as observed in several overcontact binary systems.

For J161858 we have calculated an orbital period decrease of  $dP/dt = -3.21 \times 10^{-7} \text{ day yr}^{-1} = -0.028 \text{ sec yr}^{-1}$ . Such a variation can be explained by either mass transfer from the more massive to the secondary star or by angular momentum loss (AML) due to a magnetic stellar wind. If the parabolic variation is produced by conservative mass transfer, the transfer rate is  $dM_1/dt = -4.25 \times 10^{-7} \text{ Myr}^{-1}$  (Kwee 1958).

Another possible mechanism for the parabolic variation is the AML is caused by magnetic braking. Guinan & Bradstreet (1988) derived an approximate formula for the period decrease rate due to

spin-orbit-coupled AML of binary systems as follows:

$$dP/dt = -1.1 \times 10^{-8} q^{-1} (1+q)^2 (M_1 + M_2)^{-5/3} k_2 (M_1 R_2^4 + M_2 R_1^4) P^{-7/3} \quad (7)$$

where  $k_2$  is the gyration constant. With  $k_2 = 0.1$  (see Webbink (1976)), and with the absolute dimensions of Table 6 we computed the AML rate to be

$$\left( \frac{dP}{dt} \right)_{AML} = -4.31 \times 10^{-8} \text{ day yr}^{-1} \quad (8)$$

which is too small in comparison to the observed value. Therefore, with AML alone it is difficult to fully explain the observed secular period decrease.

For J161858 spectroscopic radial velocity observations are surely necessary in order to understand the configuration of the system.

### 6.3. CSS J123609.78+341159.5 and CSS J164349.58+325637.8

The principal common characteristic of these two systems is the large mass ratio ( $q > 0.72$ ) that was first presented by Csizmadia & Klagyivik (2004).

The assumption is that in H-type contact binaries the energy transfer behavior is different than in other types of CBs, with the energy transfer rate less efficient at a given luminosity ratio.

Due to the mass ratio being close to unity, to equalize the surface temperature of the components

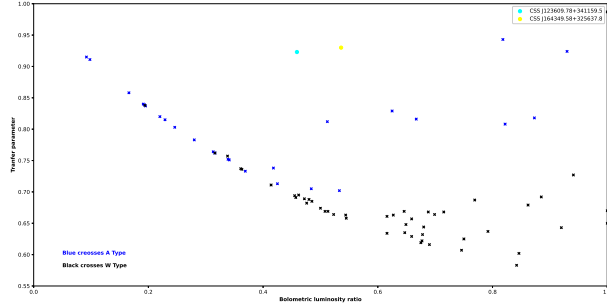


Fig. 7. Bolometric luminosity ratio  $\lambda$  vs transfer parameter  $\beta$  for J123609 and J164349. A and W-subtype are distinguished. Systems which have  $q > 0.72$  are far from the position of most of the systems of the example. The color figure can be viewed online.

less luminosity should be transferred, so they have a higher transfer parameter. The transfer parameter is defined as:

$$\beta = \frac{1 + \alpha \lambda^{5.01}}{1 + \lambda} \quad (9)$$

where  $\alpha = (T_1/T_2)^{20.01}$  and relates the temperature of the components of both the systems.

It is possible to calculate the bolometric luminosity ratio from the measured ratio in the  $V$  band via

$$\lambda = \left( \frac{L_2}{L_1} \right)_{bol} = \left( \frac{L_2}{L_1} \right)_V 10^{0.4 - (BC_1 - BC_2)}. \quad (10)$$

Using all the data of Csizmadia & Klagyivik (2004), in Figure 7 we plot the transfer parameter  $\beta$  against the bolometric luminosity ratio for our two H-systems.

Figure 7 shows that, except for the system which has  $q > 0.72$ , our systems have a good correlation between the bolometric luminosity ratio and the transfer parameter.

However, subsequent work by Sun et al. (2020) showed that in H-type CBs the energy transfer behavior is not significantly different from that of the remaining CBs, but the interest towards these H-type systems remains.

The secondary components of both systems are brighter and larger than their main sequence counterparts, as firstly suggested by the work of Lucy (1968), showing that the transfer of energy from the primary to the secondary is the cause of these discrepancies of luminosity and size of the secondary component.

Both systems are in physical contact with a high fill-out value, while the thermal contact is relatively far away.

The presence of third light obtained from our analysis in J164349 can explain, as for the above system J105924, the major fill-out value and the minor difference in temperature in respect to J123609 that did not show the presence of third light.

To achieve a good fit of the light curves a spot solution was considered with the result of a hot spot on the primary component of both systems.

#### 6.4. CSS J132308.74+424613.3

J132308 is a semi-detached system in which the primary component is slightly greater than its Roche lobe, while the secondary component fills it.

The studies of Shaw (1994) and Zhu et al. (2010) suggest that semi-detached binaries could be in the stage between a detached binary and a contact one.

The good thermal contact between the components ( $\Delta T = 271$  K), the low mass ratio ( $q = 0.202$ ), the positive fill-out of the primary component ( $f = 6.7\%$ ) and the shape of the light curves, that resemble those of contact binaries, suggest that this is a system in evolution toward a state of full geometrical and thermal contact.

A cool spot on the secondary component was necessary to better fit the light curves.

The star is clearly worthy of further investigation given its short period and its late spectral type.

This work is based upon observations carried out at the Observatorio Astronómico Nacional on the Sierra de San Pedro Mártir (OAN-SPM), Baja California, México. This work has made use of data from the European Space Agency (ESA) mission Gaia<sup>5</sup> and processed by the Gaia Data Processing and Analysis Consortium (DPAC)<sup>6</sup> Use of the International Variable Star Index (VSX) database has been made (operated at AAVSO Cambridge, Massachusetts, USA), as well as of the AAVSO Photometric All-Sky Survey (APASS) funded by the Robert Martin Ayers Sciences Fund. Also, use has been made of the VizieR catalogue access tool, CDS, Strasbourg, France. The original description of the VizieR service was published in A&AS 143, 23. We would like to thank the anonymous referee for her/his useful comments which improved the quality of this paper, and for calling our attention to the TESS data.

<sup>5</sup><https://www.cosmos.esa.int/gaia>.

<sup>6</sup><https://www.cosmos.esa.int/web/gaia/dpac/consortium>.

## REFERENCES

- Akerlof, C., Amrose, S., Balsano, R., et al. 2000, *AJ*, 119, 1901, <https://doi.org/10.1086/301321>
- Anders, F., Khalatyan, A., Queiroz, A. B. A., et al. 2022, *A&Ap*, 658, 91, <https://doi.org/10.1051/0004-6361/202142369>
- Arbutina, B. 2007, *MNRAS*, 377, 1635, <https://doi.org/10.1111/j.1365-2966.2007.11723.x>
- Bai, Y., Liu, J., Bai, Z., et al. 2019, *VizieR Online Data Catalog*, J/AJ/158/93
- Bradstreet, D. H. & Steelman, D. P. 2002, *A&AS*, 201, 7502
- Butters, O. W., West, R. G., Anderson, D. R., et al. 2010, *A&Ap*, 520, 10, <https://doi.org/10.1051/0004-6361/201015655>
- Csizmadia, S. & Klagyivik, P. 2004, *A&Ap*, 426, 1001, <https://doi.org/10.1051/0004-6361:20040430>
- Dimitrov, D. P. & Kjurkchieva, D. P. 2015, *MNRAS*, 448, 2890, <https://doi.org/10.1093/mnras/stv147>
- Drake, A. J., Graham, M. J., Djorgovski, S. G., et al. 2014, *ApJS*, 213, 9, <https://doi.org/10.1088/0067-0049/213/1/9>
- Eker, Z., Demircan, O., Bilir, S., et al. 2006, *MNRAS*, 373, 1483, <https://doi.org/10.1111/j.1365-2966.2006.11073.x>
- Flannery, B. P. 1976, *ApJ*, 205, 217, <https://doi.org/10.1086/154266>
- Gaia Collaboration, Brown, A. G. A., Vallenari, A., et al. 2018, *A&Ap*, 616, 1, <https://doi.org/10.1051/0004-6361/201833051>
- Girardi, L., Bressan, A., Bertelli, G., et al. 2000, *A&AS*, 141, 371, <https://doi.org/10.1051/aas:2000126>
- Guinan, E. F. & Bradstreet, D. H. 1988, *Formation and Evolution of Low Mass Stars*, 241, 345, [https://doi.org/10.1007/978-94-009-3037-7\\_23](https://doi.org/10.1007/978-94-009-3037-7_23)
- Jiang, D., Han, Z., Ge, H., et al. 2012, *MNRAS*, 421, 2769, <https://doi.org/10.1111/j.1365-2966.2011.20323.x>
- Jiang, L., Qian, S.-B., Zhang, J., et al. 2015, *PASJ*, 67, 118, <https://doi.org/10.1093/pasj/psv092>
- Kwee, K. K. 1958, *Bull. Astron. Inst. Netherlands*, 14, 131
- Latković, O., Čeki, A., & Lazarević, S. 2021, *ApJS*, 254, 10, <https://doi.org/10.3847/1538-4365/abeb23>
- Leung, K.-C. & Wilson, R. E. 1977, *ApJ*, 211, 853, <https://doi.org/10.1086/154994>
- Li, L., Zhang, F., Han, Z., et al. 2008, *MNRAS*, 387, 97, <https://doi.org/10.1111/j.1365-2966.2008.12736.x>
- Li, K., Xia, Q.-Q., Michel, R., et al. 2019, *MNRAS*, 485, 4588, <https://doi.org/10.1093/mnras/stz715>
- Li, K., Kim, C.-H., Xia, Q.-Q., et al. 2020, *AJ*, 159, 189, <https://doi.org/10.3847/1538-3881/ab7cda>
- Li, K., Xia, Q.-Q., Kim, C.-H., et al. 2021, *ApJ*, 922, 122, <https://doi.org/10.3847/1538-4357/ac242f>
- Li, K., Gao, X., Liu, X.-Y., et al. 2022, *AJ*, 164, 202, <https://doi.org/10.3847/1538-3881/ac8ff2>
- Liao, W.-P., Qian, S.-B., Soonthornthum, B., et al. 2017, *PASP*, 129, 124204, <https://doi.org/10.1088/1538-3873/aa8ded>
- Liu, L., Qian, S.-B., Zhu, L.-Y., et al. 2011, *MNRAS*, 415, 3006, <https://doi.org/10.1111/j.1365-2966.2011.18914.x>
- Liu, N.-P., Qian, S.-B., Soonthornthum, B., et al. 2014, *AJ*, 147, 41, <https://doi.org/10.1088/0004-6256/147/2/41>
- Liu, L., Qian, S.-B., Fernández Lajús, E., et al. 2018, *Ap&SS*, 363, 15, <https://doi.org/10.1007/s10509-017-3227-4>
- Lohr, M. E., Norton, A. J., Kolb, U. C., et al. 2013, *A&Ap*, 549, 86, <https://doi.org/10.1051/0004-6361/201220562>
- Lucy, L. B. 1967, *ZAp*, 65, 89
- . 1968, *ApJ*, 151, 1123, <https://doi.org/10.1086/149510>
- . 1976, *ApJ*, 205, 208, <https://doi.org/10.1086/154265>
- Marsh, F. M., Prince, T. A., Mahabal, A. A., et al. 2017, *MNRAS*, 465, 4678, <https://doi.org/10.1093/mnras/stw2110>
- Miller, A. A. 2015, *ApJ*, 811, 30, <https://doi.org/10.1088/0004-637X/811/1/30>
- O’Connell, D. J. K. 1951, *PRCO*, 2, 85
- Paczynski, B., Szczygieł, D. M., Pilecki, B., et al. 2006, *MNRAS*, 368, 1311, <https://doi.org/10.1111/j.1365-2966.2006.10223.x>
- Paegert, M., Stassun, K. G., Collins, K. A., et al. 2021, *arXiv:2108.04778*, <https://doi.org/10.48550/arXiv.2108.04778>
- Papageorgiou, A., Christopoulou, P.-E., Ferreira Lopes, C. E., et al. 2023, *AJ*, 165, 80, <https://doi.org/10.3847/1538-3881/aca65a>
- Prša, A., Kochoska, A., Conroy, K. E., et al. 2022, *ApJS*, 258, 16, <https://doi.org/10.26093/cds/vizier.22580016>
- Qian, S., Yang, Y., Zhu, L., et al. 2006, *Ap&SS*, 304, 25, <https://doi.org/10.1007/s10509-006-9114-z>
- Qian, S.-B., Zhu, L.-Y., Liu, L., et al. 2020, *Research in Astronomy and Astrophysics*, 20, 163, <https://doi.org/10.1088/1674-4527/20/10/163>
- Robertson, J. A. & Eggleton, P. P. 1977, *MNRAS*, 179, 359, <https://doi.org/10.1093/mnras/179.3.359>
- Ruciński, S. M. 1973, *Acta A.*, 23, 79
- . 1992, *AJ*, 103, 960, <https://doi.org/10.1086/116118>
- . 2001, *AJ*, 122, 1007, <https://doi.org/10.1086/321153>
- . 2007, *MNRAS*, 382, 393, <https://doi.org/10.1111/j.1365-2966.2007.12377.x>
- Ruciński, S. M. & Pribulla, T. 2008, *MNRAS*, 388, 1831, <https://doi.org/10.1111/j.1365-2966.2008.13508.x>
- Samus’, N. N., Kazarovets, E. V., Durlevich, O. V., Kireeva, N. N. & Pastukhova, E. N. 2017, *ARep*, 61, 80, <https://doi.org/10.1134/S1063772917010085>

- Shaw, J. S. 1994, *Mem. Soc. Astron. Italiana*, 65, 95
- Stassun, K. G., Oelkers, R. J., Pepper, J., et al. 2018, *AJ*, 156, 102, <https://doi.org/10.3847/1538-3881/aad050>
- Stassun, K. G., Oelkers, R. J., Paegert, M., et al. 2019, *AJ*, 158, 138, <https://doi.org/10.3847/1538-3881/ab3467>
- Stępień, K. 2006, *Acta A.*, 56, 347, <https://doi.org/10.48550/arXiv.astro-ph/0701529>
- . 2011, *Acta A.*, 61, 139, <https://doi.org/10.48550/arXiv.1105.2645>
- Stępień, K. & Gazeas, K. 2012, *Acta A.*, 62, 153, <https://doi.org/10.48550/arXiv.1207.3929>
- Sun, W., Chen, X., Deng, L., & de Grijs, R. 2020, *ApJS*, 247, 50, <https://doi.org/10.3847/1538-4365/ab7894>
- Tonry, J. L., Denneau, L., Flewelling, H., et al. 2018, *ApJ*, 867, 105, <https://doi.org/10.3847/1538-4357/aae386>
- Tylenda, R., Hajduk, M., Kamiński, T., et al. 2011, *A&Ap*, 528, 114, <https://doi.org/10.1051/0004-6361/201016221>
- van Hamme, W. 1993, *AJ*, 106, 2096, <https://doi.org/10.1086/116788>
- Webbink, R. F. 1976, *ApJ*, 209, 829, <https://doi.org/10.1086/154781>
- Wilson, R. E. & Devinney, E. J. 1971, *ApJ*, 166, 605, <https://doi.org/10.1086/150986>
- Wilson, R. E. 1978, *ApJ*, 224, 885, <https://doi.org/10.1086/156438>
- . 1990, *ApJ*, 356, 613, <https://doi.org/10.1086/168867>
- Wilson, R. E. & van Hamme, W., 2016, *Computing Binary Stars Observables*, <ftp.astro.ufl.edu>, directory pub/wilson/lcdc2015
- Yakut, K. & Eggleton, P. P. 2005, *ApJ*, 629, 1055, <https://doi.org/10.1086/431300>
- Yang, Y.-G., Wei, J.-Y., & Li, H.-L. 2010, *New Astronomy*, 15, 155, <https://doi.org/10.1016/j.newast.2009.07.009>
- Yang, Y.-G. & Qian, S.-B. 2015, *AJ*, 150, 69, <https://doi.org/10.1088/0004-6256/150/3/69>
- Zhang, X.-D. & Qian, S.-B. 2020, *MNRAS*, 497, 3493, <https://doi.org/10.1093/mnras/staa2166>
- Zhu, L., Qian, S.-B., Mikulášek, Z., et al. 2010, *AJ*, 140, 215, <https://doi.org/10.1088/0004-6256/140/1/215>
- Zhu, L.-Y., Qian, S.-B., Jiang, L.-Q., et al. 2015, *Living Together: Planets, Host Stars and Binaries*, ed. S. M. Ruciński, G. Torres, & M. Zejda, 496, 200
- Zhu, L.-Y., Zhao, E.-G., & Zhou, X. 2016, *RAA*, 16, 68, <https://doi.org/10.1088/1674-4527/16/4/068>

F. Acerbi: Via Zoncada 51, Codogno, LO, 26845, Italy (acerbifr@tin.it).

C. Barani: Via Molinetto 35, Triulza di Codogno, LO, 26845, Italy (cvbarani@alice.it).

M. Martignoni: Via Don G. Minzoni 26/D, Magnago, MI, 20020, Italy (massimiliano.martignoni@outlook.it).

R. Michel, H. Aceves & L. Altamirano-Dévora: Instituto de Astronomía, UNAM. A.P. 106, 22800 Ensenada, BC, Mexico (rmm, aceves, lili@astro.unam.mx).

F. J. Tamayo: Facultad de Ciencias Físico-Matemáticas, UANL, 66451 San Nicolás de los Garza, NL, México (francisco.tamayom@uanl.edu.mx).



## CCD PHOTOMETRY OF THE GLOBULAR CLUSTER NGC 5897<sup>1</sup>

A. Ruelas-Mayorga<sup>2</sup>, L. J. Sánchez<sup>2</sup>, E. Macías-Estrada<sup>2</sup>, and A. Nigoche-Netro<sup>3</sup>

*Received September 12 2023; accepted November 1 2023*

### ABSTRACT

We report CCD photometric observations of the globular cluster NGC 5897, in the Johnson system filters  $B$ ,  $V$ ,  $R$ , and  $I$ . With the values for these magnitudes we obtain various colour indices and produce several colour-magnitude diagrams. We present eight colour-magnitude diagrams:  $V$  vs  $B - V$ ,  $B$  vs  $B - V$ ,  $V$  vs  $V - I$ ,  $I$  vs  $V - I$ ,  $R$  vs  $R - I$ ,  $I$  vs  $R - I$ ,  $V$  vs  $V - R$ , and  $R$  vs  $V - R$ . In all of these diagrams we can clearly see the giant branch, the horizontal branch and the beginning of the main sequence. To the left of the main sequence turn-off point we detect a somewhat large number of blue straggler stars. We determine the mean value of the visual magnitude of the  $HB$  as  $16.60 \pm 0.46$ . This value is fainter than the value found by other authors.

### RESUMEN

Se reportan observaciones fotométricas del cúmulo globular NGC 5897 en los filtros del sistema de Johnson  $B$ ,  $V$ ,  $R$  e  $I$ . Con los valores de estas magnitudes obtenemos diferentes índices de color y producimos varios diagramas color-magnitud. Presentamos ocho diagramas color-magnitud  $V$  vs  $B - V$ ,  $B$  vs  $B - V$ ,  $V$  vs  $V - I$ ,  $I$  vs  $V - I$ ,  $R$  vs  $R - I$ ,  $I$  vs  $R - I$ ,  $V$  vs  $V - R$ , y  $R$  vs  $V - R$ . En todos estos diagramas se distinguen claramente la rama de las gigantes, la rama horizontal y el comienzo de la secuencia principal. A la izquierda del punto de salida de la secuencia principal detectamos un número relativamente grande de estrellas ‘blue stragglers’. Determinamos el promedio de la magnitud visual de la rama horizontal como  $16.60 \pm 0.46$ . Este valor es más débil que el valor encontrado por otros autores.

*Key Words:* Galaxy: general — globular clusters: individual: NGC 5897 — techniques: photometric

### 1. INTRODUCTION

The globular clusters are spherically symmetric stellar systems which may be found in all galaxies. They are very rich stellar systems that may be found in our Galaxy in remote regions of the galactic halo and also close to the galactic centre. They contain hundreds of thousands of stars within a radius  $20 - 50$  pc, having typical central densities between  $10^2$  and  $10^4$  stars/pc<sup>3</sup>. Globular clusters are dynamically very stable and may live for a long time. They represent a remnant of a primordial stellar forma-

tion epoch and may be considered as proper galactic subsystems (Ruelas-Mayorga et al. 2010).

Many Milky Way globular clusters have been known for a long time (see the Messier (1771) catalogue). Presently we think there are approximately 150-200 in our Galaxy, although this figure does not include those clusters close to the galactic plane or very low surface brightness objects, (see Monella (1985) and Harris (1996)).

Because globular clusters are very luminous systems they may be observed at very large distances. This fact makes them fundamental in the study of galactic structure.

Some characteristics of globular clusters are:

- In general, the light that comes from these objects originates in stars slightly cooler than our Sun.

<sup>1</sup>Based upon observations acquired at the Observatorio Astronómico Nacional on the Sierra San Pedro Mártir (OAN-SPM), Baja California, México.

<sup>2</sup>Instituto de Astronomía, Universidad Nacional Autónoma de México, CDMX, México.

<sup>3</sup>Instituto de Astronomía y Meteorología, Universidad de Guadalajara, Guadalajara, Jal. 44130, México.

- Morphology. In general, they are slightly elliptical in shape. The average ratio between the minor and major axes of the apparent ellipse that they project on the sky is  $b/a = 0.73$ , with only 5% of them more elongated than  $b/a = 0.8$ .
- They appear to be exclusively stellar system in which no presence of gas or dust is detected (Binney & Merrifield 1998).
- The radial distribution of stars varies between clusters, and there are some that present a strong central concentration (Mihalas & Binney 1981).
- The value of their integrated absolute magnitude  $(M_V)_0$  is usually found in the interval  $-5 > (M_V)_0 \gtrsim -10$  where the maximum of the distribution is found at  $(M_V)_0 \approx -8.5$  and with a FWHM of  $\approx \pm 1$  mag.
- Their intrinsic colour takes values in the interval  $0.4 \lesssim (B - V)_0 \lesssim 0.8$  with a maximum at  $(B - V)_0 \approx 0.57$  (Mihalas & Binney 1981).
- There are clusters with a large metallic deficiency, usually located in the galactic halo, up to those with abundances similar to that of the Sun (Mihalas & Binney (1981), Harris (2010), Pfeffer et al. (2023)).
- It is common to find clusters with metallic abundances in the interval  $-2.2 \lesssim [Fe/H] \lesssim 0.0$ .

Studies of globular clusters are important because they serve a variety of astronomical purposes, such as: determination of the galactic centre position, as indicators of the galactic gravitational potential (i.e. Ishchenko et al., 2023 and references therein), studies of the evolution of low mass and low metallicity stars, and also of chemical evolution of galactic systems. Globular clusters can also provide restrictions on galaxy formation (i.e. Strader et al. (2005), Harris et al. (2013), Beasley (2020), and Palma (2023)).

NGC 5893 is a low concentration cluster ( $c = \log r_t/r_c = 1.19$ ) Webbink (1985). There are in the literature several published colour-magnitude diagrams for this cluster (Sandage & Katem (1968), Sarajedini (1992), Ferraro et al. (1992) and Stetson (2019)). Sandage & Katem (1968) obtained  $B$  and  $V$  photometry down to  $V \approx 17$  which was just able to include the horizontal branch (HB) of this cluster. They found that  $V(HB) = 16.20$ ,  $E(B - V) = 0.11 \pm 0.02$  and  $(B - V)_{0,g} = 0.78 \pm 0.03$  (the dereddened colour of the giant branch (GB) at

the level of the HB), this allowed them to determine the metallicity of NGC 5893 to be between that of M3 and M92. The HB of this cluster is made mainly of blue stars. Wehlau (1990) found the average of the  $V$  magnitude of the RR Lyrae star in this cluster to be  $V(RR) = 16.30$ . Sarajedini (1992) obtained CCD  $B$  and  $V$  photometry of this cluster down to  $V \approx 22$ . In this paper he reached the following conclusions:

- The HB of this cluster appears to be made mainly by blue stars with  $V(HB) = 16.35 \pm 0.15$ .
- The metallicity of this cluster is  $[Fe/H] = -1.66 \pm 0.10$ . He obtains this value from his adopted value for the  $E(B - V) = 0.07 \pm 0.04$ , and the colour of the red giant branch (RGB) at the level of the HB.
- He finds that NGC 5897 is  $\approx 2$  Gyr older than the globular cluster M3.
- The luminosity function of the RGB shows an enhancement of the number of stars at the level of the HB.
- The colour-magnitude (CM) diagram of this cluster reveals a large population of blue straggler stars.

This paper is organised as follows: in § 2 we present the observations and describe the reduction of the standard stars, in § 3 the reduction of the photometry of the cluster stars is described, as well as the procedure for aligning and matching the different sections of the cluster which we observed. § 4 deals with the derivation of the fiducial lines and the introduction of the colour-magnitude diagrams, the following section (§ 5) presents the different colour-magnitude diagrams which we derived. § 6 talks about the calculation of the metallicity and the reddening using the Sarajedini & Layden method (see Sarajedini (1994) and Sarajedini & Layden (1997)). § 7 derives the distance modulus to NGC 5897, and finally, in § 8 we present our conclusions.

## 2. THE OBSERVATIONS

The globular cluster NGC 5897 is located on the constellation of Libra ( $AR(2000) : 15^h 17^m 24.5^s$ ,  $DEC(2000) : -21^\circ 00' 37.0''$ ), it contains several hundred thousands stars (see Figure 1). Its most important properties are listed in Table 1 (Harris 1996).

We obtained the observations at the Observatorio Astronómico Nacional in San Pedro Mártir (OAN-SPM), Baja California during 2006, March 20-23 and 2007, March 14.



TABLE 1

Data for the Globular Cluster NGC 5897		
Right Ascension (2000)		$15^h 17^m 24.5^s$
Declination (2000)		$-21^\circ 00' 37.0''$
Galactic Longitude		342.95
Galactic Latitude		30.29
Distance to the Sun(kpc)		12.5
Tidal radius (arcmin) (Webbink 1985)		11.5
Distance to the Galactic Centre (kpc)		7.4
Reddening $E(B - V)$		0.09
Horizontal Branch Magnitude (in $V$ )		16.27
Distance Modulus ( $m - M$ ) (in $V$ )		15.76
Integrated $V$ Magnitude		8.53
Absolute Visual Magnitude		-7.23
	$U - B$	0.08
Integrated Colour Indices	$B - V$	0.74
(no reddening correction)	$V - R$	0.50
	$V - I$	1.041
Metallicity [Fe/H]		-1.90
Integrated Spectral Type		$F7$
Heliocentric Radial Velocity (km/s)		101.5
Central Concentration		0.86
Ellipticity		0.08
Nucleus Radius (arcmin)		1.40
Mean Mass Radius (arcmin)		2.06
Central Surface Brightness (in $V$ ) (magnitudes/arcsec)		20.53
Logarithm of the luminous density at the centre ( $L_\odot/\text{pc}^3$ )		1.53



Fig. 1. The globular cluster NGC 5897. The image is 12.6' vertically (Taken from: <http://astrim.free.fr/ngc5897.htm/>).

We utilised two different CCD cameras attached to the 1.5m telescope. The characteristics of these detectors are presented in Table 2.

As stated above, the observations were collected during two observing runs, during which, we observed in a standard way obtaining bias and flat field frames in each filter, plus obtaining multiple observations of standard star regions. In Tables 3 and 4 we present the logs for both observation seasons regarding the globular cluster NGC 5897.

### 2.1. Reduction of Standard Stars

In order to express the magnitude of the stars in the globular cluster in a standard system, we performed aperture photometry of stars in some of the Landolt Standard Regions (Landolt 1992) listed in Tables 3 and 4. The photometric observations of the standard stars was carried out using the APT (Aperture Photometry Tool) (Laher et al. 2012), (see also <https://www.aperturephotometry.org/about/>).

The APT programme is a software that permits aperture photometry measurements of stellar images on a frame. The programme accepts images in the *fits* format, so no transformation of our images to other formats was necessary. The standard regions which were measured had already been processed by

TABLE 2

Characteristics of the Detectors Used in the Observations		
Characteristic	Thomson	Site1
Size (pixels)	2048 × 2048	1024 × 1024
Pixel Size ( $\mu m$ )	14 × 14	24 × 24
Quantum Efficiency	Maximum 65% at 5000 Å	
Reading noise ( $e^-$ ) (gain mode 4 binning $2 \times 2$ )	5.3	5.5 (Direct Imaging)
Dark Current ( $e^-/\text{pix/h}$ )	1.0 a $-95.2^\circ\text{C}$	7.2 approximately at $-80^\circ\text{C}$
Well Depth ( $e^-$ )	$1.23 \times 10^5$ (MPP Mode)	
Bias Level (gain mode 4 binning $2 \times 2$ )	384	547 (Direct Imaging)
Gain ( $e^-$ ) (Mode 4)	0.51	1.27
A/D Converter	16 bits	
Linearity	99%	99.5%
Plate Scale ( $''/\text{pixel}$ )	0.147	0.252

removal of hot and cosmic ray pixels, and were bias and flat-field corrected.

We propose a set of transformation equations from the observed to the intrinsic photometric system that looks as follows:

$$B_{int} - B_{obs} = A_B * X + K_B * (B - V)_{obs} + C_B, \quad (1)$$

$$V_{int} - V_{obs} = A_V * X + K_V * (B - V)_{obs} + C_V, \quad (2)$$

$$R_{int} - R_{obs} = A_R * X + K_R * (R - I)_{obs} + C_R, \quad (3)$$

$$I_{int} - I_{obs} = A_I * X + K_I * (R - I)_{obs} + C_I, \quad (4)$$

where the suffixes *int* and *obs* stand for *intrinsic* and *observed*, and  $A$ ,  $K$  and  $C$  correspond to the negative of the atmospheric absorption coefficient, the colour term and the zero point term. These are the terms that we intend to calculate using the intrinsic values for the magnitudes given in Landolt (1992), and the observed values measured with APT. The equations are solved using the least squares procedure and the coefficients obtained are shown in Tables 5, 6, 7 and 8.

In Figure 2 we plot, for magnitudes  $B$ ,  $V$ ,  $R$  and  $I$ , on the vertical axis the difference between the intrinsic magnitude of the standard stars and their calculated values using the transformation equations (equations 1, 2, 3 and 4) given above, and on the horizontal axis we plot the corresponding observed value for the magnitude. It is clear from these graphs that the calculated values minus the intrinsic values of the magnitudes for the standard stars are, in its majority, distributed around the zero value. However, there are two groups of stars that differ significantly from zero and appear displaced above and below the

rest of the stars. These anomalous stars belong in general to the regions PG0942, Rubin 152, PG 1323 and Area 98. We have checked that the stars in these regions are well identified with our observation frames. However, we have been unable to find the cause of this discrepancy; therefore, these anomalous stars were eliminated from the rest of the analysis.

The reduction of the data was done in a standard way, that is, removing dead and hot pixels produced by cosmic rays, and performing bias subtraction, and flat field correction. This reduction process was achieved using the general purpose software: Image Reduction and Analysis Facility (IRAF). Once the fields have been bias and flat field corrected we proceed to utilise the routine DAOPHOT to obtain the photometry of the many stars present in the field using the Point Spread Function (PSF) technique (Stetson 1992). As an example of an image on which we apply the DAOPHOT technique see Figure 3.

Figure 4 show graphs of the measurement errors as function of the value of the observed magnitude for  $B$ ,  $V$ ,  $R$  and  $I$ . It is clear that for brighter magnitudes the measurement errors are very small and begin to increase as we move to fainter magnitudes, becoming of the order of several tenths of magnitude by a magnitude value of  $\approx 20$ .

### 3. PHOTOMETRY OF THE CLUSTER STARS

The calculation of the different observed magnitudes of the stars in the cluster NGC 5897 was obtained by a standard application of the DAOPHOT subroutine present in IRAF to all the observed frames in each filter, after having the frames bias-subtracted and flat fielded.

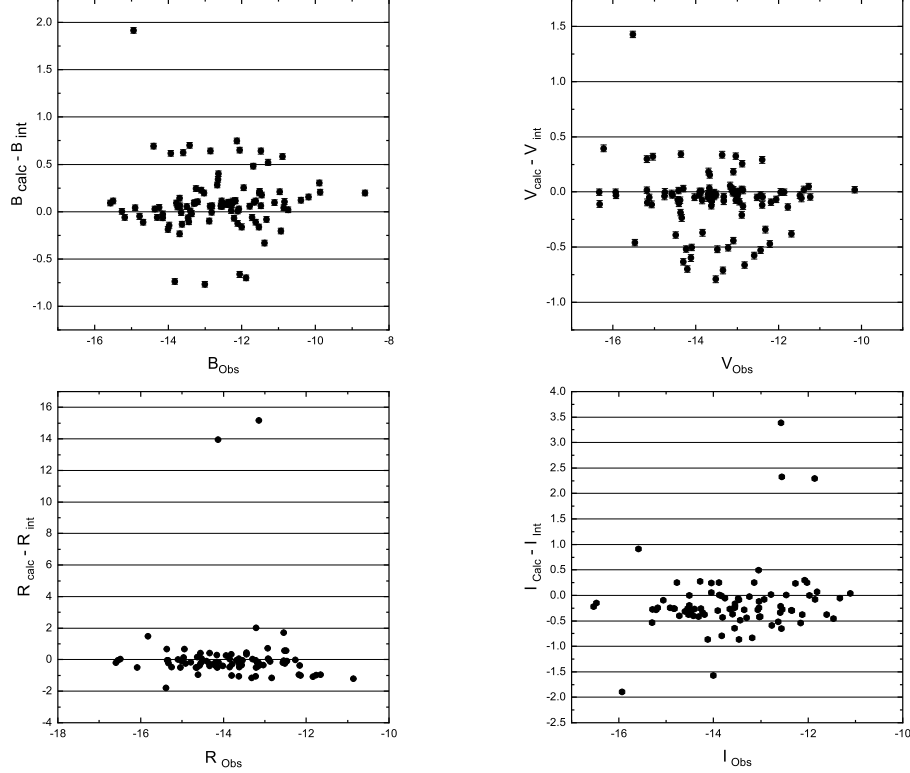


Fig. 2. Calculated minus intrinsic magnitude versus observed magnitude.

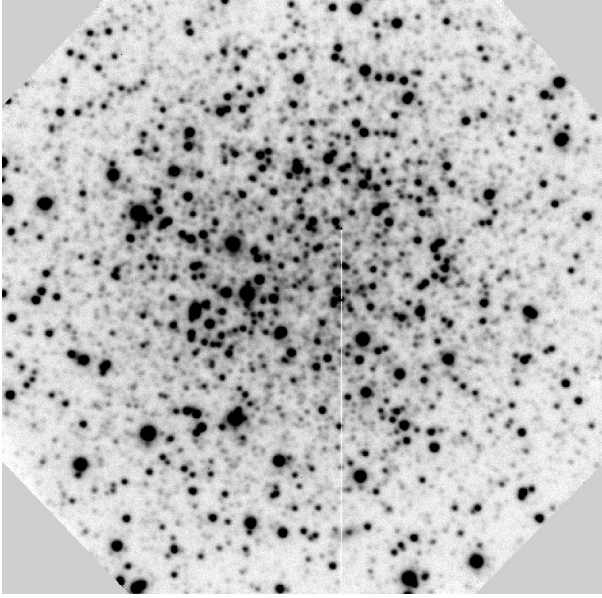


Fig. 3. Image of the central zone of the globular cluster NGC 5897 in the  $R$  filter after the process of preparation.

The magnitude catalogues produced by the subroutine ALLSTAR for the observations were combined to obtain the observed colours for the stars in the globular cluster, so that the application of

equations 1, 2, 3 and 4 with the appropriate transformation coefficients was straightforward.

### 3.1. Colour-Magnitude Diagrams

In order to construct the colour-magnitude diagrams we utilised the photometric catalogues, in the four filters of interest  $B$ ,  $V$ ,  $R$  and  $I$ , which were derived from the application of the DAOPHOT subroutines. The diagrams which we shall present are the following: ( $B$  vs  $B - V$ ), ( $V$  vs  $B - V$ ), ( $V$  vs  $V - I$ ), ( $I$  vs  $V - I$ ), ( $I$  vs  $R - I$ ), ( $R$  vs  $R - I$ ), ( $V$  vs  $V - R$ ) and ( $R$  vs  $V - R$ ). To be able to use the derived photometric catalogues, it is necessary to effect a series of steps so that the frames in all filters are compatible. It was therefore necessary to align, group, and standardise them as well as eliminate those stars that might appear repeated.

### 3.2. Alignment

To obtain the colours of the star in NGC 5897 we need to pair the different magnitude catalogues. This procedure is not a trivial one since one star does not necessarily have the same coordinates in all the frames in which it appears. We have to remember that each filter observation was taken in 5 different frames (North, South, East, West and Centre) which have to be assembled into a grand image

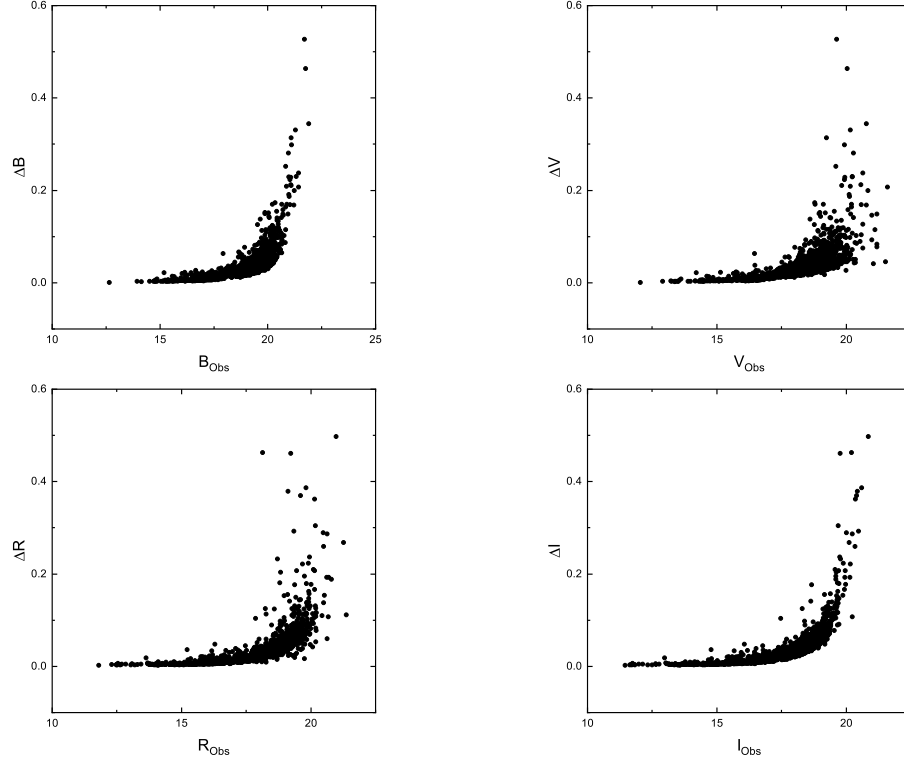


Fig. 4. Measurement error  $\Delta Mag$  vs  $Mag_{Obs}$  for  $B$ ,  $V$ ,  $R$  and  $I$ .

for the entire cluster, taking care to obtain the average of the intensity of those stars that appear on any two sections of the mosaic. Taking into consideration that we used one CCD in 2006 and a different one in 2007 the matching of the images required a positional transformation which consisted of a translation, a rotation and a stretching. Fortunately, the coefficients for rotation and stretching resulted in very small numbers, so our problem reduced itself to a simple translation of coordinates. We define as a primary reference frame the positions and the magnitudes of the stars in the central image observed for the 2007 observing season. Doing this, we ended up having photometric files for the four filters in the same positional and magnitude systems, which allowed the calculation of colours in an easy and straightforward way.

#### 4. PHOTOMETRY OF THE STARS IN NGC 5897, COLOUR CATALOGUES AND FIDUCIAL LINES

The standard magnitudes for the stars in the cluster NGC 5897 were obtained by comparison with the published photometry results for this cluster published by Stetson (2019). A number of stars were identified in our and Stetson's observations, and

a linear transformation between one set of observations and the other was proposed as follows:

$$\alpha = C_1 X_{pos} + C_2, \quad (5)$$

where  $\alpha$  represents right ascension,  $C_1$  is the longitudinal stretching coefficient,  $X_{pos}$  represents the  $X$  coordinate value in our files and  $C_2$  is the longitudinal coefficient of translation.

Analogously,

$$\delta = C_3 Y_{pos} + C_4, \quad (6)$$

where  $\delta$  represents the declination,  $C_3$  is the transversal stretching coefficient,  $Y_{pos}$  represents the  $Y$  coordinate in our files and  $C_4$  is the transversal coefficient of translation.

The values we obtained for the transformation coefficients between our positions and those of Stetson's are as follows:

- $C_1 = -9.60592 \times 10^{-5}$
- $C_2 = 229.39920$
- $C_3 = 8.76398 \times 10^{-5}$
- $C_4 = -21.06008$

TABLE 3

Observation log for March 2006		
Object Observed	Filter	Number of Images
Bias		5
Flat Field <i>B</i>	<i>B</i>	5
Flat Field <i>V</i>	<i>V</i>	5
Flat Field <i>R</i>	<i>R</i>	5
Flat Field <i>I</i>	<i>I</i>	5
Region 98	<i>B</i>	4
Region 98	<i>V</i>	4
Region 98	<i>R</i>	4
Region 98	<i>I</i>	4
Rubin 152	<i>B</i>	4
Rubin 152	<i>V</i>	4
Rubin 152	<i>R</i>	4
Rubin 152	<i>I</i>	4
Rubin 149	<i>B</i>	4
Rubin 149	<i>V</i>	4
Rubin 149	<i>R</i>	4
Rubin 149	<i>I</i>	4
PG 1323	<i>B</i>	4
PG 1323	<i>V</i>	4
PG 1323	<i>R</i>	4
PG 1323	<i>I</i>	4
PG 0942	<i>B</i>	4
PG 0942	<i>V</i>	4
PG 0942	<i>R</i>	4
PG 0942	<i>I</i>	4
PG 1525	<i>B</i>	4
PG 1525	<i>V</i>	4
PG 1525	<i>R</i>	4
PG 1525	<i>I</i>	4
PG 1528	<i>B</i>	4
PG 1528	<i>V</i>	4
PG 1528	<i>R</i>	4
PG 1528	<i>I</i>	4
NGC 5897	<i>B</i>	10
NGC 5897	<i>V</i>	10
NGC 5897	<i>R</i>	10
NGC 5897	<i>I</i>	10

The magnitude transformation results simply on an additional displacement for the four filters. This procedure is applied to our four mosaics in filters *B*,

TABLE 4

Observation log for March 2007		
Object Observed	Filter	Number of Images
Bias		10
Flat Field <i>B</i>	<i>B</i>	3
Flat Field <i>V</i>	<i>V</i>	3
Flat Field <i>R</i>	<i>R</i>	3
Flat Field <i>I</i>	<i>I</i>	3
Rubin 152	<i>B</i>	3
Rubin 152	<i>V</i>	3
Rubin 152	<i>R</i>	3
Rubin 152	<i>I</i>	3
Rubin 149	<i>B</i>	3
Rubin 149	<i>V</i>	3
Rubin 149	<i>R</i>	3
Rubin 149	<i>I</i>	3
PG 1323	<i>B</i>	3
PG 1323	<i>V</i>	3
PG 1323	<i>R</i>	3
PG 1323	<i>I</i>	3
PG 0942	<i>B</i>	3
PG 0942	<i>V</i>	3
PG 0942	<i>R</i>	3
PG 0942	<i>I</i>	3
PG 1525	<i>B</i>	3
PG 1525	<i>V</i>	3
PG 1525	<i>R</i>	3
PG 1525	<i>I</i>	3
NGC 5897 C, N, E, W	<i>B</i>	10
NGC 5897 C, N, E, W	<i>V</i>	10
NGC 5897 C, N, E, W	<i>R</i>	10
NGC 5897 C, N, E, W	<i>I</i>	10

TABLE 5

Standard System	A <sub>B</sub>	K <sub>B</sub>	C <sub>B</sub>
21-22 March 2006	-0.36496	0.19409	26.83682
22-23 March 2006	-1.23555	0.17829	26.39759
23-24 March 2006	-0.41733	0.42103	26.78603
12-13 March 2007	1.16919	0.10874	25.34031
13-14 March 2007	-0.30223	0.10583	27.47228
14-15 March 2007	-0.37970	0.13717	27.53140

TABLE 6

Standard System	A <sub>V</sub>	K <sub>V</sub>	C <sub>V</sub>
21-22 March 2006	0.94214	0.05596	25.03835
22-23 March 2006	-1.67073	0.00563	28.07604
23-24 March 2006	-0.46776	0.30053	27.38143
12-13 March 2007	0.12127	-0.02352	27.58167
13-14 March 2007	-0.25039	-0.03984	27.76332
14-15 March 2007	-0.32799	-0.02824	27.86426

TABLE 7

Standard System	A <sub>R</sub>	K <sub>R</sub>	C <sub>R</sub>
21-22 March 2006	—	—	—
22-23 March 2006	-1.83264	0.13357	28.60749
23-24 March 2006	-0.59665	0.50853	27.63788
12-13 March 2007	0.37819	-0.02996	27.22330
13-14 March 2007	-0.13806	-0.04880	27.22305
14-15 March 2007	-0.23895	-0.05205	27.75572

TABLE 8

Standard System	A <sub>I</sub>	K <sub>I</sub>	C <sub>I</sub>
21-22 March 2006	—	—	—
22-23 March 2006	-2.25859	0.14873	29.11512
23-24 March 2006	-0.56102	0.78455	27.07607
12-13 March 2007	1.14735	0.06524	25.31618
13-14 March 2007	-0.02309	0.00138	26.50840
14-15 March 2007	0.11989	-0.02645	26.57065

$V$ ,  $R$  and  $I$  producing a final set of NGC 5897 stars in four filters on a standard system of position and magnitude.

#### 4.1. Colour Catalogues

We formed four colour catalogues as follows:

- $B - V$  catalogue: 1656 stars
- $V - I$  catalogue: 1935 stars
- $R - I$  catalogue: 2026 stars
- $V - R$  catalogue: 2587 stars

The number of stars in each catalogue is different because not all stars are equally detected in the different filters and therefore, some of them may be detected in one filter and not in another.

#### 4.2. Fiducial Lines (FL) and Colour-Magnitude Diagrams (CMD)

In this section we shall present the colour magnitude diagrams which we obtained from the photometry performed on the stars of the globular cluster

NGC 5897. Each colour-magnitude diagram will be presented as a plot of magnitude versus colour, on which we have superimposed a series of lines which correspond to the fiducial line for the giant branch and part of the main sequence. The fiducial line was obtained with the following procedure:

- We calculate the maximum and minimum value of the magnitude interval.
- We divide this interval in a number of magnitude bins.
- Along each magnitude bin we find the number of stars in a number of colour bins. This allows us to find a distribution of the number of stars along a magnitude bin in bins of colour. We obtain a distribution histogram for the number of stars in each magnitude bin.
- Each one of these histograms is fitted by a Gaussian function and we obtain for this function its maximum height ( $A$ ), its central value ( $x_0$ ) and its standard deviation ( $\sigma$ ).
- The fiducial line is formed from the points with coordinates  $(x_0, m_0)$  where  $m_0$  is the average magnitude in each magnitude bin.

Table 9 presents the FL derived by Sarajedini (1992) (Columns 1 and 2), that derived by us in this paper (Columns 3, 4 and 5), an eyeball fit to our FL (Columns 6 and 7) and an eyeball fit to the Sarajedini (1992) CMD made by us (Columns 8 and 9). Tables 10 and 11 give the colours, magnitudes and colour dispersion for the fiducial lines, calculated with the procedure described above, for the  $B$  vs  $(B - V)$  and  $V$  vs  $(V - I)$  colour magnitude diagrams.

Figure 5 presents the FL derived by Sarajedini (1992) (blue) from an eyeball fitting to the points on his CMD and the FL we derived in this paper (red) following the procedure described above. We have also included in this figure an eyeball fit to our FL (pink), as well as an eyeball fit made to the CM diagram of Sarajedini's made by us (green). The FL we derived using the Gaussian technique has errors in the  $(B - V)$  colour that bring it in close agreement with the Sarajedini (1992) fiducial line. However, in the magnitude range  $14.0 \leq V \leq 16.0$  our fiducial line appears  $\approx 0.1$  units bluer than that of Sarajedini's. Even if we consider the estimated error for the  $(B - V)$  colour of our observations ( $\approx 0.03$ ) this cannot explain a shift of this magnitude. Fainter than  $V \approx 16.0$  and down to  $V \approx 19.0$  our FL and that

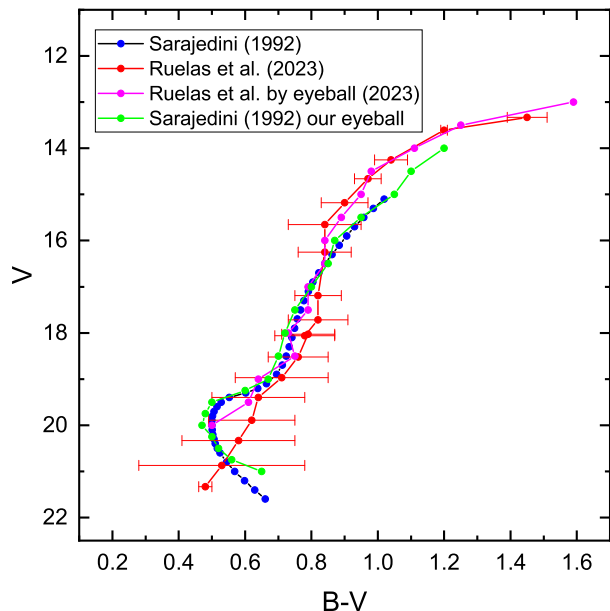


Fig. 5. The blue dots show the fiducial line derived by Sarajedini (1992) from an eyeball fit to his CMD. The red dots show the FL derived in this paper following the procedure described herein (see text); error bars for these points are also shown. The pink dots show an eyeball fit to our FL and finally, the green dots show an eyeball fit to the Sarajedini CMD made by us. The colour figure can be viewed online.

of Sarajedini's coincide within the errors. Further down than  $V \approx 19.0$  there is again a discrepancy which, in this case, is simply due to the paucity of our data at these faint magnitudes.

The difference we observe between our FL and that of Sarajedini's at brighter magnitudes baffles us and we cannot find, at this point, a reasonable explanation for it. Our observations are quite incomplete at levels deeper than  $V \approx 19$ ; that is why our FL shows neither the turn-off point nor the beginning of the main sequence.

## 5. COLOUR-MAGNITUDE DIAGRAMS

Figure 6 shows the colour-magnitude diagrams  $B$  vs  $B - V$ ,  $V$  vs  $B - V$ ,  $V$  vs  $V - I$  and  $I$  vs  $V - I$ . The lines show the fiducial Line (FL) obtained following the procedure described above and the FL displaced one and two standard deviations. We can say that those stars that lie outside the  $2\sigma$  limit and do not belong to the horizontal branch of the cluster have a very low probability ( $\approx 5\%$ ) of belonging to the globular cluster.

Figure 7 presents the colour-magnitude diagrams corresponding to the following combinations of magnitude and colour:  $V$  vs  $(V - R)$ ,  $R$  vs  $(V - R)$ ,  $R$  vs

$(R - I)$  and  $I$  vs  $(R - I)$ . On these diagrams we have not drawn the fiducial lines, but they can be easily obtained following the procedure described above.

On all the colour-magnitude diagrams presented here we can clearly appreciate the presence of the giant branch (GB) which, on the  $V$  vs  $B - V$  diagram extends from  $V \approx 13.5$  to  $V \approx 20$  where the main sequence (MS) appears to begin. Our observations are not sufficiently deep to allow us a clear detection of the MS of this cluster. However, on the  $V$  vs  $V - R$  diagram we see stars that extend down to magnitude  $V \approx 22$ , where the turn-off point (TO) and the beginning of the MS are more clearly shown on this diagram. It is also clear that there is a number of stars that most probably do not belong to the globular cluster and that most certainly are foreground and to a lesser extent background stars. As mentioned above, the FLs obtained for three of the colour-magnitude diagrams permit us to eliminate with a high degree of certainty those stars which are located far away from the calculated fiducial line for the cluster. Below the HB and to the left (bluer colours) of the GB there is a large number of stars that could possibly be blue stragglers belonging to this cluster.

The giant branch (GB) of this cluster is very well delineated on the  $R$  vs  $R - I$  and  $I$  vs  $R - I$  diagrams and it extends from  $\approx 12$  to  $\approx 18$  magnitudes.

The presence of horizontal branch (HB) stars is obvious in all the diagrams. In those diagrams that include the  $R$  and  $I$  magnitudes, it is clear that the HB stars become fainter very quickly as we move towards bluer colours. In all our photometric catalogues we separated from the bulk of our observations the HB stars, and on each one of the colour-magnitude diagrams we explicitly state the number of HB stars belonging to this diagram.

### 5.1. The Horizontal Branch

The horizontal branch (HB) of globular cluster is an interesting region of their CM diagram because: (i) it contains RR-Lyrae variable stars which have a fixed absolute magnitude (within certain restrictions). This fact is tremendously useful in the calculation of the distance of the globular cluster in question. (ii) It also presents groups of red and blue HB stars and the relative number of these red and blue stars is related to the helium abundance of the stars in the cluster.

In Table 12 we give the mean value of the magnitude values for the stars in the horizontal branch for each filter with which we observed. We shall later use these values in order to calculate a distance to

TABLE 9  
FIDUCIAL LINES FOR V VS (B-V)

$(B - V)_{Sa}$	$V_{Sa}$	$(B - V)_O$	$V_O$	$\sigma_O$	Eye $(B - V)_O$	Eye $V_O$	Eye $(B - V)_{Sa}$	Eye $V_{Sa}$
1.019	15.1	1.45	13.33	0.06	1.59	13	1.2	14
0.987	15.3	1.2	13.61	0.01	1.25	13.5	1.1	14.5
0.958	15.5	1.04	14.25	0.05	1.11	14	1.05	15
0.93	15.7	0.97	14.66	0.04	0.98	14.5	0.95	15.5
0.906	15.9	0.9	15.18	0.07	0.95	15	0.87	16
0.884	16.1	0.84	15.65	0.11	0.89	15.5	0.85	16.5
0.862	16.3	0.84	16.25	0.08	0.84	16	0.8	17
0.84	16.5	0.82	17.19	0.07	0.84	16.5	0.75	17.5
0.822	16.7	0.82	17.72	0.09	0.79	17	0.72	18
0.804	16.9	0.78	18.06	0.09	0.79	17.5	0.7	18.5
0.791	17.1	0.79	18.03	0.08	0.73	18	0.67	19
0.777	17.3	0.76	18.52	0.09	0.75	18.5	0.6	19.25
0.767	17.5	0.71	18.97	0.14	0.64	19	0.5	19.5
0.757	17.7	0.64	19.4	0.14	0.61	19.5	0.48	19.75
0.749	17.9	0.62	19.89	0.13	0.5	20	0.47	20
0.741	18.1	0.58	20.33	0.17			0.5	20.25
0.733	18.3	0.53	20.87	0.25			0.52	20.5
0.724	18.5	0.48	21.33	0.02			0.56	20.75
0.712	18.7						0.65	21
0.695	18.9							
0.664	19.1							
0.638	19.2							
0.602	19.3							
0.552	19.4							
0.528	19.5							
0.515	19.6							
0.506	19.7							
0.502	19.8							
0.5	19.9							
0.5	20							
0.501	20.1							
0.503	20.2							
0.506	20.3							
0.51	20.4							
0.516	20.5							
0.524	20.6							
0.544	20.8							
0.569	21							
0.598	21.2							
0.629	21.4							
0.661	21.6							

NGC 5897. We also indicate the value of the median colour of the stars in the HB. It is clear that on all the CMD the median colour is located very much

towards the blue edge of the HB, indicating that the majority of the stars in the HB branch are blue stars as mentioned in Sarajedini (1992).



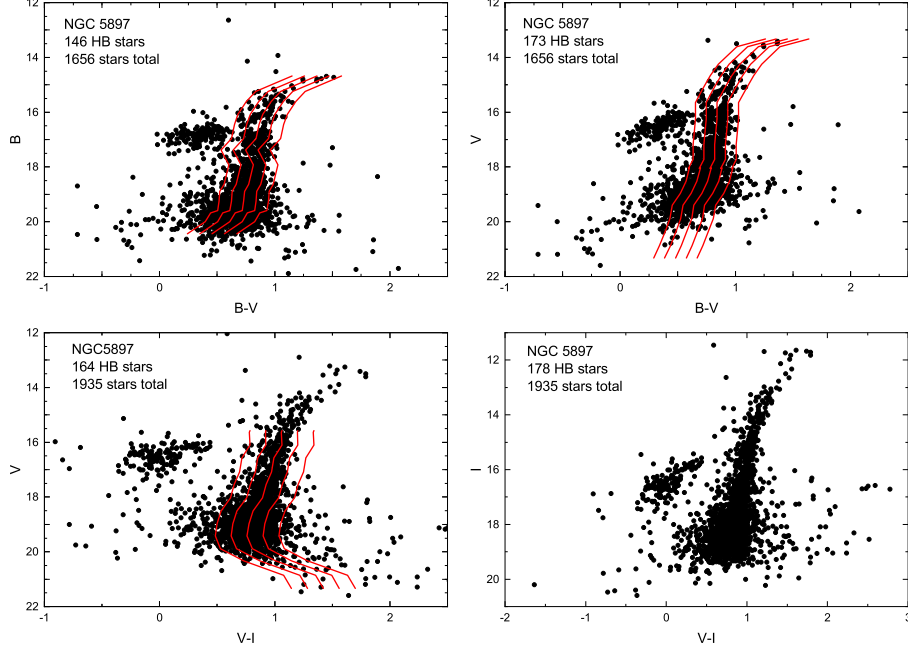


Fig. 6. Colour-magnitude diagrams for  $B$  vs  $B - V$ ,  $V$  vs  $B - V$ ,  $V$  vs  $V - I$  and  $I$  vs  $V - I$ . The central red line is the fiducial line (FL) (see text) and the other red lines indicate a  $1\sigma$  and  $2\sigma$  separation from the FL. The estimated errors are  $\approx 0.02$  for the magnitudes and  $\approx 0.03$  for the colours, smaller than the dots representing the stars. The colour figure can be viewed online.

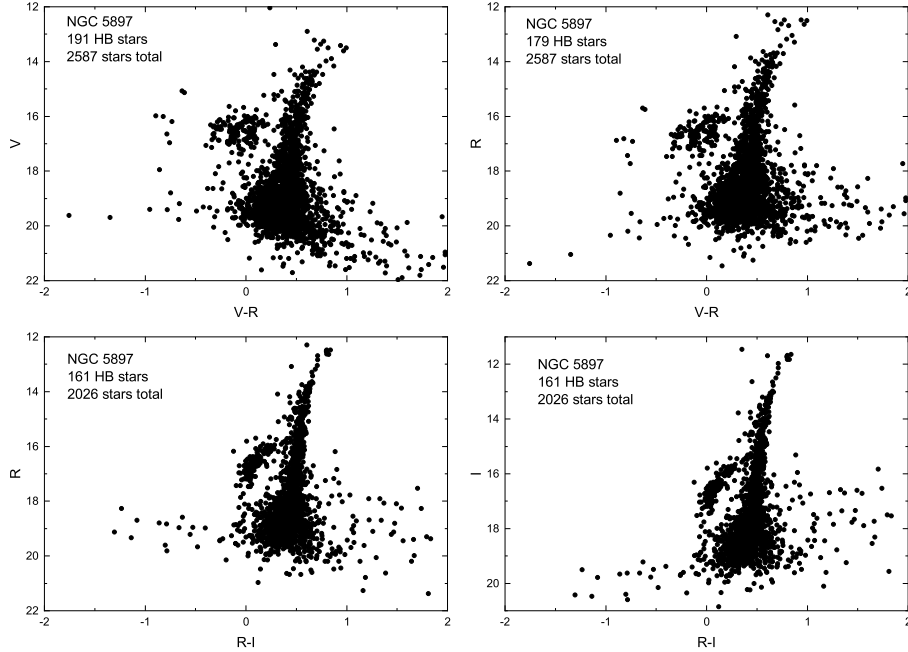


Fig. 7. Colour-magnitude diagrams for  $V$  vs  $V - R$ ,  $R$  vs  $V - R$ ,  $R$  vs  $R - I$  and  $I$  vs  $R - I$ . The estimated errors are  $\approx 0.02$  for the magnitudes and  $\approx 0.03$  for the colours, smaller than the dots representing the stars.

## 6. METALLICITY AND REDDENING

The metallicity and the reddening of a globular cluster may be determined simultaneously by the

Sarajedini method (Sarajedini, 1994 and Sarajedini & Layden, 1997), which takes into consideration the shape of the red giant branch (RGB), the observed

TABLE 10

FIDUCIAL LINE FOR  $B$  VS  $(B - V)$ 

$B - V$	$B$	$\sigma$
1.365	14.683	0.106
1.05	15.238	0.068
0.968	15.608	0.085
0.895	16.078	0.098
0.864	16.444	0.113
0.838	16.969	0.081
0.747	17.382	0.019
0.814	17.925	0.073
0.773	18.639	0.102
0.737	18.888	0.055
0.731	19.248	0.12
0.718	19.592	0.253
0.656	19.682	0.151
0.611	19.993	0.143
0.456	20.441	0.138

TABLE 11

FIDUCIAL LINE FOR  $V$  VS  $(V - I)$ 

$V - I$	$V$	$\sigma$
1.544	13.325	0.092
1.616	14.177	0.211
1.314	14.254	0.179
1.107	15.169	0.088
1.062	15.576	0.114
1.057	15.641	0.093
1.062	16.109	0.058
0.992	16.574	0.078
0.971	17.08	0.08
0.926	17.542	0.082
0.894	18.026	0.08
0.811	18.516	0.204
0.775	18.977	0.179
0.76	19.417	0.165
0.806	19.883	0.167
1.007	20.324	0.33
1.355	20.858	0.026
1.422	21.332	0.269

magnitude ( $V_{HB}$ ) of the horizontal branch (HB), the intrinsic  $(B - V)$  colour of the RGB at the level of the HB; this value will be denoted herein as:  $(B - V)_{0,g}$ , and the difference in observed  $V$  magnitude between the HB and the RGB at  $(B - V)_{int} = 1.2$  denoted by  $\Delta V_{1.2} = V_{HB\ Obs} - V_{RGB\ Obs\ at\ 1.2\ int}$ , where  $V_{RGB\ Obs\ at\ 1.2\ int}$  means the observed  $V$  magnitude of the RGB at an intrinsic  $(B - V)$  colour equal to

TABLE 12

MEAN VALUE OF THE MAGNITUDE FOR THE STARS IN THE HORIZONTAL BRANCH

CM Diagram	Mean HB Magnitude	Standard Deviation	Median Colour
$B$ vs $B - V$	$\overline{BHB} = 16.84$	0.27	0.36
$V$ vs $B - V$	$\overline{VHB} = 16.60$	0.46	0.37
$V$ vs $V - R$	$\overline{VHB} = 16.57$	0.55	-0.05
$R$ vs $V - R$	$\overline{RHB} = 16.66$	0.51	-0.05
$R$ vs $R - I$	$\overline{RHB} = 16.63$	0.44	0.08
$I$ vs $R - I$	$\overline{IHB} = 16.57$	0.50	0.08
$V$ vs $V - I$	$\overline{VHB} = 16.60$	0.44	-0.01
$I$ vs $V - I$	$\overline{IHB} = 16.58$	0.55	0.02

1.2. Defined this way,  $\Delta V_{1.2}$  results in an intrinsically positive quantity.

We applied the Sarajedini method for the stars in the  $V$  vs  $(B - V)$  and the  $V$  vs  $(V - I)$  colour-magnitude diagrams and obtained values for the metallicity  $[\text{Fe}/\text{H}]$  and colour excesses  $E(B - V)$  and  $E(V - I)$ . Unfortunately, these values were completely absurd, resulting in very high metallicities and negative colour excesses. We conducted a few numerical experiments and saw that the values of the metallicity and the colour excess are very sensitive to variations of the values of the fit coefficients. The coefficients we obtained for the FLs in the  $V$  vs  $(B - V)$  and  $V$  vs  $(V - I)$  diagrams had errors of the order 30 % which might explain the troublesome results we obtained. We therefore decided to adopt the values given in the Harris catalogue (Harris, 1996)  $[\text{Fe}/\text{H}] = -1.90$  and  $E(B - V) = 0.09$ .

The parameters discussed in this section could also be determined by means of isochrone fitting. There are in the literature several sets of isochrones which could be used (Girardi et al. (2002), Spada et al. (2013), <http://www.astro.yale.edu/demarque/yyiso.html>, and references therein, <http://stev.oapd.inaf.it/cgi-bin/cmd> and references therein. We shall report on this elsewhere.

## 7. DISTANCE MODULUS

Using the assumption that the average absolute magnitude of the HB is equal to the absolute magnitude of the RR-Lyrae stars in the cluster, we calculate the distance to the cluster we study here (for a justification of this assumption see, for example, Christy, 1966; Demarque & McClure, 1977 and Saio, 1977).

For the RR-Lyrae stars, a linear relation between absolute magnitude and metallicity of the

form  $M = a + b[\text{Fe}/\text{H}]$  is proposed in the astronomical literature. Determination of the constants  $a$  and  $b$  is achieved using the following methods: (i) statistical parallaxes, (ii) the BBW moving atmosphere method, and (iii) main sequence fitting (Sandage & Tammann (2006)).

In the following paragraphs we shall use different absolute magnitude-metallicity relations from the literature for RR-Lyraes, which combined with the metallicity and the apparent magnitude for the HB of NGC 5897, will permit us to determine the value of its distance modulus.

A compilation of statistical parallaxes of field RR-Lyrae stars has been presented by Wan et al. (1980) in a Catalogue of the Shanghai Observatory. This compilation is summarised in Table 3 of Reid (1999). There is a value for  $\langle M_V \rangle_{\text{RR}} = 0.83 \pm 0.23$  for  $\langle [\text{Fe}/\text{H}] \rangle$  values around  $-0.75$  and another  $\langle M_V \rangle_{\text{RR}} = 0.85 \pm 0.15$  for  $\langle [\text{Fe}/\text{H}] \rangle$  values around  $-1.56$ . A linear extrapolation to the metallicity of NGC 5897 ( $[\text{Fe}/\text{H}] = -1.90$ ) produces a value for

$$\langle M_V \rangle_{\text{NGC 5897}} = 0.86.$$

The extrapolation process poses a problem for this determination.

Using a combination of the infrared flux and the Baade-Wesselink analysis methods Fernley et al. (1989), Fernley et al. (1990a), Fernley et al. (1990b), Skillen et al. (1989), and Skillen et al. (1993) study 21 RR-Lyrae variable stars and obtain a mean relation for their absolute magnitude expressed as follows:

$$\langle M_V \rangle_{\text{RR}} = (0.21 \pm 0.05)[\text{Fe}/\text{H}] + (1.04 \pm 0.10),$$

which for the metallicity value of our globular cluster produces a result of

$$\langle M_V \rangle_{\text{NGC 5897}} = 0.64 \pm 0.20.$$

Fernley (1993) uses his near-IR Sandage period-shift effect (SPSE) and a theoretical pulsation relation to derive the following relation:

$$\langle M_V \rangle_{\text{RR}} = 0.19[\text{Fe}/\text{H}] + 0.84,$$

which applied to our cluster gives

$$\langle M_V \rangle_{\text{NGC 5897}} = 0.48.$$

McNamara (1997) has reanalysed these same 29 stars making use of more recent Kurucz model atmospheres and derives a steeper, more luminous calibration given as follows:

$$\langle M_V \rangle_{\text{RR}} = (0.29 \pm 0.05)[\text{Fe}/\text{H}] + (0.98 \pm 0.04),$$

The RR-Lyraes studied in the McNamara paper belong to a metallicity interval from approximately  $-2.2$  to  $0.0$ . The metallicity value for our globular cluster ( $-1.90$ ) lies within this interval, making it reasonable to apply this relation to this cluster. The value we obtain from this relation is:

$$\langle M_V \rangle_{\text{NGC 5897}} = 0.43 \pm 0.14.$$

Tsujimoto et al. (1998) have analysed data for 125 *Hipparcos* RR Lyraes in the metallicity range  $-2.49 < [\text{Fe}/\text{H}] < 0.07$  using the maximum likelihood technique proposed by Smith (1988). This technique allows simultaneous correction of the Malmquist and Lutz-Keller biases, allowing a full use of negative and low-accuracy parallaxes. They derive the following relation:

$$\langle M_V \rangle_{\text{RR}} = (0.59 \pm 0.37) + (0.20 \pm 0.63)([\text{Fe}/\text{H}] + 1.60).$$

Given that  $[\text{Fe}/\text{H}]_{\text{NGC 5897}} = -1.90$  is contained within the studied metallicity interval, applying this relation to the cluster studied in this paper produces

$$\langle M_V \rangle_{\text{NGC 5897}} = 0.53 \pm 0.56.$$

Arellano Ferro et al. (2008) using the technique of Fourier decomposition for the light curves of RR-Lyraes in several globular clusters derive the following relation:

$$\langle M_V \rangle_{\text{RR}} = +(0.18 \pm 0.03)[\text{Fe}/\text{H}] + (0.85 \pm 0.05).$$

This relation was obtained for a set of globular clusters contained within the metallicity interval  $-2.2 < [\text{Fe}/\text{H}] < -1.2$  making it appropriate for the metallicity value ( $-1.90$ ) we have for NGC 5897.

Applying this relation to our cluster we find

$$\langle M_V \rangle_{\text{NGC 5897}} = 0.51 \pm 0.10.$$

There are many different empirical and theoretical determinations of the  $\langle M_V \rangle - [\text{Fe}/\text{H}]$  relation for RR-Lyrae stars, for ample discussions see Chaboyer (1999), Cacciari & Clementini (2003) and Sandage & Tammann (2006). Determining which one is the most appropriate for NGC 5897 is beyond the scope of this paper, so we have decided to consider all of them for the calculation of the distance modulus of the globular cluster studied in this paper.

From the data presented in this paper we determine an apparent  $V$  magnitude for the HB of NGC 5897 of  $16.60 \pm 0.46$ , which combined with the values for the absolute magnitudes of the RR-Lyrae

TABLE 13

DISTANCE MODULUS FOR NGC 5897		
From the calibration given in	$\langle M_V \rangle$	$(m - M)_0$ $m_{HB} - \langle M_V \rangle - 3.1E(B - V)$
Wan et al. (1980)	$0.86 \pm 0.10$	$15.66 \pm 0.10$
Fernley (1993)	$0.48 \pm 0.10$	$16.04 \pm 0.10$
Skillen et al. (1993)	$0.64 \pm 0.20$	$16.08 \pm 0.20$
McNamara (1997)	$0.43 \pm 0.14$	$16.17 \pm 0.14$
Tsujimoto et al. (1998)	$0.53 \pm 0.56$	$16.91 \pm 0.56$
Arellano Ferro et al. (2008)	$0.51 \pm 0.10$	$16.01 \pm 0.10$

stars and the assumption that the HB and the RR-Lyraes have the same absolute magnitude yields the distance modulus values presented in Table 13.

A weighted average (by the inverse square of the errors) of these values results in an average distance modulus for NGC 5897 of  $15.96 \pm 0.64$  ( $15500^{+5200}_{-3900}$  pc). The errors we encounter represent a  $\approx \pm 34\%$  error in distance. For the most part the error in the distance modulus comes from the errors in the absolute magnitude versus metallicity relations (see Table 13, Column 2), and not from the errors in our photometry.

Benedict et al. (2002), using the HST parallax for the prototype RR-Lyrae star, determine an absolute magnitude for this star of  $M_v = 0.61 \pm 0.10$ . If we assume that the HB of NGC 5897 has this value for its absolute magnitude, then we obtain a distance modulus of:

$$(m - M)_0 = (16.60 \pm 0.46) - (0.61 \pm 0.10)$$

$$-3.1 \times (0.09 \pm 0.10) = 15.71 \pm 0.87 ,$$

which agrees, within the errors, with previous determinations. This value of the distance modulus produces a distance of  $13800^{+6800}_{-4600}$  pc to NGC 5897 with an error of  $\approx \pm 49\%$ .

We adopt as our best determination for the NGC 5897 distance modulus the average of the values obtained with the Fernley (1993) ( $16.04 \pm 0.10$ ), and the Arellano Ferro et al. (2008) ( $16.01 \pm 0.10$ ) calibrations due to the fact that these calibrations present the smallest errors. This average results in  $16.02 \pm 0.14$ .

## 8. CONCLUSIONS

In this paper we present  $B$ ,  $V$ ,  $R$  and  $I$  CCD photometry for the globular cluster NGC 5897. We obtained aperture photometry for a number of standard stars in the Landolt (1992) regions, and then

compared our observed stars with the magnitudes published by Stetson (1992). After aligning and matching the different sections of the globular cluster, we were able to produce magnitude catalogues for all the filters (a sample of these catalogues is presented in Appendix A). We formed eight colour magnitude (CM) diagrams (see Figures 6 and 7). In all these CM diagrams we can clearly see the red giant branch (RGB), the horizontal branch (HB) and the beginning of the main sequence (MS). Towards bluer colours from the MS turn-off point, we see a somewhat large number of stars that we identify as blue stragglers in this cluster. We tried to calculate the metallicity and the reddening of this cluster making use of the Sarajedini-Layden method (see Sarajedini (1994) and Sarajedini & Layden (1997)), but we were unable to do so. We calculated the distance modulus to this cluster, and it resulted in  $16.02 \pm 0.14$  which corresponds to a distance of  $16.0 \pm 1.0$  kpc.

We would like to thank the Instituto de Astronomía at Universidad Nacional Autónoma de México (IAUNAM) and the Instituto de Astronomía y Meteorología at Universidad de Guadalajara (IAMUdeG) for providing a congenial and stimulating atmosphere in which to work. We also thank the computing staff at both institutions for being always available and ready to help with random problems with our computing equipment, which arise when one least expects them. We would also like to thank Juan Carlos Yustis for help with the production of the figures in this paper. We also thank Dirección General de Asuntos del Personal Académico, DGAPA at UNAM for financial support under projects PAPIIT IN103813, IN102517 and IN102617. The help and valuable suggestions provided by an anonymous referee are gratefully acknowledged.

## APPENDIX

In Tables 14 and 15 we present samples of the magnitude catalogues for this paper. The complete catalogues are available upon request.

TABLE 14

<i>B</i> and <i>V</i> MAGNITUDES STARS IN NGC 5897			
<i>x</i> (pixels)	<i>y</i> (pixels)	Mag <i>B</i>	Mag <i>V</i>
-277.6176	547.1518	19.4144	18.689125
-260.9676	469.6858	19.8054	19.129125
-242.1806	360.0848	16.6974	16.453125
-225.8216	444.9578	18.4854	17.707125
-217.0566	868.2468	19.0594	18.111125
-211.4806	404.3458	19.1194	18.453125
-210.1306	444.8878	19.9204	19.279125
-209.5756	285.4678	18.1414	17.317125
-206.3026	784.5288	18.7414	18.202125
-203.2576	920.8858	16.9184	16.716125
-175.0646	374.1218	18.1674	17.363125
-174.9546	461.2768	20.1134	19.484125
-167.2466	948.8658	19.0664	18.332125
-165.9416	702.2378	15.4514	14.378125
-155.0016	218.2148	19.2874	18.574125
-154.4836	140.9378	19.7204	19.065125
-147.7006	607.6628	16.9474	16.747125
-128.4606	279.8978	16.5364	16.210125
-128.0146	868.9678	16.7764	16.562125
-120.0366	848.4458	18.8774	18.148125
-96.1348	422.0696	18.9894	18.215125
-88.0116	218.9878	16.1654	15.098125
-87.8078	424.5506	20.0354	19.468125
-85.0406	473.5338	19.1244	18.368125
-83.6186	457.5028	18.6764	17.788125
-80.8708	206.5076	20.0504	19.696125
-78.9268	-112.1904	20.1914	19.493125
-77.6868	463.3066	20.2104	19.453125
-77.6686	746.1548	18.2714	17.494125
-76.6066	1057.1788	20.0354	19.186125

## REFERENCES

- Arellano Ferro, A., Giridhar, S., Rojas López, V., et al. 2008, RMxAA, 44, 365
- Beasley, M. A. 2020, in Reviews in Frontiers of Modern Astrophysics; From Space Debris to Cosmology, ed. P. Kabáth, D. Jones, & M. Skarka (Springer International Publishing), 245, [https://doi.org/10.1007/978-3-030-38509-5\\_9](https://doi.org/10.1007/978-3-030-38509-5_9)

TABLE 15

<i>R</i> and <i>I</i> MAGNITUDES STARS IN NGC 5897			
<i>x</i> (pixels)	<i>y</i> (pixels)	Mag <i>R</i>	Mag <i>I</i>
-287.2978	628.6134	16.95635	16.55932
-275.8288	546.6794	18.23635	17.89732
-253.0268	552.9184	18.94435	18.63932
-241.8808	359.8734	16.36735	16.32632
-236.2428	805.0314	18.63835	18.35832
-225.3138	444.7094	17.27135	16.85532
-216.0218	867.7194	17.56735	17.18532
-210.9128	405.2264	18.09135	17.74332
-209.2018	285.3604	16.86735	16.47632
-208.7448	670.3394	17.18435	16.76832
-208.3818	945.1264	18.31335	17.93632
-205.1298	784.2834	17.87935	17.64832
-202.7348	919.9534	16.68035	16.68832
-187.5238	817.3414	18.58435	18.19432
-184.7668	573.4634	19.30235	18.93232
-174.8078	373.8214	16.89735	16.48132
-174.5678	461.5674	19.08335	18.96432
-173.3298	625.7874	18.87335	18.70232
-166.6518	948.2634	17.86835	17.49232
-165.4968	701.9594	13.74835	13.19532
-154.6808	364.3284	18.43835	18.01332
-154.1348	218.2784	18.11335	17.87332
-153.8348	353.4634	18.91635	18.60632
-153.8298	141.3604	18.79335	19.65532
-147.3108	607.1884	16.71035	16.72932
-146.6818	407.2014	18.29635	17.68232
-140.7538	880.8234	17.97135	17.56732
-138.8768	586.5374	18.46135	17.96932
-132.2968	412.4374	18.94335	18.67032
-128.3178	279.7424	16.07935	15.98132

- Benedict, G. F., McArthur, B. E., Fredrick, L. W., et al. 2002, AJ, 123, 473, <https://doi.org/10.1086/338087>
- Binney, J. & Merrifield, M. 1998, Galactic Astronomy (Princeton, NJ: PUP)
- Cacciari, C. & Clementini, G. in Stellar Candles for the Extragalactic Distance Scale, ed. D. Alloin & W. Gieren (Lecture Notes in Physics 365), 105, <https://doi.org/10.1007/b13985>
- Chaboyer, B. 1999, in Post-Hipparcos Cosmic Candles, ed. A. Heck & F. Caputo (Astrophysics and Space Science Library 237), 111, <https://doi.org/10.1007/978-94-011-4734-7>

- Christy, R. F. 1966, *ApJ*, 144, 108, <https://doi.org/10.1086/148593>
- Demarque, P. & McClure, R. D. 1977, in *Evolution of Galaxies and Stellar Populations*, ed. B. M. Tinsley & R. B. Larson (New Haven, CT: Yale University Observatory), 199
- Fernley, J. 1993, *A&A*, 268, 591
- Fernley, J. A., Lynas-Gray, A. E., Skillen, I., et al. 1989, *MNRAS*, 236, 447, <https://doi.org/10.1093/mnras/236.3.447>
- Fernley, J. A., Skillen, I., Jameson, R. F., Barnes, T. G., Kilkenny, D., & Hill, G. 1990a, *MNRAS*, 247, 287
- Fernley, J. A., Skillen, I., Jameson, R. F., & Longmore, A. J. 1990b, *MNRAS*, 242, 685, <https://doi.org/10.1093/mnras/242.4.685>
- Ferraro, F. R., Fusi Pecci, F., & Buonanno, R. 1992, *MNRAS*, 256, 376, <https://doi.org/10.1093/mnras/256.3.376>
- Girardi, L., Bertelli, G., Bressan, A., et al. 2002, *A&A*, 391, 195, <https://doi.org/10.1051/0004-6361:20020612>
- Harris, W. E. 1996, *AJ*, 112, 1478, <https://doi.org/10.1086/118116>
- . 2010, *arXiv:1012.3224*, <https://doi.org/10.48550/arXiv.1012.3224>
- Harris, W. E., Harris, G. L. H., & Alessi, M. 2013, *ApJ*, 772, 82, <https://doi.org/10.1088/0004-637X/772/2/82>
- Ishchenko, M., Sobolenko, M., Berczik, P., et al. 2023, *A&A*, 673, 152, <https://doi.org/10.1051/0004-6361/202245117>
- Laher, R. R., Gorjian, V., Rebull, L. M., et al. 2012, *PASP*, 124, 737, <https://doi.org/10.1086/666883>
- Landolt, A. U. 1992, *AJ*, 104, 340, <https://doi.org/10.1086/116242>
- McNamara, D. H. 1997, *PASP*, 109, 857, <https://doi.org/10.1086/133956>
- Mihalas, D. & Binney, J. 1981, *Galactic Astronomy & Binney, J.* (San Francisco, CA: Freeman)
- Monella, R. 1985, *Col*, 53, 225
- Palma, T. 2023, *BAAA*, 64, 136
- Pfeffer, J., Kruijssen, J. M. D., Bastian, N., Crain, R. A., & Trujillo-Gomez, S. 2023, *MNRAS*, 519, 5384, <https://doi.org/10.1093/mnras/stad044>
- Reid, I. N. 1999, *ARA&A*, 37, 191, <https://doi.org/10.1146/annurev.astro.37.1.191>
- Ruelas-Mayorga, A., Sánchez, L. J., Herrera, G., & Nigoche-Netro, A. 2010, *RMxAA*, 46, 3
- Saio, H. 1977, *Ap&SS*, 50, 93, <https://doi.org/10.1077/BF00648522>
- Sandage, A. & Katem, B. 1968, *ApJ*, 153, 569, <https://doi.org/10.1086/149687>
- Sandage, A. & Tammann, G. A. 2006, *ARA&A*, 44, 93, <https://doi.org/10.1146/annurev.astro.43.072103.150612>
- Sarajedini, A. 1992, *AJ*, 104, 178, <https://doi.org/10.1086/116229>
- . 1994, *AJ*, 107, 618, <https://doi.org/10.1086/116880>
- Sarajedini, A. & Layden, A. 1997, *AJ*, 113, 264, <https://doi.org/10.1086/118250>
- Skillen, I., Fernley, J. A., Jameson, R. F., Lynas-Gray, A. E., & Longmore, A. J. 1989, *MNRAS*, 241, 281, <https://doi.org/10.1093/mnras/241.2.281>
- Skillen, I., Fernley, J. A., Stobie, R. S., & Jameson, R. F. 1993, *MNRAS*, 265, 301, <https://doi.org/10.1093/mnras/265.2.301>
- Spada, F., Demarque, P., Kim, Y. C., & Sills, A. 2013, *ApJ*, 776, 87, <https://doi.org/10.1088/0004-637X/776/2/87>
- Stetson, P. B. 1992, *JRASC*, 86, 71
- . 2019, *Canadian Advanced Network for Astronomical Photometric Standard Fields: NGC 5897, pastime visited March 19th 2022*
- Strader, J., Brodie, J. P., Cenarro, A. J., Beasley, M. A., & Forbes, D. A. 2005, *AJ*, 130, 1315, <https://doi.org/10.1086/432717>
- Tsujiimoto, T., Miyamoto, M., & Yoshii, Y. 1998, *ApJ*, 492, 79, <https://doi.org/10.1086/311084>
- Wan, L., Mao, Y. Q., & Ji, D. S. 1980, *Annals of the Shanghai Observatory*, 2, 1
- Webbink, R. F. in *IAUS 113, Dynamics of Star Clusters*, ed. J. Goodman & P. Hut (Princeton, NJ: Dordrecht Reidel), 541
- Wehlau, A. 1990, *AJ*, 99, 250, <https://doi.org/10.1086/115324>

E. Macías-Estrada, A. Ruelas-Mayorga, and L. J. Sánchez: Instituto de Astronomía, Universidad Nacional Autónoma de México, Apartado Postal 70-264, Cd. Universitaria 04510, CDMX, México (emacias, rarm, leonardo@astro.unam.mx).

A. Nigoche-Netro: Instituto de Astronomía y Meteorología, Universidad de Guadalajara, Guadalajara, Jal. 44130, México (anigoche@gmail.com).

## THE FIRST MULTICOLOUR PHOTOMETRY OF THE V840 LYR CONTACT BINARY STAR

Mehmet Tanrıver<sup>1,2</sup>, Raúl Michel<sup>3</sup>, Ahmet Bulut<sup>4,5</sup>, Héctor Aceves<sup>3</sup>, and Ahmet Keskin<sup>1</sup>

*Received May 16 2023; accepted November 2 2023*

### ABSTRACT

Light curves for the total-eclipsing binary system V840 Lyr in the  $V$ ,  $R_c$ , and  $I_c$  bands are presented; these display the O’Connell effect. Analysis was performed with the `Phoebe031a` software revealing that V840 Lyr is a W-type contact binary with a degree of contact factor of  $f = 15.1 \pm 5.6\%$ , a mass ratio of  $q = 0.4509 \pm 0.0705$ , an inclination of  $i = 86.7^\circ$ , and a temperature difference of  $\Delta T = 45$  K. An asymmetry in the light curves was modeled assuming a cool spot located on the secondary star. The period changes of the system are examined by combining our recently found times of light minima together with those in the literature. Absolute parameters were obtained as  $M_1 = 0.74M_\odot$ ,  $M_2 = 0.34M_\odot$ ,  $R_1 = 0.74R_\odot$ , and  $R_2 = 0.51R_\odot$  from our photometric solutions, using some empirical relations. The long-term period increase and the contact configuration indicate that V840 Lyr will evolve into a fill-out overcontact binary.

### RESUMEN

Presentamos curvas de luz  $V$ ,  $R_c$ , e  $I_c$  para el sistema binario totalmente eclipsante V840 Lyr; las cuales manifiestan el efecto O’Connell. Se hace el análisis usando el paquete `Phoebe031a`; encontramos que V840 Lyr es una binaria de contacto tipo-W, con factor de contacto  $f = 15.1 \pm 5.6\%$ , razón de masa  $q = 0.4509 \pm 0.0705$ , una inclinación de  $i = 86.7^\circ$ , y diferencia de temperatura de  $\Delta T = 45$  K. Modelamos una asimetría en las curvas de luz asumiendo un mancha fría ubicada en la estrella secundaria. Los cambios de período del sistema se examinaron combinando nuestros tiempos mínimos de luz en conjunto con los de la literatura. Los parámetros absolutos obtenidos  $M_1 = 0.74M_\odot$ ,  $M_2 = 0.34M_\odot$ ,  $R_1 = 0.74R_\odot$ , y  $R_2 = 0.51R_\odot$  resultan de nuestras soluciones fotométricas y utilizando relaciones empíricas. El aumento del período a largo plazo y la configuración de contacto indican que V840 Lyr evolucionará hacia una binaria de sobrecontacto rellena.

*Key Words:* stars: binaries: eclipsing — stars: binaries: general — stars: individual: V840 Lyr

### 1. INTRODUCTION

Super Wide Angle Search for Planets (SuperWASP), an international team of many academic institutions conducting an ultra-wide angle search for exoplanets using transit photometry, discovered that V840 Lyr (1SWASP J183738.17+402427.2 = 2MASS J18373818+4024271) is an eclipsing binary star with a short period (Norton

et al. 2011). In the General Catalogue of Variable Stars (GCVS) database, V840 Lyr was identified by Samus et al. (2017) to be an eclipsing W UMa (EW) type binary. The system’s ephemeris (*Heliocentric Julian Day*-HJD) was provided by (GCVS) database (Samus et al. 2017):

$$\text{Min.}I(HJD) = 2457423.1706 + 0.221311 \times E. \quad (1)$$

New high-quality photometric observations were made in order to study this binary. The multicolor light curves of the system demonstrated an O’Connell effect in the  $V$ ,  $R_c$ , and  $I_c$  filters (see Figure 4). If the magnitude of the maximum-I is lower than that of the maximum-II, this is accepted as a positive O’Connell effect (O’Connell 1951).

<sup>1</sup>Department of Astronomy and Space Science, University of Erciyes, Türkiye (corresponding author: mtanriver@erciyes.edu.tr).

<sup>2</sup>Astronomy and Space Science Observatory Application and Research Center, University of Erciyes, Türkiye.

<sup>3</sup>Instituto de Astronomía, UNAM. Ensenada, México.

<sup>4</sup>Department of Physics, University of Çanakkale Onsekiz Mart, Türkiye.

<sup>5</sup>Astrophysics Research Centre and Observatory, University of Çanakkale Onsekiz Mart, Türkiye.



TABLE 1  
THE TARGET STARS' COORDINATES

Target	Stars	R.A.(2000) h:m:s	DEC.(2000) ° ' "	V mag	Ref
C1	V840 Lyr	18:37:38.18	40:24:27.09	14.45	(1)
C2	Comparison	18:37:27.01	40:24:56.88	12.63	(2)
C3	Comparison	18:37:25.32	40:26:03.59	13.19	(2)
C4	Comparison	18:37:34.49	40:24:44.78	14.89	(2)
C5	Comparison	18:37:47.46	40:25:29.24	14.47	(2)
C6	Check	18:37:55.51	40:25:35.25	14.36	(2)

Ref: (1) SuperWASP (Norton et al. 2011); (2) CCD photometry.

The presence of a dark cool spot on the secondary star provided an explanation for the asymmetric light curves. Their photometric investigation revealed that the V840 Lyr is a W-type over-contact binary with a small mass ratio. The binary star's derived fill-out factor of 15.14 percent indicated that it is getting close to the end of its evolution. These characteristics suggest that V840 Lyr is a promising target for additional research, which is made in part in this work. When the binary system satisfies the well-known requirement that the orbital angular momentum is less than three times the total rotational angular momentum of the components ( $J_{orb} < 3J_{rot}$ ), both components may merge into a rapidly spinning single star (Hut 1980). As a result, it is a potential progenitor for a luminous red nova (Zhu et al. 2016).

In this paper we study V840 Lyr further by analyzing light curves using a standard software package, and provide different estimates of the physical parameters for this binary star. Table 1 contains details on V840 Lyr, comparisons, and check stars. A typical binary of the EW type is V840 Lyr. The parallax for this eclipsing binary was stated as  $\pi = 2.2235 \pm 0.0214$  mas in Gaia Data Release 2-3 (Gaia Collaboration; et al. 2018).

## 2. PHOTOMETRIC OBSERVATIONS

$V$ ,  $R_c$  and  $I_c$  observations were carried out with the Mexman filter wheel mounted on the 84 cm reflecting telescope at San Pedro Martir (SPM) Observatory during the nights of 2018 July 06 (2.6h), 2019 June 06 (0.9h), 2019 June 07 (3.2h) and 2021 September 27 (2.5h) using exposure times of 60s in  $V$  and 40s both in  $R_c$  and  $I_c$ . Additional observations were carried out in 2022 June 14 (2.3h) and 2022 June 17 (6.9h) with exposure times of 20s in  $V$  and 15s in both  $R_c$  and  $I_c$ . During the 2018 run the Spectral Instruments CCD camera was employed while the Marconi 5 camera was used during the other runs. Table 1 contains the coordinates of the variable (V840 Lyr), the comparisons and the check stars

in the CCD camera's field of vision. The PHOT aperture photometry routine of IRAF was used for the reduction of the observed CCD field images.

The epoch specified in the GCVS, however, is *Heliocentric Julian Day*-HJD (Samus et al. 2017), needs to be transformed to *Barycentric Julian Day*-BJD to be compatible with TESS data. The following equation specifies the epoch as BJD:

$$BJD_{Min.I} = 2457423.0607315 + 0.221311 \times E. \quad (2)$$

To make this transformation, we used the code in the Eastman et al. (2010) study. Equation 2 specifies the epoch as BJD. In equation 2 period and epoch are taken from the GCVS catalog.

Table 2 lists the results of using the Gauss fitting method along with Monte Carlo Markov Chain (MCMC) to the following datasets: 14 CCD times of light minima from SPM observations, 18 from SWASP (Super Wide Angle Search for Planets (Pollacco et al. 2006), 3 from CRTS (Catalina Real-time Transient Survey, Drake et al. 2009), 9 from ZTF (The Zwicky Transient Facility (Bellm et al. 2019), and 10 from TESS (the Transiting Exoplanet Survey Satellite (Sullivan et al. 2015).

## 3. INVESTIGATION OF THE O-C CHANGE

Since the variable's discovery, no period change studies have been undertaken. We gather all available photoelectric and CCD times of minimum light from the other works, websites, and other surveys (SWASP, CRTS, ZTF, TESS) to examine the variations in the orbital period. Table 2 contains a list of minimum times of all primary and secondary eclipses. The seventh column of Table 2 contains a list of the (O-C) values (*O*bserved times of light minima minus *C*omputed times of light minima), which are plotted in the top panel of Figure 1 and are calculated by equation 2. In this figure, black-filled and empty circles signify data from the SPM Observatory, black-filled and empty diamonds indicate data obtained from TESS light curves, black-filled and empty squares refer to data from SWASP, black-filled and empty triangles indicate data obtained from ZTF, and the black plus and the black cross refer to data from CRTS.

The following ephemeris is provided by the (O-C) values' least-squares solution:

$$(O - C) = 1.33484(2) \times 10^{-03} + 2.10185(3) \times 10^{-07} E. \quad (3)$$

This ephemeris' linear term allows to calculate the new period and new initial minimum time. These minimum times of the binary system were used to calculate the revised orbital period, as provided by equation 4:

$$BJD(MinI) = 2457422.62012184 + 0.22131121 \times E \\ (\pm 0.00025736) \quad (\pm 0.00000002). \quad (4)$$

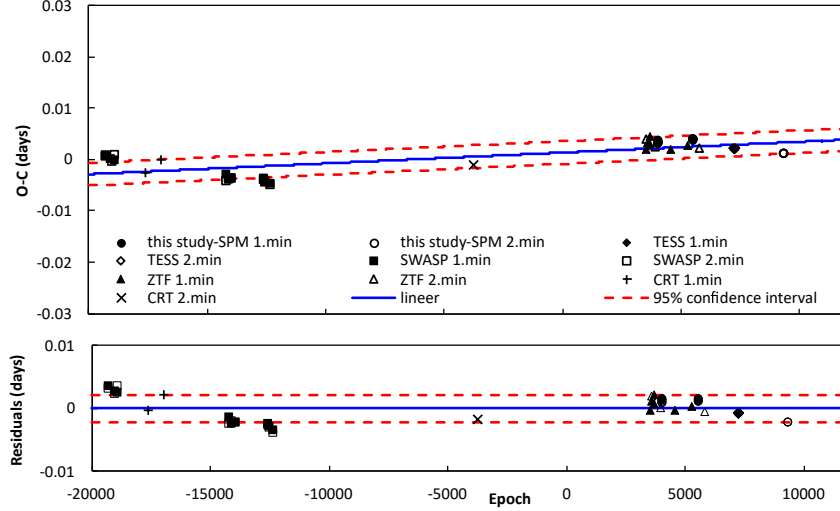


Fig. 1. According to all primary and secondary minimum times, the (O-C) diagram of the short period V840 Lyr binary. The blue solid line depicts a linear fit. In the lower panel, residuals pertaining to the linear ephemerides are shown. The red dashed lines represent a 95% confidence interval. The color figure can be viewed online.

Using equation 4, we found the revised period to be  $0^d.22131121$  for V840 Lyr.

The bottom panel of Figure 1 displays the residuals from equation 3, and Column 8 of Table 2 lists them.

#### 4. THE SOLUTION OF THE PHOTOMETRIC LIGHT CURVE

In this work, the  $V$ ,  $R_c$  and  $I_c$  light curves described above are used. The W-D code-based `Phoebe0.31a` interface program was used to analyze the light curves of V840 Lyr in order to understand its geometrical structure and evolutionary state (Wilson & Devinney 1971; Wilson 1979; van Hamme & Wilson 2003; Wilson et al. 2010; van Hamme 1993). The O’Connell effect can be seen in the binary system’s light curves, and it can be explained by dark-cool spot activity on the secondary component (Qian et al. 2017). The O’Connell effect can be modeled by placing a spot on any of the system components. At the same time, the study of Kallrath & Milone (1999) explains how to determine the hotter and cooler spot. As specified by Kallrath & Milone (1999), ‘*colour amplitudes increase when going to  $V \rightarrow R \rightarrow I$  as expected for cool spots*’. The opposite of this is valid for the hotter spot. In this study, the cooler spot was placed on the secondary component of the V840 Lyr system. Modeling can be done also by placing a cooler spot on the primary component. The best fit is obtained in the case with the cooler spot on the secondary component. We applied a second-order polynomial regression to the sample data of Berdyugina (2005) to determine the spot’s temperature factor. A polynomial fit to the change in temperature

$\Delta T$  between spot and photosphere temperatures is given by:

$$\begin{aligned} \Delta T &= (T_{phot} - T_{spot}) \\ &= 2.89 \times 10^{-5} T_{phot}^2 + 0.34 T_{phot} - 1088, \end{aligned} \quad (5)$$

where  $T_{spot}$  and  $T_{phot}$  are spot and photosphere temperatures, respectively. For the cooler spots, the temperature factor is less than 1. Several groups of spots are tested. Finally, a converged solution was found with a cooler spot on the secondary components of V840 Lyr system. The solution parameters for the V840 Lyr system are listed in Table 4. The light curves in Figure 4 demonstrate common EW-type changes that make it possible to identify accurate photometric parameters. 2MASS provided magnitudes in the  $J$ ,  $H$  and  $K$  bands (12.851, 12.299, and 12.219 mag, respectively) (Cutri et al. 2003). The spectral class of V840 Lyr is K3 or K5, according to the color indices  $J - H = 0.552$  mag and  $H - K = 0.632$  mag. The Planck function representing the black-body radiation is given by

$$B_\lambda(\lambda, T) = \frac{2hc^2}{\lambda^5} \frac{1}{\exp(\frac{hc}{\lambda kT}) - 1}, \quad (6)$$

where  $B_\lambda$ ,  $h$ ,  $c$ ,  $\lambda$ ,  $k$ , and  $T$  represent the spectral radiance, the Planck constant, the speed of light, the wavelength, the Boltzman constant, and the temperature, respectively. This function was fitted to the Gaia energy distribution spectrum of the V840 Lyr binary star system. The temperature that provided the best fit was 4820 K (see Figure 2). The light curve solutions were carried out by keeping this temperature value (4820 K) constant.

TABLE 2  
NEW CCD MINIMUM TIMES FOR V840 LYR, FROM SPM AND OTHER SURVEYS

Observed BJDmin(2.4M+)	Instrument (filter)	Min I/II	Ref.	Observed BJDmin(2.4M+)	Instrument (filter)	Min I/II	Ref.
53143.68187	CCD	Min.II	(1)	58305.76370	$I_c$	Min.II	(4)
53144.67801	CCD	Min.I	(1)	58305.87452	$R_c$	Min.I	(4)
53201.55432	CCD	Min.I	(1)	58305.87460	$I_c$	Min.I	(4)
53204.54147	CCD	Min.II	(1)	58305.87476	$V$	Min.I	(4)
53231.54280	CCD	Min.II	(1)	58305.98481	$V$	Min.II	(4)
53232.53755	CCD	Min.I	(1)	58305.98539	$R_c$	Min.II	(4)
53526.87864	CCD	Min.I	(2)	58427.59401	CCD	Min.I	(3)
53669.62683	CCD	Min.I	(2)	58588.93059	CCD	Min.I	(3)
54275.57350	CCD	Min.I	(1)	58640.93952	$I_c$	Min.I	(4)
54276.56826	CCD	Min.II	(1)	58640.93956	$R_c$	Min.I	(4)
54297.59319	CCD	Min.II	(1)	58640.93980	$V$	Min.I	(4)
54298.58886	CCD	Min.I	(1)	58641.93571	$I_c$	Min.II	(4)
54327.47016	CCD	Min.II	(1)	58641.93576	$V$	Min.II	(4)
54328.46606	CCD	Min.I	(1)	58641.93584	$R_c$	Min.II	(4)
54628.56379	CCD	Min.I	(1)	58700.80260	CCD	Min.II	(3)
54628.67418	CCD	Min.II	(1)	59012.18724	CCD	Min.II	(5)
54644.49783	CCD	Min.I	(1)	59012.51913	CCD	Min.I	(5)
54645.49342	CCD	Min.II	(1)	59019.82226	CCD	Min.I	(5)
54683.44789	CCD	Min.I	(1)	59019.93293	CCD	Min.II	(5)
54684.44347	CCD	Min.II	(1)	59023.36325	CCD	Min.I	(5)
56592.59073	CCD	Min.II	(2)	59023.47392	CCD	Min.II	(5)
58204.95510	CCD	Min.I	(3)	59024.35929	CCD	Min.II	(5)
58205.95317	CCD	Min.II	(3)	59024.46998	CCD	Min.I	(5)
58210.93182	CCD	Min.I	(3)	59034.53962	CCD	Min.II	(5)
58235.93964	CCD	Min.I	(3)	59034.87159	CCD	Min.I	(5)
58237.93292	CCD	Min.I	(3)	59484.68517	$I_c$	Min.II	(4)
58290.93488	CCD	Min.II	(3)	59484.68518	$R_c$	Min.II	(4)
58305.76346	$V$	Min.II	(4)	59484.68519	$V$	Min.II	(4)
58305.76355	$R_c$	Min.II	(4)				

Equation 2 is used to calculate the minima, with Min.I denoting the primary minimum and Min.II denoting the secondary minimum. Ref: (1) SWASP, (2) CRTS, (3) ZTF, (4) SPM-This study, (5) TESS-This study.

This temperature value (4820 K) is among the temperature values found from other surveys and catalogues in Table 3. Therefore,  $T_1 = 4820$  K was chosen as the major component's effective temperature, and we kept this temperature value constant during the solution process and analysis. Estimated values for the relevant effective temperatures obtained from the other surveys and catalogues are between 4910 K and 4535 K. A list showing these temperature values is given in Table 3.

The depths of both minima in the light curves are approximately equal, indicating that both components are roughly at the same temperature. The gravity-darkening coefficients and bolometric albedo are therefore set to the same values for both components,  $g_1 = g_2 = 0.32$  (Lucy

1967) and  $A_1 = A_2 = 0.5$  (Ruciński 1969). According to Claret & Gimenez (1990), the bolometric and band-pass limb-darkening coefficients ( $x$  and  $y$ ) were applied to model the light curves. The parameters include the star 1 and star 2's dimensionless potential ( $\Omega_1 = \Omega_2$  for mode 3-overcontact configuration), star 1's orbital inclination ( $i$ ), star 2's mean temperature ( $T_2$ ), and the star 1's monochromatic luminosities ( $L_{1,V}$ ,  $L_{1,R_c}$ ,  $L_{1,I_c}$ ).

The mass ratio of the system was determined using the  $q$ -search technique ( $q = M_2/M_1$ ). For a variety of mass ratio values, solutions were obtained. We discovered that the answers typically converged to mode 3 for each value of  $q$ . The calculation began in mode 2 (detached mode) for each value of  $q$ . Figure 3 shows

TABLE 3  
EFFECTIVE TEMPERATURE AND SPECTRAL CLASSIFICATIONS FOR V840 LYR ACCORDING TO SEVERAL CATALOGUES

Catalogue / Survey	$(J-H)_0$	$\pm\sigma$	$T_{eff}^a$	$BC^b$	Spt.Type <sup>c</sup>
2MASS (Cutri et al. 2003)	0.537	0.115	4535*	-0.61*	K4.5*
TESS Input Catalog (Paegert et al. 2021)	0.455	0.122	4910*	-0.37*	K2.6*
APASS DR9 (Henden et al. 2015)	0.505	0.085	4718*	-0.49*	K3.6*
Worthey & Lee (2011)	0.540	0.101	4758	-0.41	K3.4*
Gaia DR2 (Gaia Collaboration et al. 2018)	0.485	0.075	4801	-0.43*	K3.2*
Drilling & Landolt (2000)	0.537	0.135	4718	-0.50	K3.3

$E(J-H) = 0.015$  mag,  $a$  :  $T_{eff}$  of the primary component,  $b$  : bolometric correction,  $c$  : spectral class of the primary component, \* : estimated by Pecaut & Mamajek (2013).

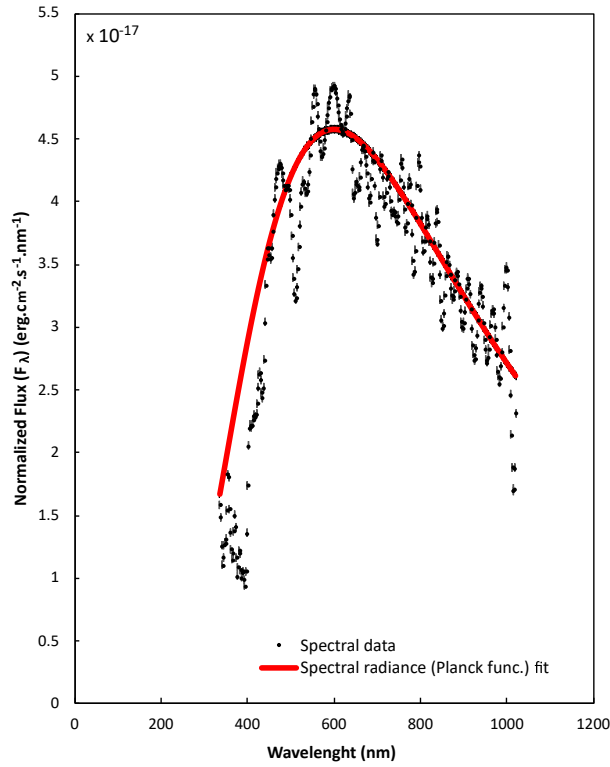


Fig. 2. The Gaia energy distribution spectrum of the V840 Lyr binary star system. The black dots along with the errors show the spectral data of the system. The red solid line depicts a black-body (Planck function) fit. The color figure can be viewed online.

the relationship between  $q$  and the sum of the results of the weighted squared deviations,  $\chi^2$ . A minimum is discovered at  $q = 0.45$ , as represented in the figure. At  $q = 0.45$ , the value of  $\chi^2$  is 0.00016. As a result, we decided to make  $q$  an adjustable parameter and set its initial value at 0.45. Models were solved by considering together the light curves of SPM observations in the  $V$ ,  $R_c$  and  $I_c$  bands and TESS observations. Dur-

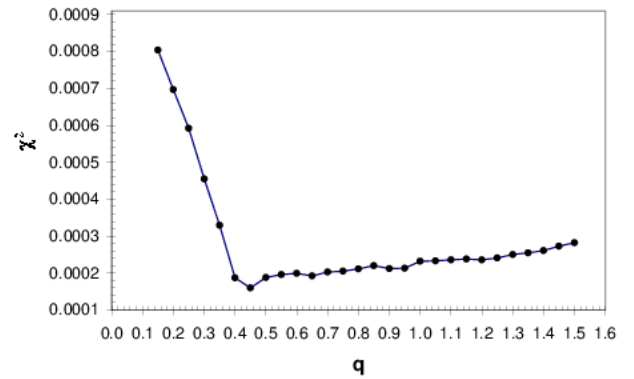


Fig. 3. The relation between  $\chi^2$  and  $q$  for V840 Lyr, and the minimum is found at  $q = 0.45$ . The color figure can be viewed online.

ing the light curve-LC analysis processes of SPM and TESS, we kept the primary temperature  $T_1$ , the initial epoch  $T_0$ , the period of the system  $P$ , and semi-major axis ( $SMA$ ) –  $a(R_\odot)$  parameters constant and left free the mass ratio  $q$ , the inclination of the system  $i$ , the secondary temperature  $T_2$ , the potential of the components  $\Omega_1 = \Omega_2$ . The  $q$  value changed little from the initial value determined by the  $q$  – search process during the analysis process. In the analysis processes, the third light contribution was also investigated. Observational errors are in the range of 0.01 to 0.02 by taking into account weights on data in the standard  $1/\sigma^2$  form. The light curve analysis was performed by taking into account the observation weights. The propagation errors of the solution parameters were determined using the well-known astrophysical equations. These errors are given in Table 4 and Table 5.

Final solutions were derived after applying differential corrections until they converged. For no third light and third light, our solution respectively converged at  $q = 0.4509 \pm 0.0705$  and  $q = 0.4543 \pm 0.0710$ . The synthetic/model light curves estimated using those photo-

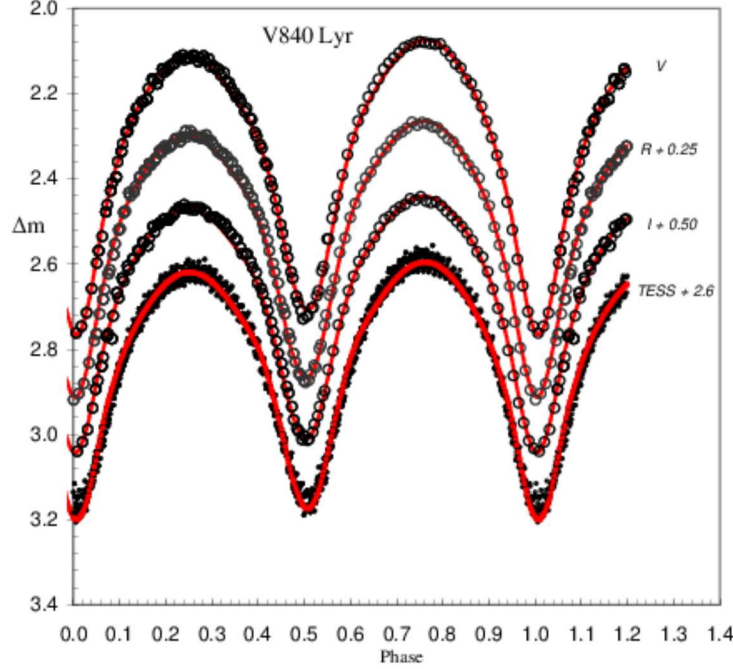


Fig. 4. The photometric light curves and synthetic/model fit with the dark-colder spot (solid-red line) of V840 Lyr in the  $V$ ,  $R_c$  and  $I_c$  filters. The observational light curve and synthetic/model fit of TESS data are given at the bottom. The color figure can be viewed online.

metric solution parameters which are given in Columns 3 and 5 of Table 4, are presented in Figure 4. Because of how asymmetric the light curves are, the spotted solution is required. The solution reveals that V840 Lyr is a W-subtype W UMa contact binary with a mass ratio of  $q = 0.4509 \pm 0.0705$  and a degree of contact factor of  $f = 15.14\% \pm 5.68\%$ . Figures 5 and 6 display the Roche geometrical structures of the system at different phases as well as the outline of the Roche surface.

## 5. ABSOLUTE PARAMETERS

For V840 Lyr a W-subtype W UMa binary system, we estimated the absolute parameters listed in Table 5 using the best model for the 2020 light curves as a guide. Without radial velocity information, the total mass cannot be calculated directly. The binary stars' masses, radii, and luminosities are, however, listed from the literature.

The absolute parameters were calculated using statistical relationships. For short period binaries with  $P < 0^d.27$ , which include radial velocity and contemporary light curve solutions, Dimitrov & Kjurkchieva (2015) discovered an empirical relation that is well defined between the  $a$ -semi major axis and  $P$ -period. Because we lacked information on radial velocity, we used their relationship to estimate the  $a$ -semi major axis of the system orbit, which is given by

$$a(R_\odot) = -1.154 + 14.633 \times P - 10.319 \times P^2, \quad (7)$$

with the parabolic fit's standard error given as  $0.05R_\odot$ . The semi major axis of the target system V840 Lyr is estimated to be  $a(R_\odot) = 1.57903 \pm 0.08059$  using its orbital period. During the photometric solution using *Phoebe*0.31a, this value is fixed. Equation 7 was used to obtain the error in  $a$  from the error in  $P$  and is responsible for the error value of 0.08059 stated for the semi-major axis.

The V840 Lyr eclipsing binary system's  $q$  mass ratio was estimated to be  $0.4509 \pm 0.0705$ . We calculated the primary star's mass for the V840 Lyr eclipsing binary system using the  $a(R_\odot)$ -semi major axis values, the  $q$ -mass ratio,  $q = M_2/M_1$ , and the corrected third law of Kepler,  $M_1(1 + q) = a^3/P^2$ . Thus it was calculated to be  $M_1 = 0.744 \pm 0.097M_\odot$ . Then, using the fractional radii ( $r_{1,2}$ ) and the semimajor axis values- $a(R_\odot)$ , we calculated the radii of the target system's component stars in units of solar radii using the formula  $r_{1,2} = R_{1,2}/a$ . Table 5 shows the outcomes of our calculations using equation 7 for the absolute parameters. In addition, the final information about the system obtained from GaiaDR3 (Gaia Collaboration 2022) and TESS (Stassun et al. 2019) observation results is given in Table 5. Also, the additional photometric elements-based absolute parameters for the V840Lyr system were  $M_2 = 0.336 \pm 0.052M_\odot$ ,  $R_1 = 0.735 \pm 0.039R_\odot$ , and  $R_2 = 0.508 \pm 0.029R_\odot$ .

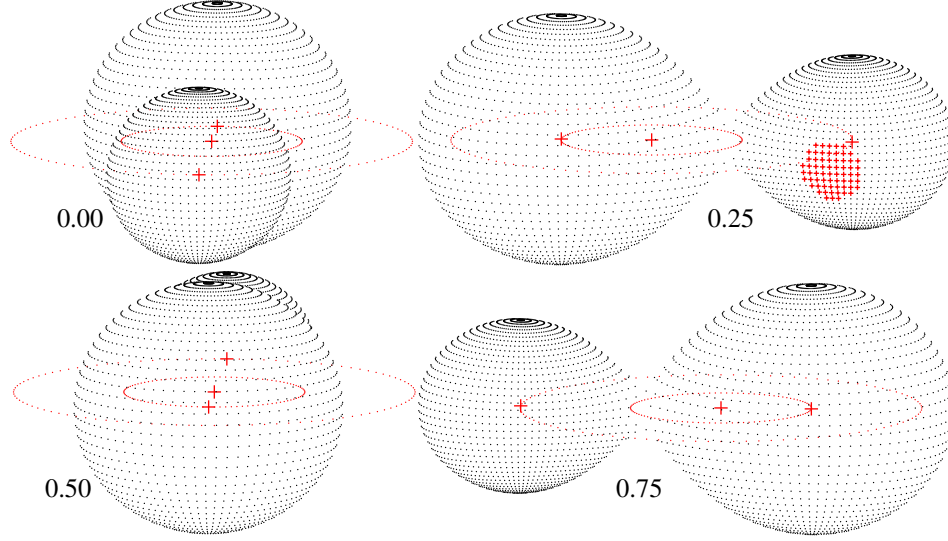


Fig. 5. The W-type contact binary V840 Lyr's Roche configuration at phases 0.00, 0.25, 0.50, and 0.75. The color figure can be viewed online.

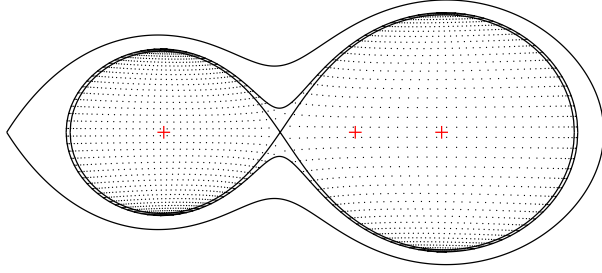


Fig. 6. The V840 Lyr binary system Roche surface outline pattern. The color figure can be viewed online.

Lucy & Wilson (1979) calculated the fill-out parameter ( $f$ ), which indicates the degree of contact between companion stars in a binary system using the formula  $f = (\Omega_{inner} - \Omega)/(\Omega_{inner} - \Omega_{outer})$ . Here,  $\Omega_{outer}$  stands for the outer critical Lagrangian/Roche equipotential,  $\Omega_{inner}$  is the critical Lagrangian equipotential of the inner critical Roche surface, and  $\Omega = \Omega_{1,2}$  indicates the surface Lagrangian/Roche equipotential of the component stars and varies from 0 (the inner critical Roche surface) to 1 (the outer critical Roche surface). Since the computed fill-out parameter of V840 Lyr was  $f = 0.1514$ , we came to the conclusion that the target system is a contact binary.

Using the astrophysical well-known equations:

$$\frac{L_{\star}}{L_{\odot}} = 10^{-0.4(M_{bol,\star} - M_{bol,\odot})}, \quad (8)$$

$$M_{bol,sys} = M_{bol,\star} + 2.5 \log \frac{L_{\star}}{L_{sys}},$$

where the prefix ( $\star$ ) refers to system component stars, and  $M_{bol,\odot} = 4.74$  mag (Cox 2000).  $M_{bol,system} = 5^m.83$  is the system's bolometric absolute magnitude, we calculated the system's bolometric absolute magnitude from the individual bolometric absolute magnitudes ( $M_{bol,1} = 6^m.26$ ,  $M_{bol,2} = 7^m.05$ ) of the components obtained from the `Phoebe` solution and also the luminosities of the component stars.

The  $\log(g)$  values of V840 Lyr are compatible with the values calculated to be  $\log(g_1) = 4.58 \pm 0.10$  cgs,  $\log(g_2) = 4.55 \pm 0.11$  cgs using the primary and secondary component's masses and radii within an error range. The equations of Mochnacki (1981) were used to get the components' mean densities of the V840 Lyr binary system and the components' mean densities were computed to be  $\rho_1 = 2.80 \pm 0.14$  gr cm $^{-3}$  and  $\rho_2 = 3.67 \pm 0.20$  gr cm $^{-3}$ .

We used the IPAC's database given in NASA/Extragalactic and the reddening maps from Schlafly & Finkbeiner (2011) for the interstellar extinction value ( $A_v$ ) to the distance of the V840 Lyr binary system,

$$d(\text{pc}) = 10^{(m - M_v - A_v + 5)/5}, \quad (9)$$

to be  $443.6 \pm 28.2$  pc using  $M_{bol}(\text{system}) = 5.83$  mag and  $BC = -0.02$  mag, assuming that they are main sequence stars and considering  $A_v = 0.1918$  for the interstellar extinction. The Gaia EDR3 catalogue lists V840 Lyr's parallax as  $2.2298 \pm 0.0214$  mas. The system's Gaia distance is  $448.5 \pm 5.3$  pc. This value is consistent with our distance estimation.



TABLE 4  
V840 LYR'S SOLUTION PARAMETERS WITH DARK, COOLER SPOT

Description	Parameters	No third light		Third light	
		Values	$\pm\sigma$	Values	$\pm\sigma$
The initial point of the ephemeris	$T_0$ (HJD)	2457422.6180	fixed	2457422.618	fixed
Orbital period	$P$ (days)	0.221311	fixed	0.221311	fixed
Semi major axis	$SMA$ ( $R_\odot$ )	1.57903	fixed	1.57903	fixed
Mass ratio	$q$	0.4509	0.0705	0.4543	0.0710
Orbital inclination	$i$	80.44	0.09	80.49	0.07
Fill-out parameter	$f$	0.1514	0.0568	0.2323	0.0871
The ratio of frac. radii	$k = r_2/r_1$	0.6919		0.6986	
Temperature ratio	$T_2/T_1$	0.9907		0.9913	
Temperature of primary comp.	$T_1$ (K)	4820	fixed	4820	fixed
Temperature of secondary comp.	$T_2$ (K)	4775	110	4778	112
Surface potential of components	$\Omega_1 = \Omega_2$	2.7389	0.0052	2.7234	0.0044
Bol. albedo of components	$A_1 = A_2$	0.50		0.50	
Gravity darkening exponents	$g_1 = g_2$	0.32		0.32	
Bolometric limb darkening	( $V$ )	0.800, 0.066		0.800, 0.066	
Logarithmic coefficients of pri. component ( $x_1, y_1$ )	( $R_c$ )	0.721, 0.146		0.721, 0.146	
	( $I_c$ )	0.625, 0.175		0.625, 0.175	
	( $V$ )	0.800, 0.066		0.800, 0.066	
Bolometric limb darkening Logarithmic coefficients of sec. component ( $x_2, y_2$ )	( $R_c$ )	0.721, 0.146		0.721, 0.146	
	( $I_c$ )	0.625, 0.175		0.625, 0.175	
	( $V$ )	0.800, 0.066		0.800, 0.066	
The fractional luminosities of primary component	( $V$ )	0.6816	0.0251	0.6778	0.0820
	( $R_c$ )	0.6802	0.0260	0.6736	0.0891
	( $I_c$ )	0.6794	0.0272	0.6656	0.0942
The fractional luminosities of secondary component	( $V$ )	0.3184	0.0252	0.3222	0.0822
	( $R_c$ )	0.3198	0.0263	0.3264	0.0890
	( $I_c$ )	0.3205	0.0271	0.3344	0.0941
Third light	$l_3$ ( $V$ )	0		0.0020	0.0007
	$l_3$ ( $R_c$ )	0		0.0011	0.0008
	$l_3$ ( $I_c$ )	0		0.0033	0.0009
The frac. radii of primary component	$r_1(pole)$	0.4351	0.0012	0.4302	0.0010
	$r_1(side)$	0.4658	0.0014	0.4595	0.0011
	$r_1(back)$	0.4969	0.0039	0.4899	0.0033
The frac. radii of secondary component	$r_2(pole)$	0.2994	0.0014	0.2993	0.0011
	$r_2(side)$	0.3138	0.0017	0.3133	0.0013
	$r_2(back)$	0.3539	0.0031	0.3513	0.0023
The mean frac. radii of pri. comp.	$r_{1,mean}$	0.4659	0.0018	0.4598	0.0015
The mean frac. radii of sec. comp.	$r_{2,mean}$	0.3224	0.0020	0.3213	0.0016
Spot parameters of the secondary component					
Spot co-latitude	$\Theta$ [ $^\circ$ ]	100.00	3.82	100.00	3.82
Spot longitude	$\phi$ [ $^\circ$ ]	80.00	1.93	80.00	1.93
Angular radius	$r_s$ [ $^\circ$ ]	20.00	1.75	20.00	1.75
Temperature factor	fraction	0.7376		0.7376	

Note: The errors ( $\pm\sigma$ ) are solely formal errors generated by Phoebe0.31a. They are the modeling-related propagating uncertainties.



TABLE 5  
THE ABSOLUTE PARAMETERS OF V840 LYR

Description	Parameters	This Study values $\pm \sigma$	Gaia-DR3 <sup>a</sup> values $\pm \sigma$	Tess <sup>b</sup> values $\pm \sigma$
The first Lagrangian point's equipotential	$\Omega(L_1)$	2.773046		
The second Lagrangian point's equipotential	$\Omega(L_2)$	2.502974		
The primary comp.'s mass	$M_1(M_\odot)$	$0.744 \pm 0.097$	$0.754 \pm 0.043$	0.760
The secondary comp.'s mass	$M_2(M_\odot)$	$0.336 \pm 0.052$	$0.341 \pm 0.019$	0.343
The primary comp.'s radius	$R_1(R_\odot)$	$0.735 \pm 0.039$	$0.757 \pm 0.018$	0.774
The secondary comp.'s radius	$R_2(R_\odot)$	$0.508 \pm 0.029$	$0.523 \pm 0.013$	0.535
The primary comp.'s temperature	$T_1(K)$	4820	$4829 \pm 33$	$4726 \pm 155$
The secondary comp.'s temperature	$T_2(K)$	$4775 \pm 110$	$4784 \pm 33$	$4682 \pm 155$
The primary comp.'s bol. absolute magnitude	$M_1^{bol}(\text{mag})$	$6.26 \pm 0.12$		
The secondary comp.'s bol. absolute magnitude	$M_2^{bol}(\text{mag})$	$7.05 \pm 0.13$		
The primary comp.'s logarithmic surface gravity	$\log(g_1)(\text{cgs})$	$4.58 \pm 0.10$	$4.56 \pm 0.02$	4.54
The secondary comp.'s logarithmic surface gravity	$\log(g_2)(\text{cgs})$	$4.55 \pm 0.11$	$4.53 \pm 0.02$	4.51
The primary comp.'s luminosity	$L_1(L_\odot)$	$0.257 \pm 0.052$	$0.257 \pm 0.007$	0.269
The secondary comp.'s luminosity	$L_2(L_\odot)$	$0.119 \pm 0.025$	$0.119 \pm 0.003$	0.125
The primary comp.'s density	$\rho_1(\text{gr cm}^{-3})$	$2.80 \pm 0.14$	$2.45 \pm 0.01$	2.31
The secondary comp.'s density	$\rho_2(\text{gr cm}^{-3})$	$3.67 \pm 0.20$	$3.35 \pm 0.01$	3.03
Distance of the system	$d(\text{pc})$	$443.6 \pm 28.2$	$448.5 \pm 5.3$	$444.0 \pm 4.2$
Total mass	$M_t(M_\odot)$	$1.080 \pm 0.149$	$1.094 \pm 0.062$	1.103
The system's mass function	$f(M_t)(M_\odot)$	$1.036 \pm 0.151$	$1.049 \pm 0.068$	1.057

a; Ref; Gaia Collaboration (2022), b; Ref; Stassun et al. (2019).

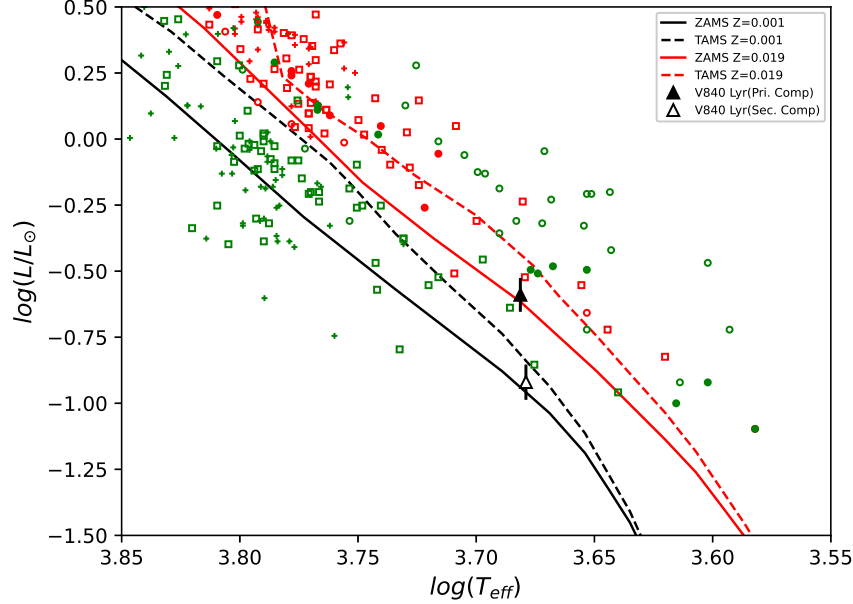


Fig. 7. The locations of V840 Lyr along the ZAMS and TAMS lines from Girardi et al. (2000) ( $Z = 0.001$  and  $0.0019$ ) on the HR diagram. The black-filled and empty triangles display V840 Lyr's primary and secondary stars. The example systems of Yakut & Eggleton (2005) are presented. '□'; W-type, '+'; A-type example contact W UMa binaries, '○'; example binaries close to contact, and '●'; detached example binaries. Red colors represent every primary star, green colors every secondary star. Temperature errors stay within the symbol size. The color figure can be viewed online.

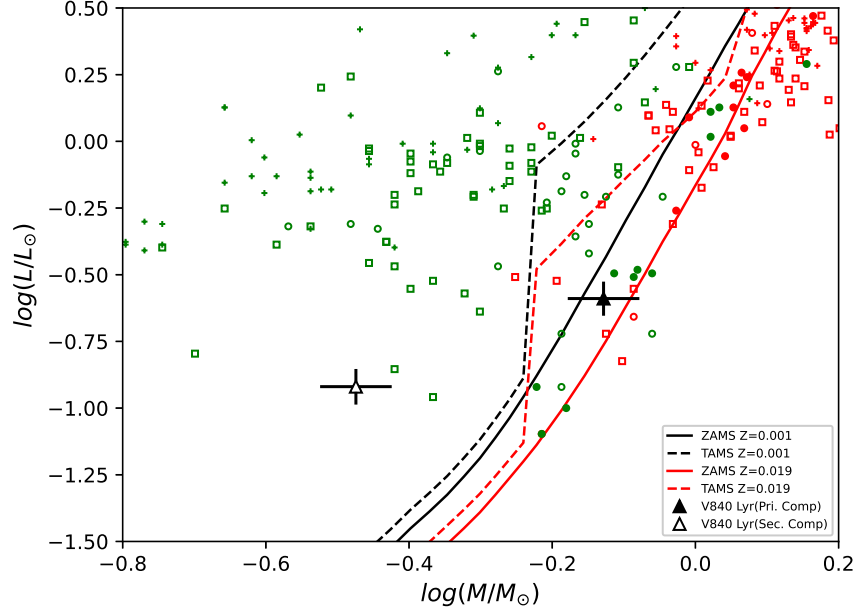


Fig. 8. V840 Lyr's location on the mass-luminosity diagram. The sample systems, symbols, and other details are indicated in Figure 7. The color figure can be viewed online.

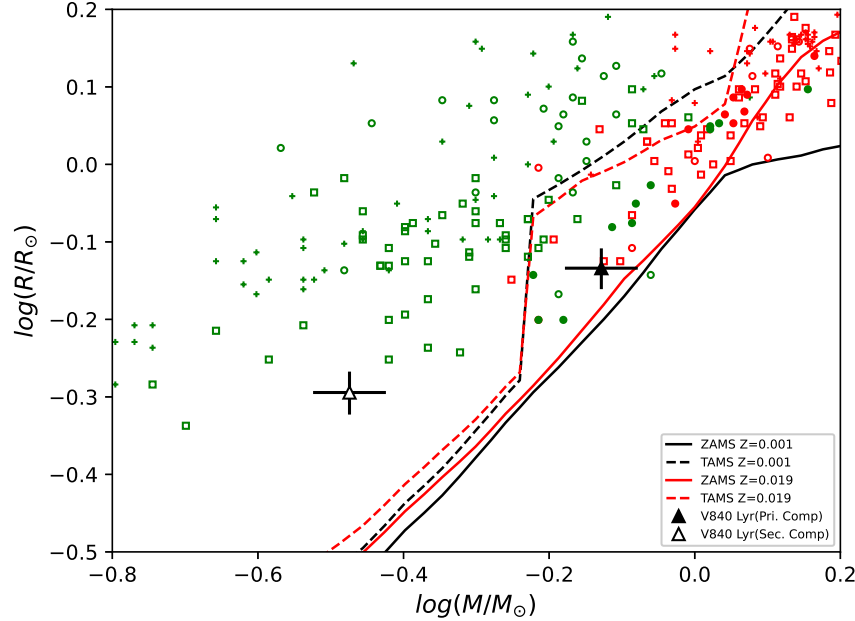


Fig. 9. V840 Lyr location on the mass-radius diagram. The sample systems, symbols, and other details are indicated in Figure 7. The color figure can be viewed online.

We display on the *HR* (*Hertzsprung Russell*),  $M$  (*mass*) –  $L$  (*luminosity*),  $M$  (*mass*) –  $R$  (*radius*),  $M$  (*mass*) –  $J_0$  (*momentum*) diagrams and also on the *HR* diagram with the evolutionary tracks, the position of V840 Lyr together with the other contact binaries in Figures 7-11, respectively.

## 6. DISCUSSION AND CONCLUSIONS

The asymmetrical light curves of V840 Lyr we acquired from the SPM observatory show the O'Connell effect. It is clear that the maximum level at phase 0.75 of our multicolour light curves is, respectively, around 0.033 mag, 0.030 mag, and 0.024 mag higher than those

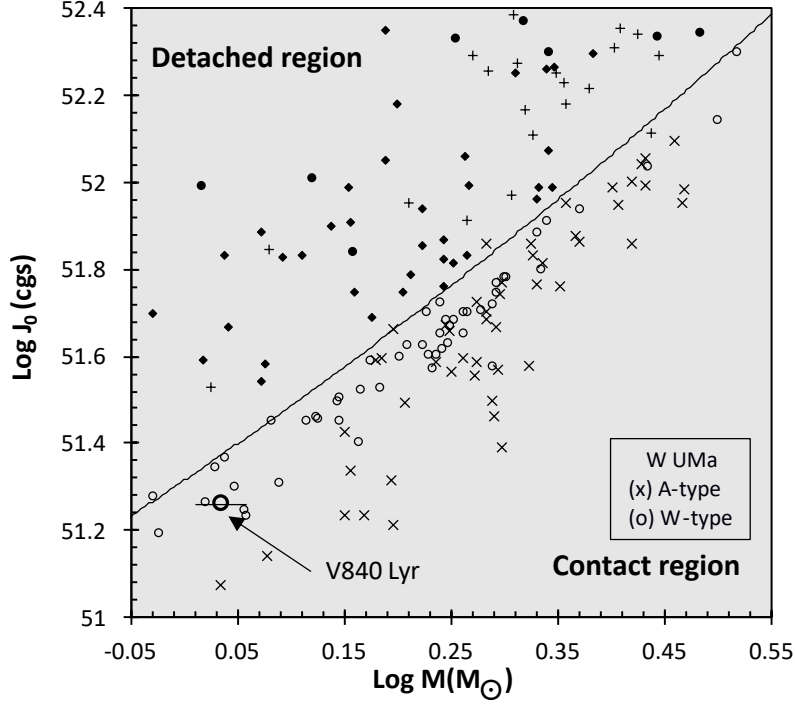


Fig. 10. The location of V840 Lyr on the mass-angular momentum diagram according to Eker et al. (2006), under the  $J_{lim}$  borderline dividing detached and contact binaries. The symbols are the same ones that are described in Figures 1 and 4 of Eker et al. (2006)'s study. The circles show the W-subtype systems, whereas the crosses stand for the A-subtype systems. The error of  $\log J_0$  is within the size of the symbol. The color figure can be viewed online.

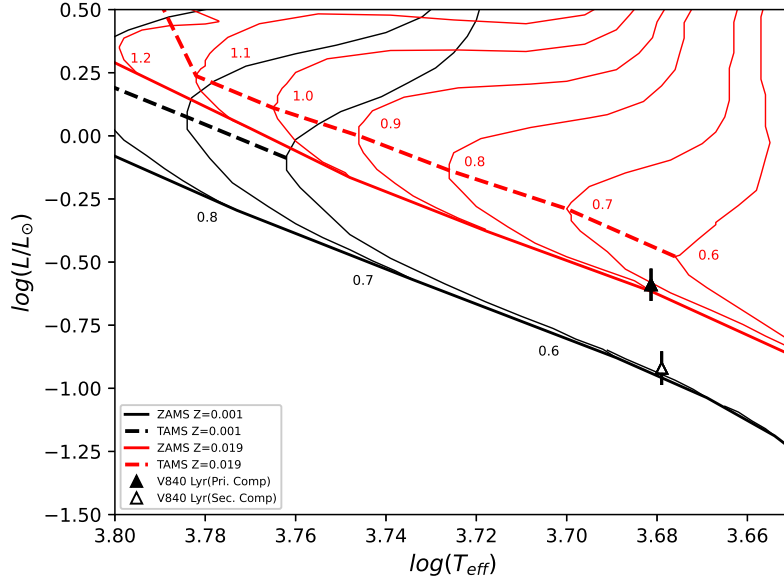


Fig. 11. V840 Lyr's components (triangles) plotted in the HR diagram with ZAMS, TAMS, evolutionary tracks and isochrone derived from Girardi et al. (2000) for  $Z = 0.001$  and  $0.019$ . The errors are within the symbol's size. The color figure can be viewed online.

at phase 0.25 despite the fact that the Min-I and Min-II minimum depths of our multicolour light curves are nearly equal. The light curves we acquired do not demon-

strate a large scatter, as shown in Figure 4. This suggests that more credible solutions might be found using our light curves.

The secondary component's dark-cool spot was considered to account for the asymmetries in our light curves. With the help of the `Phoebe0.31a` interface software based on the WD method, we discovered that V840 Lyr is an extreme mass ratio ( $q = 0.4509$ ) W-subtype contact W UMa type binary star with a 15.14% fill-out factor. The photometric results showed that the more massive component's temperature is about 45 K higher than that of the less massive component. Over four years, V840 Lyr was observed, and 17 times of light minima were discovered.

According to the absolute parameters estimated in this work, the angular momentum  $\log J_0$  value of V840 Lyr is 51.261 in cgs units, and the  $\log J_{lim} = 51.371$  in cgs units using the angular momentum expression of Eker et al. (2006). These values of  $\log J_0$  are less than those of  $\log J_{lim}$  ( $\log J_0 < \log J_{lim}$ ). This result shows that V840 Lyr, according to the absolute parameter estimations, is located in the contact configuration region of the angular momentum diagram obtained by Eker et al. (2006) (see Figure 10).

We compared the component locations of the target system with LTCBs (A type), LTCBs (W type), NCBs, and DCBs samples in the  $M - L$ ,  $M - R$ ,  $M - J_0$ , and  $T_{eff} - L$  diagrams with ZAMS and TAMS provided by Girardi et al. (2000), taking into account the absolute parameters we obtained for the V840 Lyr binary system (see Figures 7-11). V840 Lyr resembles other contact binary systems (Yakut & Eggleton 2005; Eker et al. 2006). Using evolutionary tracks and isochrones, we also determine the evolutionary status of the V840 Lyr binary system.

Regarding the absolute parameters of the primary component, V840 Lyr is also compatible with the evolutionary tracks for  $0.74 M_{\odot}$ , a single star with metallicities of  $Z=0.019$  and  $Z=0.001$ . It is possible to determine that the V840 Lyr's primary and secondary components positions in the HR diagram, compared with stellar evolutionary paths, are appropriate for the binary system masses. The primary and secondary stars of the V840 Lyr were positioned on the ZAMS with a  $Z=0.019$  and  $Z=0.001$  metallicity, respectively, as shown in Figures 7 and 9. It is plausible that the system's constituents were exchanging mass with one another; from the secondary to the primary star (see Figure 1).

Using the Binary Maker 3.0 tool (Bradstreet & Steelman 2002), we created Roche configurations of the components that make up the V840 Lyr in accordance with the target system's absolute parameters (see Figure 5-6).

Using the estimated absolute parameters, we computed the distance of the V840 Lyr to be  $d = 443.6 \pm 28.2$  pc, consistent with the distance ( $d = 448.5 \pm 5.3$  pc) obtained from the Gaia EDR3's parallax ( $2.2298 \pm$

$0.0214$  mas) (see Table 5). Additionally, the absolute parameters obtained in this study were compared with GaiaDR3 (Gaia Collaboration 2022) and TESS (Stassun et al. 2019) data and are given in Table 5. As a result of this comparison, it can be seen that the absolute parameters obtained from the analysis are consistent with the results of GaiaDR3 and TESS.

In summary, V840 Lyr is quite remarkable and seems to be an overcontact binary star. The stars that make up our target binary system have filled Roche lobes. The target system V840 Lyr's estimated absolute parameters are roughly within the predicted limits, as demonstrated by a comparison with the other W UMa stars. However, the absolute solution parameters of the target system V840 Lyr in this work should be considered as preliminary values in the absence of spectroscopic studies, which are necessary for the more reliable identification of the spectral types, the semi-major axis, and the mass ratio.

Combining more sensitive photometric and spectroscopic observations of this binary star would be a significant step forward in advancing our comprehension of contact binaries, validating the existing results, and revealing the true structure of this system. We encourage researchers to do the appropriate photometric and spectroscopic measurements to confirm the existence of starspots and establish their locations. This will help us to learn more about this system.

We thank the San Pedro Martir National Astronomical Observatory (SPM) for its support in allowing us the use of its T84 telescope, and Edilberto Sánchez-Moreno (IAUNAM) for help with some of our figures. We gratefully acknowledge the SIMBAD, ADS, CRTS, TESS, BRNO O-C Gateway, Kraków O-C Atlas, NASA/IPAC, and Gaia EDR3 databases for also providing data. We acknowledge with thanks the variable star observations from the AAVSO International Database contributed by observers worldwide and used in this research. This publication makes use of data products from the Two Micron All Sky Survey, which is a joint project of the University of Massachusetts and the Infrared Processing and Analysis Center/California Institute of Technology, funded by the National Aeronautics and Space Administration and the National Science Foundation. We also thank the anonymous referee for her/his valuable comments to improve this article.

## REFERENCES

- Bellm, E. C., Kulkarni, S. R., Graham, M. J., et al. 2019, *PASP*, 131, 018002, <https://doi.org/10.1088/1538-3873/aaecbe>
- Berdugina, S. V. 2005, *LRSP*, 2, 8, <https://doi.org/10.12942/lrsp-2005-8>

- Bradstreet, D. H. & Steelman, D. P. 2002, *AAS*, 34, 1224
- Claret, A. & Gimenez, A. 1990, *A&A*, 230, 412
- Cox, A. N. 2000, *Allen's astrophysical quantities*, 4th ed. (New York, NY: AIP)
- Cutri, R. M., Skrutskie, M. F., van Dyk, S., et al. 2003, *VizieR Online Data Catalog*, II/246
- Dimitrov, D. P. & Kjurkchieva, D. P. 2015, *MNRAS*, 448, 2890, <https://doi.org/10.1093/mnras/stv147>
- Drake, A. J., Djorgovski, S. G., Mahabal, A., et al. *ApJ*, 696, 870, <https://doi.org/10.1088/0004-637X/696/1/870>
- Drilling, J. S. & Landolt, A. U. 2000, in *Allen's Astrophysical Quantities*, ed. A. N. Cox, 381
- Eastman, J., Siverd, R., & Gaudi, B. S. 2010, *PASP*, 122, 935, <https://doi.org/10.1086/655938>
- Eker, Z., Demircan, O., Bilir, S., & Karataş, Y. 2006, *MNRAS*, 373, 1483, <https://doi.org/10.1111/j.1365-2966.2006.11073.x>
- Gaia Collaboration. 2022, *VizieR Online Data Catalog*, I/355
- Gaia Collaboration; Brown, A. G. A., Vallenari, A., et al. 2018, *A&A*, 616, 1, <https://doi.org/10.1051/0004-6361/201833051>
- Girardi, L., Bressan, A., Bertelli, G., & Chiosi, C. 2000, *A&AS*, 141, 371, <https://doi.org/10.1051/aas:2000126>
- Henden, A. A., Levine, S., Terrell, D., & Welch, D. L. 2015, *AAS*, 225, 336.16
- Hut, P. 1980, *A&A*, 92, 167
- Kallrath, J. & Milone, E. F. 1999, in *Eclipsing binary stars: modeling and analysis* (New York, NY: Springer-Verlag), <https://doi.org/10.1007/978-1-4419-0699-1>
- Lucy, L. B. 1967, *ZA*, 65, 89
- Lucy, L. B. & Wilson, R. E. 1979, *ApJ*, 231, 502, <https://doi.org/10.1086/157212>
- Mochmacki, S. W. 1981, *ApJ*, 245, 650, <https://doi.org/10.1086/158841>
- Norton, A. J., Payne, S. G., Evans, T., et al. 2011, *A&A*, 528, 90, <https://doi.org/10.1051/0004-6361/201116448>
- O'Connell, D. J. K. 1951, *PRCO*, 2, 85
- Paegert, M., Stassun, K. G., Collins, K. A., et al. 2021, *arXiv:2108.04778*, <https://doi.org/10.48550/arXiv.2108.04778>
- Pecaut, M. J. & Mamajek, E. E. 2013, *ApJS*, 208, 9, <https://doi.org/10.1088/0067-0049/208/1/9>
- Pollacco, D., Skillen, I., Collier Cameron, A., et al. 2006, *Ap&SS*, 304, 253, <https://doi.org/10.1007/s10509-006-9124-x>
- Qian, S.-B., Han, Z.-T., Zhang, B., et al. 2017, *ApJ*, 848, 131, <https://doi.org/10.3847/1538-4357/aa8bb8>
- Ruciński, S. M. 1969, *AcA*, 19, 245
- Samus', N. N., Kazarovets, E. V., Durlevich, O. V., Kireeva, N. N., & Pastukhova, E. N. 2017, *ARep*, 61, 80, <https://doi.org/10.1134/S1063772917010085>
- Schlaflly, E. F. & Finkbeiner, D. P. 2011, *ApJ*, 737, 103, <https://doi.org/10.1088/0004-637X/737/2/103>
- Stassun, K. G., Oelkers, R. J., Paegert, M., et al. 2019, *AJ*, 158, 138, <https://doi.org/10.3847/1538-3881/ab3467>
- Sullivan, P. W., Winn, J. N., Berta-Thompson, Z. K., et al. 2015, *ApJ*, 809, 77, <https://doi.org/10.1088/0004-637X/809/1/77>
- TESS. 2021, *Observations from the Transiting Exoplanet Survey Satellite (TESS) International Database*, <https://archive.stsci.edu/missions-and-data/tess>
- van Hamme, W. 1993, *AJ*, 106, 2096, <https://doi.org/10.1086/116788>
- van Hamme, W. & Wilson, R. E. 2003, *ASPC*, 298, 323
- Wilson, R. E. 1979, *ApJ*, 234, 1054, <https://doi.org/10.1086/157588>
- Wilson, R. E. & Devinney, E. J. 1971, *ApJ*, 166, 605, <https://doi.org/10.1086/150986>
- Wilson, R. E., van Hamme, W., & Terrell, D. 2010, *ApJ*, 723, 1469, <https://doi.org/10.1088/0004-637X/723/2/1469>
- Worthey, G. & Lee, H.-C. 2011, *ApJS*, 193, 1, <https://doi.org/10.1088/0067-0049/193/1/1>
- Yakut, K. & Eggleton, P. P. 2005, *ApJ*, 629, 1055, <https://doi.org/10.1086/431300>
- Zhu, L.-Y., Zhao, E.-G., & Zhou, X. 2016, *RAA*, 16, 68, <https://doi.org/10.1088/1674/4527/16/4/068>
- H. Aceves & R. Michel: Instituto de Astronomia, UNAM. A.P. 877, 22800 Ensenada, BC, México (aceves, rmm@astro.unam.mx).
- A. Bulut: Department of Physics, Faculty of Science, University of Çanakkale Onsekiz Mart, Terzioğlu Campus, TR-17020, Çanakkale, Türkiye.
- A. Bulut: Astrophysics Research Centre and Observatory, University of Çanakkale Onsekiz Mart, Terzioğlu Campus, TR-17020, Çanakkale, Türkiye.
- A. Keskin & M. Tanrıver: Department of Astronomy and Space Science, Faculty of Science, University of Erciyes, TR-38039, Kayseri, Türkiye (mtanriver@erciyes.edu.tr).
- M. Tanrıver: Astronomy and Space Science Observatory Application and Research Center, University of Erciyes, TR-38039, Kayseri, Türkiye.



# COMPACT RADIO SOURCES IN THE FIELD OF TYCHO’S SUPERNOVA REMNANT

Luis F. Rodríguez<sup>1</sup>, Vanessa Yanza<sup>1</sup>, and Sergio A. Dzib<sup>2</sup>

*Received August 13 2023; accepted November 20 2023*

## ABSTRACT

We present sensitive, high angular resolution Jansky Very Large Array observations made in 2014 at 1.50 GHz toward the field of Tycho’s supernova remnant. We detect a total of 36 compact sources in a field with radius of 13 arcmin. This number is consistent with the expected number of background sources. We use older observations made with the classic Very Large Array to compare with the 2014 observations and search for sources showing large proper motions that could be related to the donor companion of the exploding white dwarf that produced the supernova in 1572. The comparison of the positions for the two sets of observations does not show sources with large proper motions and supports the conclusion that all sources detected are extragalactic and unrelated to the supernova field.

## RESUMEN

Presentamos observaciones sensitivas de alta resolución angular hechas en 2014 con el Jansky Very Large Array a 1.50 GHz hacia el campo de la remanente de supernova de Tycho. Detectamos un total de 36 fuentes compactas en un campo con radio de 13 minutos de arco. Usamos observaciones más antiguas hechas con el VLA clásico para comparar con los datos de 2014 buscando fuentes con movimientos propios grandes que pudieran estar relacionadas con la compañera donante de la enana blanca que explotó y produjo la supernova en 1572. La comparación de posiciones entre los dos conjuntos de observaciones no revela fuentes con grandes movimientos propios y apoya la conclusión de que todas las fuentes detectadas son fuentes extragalácticas de fondo sin relación con el campo de la supernova.

*Key Words:* astrometry — ISM: supernova remnants — radio continuum: general — stars: general

## 1. INTRODUCTION

Tycho’s 1572 supernova (SN 1572, 3C 10, B Cas) has been classified as a standard type Ia on the basis of its light-echo spectrum (Krause et al. 2008). This supernova type is very important since it is a cosmological standard candle that has allowed to determine the accelerated expansion history of the Universe (Riess et al. 1998; Perlmutter et al. 1999). It is produced by the thermonuclear explosion of a white dwarf accreting from a companion in a close binary system. In the most favored model the white dwarf is fully disrupted when it reaches the Chandrasekhar limit, leaving no collapsed object. The companion then leaves the original position of the binary with

the orbital velocity it had at the moment of the explosion, that can be as large as  $\approx 1,000 \text{ km s}^{-1}$  (Geier et al. 2015). The nature of the companion is poorly understood, and it can be a main sequence, subgiant, red giant, AGB, He star or even another white dwarf (Iben 1997; Ruiz-Lapuente 2019).

The determination of the nature of the progenitor (the exploding star) of type Ia supernovae has been the subject of many studies (e.g. Maoz et al. 2014). Less effort has gone into understanding the surviving donor companion (e.g. Ruiz-Lapuente 2019). Only a handful of nearby type Ia supernova remnants (SNRs) have been inspected in search of the companion star (Pan et al. 2014). Importantly, the search for the binary companion of Tycho’s SN 1572 has yielded a candidate: a G-type subgiant star labelled Tycho-G (Ruiz-Lapuente 2004; González-Hernández

<sup>1</sup>Instituto de Radioastronomía y Astrofísica, UNAM, México.

<sup>2</sup>Max-Planck-Institut für Radioastronomie, Germany.



2009). The star is relatively close to the center of the supernova remnant, its distance is compatible with it being inside the SNR, it has significantly higher radial velocity and proper motions than other stars at the same location in the Galaxy, and it shows signs of pollution from the supernova ejecta. However, other studies have questioned Tycho-G as the companion donor star because they do not find the expected large stellar rotation (Kerzendorf et al. 2009), they do not confirm the unusual chemistry (Kerzendorf et al. 2013), or their proposed explosion center does not overlap with the past stellar position at the time of the explosion (Xue & Schaefer 2015; Millard et al. 2022). An additional problem is that the Gaia DR3 (Gaia collaboration et al. 2016; 2022) distance of Tycho-G (Gaia DR3 431160359413315328 in the Gaia designation) is  $1.93^{+0.45}_{-0.31}$  kpc while the distance to the supernova is  $2.8 \pm 0.4$  kpc (Kozlova & Blinnikov 2018). Then, the  $\pm 1\text{-}\sigma$  error bars fall close but do not overlap. More accurate distances could help solve this problem.

The lack of clearly confirmed donor companion stars in type Ia SNRs (Schaefer & Pagnotta 2012; González Hernández et al. 2012; Di Stefano & Kilic 2012; Pan et al. 2014; Ruiz-Lapuente et al. 2018) has led to a questioning of the favored ‘single-degenerate’ path (mass transfer from a normal companion star to a ultimately exploding white dwarf) in favor of the ‘double-degenerate’ scenario, in which the merger of two white dwarfs produces an explosion that leaves no stellar remnant.

The field of Tycho’s SNR has been studied in radio with emphasis on the morphology and proper motions of the extended synchrotron shell (Dickel et al. 1991; Reynoso et al. 1997; Williams et al. 2016). In this paper we present a study of the compact (taken to be  $\leq 6''$ ) radio sources in this field to search for a source with large proper motion that could be related to the companion star. Stars of low optical luminosity on the main sequence are very rarely detected in radio (Kimball et al. 2009). As noted by Gaidos et al. (2000), the radio emission of normal, single solar analogs rapidly declines to undetectable levels after a few hundred million years. On the other hand, it is known that rotation is the main agent responsible for the level of magnetic activity in cool stars (Güdel 2002). Large magnetic fields facilitate the production of radio emission via mechanisms such as gyrosynchrotron. The possible relation between rotation and radio emission is supported by the study of McLean et al. (2012) who find that rapidly rotating ( $v \sin i \geq 20 \text{ km s}^{-1}$ ) ultracool dwarfs have a higher radio detection frac-

tion by about a factor of three compared to objects with  $v \sin i \leq 10 \text{ km s}^{-1}$ . Also, Lim & White (1995) detected at 3.6 cm three of the four ultra-fast ( $v \sin i \geq 30 \text{ km s}^{-1}$ ) rotators in the Pleiades. The justification for our search is that the companion donor stars are expected to have large rotation velocities ( $v \geq 20 \text{ km s}^{-1}$  for a donor mass  $\geq 0.2 M_{\odot}$ ; Kerzendorf et al. 2009) that could enhance their radio emission. It should be pointed out, however, that there are a variety of mechanisms that can produce detectable radio emission in stars (Güdel 2002; Dzib et al. 2013). In § 2 we present the observations, while in § 3 we discuss some individual sources. Finally, in § 4 we present our conclusions.

## 2. OBSERVATIONS

### 2.1. 1.50 GHz Observations for Epoch 2014 February 20

The main set of data used in this paper corresponds to observations made with the Karl G. Jansky Very Large Array (VLA) of NRAO<sup>3</sup> in the A configuration on 2014 February 20 (2014.140). The observations were taken under project 13A-426 in the L-band (0.96-1.97 GHz) using 16 spectral windows, each 64 MHz wide. The amplitude calibrator was J0137+3309 (3C48) and the gain calibrator was J0217+7349. The phase center of the observations was at  $RA(J2000) = 00^h 25^m 18^s.966$ ;  $DEC(J2000) = 64^{\circ} 08' 20''.41$ . The data were edited and calibrated following the standard procedures inside the CASA (Common Astronomy Software Applications; McMullin et al. 2007) package of NRAO and the pipeline provided for VLA<sup>4</sup> observations.

We made images using a robust weighting (Briggs 1995) of 0 and visibilities with baselines larger than 6 kλ, to suppress structures larger than  $\approx 30$  arcsec. The final image had an rms noise of  $28 \mu\text{Jy beam}^{-1}$  at the phase center and a synthesized beam of  $1''.44 \times 0''.83$ ; PA =  $-88^{\circ}$ . The images were corrected for the primary beam response. The images were also corrected for wide-field effects using the gridding option *widefield* with  $10 \times 10$  subregions in the task TCLEAN. A region with a radius of 13 arcmin was inspected for sources with peak emission above  $6\text{-}\sigma$  ( $168 \mu\text{Jy beam}^{-1}$ ). We detected a total of 36 sources. Their positions, flux densities, spectral indices, angular sizes and counterparts, when found, are given in

<sup>3</sup>The National Radio Astronomy Observatory is a facility of the National Science Foundation operated under cooperative agreement by Associated Universities, Inc.

<sup>4</sup><https://science.nrao.edu/facilities/vla/data-processing/pipeline>.

Table 1. The positions and flux densities were determined using the task IMFIT of CASA. The spectral indices were determined by splitting the total bandwidth in four bandwidths of 256 MHz each, making images and fitting the four flux densities obtained for each source as a function of frequency with a linear regression in the log-log plane.

Following the procedure of Anglada et al. (1998) we determine that  $37 \pm 6$  background sources were expected. This estimate suggests that most, and probably all, of the sources detected are background objects unrelated to the remnant region. Nevertheless, within the uncertainty, it cannot be ruled out that a few sources could be associated with the remnant.

### 2.2. Observations with the Classic VLA

To gain information on the time variability and possible proper motions of the sources found in the 2014 image, we analyzed classic VLA observations made in the A configuration on the three epochs listed in Table 2. As in the 2014 data, the amplitude calibrator was J0137+3309 (3C48) and the gain calibrator was J0217+7349 for the three epochs. The data were concatenated to gain signal to noise ratio and assigned an average epoch of 1993.468 and an average frequency of 1.43 GHz. The data were edited and calibrated using the software package Astronomical Image Processing System (AIPS) of NRAO. We made images using a robust weighting (Briggs 1995) of 0 and visibilities with baselines larger than 6 k $\lambda$ , to suppress structures larger than  $\approx 30$  arcsec.

The final image had an rms noise of  $75 \mu\text{Jy beam}^{-1}$  at the phase center and a synthesized beam of  $1''.39 \times 1''.33$ ; PA =  $+28^\circ$ . As for the 2014 image, a region with radius of 13 arcmin was inspected for sources with peak emission above  $6\sigma$  ( $450 \mu\text{Jy beam}^{-1}$ ). We detected a total of 17 sources. Again, following the procedure of Anglada et al. (1998) we determined that  $18 \pm 4$  background sources were expected. As in the more sensitive 2014 data, this estimate suggests that most, and probably all, of the sources detected are background objects unrelated to the remnant region. Their positions and flux densities are given in Table 3. In this Table we also list the difference in RA and DEC between the 2014 positions and those obtained from the classic VLA data.

All 17 sources detected in the image from the classic VLA data were detected in the more sensitive (by a factor of 2.7) 2014 observations. To compare the flux densities at the two epochs we corrected the 2014 flux densities from 1.50 to 1.43 GHz using the spectral indices listed in Table 1. This correction is

small, of order 5-10%. In the last column of Table 3 we list the ratio of the flux densities. Eight of the 17 sources have a ratio consistent within noise with 1 and thus no variability. Only source 6 shows a variability larger than a factor of 2, decreasing by a factor of 4 between databases.

### 2.3. Upper Limits to the Proper Motions

Analyzing Table 3 we find that the position differences between the 2014 image and the classic VLA image (Columns 5 and 6) are above a conservative  $5\sigma$  value only for sources 19, 31, 34 and 35. Should these possible small proper motions be considered as real? Sources 31, 34 and 35 are resolved angularly (see Table 1) and this characteristic could well account for the small difference in position between epochs due to differences in the beam shape. The position differences for the remaining source 19 are of order of only  $\approx 0''.1$ . Taking this displacement as an upper limit to the true proper motions, we can crudely set an upper limit to the velocity of the sources in the plane of the sky. Given the time interval of 20.672 yr between the two datasets and a distance of 2.8 kpc to the supernova (Kozlova & Blinnikov 2018) this results in an upper limit of  $65 \text{ km s}^{-1}$  for the velocity of the radio sources in the plane of the sky, if they were located at the distance of the supernova. As noted before, it is most probable that all sources are extragalactic and that the small position differences measured are the result of noise and not true displacements. Supporting the extragalactic interpretation is the fact that none of the 36 radio sources has a counterpart in the Gaia DR3 catalog (Gaia collaboration et al. 2016; 2022). Tycho's SNR is almost in the plane of the Galaxy (it has a galactic latitude of  $1.4^\circ$ ). Then, extragalactic objects in this direction will be heavily obscured in the optical and very difficult to detect in the observations of the Gaia project.

### 2.4. The Non Detection of Tycho-B

The star Tycho-G was not detected in our observations. Perhaps more interestingly, the star Tycho-B was not detected either. Tycho-B is a fast-rotator A-type star that has been proposed as a candidate to be the donor companion of the exploding white dwarf that produced SN 1572 (Kerzendorf et al. 2013), although this proposal has been questioned later (Kerzendorf et al. 2018).

The best studied case of radio emission from a rapidly rotating A-type star is that of Altair ( $\alpha$  Aql; White et al. 2021). From the model of these authors we estimate that Altair is expected to have

TABLE 1  
PARAMETERS OF COMPACT RADIO SOURCES AT 1.50 GHz (2014 FEBRUARY 20)

No.	Position <sup>a</sup>		Flux	Spectral	Angular Dimensions <sup>b</sup>	Counterpart
	RA(J2000)	DEC(J2000)	Density( $\mu$ Jy)	Index	( $\theta_{maj} \times \theta_{min}; PA$ )	
1	00 23 16.800 $\pm$ 0.007	64 20 25.46 $\pm$ 0.03	1808 $\pm$ 200	+0.00 $\pm$ 0.52	1.4 $\pm$ 0.2 $\times$ 0.9 $\pm$ 0.3; 31 $\pm$ 25	...
2	00 23 24.220 $\pm$ 0.010	63 59 07.43 $\pm$ 0.02	840 $\pm$ 95	-1.35 $\pm$ 0.45	$\leq$ 0.5	...
3	00 23 30.774 $\pm$ 0.013	64 08 04.34 $\pm$ 0.05	528 $\pm$ 75	-1.14 $\pm$ 0.48	$\leq$ 0.5	...
4	00 23 40.826 $\pm$ 0.011	64 10 52.87 $\pm$ 0.03	416 $\pm$ 46	-1.45 $\pm$ 0.47	$\leq$ 0.5	...
5	00 24 11.264 $\pm$ 0.007	64 09 50.02 $\pm$ 0.01	521 $\pm$ 31	-0.04 $\pm$ 0.30	$\leq$ 0.5	...
6	00 24 18.177 $\pm$ 0.012	63 58 58.03 $\pm$ 0.12	429 $\pm$ 62	+0.02 $\pm$ 0.54	$\leq$ 0.5	...
7	00 24 30.749 $\pm$ 0.009	64 02 00.33 $\pm$ 0.03	348 $\pm$ 44	-0.59 $\pm$ 0.54	$\leq$ 0.5	...
8	00 24 39.839 $\pm$ 0.013	64 01 05.93 $\pm$ 0.05	381 $\pm$ 51	-1.31 $\pm$ 0.53	$\leq$ 0.5	...
9	00 24 41.071 $\pm$ 0.006	64 03 56.91 $\pm$ 0.01	596 $\pm$ 37	+0.03 $\pm$ 0.30	$\leq$ 0.5	...
10	00 24 44.695 $\pm$ 0.006	64 04 53.40 $\pm$ 0.05	561 $\pm$ 51	-1.63 $\pm$ 0.42	$\leq$ 0.5	...
11	00 24 46.084 $\pm$ 0.006	64 12 36.46 $\pm$ 0.02	528 $\pm$ 37	-1.27 $\pm$ 0.34	$\leq$ 0.5	...
12	00 24 51.749 $\pm$ 0.006	63 59 08.33 $\pm$ 0.02	601 $\pm$ 55	-0.89 $\pm$ 0.42	$\leq$ 0.5	...
13	00 24 56.742 $\pm$ 0.007	64 17 50.66 $\pm$ 0.03	607 $\pm$ 44	-1.69 $\pm$ 0.34	$\leq$ 0.5	...
14	00 24 58.631 $\pm$ 0.009	64 10 56.82 $\pm$ 0.03	486 $\pm$ 53	-1.03 $\pm$ 0.37	$\leq$ 0.5	...
15	00 25 01.637 $\pm$ 0.005	64 07 47.75 $\pm$ 0.01	843 $\pm$ 46	-1.49 $\pm$ 0.20	$\leq$ 0.5	...
16	00 25 10.166 $\pm$ 0.003	64 16 28.06 $\pm$ 0.01	1258 $\pm$ 53	-0.64 $\pm$ 0.20	$\leq$ 0.5	...
17	00 25 14.131 $\pm$ 0.027	64 00 15.08 $\pm$ 0.12	1652 $\pm$ 288	-1.98 $\pm$ 0.61	4.8 $\pm$ 1.1 $\times$ 2.2 $\pm$ 0.7; 45 $\pm$ 14	...
18	00 25 16.087 $\pm$ 0.016	63 59 40.96 $\pm$ 0.14	796 $\pm$ 108	-0.99 $\pm$ 0.63	2.3 $\pm$ 0.5 $\times$ 1.3 $\pm$ 0.5; 168 $\pm$ 27	...
19	00 25 19.270 $\pm$ 0.001	64 08 53.28 $\pm$ 0.01	5150 $\pm$ 68	-1.30 $\pm$ 0.06	$\leq$ 0.5	[RMG97] 002231.23+635216.9
20	00 25 26.037 $\pm$ 0.002	64 04 40.89 $\pm$ 0.01	3575 $\pm$ 90	-1.11 $\pm$ 0.08	$\leq$ 0.5	[RMG97] 002237.96+634804.7
21	00 25 34.981 $\pm$ 0.004	64 08 43.06 $\pm$ 0.01	741 $\pm$ 33	-0.70 $\pm$ 0.27	$\leq$ 0.5	...
22	00 25 36.024 $\pm$ 0.007	64 10 39.81 $\pm$ 0.01	330 $\pm$ 33	-1.31 $\pm$ 0.52	$\leq$ 0.5	...
23	00 25 40.204 $\pm$ 0.005	64 13 05.95 $\pm$ 0.01	537 $\pm$ 40	-0.10 $\pm$ 0.35	$\leq$ 0.5	...
24	00 25 40.601 $\pm$ 0.006	64 11 33.72 $\pm$ 0.02	607 $\pm$ 53	-0.92 $\pm$ 0.33	$\leq$ 0.5	...
25	00 25 50.714 $\pm$ 0.022	64 09 28.82 $\pm$ 0.17	1058 $\pm$ 115	-0.95 $\pm$ 0.49	4.6 $\pm$ 0.7 $\times$ 2.3 $\pm$ 0.5; 7 $\pm$ 11	Nucleus of radio galaxy
26	00 26 05.112 $\pm$ 0.002	64 17 13.89 $\pm$ 0.01	2306 $\pm$ 81	-0.93 $\pm$ 0.14	$\leq$ 0.5	...
27	00 26 08.967 $\pm$ 0.006	64 16 33.89 $\pm$ 0.02	590 $\pm$ 51	-0.98 $\pm$ 0.36	$\leq$ 0.5	...
28	00 26 16.279 $\pm$ 0.014	64 21 33.46 $\pm$ 0.14	3476 $\pm$ 209	-1.60 $\pm$ 0.40	5.7 $\pm$ 0.6 $\times$ 1.2 $\pm$ 0.3; 29 $\pm$ 3	Disk galaxy 2MFGC 305
29	00 26 23.102 $\pm$ 0.007	64 12 32.06 $\pm$ 0.01	581 $\pm$ 35	-1.61 $\pm$ 0.35	$\leq$ 0.5	...
30	00 26 23.656 $\pm$ 0.010	64 04 42.34 $\pm$ 0.04	253 $\pm$ 46	-1.33 $\pm$ 0.55	$\leq$ 0.5	...
31	00 26 24.059 $\pm$ 0.003	63 56 24.03 $\pm$ 0.01	1725 $\pm$ 123	-0.30 $\pm$ 0.32	1.0 $\pm$ 0.1 $\times$ 0.6 $\pm$ 0.3; 0 $\pm$ 17	...
32	00 26 28.133 $\pm$ 0.012	63 58 36.78 $\pm$ 0.08	508 $\pm$ 62	+1.05 $\pm$ 0.39	$\leq$ 0.5	...
33	00 26 30.651 $\pm$ 0.017	64 14 36.13 $\pm$ 0.06	352 $\pm$ 57	+0.49 $\pm$ 0.62	$\leq$ 0.5	...
34	00 26 50.729 $\pm$ 0.002	64 10 25.52 $\pm$ 0.01	3324 $\pm$ 112	-1.01 $\pm$ 0.14	1.0 $\pm$ 0.1 $\times$ 0.6 $\pm$ 0.1; 62 $\pm$ 7	...
35	00 26 51.389 $\pm$ 0.002	64 02 20.16 $\pm$ 0.01	20284 $\pm$ 682	-0.99 $\pm$ 0.11	1.3 $\pm$ 0.1 $\times$ 0.8 $\pm$ 0.1; 69 $\pm$ 1	Radio source EQ 0024+638
36	00 27 11.599 $\pm$ 0.017	64 12 44.78 $\pm$ 0.02	462 $\pm$ 73	+0.25 $\pm$ 0.55	$\leq$ 0.5	...

<sup>a</sup>Right ascension (RA) is given in hours, minutes, and seconds. Declination (DEC) is given in degrees, arcminutes, and arcseconds.

<sup>b</sup>The deconvolved major ( $\theta_{maj}$ ) and minor ( $\theta_{min}$ ) axes are given in arcsec. The position angle ( $PA$ ) is given in degrees.

TABLE 2  
OBSERVATIONS WITH THE CLASSIC VLA IN A CONFIGURATION

Project	Epoch	Amplitude	Gain	Frequency	Bandwidth
		Calibrator	Calibrator	(GHz)	(MHz)
AV84	1983 Nov 13 (1983.868)	J0137+3309	J0217+7349	1.38	6.25
AM437	1994 Mar 18 (1994.211)	J0137+3309	J0217+7349	1.51	6.25
AR464	2002 Apr 29 (2002.326)	J0137+3309	J0217+7349	1.41	6.25

a flux density of  $\simeq 10 \mu\text{Jy}$  at the frequency of 1.5 GHz. Tycho-B, with position  $RA(J2000) = 00^h 25^m 19^s 985$ ;  $DEC(J2000) = +64^\circ 08' 17'' 19$ , is located at a distance of 2.7 kpc (Gaia Collaboration 2020). On the other hand, Altair is located at

a distance of only 5.1 pc (van Leeuwen 2007). We then conclude that if Tycho-B had a similar radio emission to that of Altair, its flux density would be  $(2700/5.1)^2 = 2.8 \times 10^5$  weaker and undetectable with present instrumentation.

TABLE 3  
PARAMETERS OF COMPACT RADIO SOURCES FROM CLASSIC VLA DATA

No.	Position <sup>a</sup>		Flux Density( $\mu$ Jy)	$\Delta$ RA <sup>b</sup> (seconds)	$\Delta$ DEC <sup>b</sup> (arcseconds)	Flux Ratio (2014/1983)
	RA(J2000)	DEC(J2000)				
6	00 24 18.052 $\pm$ 0.099	63 58 58.73 $\pm$ 1.02	1903 $\pm$ 414	0.125 $\pm$ 0.099	-0.70 $\pm$ 1.03	0.23 $\pm$ 0.06
9	00 24 41.071 $\pm$ 0.014	64 03 56.99 $\pm$ 0.09	663 $\pm$ 163	0.000 $\pm$ 0.015	-0.08 $\pm$ 0.09	0.90 $\pm$ 0.23
10	00 24 44.701 $\pm$ 0.013	64 04 53.39 $\pm$ 0.15	692 $\pm$ 182	-0.006 $\pm$ 0.010	0.01 $\pm$ 0.16	0.87 $\pm$ 0.24
12	00 24 51.749 $\pm$ 0.016	63 59 07.99 $\pm$ 0.17	815 $\pm$ 107	0.000 $\pm$ 0.017	0.34 $\pm$ 0.17	0.77 $\pm$ 0.12
13	00 24 56.718 $\pm$ 0.023	64 17 50.48 $\pm$ 0.16	582 $\pm$ 193	0.024 $\pm$ 0.024	0.18 $\pm$ 0.16	1.13 $\pm$ 0.38
15	00 25 01.648 $\pm$ 0.009	64 07 47.89 $\pm$ 0.07	1130 $\pm$ 179	-0.011 $\pm$ 0.010	-0.14 $\pm$ 0.07	0.80 $\pm$ 0.13
16	00 25 10.161 $\pm$ 0.008	64 16 27.85 $\pm$ 0.06	1735 $\pm$ 197	0.005 $\pm$ 0.009	0.21 $\pm$ 0.06	0.75 $\pm$ 0.09
17	00 25 14.076 $\pm$ 0.097	64 00 13.84 $\pm$ 0.69	3782 $\pm$ 530	0.055 $\pm$ 0.101	1.24 $\pm$ 0.70	0.48 $\pm$ 0.11
19	00 25 19.282 $\pm$ 0.001	64 08 53.40 $\pm$ 0.01	6657 $\pm$ 166	-0.012 $\pm$ 0.001	-0.12 $\pm$ 0.01	0.82 $\pm$ 0.02
20	00 25 26.046 $\pm$ 0.002	64 04 40.97 $\pm$ 0.02	3831 $\pm$ 168	-0.010 $\pm$ 0.003	-0.08 $\pm$ 0.02	0.98 $\pm$ 0.05
21	00 25 34.987 $\pm$ 0.011	64 08 43.23 $\pm$ 0.07	974 $\pm$ 173	-0.006 $\pm$ 0.012	-0.17 $\pm$ 0.07	0.79 $\pm$ 0.14
24	00 25 40.605 $\pm$ 0.017	64 11 34.00 $\pm$ 0.11	675 $\pm$ 176	-0.004 $\pm$ 0.018	-0.28 $\pm$ 0.11	0.94 $\pm$ 0.26
26	00 26 05.110 $\pm$ 0.009	64 17 13.62 $\pm$ 0.05	2229 $\pm$ 216	0.002 $\pm$ 0.009	0.27 $\pm$ 0.06	1.08 $\pm$ 0.11
28	00 26 16.278 $\pm$ 0.053	64 21 32.73 $\pm$ 0.35	6157 $\pm$ 1010	0.012 $\pm$ 0.055	0.57 $\pm$ 0.37	0.61 $\pm$ 0.11
31	00 26 24.054 $\pm$ 0.014	63 56 23.45 $\pm$ 0.07	1338 $\pm$ 214	0.005 $\pm$ 0.014	0.58 $\pm$ 0.07	1.31 $\pm$ 0.23
34	00 26 50.724 $\pm$ 0.005	64 10 25.28 $\pm$ 0.03	3564 $\pm$ 222	0.005 $\pm$ 0.005	0.24 $\pm$ 0.03	0.98 $\pm$ 0.08
35	00 26 51.364 $\pm$ 0.002	64 02 19.78 $\pm$ 0.01	20092 $\pm$ 263	0.025 $\pm$ 0.003	0.38 $\pm$ 0.01	1.06 $\pm$ 0.04

<sup>a</sup>Right ascension (RA) is given in hours, minutes, and seconds. Declination (DEC) is given in degrees, arcminutes, and arcseconds.

<sup>b</sup>Position differences given by 2014 positions minus classic VLA positions.

### 3. INDIVIDUAL SOURCES

To gain information on the sources detected we used the SIMBAD database to search for counterparts within a few arcsec of the radio position.

#### 3.1. Sources 19 and 20

These sources are reported by Reynoso et al. (1997) in their study of the expansion of the supernova remnant. They used them to align their images at different epochs. Their compact size and negative spectral index (see Table 1) suggest they are background active galactic nuclei.

#### 3.2. Source 25

This source seems to be the nucleus of a radio galaxy (see Figure 1). The lobes of the radio galaxy extend over  $\approx 35''$  in the north-south direction. Since they are clearly extended, the lobes are not reported in our list of compact sources. The nucleus is elongated along the axis defined by the radio lobes and probably traces more recent ejections.

#### 3.3. Source 28

This source was initially catalogued in the 2MASS-selected Flat Galaxy Catalog (2MFGC;

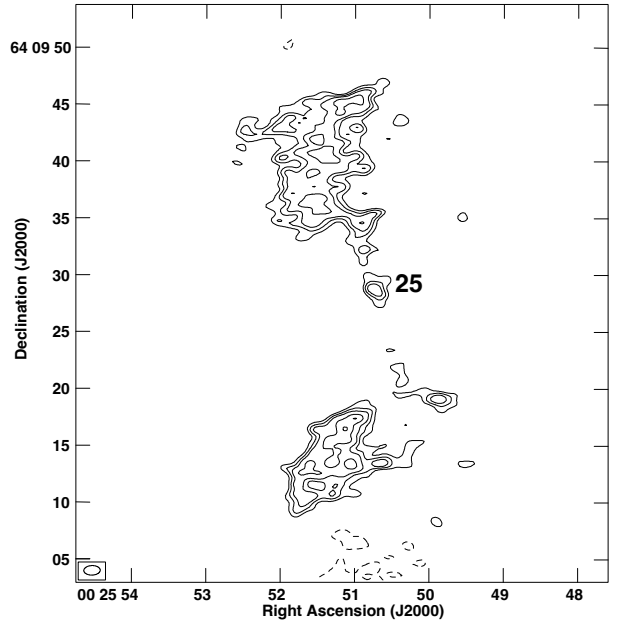


Fig. 1. Radio galaxy related to source 25. Contours are -4, 4, 5, 6, 8 and 10  $\mu$ Jy beam $^{-1}$ , the rms noise of this region of the image. The synthesized beam ( $1.44'' \times 0.83''$ ;  $-88^\circ$ ) is shown in the bottom left corner.

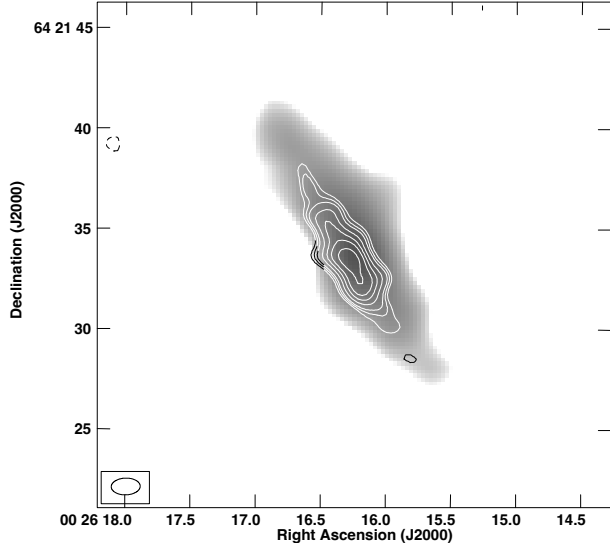


Fig. 2. The radio source 28 is shown in white contours in this image. The contours are -4, 4, 5, 6, 8, 10, 12 and 15 times  $11 \mu\text{Jy beam}^{-1}$ , the rms noise of this region of the image. The synthesized beam ( $1''.44 \times 0''.83; -88^\circ$ ) is shown in the bottom left corner. The infrared image from the Two Micron All Sky Survey (2MASS) in the  $K_s$  band is shown in greyscale.

Mitronova et al. 2006). The sources in this catalog are expected to be disk galaxies selected from the Extended Source Catalog of the Two Micron All-Sky Survey (XSC 2MASS; Jarrett et al. 2000) on the basis of their 2MASS axial ratio being  $a/b \geq 3$ . We find that the infrared and radio images approximately coincide and show similar elongated morphology (Figure 2).

#### 3.4. Source 32

This source is interesting because it shows a clearly positive spectral index ( $+1.05 \pm 0.39$ ; Table 1). All other sources in Table 1 have spectral indices that are consistent within noise with a negative spectral index. Background radio sources usually show clearly negative spectral indices, taken to be indicative of optically-thin synchrotron emission. For example, Smolčić et al. (2016) obtained accurate spectral indices for 159 sources by combining Australia Telescope Compact Array (ATCA) 2.1 GHz observations with Sydney University Molonglo Sky Survey (SUMSS) 843 MHz data. Only three of the sources show positive spectral indices ( $\alpha > 0$ ).

Source 32 could be a high frequency peaker (HFP). These are compact, sometimes powerful extragalactic radio sources with well-defined peaks in their radio spectra above a few GHz, with most of them being high redshift quasars (Dallacasa et al.

2000). A possible explanation for the HFP radio sources is that we are observing synchrotron emission produced by blazars caught during a flare, when a highly self-absorbed (optically-thick) component dominates the emission (Tinti et al. 2005)

#### 3.5. Source 35

This is the brightest compact source in the region considered. It was reported previously by Schwarz et al. (1995) from HI VLA observations made in 1993 in the C configuration. These authors proposed that it is a background source. It is an elongated source (see Table 1) and it could be a disk galaxy seen edge-on or an unresolved radio galaxy.

### 4. CONCLUSIONS

Our main conclusions are the following:

(1) We compared observations made in the L-band toward the Tycho supernova remnant in 2014 with the Jansky VLA and previously with the classic VLA. The purpose of this comparison was to search for radio sources showing large proper motions that could be related to the donor companion of the exploding white dwarf that produced the supernova in 1572. We failed to find radio sources with large proper motions ( $\geq 65 \text{ km s}^{-1}$ ) and conclude that most, and probably all, of the sources detected are background extragalactic objects. However, we argue that these donor companions could be radio sources and believe that its search in other Type Ia supernova remnants is worthwhile.

(2) We discussed several sources individually and concluded that their characteristics are compatible with them being most likely background extragalactic sources. Source 28 is most probably a disk galaxy seen edge-on. Source 32 could be a high frequency peaker, possibly a blazar caught during a flare.

This publication makes use of data products from the Two Micron All Sky Survey, which is a joint project of the University of Massachusetts and the Infrared Processing and Analysis Center, funded by the National Aeronautics and Space Administration and the National Science Foundation. This research has made use of the SIMBAD database, operated at CDS, Strasbourg, France.

### REFERENCES

- Anglada, G., Villuendas, E., Estalella, R., et al. 1998, *AJ*, 116, 2953, <https://doi.org/10.1086/300637>
- Bridle, A. H. & Schwab, F. R. 1999, *ASPC* 180, *Synthesis Imaging in Radio Astronomy II*, ed. G. B. Taylor, C. L. Carilli, and R. A. Perley, 371

- Briggs, D. S. 1995, *AAS*, 187, 11202
- Dallacasa, D., Stanghellini, C., Centonza, M., & Fanti, R. 2000, *A&A*, 363, 887, <https://doi.org/10.48550/arXiv.astro-ph/0012428>
- Dickel, J. R., van Breugel, W. J. M., & Strom, R. G. 1991, *AJ*, 101, 2151, <https://doi.org/10.1086/115837>
- Di Stefano, R. & Kilic, M. 2012, *ApJ*, 759, 56, <https://doi.org/10.1088/0004-637X/759/1/56>
- Dzib, S. A., Rodríguez, L. F., Loinard, L., et al. 2013, *ApJ*, 763, 139, <https://doi.org/10.1088/0004-637X/763/2/139>
- Gaia Collaboration, Prusti, T., de Bruijne, J. H. J., et al. 2016, *A&A*, 595, 1, <https://doi.org/10.1051/0004-6361/201629272>
- Gaia Collaboration 2020, *VizieR Online Data Catalog*, I/350, <https://doi.org/10.26093/cds/vizier.1350>
- Gaia Collaboration, Vallenari, A., Brown, A. G. A., et al. 2022, *arXiv:2208.00211*, <https://doi.org/10.48550/arXiv.2208.00211>
- Gaidos, E. J., Güdel, M., & Blake, G. A. 2000, *Geophys. Res. Lett.*, 27, 501, <https://doi.org/10.1029/1999GL010740>
- Geier, S., Fürst, F., Ziegerer, E., et al. 2015, *Sci*, 347, 1126, <https://doi.org/10.1126/science.1259063>
- González Hernández, J. I., Ruiz-Lapuente, P., Filippenko, A. V., et al. 2009, *ApJ*, 691, 1, <https://doi.org/10.1088/0004-637X/691/1/1>
- González Hernández, J. I., Ruiz-Lapuente, P., Tabernero, H. M., et al. 2012, *Nat*, 489, 533, <https://doi.org/10.1038/nature11447>
- Güdel, M. 2002, *ARA&A*, 40, 217, <https://doi.org/10.1146/annurev.astro.40.060401.093806>
- Iben, I. 1997, *Thermonuclear Supernovae*, 486, 111, [https://doi.org/10.1007/978-94-011-5710-0\\_8](https://doi.org/10.1007/978-94-011-5710-0_8)
- Jarrett, T. H., Chester, T., Cutri, R., et al. 2000, *AJ*, 119, 2498, <https://doi.org/10.1086/301330>
- Kerzendorf, W. E., Schmidt, B. P., Asplund, M., et al. 2009, *ApJ*, 701, 1665, <https://doi.org/10.1088/0004-637X/701/2/1665>
- Kerzendorf, W. E., Yong, D., Schmidt, B. P., et al. 2013, *ApJ*, 774, 99, <https://doi.org/10.1088/0004-637X/774/2/99>
- Kerzendorf, W. E., Long, K. S., Winkler, P. F., et al. 2018, *MNRAS*, 479, 5696, <https://doi.org/10.1093/mnras/sty1863>
- Kimball, A. E., Knapp, G. R., Ivezić, Ž., et al. 2009, *ApJ*, 701, 535, <https://doi.org/10.1088/0004-637X/701/1/535>
- Kozlova, A. V. & Blinnikov, S. I. 2018, *Journal of Physics Conference Series*, 1038, 012006, <https://doi.org/10.1088/1742-6596/1038/1/012006>
- Krause, O., Tanaka, M., Usuda, T., et al. 2008, *Nature*, 456, 617, <https://doi.org/10.1038/nature07608>
- Lim, J. & White, S. M. 1995, *ApJ*, 453, 207, <https://doi.org/10.1086/176380>
- Maoz, D., Mannucci, F., & Nelemans, G. 2014, *ARA&A*, 52, 107, <https://doi.org/10.1146/annurev-astro-082812-141031>
- McLean, M., Berger, E., & Reiners, A. 2012, *ApJ*, 746, 23, <https://doi.org/10.1088/0004-637X/746/1/23>
- McMullin, J. P., Waters, B., Schiebel, D., et al. 2007, *ASPC 376, Astronomical Data Analysis Software and Systems*, ed. R. A. Shaw, F. Hill, & J. Bell (Tucson, AZ: ASPC), 127
- Millard, M. J., Park, S., Sato, T., et al. 2022, *ApJ*, 937, 121, <https://doi.org/10.3847/1538-4357/ac8f30>
- Mitronova, S. N., Karachentsev, I. D., Karachentseva, V. E., Jarett, T. H., & Kudrya, Y. N. 2006, *VizieR Online Data Catalog (other)*, 0110, J/other/BSAO/57
- Pan, K.-C., Ricker, P. M., & Taam, R. E. 2014, *ApJ*, 792, 71, <https://doi.org/10.1088/0004-637X/792/1/71>
- Perlmutter, S., Aldering, G., Goldhaber, G., et al. 1999, *ApJ*, 517, 565, <https://doi.org/10.1086/307221>
- Reynoso, E. M., Moffett, D. A., Goss, W. M., et al. 1997, *ApJ*, 491, 816, <https://doi.org/10.1086/304997>
- Riess, A. G., Filippenko, A. V., Challis, P., et al. 1998, *AJ*, 116, 1009, <https://doi.org/10.1086/300499>
- Ruiz-Lapuente, P., Comeron, F., Méndez, J., et al. 2004, *Nature*, 431, 1069, <https://doi.org/10.1038/nature03006>
- Ruiz-Lapuente, P., Damiani, F., Bedin, L., et al. 2018, *ApJ*, 862, 124, <https://doi.org/10.3847/1538-4357/aac9c4>
- Ruiz-Lapuente, P. 2019, *NewAR*, 85, 101523, <https://doi.org/10.1016/j.newar.2019.101523>
- Schwarz, U. J., Goss, W. M., Kalberla, P. M., & Bengali, P. 1995, *A&A*, 299, 193
- Schaefer, B. E. & Pagnotta, A. 2012, *Nature*, 481, 164, <https://doi.org/10.1038/nature10692>
- Smolčić, V., Delhaize, J., Huynh, M., et al. 2016, *A&A*, 592, 10, <https://doi.org/10.1051/0004-6361/201526818>
- Tinti, S., Dallacasa, D., de Zotti, G., Celotti, A., & Stanghellini, C. 2005, *A&A*, 432, 31, <https://doi.org/10.1051/0004-6361/20041620>
- van Leeuwen, F. 2007, *A&A*, 474, 653, <https://doi.org/10.1051/0004-6361:20078357>
- White, J. A., Tapia-Vázquez, F., Hughes, A. G., et al. 2021, *ApJ*, 912, 5, <https://doi.org/10.3847/2041-8213/abf6da>
- Williams, B. J., Chomiuk, L., Hewitt, J. W., et al. 2016, *ApJ*, 823, 32, <https://doi.org/10.3847/2041-8205/823/2/L32>
- Xue, Z. & Schaefer, B. E. 2015, *ApJ*, 809, 183, <https://doi.org/10.1088/0004-637X/809/2/183>

Sergio A. Dzib: Max-Planck-Institut für Radioastronomie, Auf dem Hügel 69, D-53121 Bonn, Germany.

Luis F. Rodríguez and Vanessa Yanza: Instituto de Radioastronomía y Astrofísica, Universidad Nacional Autónoma de México, Apartado Postal 3-72, 58090 Morelia, Michoacán, México (l.rodriguez@irya.unam.mx).





## ASTRONOMICAL TESTS OF A MEDIUM FORMAT DIGITAL CAMERA ON A LARGE SCHMIDT TELESCOPE

F. Della Prugna

Centro de Investigaciones de Astronomía, CIDA.

*Received November 22 2023; accepted December 22 2023*

### ABSTRACT

Installation, testing and astronomical capabilities of a medium format digital camera (Fujifilm GFX 50R) on the 1-meter Schmidt Telescope at the National Astronomical Observatory of Venezuela are described. Main useful features and drawbacks are also discussed.

### RESUMEN

Se describen la instalación, las pruebas y el potencial astronómico de una cámara digital de formato medio (Fujifilm GFX 50R) en el telescopio Schmidt de 1 metro del Observatorio Astronómico Nacional de Venezuela. También se muestran las características importantes y algunas desventajas de esta cámara.

*Key Words:* instrumentation: detectors — telescopes

### 1. INTRODUCTION

On December 2023 CIDA-National Astronomical Observatory of Venezuela (OAN) celebrated its 48th anniversary. Plans for a large astronomical observatory to be originally installed in Caracas date back from the early fifties, when Dr. Eduardo Röhl, then director of Cagigal Naval Observatory, ordered four large instruments from two German firms, Carl Zeiss Oberkochen and Askania Werke (Stock 1981). One of them, the 1-meter,  $f/3$  Schmidt telescope, is among the largest in the world and, at an elevation of 3600 meters in the Andes, is indeed the largest near the equator (Classen & Sperling 1981). Originally equipped with a  $28 \times 28$  cm<sup>2</sup> placeholder, this instrument covered a 4.7 deg circular field of view. After using several small, single-CCD cameras, a major collaboration was signed by CIDA, Yale and Indiana Universities to develop a large  $4 \times 4$ -CCD array to be used for the QUEST survey (Baltay et al. 2002). First light of the QUEST camera installed on the CIDA Schmidt telescope was on November 1998. Since then, serious research was carried out and many important discoveries were made, mainly by the QUEST collaboration, but also within several other domestic and international research projects. Unfortunately, by the onset of the Covid-19 pandemic, many serious hardware and software issues, basically due to the obsolescence of critical components, put the QUEST camera down and in wait for

a major upgrade. In the meanwhile, we seriously considered the possibility of using a medium format digital camera as a relatively cheap, simple and almost plug-and-play temporary replacement to resume observations with the Schmidt telescope, especially those that do not require state-of-the-art CCD sensors or special optical filters. After an exhaustive review of medium format digital cameras available on the market, we pinpointed the Fujifilm GFX 50R as the best choice, especially considering the top performance, for the money, of its sensor.

### 2. CAMERA

The Fujifilm GFX 50R body features a 51 Mpix ( $8256 \times 6192$ ),  $5.3 \times 5.3$   $\mu\text{m}^2$  pixels, RGB Bayer filter, 14 bits/channel CMOS sensor with a peak quantum efficiency (QE) of  $\simeq 0.5$ , which covers a field of  $52 \times 39$  arcmin<sup>2</sup> at the focal plane of the CIDA Schmidt, with a scale of 0.38 arcsec/pix. This camera shows a very low read-out noise of  $\simeq 3e^-$  at ISO 100 (Claff 2023). Being a mirrorless camera, the flange to sensor distance is only 26.7 mm. However, this value sets an inferior limit to the minimum distance from the much larger original field flattener lens (Figure 1), resulting in a slight but evident degradation of images at the very edge of the field (Figure 2) and a small amount of distortion that must be taken into account in astrometric reductions. Also, the rectangular frame of the me-

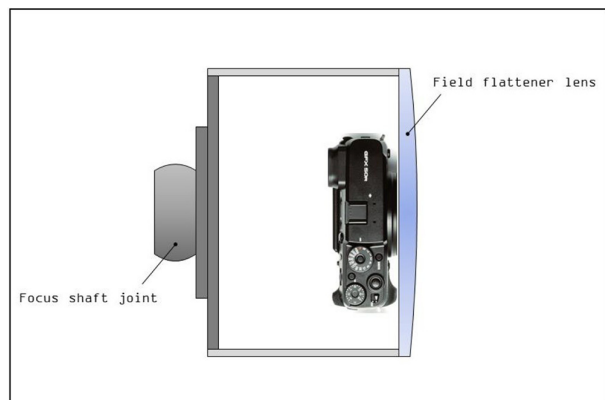


Fig. 1. The GFX 50R body inside its housing just in contact with the field flattener lens.

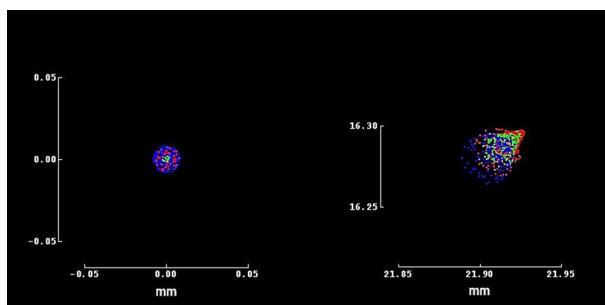


Fig. 2. Left, on-axis polychromatic spot diagram of a stellar image and at right, at the upper right corner of the field. The additional small amount of chromatism and coma is caused by the field flattener lens. The color figure can be viewed online.

chanical shutter in front of the sensor causes a visible vignetting of the  $f/3$  beam at the extreme edge (Figure 3) that must be corrected by flat-fielding. Image acquisition, exposure settings and shutter release are remotely controlled by a PC via the USB port.

### 3. PHOTOMETRIC TESTS

Lacking a temperature control, all tests were carried out with the camera already installed at the focus of the CIDA Schmidt to determine performance at ambient temperature inside the telescope, which typically drops to a few degrees above  $0^\circ\text{C}$  at night. After several trials, we resolved to use a single, 1-min exposure at ISO 1600 to carry out astronomical tests. With these settings, sky background is already clearly visible in the image as well as faint,  $m_v \simeq 20$  stars with a signal-to-noise ratio (SNR)  $\simeq 4$ . A stretched, histogram-equalized mean bias frame is shown in Figure 4. The mean dark signal at  $10^\circ\text{C}$  is shown in Figure 5. All images were stored using the lossless, compressed Fujifilm RAW format (.RAF) and linearly converted to 16-



Fig. 3. Flat field image. Vignetting of the  $f/3$  beam is caused by the rectangular frame of the mechanical shutter in front of the sensor.

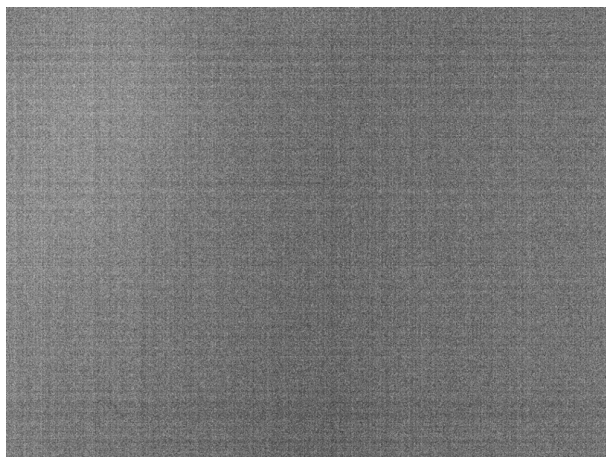


Fig. 4. A stretched, histogram-equalized mean bias image.

bits Tiffs for analysis. Photometric capabilities were determined by carrying out aperture photometry of stars in the range  $9 < m_v < 20$  from Selected Area (SA) 51 (Chiu 1980) using the G-channel image of the GFX 50R. Results are shown in Figure 6, where only a zero-point magnitude correction was applied. Linearity starts at  $m_v \simeq 12.5$  and is very good up to the faintest recorded  $m_v \simeq 20$  stars. At ISO 100, linearity increases to a range of  $\simeq 9$  magnitudes (Claff 2023), but a longer exposure time is needed to record faint stars. Figure 7 shows the SNR dependence on magnitude and Figure 8 the expected magnitude uncertainty determined from SNR values. The latter can be effectively improved by stacking several images of the same field. Also, RGB Bayer filters do not exactly match the BVR Johnson-Cousins pho-

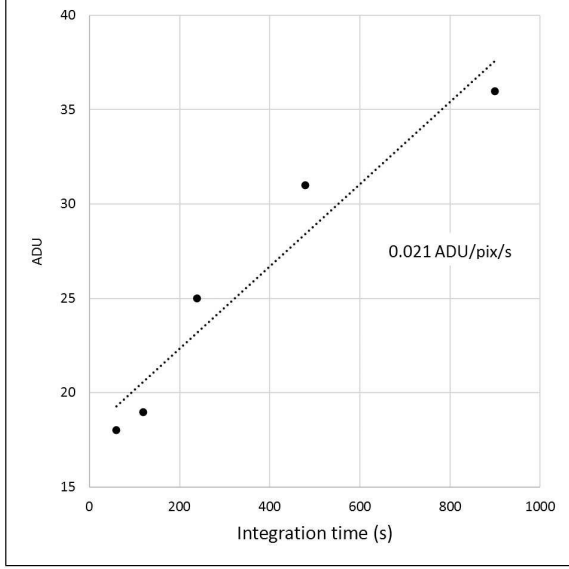
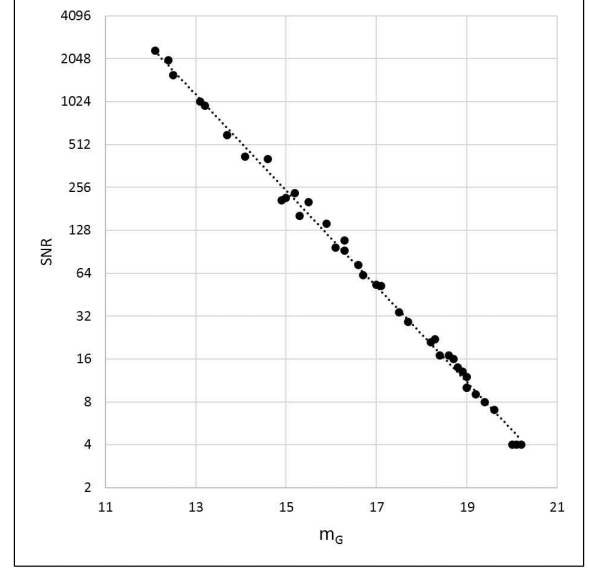
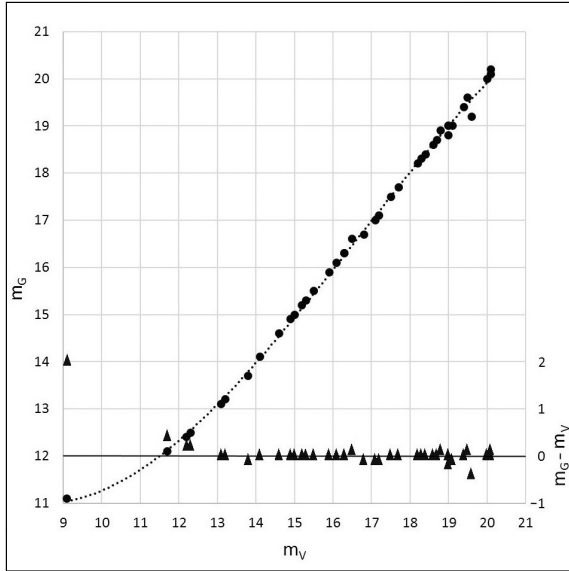
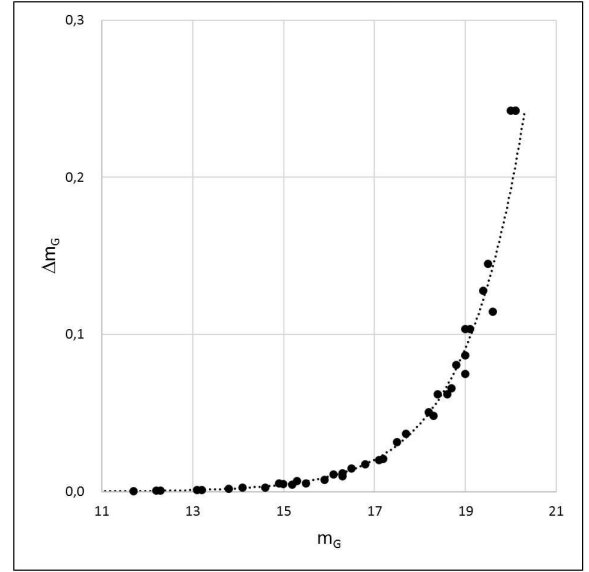


Fig. 5. Mean dark signal at 10°C ISO 1600.

Fig. 7.  $m_G$  vs. SNR. ISO 1600 single 1-min exposure.Fig. 6.  $m_V$  vs.  $m_G$  of stars from SA 51 (dots). Triangles show  $m_G - m_V$ . The solid, horizontal line corresponds to  $m_G - m_V = 0$ . ISO 1600 single 1-min exposure.Fig. 8. Expected  $m_G$  uncertainty. ISO 1600 single 1-min exposure.

tometric standard and transformations are needed (Park et al. 2016).

#### 4. DISCUSSION

CMOS sensors have been steadily replacing CCDs in common, digital cameras for several reasons, among them cost, read-out speed and low noise. Recently, also critical low-light applications are being carried out by state-of-the-art CMOS (Jorden et al. 2017). A special, large  $\approx 200 \times 200$  mm<sup>2</sup> CMOS sensor covering  $3.3 \times 3.3$  deg<sup>2</sup>

has already been tested on a large Schmidt telescope, albeit with a low resolution (Watanabe et al. 2013). The GFX 50R's sensor covers a field of  $52 \times 39$  arcmin<sup>2</sup> (Figure 9) at the focal plane of the CIDA Schmidt with a scale of 0.38 arcsec/pix, which allows us to easily attain an astrometric accuracy of  $0.1 \approx 0.2$  arcsec (Abad 1995). Among regular observations with the CIDA Schmidt, are detection and determination of accurate positions of asteroids, space debris in the geostationary ring and objective-prism stellar spectroscopy, which can be appropri-



Fig. 9. A HDR image of the Orion Nebula showing the field covered by the GFX 50R's CMOS sensor. The color figure can be viewed online.

ately carried out with the GFX 50R. However, at the time this is written, the image EXIF data only contain the internal GFX 50R's parameters, without any information of telescope's position nor relevant observing data that are usually found in astronomical images' headers. We hope to solve this issue soon by including into the image EXIF the required instrumental parameters which are digitally available from the telescope's control console. A lossless compressed raw image has a file size of  $\approx 50$  MB, but when converted to 16-bits Tiff this value can reach  $200 \approx 300$  MB. Since a scale of  $0.38 \text{ arcsec/pix}$  is oversampling the typical seeing disk at the OAN of  $\approx 1.5 \text{ arcsec}$ , we found that a post capture  $2 \times 2$  binning is useful to both reduce the file size fourfold and increase the SNR, without significantly diminishing photometric or astrometric accuracies. A 2-min exposure in drift-scan mode from the QUEST camera and a GFX 50R 1-min exposure at ISO 1600 show similar limiting magnitudes, with the latter reaching a bit fainter, probably due to the slightly better QE of the CMOS sensor compared with the now old QUEST's CCDs. Moreover, use of the camera is quite straightforward, since there are no cooling and related vacuum equipment, nor long-exposures tracking issues involved. Image stacking will improve SNR, allowing fainter magnitudes to be reached. Also, the field of view can be increased by mosaicking several overlapping images. A  $2 \times 2$ -image mosaic with a 20% overlap will allow to cover  $1.6 \times 1.2 \text{ deg}^2$ , and a  $3 \times 3$ -image  $2.3 \times 1.7 \text{ deg}^2$ .

## 5. SUMMARY

A medium format digital camera has been installed and tested at the focus of the 1-meter f/3 Schmidt telescope at the National Astronomical Observatory of Venezuela. We believe the results are quite encouraging, especially considering the very simple arrangement and operation, low cost and easy installation. Field coverage apart, astrometric and photometric accuracies are on par, or even better, with those from the QUEST camera, provided that the necessary calibration images (bias, flat, and dark) are taken into account. This low-cost solution could be of interest to other observatories with mid-sized or large telescopes on a limited budget. We found that on the CIDA Schmidt, a single, 1-min exposure at ISO 1600 will properly record sky background and faint,  $m_v \simeq 20$  stars. Stacking will further improve both limiting magnitude and SNR, and mosaicking will significantly expand field coverage. We foresee that in the near future, back-side illuminated CMOS sensors (BSI CMOS), will further improve the astronomical capabilities of common, digital cameras at modest costs.

The Fujifilm GFX 50R and a Desktop PC were made available by Ministerio para Ciencia y Tecnología (MinCyT). The author would like to thank Gerardo Sánchez, Gustavo Sánchez and Gustavo Barroeta for support and advice, Richard Rojas for assistance during the night tests at the OAN and Carlos Abad for astrometric processing.

## REFERENCES

- Abad, C. 1995, *A&AS*, 111, 369
- Baltay, C., Snyder, J. A., Andrews, P., et al. 2002, *PASP*, 114, 780, <https://doi.org/10.1086/341705>
- Chiu, L.-T. G. 1980, *ApJS*, 44, 31, <https://doi.org/10.1086/190684>
- Claff, W. J. 2023, <https://photonstophotos.net>
- Classen, J. & Sperling, N. 1981, *S&T*, 61, 303
- Jorden, P. R., Jerram, P. A., Fryer, M., & Stefanov, K. D. 2017, *JInst*, 12, 07, <https://doi.org/10.1088/1748-0221/12/07/C07008>
- Park, W., Pak, S., Shim, H., et al. 2016, *AdSpR*, 57, 509, <https://doi.org/10.1016/j.asr.2015.08.004>
- Stock, J. 1981, *RMxAA*, 6, 13
- Watanabe, J., Kasuga, T., Terai, T., et al. 2014, *The Meteoroids 2013*, ed. T. J. Jopek, F. J. M. Rietmeijer, J. Watanabe, & I. P. Williams, 325

## SN Ia DETECTION ANALYSIS RESULTS FROM REAL AND SIMULATED IMAGES USING SPECIALIZED SOFTWARE

Juan Pablo Reyes<sup>1,2</sup>, Marcela Hernández Hoyos<sup>1</sup>, and Dominique Fouchez<sup>2</sup>

*Received April 28 2023; accepted January 10 2024*

### ABSTRACT

The detection of transient events, Type Ia supernovae in particular, has become an important research subject in today's astronomy. We use as a base tool the software suite for astronomical image processing called LSSTsp and adapt it to assemble a Type Ia supernova detection pipe. We study some straightforward changes of the overall pipeline by selecting better quality inputs to perform a coaddition of reference images, we analyze the different residual sources detected on the difference images and, lastly, we build light curves by taking into account the features of detected difference image analysis sources. Finally, we build a catalog of supernova candidates by using a random forest classification, and check the relevance of these additions. We reduce the overall source detection density with our changes while finding between 82% and 85% of the present Type Ia supernovae.

### RESUMEN

La detección de eventos transientes, especialmente de las supernovas tipo Ia (SNIa), es un tema de particular importancia en la astronomía contemporánea. Usando como herramienta de base el paquete de software llamado LSSTsp, adaptamos el código para ensamblar un *pipeline* de detección SNIa y estudiar el impacto de incorporar cambios directos sobre la selección de entradas intermedias para la coadición de imágenes de referencia, analizar las fuentes detectadas en imágenes de diferencia y finalmente construir curvas de luz teniendo en cuenta las características de las detecciones residuales de fuentes. Finalmente, construimos y reportamos un conjunto de posibles supernovas usando un algoritmo de clasificación de *random forest*, verificando también la relevancia de las adiciones estudiadas. Redujimos la densidad de detecciones con nuestros cambios, hallando entre un 82% y un 85% de las SNIa presentes.

*Key Words:* methods: data analysis — supernovae: general — techniques: image processing

### 1. INTRODUCTION

Transient events are phenomena with a short lifespan when compared with everything else in the universe. However, since their behavior and duration can vary from one object to another, they present a great diversity, even within same class of events. Gamma ray bursts can last less than a second while microlensing or supernovae events remain visible from a few days to several weeks.

Type Ia supernovae (SNIa) are among the most important types of transients for cosmological anal-

ysis. This particular type of transient has been key for the determination of the expansion history of the universe by comparing the observed flux of these objects with their redshifts. Thanks to SNIa, the recent acceleration of the universe expansion has been derived and measured (Riess et al. 1998; Perlmutter et al. 1999; Betoule et al. 2014).

With the advent of more powerful and complete all-sky photometric surveys, either from ground telescopes or satellites, an increasing amount of data will be delivered to the scientific community. This enormous volume of data requires more sophisticated and efficient methods to analyze them and report important findings, such as SNIa. The more data

<sup>1</sup>Universidad de los Andes, Bogotá, Colombia.

<sup>2</sup>Aix Marseille Univ, CNRS/IN2P3, CPPM, Marseille, France.

modern telescopes are capable of gathering, the more latent is the necessity of algorithms, big data techniques and automation strategies to fully study and leverage such amount of information.

Dedicated rolling search has been employed in several surveys to search for transients in specific regions of the sky and to perform photometric follow-up of these events. Some of these surveys are the Supernova Legacy Survey (SNLS) (Guy et al. 2010), the Panoramic Survey Telescope and Rapid Response System (Pan-STARRS) (Scolnic et al. 2018), the Sloan Digital Sky Survey (SDSS) (Sako et al. 2018), the Hyper Suprime-Cam Subaru Strategic Program (HSC SSP) (Aihara et al. 2018) the Dark Energy Survey (DES). Smith et al. (2020) have developed programs in search of SNIa.

The Vera C. Rubin Observatory Legacy Survey for Space and Time (LSST) is one of these surveys whose objective is to provide an unprecedented volume of images and information, using the largest digital camera ever constructed (Ivezić et al. 2019). Along with the LSST, there is an important effort to provide a software backbone for the processing and generation of LSST data in the form of the LSST Science Pipelines, the LSSTsp, for short (Jurić et al. 2017; Bosch et al. 2018). The LSSTsp is a suite of software packages capable of enabling the creation of dedicated data products with high quality and great performance (Axelrod et al. 2010). This is the base tool the LSST survey will use to accomplish its science goals and that this work employs to analyze and study SNIa in real and simulated images.

Other surveys have developed tool sets to analyze transients. For instance, Perrett et al. (2010) developed a pipeline for SNLS that involved calibrating, warping and subtracting the images; then using photometry fittings; and finally, generating triplets of transient candidates that were visually confirmed by experts, relying on manual classification.

Another example is Kessler et al. (2015), which described the DES-SN difference imaging pipeline used to detect transients for DES. This pipeline is based on selecting objects, mixing thresholding images and matching catalogs. They use Hotpants (Becker 2015), an implementation of the Optimal Image Subtraction (OIS) (Alard & Lupton 1998), and Autoscan, a machine learning code to replace human intervention when identifying transient objects (Goldstein et al. 2015).

Recently, Sánchez et al. (2022) worked using a difference image pipeline built on the LSSTsp to analyze simulated images that included SN Ia light curves. It also measured cosmic distances and cosmological

parameters from the SNIa to monitor the detection efficiency of the LSSTsp. Sánchez et al. (2022) employed the LSSTsp systems as a tool to study images from different characteristics for the needs of current and future surveys.

As powerful as difference imaging is, recent works have also leveraged machine learning to further refine the detection transients. For instance, Goldstein et al. (2015) proposed a random forest approach to identify artifacts among the objects extracted from difference images in the DES-SN transient detection pipeline (Kessler et al. 2015). Their method presented a missed detection rate of 5% and a false positive rate of 2.5%.

An example of classification of detected transients within the LSST comes from Pasquet et al. (2019), which proposes a complex deep learning architecture to characterize and classify supernovae of different types, based on previous applications of the same strategy to other similar problems in astronomy. They tested it with simulated data from the Supernova Photometric Classification Challenge SNPhotCC, which is a set of simulated supernovae on DES images (Kessler et al. 2010). This algorithm presents an accuracy of over 86% for SNPhotCC with an AUC of 0.937, and despite some uncertainties, it obtained an accuracy of between 90% and 97% with an AUC of between 0.990 and 0.997 for simulated SNIa in the LSST Deep Fields.

Another example comes from Boone (2019) which proposed Avocado: a Gaussian process augmentation applied over light curves in all bands, used to train a decision tree to classify different types of transients for the Photometric LSST Astronomical Time-Series Classification Challenge or PLAsTiCC (The PLAsTiCC team et al. 2018). PLAsTiCC is a community-wide challenge to foster the development of machine learning classification algorithms on a set of realistic LSST simulations of transient events. Avocado was the winner of this challenge, achieving an AUC of 0.957 for the classification of SNIa.

Lastly, Neira (2020) used a Random Forest based classification for binary classification (transient/non-transient) and eight-class classification. We use their approach with their base features as well as some modifications to understand the relevance of the studied additions.

In this paper we present a study of detection techniques to select SNIa on images from big telescopes. To obtain and analyze our results we use the LSSTsp. Our main objective is to show how it is possible to explore and design procedures that contribute to the

exploration and analysis of data for the astrophysics field through the use of powerful computational tools.

## 2. MATERIALS

This section presents the characteristics of the images used to test the proposed pipeline. We employ real data and try to find genuine supernovae present in the images. We also work with simulated data, creating and injecting supernovae in the input images, to help us understand the behavior of the different tasks with varying inputs. As these new images are virtually equivalent to normal acquisitions, we can use them as inputs to determine the sensitivity of our processing by counting the SNIa detected after simulations, as if these were real phenomena.

### 2.1. Real Data

We employ two types of real data: images obtained from the Canada France Hawaii Telescope (CFHT) and light curves from SNIa found in these images by the Supernovae Legacy Survey (SNLS). The SNLS has developed a major program on supernova detection that includes an image processing pipeline. It has detected more than 300 SNIa in its first five years of observation (Guy et al. 2010).

#### 2.1.1. Images

Images from CFHT datasets belong to one of the four deep fields (noted D1, D2, D3 and D4) during the first three years of the survey: the D3 field. We use this field as a limited sample that allows us to test our contributions within the limits of our technical resources. These first three years, from 2004 to 2006, have available valuable results regarding the detection of SNIa among the images (Guy et al. 2010). These images are obtained using the Megacam camera. The Megacam has 36 charge-coupled devices (CCD) capable of providing an image. The number of images per filter varies as shown in Table 1; the total number of images in the used field is 54614. It is noticeable that most images use filters  $r$  and  $i$ , which justifies why we focus some of our results on the former.

These deep fields have the following characteristics:

- An observation set every 5 nights on average.
- When a night is observed, 5 observations are gathered on average.
- $1 \text{ deg}^2$  of sky observed during almost 6 consecutive months every year.
- A full focal plane composed of 36 CCDs.

- Each CCD is  $2048 \times 4612$  pixels
- Each pixel is 0.186 arcsec.
- The limit magnitude of four fields are  $u = 27.5$ ,  $g = 27.9$ ,  $r = 27.7$ ,  $i = 27.4$  and  $z = 26.2$ .
- Depth per night is about magnitude 3.
- Seeing range between approximately 0.6 and 1.1 with an average of 0.8

TABLE 1

TOTAL OF ORIGINAL CCDS IMAGES PER FILTER FOR THE FIRST THREE YEARS OF CFHT OBSERVATION IN FIELD D3

Filter	Number of images
$r$	13242
$i$	18033
$g$	10828
$z$	12511

#### 2.1.2. Light Curves

To validate our results, we use the SNIa reported by the SNLS and identified using spectroscopy. This survey has identified and measured the photometric properties of 252 SNIa with a redshift range of between 0.15 and 1.1 (Guy et al. 2010) and reported at least 485 SNIa candidates (Bazin et al. 2011). The first SNLS sample provides one of the most uniform sets of SNIa available, but the actual number of objects per deep field is low, providing only 75 SNIa for the D3 field in the three years of observation. Nevertheless, these supernovae serve as the ground truth for the detection.

### 2.2. Simulated Data

We present here the simulation of SNIa injected on real images. We simulate type SNIa through the Supernova Analysis Software or SNANA (Kessler et al. 2009) using the Spectral Adaptive Lightcurve Template 2 model, also known as SALT2 (Guy et al. 2007), and then inject them into the CFHT images, to create an effective sample of time series for testing our analysis using machine learning algorithms along with Poisson noise from the source. We generate 5000 SNIa for the CFHT deep field D3, and we inject each one on the successive visits during the season and the field. Each injection is individually given a coordinate in the images and then added to it.

We inject simulated point sources on real CFHT images. We choose a random date and a random location from the CFHT image set to inject the simulated



supernovae. The selection of the random location is achieved by employing an external catalog to select any galaxy in the field as a host. This external source catalog provides the location of galaxies within a sequence of images. At this point, all injections are then handled as single image simulations: we locate the coordinates of such galaxy in the map of the sky so we know which images we need to retrieve. Subsequently, we get the respective image in the located coordinates for every observation in the simulated curve. After that, we calculate the local PSF values using principal component analysis to give shape to the supernovae; then we inject the simulated supernovae with an intensity added to that of the host galaxy, with a random off-set to the location within the confines of the host galaxy.

### 3. METHODS

We use the LSSTsp as the base tool to detect the SNIa. We present in this section the main tasks used and some custom tasks we developed for our specific needs.

#### 3.1. The LSST Science Pipelines

The LSST Science Pipelines (LSSTsp) was developed for the purpose of processing data for the Vera C. Rubin Observatory Legacy Survey for Space and Time. It is developed in Python and C++ (Kantor et al. 2007; Bosch et al. 2018) and it has been tested through data challenges with different levels of complexity and being constantly prototyped. Currently, it has more than 40 packages that perform a large variety of image and data processing operations; it includes efficiently designed C++ algorithms wrapped in SWIG. It provides architectures to process inputs and to generate the required results (Ivezić et al. 2019).

The LSSTsp has several different tasks for image processing. Each task has its own independent responsibilities, but when put together, it is possible to employ the intermediate products to detect transients by means of a pipeline. Our work relies on the LSSTsp v14 for assembling a processing pipeline for SNIa detection, through the use of some Difference Image Analysis (DIA) tasks and routines. We acknowledge that more recent versions of the LSSTsp have included new features related to the analysis presented in this paper, but we still use this version to ensure compatibility with our previous work and this does not change the relevance of our results.

As there is not an official transient detection pipeline for CFHT images within the LSSTsp, we assemble one as a starting point. This pipeline is shown

in Figure 1. It has three main stages: First, the Generation of Difference Images, which encompasses the pre-processing, coaddition, and subtraction of images using the OIS. The second stage is the Candidate Selection, which comprises the optimization of the detection of sources in the difference images, the association of sources to produce multi-channel source associations (up to 5 pixels) to produce light curves, and the selection of transient candidates based on their light curves. In this stage, all operations that use the difference image are noted with the prefix DIA (Difference Image Analysis). The third and last stage is the Type Ia Supernova Identification, which applies a machine learning algorithm to the candidates to recognize the SNIa.

Figure 1 highlights elements that we use, adapted and created for the pipeline. Tasks in blue are used without any modification, tasks in purple have been extended to help them fit better into the new pipeline. Tasks in red are new and they are programmed using the task architecture of the LSSTsp and developed completely to answer the need of processing for particular points of the pipeline.

#### 3.2. Generation of Difference Images

The purpose of this stage is to generate the difference images for each reference and science image input. As shown in Figure 1a, the tasks involved in this stage are the Image Pre-processing; the Image Coaddition tasks (Day Coaddition and Deep Coaddition tasks) to generate the respective input images for the image subtraction; and the Optimal Image Subtraction itself. Here we study the impact on the existing software of implementing a task to select better reference images (calexps) for the Deep Coaddition.

##### 3.2.1. Image Pre-Processing Task

Firstly, the Image Pre-Processing task encompasses the calibration of the initial exposures, the artifact correction, the detection of visible sources, and the masking of saturated and edge pixels. This processing provides a relatively clean set of images with noise corrections, masked saturated pixels and cosmic rays. These images are used as inputs for the Image Coaddition tasks. The result of this first task is a set of calibrated exposures or calexps.

##### 3.2.2. Image Coaddition and Input Selection

Typically, when using coadditions in LSSTsp, the final user is in charge of selecting calibrated exposure inputs and there are no enforced rules within the code to differentiate between a coaddition for a reference



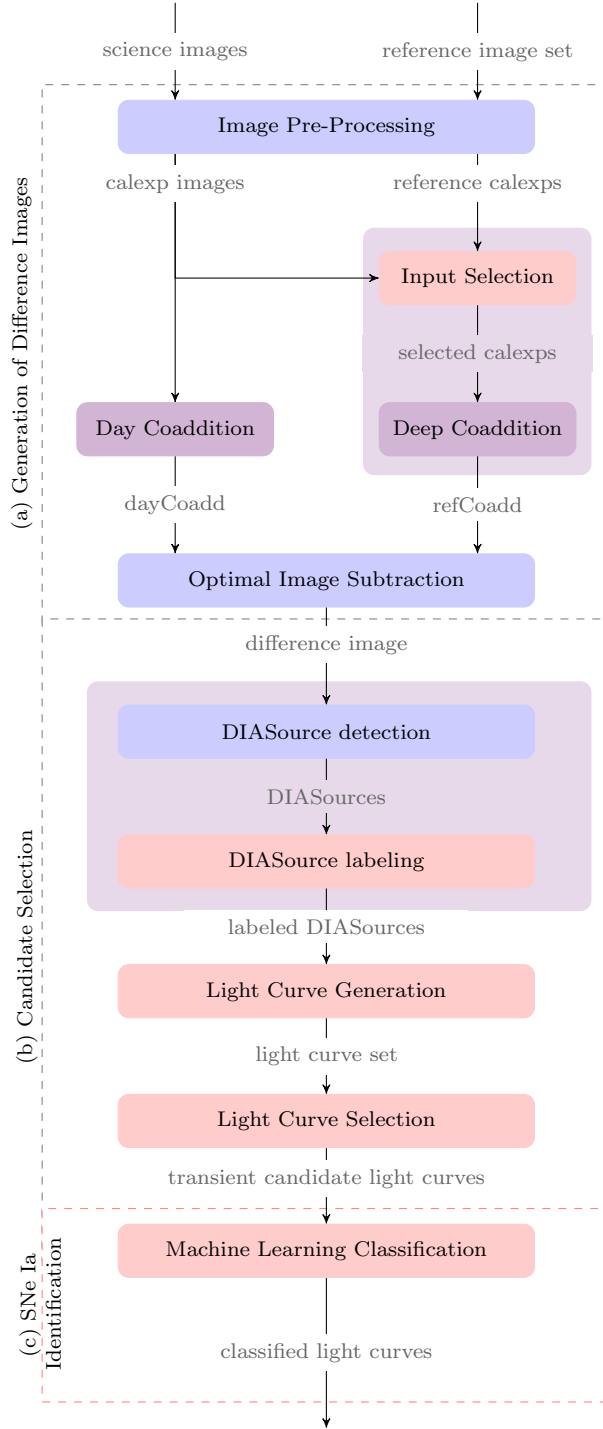


Fig. 1. The Supernova Detection Pipeline divided in three stages: (a) Generation of Difference Images; (b) Candidate Selection; and (c) SNe Ia Identification. Blue tasks are left untouched, purple tasks have been modified and red ones are tasks we created for the LSSTsp. The color figure can be viewed online.

image and one for a science image. This process is reached through the use of two tasks and it is indifferent to the purpose of the output. In the pipeline, we opt to fuse both generation and assembly tasks together and then specialize each one to generate the coaddition for science and reference calexp. We call these the Day Coaddition and the Deep Coaddition tasks. This allows us more control over each process independently, without affecting the other. From a technical perspective, this also mitigates the impact of bottlenecks for global field processing and allows the new tasks to be more time efficient when generating the deep coadditions.

Selecting high quality inputs is vital to ensure a good coaddition and subsequently good difference images. Using low quality inputs without any sort of quality metric has the potential of propagating noticeable errors and aberrations from the coaddition, all the way to the detection of transient candidates. Errors on the images come from the sky background and increase as the square root of the signal, bad atmospheric conditions or deficient seeing. As the image subtraction operation alters the inherent noise of the inputs through convolution, they become problematic and the artifacts become more visible most of the time. We choose to address this issue for deep coadditions.

#### Day Coaddition Task

The objective of this task is to generate a high quality science coaddition image, as mentioned before. Day coadditions, or dayCoadds, are built by using the different exposures acquired on a given night. As there is a limited number of acquisitions per night (between 4 and 10 in most cases), we use all available exposures to ensure the best possible quality without performing a selection of high quality inputs. This way of generating day coadditions means that very short-lived objects (less than one night) are not registered in the detections or might appear as single point detections.

As with science images, we expect the transient and variable objects to be present here; thus, when performing the OIS, we match their PSF to that of the astrometrically corresponding deep coaddition to detect them after subtracting both.

#### Deep Coaddition Task

Deep coadditions created from a reference image set are referred to as refCoadds. These coadded exposures, which come from a wider time frame belonging to an outside acquisition year, help to detect all changes in science images during the subtraction. As

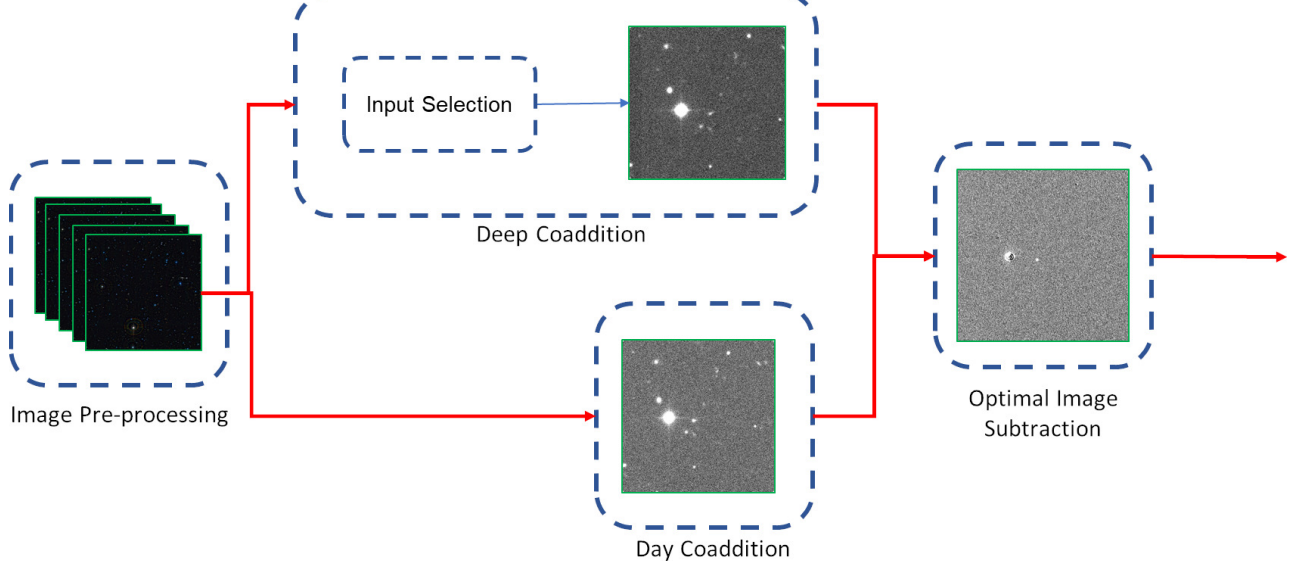


Fig. 2. First part of the pipeline: the generation of difference images. The tasks here are responsible for generating the reference and science image coadditions, and then performing the subtraction using the OIS algorithm. The Deep Coaddition task generates the reference image, whereas the Day Coaddition task creates the science image. The Image Subtraction task generates the difference image as final result.

explained before, the convolution Kernel that calculates the OIS when matching with the day coaddition modifies these images. High quality images provide better and less complex PSFs to be parametrized by the sum of Gaussians via the OIS, reducing the overall artifacts later when a subtraction is performed.

Ensuring the quality of the inputs is especially important when constructing the deep coaddition, because input datasets for these can span up to hundreds of different images acquired during several months of operation. Therefore, we construct these references guaranteeing high signal-to-noise on the result and thus obtaining high quality difference images. To achieve this, we perform an selection using the noise variance levels on the input images after warping and adjusting them to their respective patch in the skymap, but before assembling the final coaddition. As noise levels change locally within the image and can present variation between the original calexps and the smaller patches used for the coaddition, it follows that the optimal approach is to use the values in the patches as criteria for the selection. We call this process the Input Selection.

### 3.2.3. Optimal Image Subtraction

As already mentioned, we use the OIS (Alard & Lupton 1998; Alard 2000) LSSTsp task with the new dayCoadds and refCoadds as inputs. We use the default parameters of 3 Gaussians with degrees 4, 2 and 2. As expected, the OIS generates a difference

image that is the output of the current stage and will be the input of the next one

## 3.3. Candidate Selection

The main objective of this stage is to produce a set of plausible candidates, from the detections in the difference images, to be transient objects. The tasks involved in this stage are the DIASource Selection, the Light Curve Generation and the Light Curve Selection. These tasks are shown in Figure 1b. We perform a quality analysis for the sources detected in the difference images through the use of footprint analysis.

### 3.3.1. DIASource Selection

This first task of this stage is divided in two phases: The DIASource detection and the DIASource labeling.

#### DIASource Detection

The detection of sources in difference images is performed using the default single frame measurement algorithm of the LSSTsp that searches positive and negative local peaks, and using a detection threshold of  $5\sigma$ . Each detected source is then stored into a catalog created for each patch of the defined skymap. Every source is characterized by its coordinates, its flux measurement and its flux error which are calculated from the aperture flux. We use an aperture with a radius of 4.5 pixels that has consistently

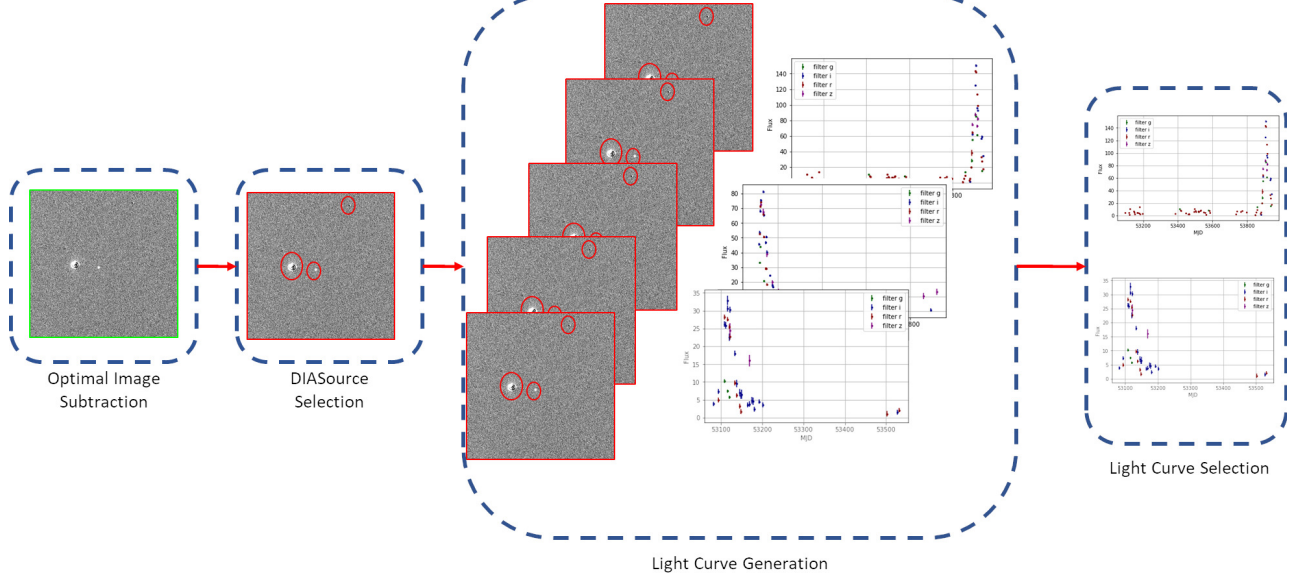


Fig. 3. Second part of the pipeline: Light curve detection and selection. The tasks here include the detection of DIASources; and the detection and selection of light curves.

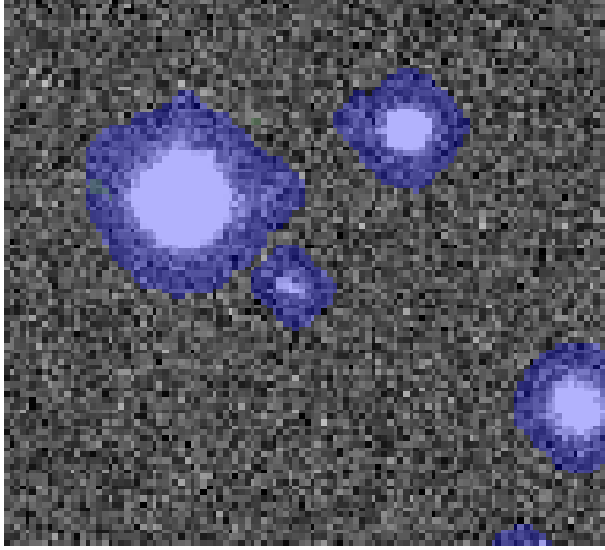


Fig. 4. Example of sources with footprints overlaid as semi-transparent blue groups of pixels. The color figure can be viewed online.

yielded the most stable results of flux measurements while reducing the overall measurement error in our experiments.

Previous analysis using the LSSTsp suggest that an underestimation of noise in the CFHT images ends up generating a high number of detections during this step (Slater 2016). To mitigate this, we re-estimate the value of background noise on the images using the algorithm in the LSSTsp and then recalculate the threshold value defined for the image in the given

band. This process, even if time-consuming, ensures that there are less bogus detections in the images, and guarantees that the noise is not inflated.

When a DIASource is detected, one or two footprints are calculated on a  $20 \times 20$  local neighborhood centered around the source. Footprints  $F$  are connected regions that start as contiguous patches of high-intensity pixels that are then expanded to include up to 4 pixels away from the initial pixels. As these footprints can be calculated in difference images, the possible footprints will group pixels with positive or negative values. Overlapping footprints with the same sign are merged. Figure 4 shows an example of positive footprints calculated on a calibrated image. Consequently, a given DIASource can have either one positive  $F^+$  footprint, one negative  $F^-$  footprint or both at the same time. Footprints are defined as follows:

$$F^+ = \bigcup_i R'_{i+}, \quad (1)$$

$$F^- = \bigcup_i R'_{i-}, \quad (2)$$

where  $R'$  is the result of a region growth over an initial group of pixels  $R_+$  or  $R_-$  such as:

$$(x, y) \in R' \iff \exists (x', y') \in R : d((x', y'), (x, y)) < g. \quad (3)$$

Here,  $d((x', y'), (x, y))$  is the Euclidean distance between pixels  $I(x', y')$  and  $I(x, y)$ .  $g$  is the growth value of the region.

$R_+$  and  $R_-$  are initial groups of at least 5 pixels for which:

$$(x, y) \in R_+ \iff I(x, y) > th * \sigma, \quad (4)$$

$$(x, y) \in R_- \iff I(x, y) < -th * \sigma. \quad (5)$$

Here  $th$  is the threshold value, and  $x$  and  $y$  represent the pixel coordinates.

Notice that, as the region growing algorithm determined by equation 3 does not take into account pixel values, footprints  $F^+$  and  $F^-$  can have intersections.

#### DIASource Labeling

Once the footprints of a DIASource are calculated, the number of pixels and their flux are measured. These values are used to label the corresponding DIASource. The analysis of DIASources is a custom task independent from similar ones currently present in more recent versions of the LSSTsp such as DipoleAnalysis. The possible labels that we assign are:

- **Positive:** DIASources that only have  $F^+$ . Their presence is the result of a transient object in the science image.
- **Negative:** DIASources that only have  $F^-$ . These are rare residuals and they sometimes indicate transients present in the reference images.
- **Dipole:** DIASources with  $F^+$  and  $F^-$  with balanced flux and size with low geometric overlapping.
- **Fringe:** DIASources with  $F^+$  and  $F^-$  with balanced flux and size with high geometric overlapping.
- **Artifact:** DIASources that do not fit in any of the previous categories.

Let us define:

$$\bar{F} = F^+ \cup F^- . \quad (6)$$

To determine whether a DIASource is a Dipole or a Fringe, we define two properties: Geometric Dipoles  $GD(\bar{F})$  and Photometric Dipoles  $PD(\bar{F})$ .

A Geometric Dipole  $GD(\bar{F})$  is defined using the following equation:

$$GD(\bar{F}) = \begin{cases} 1 : \text{if } \sum_{(x,y) \in F^+} 1 \leq \frac{2}{3} \sum_{(x,y) \in \bar{F}} 1 \wedge \\ \sum_{(x,y) \in F^-} 1 \leq \frac{2}{3} \sum_{(x,y) \in \bar{F}} 1 \\ 0 : \text{otherwise.} \end{cases} \quad (7)$$

A Photometric Dipole  $PD(\bar{F})$  is defined using the following equation:

$$PD(\bar{F}) = \begin{cases} 1 : \text{if } \sum_{(x,y) \in F^+} |I(x, y)| \leq \frac{2}{3} \sum_{(x,y) \in \bar{F}} |I(x, y)| \wedge \\ \sum_{(x,y) \in F^-} |I(x, y)| \leq \frac{2}{3} \sum_{(x,y) \in \bar{F}} |I(x, y)| \\ 0 : \text{otherwise.} \end{cases} \quad (8)$$

Therefore, using the properties defined in equations 7 and 8, we define a Dipole  $D(\bar{F})$  as:

$$D(\bar{F}) = \begin{cases} 1, & \text{if } PD(\bar{F}) = 1 \wedge GD(\bar{F}) = 1 \\ 0, & \text{otherwise.} \end{cases} \quad (9)$$

And a Fringe  $Fr(\bar{F})$  as:

$$Fr(\bar{F}) = \begin{cases} 1, & \text{if } PD(\bar{F}) = 1 \wedge GD(\bar{F}) = 0 \\ 0, & \text{otherwise.} \end{cases} \quad (10)$$

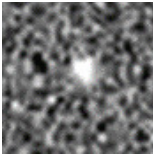
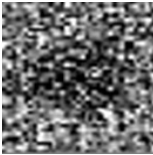
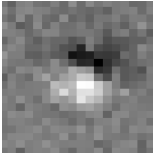
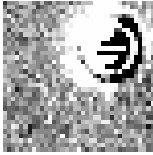
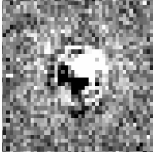
To summarize, we evaluate the amount of overlapping in terms of pixels and calculated flux to determine the label for a given footprint. The proportions are empirically determined, leaving the possibility of a more in-depth study and refinement of these categories. Visual examples of their aspect are presented in Table 2.

#### 3.3.2. Light Curve Generation

From the detected and labeled DIASources obtained from the previous step, we match all DIASources that are located at the same coordinates within a 1 arcsec of radius in all the different images along all the seasons, under the assumption that all these detections belong to the same object. For each set of matched DIASources, we build a light curve and assign an object ID to it. Consequently, each

TABLE 2

FOOTPRINT LABELS DEFINED FOR EVERY SOURCE DETECTION BASED ON THEIR FOOTPRINTS\*

Label	Visual Aspect	Description
Positive		Sources that only have positive footprints. Their presence usually is the result of a transient object in the science image.
Negative		Sources that only have negative footprints. These are rare residuals and they sometimes indicate transients present in the reference images.
Dipole		Sources with positive and negative footprints. These artifacts occur when there are alignment problems between the images.
Fringe		Sources with positive and negative footprints. These artifacts occur when there are inaccuracies in the PSF matching algorithm.
Artifact		Sources with both positive and negative footprints, but that do not fall in the Dipoles or Fringes categories.

\*The Visual Aspect column shows a general idea of the type of objects labeled as such.

light curve may be composed of several DIASources and always has at least one.

The output of this task is a catalog of the light curves for every filter. Each light curve is stored as set of DIASources with all the relevant information such as the coordinates, flux, error, magnitude, filter, and date (MJD format). The study of the DIASources and its classification is helpful to identify which type of object is being described by the light curve.

### 3.3.3. Light Curve Selection

A consequence of the previous task is that a detected light curve can technically contain, in the worst case, a single point. Isolated detections of an object do not strongly indicate the presence of supernova-like transients; in fact, they can be indicative of anomalous subtractions, short-lived events, or transients who vary in intensity and position at the same time. The Light Curve Selection task is implemented so that it chooses only curves that satisfy two criteria: at least five total detections and data present in

at least two different bands. This ensures that the object has a certain continuity between observations and that its residual light intensity can be picked in different bands.

Although these criteria might appear to be simplistic, they perform a considerable reduction of the candidate set, while also being conservative enough not to reject true transients.

### 3.4. Type Ia Supernovae Identification

The final stage of the pipeline classifies the transient candidate light curves to identify real SNIa, using the machine learning classification method proposed by Neira (2020). Figure 1c depicts this task in the pipeline. We use the identification part of the pipeline to validate the impact of our studies and characterization, specially when introducing new variables calculated after obtaining better quality light curves.

Regarding the identification, we worked on four fronts: First, the adaption of the method to binary

TABLE 3  
FEATURES CALCULATED FOR MACHINE LEARNING TRAINING OF LIGHT CURVES

Feature	Category	Description
<code>skew</code>	moment-based	Asymmetry of the curve
<code>kurtosis</code>	moment-based	Measure of extreme values in either tail of the curve
<code>small kurtosis</code>	moment-based	Small sample kurtosis
<code>std</code>	moment-based	Standard deviation
<code>beyondstd</code>	moment-based	Percentage of magnitudes beyond one standard deviation from the weighted mean.
<code>stetson j</code>	moment-based	Each weight is calculated as the inverse of the photometric error
<code>stetson k</code>	moment-based	The Welch-Stetson J variability. A robust standard deviation
<code>max slope</code>	flux-based	The Welch-Stetson K variability. A robust kurtosis
<code>amplitude</code>	flux-based	Maximum absolute slope between two consecutive observations
<code>median absolute deviation</code>	flux-based	Difference between maximum and minimum intensity
<code>median buffer range percentage</code>	flux-based	Median discrepancy of fluxes from the median magnitude
<code>pair slope trend</code>	flux-based	Percentage of points within 10% of the median flux.
<code>pair slope trend last 30</code>	flux-based	Percentage of all pairs of consecutive positive slope measurements
<code>resPos</code>	flux-based	Percentage of the last 30 pairs of consecutive positive slope measurements minus percentage of last 30 pairs of consecutive negative slope measurements.
<code>percent amplitude</code>	percentile-based	Percentage of footprints labeled as positive in light curve
<code>percent difference flux percentile</code>	percentile-based	Largest percentage difference between absolute max. magnitude and the median.
<code>flux percentile ratio mid20,35,50,65,80</code>	percentile-based	Ratio of $F_{5,95}$ and the median flux.
<code>poly1.a</code>	fitting-based	Ratio of percentile and $F_{5,95}$
<code>poly2.a,b</code>	fitting-based	Coefficient of the monomial curve fitting
<code>chi2SALT2</code>	fitting-based	Coefficients of the quadratic curve fitting
<code>chi2sGauss</code>	fitting-based	$\chi^2$ goodness-of-fit value using the SALT2 model
		$\chi^2$ goodness-of-fit value using the Skewed Gaussian model

classification (SNIa and non-SNIa). Secondly, the selection of relevant data features and the introduction of three new ones in the form of the  $\chi^2$  goodness-of-fit statistic for the SALT2 and the Skewed Gaussian models. Third, we extend the classification to use real data from all the filters, given that the original implementation classifies light curves, one band at a time. Finally, the use of simulated data as well as other real non SNIa objects detected in the difference images to train and validate the algorithm, as the dataset does not contain enough real SNIa on CFHT images for a viable classification effort.

Before classifying, the method uses dimension reduction via feature extraction. Light curve observations are not sampled at regular intervals and all of them do not have the same number of observations. This makes it very challenging to use the time-series data directly for classification using traditional methods. To solve this difficulty, a set of characteristic features is extracted from each light curve instead, using statistical and model-specific fitting techniques. From the original implementation, we only use 23 features that are strictly geometrical and statistical (Table 3). These features are categorized in the following four groups: moment-based, magnitude-based, percentile-based and fitting-based.

The three new features we introduce are:

- The  $\chi^2$  statistic for a fit of the light curve with the SALT2 model, denoted as `chi2SALT2`. The

$\chi^2$  goodness-of-fit coefficient is calculated for the candidate light curves obtained from the previous stage of the pipeline.

- The  $\chi^2$  statistic for a fit of the light curve with the Skewed Gaussian model, denoted as `chi2sGauss`. Both this and the previous  $\chi^2$  statistic are calculated by fitting the models to the points of the light curve.
- The percentage of DIASources labeled as positive present in the light curve of a given object, denoted as `resPos`. This feature is obtained by calculating the number of footprints labeled as positive as a percentage of the total number of sources present in the light curve.

#### 4. RESULTS

We present here the results of our analyses in each stage using our pipeline: Generation of Difference Images, Candidate Selection, and Type Ia Supernova Identification. We show the results when applying the different options offered by the pipeline.

##### 4.1. Tuning the OIS

We tested the effect of modifying the OIS parameters to better adapt it to our input images using the simulated inputs with various fluxes. Among the many parameters that can be tuned to optimize the OIS, we varied the cell size, the Spatial Kernel Order and the number of Gaussians used to model



TABLE 4  
NUMBER AND DENSITY OF SOURCE  
DETECTIONS BEFORE AND AFTER INPUT  
SELECTION ON FILTER R

	Number of Sources	Sources per square degree
Before input selection	4215406	48452.9
After input selection	87042	1000.5

the PSF for different patches in the images and then we applied a grid search test to find the better parameter combinations. For the cell size, we tested values between 50 and 500 pixels, we varied the number of Gaussians between 3 and 8 and for the Spatial Kernel Order we used several combinations of degrees between 1 and 9. There were no improvements of more than 1.2% in the number of detections. For all the studied parameters, we concluded that the default values fixed by the Rubin Observatory Data Management team are the optimal ones for our data as well (real CFHT data with simulated supernovae).

#### 4.2. Generation of Difference Images

To measure the impact of the pipeline different options on the Deep Coaddition task, we compared the number of DIASources detected on the CFHT image dataset with and without input analysis and then we analyzed the quality of such sources using the footprint labeling. Figure 6 presents the number of detections as a function of the number of input coadded images in three situations: (a) when using Input Selection to select low variance images, (b) when selecting random input images, and (c) when averaging the results for several images while using low variance, high variance, and without Input Selection (noted as random). Figure 7 shows the same results, but instead of variance, it depicts Input Selection based on PSF radius size. From these results, we infer that the number of detections in coadditions is reduced when selecting input images with low variance and low PSF radius size.

We can consider that the higher the number of DIASources detected, the more spurious detections are present among them. As such, a precise pipeline should strive to reduce the overall number of detections while preserving real transients. Consequently, better coadditions should have fewer detections with unchanged efficiency of detecting transients. The efficiency of detecting transient is evaluated with the

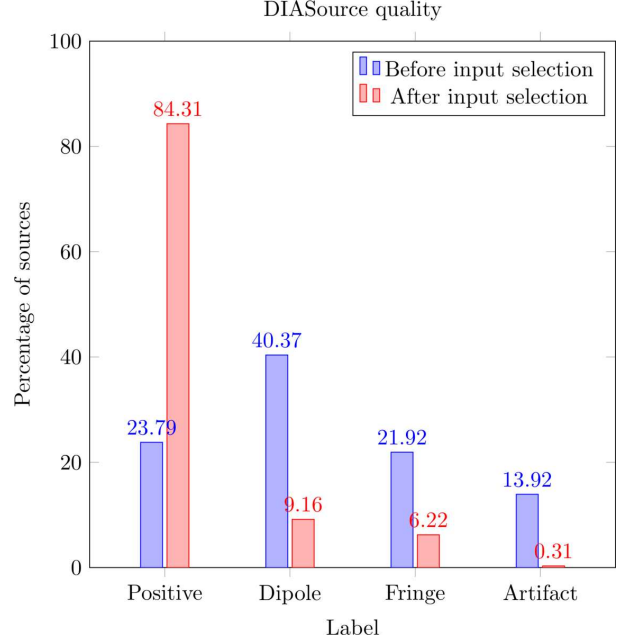


Fig. 5. Comparative percentage of labeled DiaSources. Not only does the original pipeline have more detections, but the proportion of spurious detections (non-positive) is consistently higher than when using Input Selection. The color figure can be viewed online.

simulated data and does not vary significantly with the coaddition. Our results show that increasing the number of input images for the coaddition reduces the number of detections as well.

By Input Selection and DIASource analysis, we were able to reduce the overall source detection density for one filter as shown in Table 4. This represents a reduction of 80% of detections, a percentage that is greater if other filters are taken into consideration. This result is comparable with the artifact density found by Sánchez et al. (2022), which also uses a strategy to ensure high quality template images, with the difference that we use straightforward modifications with real data.

Another measure of the impact of our contributions is the proportion of positive and dipole labeled DIASources. Firstly, we obtained around 85% of positive labeled DIASources, against only 24% before our additions. We were also able to reduce the number of dipoles from 40% to 9%. Similar reductions in artifacts and fringes are measured, as illustrated by Figure 5.

By enhancing the quality of the inputs we reduce the total number of detections while yielding higher quality transient-like candidates.

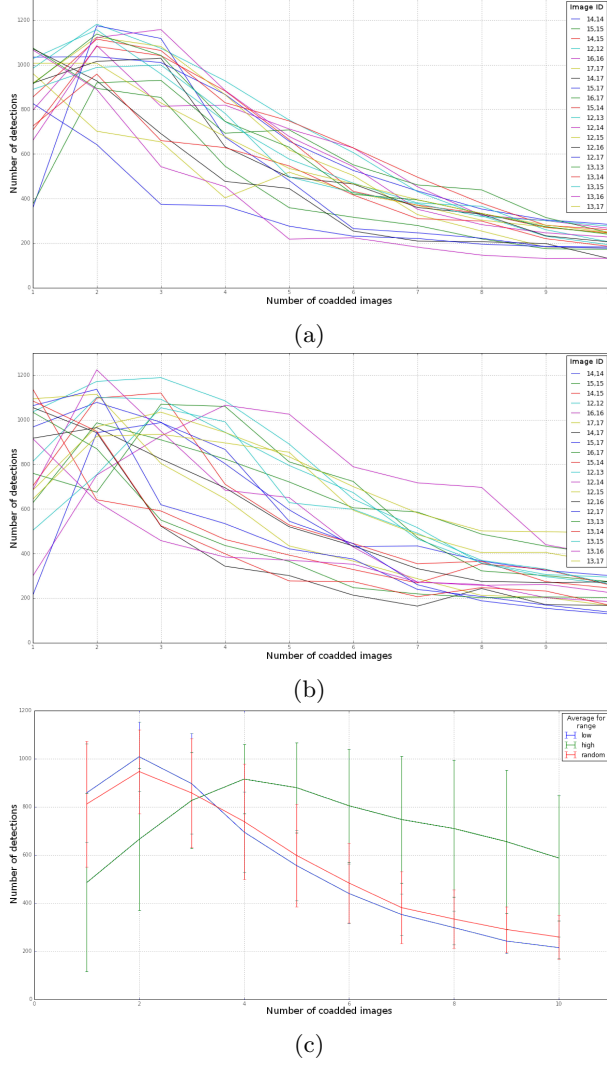


Fig. 6. Analysis of the number of detections with different amounts of coadded images using Input Selection to coadd images with: (a) low variance inputs and (b) random variance inputs. (c) Analysis of the number of average detections for low, high and random variance input coadded images. Image ID indicates the location of the image in the skymap. The color figure can be viewed online.

#### 4.3. Candidate Selection

We present the results of selecting SNIa candidates in the pipeline with the different options presented with simulated and real data.

##### *Real data*

When we tested our pipeline with real data (CFHT images), it preserved among the candidates 85% of the supernovae reported by SNLS (64 out of 75).

We also determined the quality of the supernova-like candidates by measuring the proportions of

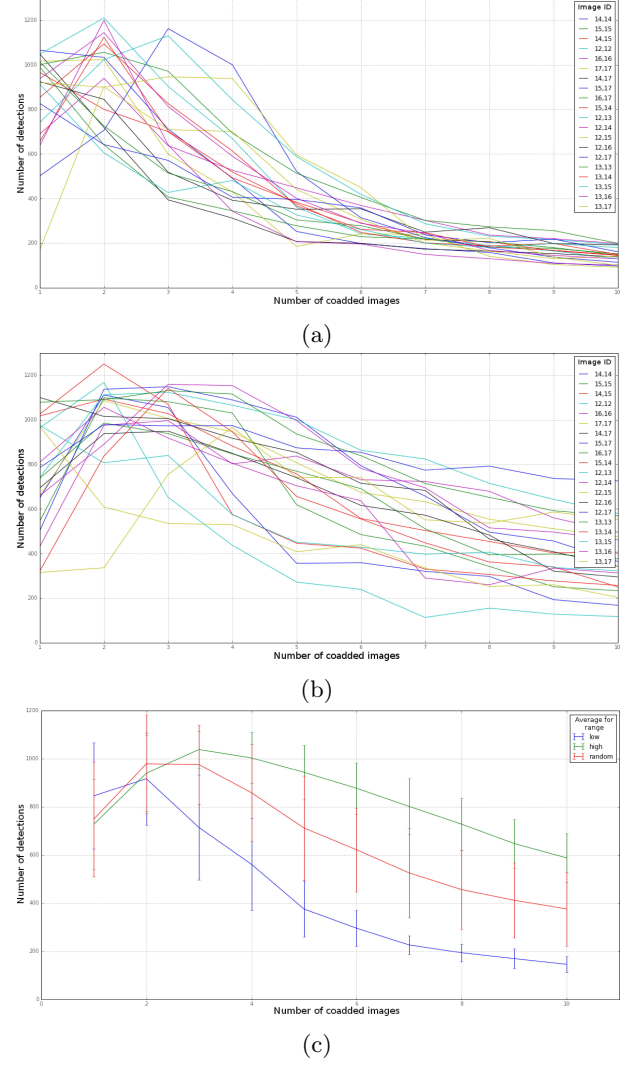


Fig. 7. Analysis of the number of detections with different amounts of coadded images using Input Selection to coadd images with: (a) low PSF Radius inputs and (b) random PSF Radius inputs. (c) Analysis of the number of average detections for low, high and random PSF Radius input coadded images. Image ID indicates the location of the image in the skymap. The color figure can be viewed online.

DIASource labels per object. Results on the CFHT images show that, before Input Selection, at least 33% of the objects presented light curves with 70% or more detections labeled as artifacts, whereas after the Input Selection only around 6% presented this property. For the dipoles, the difference was less stringent, as some of the built light curves still had a mixture of dipole and positive detections, that can be probably attributed to subtraction problems and other imaging issues.



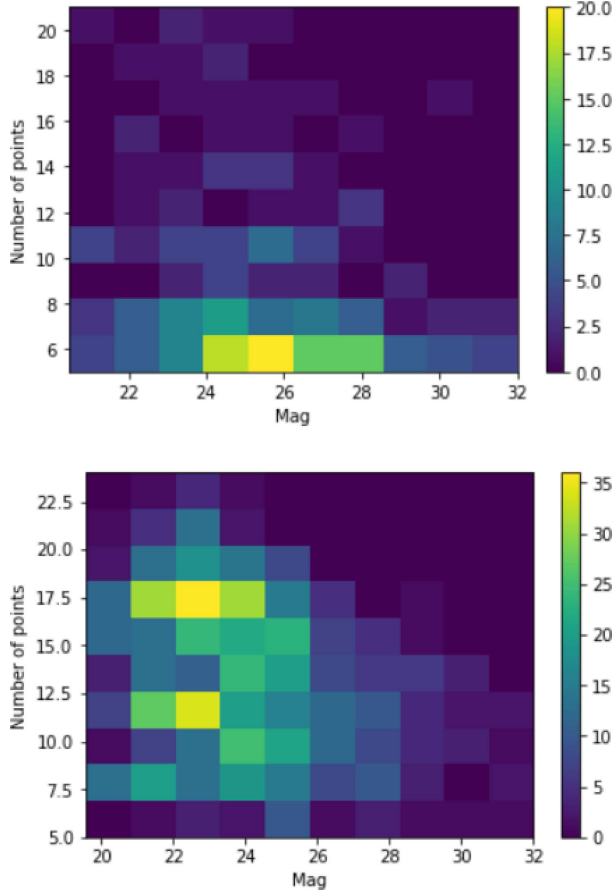


Fig. 8. Heatmap of light curves per configuration of maximum magnitude values vs number of points for the simulated curves that were not found (Top) and the simulated curves that were successfully found by the algorithm (Bottom). The color figure can be viewed online.

Before Input Selection, the distribution of positives per light curve was so low that there were no strong candidates with this quality. Our results show that 72% of the light curves have 80% of DIASources labeled as positive. The reduction of the number of artifacts with the extra options of the pipeline is notable: originally, at least 33% of objects we obtained have light curves with 70% or more detections that were labeled as artifacts, whereas for our pipeline only less than 1% presented this quality.

#### *Simulated Data*

In the case of simulations, we tested the Candidate Selection by injecting 5000 artificial supernovae. While obtaining 80% less total detections, we were able to find 75% of the injected supernovae. By creating simulations that avoided injecting SNIa too near the edges of patches we were able to increase the

number of found SNIa to between 75% and 78%. The detection efficiency drops at a redshift of about 0.8.

Figure 8 illustrates that most of the light curves that were not found by the algorithm have a low number of individual points and a considerable number of high magnitude points. These qualities make these curves more susceptible to be missed, thus reducing the overall efficiency. By using curves with points with a lower magnitude, and a slightly higher number of points, we improved the pipeline’s response to the simulated events.

The results in this case are highly dependant on the simulated curves and the magnitude used. It is possible to vary the threshold to allow more candidates, at the cost of more spurious candidates.

The distribution of positive residuals among the simulated type Ia supernova light curves showed that 95% of these detected supernovae had at least 90% or more of their individual detections labeled as positive residuals. Thus, they have an overall higher quality and demonstrate that we are able to obtain a cleaner candidate set.

It is important to notice that, even if we are able to greatly reduce the load by sacrificing some accuracy, other works provide better insights on how to improve these results. For instance, Goldstein et al. (2015) use machine learning methods to reduce by 11% the load of candidates to evaluate with a loss of only 1%. We also believe that an adapted threshold for detection might mitigate this loss, at the cost of augmenting again the number of candidates.

Given the fact that the proportion of positive labels among all objects rose in the light curves we obtained, we assert that our enhancements go in the right direction. Reducing the number of DIASources and increasing their quality provides a more accurate detection of transients. This accuracy is not only susceptible to increase by applying methods to automatically classify SNIa, but also when using high quality datasets with strategies such as Input Selection.

#### *4.4. Type Ia Supernova Identification*

In order to assess the efficiency of the algorithm to classify candidate light curves in two classes, SNIa or non-supernova objects, we used:

- A balanced training set composed of 1333 simulated light curves of each class (simulated SNIa and real non-SNIa light curves).
- An unbalanced validation set that contains 1404 simulated supernovae and 444 real non-

TABLE 5

RESULTS OF THE MACHINE LEARNING BINARY CLASSIFICATION OF SUPERNOVAE AND NON-SUPERNOVAE OBJECTS\*

Test	F1-score	Precision	Recall	AUC
Base features in filter $r$	0.899	0.853	0.950	0.983
All features in filter $r$	0.911	0.883	0.941	0.984
Base features in all filters	0.951	0.958	0.943	0.995
All features in all filters	0.960	0.970	0.949	0.996

\*Using simulated data: 1404 simulated supernovae and 444 real non-supernova light curves.

TABLE 6

RESULTS OF THE MACHINE LEARNING BINARY CLASSIFICATION OF SUPERNOVAE AND NON-SUPERNOVAE OBJECTS\*

Test	F1-score	Precision	Recall	AUC
Base features in filter $r$	0.744	0.690	0.807	0.968
All features in filter $r$	0.754	0.650	0.900	0.971
Base features in all filters	0.901	0.926	0.876	0.996
All features in all filters	0.918	0.891	0.946	0.997

\*Using real data: 130 oversampled instances of 75 real supernovae and 444 real non-supernova light curves.

supernova light curves randomly selected from photometric classification from previous analyses. Table 5 shows the classification results for this set.

- A second validation set consisting of 130 real SNIa light curves and 444 real non-supernovae light curves. To supply the real SNIa light curves we use the 75 real SNIa instances detected by SNLS and then we oversampled to generate the remaining ones using the technique described by Neira (2020). Table 6 depicts the results for this set.

The classification algorithm had an f-score of 0.899 and 0.744 on simulated and real data respectively, using only the original base features proposed by Neira (2020). When using the base features, the features we added and light curves with detection on several filters, we went from an f-score of 0.911 and 0.901 up to 0.960 and 0.918 for simulated and real data respectively. In both cases there was a slight improvement in the classification performance.

We also calculated the comparative ROC curves for simulated data using the base features and our new features. Figures 9 and 10 show the comparison of the curves when classifying light curves in all filters and in one selected filter. Here, a marginal improvement was still noticeable when expanding the features for the classification. Additional research is necessary to keep finding the ideal combination while also reducing

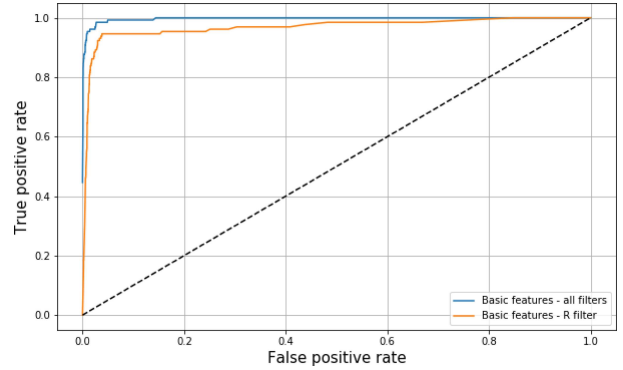


Fig. 9. ROC curve for the efficiency of the classification using only base features with information from the filter  $r$  (orange) and information from all the filters (blue). The color figure can be viewed online.

the number of features and still maintaining a high classification performance.

The importance of all features is shown in Figure 11. The selected features, already studied by Neira (2020), proved to be effective. With a 97% precision on other simulated curves and a 89% precision on real supernovae, we can see that the classification with new features was successful, even if the contribution to the efficiency was small. As a matter of fact, even with the possible issues with the flux of simulated supernovae on images, this performance on

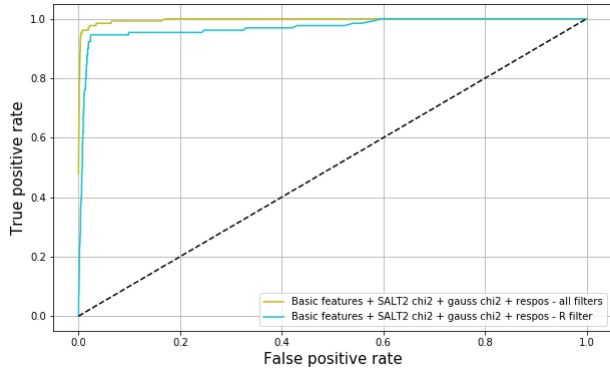


Fig. 10. ROC curve for the efficiency of the classification using all features with information from the filter  $r$  (blue) and information from all the filters (green). The color figure can be viewed online.

a real dataset indicates that the algorithm remains flux invariant.

When compared with similar classification methods such as the ones proposed by Pasquet et al. (2019) and Muthukrishna et al. (2019), our results were in line with these works in terms of the AUC values. While we obtained between 0.971 and 0.997 for real data and 0.984 and 0.996 for simulated data and, Pasquet et al. (2019) reported between 0.984 and 0.996 for simulated and real data in three different datasets similar to the CFHT ones, whereas Muthukrishna et al. (2019) obtained between 0.940 and 0.970, using the PLAsTiCC dataset (The PLAsTiCC team et al. 2018). Both works used deep learning and included more source characteristics such as photometric redshift. Further comparisons might be needed using similar datasets; however, we do show that quality improvements along the pipeline and an increase in the amount of information available to find light curves impact positively the results for SNIa detection. We are cautiously optimistic about these results, as they may open new research paths on this subject, in particular, applying these ideas to classify more kinds of supernovae and even other types of transients.

## 5. CONCLUSIONS

In this paper we presented an exploration of possible optimizations for type Ia supernovae detection using the LSSTsp as a base tool. Using this framework, we focused our contributions on studying some changes to the Generation of Difference Images, the Candidate Selection, and the Type Ia Supernova Identification stages.

Our studies demonstrates the importance of fine-tuning a transient detection pipeline through improving the quality of inputs, and consequently, helping the pipeline detect and classify candidates.

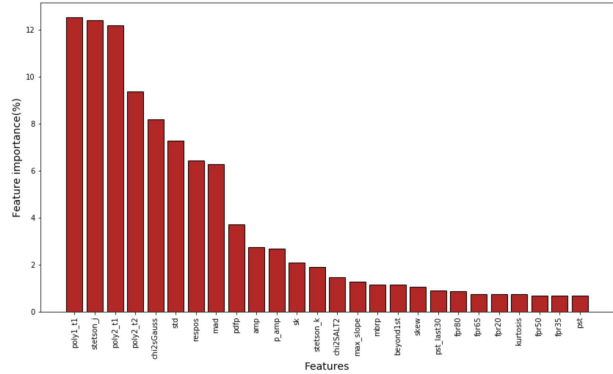


Fig. 11. Feature importance for binary classification of supernovae. The new features (chiSALT, chi2sGauss and respos) have variable non-negligible importance on the classification. The color figure can be viewed online.

We have achieved a relatively high efficiency in the identification of Type Ia Supernovae, and we have showcased how a framework such as the LSSTsp could be used to leverage new studies and open the door to new possibilities exploring the intersection between the application of computational methods, machine learning, and image processing to astronomical surveys.

Overall, we presented different approaches, tweaks, and adaptations to traditional transient detection pipelines. We believe our results are significant enough to justify further exploration in this area.

This work was possible thanks to the financing of the Administrative Department of Science, Technology and Innovation of Colombia (Colciencias), and the “Becas de doctorado - convocatoria 617”.

This work was also financed by the Eiffel scholarship program of excellence for PhD students.

This paper makes use of software developed for the Large Synoptic Survey Telescope. We thank the LSST Project for making their code available as free software at <http://dm.lsst.org>.

This work has also been carried out thanks to the support of the OCEVU Labex (ANR-11-LABX-0060) and of the Excellence Initiative of Aix-Marseille University - A\*MIDEX, part of the French “Investissements d’Avenir” programme.

## REFERENCES

- Aihara, H., Arimoto, N., Armstrong, R., et al. 2018, PASJ, 70, S4. <https://doi.org/10.48550/arXiv.1704.05858>
- Alard, C. & Lupton, R. H. 1998, ApJ, 503, <https://doi.org/10.48550/arXiv.astro-ph/9712287>

- Alard, C. 2000, *A&AS*, 144, 363. <https://doi.org/10.1051/aas:2000214>
- Axelrod, T., Kantor, J., Lupton, R. H., et al. 2010, *Proc. SPIE*, 7740, 774015. <https://doi.org/10.1117/12.857297>
- Bazin, G., Ruhlmann-Kleider, V., Palanque-Delabrouille, N., et al. 2011, *A&A*, 534, A43. <https://doi.org/10.1051/0004-6361/201116898>
- Becker, A. 2015, *Astrophysics Source Code Library*. <https://www.ascl.net/1504.004>
- Betoule, M., Kessler, R., Guy, J., et al. 2014, *A&A*, 568, A22. <https://doi.org/10.1051/0004-6361/201423413>
- Boone, K. 2019, *AJ*, 158, 257. <https://doi.org/10.3847/1538-3881/ab5182>
- Bosch, J., Armstrong, R., Bickerton, S., et al. 2018, *PASJ*, 70, S5. <https://doi.org/10.1093/pasj/psx080>
- Goldstein, D. A., D’Andrea, C. B., Fischer, J. A., et al. 2015, *AJ*, 150, 82. <https://doi.org/10.1088/0004-6256/150/3/82>
- Guy, J., Astier, P., Baumont, S., et al. 2007, *A&A*, 466, 11. <https://doi.org/10.1051/0004-6361:20066930>
- Guy, J., Sullivan, M., Conley, A., et al. 2010, *A&A*, 523, A7. <https://doi.org/10.1051/0004-6361/201014468>
- Ivezić, Ž., Kahn, S. M., Tyson, J. A., et al. 2019, *ApJ*, 873, 111. <https://doi.org/10.3847/1538-4357/ab042c>
- Jurić, M., Kantor, J., Lim, K.-T., et al. 2017, *Astronomical Data Analysis Software and Systems XXV*, 512, 279
- Kantor, J., Axelrod, T., Becla, J., et al. 2007, *Astronomical Data Analysis Software and Systems XVI*, 376, 3
- Kessler, R., Bernstein, J. P., Cinabro, D., et al. 2009, *PASP*, 121, 1028. <https://doi.org/10.1086/605984>
- Kessler, R., Bassett, B., Belov, P., et al. 2010, *PASP*, 122, 1415. <https://doi.org/10.1086/657607>
- Kessler, R., Marriner, J., Childress, M., et al. 2015, *AJ*, 150, 172. <https://doi.org/10.1088/0004-6256/150/6/172>
- Muthukrishna, D., Narayan, G., Mandel, K. S., et al. 2019, *PASP*, 131, 118002. <https://doi.org/10.1088/1538-3873/ab1609>
- Neira, M., Gómez, C., Suárez-Pérez, J. F., et al. 2020, *ApJS*, 250, 11. <https://doi.org/10.3847/1538-4365/aba267>
- Pasquet, J., Pasquet, J., Chaumont, M., et al. 2019, *A&A*, 627, A21. <https://doi.org/10.1051/0004-6361/201834473>
- Perlmutter, S., Aldering, G., Goldhaber, G., et al. 1999, *ApJ*, 517, 565. <https://doi.org/10.1086/307221>
- Perrett, K., Balam, D., Sullivan, M., et al. 2010, *AJ*, 140, 518. <https://doi.org/10.1088/0004-6256/140/2/518>
- Riess, A. G., Filippenko, A. V., Challis, P., et al. 1998, *AJ*, 116, 1009. <https://doi.org/10.1086/300499>
- Sako, M., Bassett, B., Becker, A. C., et al. 2018, *PASP*, 130, 064002. <https://doi.org/10.1088/1538-3873/aab4e0>
- Sánchez, B. O., Kessler, R., Scolnic, D., et al. 2022, *ApJ*, 934, 96. <https://doi.org/10.3847/1538-4357/ac7a37>
- Scolnic, D. M., Jones, D. O., Rest, A., et al. 2018, *ApJ*, 859, 101. <https://doi.org/10.3847/1538-4357/aab9bb>
- Slater, C. 2016, *DM Technotes*, 2016. <https://doi.org/10.5281/zenodo.192828>
- Smith, M., D’Andrea, C. B., Sullivan, M., et al. 2020, *AJ*, 160, 267. <https://doi.org/10.3847/1538-3881/abc01b>
- The PLAsTiCC team, Allam, T., Bahmanyar, A., et al. 2018, *arXiv:1810.00001*. <https://doi.org/10.48550/arXiv.1810.00001>

Dominique Fouchez: Centre de physique des particules de Marseille, Avenue de Luminy, 13009 Marseille, France (fouchez@cppm.in2p3.fr).

Marcela Hernández Hoyos and Juan Pablo Reyes: Systems and Computing Engineering Department, Universidad de los Andes, Bogotá, Colombia, Cra 1 N° 18A - 12, 111711, Bogotá, Colombia (marc-her, jp.reyes39@uniandes.edu.co).

## TESTING AN ENTROPY ESTIMATOR RELATED TO THE DYNAMICAL STATE OF GALAXY CLUSTERS

J. M. Zúñiga<sup>1</sup>, C. A. Caretta<sup>1</sup>, A. P. González<sup>2</sup>, and E. García-Manzanárez<sup>1</sup>

*Received February 23 2023; accepted January 12 2024*

### ABSTRACT

We propose the entropy estimator  $H_Z$ , calculated from global dynamical parameters, in an attempt to capture the degree of evolution of galaxy systems. We assume that the observed (spatial and velocity) distributions of member galaxies in these systems evolve over time towards states of higher dynamical relaxation (higher entropy), becoming more random and homogeneous in virial equilibrium. Thus, the  $H_Z$ -entropy should correspond to the gravitational assembly state of the systems. This was tested in a sample of 70 well sampled clusters in the Local Universe whose gravitational assembly state, classified from optical and X-ray analysis of substructures, shows clear statistical correlation with  $H_Z$ . This estimator was also tested on a sample of clusters (halos) from the IllustrisTNG simulations, obtaining results in agreement with the observational ones.

### RESUMEN

Proponemos el estimador de entropía  $H_Z$ , calculado a partir de parámetros dinámicos globales, en un intento de capturar el grado de evolución de los sistemas de galaxias. Asumimos que las distribuciones (espaciales y de velocidad) observadas de galaxias miembros de estos sistemas evolucionan en el tiempo hacia estados de mayor relajación dinámica (mayor entropía), y se vuelven más aleatorias y homogéneas en el equilibrio virial. Así, la entropía  $H_Z$  debería corresponder con el estado de ensamblaje gravitacional de los sistemas. Esto se probó en una muestra de 70 cúmulos bien estudiados del Universo Local, cuyo estado de ensamblaje gravitacional, clasificado a partir del análisis óptico y de rayos X de las subestructuras, mostró una clara correlación estadística con  $H_Z$ . Este estimador también se probó en una muestra de cúmulos (halos) de las simulaciones IllustrisTNG, y se obtuvieron resultados acordes con los obtenidos para los cúmulos observados.

*Key Words:* equation of state — galaxies: clusters: general — galaxies: kinematics and dynamics — galaxies: statistics — gravitation

### 1. INTRODUCTION

Galaxies are not uniformly distributed in the Universe, instead they undergo gravitational clustering that leads to an intricate three-dimensional structure in the shape of a network of knots, filaments, walls and voids (Libeskind et al. 2018). This cosmic web, revealed in both the observed distribution of galaxies (Geller & Huchra 1989; Santiago-Bautista et al. 2020) and in cosmological simulations (Davis et al. 1985; Springel et al. 2005), is called

the Large-Scale Structure of the Universe (LSS, Peebles 1980; Einasto 2010), and contains systems of galaxies at different scales embedded in it (Einasto et al. 1984; Cautun et al. 2014). Such systems go from small groups, like the Local Group that hosts the Milky Way, to superclusters, the largest and youngest coherent structures formed under gravitational influence in the Universe (reaching up to  $\approx 100$  Mpc long, e.g., Oort 1983; Böhringer & Chon 2021).

Knot-shaped regions, that is, quasi-spherical overdensities of galaxies with radii ranging from  $\approx 1.0$  to  $\approx 5.0$  Mpc, are commonly known as galaxy

<sup>1</sup>Departamento de Astronomía, Universidad de Guanajuato, México.

<sup>2</sup>Departamento de Matemáticas, Universidad del Cauca, Colombia.

groups or clusters. If we define the galaxy system richness in terms of galaxies with masses of the order of the Milky Way or greater, it is usually considered that groups have between 3 and 30 galaxies, poor clusters have between 30 and 50 galaxies, and rich clusters have more than 50 galaxies, counting them over a projected sky area of radius  $R_A \approx 2.1$  Mpc according to the criteria first proposed by Abell (1958) (see also, Abell et al. 1989; Bahcall 1996). However, this classification is only an *ad hoc* criterion since there is actually a continuum in the richness of these systems and their physical limits are uncertain. A more elegant and physically motivated way to characterize clusters is to define them based on their expected virialized zones, that is, as galaxy regions where the mean density is  $\Delta_c$  times the critical density of the Universe at the considered redshift (typical values are  $\Delta_c \approx 100 - 200$ , e.g., Carlberg et al. 1997b; Bryan & Norman 1998; Tully 2015), which provides better estimates of their mean dimensions and dynamical properties in the cosmology used.

The baryonic —stellar and gaseous— matter contained in galaxies and in the form of intracluster X-ray emitting hot gas (intracluster medium, ICM, e.g., Böhringer & Werner 2010) is estimated (White 1992; Lima-Neto et al. 2005) to account for only 15% of the total mass of a galaxy system, while the remaining 85% is provided by the dark matter (DM). Nevertheless, as a first approximation, one can consider a group/cluster as a collisionless ensemble of galaxies moving in the mean gravitational field generated by its total mass (e.g., Schneider 2015). In this context, galaxies may be taken as fundamental observational tracers (or primary units, e.g., Padmanabhan 1993) of the global dynamical properties of the galaxy system.

The process of formation and evolution of a cluster from a matter density perturbation to a galaxy system in dynamical equilibrium is driven both by the initial cosmological conditions and by various physical and stochastic mechanisms (Binney & Tremaine 2008). Initially, both the homogeneous background and the matter perturbation expand with the Hubble flow; however, a fraction of this matter condenses into a set of galaxies that decouple from the expansion. The cluster itself, in the course of time, decouples from the expansion, forming now a gravitationally bound system, which turns around and begins a process of collapse that ends in an eventual virialization (Gunn & Gott III 1972). This is a state of statistical equilibrium of internal gravitational forces, reflected in the averages of the total kinetic and potential energies of galaxies (Lim-

ber & Mathews 1960). Analyzing the transitory evolutionary state of galaxy systems is not a trivial task, even when gravity is the sole driving force shaping their evolutionary processes. Here, we use the term ‘evolutionary state’ to refer to the degree of progress a galaxy system has in its evolutionary line, starting from its formation and ending at equilibrium (relaxation).

In this work we present a method to characterize the evolutionary state of galaxy systems by estimating the entropy component that depends only on the macroscopic state of their galaxy ensembles. For this, we propose a specific entropy estimator ( $H_Z$ ) that combines (optical) observational parameters of the systems such as virial mass, volume, and galaxy velocity dispersion. Our fundamental premise is that a galaxy ensemble should evolve in the sense of increasing entropy, modifying its distribution of galaxies in the observed phase-space (which includes radial, angular and velocity coordinates) to a more random and dynamically relaxed one where there are no macroscopic movements or special configurations (Landau & Lifshitz 1980; Saslaw & Hamilton 1984). This means that the spatial and velocity distributions of member galaxies change as the system evolves, starting from more substructured ensembles (with less entropy) towards more homogeneous ones in dynamical relaxation (with higher entropy). Of course, the parameters associated with the global dynamics of the system also change in the process, and may be useful for the estimation of state functions such as entropy. No assumption is made here about the distribution of DM and ICM within the cluster (Lokas & Mamon 2003; Lima-Neto et al. 2005), but only about their important contribution to the total gravitational potential that determines the dynamics of the galaxy ensemble.

To evaluate the  $H_Z$ -entropy estimator we make use of different tests. The first is the comparison between  $H_Z$ -entropy estimator and a discrete classification of assembling states applied to an observational samples of 70 nearby clusters ( $z \lesssim 0.15$ ). The second test is the calculation of the Shannon entropy, which provides a quantitative measure of the degree of disorder (or uncertainty) in the distribution of galaxies in different regions within each cluster phase-space. Substructures are considered as special configurations and their presence reduces the Shannon entropy, so more relaxed systems (with a more random galaxy distribution in the phase-space) are expected to have higher entropies. In this test, galaxy systems are considered as data sets whose information entropies can be calculated. Both the observational

cluster sample and another from simulated cluster halos, with their respective subhalos, are used to compare  $H_Z$  and Shannon entropies. As complementary validations, different approaches are used, including the analysis of the relaxation probability of the systems (based on statistical distances between empirical and reference galaxy distributions) and the study of correlations between  $H_Z$  and other continuous parameters commonly associated to the dynamical state of the systems.

In § 2, we extend the discussion about the dynamical equilibrium and stability of galaxy clusters, together with a brief description of the way evolutionary state is commonly characterized from observed and simulated data. In § 3, we focus on the entropy-based estimator and present our proposal to quantify the dynamical state of galaxy systems. In § 4, we apply our method to a sample of 70 well-sampled galaxy clusters in the nearby Universe, from very rich to poor ones. In § 5 we calculate the Shannon entropy for both the observational sample and a sample of 248 cluster halos from the IllustrisTNG simulation. Then, we compare this parameter with  $H_Z$ . Other dynamical parameters are evaluated in § 6 also for validating  $H_Z$ . Discussion and conclusions are presented in § 7. Throughout this paper we assume a flat  $\Lambda$ CDM cosmology with the following parameters: Hubble constant  $H_0 = 70 \text{ km s}^{-1} \text{ Mpc}^{-1}$ , matter density  $\Omega_M = 0.3$  and dark energy density  $\Omega_\Lambda = 0.7$ .

## 2. EVOLUTION, EQUILIBRIUM AND STABILITY OF GALAXY CLUSTERS

### 2.1. *Reaching Virial Equilibrium*

The evolution of galaxy systems at various scales is understood today through the hierarchical formation model (Peebles 1980; Padmanabhan 1993; Zakhozhay 2018) in a  $\Lambda$ CDM scenario. According to this model, the smallest systems (galaxy groups and poor clusters) merge —via gravity— to form the largest ones (rich clusters and superclusters), being the observed substructuring a consequence of this process. Subsequently, these galaxy ensembles undergo a non-linear gravitational collapse during which a combination of physical and stochastic mechanisms (Lynden-Bell 1967; Saslaw 1980; Padmanabhan 1990) drive the systems into a further state of dynamical relaxation —the virial equilibrium— in which their substructures vanish (Araya-Melo et al. 2009).

Galaxy clustering is an irreversible process where, as galaxies accumulate, different mechanisms tend to increase the number of ways in which, in a statistical sense, internal energy can be distributed within the systems (Saslaw 1980; Saslaw & Hamilton 1984). Once bound and during collapse, the galaxy system undergoes internal —dissipationless— processes (e.g., violent relaxation, phase mixing, energy equipartition, galaxy mergers, fading of substructures and density or temperature gradients, among others, see, White 1996; Dehnen 2005; Binney & Tremaine 2008) that lead to states of greater dynamical relaxation. All these processes are dominated by gravitational interactions that, during the relaxation time, tend to homogenize the spatial distribution of the member galaxies and to distribute their radial velocities in a Gaussian way —inside the clusters, galaxies are scattered randomly (achieving a quasi-Maxwellian velocity distributions as they tend to virialization, e.g., Saslaw & Hamilton 1984; Sampaio & Ribeiro 2014), causing the tendency for macroscopic motions to disappear. This requires the individualization of the motions of the galaxies, so that any substructure (e.g., accreted groups) will be ‘dissolved’ before the cluster virializes. The thermodynamic perturbations and the changes in the distribution of the ICM inside the clusters during their evolution also produce increases in the total entropy of these systems (Tozzi & Norman 2001; Voit 2005).

The equilibrium state can be understood, in a first approximation, as that in which the gravitational collapse is supported by the effect of inertial —centrifugal or dispersion— forces, achieving relaxed internal configurations (called states of dynamical relaxation), that is, in which there are no unbalanced potentials, such as gravitational-driving forces, within galaxy systems. In this sense, collisionless systems in equilibrium are analogous to self-gravitating fluids because they support gravitational collapse through “pressure gradients” proportional to the velocity dispersion that, at each point, tend to disperse any local increase in particle density (Binney & Tremaine 2008). Furthermore, dynamical equilibrium is characterized by the statistical equality of the cluster mass profiles obtained from different galaxy populations within the cluster (Carlberg et al. 1997a), implying that all these populations are in equilibrium with the cluster potential according to the hydrodynamical equilibrium model by Jeans.

Throughout the evolution of an isolated cluster, its total internal energy  $U = K + W$  is conserved so that, as the member galaxies get closer together (spontaneous reduction of inter-particle distance  $r_{ij}$



by mutual attraction), the gravitational potential energy  $W$  decreases (becoming more negative) and consequently the total internal kinetic energy  $K$  increases. This is reflected observationally as an increase in the velocity dispersion of galaxies, which can stop the collapse. Thus, when the system finds some route to dynamical equilibrium, the increase in  $K$  at the expense of the decrease in  $W$  does not continue indefinitely, but evolves toward configurations in which the ratio

$$b = -\frac{W}{2K}, \quad (1)$$

tends to one ( $b \rightarrow 1$ , Saslaw & Hamilton 1984; Binney & Tremaine 2008). The asymptotic limit,  $b = 1$ , of this tendency is the virial equilibrium:

$$W = -2K, \quad (2)$$

a state in which dynamical parameters that characterize the global configuration of the system remain, at least temporarily, stationary (relaxed). The virial theorem expresses a statistical equilibrium between the temporal averages of the total internal kinetic and gravitational potential energies, *i.e.*,  $\langle W \rangle_\tau = -2\langle K \rangle_\tau$ , but these energies are also the result of an ensemble of interacting galaxies (Limber & Mathews 1960), so it is reasonable to approximate the temporal averages by the average of the ensemble expressed in (2). Virial equilibrium is assumed to be the type of dynamical equilibrium reached by self-gravitating systems.

## 2.2. Stability

Going beyond the description of equilibrium in galaxy systems, we need to discuss if this equilibrium is stable and this topic requires involving the concept of ‘entropy’. As any thermodynamic system, self-gravitating systems progress in the sense of increasing entropy (Lifshitz & Pitaevskii 1981; Tremaine, Hénon & Lynden-Bell 1986; Pontzen & Governato 2013) towards the state of dynamical equilibrium described above. Galaxy clustering simulations also confirm this fact (Saslaw & Hamilton 1984; Iqbal et al. 2006, 2011). Due to the scattering experienced by galaxies in the phase-space of clusters, these become the regions within the LSS where first-order entropy production occurs by increasing the randomness of the motion of galaxies during their gravitational accumulation. Even if galaxy clusters are isolated, some entropy is generated—or produced—due to the presence of internal irreversibilities. The peculiarity here is that the virial equilibrium is not unique, but only a *metastable equilibrium state*

(Antonov 1962; Lynden-Bell & Wood 1968; Padmanabhan 1990; Chavanis et al. 2002). This means that the entropy of self-gravitating systems can grow indefinitely without reaching a global maximum, that is, the virial equilibrium is only a state of local extreme of entropy (Padmanabhan 1989).

The dynamical equilibrium of a galaxy cluster can be disturbed if it actively interacts with its surroundings, for example through mergers with other clusters and/or group accretions or tidal forces. As a result, the cluster takes a route towards a new equilibrium, in a state of higher entropy. Concerning the impact of the interaction, if the accreted groups are very small, the clusters can be kept unperturbed in states close to equilibrium. In more extreme cases, the merger of two massive clusters completely removes the systems from their equilibrium. In dense environments, such as supercluster cores, the accretion of galaxies and groups by the most massive clusters continually disturbs their dynamical states. On the other hand, in less dense environments, such as along filaments or edges near voids, clumpy clusters evolve as quasi-isolated systems, reaching dynamical relaxation possibly faster, without many significant disturbances, but accessing lower entropy levels compared to clusters in “busy” environments. That is, depending on the cosmological environment inside the LSS in which a cluster evolves, its relaxation process may be affected several times—or not—given the amount of matter available in its surroundings.

The most stable states of a galaxy cluster—of mass  $\mathcal{M}$  and radius  $R$ —are favored when the density contrast between its center and its edge is  $\rho_0/\rho(R) < 709$  and the internal energy is  $U > -0.335G\mathcal{M}^2/R$  (the Antonov instability or gravothermal catastrophe, Antonov 1962; Lynden-Bell & Wood 1968), and under these conditions the virial equilibrium corresponds to a local maximum of entropy (Padmanabhan 1989, 1990). In fact, the most stable dynamical configurations that self-gravitating systems can access are those in which the particle—or matter—distribution settles on a core-halo structure (Binney & Tremaine 2008; Chavanis et al. 2002). This theoretical structure, characterized by a collapsed core coexisting with a regular halo, has also been confirmed by simulations (Cohn 1980; Balberg, Shapiro & Inagaki 2002) and recognized by the distributions of galaxies (Sarazin 1988; Adami et al. 1998) and the ICM in observed clusters (Tozzi & Norman 2001; Cavagnolo et al. 2009).

### 2.3. Estimating the Evolutionary State of Galaxy Systems

Observationally, a cluster close to dynamical equilibrium is distinguished from a non-relaxed one by exhibiting a more regular morphology (Sarazin 1988), both in the optical and X-rays, and a more homogeneous —projected— spatial distribution of member galaxies (without the presence of significant substructures, Caretta et al. 2023, and references therein), as well as by having a more isotropic galaxy velocity distribution (or Gaussian in the line-of-sight, Girardi & Mezzetti 2001; Sampaio & Ribeiro 2014).

Concerning global morphology, the most dynamically relaxed clusters tend to present low ellipticity shapes in the projected distribution of galaxies and X-ray surface brightness maps, with a —possible— single peak at their centers. Several morphological classifications have been proposed following this premise (Sarazin 1988, and references therein). There are also indicators of the internal structure of the galaxy systems, such as the radial profile and the degree of concentration of galaxies (Adami et al. 1998; Tully 2015; Kashibadze et al. 2020), as well as a measure of the presence of substructures within them using 1D, 2D and 3D tests (Geller & Beers 1982; Dressler & Shectman 1988; Caretta et al. 2023).

In this sense, a significantly substructured system, either from optical observation of galaxy subclumps (e.g., Geller & Beers 1982; Bravo-Alfaro et al. 2009; Caretta et al. 2023) or the detection of multiple peaks in X-ray emission (e.g., Jones & Forman 1984; Buote & Tsai 1995; Laganá et al. 2019), cannot be considered in dynamical equilibrium. Thus, the presence and significance of substructures reveal how far the galaxy system is from a relaxed and homogeneous global potential. A description of the cluster level of internal structuring is called its gravitational assembly state (Caretta et al. 2023).

In principle, one can also measure global parameters related to the internal dynamics (Carlberg et al. 1996; Girardi & Mezzetti 2001) —or dynamical state— of the galaxy system. These parameters are associated, for example, with the mass, radius and velocity dispersion of the system. Such approach supposes that both the observable aspect and structure and the dynamical parameters of the system change in a correlated manner during its evolution, dominated by mechanisms that take it from more irregular and substructured configurations to those with more homogeneous galaxy distributions and more dynamically relaxed (Araya-Melo et al. 2009).

Furthermore, from X-ray observations one can construct entropy (or temperature or density) profiles that account for the evolutionary history, structure and thermodynamic state of the ICM inside the clusters (Tozzi & Norman 2001; Voit 2005; Cavagnolo et al. 2009), which also contributes to the study of the degree of relaxation —or disturbance— of their gravitational potentials (analysis of self-similarity of clusters). Nevertheless, we are not always fortunate enough to detect X-ray emission from clusters nor to have the amount of data necessary to carry out massive studies, so for this we are still limited to optical surveys.

### 3. ENTROPY OF GALAXY SYSTEMS FROM GLOBAL PARAMETERS

Based on the ‘classical’ concept of entropy of a particle system, it is possible to construct an estimator for the entropy component related to the set of member galaxies of a cluster, the ‘galaxy ensemble’. The depth of the cluster’s global potential well, which determines how fast the bound galaxies must move, is proportional to the total mass of the cluster that can be estimated, with negligible bias (see, Biviano et al. 2006), by the virial mass estimator

$$\mathcal{M}_{\text{vir}} = \frac{\alpha\pi}{2G}\sigma_{\text{LOS}}^2 R_p, \quad (3)$$

where  $\sigma_{\text{LOS}}$  is the line-of-sight (LOS) velocity dispersion of the sampled galaxies,  $\alpha$  is a deprojection parameter for  $\sigma_{\text{LOS}}$  assuming anisotropy in the galaxy velocity distribution ( $\alpha = 3$  if orbits have an isotropic and isothermal distribution, e.g., Tully 2015, and references therein), and

$$R_p = \frac{N(N-1)}{\sum_{k<l} 1/R_{kl}}, \quad (4)$$

is the projected mean radius of the distribution of cluster galaxies, where  $R_{kl}$  is the projected distance (in Mpc) between pairs of the  $N$  sampled galaxies. The factor  $\pi/2$  in (3) is the radius deprojection factor (Limber & Mathews 1960) so that statistically  $R_{\text{vir}} \simeq \pi R_p/2$  is the three-dimensional virial radius of the cluster (Carlberg et al. 1996; Girardi & Mezzetti 2001), a measure of the region of gravitational confinement of its member galaxies.

Now, as a first approximation, we can imagine the set of cluster galaxies as a system of particles with mean kinetic energy (Schneider 2015)

$$K = \frac{\alpha}{2}\mathcal{M}_{\text{vir}}\sigma_{\text{LOS}}^2, \quad (5)$$

and confined in a region of volume

$$V = \frac{4}{3}\pi R_{\text{vir}}^3. \quad (6)$$

We assume that the velocity dispersion of galaxies is proportional to the ‘temperature’  $T$  of the galaxy ensemble<sup>3</sup>, so that  $\sigma_{LOS}^2 = \beta T$ , with  $\beta$  being a proportionality constant that transforms temperature units into squared velocity units. Furthermore, the mean ‘pressure’ of the galaxy ensemble, commonly approximated as  $P = \bar{\rho}\sigma_{LOS}^2$ , where  $\bar{\rho}$  is the mean mass density of the system (Schneider 2015), can be conveniently modified to the form  $P = \bar{\rho}\sigma_{LOS}^2(1 - 2b)$ , where the factor  $(1 - 2b)$  has been introduced to generalize the expression (see, for example, Saslaw & Hamilton 1984). Thus,  $P > 0$  for unbound systems ( $b = 0$ ), just like an ordinary gas of particles enclosed in a hypothetical sphere of volume  $V$  with no gravitational potential; while  $P < 0$  in self-gravitating bound systems ( $b > 0.5$ ). The mean value of the pressure in a marginal virial equilibrium ( $b \rightarrow 1$ ), for a system with  $\bar{\rho} = \mathcal{M}_{\text{vir}}/V$ , is

$$P = -\bar{\rho}\sigma_{LOS}^2 = -\frac{2K}{\alpha V}, \quad (7)$$

matching the definition of the so-called gravitational pressure (Padmanabhan 2000),  $P = W/3V$ , when  $\alpha \rightarrow 3$ .

In virial equilibrium, the internal energy of the galaxy ensemble is  $U = K + W = -K$ , according to (2). However, for any state of the system including those prior to equilibrium, the internal energy can be generalized, as in Saslaw & Hamilton (1984), in the form  $U = K(1 - 2b)$ , where, for unbound systems ( $b = 0$ ) the internal energy is only kinetic, while for bound and virialized systems ( $b \rightarrow 1$ ) we get the marginal value

$$U = -\frac{\alpha}{2}\mathcal{M}_{\text{vir}}\beta T, \quad (8)$$

where  $\sigma_{LOS}^2 = \beta T$ , as before. Note that the mean potential energy of the galaxy system does not appear explicitly in its ‘thermodynamic description’.

As can be inferred from (3), galaxy systems of fixed mass internally heat up ( $T$  increases) when they contract ( $R_{\text{vir}}$  decreases) and cool down ( $T$  decreases) when they expand ( $R_{\text{vir}}$  increases). In addition, from (8) it is possible to appreciate an atypical behavior of virialized self-gravitating systems. If we allow the galaxy systems to exchange energy—but not matter—with the environment, then they cool

down ( $dT < 0$ ) by receiving energy ( $dU > 0$ ) from the environment and warm up ( $dT > 0$ ) by releasing energy ( $dU < 0$ ) to it. These types of systems are said to have negative specific heats ( $dU/dT < 0$ , Lynden-Bell D. & Lynden-Bell R. 1977).

A fundamental expression of the form  $u = u(s, v)$ , which relates the specific variables  $u$ ,  $s$  and  $v$  of internal energy, entropy and volume respectively, must be satisfied by a single-component thermodynamic system (Saslaw & Hamilton 1984). Differentiating, we get that  $du = (\partial u/\partial s)_v ds + (\partial u/\partial v)_s dv$ , obtaining the standard Gibbs  $Tds$  relation  $du = Tds - Pdv$ , with  $T \equiv (\partial u/\partial s)_v$  and  $P \equiv -(\partial u/\partial v)_s$  being respectively the temperature and pressure of the system. Let  $u = U/\mathcal{M}_{\text{vir}}$ ,  $\kappa = K/\mathcal{M}_{\text{vir}}$ ,  $s = S/\mathcal{M}_{\text{vir}}$ , and  $v = V/\mathcal{M}_{\text{vir}}$  the specific variables per unit of mass for internal and kinetic energies, entropy and volume, respectively. It is evident that Gibbs  $Tds$  relation does not fit in its original form to self-gravitating systems. For ordinary systems of particles, both adiabatic compression ( $dv < 0$ ) and isocoric heat input from the environment ( $Tds > 0$ ) imply an increase in their internal energy ( $du > 0$ ). Instead, for self-gravitating system of particles, compressions imply ‘heating’ ( $dT, d\kappa > 0$ ), but with a decrease in internal energy ( $du < 0$ ), which leads to an increase in the entropy of the system ( $ds > 0$ ) according to the direction of the spontaneous process of gravitational accumulation.

It is necessary to use an expression analogous to the Gibbs  $Tds$  equation, but which conforms to the thermodynamic behavior of self-gravitating systems described above. In the considered galaxy ensemble the entropy increases along with the internal kinetic energy as they virialize (see, § 2). Then, we can impose that, in systems of point galaxies,  $s = s(\kappa, v)$  with differential form

$$ds = \left(\frac{\partial s}{\partial \kappa}\right)_v d\kappa + \left(\frac{\partial s}{\partial v}\right)_\kappa dv, \quad (9)$$

where, by analogy with the well-known thermodynamic expressions for temperature and pressure in the Gibbs  $Tds$  equation, we have

$$\left(\frac{\partial s}{\partial \kappa}\right)_v = \frac{1}{T}, \quad \text{and} \quad \left(\frac{\partial s}{\partial v}\right)_\kappa = \frac{P}{T}. \quad (10)$$

Note that, for self-gravitating galaxy systems in general, we need the  $1/T > 0$  and  $P/T < 0$  conditions to be satisfied. The last condition is required to obtain entropy increases during the gravitational collapse processes (in which the systems undergo contractions,  $dv < 0$ ). This suggests a negative pressure

<sup>3</sup>Thought, simplistically, as a system of point masses (particles).

in this type of systems (like systems in phase transitions or metastable states in liquids, e.g., Imre 2007) that causes a “repulsion” and prevents a singular collapse, just as proposed by the expression (7).

Finally, in order to obtain an estimator for the entropy of galaxy clusters, we will solve the system of differential equations (10) assuming that  $1/T = \alpha\beta/2\kappa$  and  $P/T = -\beta/v$ , obtained by combining (5) and (7). Thus, the solution can be verified to be of the form

$$s(\kappa, v) = \beta \ln(\kappa^{\frac{\alpha}{2}} v^{-1}) + s_0, \quad (11)$$

where  $s_0$  is an integration constant possibly related to the initial entropy of the galaxy ensemble, e.g., the entropy it had when the distribution of galaxies was not yet concentrated before gravitational clustering (see, § 2). Replacing the expressions  $\kappa = (\alpha/2)\sigma_{LOS}^2$  and  $v = (4/3)\pi R_{vir}^3 \mathcal{M}_{vir}^{-1}$  in (11) we get the dimensionless estimator

$$H_Z \equiv \frac{s - s_0}{\beta} = \ln\left(\frac{\mathcal{M}_{vir}}{\frac{4}{3}\pi R_{vir}^3}\right) + \frac{\alpha}{2} \ln\left(\frac{\alpha}{2}\sigma_{LOS}^2\right), \quad (12)$$

defined only in terms of observational parameters that can be obtained through optical data (e.g., galaxy coordinates and redshifts).

#### 4. TESTING THE $H_Z$ ENTROPY ESTIMATOR IN GALAXY SYSTEMS

##### 4.1. *Observational Data*

We use data from Caretta et al. (2023), a sample of 67 galaxy clusters, from Abell/ACO (Abell 1958; Abell et al. 1989) catalogs, with redshifts up to  $z \approx 0.15$ . These clusters were selected because they are among the most well sampled galaxy systems in the nearby Universe, and cover roughly uniformly from poor to rich systems (with ICM-temperatures from 1 to 12 keV), being balanced for including all BM (Bautz & Morgan 1970) types. Three other non-Abell clusters with similar characteristics were included in our sample (AM0227-334, SC1329-313 and MKW03S), which allows us to call (for short) our observational sample *Top70* from now on (Table 1). For each cluster, a sample of spectroscopically confirmed member galaxies is available, selected inside the cluster caustics up to a fiducial aperture of  $1.3 \times r_{200}$  from the center of the cluster (chosen to be the Central Dominant Galaxy, CDG). The numbers of these presumably virialized members range from 21 to 919 (average 154), while originally at least 100 spectroscopic redshifts were available for each cluster (see Caretta et al. 2023, for the details of the

process for determining membership, caustics and virial radius). One should note that the richness of a cluster is related to both intrinsic and observational conditions —more massive clusters are richer, while nearby clusters tend to be preferentially observed. However, the numbers of members we have are adequate for minimizing observational biases by counting them in bins. Astrometric positions of galaxies have uncertainties of  $\pm 0.25''$ , and radial velocities of  $\pm 60 \text{ km s}^{-1}$  (see, Caretta et al. 2023, and references therein).

By using different 1D, 2D and 3D methods (e. g., Dressler & Shectman 1988), applied to the distribution of the members inside the caustics, these authors searched for optical substructures in the cluster sample, supplementing their analysis with X-rays and radio literature data. They found that at least 70% of the clusters in their sample present clear signs of substructuring, with 57% being significantly substructured. The significance of the identified substructures in each cluster was estimated by the fraction of galaxies they contain with respect to the total richness.

The clusters were classified into five assembly state levels according to the presence —or not— and relative importance of substructures: unimodal systems, made up of a regular structure (U); low mass unimodal systems (L); systems with a primary structure and only low significance substructures (P); significantly substructured systems with one main substructure (S); and multimodal conglomerates with more than one main substructure (M). While the L clusters are young poor galaxy systems, representing evolutionary states prior to amalgamation processes but already relatively placidly evolved, the U clusters are old and massive, which have probably grown by mergers and accretions and have already settled close to a relaxation state. P clusters are also old and massive, but still present signs of recent accretions; since these accretions are minor, the relaxation state of the cluster is almost unaffected. Finally, S and M clusters are systems during merging processes, the difference being whether these mergers are minor or major, respectively.

The benefit of using this sample lies in the availability of this discrete classification of gravitational assembly states (see Column 2 of Table 2 below). This will serve to establish correlations between the  $H_Z$  estimator applied to the ensemble of galaxies of each cluster and the evolutionary state obtained from direct observational methods.

The observational cluster sample is reported in Table 1: Column 1 shows the name of clusters;

TABLE 1  
CLUSTER SAMPLE (TOP70)

Name <sup>a</sup>	Optical data				X-ray data <sup>b</sup>		Basic properties		
	RA <sub>CDG</sub> [deg] <sub>J2000</sub>	Dec <sub>CDG</sub> [deg] <sub>J2000</sub>	$\bar{z}$	$N_a$	$r_{500}$ [Mpc]	$kT_X$ [keV]	$\sigma_{LOS}$ [km/s]	$\mathcal{M}_{vir}$ [ $10^{14} \mathcal{M}_{\odot}$ ]	$R_{vir}$ [Mpc]
(1)	(2)	(3)	(4)	(5)	(6)	(7)	(8)	(9)	(10)
A2798B	9.37734	-28.52947	0.1119	60	0.7476	3.39	757	6.01	1.75
A2801	9.62877	-29.08160	0.1122	35	...	3.20	699	6.94	1.83
A2804	9.90754	-28.90620	0.1123	48	...	1.00	516	3.11	1.40
A0085A	10.46052	-9.30304	0.0553	318	1.2103	7.23	1034	19.75	2.65
A2811B	10.53718	-28.53577	0.1078	103	1.0355	5.89	947	13.94	2.32
A0118	13.75309	-26.36238	0.1144	72	...	...	680	6.16	1.76
A0119	14.06709	-1.25549	0.0444	294	0.9413	5.82	853	9.51	2.08
A0122	14.34534	-26.28134	0.1136	28	0.8165	3.70	677	4.98	1.64
A0133A	15.67405	-21.88215	0.0562	86	0.9379	4.25	778	7.30	1.90
A2877-70	17.48166	-45.93122	0.0238	112	0.6249	3.28	679	4.20	1.60
AM0227-334	37.33891	-33.53196	0.0780	30	...	...	625	4.11	1.56
A3027A	37.70601	-33.10375	0.0784	82	0.7200	3.12	713	7.52	1.90
A0400	44.42316	6.02700	0.0232	51	0.6505	2.25	343	0.68	0.87
A0399	44.47120	13.03080	0.0705	69	1.1169	6.69	950	11.65	2.21
A0401	44.74091	13.58287	0.0736	114	1.2421	7.06	1026	15.11	2.41
A3094A	47.85423	-26.93122	0.0685	84	0.6907	3.15	637	4.83	1.65
A3095	48.11077	-27.14017	0.0652	21	...	...	327	0.65	0.84
A3104	48.59055	-45.42024	0.0723	28	0.8662	3.56	498	1.77	1.18
S0334	49.08556	-45.12110	0.0746	26	...	...	534	2.11	1.25
S0336	49.45997	-44.80069	0.0773	32	...	...	538	3.02	1.40
A3112B	49.49025	-44.23821	0.0756	74	1.1288	5.49	705	8.45	1.98
A0426A	49.95098	41.51168	0.0176	314	1.2856	6.42	1029	13.50	2.36
S0373	54.62118	-35.45074	0.0049	98	0.4017	1.56	390	0.43	0.75
A3158	55.72063	-53.63130	0.0592	249	1.0667	5.42	1066	13.93	2.35
A0496	68.40767	-13.26196	0.0331	279	0.9974	4.64	712	6.31	1.82
A0539	79.15555	6.44092	0.0288	92	0.7773	3.04	698	3.92	1.56
A3391	96.58521	-53.69330	0.0560	75	0.8978	5.89	817	7.74	1.94
A3395	96.90105	-54.44936	0.0496	199	0.9298	5.10	746	6.42	1.82
A0576	110.37600	55.76158	0.0379	191	0.8291	4.27	866	11.18	2.20
A0634	123.93686	58.32109	0.0268	70	...	...	395	1.13	1.03
A0754	137.13495	-9.62974	0.0542	333	1.1439	8.93	820	9.10	2.05
A1060	159.17796	-27.52858	0.0123	343	0.7015	2.79	678	3.99	1.57
A1367	176.00905	19.94982	0.0215	226	0.9032	3.81	597	3.76	1.54
A3526A	192.20392	-41.31167	0.0100	126	0.8260	3.40	564	2.43	1.34
A3526B	192.51645	-41.38207	0.0155	45	...	...	317	0.44	0.75
A3530	193.90001	-30.34749	0.0536	94	0.8043	3.62	631	4.63	1.63
A1644	194.29825	-17.40958	0.0470	288	0.9944	5.25	1008	13.98	2.36
A3532	194.34134	-30.36348	0.0557	58	0.9201	4.63	443	1.66	1.16
A1650	194.67290	-1.76139	0.0842	146	1.1015	5.72	723	7.55	1.90
A1651	194.84383	-4.19612	0.0849	158	1.1252	7.47	876	12.48	2.25
A1656	194.89879	27.95939	0.0233	919	1.1378	7.41	995	15.66	2.47
A3556	201.02789	-31.66996	0.0482	90	...	3.08	520	2.59	1.35
A1736A	201.68378	-27.43940	0.0350	36	0.9694	3.34	386	1.30	1.08
A1736B	201.86685	-27.32468	0.0456	126	...	...	844	8.82	2.03
A3558	201.98702	-31.49547	0.0483	469	1.1010	5.83	955	15.75	2.46
SC1329-313	202.86470	-31.82058	0.0448	46	...	...	383	1.01	0.99
A3562	203.39475	-31.67227	0.0486	82	0.9265	5.10	594	3.94	1.55
A1795	207.21880	26.59301	0.0630	154	1.2236	6.42	780	7.09	1.88
A2029	227.73377	5.74491	0.0769	155	1.3344	8.45	931	7.82	1.93
A2040B	228.19782	7.43426	0.0451	104	...	2.41	627	4.77	1.65

TABLE 1. CONTINUED

Name <sup>a</sup>	Optical data				X-ray data <sup>b</sup>		Basic properties		
	RA <sub>CDG</sub> [deg] <sub>J2000</sub>	Dec <sub>CDG</sub> [deg] <sub>J2000</sub>	$\bar{z}$	$N_a$	$r_{500}$ [Mpc]	$kT_X$ [keV]	$\sigma_{LOS}$ [km/s]	$\mathcal{M}_{vir}$ [ $10^{14} \mathcal{M}_\odot$ ]	$R_{vir}$ [Mpc]
(1)	(2)	(3)	(4)	(5)	(6)	(7)	(8)	(9)	(10)
A2052	229.18536	7.02167	0.0347	120	0.9465	2.88	648	4.28	1.60
MKW03S	230.46613	7.70888	0.0443	75	...	...	607	3.46	1.49
A2065	230.62053	27.71228	0.0730	168	1.0480	6.59	1043	17.01	2.50
A2063A	230.77210	8.60918	0.0345	142	0.9020	3.34	762	6.18	1.81
A2142	239.58345	27.23335	0.0902	157	1.3803	11.63	828	11.06	2.16
A2147	240.57086	15.97451	0.0363	397	0.9351	4.26	935	15.70	2.47
A2151	241.28754	17.72997	0.0364	276	0.7652	2.10	768	8.35	2.00
A2152	241.37175	16.43579	0.0443	64	0.5783	2.41	406	1.56	1.14
A2197	246.92114	40.92690	0.0304	185	0.5093	2.21	573	4.21	1.59
A2199	247.15949	39.55138	0.0303	459	1.0040	4.04	779	7.21	1.91
A2204A	248.19540	5.57583	0.1518	38	1.3998	10.24	1101	20.33	2.59
A2244	255.67697	34.06010	0.0993	102	1.1295	5.99	1161	18.35	2.55
A2256	256.11353	78.64056	0.0586	280	1.1224	8.23	1222	20.63	2.68
A2255	258.11981	64.06070	0.0805	179	1.0678	7.01	1000	16.44	2.47
A3716	312.98715	-52.62983	0.0451	123	...	2.19	783	6.99	1.88
S0906	313.18958	-52.16440	0.0482	26	...	...	440	1.46	1.11
A4012A	352.96231	-34.05553	0.0542	39	...	...	575	3.15	1.44
A2634	354.62244	27.03130	0.0309	166	0.7458	3.71	717	5.87	1.78
A4038A-49	356.93768	-28.14071	0.0296	180	0.8863	2.84	753	5.95	1.79
A2670	358.55713	-10.41900	0.0760	251	0.9113	4.45	970	9.91	2.09

<sup>a</sup>A capital letter after the ACO name indicates the line-of-sight component of the cluster.

<sup>b</sup>Taken from Caretta et al. (2023) and references therein.

Columns 2, 3 and 4 present their right ascension, declination and mean redshift, respectively; Column 5 presents the number of presumably virialized sampled galaxies belonging to the system (inside the caustics and the aperture  $1.3 \times r_{200}$ ); Column 6 presents the radius  $r_{500}$  at which the mean interior overdensity is 500 times the critical density at the corresponding redshift; and Column 7 presents the X-ray temperature of the clusters.

For each observed cluster, the virial mass was estimated using (3) and the virial radius by

$$R_{vir}^3 = \frac{3\mathcal{M}_{vir}}{4\pi\rho_{vir}} = \frac{\alpha\sigma_{LOS}^2 R_p}{18\pi H^2(z)}. \quad (13)$$

where  $\rho_{vir} = 18\pi^2[3H^2(z)/8\pi G]$  is the virialization density assuming a spherical model for nonlinear collapse (e.g., Bryan & Norman 1998). In all calculations we used  $\alpha = 2.5$ , assuming a weak anisotropy (e.g., Tully 2015; Kashibadze et al. 2020). The line-of-sight velocity dispersions were computed using the Tukey's biweight robust estimator (Beers et al. 1990). The results of  $\sigma_{LOS}$ ,  $\mathcal{M}_{vir}$  and  $R_{vir}$  are shown, respectively, in Columns 8, 9 and 10 of Table 1.

#### 4.2. Simulation Data

In addition, we use data from the IllustrisTNG simulation (Springel et al. 2018; Nelson et al. 2019),

a set of cosmological simulations that assumes initial conditions consistent with the Planck Collaboration (2016) results and takes into account magnetohydrodynamical effects. In particular, we use the TNG300-1 data cube that contemplates the largest volume allowing the study of the distribution of galaxies and massive objects such as clusters. We take halos (equivalent to galaxy clusters) from the TNG300-1 simulation at redshift  $z = 0$ ,<sup>4</sup> which has a resolution of  $2500^3$  dark matter particles and  $2500^3$  baryonic matter particles. We sampled 248 halos with masses greater than  $10^{14} h^{-1} \mathcal{M}_\odot$  with 370,119 member subhalos, of which 366,940 are classified as galaxies. Information related to the peculiar velocity, mass and position of the center of each halo and subhalo was extracted.

Each halo in the simulation contains, on average, 1,300 subhalos within its virial radius, greatly outnumbering the tracers (galaxies) in our observational sample of clusters. This large difference is due to the number of low-mass systems (dwarf galaxies subhalos) entering the count of TNG300-1; these galaxies are hard to detect in real clusters due to their low

<sup>4</sup>The positions are given in rectangular coordinates of the form  $(x, y, z) ah^{-1}$  kpc, where  $a$  is the cosmological scale factor, being  $a = 1$  in  $z = 0$ , and  $h = H_0/(100 \text{ km s}^{-1} \text{ Mpc}^{-1})$ , for which a value of  $h = 0.7$  was assumed here.

luminosity. Thus, to avoid statistical differences between the parameters estimated from observational and simulated data, we limit the selection of member subhalos by taking only those with mass greater than  $2.0 \times 10^{10} h^{-1} \mathcal{M}_{\odot}$ . For each halo, all member subhalos up to a distance of  $1.3 \times r_{200}$  from the center (the particle with the least gravitational potential energy) were taken. Also,  $\sigma_{LOS}$ ,  $\mathcal{M}_{\text{vir}}$  and  $R_{\text{vir}}$  were calculated reproducing the observational procedure.

Figure 1 shows the projected distribution of member subhalos for two halos in the sample, one high-entropy (left) and one low-entropy (right). Note that, as expected, the distribution of subhalos is more random and homogeneous in a high entropy halo, while more substructured and elongated in a low entropy halo. This also happens in the observed clusters, reinforcing our hypothesis that evolutionary changes in galaxy systems progress in the direction in which the system dissolves substructures, becoming observationally more regular and homogeneous, with higher entropy values.

#### 4.3. Results on the Assembly State of Observed Clusters

To appreciate the correlation between the  $H_Z$  entropy (shown in Column 3 of Table 2 below) and the gravitational assembly level—and therefore with the evolutionary state—of galaxy systems, we present in Figure 2 the distributions of the  $H_Z$  values with respect to the assembly state classes. These are displayed in the form of boxplots, which allow graphically describing the locality, dispersion and asymmetry of data classes (groups) of a quantitative variable through its quartiles (Heumann & Shalabh 2016). The classes were ordered from more to less relaxed systems. Although the box overlap does not allow one to unambiguously discriminate the class to which an arbitrary individual cluster should belong, the statistical correlation is clear: the sequence U-P-S-M-L follows directly the decreasing median values of entropy. The only marginal difference case is between U and P systems, which is understandable if we consider that the primary systems (with only low significance substructures) are dynamically very similar to the unimodal ones—both tend to be relatively massive and evolved systems. This discussion will be resumed later.

### 5. TESTING STATISTICALLY THE $H_Z$ -ENTROPY ESTIMATOR

#### 5.1. Shannon Entropy of Galaxy Distributions in Phase-Spaces

Another way to evaluate the entropy estimates that  $H_Z$  can provide is by using a method that

does not take into account equilibrium assumptions, but allows us to characterize the internal states of a galaxy system from the raw distribution of its member galaxies. In information theory, for example, entropy is a measure of the uncertainty of a random variable (or source of information, e.g., Shannon 1948; Cover & Thomas 2006). If  $X$  is a discrete random variable with possible observable values  $x \in \mathcal{X}$ , which occur with probability  $p(x) = \Pr\{X = x\}$ , the Shannon (or information) entropy of  $X$  is defined as

$$H_S(X) \equiv - \sum_{x \in \mathcal{X}} p(x) \log_{\lambda} p(x), \quad (14)$$

where the sum is performed over all possible values of the variable, and the base  $\lambda$  of the logarithm is chosen according to the entropy ‘units’ to use (*nats*,  $\lambda = e$ ; *bits*,  $\lambda = 2$ ; *bans*,  $\lambda = 10$ ). One of the criteria used by Shannon (1948) to define  $H_S$  ensures that it increases as the possible values of  $X$  begin to appear with equal frequency, taking higher values when they become equiprobable, *i.e.*, when there are no special configurations in the data distribution that provide more information, increasing the uncertainty.

Now, the raw coordinates of the galaxies in a cluster, *i.e.* the observable set of triples (RA, Dec,  $z$ ) of right ascension, declination and redshift, are distributed within a solid angle, which can be approximated by a cylinder with a circular base in the plane of sky and depth along the line-of-sight (see, Figure 3, left panel). Inside the cylinder, the position of each galaxy can be expressed in the form  $x = (r, \theta, z)$ , where  $r$  is its projected distance from the cluster center,  $\theta$  its—azimuthal—angle with respect to the local north direction in the projected sky distribution (see, Figure 3, right panel), and the redshift  $z$  is a measure of its radial velocity. In fact, the cylinder of  $x$ -coordinates (two spatial and one velocity) may be considered a—projected—phase-space for the galaxy ensemble, and the distribution of the variables  $(r, \theta, z)$  inside it depends on the dynamical state of the galaxy cluster.

By considering the cylinder of sampled galaxies as a source of information for the  $x$ -distribution, the probability of finding a galaxy in the neighborhood of position  $x$  (*i.e.*, the probability that the position random variable  $X$  takes a value very close to  $x$  inside the cylinder) can be approximated as  $p(x) \simeq \bar{f}_{r\theta z}(x) \Delta x$ , where  $\bar{f}_{r\theta z}$  must be the observed—or empirical—joint probability density function (PDF) that represents the actual distribution of the galaxy ensemble in the variable  $x$ . Replacing this in (14), one can compute the Shannon entropy of the



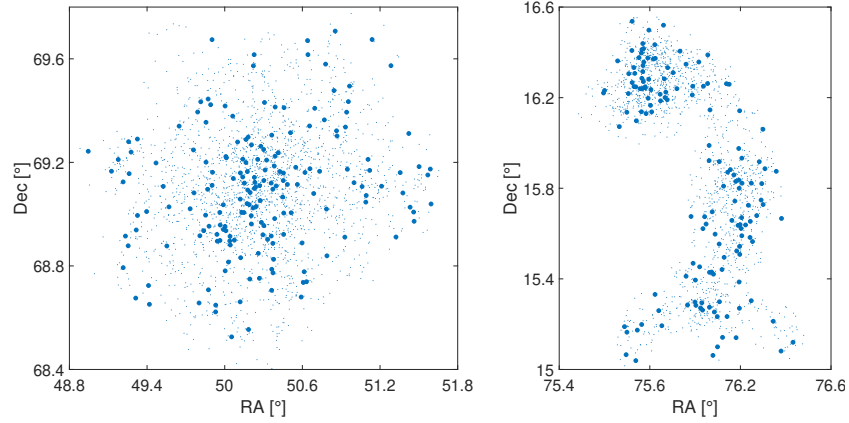


Fig. 1. Two examples of sampled TNG300 halos. *Left*: subhalo distribution for a high entropy halo (TNG-halo-34). *Right*: subhalo distribution for a low entropy halo (TNG-halo-87). Each dot represents a member subhalo: the small dots are subhalos with masses less than  $2.0 \times 10^{10} M_\odot$  while the big dots are the subhalos taken for our analysis.

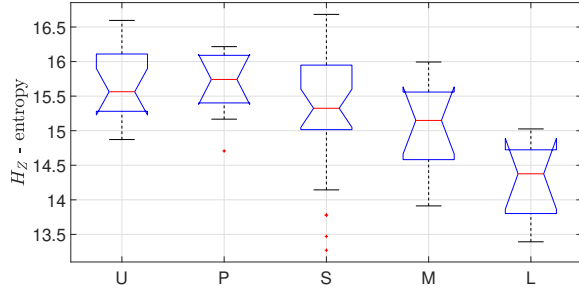


Fig. 2. Boxplots of  $H_Z$ -entropy for the five assembly classifications of clusters. The lower and upper extremes of each box are the 25th and 75th percentiles, respectively, while the central red line marks the median. Whiskers extend to the most extreme non-outlier data, while outliers are represented by red ‘+’ symbols. The color figure can be viewed online.

galaxy distribution for a cluster in the form

$$H_S = - \sum_{x \in \mathcal{X}} [\bar{f}_{r\theta z}(x) \Delta x] \ln \{ \bar{f}_{r\theta z}(x) \Delta x \}, \quad (15)$$

where  $\lambda = e$  has been chosen, and the sum is performed over all the  $n$  discrete partitions  $\Delta x$  made to the domain  $\mathcal{X} = [0, R_{\text{vir}}] \times [0, 360] \times [z_{\text{min}}, z_{\text{max}}]$  of the observed joint PDF. Here,  $z_{\text{min}}$  and  $z_{\text{max}}$  are the minimum and maximum values of redshift in the sample of galaxies of each cluster.

Shannon entropy is a well-established measure for quantifying disorder or uncertainty in a system (Cover & Thomas 2006). In this context,  $H_S$  provides a measure of the degree of randomness in

the distribution of galaxies in the phase-space of a cluster (or any other galaxy system). By calculating this entropy, we are evaluating the information contained in the galaxy ensemble and how galaxies are distributed in different regions of phase-space. Close to equilibrium, the memory (information) of the initial conditions of cluster formation is lost (Binney & Tremaine 2008; Araya-Melo et al. 2009). The general character of  $H_S$  comes from the fact that it is not restricted only to thermodynamic variables, but to any type of data  $X$  that contains information about the state of a system, so it can be used to study characteristics of non-equilibrium systems as they evolve. In addition, it does not consider the microstates of a system as equiprobable, keeping a certain relationship in mathematical form and meaning with the Gibbs entropy (Jaynes 1957).

## 5.2. Shannon Entropy Estimations

To calculate the Shannon entropy, we first established the observed joint PDF  $\bar{f}_{r\theta z}(x)$  of each cluster in two different ways. First, by counting galaxies independently in bins of width  $\Delta r$ ,  $\Delta \theta$  and  $\Delta z$  in the radial- $r$ , azimuthal- $\theta$  and redshift- $z$  directions, respectively, we constructed 1D-histograms that describe the observed distribution of that variable in the galaxy ensemble. Then, by a smoothing technique, the *observed PDFs*  $\bar{f}_r(r)$ ,  $\bar{f}_\theta(\theta)$  and  $\bar{f}_z(z)$  were obtained for the variables from their respective normalized histograms (see, red solid lines on graphs in Figure 4). For this, we used a kernel density estimator that allows a non-parametric fit of PDFs of random variables, adapting directly

TABLE 2  
DYNAMICAL PARAMETERS FOR TOP70 CLUSTER SAMPLE

Name	$\mathcal{A}^a$	$H_Z$	$H_S$ [nat]	$r'_c$ [Mpc]	$\mathcal{P}_{\text{relax}}$	$c_K$	$c_{\text{NFW}}$	$c_{\text{ICM}}$
(1)	(2)	(3)	(4)	(5)	(6)	(7)	(8)	(9)
A2798B	U	15.54	10.85	0.28	0.808	7.85	3.91	2.33
A2801	U	15.34	10.60	0.29	0.794	3.94	1.22	...
A2804	M	14.58	10.16	0.22	0.668	3.41	1.55	...
A0085A	S	16.26	12.48	0.42	0.816	4.76	1.89	2.18
A2811B	S	16.09	11.69	0.37	0.762	5.42	1.77	2.23
A0118	S	15.27	11.25	0.28	0.680	1.76	1.17	...
A0119	S	15.77	11.90	0.33	0.893	7.00	3.88	2.21
A0122	U	15.26	10.72	0.26	0.839	8.29	5.03	2.00
A0133A	S	15.55	11.26	0.30	0.792	7.10	3.36	2.02
A2877-70	S	15.18	10.99	0.25	0.828	10.59	6.95	2.55
AM0227-334	L	15.03	9.36	0.25	0.650	3.72	1.97	...
A3027A	S	15.36	11.20	0.30	0.825	3.32	1.26	2.64
A0400	S	13.47	8.65	0.14	0.816	7.32	3.46	1.33
A0399	U	16.07	12.03	0.35	0.775	6.43	4.61	1.97
A0401	U	16.26	12.25	0.38	0.841	8.86	5.43	1.93
A3094A	U	15.06	11.13	0.26	0.865	3.93	1.28	2.38
A3095	L	13.39	7.66	0.13	0.645	1.95	0.56	...
A3104	S	14.45	9.54	0.19	0.704	7.52	4.44	1.35
S0334	L	14.63	9.77	0.20	0.757	12.41	7.42	...
S0336	L	14.65	9.39	0.22	0.730	4.84	1.38	...
A3112B	S	15.33	11.11	0.32	0.756	1.98	1.32	1.75
A0426A	P	16.22	12.48	0.38	0.824	11.44	7.29	1.83
S0373	S	13.78	9.13	0.12	0.823	6.11	2.58	1.86
A3158	S	16.34	12.28	0.37	0.761	10.73	8.35	2.20
A0496	S	15.31	11.54	0.29	0.919	6.26	2.99	1.82
A0539	S	15.26	10.91	0.25	0.814	10.51	5.45	2.00
A3391	U	15.67	11.38	0.31	0.804	9.75	5.43	2.15
A3395	M	15.44	11.50	0.29	0.781	6.67	3.64	1.96
A0576	S	15.80	11.98	0.35	0.830	6.26	2.93	2.65
A0634	L	13.83	9.31	0.16	0.746	2.41	0.68	...
A0754	M	15.68	12.07	0.33	0.836	4.88	2.04	1.78
A1060	P	15.17	11.29	0.25	0.874	9.76	6.62	2.24
A1367	M	14.86	10.64	0.24	0.848	4.10	1.61	1.70
A3526A	P	14.71	10.33	0.21	0.823	8.40	4.62	1.61
A3526B	S	13.27	7.57	0.12	0.725	4.26	1.16	...
A3530	S	15.03	11.07	0.26	0.888	5.42	2.24	2.02
A1644	P	16.19	12.39	0.38	0.838	7.51	5.26	2.37
A3532	S	14.14	9.75	0.18	0.778	3.59	1.19	1.26
A1650	U	15.40	11.32	0.30	0.846	3.42	1.26	1.72
A1651	P	15.88	11.97	0.36	0.833	4.42	1.67	1.99
A1656	S	16.14	12.73	0.39	0.861	7.79	4.11	2.17
A3556	M	14.54	10.85	0.21	0.744	3.79	1.49	...
A1736A	S	13.78	9.34	0.17	0.783	2.75	0.71	1.10
A1736B	S	15.75	11.77	0.32	0.775	5.74	3.64	...
A3558	P	16.06	12.60	0.39	0.826	4.89	2.12	2.23
SC1329-313	L	13.77	8.65	0.16	0.744	4.63	2.34	...
A3562	U	14.87	10.70	0.25	0.841	4.15	1.74	1.67
A1795	U	15.56	11.51	0.30	0.893	9.47	5.04	1.53
A2029	U	16.02	11.81	0.31	0.838	12.94	6.92	1.44
A2040B	S	15.00	10.76	0.26	0.838	4.28	1.10	...

TABLE 2. CONTINUED

Name	$\mathcal{A}^a$	$H_Z$	$H_S$	$r'_c$	$\mathcal{P}_{\text{relax}}$	$c_K$	$c_{\text{NFW}}$	$c_{\text{ICM}}$
(1)	(2)	(3)	(4)	(5)	(6)	(7)	(8)	(9)
A2052	S	15.08	10.98	0.25	0.850	6.82	3.69	1.69
MKW03S	U	14.92	11.30	0.24	0.881	6.58	4.01	...
A2065	U	16.30	12.19	0.40	0.882	9.11	5.24	2.38
A2063A	P	15.48	11.50	0.29	0.899	9.51	5.19	2.00
A2142	P	15.74	12.12	0.34	0.866	4.54	1.82	1.56
A2147	M	15.99	12.00	0.39	0.829	3.62	1.64	2.63
A2151	M	15.50	11.85	0.32	0.823	4.18	1.36	2.61
A2152	M	13.91	9.38	0.18	0.758	1.99	0.75	1.96
A2197	M	14.76	10.65	0.25	0.699	1.59	1.06	3.12
A2199	P	15.53	12.02	0.30	0.884	7.41	4.23	1.89
A2204A	S	16.51	11.16	0.41	0.769	3.92	1.72	1.84
A2244	U	16.60	12.33	0.41	0.821	10.46	7.81	2.25
A2256	S	16.68	12.47	0.43	0.607	10.87	8.49	2.39
A2255	S	16.20	12.31	0.39	0.789	6.54	3.42	2.31
A3716	M	15.56	11.56	0.30	0.769	5.53	3.17	...
S0906	L	14.12	9.30	0.18	0.793	2.94	0.74	...
A4012A	L	14.80	10.13	0.23	0.834	4.26	1.63	...
A2634	S	15.32	11.60	0.28	0.861	6.69	3.81	2.38
A4038A-49	S	15.45	11.35	0.28	0.820	9.73	5.12	2.01
A2670	U	16.12	11.92	0.33	0.859	10.24	6.01	2.29

<sup>a</sup>Gravitational assembly classes from Caretta et al. (2023).

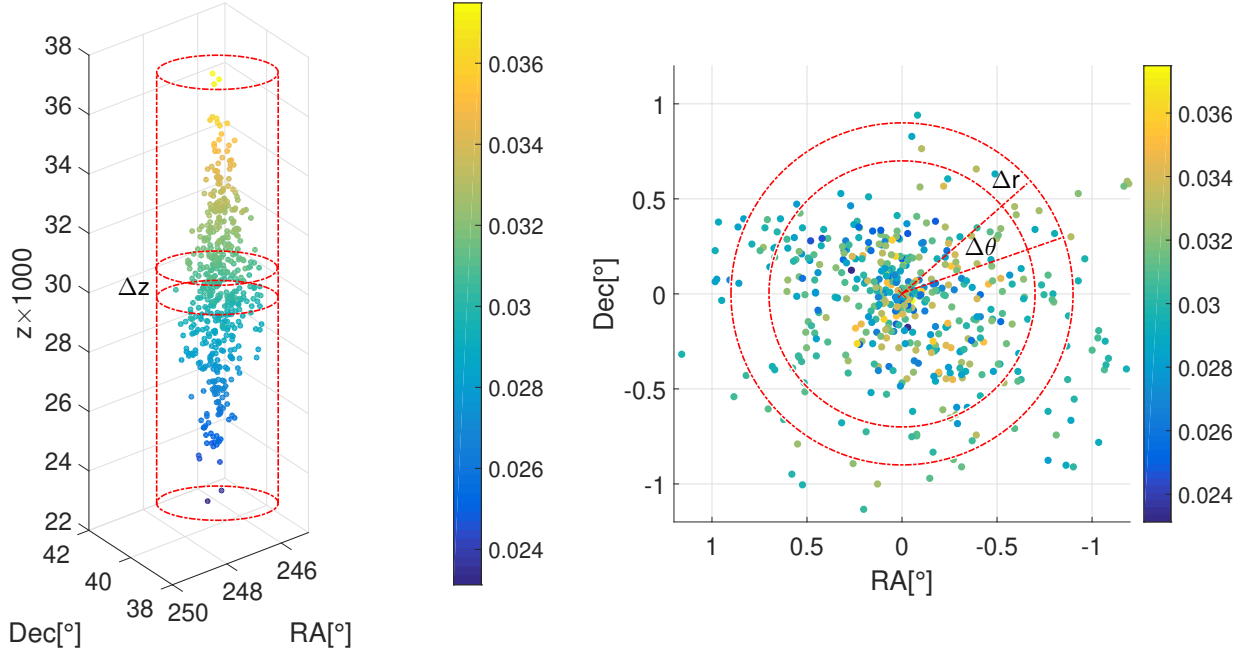


Fig. 3. Sample of galaxies for A2199 cluster in Caretta et al. (2023). Color bars represent the redshift ( $z$ ) distribution. *Left panel*: the cylinder along the line-of-sight direction. *Right panel*: projected distribution in the sky plane with RA and Dec coordinates transported to the origin (the FRG, see the text). The color figure can be viewed online.

to the data (e.g., Heumann & Shalabh 2016). This method is particularly useful when the actual distribution of a data set is unknown, as is the case

for the galaxy distributions inside the (phase-space) cylinders. A standard Gaussian smoothing kernel was used with bins of widths  $\Delta r = 0.15$  Mpc,

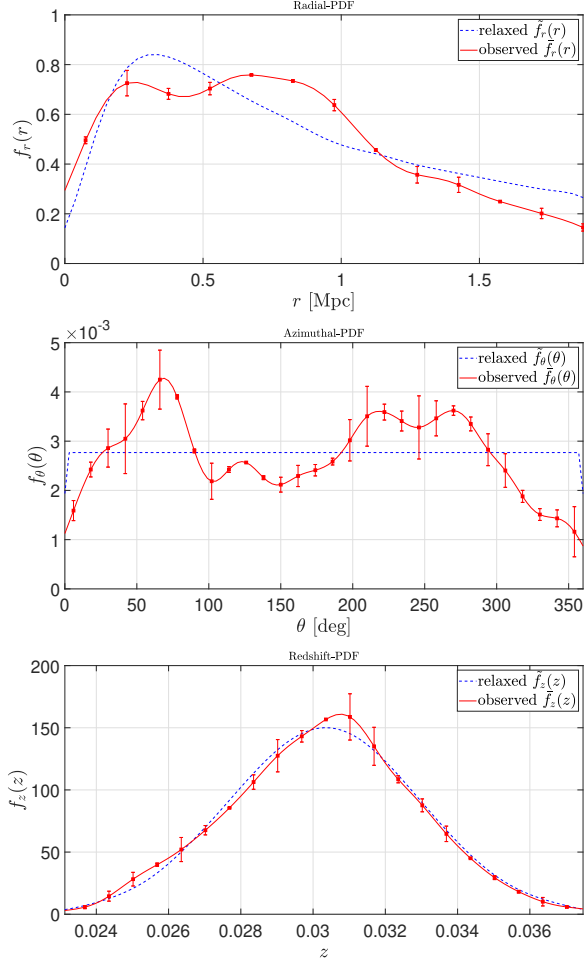


Fig. 4. Probability density functions for the radial- $r$ , azimuthal- $\theta$  and redshift- $z$  distributions of member galaxies in the A2199 cluster. The red solid lines represent the *observed PDFs* obtained by smoothing (normal kernel) from observational data histograms, while dashed blue lines represent the *relaxed PDFs* of equilibrium distributions. The error bars represent the difference between the height of the smoothed curve and the height of the corresponding bin in each 1D-histogram. The color figure can be viewed online.

$\Delta\theta = 12^\circ$ ,  $c\Delta z = 200 \text{ km s}^{-1}$  and supports in the intervals  $[0, R_{\text{vir}}]$ ,  $[0, 360]$  and  $[z_{\text{min}}, z_{\text{max}}]$  for the  $\bar{f}_r$ ,  $\bar{f}_\theta$  and  $\bar{f}_z$  distributions, respectively. Finally, we took  $\bar{f}_{r\theta z}(r, \theta, z) = \bar{f}_r(r)\bar{f}_\theta(\theta)\bar{f}_z(z)$  assuming statistical independence of the variables  $r$ ,  $\theta$  and  $z$  in the galaxy distributions.

On the other hand, as is evident in the right panel of Figure 3, galaxies with the highest and lowest redshifts prefer the center of the projected distribution of the cluster. This correlation between the variables  $r$  and  $z$  is physically justified since the galaxies acquire a greater speed during their tran-

sit through the central regions of the clusters (*i.e.*, where the gravitational potential well is the deepest). Projection effects can also occur, especially for halo galaxies that are located in front or behind the core and close to the line-of-sight. No significant correlation was detected between the variables  $r$  or  $z$  with  $\theta$  instead. Thus, to construct the observed joint PDF in the second way we only took into account the correlation between  $r$  and  $z$ , such that  $\bar{f}'_{r\theta z}(r, \theta, z) = \bar{f}_{rz}(r, z)\bar{f}_\theta(\theta)$ , where the  $\bar{f}_{rz}$  functions were obtained by counting galaxies in bi-dimensional bins of “area”  $\Delta r\Delta z$  and smoothed by a multivariate Gaussian surface kernel, using the same bin width values as above.

Two statistical tests, Kolmogorov-Smirnov and Rank-Sum, showed no significant differences between both methods, confirming the null hypothesis that the PDFs  $\bar{f}_{r\theta z}$  and  $\bar{f}'_{r\theta z}$  represent the same distribution with a confidence level of 95% in both tests. This is probably because the fraction of galaxies that present a strong  $rz$ -correlation is very small, implying a low statistical weight. Then, for simplicity we choose the first option (*i.e.*, that with the three variables assumed to be statistically independent, see Figure 4) to compute the probability values

$$p(x) \simeq \bar{f}_{r\theta z}(x)\Delta x = [\bar{f}_r(r)\Delta r][\bar{f}_\theta(\theta)\Delta\theta][\bar{f}_z(z)\Delta z], \quad (16)$$

varying one of the variables in its respective domain (e.g.,  $r \in [0, R_{\text{vir}}]$ ,  $\theta \in [0, 360]$  and  $z \in [z_{\text{min}}, z_{\text{max}}]$ ), while keeping the other two constant. Thus,  $p(x)$  was obtained in about 1,000 positions  $x = (r, \theta, z)$  inside the data cylinder of each real (and simulated) cluster and these values were used to compute the respective  $H_S$ -entropies by (15) for the galaxy ensembles. The results for *Top70* clusters are shown in Column 4 of Table 2.

### 5.3. Results on the Shannon Entropy for Observed and Simulated Clusters

The relation between the  $H_Z$ -entropy estimator, proposed in the present work, and the Shannon entropy  $H_S$  of the real galaxy distributions can be seen in Figure 5, where the dashed line represents the best fit curve, with a coefficient of determination ( $\mathcal{R}^2$ , Heumann & Shalabh 2016) of 0.886. This figure shows a high degree of correlation (almost linear) between the  $H_Z$  and  $H_S$  entropies that, when measured by the Pearson and Spearman coefficients (e.g., Gibbons & Chakraborti 2003; Heumann & Shalabh 2016), gives the values 0.932 and 0.922, respectively. Below (see, § 7), we offer what we believe to be a possible explanation for such an explicit correlation. In addition, the figure also shows the association of

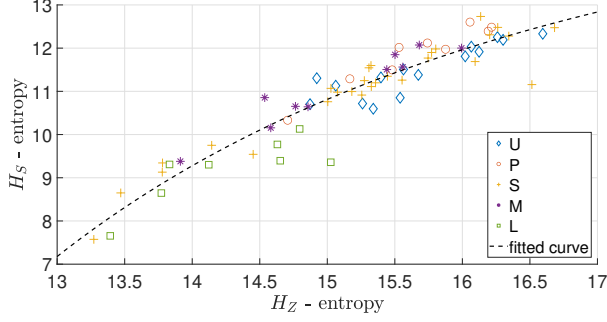


Fig. 5. Scatter plot of  $H_Z$  vs.  $H_S$  made with the entropy values estimated for the *Top70* clusters. The symbols and color scale of the points represent the U-P-S-M-L assembly level classification of clusters performed by Caretta et al. (2023). The dashed line represents the best —power law— fit with  $\mathcal{R}^2 = 0.886$ . The color figure can be viewed online.

these  $H_Z$  and  $H_S$  entropy values with the assembly state of the clusters (represented by the U-P-S-M-L classes). Although the correlation is not evident, it is noticeable that all U and P clusters are placed in the locus of points with higher values of both  $H_Z$  and  $H_S$ , while all L are located in the region with lower values of these entropies.

A procedure similar to that performed with *Top70* clusters was applied to the TNG300 sample to compare the  $H_Z$  and  $H_S$  entropies estimated for the simulated halos. Figure 6 shows a significant correlation, with Pearson and Spearman coefficients of 0.709 and 0.678, respectively, between the dynamical and Shannon entropies, which are very similar to those of real clusters. We did not carry out a classification of simulated clusters in their different assembly levels ( $\mathcal{A}$ ) that allows us to analyze the distribution of  $H_Z$  in each class, as in the case of real clusters. We hope to do this in future work.

## 6. OTHER VALIDATIONS FOR $H_Z$

### 6.1. The Relaxation Probability of Galaxy Systems

Several studies reveal that clusters close to dynamical equilibrium have distributions of galaxies whose radial density and LOS velocity profiles tend to ones that can be represented by specific mathematical functions (Saslaw & Hamilton 1984; Sarazin 1988; Adami et al. 1998; Sampaio & Ribeiro 2014). The above is also true for the ICM entropy profiles in X-ray observations (e. g., Voit 2005) or for the distribution of DM subhalos in cosmological simulations (e. g., Navarro, Frenk & White 1996). Thus, we consider that it is also possible to characterize the

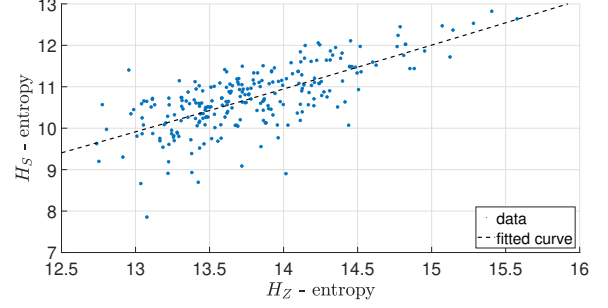


Fig. 6. Scatter plot of  $H_S$  vs.  $H_Z$  entropies made with the data of the complete TNG300 sample. The dashed line represents the best power law fit with  $\mathcal{R}^2 = 0.505$ .

evolutionary state of a galaxy system by measuring how far the currently *observed PDFs* are from their expected equilibrium functional shapes. For this, we need to use (or choose) a consistent reference equilibrium model that describes the distribution when the galaxy ensemble is relaxed, as well as a metric that allows us to estimate the distance of the observed distribution from that of the equilibrium model.

We limit ourselves to a simple reference equilibrium model, considering clusters represented by a spherical distribution of galaxies, with a homogeneous core-halo spatial configuration and an isotropic velocity distribution without net angular momentum.

In principle, the radial distribution of galaxies can be well described (see Adami et al. 1998) by different single mass profiles proposed for clusters in the literature, both *core-* (King 1962; Einasto 1965) and *cuspy-* (Hernquist 1990; Navarro, Frenk & White 1996) dominated ones. Nonetheless, there has been a tendency, especially for fitting DM halos, to use more complex functions, with a larger number of free parameters (Dehnen 1993; Fielder et al. 2020; Diemer 2023) —although they are essentially double and/or truncated power laws— in order to better accommodate the inner and outer slopes. On the other hand, since *core-*dominated profiles usually perform slightly better for real clusters (Sarazin 1988; Adami et al. 1998; García-Manzanárez 2022) —as commented before, the core-halo structure is the one expected for self-gravitating systems at equilibrium— and considering the simplest possible analytical form, we choose the King density profile at this point. Such a profile can be approximated analytically by the form

$$\rho(r) = \rho_0 \left[ 1 + \left( \frac{r}{r_c} \right)^2 \right]^{-\gamma}, \quad (17)$$

suggesting a finite central density  $\rho_0 = \rho(0)$  and the existence of a core of radius  $r_c$ . The parameters  $r_c$ ,  $\rho_0$  and  $\gamma$  can be determined by the best fit of the model (17) to the spatial distribution of galaxies. For three-dimensional distributions it has been found that  $\gamma = 3/2$  and  $\rho_0 = 9\sigma_{LOS}^2/4\pi Gr_c^2$ , while for observed two-dimensional (or projected) distributions  $\gamma = 1$  and  $\rho_0 = 9\sigma_{LOS}^2/2\pi Gr_c$  (see, Rood et al. 1972; Schneider 2015), where  $G$  is the gravitational constant. Thus, here we consider the projection (on the RA-Dec plane) of a cluster in equilibrium to have a King-type radial distribution of galaxies described by the (1D) radial-PDF of the form

$$f_r^{\text{eq}}(r) = \frac{6r}{\pi r'_c R_{\text{vir}}} \left[ 1 + \left( \frac{r}{r'_c} \right)^2 \right]^{-1}, \quad (18)$$

in which the count of galaxies must be performed in bins of length  $\Delta r$  instead of rings of area  $\Delta A = 2\pi r \Delta r$ , that is, counting the number of galaxies located between  $r$  and  $r + \Delta r$  for each distance from the cluster center. Integrating (18) from 0 to  $R_{\text{vir}}$ , the normalization condition to find the ‘relaxed’ core radius ( $r'_c$ ) in virial equilibrium is

$$\ln \left( 1 + \frac{R_{\text{vir}}^2}{r'^2_c} \right) = \frac{\pi R_{\text{vir}}}{3r'_c}. \quad (19)$$

For the azimuthal distribution of galaxies on the RA-Dec projected plane of a regular cluster we expect a continuous uniform azimuthal-PDF of the form

$$f_\theta^{\text{eq}}(\theta) = \begin{cases} 1/360, & \text{for } \theta \in [0, 360] \\ 0, & \text{otherwise,} \end{cases} \quad (20)$$

since, under the assumed equilibrium model, the probability of finding galaxies in any direction of the plane must be the same if there are no deformities (flattening or elongation) in the cluster morphology and no substructures when counting galaxies in slices of width  $\Delta\theta$  at fixed radius.

Finally, for the (3D) galaxy velocities inside clusters in equilibrium we expect a quasi-Maxwellian distribution (isotropic, e.g., Sarazin 1988; Sampaio & Ribeiro 2014), so that the LOS components of velocities have a normal distribution described by the redshift-PDF

$$f_z^{\text{eq}}(z) = \frac{c}{\sigma_{LOS}\sqrt{2\pi}} \exp \left\{ -\frac{c^2}{2} \left( \frac{z - \bar{z}}{\sigma_{LOS}} \right)^2 \right\}, \quad (21)$$

where  $c$  is the speed of light and  $c\bar{z}$  is the mean LOS velocity of the cluster.

The construction of the reference PDFs associated to the data is done in three steps. First, we determine numerically the relaxed core radius  $r'_c$  (see, Column 5 of Table 2 for observational sample), taking into account the normalization condition (19), to be used in  $f_r^{\text{eq}}$ . For  $R_{\text{vir}}$ , also used in  $f_r^{\text{eq}}$ , and for  $c\bar{z}$  and  $\sigma_{LOS}$ , the last ones for  $f_z^{\text{eq}}$ , we take the previously calculated parameters (see, Columns 10, 4 and 8, respectively, of Table 1 for observational sample). The  $f_\theta^{\text{eq}}$  distribution is trivial and does not require observational parameters of clusters.

Next, for each cluster we construct its corresponding relaxed mock cluster, which has as many particles as observed galaxies but distributed according to (or following) the corresponding  $f_r^{\text{eq}}$ ,  $f_\theta^{\text{eq}}$  and  $f_z^{\text{eq}}$  equilibrium PDFs.

The third step is done by fitting the tuned equilibrium models to the particle distributions of the mock clusters in the radial, azimuthal, and redshift components, using bin widths and smoothing levels equal to those used in the *observed PDFs*. With this, we are able to construct the *relaxed PDFs*,  $\tilde{f}_r$ ,  $\tilde{f}_\theta$  and  $\tilde{f}_z$ , *i.e.*, the ones expected in the dynamical relaxation state. Figure 4 shows an example of the *observed* and *relaxed PDFs* for the A2199 cluster.

Now, the relaxation probability of a galaxy system can be defined as a distance between the *observed PDFs* and the *relaxed* ones, *i.e.*, between the current dynamical state of the galaxy ensemble (characterized by  $\tilde{f}_r$ ,  $\tilde{f}_z$  and  $\tilde{f}_\theta$ ) and its most probable equilibrium state (characterized by  $\tilde{f}_r$ ,  $\tilde{f}_\theta$  and  $\tilde{f}_z$ ), in the probability space. For this, we use the Hellinger distance (Hellinger 1909), a metric used to quantify the similarity between two distributions in the same probability space so that, if  $f_1$  and  $f_2$  represent two PDFs for the same variable, the Hellinger distance between them is defined as

$$H(f_1, f_2) \equiv \left[ \frac{1}{2} \int \left( \sqrt{f_1(x)} - \sqrt{f_2(x)} \right)^2 dx \right]^{1/2}, \quad (22)$$

where the integration must be carried out over the domain of the functions, and the property  $0 \leq H(f_1, f_2) \leq 1$  allows us to define the relaxation probability,  $\mathcal{P}_{\text{relax}} \equiv 1 - H$ , of a galaxy ensemble. Thus, the closer the  $\tilde{f}_i$  and  $\tilde{f}_i$  functions are to each other, the more relaxed a galaxy system can be considered. For a system close to equilibrium  $H \rightarrow 0$  and  $\mathcal{P}_{\text{relax}} \rightarrow 1$ .

Under the same assumption of statistical independence between the variables  $r$ ,  $\theta$  and  $z$  used for the observed joint PDFs, the relaxed joint PDFs were then defined as  $\tilde{f}_{r\theta z}(r, \theta, z) = \tilde{f}_r(r)\tilde{f}_\theta(\theta)\tilde{f}_z(z)$ . For calculations of  $H$ , we take  $f_1 = \tilde{f}_{r\theta z}$  and  $f_2 =$

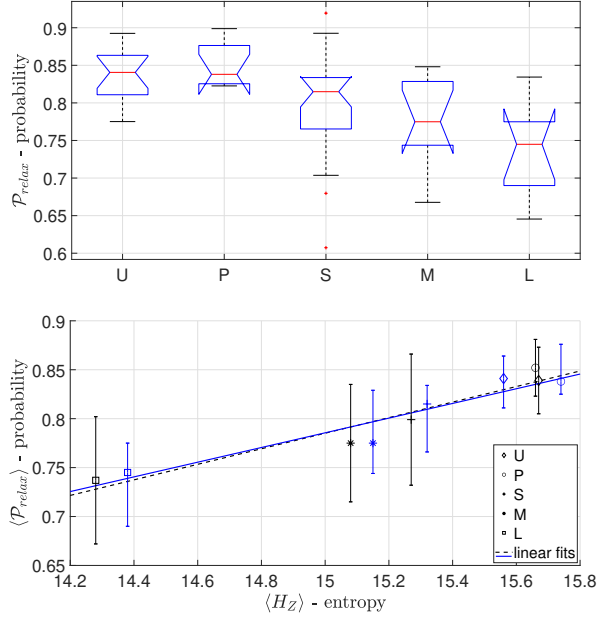


Fig. 7. *Top panel:* Boxplots of  $\mathcal{P}_{\text{relax}}$  values for the five assembly states of clusters from Caretta et al. (2023). *Bottom panel:* Scatter plot of  $\langle \mathcal{P}_{\text{relax}} \rangle$  vs.  $\langle H_Z \rangle$  made with the mean (black markers) and median (blue markers)  $H_Z$  and  $\mathcal{P}_{\text{relax}}$  values presented in Table 3. The symbols of the points represents the U-P-S-M-L assembly level classes. The black dashed and blue solid lines represents the linear fits to the mean and median data, with  $\mathcal{R}^2$  of 0.964 and 0.950, respectively. The color figure can be viewed online.

$\tilde{f}_{r\theta z}$  in (22) for each galaxy cluster. The calculated values for the relaxation probability,  $\mathcal{P}_{\text{relax}}$ , for the observed clusters are shown in Column 6 of Table 2.

In addition, the top panel of Figure 7 shows the distribution of  $\mathcal{P}_{\text{relax}}$  values with respect to the assembly state classes. Like what happened with the  $H_Z$ -entropy, there is a clear correlation between the relaxation probability and the level of gravitational assembly of a system: the sequence U-P-S-M-L considered here goes from the most likely relaxed to the least relaxed systems with respect to the chosen equilibrium model. The triple correlation between the dynamical entropy, the relaxation probability and the assembly level of clusters can be seen in the bottom panel of Figure 7, a scatter plot of  $\langle \mathcal{P}_{\text{relax}} \rangle$  vs.  $\langle H_Z \rangle$  built with the mean and median values (see Table 3) obtained for  $H_Z$  and  $\mathcal{P}_{\text{relax}}$  in each assembly classification.

Finally, we applied a Kolmogorov-Smirnov (KS-) test to evaluate, with a confidence level set at 90%

(or significance level of 0.1), the null hypothesis that the  $H_Z$  or  $\mathcal{P}_{\text{relax}}$  values for the galaxy systems classified into two different assembly classes (U, P, S, M and L) come from the same continuous distribution. Table 4 shows the  $p$ -values, in the range  $[0, 1]$ , that resulted from the KS-test. The closer a  $p$ -value is to 1, the more similar are the distributions of  $H_Z$  and  $\mathcal{P}_{\text{relax}}$  values in two different assembly ( $\mathcal{A}$ ) classes.

## 6.2. Relation Between $H_Z$ and the Cluster Concentration Indices

Apart from the discrete characterization of the assembly state used in the previous sections, one can also probe some continuous parameters, estimated from optical or X-ray data (Carlberg et al. 1996; Girardi & Mezzetti 2001; Zhang et al. 2011; Caretta et al. 2023, and references therein), that are expected to correlate with the evolutionary state of the galaxy system. Here we present, for instance, the concentration indices of a cluster, both from optical galaxy distributions and X-ray from ICM: more relaxed clusters tend to be denser at their centers and have higher values for these indices.

For the optical data, we use the Maximum Likelihood Estimation method (MLE) to determine the optimal concentration indices for the King and NFW radial profiles fitted to the observed projected distributions of galaxies in the clusters of the *Top70* sample. The King profile employed for the fitting is the one described by equation (17), while the NFW profile takes the form

$$\rho(r) = \rho_0 \left[ \left( \frac{r}{r_s} \right) \left( 1 + \frac{r}{r_s} \right)^2 \right]^{-\gamma}, \quad (23)$$

where  $r_s$  is the scale radius of the galaxy cluster. The concentration indices of each cluster are related to its respective virial and characteristic radii ( $r_c$  or  $r_s$  obtained by MLE) in the form  $c_K = R_{\text{vir}}/r_c$  and  $c_{\text{NFW}} = R_{\text{vir}}/r_s$  (Binney & Tremaine 2008), and the obtained values are compiled in Columns 7 and 8 of Table 2. We also probed the ratio  $c_{500} = R_{\text{vir}}/r_{500}$  (using the available X-ray data in Table 1); the obtained values are shown in Column 9 of the Table 2.

Figure 8 shows the relationship between the  $H_Z$ -entropy and the estimated—cluster—concentration indices for the *Top70* sample. The Pearson correlation coefficients between the  $H_Z$ -entropy values and those corresponding to the indices  $c_K$ ,  $c_{\text{NFW}}$  and  $c_{500}$  are 0.448, 0.512, 0.429, respectively. Despite the not strong statistical significance and the remarkable dispersion, an evident growing trend can be seen in the concentration indices with the growth of the  $H_Z$ -entropy in the systems. This tendency is also subtly



TABLE 3

MEAN (WITH STANDARD DEVIATION) AND MEDIAN (WITH THE FIRST-25% AND THIRD-75% QUANTILES) VALUES FOR  $H_Z$  AND  $\mathcal{P}_{\text{RELAX}}$  IN EACH OF THE ASSEMBLY STATE CLASSES

Assembly level class	Mean $\pm$ std		Median $^{+Q^3}_{-Q^1}$	
	$H_Z$	$\mathcal{P}_{\text{relax}}$	$H_Z$	$\mathcal{P}_{\text{relax}}$
U	$15.67 \pm 0.53$	$0.839 \pm 0.034$	$15.56^{+0.55}_{-0.28}$	$0.841^{+0.023}_{-0.030}$
P	$15.66 \pm 0.50$	$0.852 \pm 0.029$	$15.74^{+0.35}_{-0.34}$	$0.838^{+0.038}_{-0.013}$
S	$15.27 \pm 0.91$	$0.799 \pm 0.067$	$15.32^{+0.62}_{-0.31}$	$0.815^{+0.019}_{-0.049}$
M	$15.08 \pm 0.65$	$0.775 \pm 0.060$	$15.15^{+0.41}_{-0.56}$	$0.775^{+0.054}_{-0.031}$
L	$14.28 \pm 0.58$	$0.737 \pm 0.065$	$14.38^{+0.35}_{-0.57}$	$0.745^{+0.030}_{-0.055}$

TABLE 4

$P$ -VALUES OF KOLMOGOROV-SMIRNOV TEST COMPARING THE DISTRIBUTIONS OF  $H_Z$ -ENTROPY (LEFT VALUES) AND RELAXATION PROBABILITY  $\mathcal{P}_{\text{RELAX}}$  (RIGHT VALUES)\*

Class	P		S		M		L	
U	0.958	0.500	0.417	0.024	0.065	0.024	2.003e-04	7.725e-04
P	-	-	0.205	0.006	0.203	0.037	7.652e-04	9.766e-04
S	-	-	-	-	0.509	0.714	7.044e-04	0.019
M	-	-	-	-	-	-	0.148	0.243

\*For galaxy clusters in different classifications. The confidence level for the KS-test was 90%.

manifested in the assemblage classes (represented by the marker symbols in Figure 8): the U and P clusters tend to have higher concentration indices, while the L clusters tend to present lower values of these. S and M clusters appear with a more extended range of concentration indices. It is interesting to note that if we leave only U and P clusters in the above relation, for example for  $c_{500}$ , the correlation increases from 0.429 to 0.603 —these are the typical clusters that appear in studies based on X-rays emission of ICM.

We have also probed other continuous dynamical parameters, obtained from X-rays emission of ICM, associated to the evolutionary state of galaxy systems: the concentration  $c$  and the luminosity concentration  $c_L$  (resepctively from Parekh et al. 2015; Zhang et al. 2017), the Gini and  $M_{20}$  morphological coefficients (from Parekh et al. 2015; Lovisari et al. 2017), the substructure level  $S_C$  (from Andrade-Santos et al. 2012), and the  $C_{\text{SB}}$  and  $C_{\text{SB4}}$  concentration parameters (from Andrade-Santos et al. 2017). Although the statistics are usually poor, and the aspects captured from X-ray data are not necessarily similar to the ones captured by optical data (which include  $H_Z$ ), the results are all similar to the ones showed for  $c_{500}$ , for example increasing correlation when only U and P clusters are considered.

It is remarkable that the only parameter that correlates very well with  $H_Z$  is  $r'_c$  (with a Pearson coef-

ficient of 0.972). The theory states that the natural tendency of a gravitational system towards its evolution is establishing a structure core-halo. This is exactly what the correlation of  $H_Z$  and  $r'_c$  may be suggesting: the core radius grows with the entropy of the cluster.

We consider that  $H_Z$  is an efficient parameter for estimating the relaxation/dynamical state of galaxy clusters, maybe better than the others we have compared in this incomplete exercise, because it can capture more important aspects of such an evolutionary snapshot. However, it is important to note that no parameter can, alone, account for all the evolutionary aspects, such as interaction with the cosmological environment, collapse and mass growth, galaxy formation, AGN activity, feedback processes, among others, making paramount to consider different observations and analyses for constructing the most complete picture possible.

## 7. DISCUSSION AND CONCLUSIONS

In this work we have proposed an entropy estimator,  $H_Z$ , which can be calculated from global dynamical parameters (virial mass, projected virial radius and velocity dispersion), to characterize the dynamical state of galaxy systems. Initially, a slight modification of the standard  $T ds$  Gibbs relation was carried out to include the peculiar behavior of self-gravitating systems and, as a result, an expression



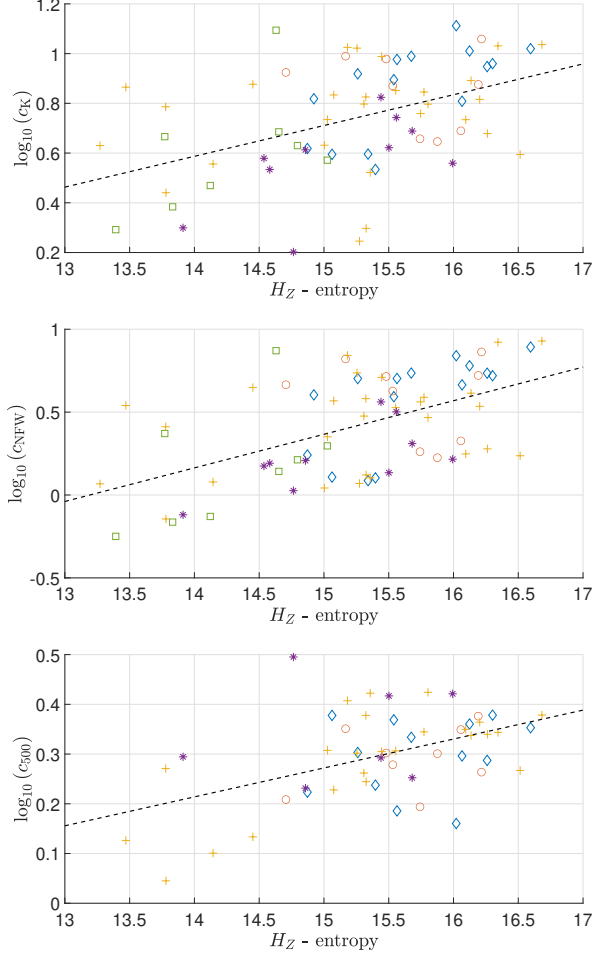


Fig. 8. Scatter plots of  $H_Z$ -entropy *vs.* concentration indices ( $c_K$ ,  $c_{NFW}$ , and  $c_{500}$ ) for the *Top70* cluster sample. The symbols used for the markers have the same meaning as in Figure 5. The dashed line represents the best linear fit to the data, with  $\mathcal{R}^2$  of 0.203, 0.264 and 0.215, respectively from top to bottom. The color figure can be viewed online.

was obtained for the entropy component  $s$  related only to the galaxy ensemble, which is a function of the internal kinetic energy and the volume of the systems.

The direct association of the  $H_Z$ -entropy estimator to the dynamical state of the galaxy systems comes from the second law of thermodynamics, according to which entropy increases as the systems advance towards more stable states, reaching a local maximum in virial equilibrium. This does not assert that the galaxy system reaches a stable state of equilibrium, which would be determined by a global maximum of entropy, but rather a state of greater stability than its previous evolutionary configurations, the

so-called dynamical relaxation. Thus, although the virial theorem is fulfilled in relaxed states with a local entropy maximum, these are *metastable equilibria* that can be broken if the galaxy system significantly interacts with its environment, such as through accretions and mergers with other systems. However, if the system is isolated (or its interaction with the environment is negligible), its entropy value remains in the vicinity of the maximum and its behavior in such state will be indistinguishable from dynamical relaxation.

In order to evaluate the power of this entropy to represent the evolutionary state of a galaxy system, we correlated it to four independent estimators: two observational and two statistical. The two observational ones come from analyses of the internal structure of real clusters, particularly the discrete gravitational assembly state (obtained from optical data) and three continuous concentration indices (both from optical and X-ray data), applied to a sample of 70 well spectroscopically-sampled nearby galaxy clusters. The statistical estimators include the Shannon (information) entropy and the relaxation probability, calculated for the same sample of observed clusters and for a sample of 248 halos (simulated clusters) from IllustrisTNG.

The first striking result of our analysis is that the  $H_Z$ -entropy correlates very well with the gravitational assembly state of the clusters obtained from observational optical data. The  $H_Z$ -entropy increases with the decrease in the level of substructuring, which is interpreted as the less relaxed a cluster is, the more information is lost when treating it as a virialized system. Specifically, both U and P clusters show the highest entropies, while L present the lowest values for this property. Since P clusters are massive, while possessing only low significance substructures (low mass accretions), they resemble the unimodal U clusters. On their turn, L clusters are, as pointed by Caretta et al. (2023), the ‘less evolved’, in the sense that they are the poorest, less massive and have not suffered significant merging processes yet. S and M clusters present a large range of entropies. This happens because both less or more massive clusters (and both less and more evolved ones) can suffer new mergings or accretion at any time.

The  $H_Z$ -entropy estimator was derived based on specific variables (e.g., per mass unit), which allow comparisons between galaxy systems of different masses ( $\mathcal{M}_{\text{vir}}$ ) and sizes ( $R_{\text{vir}}$ ). Moreover, equation (12) shows a clear functional dependence of the entropy on the galaxy velocity dispersion (*i.e.*, on the specific internal kinetic energy  $\kappa = (\alpha/2)\sigma_{\text{LOS}}^2$  of

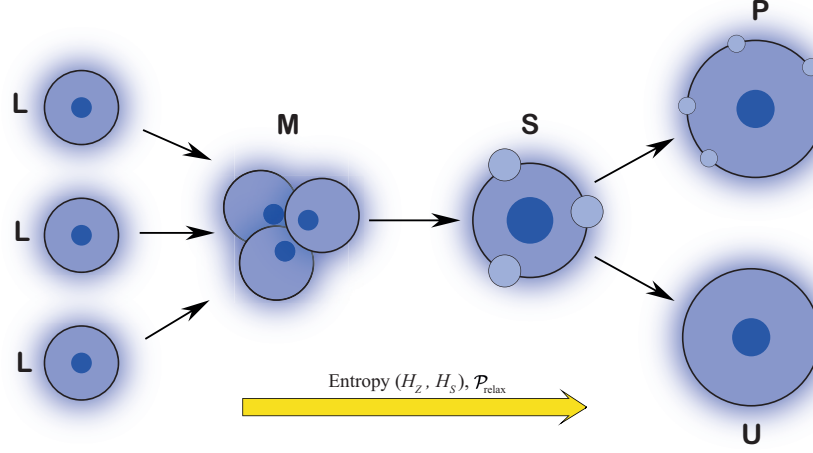


Fig. 9. Diagram of a possible evolutionary line between systems in the different assembly levels (U-P-S-M-L). The entropy levels of the galaxy systems, obtained using the  $H_Z$  and  $H_S$  estimators, increase as they progress towards more dynamically relaxed states (with a higher probability of relaxation,  $\mathcal{P}_{\text{relax}}$ ), *i.e.*, states with more homogeneous and less substructured galaxy distributions (or where the substructures are insignificant for the dynamics of the systems).

the galaxy ensemble). This implies that although groups and poor clusters can reach virial equilibrium like rich clusters, the relaxation state of the latter will be characterized by higher entropy values given their higher velocity dispersions. It is possible to verify that, by calculating  $H_Z$  without taking into account the term that depends on  $\sigma_{LOS}$  in (12), then the entropy values of all sampled clusters are very closely distributed around a central value  $\langle H_Z \rangle$  that depends on the units chosen for  $\mathcal{M}_{\text{vir}}$  and  $R_{\text{vir}}$ .

A possible evolutionary line between systems at different assembly levels has been schematized in Figure 9. Multimodal (M) systems could be formed by the merger of two or more low-mass unimodal (L) systems. These mergers increase the entropy level of the systems due to the increase in mass and number of particles (*i.e.*, galaxies). As gravity further assembles the fused parts, a main structure is formed in the clusters, and, when still dynamically significant substructures remain, we have substructured systems (S). In this process, the entropy increases because the main structure, which is larger than the rest of the substructures, begins a virialization process and dominates the dynamics of the cluster. The substructures are special configurations in the distribution of galaxies, macroscopic movements that can slightly affect the dynamics of the system. However, these are little by little accreted and dissolved by the main structure, until they become less significant and the clusters evolve marginally towards the more assembled states primaries (P) and unimodals (U),

where the entropy is greater given the large homogeneity of the distribution of galaxies, large velocity dispersion and the proximity to virialization.

It is important to highlight that, despite the notable tendency of  $H_Z$ -entropy to increase with the  $L \rightarrow M \rightarrow S \rightarrow P/U$  sequence of assembly states, an individual cluster could not be assigned to a specific  $\mathcal{A}$  class only knowing its  $H_Z$ -entropy value, since this classification requires the knowledge of more observational (optical and X-ray) features of the cluster. However, the  $H_Z$ -entropy values allow us to know statistically which clusters are likely to be more relaxed—and probably with a higher assembly level—than others when working with a large sample of clusters, *e.g.*, as in the case of the *Top70* or TNG300 sample. In addition, if by qualitative methods two clusters appear similar, their  $H_Z$  values can help to discriminate if they are at the same evolutionary state or if one of them is more advanced (or delayed) than the other, like is the case of L and U clusters.

Resuming the question about unimodal clusters, we have also verified that L clusters lack the core-halo spatial configuration, unlike U clusters that exhibit a clear central concentration of galaxies. In fact, as can be seen from the galaxy concentration indices, U clusters generally achieve the highest concentration indices while L clusters have the lowest. Thus, the Hellinger distance between the respective *observed* and *relaxed PDFs* of a cluster becomes larger when the latter lack a central concentration.

Concerning the statistical estimators we used to test  $H_Z$ -entropy, we found that the Shannon —or information— entropy  $H_S$  presents a remarkable (almost linear) correlation with it.

Information entropy does not necessarily have a simple correspondence with physical entropy, but we can provide a possible explanation for the correlation between the  $H_Z$  and  $H_S$  entropies as follows. Given that the cylinder of  $x$ -points of observational data constitutes a projected phase-space (e.g., it contains 2D-position and 1D-velocity coordinates of particles in a system that evolves with time) for each cluster,  $\bar{f}_{r\theta z}$  is like a ‘coarse-grained distribution function’ obtained for a fixed time —the observing time— in this phase-space. Thus, the Shannon entropy  $H_S(\bar{f}_{r\theta z})$  meets in this context the criteria to be an H-function (see Tremaine, Hénon & Lynden-Bell 1986; do not confuse it with the Hellinger distance in Eq. 22) and, therefore, it always increases with the evolution of the galaxy ensemble.

On the other hand, the argument  $\kappa^{\alpha/2}v^{-1}$  in (11) is equivalent, by analogy with statistical mechanics concepts, to the  $\mathcal{Z}$  partition function of the galaxy ensemble. Every  $\mathcal{Z}$  function is defined in the phase-space of a system (Hill 1956; Landau & Lifshitz 1980), taking higher values in states of —or close to— equilibrium, where dynamical relaxation increases the randomness of the particle distribution and offers a greater number of ways in which energy can be distributed inside the system, *i.e.*, in states of higher entropy since  $s \propto \mathcal{Z}$ . The  $\bar{f}_{r\theta z}$  distributions and  $\mathcal{Z}$  functions are intrinsically related in the thermodynamic limit of a system (Jaynes 1957), even in self-gravitating ones (Chavanis 2003, 2006), this is why both  $H_Z$  and  $H_S$  are related between them and to the dynamical state of the galaxy ensemble, and allows us to measure how close it is to virial equilibrium.

This interpretation is reinforced by the relaxation probability  $\mathcal{P}_{\text{relax}}$  which shows that the closer the galaxy cluster is to the virialization, the smaller is the distance between its observed distribution of galaxies and the expected theoretical equilibrium one.

The entropy estimations presented here are very promising because, once one has a representative sample of galaxy members for the cluster, the calculation of the input parameters is straight forward. This low-cost analysis is much easier than the broader one presented in Caretta et al. (2023), and can also be used as a complementary analysis in the study of the assembly state of the galaxy systems. It is still lacking a deeper analysis of the implications

of the results presented here, which we plan to do in a future work. We also intend to extend this analysis to other scales of galaxy clustering, especially in the direction of the evolution of the large scale structures like the superclusters of galaxies.

Our main conclusions are the following:

- The  $H_Z$ -entropy estimator, which depends solely on observational (optical) parameters, adequately captures the entropy of clusters manifested in the (spatial and velocity) distribution of their member galaxies.
- The  $H_Z$ -entropy is related, through the second law of thermodynamics, to the evolutionary state of galaxy systems. Entropy increases as systems evolve towards more stable states, reaching a local (non-unique) maximum at virial equilibrium.
- There is a significant correlation between the  $H_Z$ -entropy of galaxy systems and their gravitational assembly states (A, Caretta et al. 2023), presenting an entropy growth in the L→M→S→P/U sequence, the direction in which the relaxation probability  $\mathcal{P}_{\text{relax}}$  of the clusters also increases.
- There is a remarkable (almost linear) correlation between  $H_Z$ -entropy and the Shannon (information) entropy,  $H_S$ , reinforcing that the dynamical entropy we propose can capture the increase in disorder and loss of information in the process of virialization.
- Clusters with higher velocity dispersions of member galaxies tend to have higher  $H_Z$  and  $H_S$  entropy values, indicating more random galaxy distributions.
- The  $H_Z$ -entropy estimator shows a great capacity to capture the state of relaxation and evolution of the galaxy systems, maybe better than the one presented by other conventional continuous parameters used for this purpose.
- The  $H_Z$ -entropy estimator provides valuable information on the dynamical state and assembly levels of galaxy clusters, which may have significant applications in studying the evolution of galaxy systems and understanding their dynamics.

The authors JMZ, CAC and EGM thank financial support from *Universidad de Guanajuato*

(DAIP), *Convocatoria Institucional de Investigación Científica*, projects 096/2021 and 162/2022. JMZ acknowledges funding from CONACyT PhD grant and appreciates the manuscript revision by Manuela Paz. APG acknowledges support from *Departamento de Matemáticas, Universidad del Cauca*. The authors are grateful to Dr. Roger Coziol and Dr. Francisco Escamilla for the discussions that helped to improve the manuscript.

## REFERENCES

- Abell, G. 1958, *ApJS*, 3, 211, <https://doi.org/10.1086/190036>
- Abell, G., Corwin, H. G. Jr., & Olowin, R. P. 1989, *ApJS*, 70, 1, <https://doi.org/10.1086/191333>
- Adami, C., Mazure, A., Katgert, P., & Biviano, A. 1998, *A&A*, 336, 63, <https://doi.org/10.48550/arXiv.astro-ph/9804172>
- Andrade-Santos, F., Lima-Neto, G. B., Laganá, T. F. 2012, *ApJ*, 746, 139, <https://doi.org/10.1088/0004-637X/746/2/139>
- Andrade-Santos, F., Jones, C., Forman, W. R., et al. 2017, *ApJ*, 843, 76, <https://doi.org/10.3847/1538-4357/aa7461>
- Antonov, V. A. 1962, Solution of the problem of stability of stellar system Emden's density law and the spherical distribution of velocities, *Vestnik Leningradskogo Universiteta*. (Translated, 1985, in *IAUS 113, Dynamics of star clusters.*, ed, J. Goodman & P. Hut, Goodman, Reidel, Dordrecht, 525
- Araya-Melo, P., Reisenegger, A., Meza, A., van de Weygaert, R., Dünner, R., & Quintana, H. 2009, *MNRAS*, 399, 97, <https://doi.org/10.1111/j.1365-2966.2009.15292.x>
- Bahcall, N. A. 1996, *arXiv:astro-ph/9611148*, <https://doi.org/10.48550/arXiv.astro-ph/9611148>
- Balberg, S., Shapiro, S. L., & Inagaki, S. 2002, *ApJ*, 568, 475, <https://doi.org/10.1086/339038>
- Bautz, L. P., & Morgan, W. W. 1970, *ApJ*, 162, 149, <https://doi.org/10.1086/180643>
- Beers, T. C., Flynn, K., & Gebhardt, K. 1990, *AJ*, 100, 32, <https://doi.org/10.1086/115487>
- Binney J., & Tremaine, S. 2008, *Galactic Dynamics* 2nd ed. (Princeton, NJ: PUP)
- Biviano, A., Murante, G., Borgani, S., Diaferio, A., Dolag, K., & Girardi, M. 2006, *A&A*, 456, 23, <https://doi.org/10.1051/0004-6361:20064918>
- Böhringer, H., & Werner, N. 2010, *A&A Rev.*, 18, 127, <https://doi.org/10.1007/s00159-009-0023-3>
- Böhringer, H., & Chon, G. 2021, *A&A*, 656, 144, <https://doi.org/10.1051/0004-6361/2021141341>
- Bravo-Alfaro, H., Caretta, C. A., Lobo, C., Durret, F., & Scott, T. 2009, *A&A*, 495, 379, <https://doi.org/10.1051/0004-6361:200810731>
- Bryan, G. L., & Norman, M. L. 1998, *ApJ*, 495, 80, <https://doi.org/10.1086/305262>
- Buote, D. A., & Tsai, J. C. 1995, *AJ*, 452, 522, <https://doi.org/10.1086/176326>
- Caretta, C. A., Andernach, H., Chow-Martínez, M., Coziol, R., et al. 2023, *RMxAA*, 59, 345, <https://doi.org/10.22201/ia.018511101p.2023.59.02.13>
- Carlberg, R. G., et al. 1996, *ApJ*, 462, 32, <https://doi.org/10.1086/177125>
- Carlberg, R. G., et al. 1997a, *ApJ*, 476, 7, <https://doi.org/10.1086/310497>
- Carlberg, R. G., et al. 1997b, *ApJ*, 485, 13, <https://doi.org/10.1086/310801>
- Cavagnolo, K. W., Donahue M., Voit G. M., Sun M. 2009, *ApJS*, 182, 12, <https://doi.org/10.1088/0067-0049/182/1/12>
- Cautun, M., van de Weygaert, R., Jones, B. J .T., & Frenk, C. S. 2014, *MNRAS*, 441, 2923, <https://doi.org/10.1093/mnras/stu768>
- Chavanis, P. H., Rosier, C., & Sire, C. 2002, *PhRvE*, 66, 036105, <https://doi.org/10.1103/PhysRevE.66.036105>
- Chavanis, P. H. 2003, *A&A*, 401, 15, <https://doi.org/10.1051/0004-6361:20021779>
- . 2006, *IJMPB*, Vol. 20, 22, 3113, <https://doi.org/10.1142/S0217979206035400>
- Cohn, H. 1980, *ApJ*, 242, 765, <https://doi.org/10.1086/158511>
- Cover, T. M., & Thomas, J. A. 2006, *Elements of Information Theory* (2nd ed.; Hoboken, NJ: Wiley-Interscience)
- Davis, M., Efstathiou, F., Frenk, C. S., & White, S. D. M., 1985, *ApJ*, 292, 371, <https://doi.org/10.1086/163168>
- Dehnen, W. 1993, *MNRAS*, 265, 250, <https://doi.org/10.1093/mnras/265.1.250>
- Dehnen, W. 2005, *MNRAS*, 360, 892, <https://doi.org/10.1111/j.1365-2966.2005.09099.x>
- Diemer, B. 2023, *MNRAS*, 519, 3292, <https://doi.org/10.1093/mnras/stac3778>
- Dressler, A., & Shectman, S. A., 1988, *AJ*, 95, 985, <https://doi.org/10.1086/114694>
- Einasto, J. 1965, *TrAlm*, 5, 87
- Einasto, J., Klypin, A., Saar, E., & Shandarin, S., 1984, *MNRAS*, 206, 529, <https://doi.org/10.1093/mnras/206.3.529>
- Einasto, J. 2010, *AIPC 1205, THE SUN, THE STARS, THE UNIVERSE AND GENERAL RELATIVITY: International Conference in Honor of Ya.B. Zel'dovich's 95th Anniversary*, 1205, 72, <https://doi.org/10.1063/1.3382336>
- Fielder, C. E., Mao, Y.-Y., Zentner, A. R., Newman, J. A., Wu, H.-Y., Wechsler, R. H. 2020, *MNRAS*, 499, 2426, <https://doi.org/10.1093/mnras/staa2851>
- García-Manzanárez, E. 2022, *MSc. Thesis*, Universidad de Guanajuato, Mexico
- Geller, M. J., & Beers, T. C., 1982, *PASP*, 94, 421, <https://doi.org/10.1086/131003>
- Geller, M. J., & Huchra, J. P., 1989, *Science*, 246, 897, <https://doi.org/10.1126/science.246.4932.897>

- Gibbons, J. D., & Chakraborti, S. 2003, *Nonparametric Statistical Inference* (4th ed.; New York: Marcel Dekker)
- Girardi, M., & Mezzetti, M. 2001, *ApJ*, 548, 79, <https://doi.org/10.1086/318665>
- Gunn, J. E., & Gott III, J. R. 1972, *ApJ*, 176, 1, <https://doi.org/10.1086/151605>
- Hellinger, E. 1909, *Journal für die reine und angewandte Mathematik*, 136, 210
- Hernquist, L. 1990, *AJ*, 356, 359, <https://doi.org/10.1086/168845>
- Heuman, C., & Shalabh, M. S. 2016, *Introduction to Statistics and Data Analysis* (Springer)
- Hill, T. L. 1956, *Statistical Mechanics* (New York: McGraw-Hill)
- Imre, A. R. 2007, How to generate and measure negative pressure in liquids? in *NATO Science Series II: Mathematics, Physics and Chemistry*. Vol 242, *Soft Matter under Exogenic Impacts*, eds. S. J. Rzoska & V. A. Mazur (Dordrecht: Springer), 379
- Iqbal, N., Ahmad, F., & Khan, M. S. 2006, *JApA*, 27, 373, <https://doi.org/10.1007/BF02709363>
- Iqbal, N., Khan, M. S., & Masood, T. 2011, *Natural Science*, 3, 1
- Jaynes, E. T. 1957, *PhRv*, 106, 4, <https://doi.org/10.1103/PhysRev.106.620>
- Jones, C., & Forman, W. 1984, *ApJ*, 276, 38, <https://doi.org/10.1086/161591>
- Kashibadze, O. G., Karachentsev, I. D., & Karachentseva, V. E. 2020, *A&A*, 635, 135, <https://doi.org/10.1086/161591>
- King, I. R. 1962, *AJ*, 67, 471, <https://doi.org/10.1086/108756>
- Laganá, T. F., Durret, F., & Lopes, P. A. A. 2019, *MNRAS*, 484, 2807, <https://doi.org/10.1093/mnras/stz148>
- Landau, L. D. & Lifshitz, E. M. 1980, *Statistical Physics, Course of Theoretical Physics*. Vol. 5 (3rd ed.; Butterworth-Heinemann)
- Libeskind, N. I., van de Weigert, R., Cautun, M., et al. 2018, *MNRAS*, 473, 1195, <https://doi.org/10.1093/mnras/stx1976>
- Lifshitz, E. M., & Pitaevskii, L. P. 1981, *Physical Kinetics* (Oxford: Pergamon)
- Lima-Neto, G. B. 2005, *BrJPh*, 35, 4b, <https://doi.org/10.1590/S0103-97332005000700042>
- Limber, D. N., & Mathews, W. G. 1960, *ApJ*, 132, 286, <https://doi.org/10.1086/146928>
- Lokas, E. L. & Mamon, G. A. 2003, *MNRAS*, 343, 401, <https://doi.org/10.1046/j.1365-8711.2003.06684.x>
- Lovisari, L., Forman, W., Jones, C., et al. 2017, *ApJ*, 846, 51, <https://doi.org/10.3847/1538-4357/aa844f>
- Lynden-Bell, D. 1967, *MNRAS*, 136, 101, <https://doi.org/10.1093/mnras/136.1.101>
- Lynden-Bell, D., & Wood, R. 1968, *MNRAS*, 138, 495, <https://doi.org/10.1093/mnras/138.4.495>
- Lynden-Bell, D., & Lynden-Bell, R. 1977, *MNRAS*, 181, 405, <https://doi.org/10.1093/mnras/181.3.405>
- Navarro, J. F., Frenk, C. S., & White, S. D. M. 1996, *ApJ*, 462, 563, <https://doi.org/10.48550/arXiv.astro-ph/9508025>
- Nelson, D., Springel, V., Pillepich, A., et al. 2019, *ComAC*, 6, 2, <https://doi.org/10.1186/s40668-019-0028-x>
- Oort, J. H. 1983, *ARA&A*, 21, 373, <https://doi.org/10.1146/annurev.aa.21.090183.002105>
- Padmanabhan, T. 1989, *ApJS*, 71, 651, <https://doi.org/10.1086/191391>
- \_\_\_\_\_. 1990, *PhR*, 188, 5, [https://doi.org/10.1016/0370-1573\(90\)90051-3](https://doi.org/10.1016/0370-1573(90)90051-3)
- \_\_\_\_\_. 1993, *Structure formation in the Universe* (Cambridge, MA: CUP)
- \_\_\_\_\_. 2000, *Theoretical Astrophysics. Vol. I, Astrophysical Processes* (Cambridge, MA: CUP)
- Parekh, V., van der Heyden, K., Ferrari, C., et al. 2015, *A&A*, 575, 127, <https://doi.org/10.1051/0004-6361/201424123>
- Peebles, P. J. E. 1980, *The Large-Scale Structure of the Universe*. (Princeton, NJ: PUP)
- Pontzen, A. & Governato, F. 2013, *MNRAS*, 430, 121, <https://doi.org/10.1093/mnras/sts529>
- Planck Collaboration: Ade, P. A. R., et al. 2016, *A&A*, 594, 27, <https://doi.org/10.1051/0004-6361/201525823>
- Rood, H. J., Page, T. L., Kintner, E. C., & King, I. R. 1972, *ApJ*, 175, 627, <https://doi.org/10.1086/151585>
- Sampaio, F. S. & Ribeiro, A. L. B. 2014, *NewA*, 27, 41, <https://doi.org/10.1016/j.newast.2013.08.008>
- Santiago-Bautista, I., Caretta, C. A., Bravo-Alfaro, H., Pointecouteau, E., & Andernach, H. 2020, *A&A*, 637, 31, <https://doi.org/10.1051/0004-6361/201936397>
- Sarazin, C. L. 1988, *X-ray Emission from Clusters of Galaxies* (Cambridge, MA: CUP)
- Saslaw, W., 1980, *ApJ*, 235, 299, <https://doi.org/10.1086/157634>
- Saslaw, W. & Hamilton, A. 1984, *ApJ*, 276, 13, <https://doi.org/10.1086/161589>
- Schneider, P. 2015, *Extragalactic Astronomy and Cosmology: An Introduction* (2nd ed.; Springer)
- Shannon, C. E. 1948, *Bell Syst. Tech. J.* 27, 379
- Springel, V., White, S. D. M., Jenkins, A., et al. 2005, *Natur*, 435, 629, <https://doi.org/10.1038/nature03597>
- Springel, V., Pakmor, R., Pillepich, A., et al. 2018, *MNRAS*, 475, 676, <https://doi.org/10.1093/mnras/stx3304>
- Tozzi, P. & Norman, C. 2001, *ApJ*, 546, 63, <https://doi.org/10.1086/318237>
- Tremaine, S., Hénon, M., & Lynden-Bell, D., 1986, *MNRAS*, 219, 285, <https://doi.org/10.1093/mnras/219.2.285>

- Tully, R. B. 2015, *AJ*, 149, 54, <https://doi.org/10.1088/0004-6256/149/2/54>
- Voit, G. M. 2005, *RvMP*, 77, 207, <https://doi.org/10.1103/RevModPhys.77.207>
- White, S. D. M. 1992, in *Clusters and Superclusters of Galaxies*, ed. A. C. Fabian (Dordrecht: Kluwer), 17
- White, S. D. M. 1996, preprint (arXiv:astro-ph/9602021v1), <https://doi.org/10.48550/arXiv.astro-ph/9602021>
- Zakhozay, V. A. 2018, *OAP*, 30, 56, <https://doi.org/10.18524/1810-4215.2018.31.148048>
- Zhang, Y.-Y., Andernach, H., Caretta, C. A., et al. 2011, *A&A*, 526, 105, <https://doi.org/10.1051/0004-6361/201015830>
- Zhang, Y.-Y., Reiprich, T. H., Schneider, P., et al. 2017, *A&A*, 599, 138, <https://doi.org/10.1051/0004-6361/201628971>

C. A. Caretta, E. García-Manzanárez, and Johan M. Zúñiga: Departamento de Astronomía, Universidad de Guanajuato, Apartado Postal 36000, Guanajuato, Gto., México (jm.zuniga@ugto.mx).

A. P. González: Departamento de Matemáticas, Universidad del Cauca, Colombia.

# ASTRONOMICAL SIGNALS IN THE BRIGHTEST FIREBALLS THAT FALL ON EARTH

D. Maravilla<sup>1</sup>, M. Pazos<sup>2</sup>, and G. Cordero<sup>1</sup>

*Received January 25 2023; accepted February 2 2024*

## ABSTRACT

In this work a wavelet spectral study of a time series of brightest fireballs is presented. The wavelet analysis shows that there are two solar periodicities around 27 and 13.5 days. These periodicities have been associated to Carrington rotation and lunar motions and indicate that both Solar and Lunar rotations could have an influence on the brightest fireballs that fall on Earth. A third periodicity around 2.5 days was also identified in almost all spectra but it could be a harmonic of those periods.

## RESUMEN

En este trabajo se presenta un estudio espectral de series de tiempo de la entrada de meteoroides pequeños a la atmósfera terrestre usando la técnica wavelet. El análisis muestra que hay dos señales alrededor de 27 y 13.5 días. Estas periodicidades han sido asociadas a la rotación Carrington y a los periodos lunares que podrían estar influenciando la caída de este tipo de objetos sobre la Tierra. Una tercera periodicidad alrededor de 2.5 días fue identificada en casi todos los espectros obtenidos y podría ser una señal armónica de las periodicidades lunar y solar.

*Key Words:* meteorites, meteors, meteoroids — Moon — Sun: rotation

## 1. INTRODUCTION

There are many phenomena that can be observed in the atmosphere of our planet, from the formation of clouds to the arrival of bodies that come from space and cross the different layers of the atmosphere, producing luminous phenomena such as meteors and meteor showers. An average of 100,000 metric tons of material from space arrives on Earth yearly (Brownlee 2001; Trigo-Rodríguez 2019). Part of this material ablates in the atmosphere while the rest can survive and be deposited as meteorites on the Earth's surface, at the bottom of the oceans or on the ice of Antarctica, where it can be collected. A particular case of extraterrestrial material that reaches Earth are dust particles (IDPs), also called Brownlee particles, which can remain suspended in the stratosphere and be collected by planes to be analyzed in laboratories (Duprat et al. 2007) or become embedded in spacecrafts where they impact (Moorhead et al. 2020). The IDPs contain information on the compounds that come from the cloud of

gas and dust that gave rise to our Solar System, as well as information from the pre-solar period. These bodies come mainly from comets and probably from asteroids (Bradley et al. 1996; Vernazza et al. 2015).

From recent studies carried out on meteorites it is known that much of the extraterrestrial material comes mainly from undifferentiated bodies, small asteroids and comets (Trigo-Rodríguez 2019). In particular, it has been observed that the extraterrestrial material that reaches the surface of our planet is mainly of a chondritic nature. On the other hand, material that has an origin in differentiated bodies can also reach Earth, as is the case of achondritic meteorites whose origin may be Mars, as the ALH84001 meteorite (McKay et al. 1996; McSween & Harry 1996), the asteroid Vesta from which the Tatahouine meteorite comes from (Maravilla et al. 2013) or the Moon, as the lunar meteorites found and collected in Northern Africa (Korotev & Irving 2021; Heiken et al. 1991).

A particularity of asteroids and comets is that they are constantly subjected to erosion processes, which makes them one of the main sources of meteoroids that form the zodiacal cloud. While aster-

<sup>1</sup>Instituto de Geofísica, UNAM, México.

<sup>2</sup>Instituto de Cambio Climático, y Ciencias de la Atmósfera, UNAM, México.

oidal meteoroids are produced by impacts, cometary meteoroids come from the degassing of their parent bodies (Jenniskens 1998; Trigo-Rodríguez 2019) considering that comets were formed in distant regions of the protoplanetary disk from the accretion of primordial materials made up of ice, organic material and dust grains (Trigo-Rodríguez & Blum 2022), and asteroids were formed in the inner solar system and are made up fundamentally of minerals (JPL NASA CNEOS: NEO Basics, <https://cneos.jpl.nasa.gov/fireballs/>). When comets approach the Sun, they sublimate, generating jets that emit large quantities of meteoroids into space. These meteoroids form beams of dust that can remain in stable orbits around the Sun for thousands of years (Williams 2002) and can be intercepted by planets such as the Earth. To exemplify this fact, the Earth receives tens of kilograms of material that comes from meteor showers such as the Leonids or the Perseids (Trigo-Rodríguez & Blum 2009) that have their origin in the comets 55P/Tempel-Tuttle and 109P/Swift-Tuttle respectively.

In recent years, it was discovered by the JUNO space mission that Mars is the main source of dust in the zodiacal cloud between 1 and 2.8 AU (Jorgensen et al. 2020), becoming the third source of material that feeds the zodiacal cloud. When cometary or asteroidal meteoroids impact a planetary atmosphere, they will be decelerated, fragmented, evaporated and/or pulverized. The speed of a meteoroid that impacts the atmosphere is in the range of 11 to 72 km/s. As cometary meteoroids are made up of organic matter, micrometric dust and volatiles, they cannot survive their passage through the atmosphere (Trigo-Rodríguez & Blum 2009). As a result of the collision of a meteoroid with the atmosphere, ionization, ablation, fragmentation and light generation can occur (fireballs) (Trigo-Rodríguez 2019; Mas Sanz et al. 2020).

Trigo-Rodríguez & Blum (2022) presented the results of an investigation based on the study of meteoroid stream flux and mass distribution of cometary material that arrives on Earth. The fundamental results of this work show that there is a gap between the mass distribution of cometary dust and the largest IDPs collected in the atmosphere, and show that the typical sizes of cometary meteoroids (3 cm) cannot survive their passage through the atmosphere; but if fragmentation occurs in the upper atmosphere, then the meteoroids may not undergo ablation and therefore some of the IDPs could be fragments of low-velocity meteoroids. The results also indicate that the direct flow coming from the

meteoroid streams has a minor contribution from cometary meteoroids accreting on the Earth (of the order of 500 tons/y). The same work also mentions that comets could have participated in the massive delivery of sodium and organic compounds to the early Earth.

The study from a scientific point of view of the extraterrestrial material that reaches our planet has been carried out since the last century through the construction of observation networks, detection instruments and monitoring networks; highlights are the US Government sensors (USG) that have documented the entry of fireballs around the world since 1988 (Tagliaferri et al. 1994) and the worldwide FRIPON network, which has monitored the entry of 4000 meteoroids since 2016 (Colas et al. 2020) above part of western Europe and characterized its physical and dynamic properties. With this network, the flux of meteorites larger than 100g has been estimated, being of the order of  $14/\text{yr}/10^6 \text{ km}^2$ . According to Ceplecha et al. (1998) and Rubin & Grossman (2010), once a body coming from the interplanetary medium travels across the terrestrial atmosphere, it can produce a luminous phenomenon called meteor if its size is larger or equal than 100 microns. Fireballs are meteors whose magnitude is  $-4$  or brighter (Blanch et al. 2017). This phenomenon can be registered by different instrument such as optical telescopes, radar, lidar, and infrasound sensors (Edwards et al. 2005; Brown et al. 2008; Trigo-Rodríguez et al. 2008).

Peña-Asensio et al. (2022) reported the orbits of the meter-sized hazardous projectiles that impacted the Earth's atmosphere and investigated the possible connection that the projectiles could have with cometary and asteroidal meteoroid streams and NEO's (Near Earth Objects). The authors used the series of superbolide events from the CNEOS database recorded by the United States Government sensors. Of the 887 events in the database, only 255 were analyzed because they had enough information to calculate their heliocentric orbit. The results of this research indicate that only 58 of the events probably have a cometary or asteroidal origin. These 58 events represent 23 % of the total number of meter-sized projectiles that produce large bolides, which implies that one in four superbolides is originated by near-Earth objects (NEO's). The authors, based on the height and speed of each event in the database (CNEOS), found that 61.9 % of the projectiles are rocky or rocky-iron, 35.7 % are carbonaceous and 2.4 % are cometary. In relation to their heliocentric orbit, 85.5 % have orbital elements similar to



those of asteroids and 9.8 % correspond to comets of the Jupiter family. Of the events analyzed, the researchers identified 5 events with hyperbolic orbits and identified the orbital elements of the first interstellar superbolide detected on January 8, 2014, concluding that at least 1 % of the large meteoroids that impact the Earth's atmosphere could be of interstellar origin.

The Earth and the Moon are under the gravitational and electromagnetic influence of the Sun. The effects on the Earth have been identified through spectral analysis of time series of solar phenomena or events such as sunspots, the magnetic solar cycle or solar cosmic rays. Through spectral analysis using different techniques, several short, medium and long-term periodicities have been identified, ranging from days to years. Some of these periodicities have been identified in terrestrial phenomena from geomagnetic, atmospheric and oceanographic points of view, showing that there is a relationship between the Sun and the Earth. But just as this relationship exists, the Sun has also influence on other bodies of the Solar System, such as meteoroids, comets and asteroids; there is also a strong gravitational influence of the Earth and the Moon on the bodies living in the terrestrial vicinity.

## 2. THE BRIGHTEST FIREBALLS DATA

In this research a time series related to registered fireballs corresponding to the last 33 years is spectrally studied taking into account 852 events with energies greater than 0.073 Kt from 15 April 1988 to 29 December 2020. The data were provided by the United States Government sensors homepage and released to the Near Earth Object Program (<https://cneos.jpl.nasa.gov/fireballs/>); they contain the following information: peak brightness data/time, geographical location, altitude and speed when the object reaches its maximum brightness, approximate total optical energy and calculated total impact energy.

### 2.1. *The Spectral Method*

When astronomical and astrophysical data are analyzed we can expect gaps or errors due to different record techniques and times (Jopek & Kaňuchová 2017; Soon et al. 2019). Spectral analysis has been used to study time series with missing astronomical and astrophysical data (Feigelson 1997; Scargle 1997; Ding et al. 1998). The Fourier transform (FT) can be applied to analyze the time series. However, this method might not be suitable for non-stationary and irregularly spaced time series;

therefore, another method is required to study a time series with gaps such as the brightest fireball events. The classical wavelet technique (Torrence & Compo 1998; Velasco et al. 2017) is used for non-stationary time series. The wavelet method is useful for analyzing local variations of power within a single non-stationary time series at multiple periodicities. We applied this method using the Morlet function specially developed for geophysical phenomena, which provides a good time resolution (Torrence & Compo 1998). We also applied the Morlet mother function to analyze the power spectral density (PSD) of the brightest fireballs, since this mother function does not only provide a higher periodicity resolution but is also a complex function that allows to calculate the inverse wavelet transform (Torrence & Compo 1998; Soon et al. 2011; Velasco et al. 2017; Soon et al. 2019). The meaningful wavelet periodicities with a confidence level greater than 85% must be inside the cone of influence (COI), and the interval of 85% confidence (Torrence & Compo 1998) is marked by thin black contours in the spectra. The global spectra have been included in all wavelet plots to show the power contribution of each periodicity inside the COI (See Figure 1, for example). Also, we established the significance levels in the global wavelet spectra with a simple red noise model where the power increases at lower frequencies (Gilman et al. 1963). The uncertainties are obtained by dividing the maximum peak width and measuring both halves at the base, related to the period scale (Mendoza et al. 2006). By applying this method to the whole time series of the brightest fireballs and using the toolbox developed by Grinstead et al. (2014) we obtained periodicities of different time scales, ranging from days to years. We aimed to focus on periodicities of higher frequency (scale of days), and then we filtered the data with a high pass band filter. The periodicities found with the wavelet method were validated using Redfit-X (Björg Ólafsdóttir, et al. 2016).

## 3. RESULTS AND DISCUSSION

The first wavelet PSD was obtained with the complete time series. Later, this time series was filtered and spectrally analyzed by short intervals consisting of the brightest fireball series related to the ascending and descending phases of the solar cycle. Based on the span of the brightest fireball time series used, we found three short intervals associated with the descending solar phases and corresponding to solar cycles 22, 23 and 24, and two related to the ascending solar phase of solar cycles 23 and 24, respectively. The short time series associated with

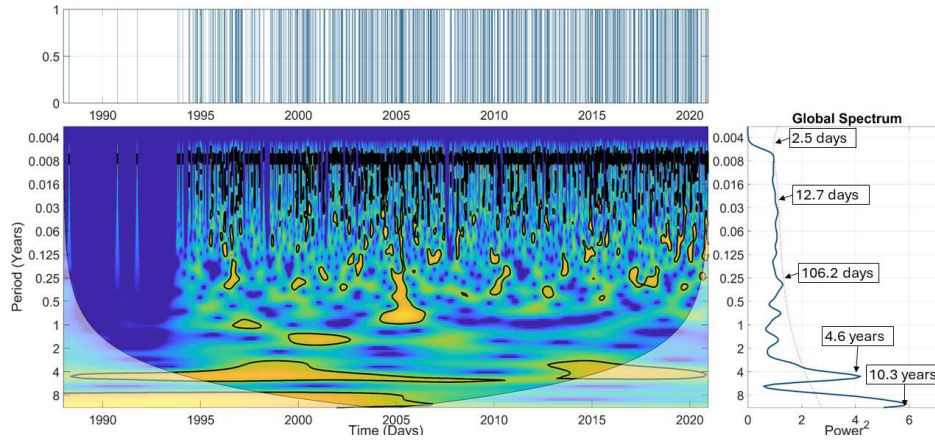


Fig. 1. Wavelet spectrum of the brightest fireball meteor data provided by United States Government sensors from 1988 to 2020. On the right side the global spectrum shows significant periodicities at 2.5, 12.7 and 106.2 days, and 4.6 and 10.3 years. The red dotted line represents the 85 % confidence level. The PSD spectrum is shown in the middle of the figure. The time series of the brightest fireballs is presented above the PSD. The color figure can be viewed online.

the descending solar phases correspond to the following intervals: 1991 to 1996 for solar cycle 22; 2000 to 2008 for solar cycle 23 and 2014 to 2020 for solar cycle 24. The short time series related to the ascending solar phases correspond to the following intervals: 1996 to 2000 for solar cycle 23 and 2008 to 2014 for solar cycle 24.

### 3.1. Wavelet Analysis

#### 3.1.1. The Complete Time Series of the Brightest Fireballs

The wavelet spectrum of the complete time series of the brightest fireballs shows five significant periodicities (Figure 1). From an inspection of Figure 1, the peak with the highest power is located at 10.3 years while the next one is at 4.6 years. The other three periodicities are located at 106.2 days, 12.7 days and 2.5 days, respectively (Table 1). All these periodicities are related to an 85% confidence level. Ge (2007), describes accurately that the significance test of the wavelet method developed by Torrence and Compo addresses the issue of how to distinguish statistically significant results from those due to pure randomness when only one sample of the population is studied, as is the case of the time series of fireballs used in this research. The confidence level is also calculated by the program and has been established in the results by the red noise line. The length of the time series and the temporal resolution are related with this level of confidence. The longest and highest resolution of data in a time series increases the confidence level.

TABLE 1  
PERIODICITIES OF THE COMPLETE TIME SERIES<sup>a</sup>

Periodicity	+	-
2.5 d	0.9	0.25
12.7 d	5.5	3.2
106.2 d	36.5	21.9
4.6 y	0.9	1.15
10.3 y	1.3	4.16

<sup>a</sup>The uncertainties are indicated with the signs + and - respectively. Days - d; Years - y.

#### 3.1.2. Filtered Short Time Series of Brightest Fireballs

##### a) Solar descending phases

In order to obtain the PSD spectra, the wavelet technique was used again in all short time series. Figures 2, 3 and 4 show the spectra of the brightest fireball time series associated with the descending phase of solar cycles 22, 23 and 24, respectively. Figure 2 shows the PSD related to solar cycle 22. In this figure two periodicities can be observed around 2.5 and 117 days (Table 2). Only the peak at 117 days is above the 85% confidence level. Figure 3 shows the wavelet PSD spectrum of the brightest fireball meteors linked to the descending solar cycle 23. In this figure it can be seen that there are five periodicities at 3.1, 5.8, 14.7, 22 and 280.1 days (Table 2), all of them under the 85% confidence level. The wavelet PSD spectrum associated with the descending solar phase of solar cycle 24 appears in Figure 4. In this plot, four periodicities appear at 2.5, 7.4, 29.5 and

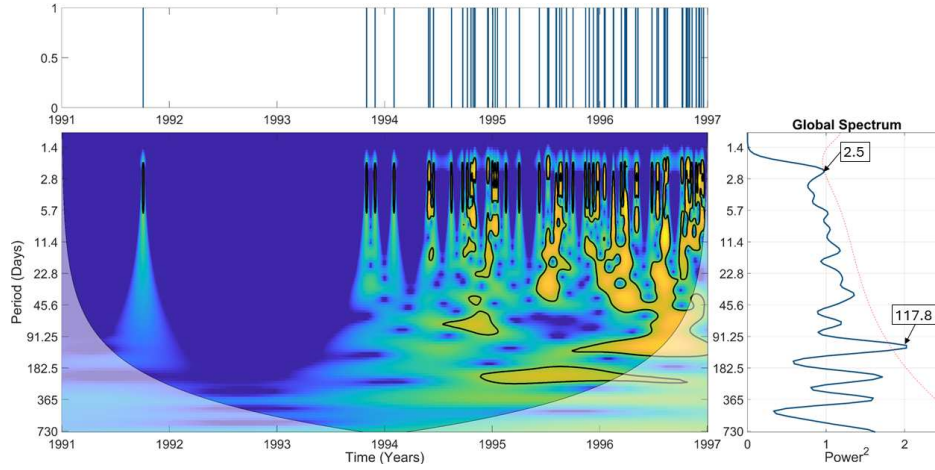


Fig. 2. PSD spectrum of the brightest fireball time series associated to the descending solar phase of solar cycle 22. The red dotted line represents the 85 % confidence level. The color figure can be viewed online.

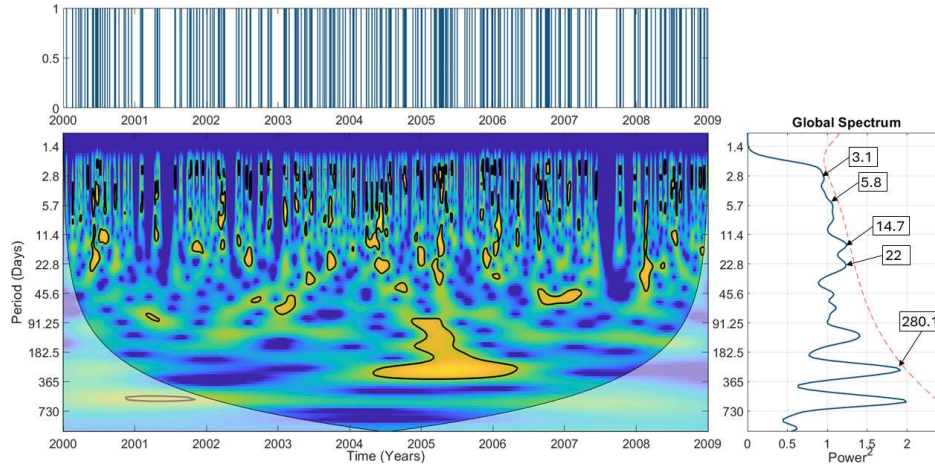


Fig. 3. Wavelet PSD of the brightest fireball time series linked to the solar descending phase of solar cycle 23. All peaks are under the dotted red line that corresponds to the 85 % confidence level. The color figure can be viewed online.

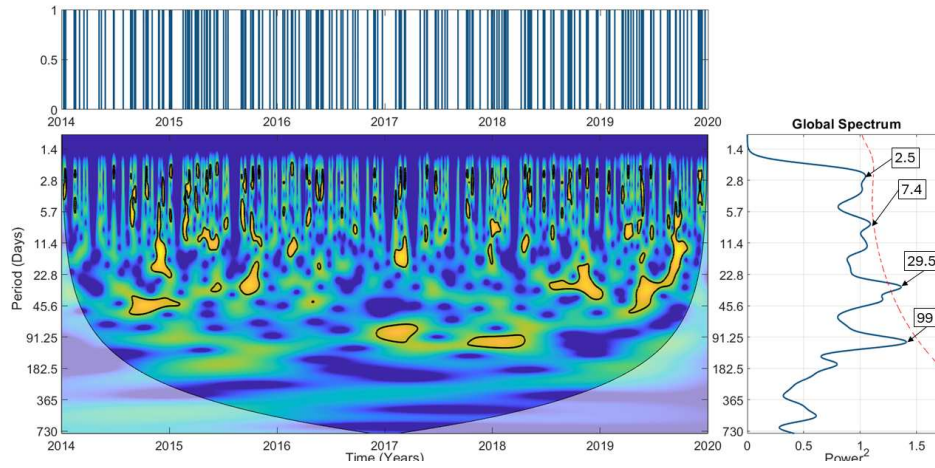


Fig. 4. Wavelet PSD of the brightest fireball time series linked to the descending solar phase of solar cycle 24. All peaks are under the dotted red line that corresponds to the 85 % confidence level. The color figure can be viewed online.

TABLE 2  
PERIODICITIES IN SOLAR CYCLES  
(DESCENDING PHASE<sup>a</sup>)

Solar cycle	Interval (years)	Periodicity (days)	(+)	(-)
22	1991 – 1996	2.5	0.8	0.4
...	...	117	22.3	29.5
23	2000 – 2008	3.1	0.6	0.6
...	...	5.8	0.7	0.3
...	...	14.7	3.9	2.3
...	...	22.0	5.7	3.5
...	...	280.1	93.8	82.1
24	2014 – 2020	2.5	0.8	0.2
...	...	7.4	1.9	0.8
...	...	29.5	7.7	3.2
...	...	99	25.9	20.4

<sup>a</sup>Uncertainties are indicated with the signs + and - and are stated in days(d).

99 days and only the periodicity around 29.5 days is above the 85% confidence level (Table 2).

b) Solar ascending phases

Figure 5 shows the PSD spectrum of the fireball time series connected with the ascending phase of solar cycle 23. In this plot four periodicities appear at 2.6, 4.4, 12.4 and 105 days (Table 3). The red line represents the 85% confidence level and all peaks are under this line.

The plot associated with the ascending phase of solar cycle 24 is presented in Figure 6 where three periodicities at 2.5, 3.7 and 29.5 days can be seen. Only the last one is above the 85% confidence level. Analyzing the periodicities observed in Figure 1 and considering uncertainties, the peak at 12.7 days could be linked to the Carrington rotation (27.275 days) as well as to the four Moon periods: synodic, sideral, nodical or draconic, and anomalistic (SSNA). The synodic period has a duration of 29.531 days, the sideral period has a duration of 27.322 days. The nodical or draconic period is of 27.212 days and the anomalistic month has a duration of 27.555 days (Karttunen et al. 2017). The periodicity at 12.7 days in Figure 1 could be a harmonic of all these periodicities (around 13.5 days). Both the Carrington rotation and the 13.5 days period have been observed in many solar-terrestrial parameters such as sunspot number, solar magnetic emergence, solar wind, the Ca-K-line plage index, sudden storm commencements, and others (Mursula & Zieger 1996; Prabhakaran et al. 2001, 2002, 2004; Emery et al. 2011; Singh & Badruddin 2014). It is important to

TABLE 3  
PERIODICITIES IN SOLAR CYCLES  
(ASCENDING PHASE<sup>a</sup>)

Solar cycle	Interval (years)	Periodicity (days)	(+)	(-)
22	1988 – 1991	...	...	...
23	1996 – 2000	2.6	0.3	0.3
...	...	4.4	0.5	0.3
...	...	12.4	2.3	2.5
...	...	105	27.3	21.7
24	2008 – 2014	2.5	0.8	0.2
...	...	3.7	0.6	0.6
...	...	29.5	7.7	3.2

<sup>a</sup>Uncertainties are indicated with the signs + and - and are stated in days(d).

point out here that the 13.5 days periodicity has also been reported in several scientific papers and is related e.g., to solar wind and ionospheric parameters; its dependence on the solar radiation wavelength has been also found by Donnelly & Puga (1990) and it could be also the lunar periods (SSNA) first harmonic. The peak at 10.3 years could be associated to the sunspots cycle while the peak at 4.6 years may be the first harmonic of that spectral signal. From the spectral analysis of the short time series of the brightest fireball data associated with descending phases of the considered solar cycles (22, 23 and 24), the periodicities at 22 days (solar cycle 23, Figure 3) and at 29.5 days (solar cycle 24, Figure 4) are related to the Carrington rotation period (27.275 days) and the latter periodicity could be associated with the lunar periods (SSNA) if uncertainties are taken into account. In Figure 3, the peak at 14.7 days (solar cycle 23) could have a connection with the solar rotation period (27.275 days) and the Moon periods (SSNA), being its first harmonic. Analyzing the results obtained from the wavelet spectral analysis of the short time series of the brightest fireball data linked to the ascending phases of solar cycles 23 and 24, a peak at 29.5 days is observed in Figure 6 (solar cycle 24), possibly connected with the Carrington rotation and the lunar signals (SSNA), whereas a peak at 12.4 days is observed in Figure 5 (solar cycle 23), which could be a harmonic of the 27.175 days solar rotation and lunar periodicities (SSNA).

Summarizing, the Carrington rotation signal (27.275 days) and the lunar periods (SSNA) are manifested in the spectra of the brightest fireball time series related with descending phases of solar cycles 23 and 24 (Figures 3 and 4) and with the ascending



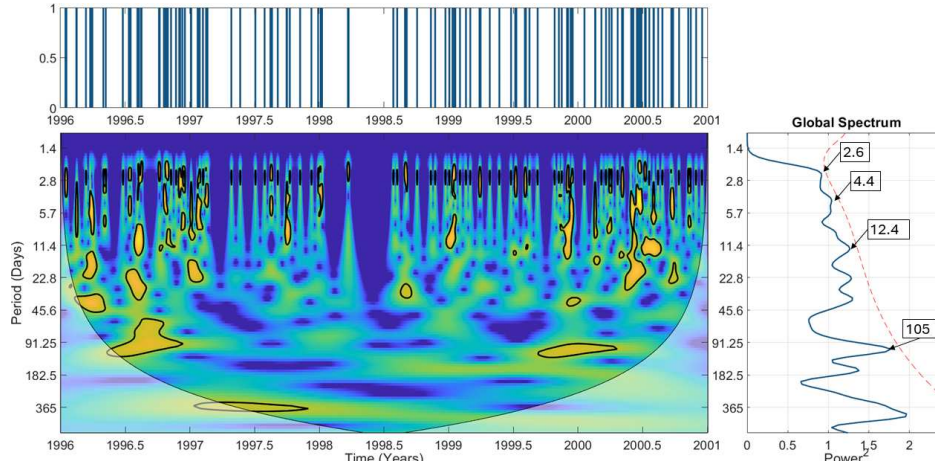


Fig. 5. Wavelet PSD of the brightest fireball time series linked to the solar ascending phase of solar cycle 23. All peaks are under the 85 % confidence level (dotted red line). The color figure can be viewed online.

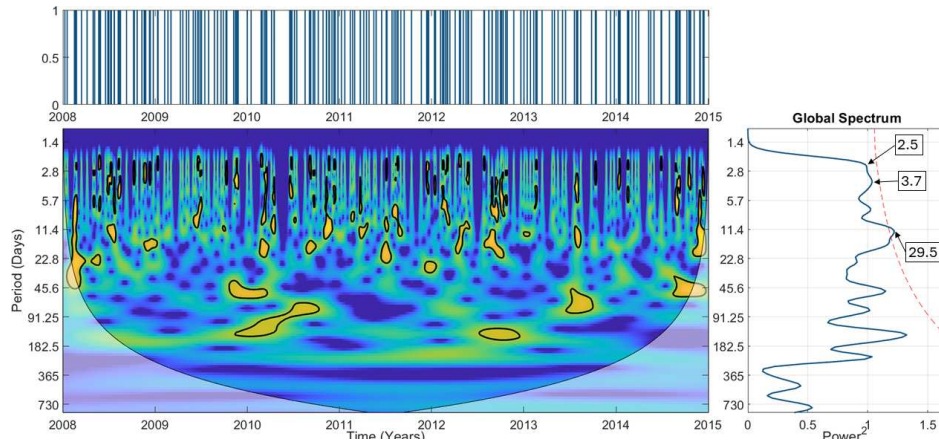


Fig. 6. Wavelet PSD of the brightest fireball time series linked to the solar ascending phase of solar cycle 24. The peak at 29.5 days is above the dotted red line that corresponds to the 85 % confidence level. The color figure can be viewed online.

solar phase of cycle 24 (Figure 6). The first harmonic of the Carrington rotation (13.5 days) could be present in the PSD of the brightest fireball meteor spectra associated with the entire solar cycle 23 (Figures 3 and 5). The presence of a periodicity close to the Carrington rotation period (27.275 days) and the Moon periods (SSNA) in the wavelet spectra of cycles 23 and 24 indicates that the solar rotation and lunar signals have left their mark in the brightest fireballs detected in the terrestrial atmosphere and could be modulating the fall of these extraterrestrial bodies on Earth. Additionally, a periodicity around 2.5 days appears in almost all spectra of the complete and short time series of the brightest fireballs associated with the considered solar cycles (ascending and

descending phases), (Tables 2 and 3) although the 3.1 days periodicity in the descending solar phase of solar cycle 23 could be also included here if the uncertainty associated with this peak, is considered. The physical reason for this periodicity is unknown though it could be a minor order harmonic of both the Carrington rotation and the Moon periods.

In order to look for the periodicities we found in the previous analysis (Figures 1-6) and possibly other ones, an additional wavelet analysis was done using the maximum velocity e.g. the entry velocity of meteoroids into the Earth's atmosphere (<https://cneos.jpl.nasa.gov/fireballs/>). We use the data from 2000 to 2020 because there is no maximum velocity registered before 2000. Separating the max-

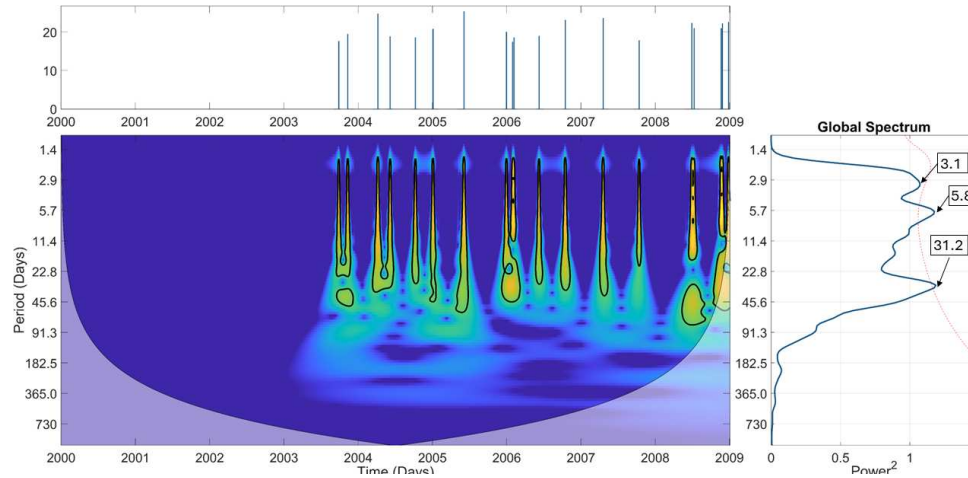


Fig. 7. PSD spectrum of the maximum velocity time series related to solar cycle 23 from 2000 to 2008 years (descending phase). The red dotted line represents the 85 % confidence level. The color figure can be viewed online.

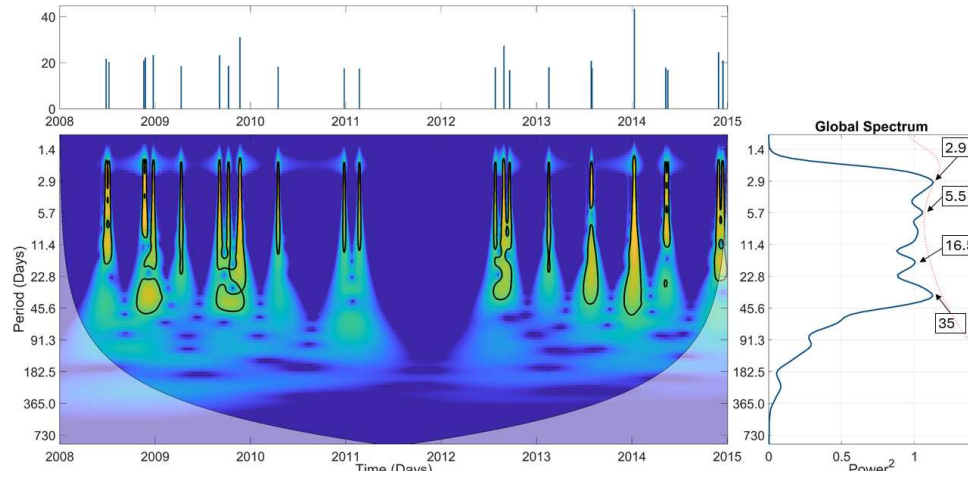


Fig. 8. PSD spectrum of the maximum velocity time series related to solar cycle 24 from 2008 to 2014 years (ascending phase). The red dotted line represents the 85 % confidence level. The color figure can be viewed online.

imum velocity time series based on the solar cycle length, three different intervals were selected corresponding to two descending solar phases from 2000 to 2008 (solar cycle 23) and from 2014 to 2020 (solar cycle 24), (Figures 7 and 9) and one ascending solar phase from 2008 to 2014 (solar cycle 24), (Figure 8), (Table 4).

In the descending period from 2000 to 2008, three periodicities are present at 3.1 days, 5.8 days and 31.2 days, while in the descending period from 2014 to 2020, the periodicities we found are located at 2.8 days, 4.4 days, 6.9 days and 19.7 days. In the ascending phase from 2008 to 2014, five different periodicities were identified, at 2.9 days, 5.5 days, 8.7 days, 16.5 days and 35 days respectively. Taking into

account the uncertainties, the lunar periods (SSNA) and the Carrington rotation period (27.275 days) are present in the descending solar phase from 2000 to 2008 and in the interval from 2008 to 2014, corresponding to an ascending solar phase. Analyzing these results from the spectral wavelet analysis we note that regarding the periodicity we observe in solar cycle 23 (Figure 7) at 31.2 days (solar descending phase), the periodicity at 35 days in solar cycle 24 (Figure 8), (solar ascending phase) and the periodicity at 19.7 days in the descending phase of solar cycle 24, all of them could be related to the Moon periods (SSNA) as well, if we consider the uncertainties. The other periodicities (Table 4) could be minor order harmonics of these last periods. If we assume that

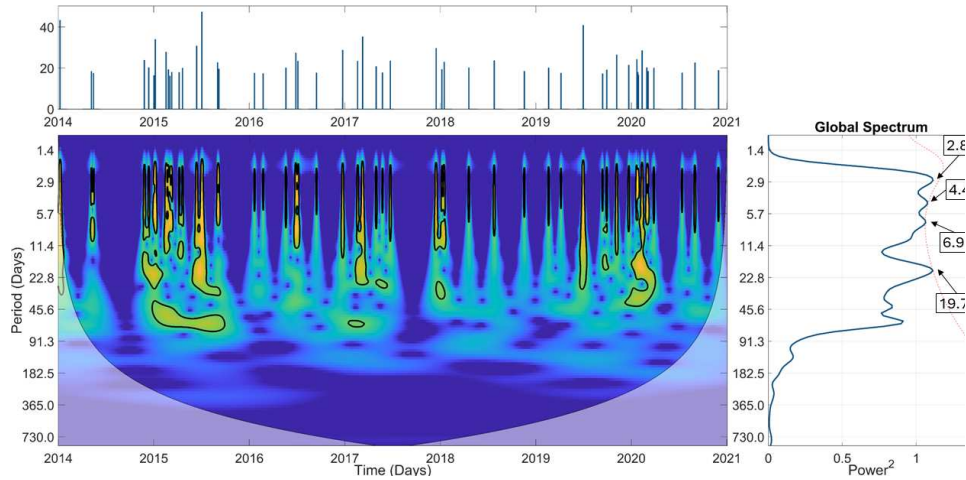


Fig. 9. PSD spectrum of the maximum velocity time series related to solar cycle 24 from 2014 to 2020 years (descending phase). The red dotted line represents the 85 % confidence level. The color figure can be viewed online.

TABLE 4

PERIODICITIES IN THE VELOCITY VECTOR TIME SERIES<sup>a</sup>

Solar cycle	Interval (years)	Periodicity (days)	(+)	(-)
23 descending phase	2000–2008	3.1	1.27	0.78
...	...	5.8	2.96	1.42
...	...	31.2	12.92	6.44
24 ascending phase	2008–2014	2.9	1.48	0.6
...	...	5.5	1.1	0.9
...	...	8.7	3.7	1.3
...	...	16.5	5.6	2.6
...	...	35	9.1	11.6
24 descending phase	2014–2020	2.8	0.7	0.5
...	...	4.4	1.1	0.7
...	...	6.9	1.9	1.1
...	...	19.7	11.5	5.0

<sup>a</sup>Uncertainties are indicated with the signs + and – and are stated in days(d).

the fireballs that arrive to our planet could be associated with a potential source of meter-size projectiles as is the case of Near Earth Objects (NEO's), (Peña-Asensio et al. 2022) and since NEO's are closer to the Moon, our satellite has a strong gravitational influence on the NEO's dynamics and the lunar signals are present in the time series analyzed, as shown in the wavelet spectra.

Peña-Asensio et al. (2022) reported that ‘certain meteoroid streams’ could be another important source of meter-sized hazardous projectiles; then, meteoroid streams could have a significant role as a source of fireballs arriving to Earth as is the case of fragments of comets and asteroids. One example of this are the Taurids (streams and showers) that have been associated not only with NEO's but also with a cometary origin. In this case the comet associated is 2P/Encke (Peña-Asensio et al. 2022).

#### 4. CONCLUSIONS

1. A periodicity around 27 days was found in the time series of the brightest fireball meteors, indicating that the Carrington rotation and the Moon (SSNA periods) are modulating the fall of meteors on Earth.

2. The periodicity around 13.5 days is barely present in several wavelet spectra of the short fireballs time series. This periodicity could be a harmonic of the main peak observed around the Carrington rotation and the Moon periods (SSNA), respectively.

3.- The periodicities found around 30 days in the maximum velocity analysis are close to both the Carrington rotation and the lunar periods (SSNA).

4. A peak at 2.5 days was found in almost all spectra (brightest fireball time series) and could be a small harmonic of the Carrington rotation period and lunar signals. On the other hand, this peak is under the 85% confidence level in all spectra of the short time series and is only significant considering the complete time series (Figure 1).

5.- Because most of the fireballs used for the wavelet analysis are less than 10 meters in size, they are not affected by the Yarkovsky effect, but they could be affected by radiation pressure or by the periodical gravity force of the Moon.

## REFERENCES

- Björg Ólafsdóttir, K., Schulz, M., & Mudelsee, M. 2016, *Comp. & Geosci.*, 91, 11
- Blanch, E., Trigo-Rodríguez, J. M., Madiedo, J. M., et al. 2017, in *Assessment and Mitigation of Asteroid Impact Hazards*, ed. J. M. Trigo-Rodríguez, M. Gritsevich & H. Palme (Switzerland: Springer), 185
- Bradley, J. P., Keller, L. P., Brownlee, D. E., & Thomas, K. L. 1996, *M&PS*, 31, 394, <https://doi.org/10.1111/j.1945-5100.1996.tb02077.x>
- Brown, P., Weryk, R. J., Wong, D. K., & Jones, J. 2008, in *Advances in Meteoroid and Meteor Science*, ed J. M. Trigo-Rodríguez, F. J. M. Rietmeijer, J. Llorca, & D. Janches (New York, NY: Springer), 209
- Brownlee, D. E. 2001, in *Accretion of Extraterrestrial Matter Throughout Earth's History*, ed B. Peucker-Ehrenbrink & B. Schmitz (New York, NY: Kluwer Academic/Plenum Publishers)
- Cepilecha, Z., Borovička, J., Elford, W. G., et al. 1998, *SSRv*, 84, 327, <https://doi.org/10.1023/A:1005069928850>
- Colas, F., Zanda, B., Bouley, S., et al. 2020, *A&A*, 644, 53, <https://doi.org/10.1051/0004-6361/202038649>
- Ding, Y. R., Zhao, H., & Li, Z. Y. 1998, *ChA&A*, 22, 235, [https://doi.org/10.1016/S0275-1062\(98\)00032-0](https://doi.org/10.1016/S0275-1062(98)00032-0)
- Donnelly, R. F. & Puga, L. C. 1990, *SoPh*, 130, 369, <https://doi.org/10.1007/BF00156800>
- Duprat, J., Engrand, C. Maurette, M. et al. 2007, *AdSpR*, 39, 605, <https://doi.org/10.1016/j.asr.2006.05.029>
- Edwards, W. N., Brown, P., & Revelle, D. O. 2005, in *Modern Meteor Science. An Interdisciplinary View*, ed. R. Hawkes, I. Mann, & P. Brown (Dordrecht: Springer)
- Emery, B. A., Richardson, I. G., Evans, D. S., Rich, F. J., & Wilson, G. R. 2011, *SoPh*, 274, 399, <https://doi.org/10.1007/s11207-011-9758-x>
- Feigelson, E. D. 1997, in *Astronomical Time Series*, ed. D. Maoz, A. Sternberg, & E. M. Leibowitz (Dordrecht: Springer)
- Ge, Z. 2007, *AnGeo*, 25, 2259, <https://doi.org/10.5194/angeo-25-2259-2007>
- Gilman, D. L., Fuglister, F. J., & Mitchell Jr., M. M. 1963, *JAtS*, 20, 182, [https://doi.org/10.1175/1520-0469\(1963\)020<0182:OTPSON>2.0.CO;2](https://doi.org/10.1175/1520-0469(1963)020<0182:OTPSON>2.0.CO;2)
- Grinstead, J. W., Wang, D., Bhat, H., et al. 2014, *Proc. Intl. Soc. Mag. Reson. Med.*, 22
- Heiken, G. H., Vaniman, D. T., & French, B. M. 1991, *Lunar Sourcebook, A User's Guide to the Moon*, (Cambridge, MA: CUP)
- Jenniskens, P. 1998, *EP&S*, 50, 555, <https://doi.org/10.1186/BF03352149>
- Jopek, T. J. & Kaňuchová, Z. 2017, *P&SS*, 143, 3, <https://doi.org/10.1016/j.pss.2016.11.003>
- Jorgensen, J. L., Benn, M., Connerney, J. E. P., et al. 2020, *JGR Planets*, 126, e2020JE006509, <https://doi.org/10.1029/2020JE006509>
- Karttunen, H., Kröger, P., Oja, H., Poutanen, M. & Donner, K. J. 2017, *Fundamental Astronomy* (Berlin: Springer-Verlag), <https://doi.org/10.1007/978-3-662-53045-0>
- Korotev, R. L. & Irving, A. J. 2021, *M&PS*, 56, 206, <https://doi.org/10.1111/maps.13617>
- Maravilla, D., Arenas-Alatorre, J., & Cañetas-Ortega, J. 2013, *J. Adv. Microsc. Res.*, 8, 252, <https://doi.org/10.1166/jamr.2013.1166>
- Mas Sanz, E., Trigo Rodríguez, J. M., Silber, E. A., et al. *LPSC*, 51, 2155
- McKay, D. S., Gibson Jr., E. K., Thomas-Keptra, K. L., et al. 1996, *Sci*, 273, 924, <https://doi.org/10.1126/science.273.5277.924>
- McSween Jr., H. Y. 1996, *M&PS*, 31, 691, <https://doi.org/10.1111/j.1945-5100.1996.tb02045.x>
- Mendoza, B., Velasco, V. M., & Valdés-Galicia, J. F. 2006, *SoPh*, 233, 319, <https://doi.org/10.1007/s11207-006-4122-2>
- Moorhead, A. V., Kingery, A., & Ehlert, S. 2020, *JSpRo*, 57, 160, <https://doi.org/10.2514/1.A34561>
- Mursula, K. & Zieger, B. 1996, *JGR*, 101, 27077, <https://doi.org/10.1029/96JA02470>
- Prabhakaran Nayar, S. R., Nair, V. S., Radhika, V. N., & Revathy, K. 2001, *SoPh*, 201, 405, <https://doi.org/10.1023/A:1017599621110>
- Prabhakaran Nayar, S. R., Radhika, V. N., Ramadas, V., & Revathy, K. 2002, *SoPh*, 208, 359, <https://doi.org/10.1023/A:1020565831926>
- Prabhakaran Nayar, S. R., Alexander, L. P., Radhika, V. N., et al. 2004, *AnGeo*, 22, 1665, <https://doi.org/10.5194/angeo-22-1665-2004>
- Peña-Asensio, E., Trigo-Rodríguez, J. M., Josep, M., & Rimola, A. 2022, *AJ*, 164, 76, <https://doi.org/10.3847/1538-3881/ac75d2>
- Rubin, A. E. & Grossman, J. N. 2010, *M&PS*, 45, 114, <https://doi.org/10.1111/j.1945-5100.2009.01009.x>
- Scargle, J. D. 1997, in *Astronomical time series*, ed. D. Maoz, A. Sternberg, & E. M. Leibowitz (Dordrecht: Springer)
- Singh, Y. P. & Badruddin 2014, *P&SS*, 96, 120, <https://doi.org/10.1016/j.pss.2014.03.019>
- Soon, W., Dutta, K., Legates, D. R., Velasco, V., & Zhang, W. 2011, *JASTP*, 73, 2331, <https://doi.org/10.1016/j.jastp.2011.07.007>
- Soon, W., Velasco Herrera, V. M., Cionco, R. G., et al. 2019, *MNRAS*, 483, 2748, <https://doi.org/10.1093/mnras/stz2748>



- 1093/mnras/sty3290
- Tagliaferri, E., Spalding, R., Jacobs, C., Worden, S. P., & Erlich, A. 1994, in Hazards due to comets and asteroids, ed. T. Gehrels, M. S. Matthews, & A. Schumann (Arizona, AZ: UAP)
- Torrence, Ch. & Compo, G. P. 1998, BAMS, 79, 61, [https://doi.org/10.1175/1520-0477\(1998\)079<0061:APGTWA>2.0.CO;2](https://doi.org/10.1175/1520-0477(1998)079<0061:APGTWA>2.0.CO;2)
- Trigo-Rodríguez, J. M., Madieto, J. M., Gural, P. S., et al. 2008, in Advances in Meteoroid and Meteor Science, ed. J. M. Trigo-Rodríguez, F. J. M. Rietmeijer, J. Llorca, & D. Janches (New York, NY: Springer)
- Trigo-Rodríguez, J. M. & Blum, J. 2009, PASA, 26, 289, <https://doi.org/10.1071/AS08070>
- Trigo-Rodríguez, J. M. 2019, in Hypersonic meteoroid entry physics, ed. G. Colonna, M. Capitelli, & A. Laricchiuta (Bristol, UK: IOP Publishing)
- Trigo-Rodríguez, J. M. & Blum, J. 2022, MNRAS, 512, 2277, <https://doi.org/10.1093/mnras/stab2827>
- Velasco Herrera, V. M., Soon, W., Velasco Herrera, G., Traversi, R. & Horiuchi, K. 2017, NewA, 56, 86, <https://doi.org/10.1016/j.newast.2017.04.012>
- Vernazza P., Marset M., Beck, P., et al. 2015, ApJ, 806, 204, <https://doi.org/10.1088/0004-637X/806/2/204>
- Williams I. P. 2002, in Meteors in the Earth's atmosphere, ed. E. Murad & I. P. Williams (Cambridge, UK: CUP)

G. Cordero and D. Maravilla: Instituto de Geofísica, Universidad Nacional Autónoma de México, (dmaravil@igeofisica.unam.mx).

M. Pazos: Instituto de Cambio Climático, y Ciencias de la Atmósfera, UNAM, México.



## CCD PHOTOMETRY OF TRAPEZIA STARS I<sup>1</sup>

A. Ruelas-Mayorga<sup>2</sup>, L. J. Sánchez<sup>2</sup>, A. Páez-Amador<sup>2</sup>, O. Segura-Montero<sup>2</sup>, and A. Nigoche-Netro<sup>3</sup>

*Received November 21 2023; accepted February 15 2024*

### ABSTRACT

We present photometric CCD observations of stars in four stellar trapezia ADS 15184, ADS 4728, ADS 2843, and ADS 16795. This study is performed on images obtained at the Observatorio Astronómico Nacional (OAN) at San Pedro Mártir, Baja California, México. In this work we utilise aperture photometry to measure the  $U$ ,  $B$ ,  $V$ ,  $R$  and  $I$  magnitudes of some of the stars in these dynamically unstable stellar clusters (trapezia). Using the  $Q = (U - B) - 0.72(B - V)$  parameter we obtain the spectral type of the studied stars as well as their distance to the Sun and their reddening. Slight differences between the  $Q$ -derived spectral types and those listed in SIMBAD might be due to a value different from 0.72 for the slope of the reddening line on the two-colour diagram.

### RESUMEN

Presentamos fotometría CCD de las estrellas en cuatro trapecios estelares ADS 15184, ADS 728, ADS 2843, y ADS 16795. El estudio se hace a partir de imágenes tomadas en el Observatorio Astronómico Nacional de San Pedro Mártir (OAN), Baja California, México. El presente trabajo utiliza la técnica de fotometría de apertura para medir las magnitudes  $U$ ,  $B$ ,  $V$ ,  $R$  e  $I$  de algunas estrellas en estos cúmulos abiertos dinámicamente inestables (trapecios). Usando el parámetro  $Q = (U - B) - 0.72(B - V)$  se obtuvo el tipo espectral de las estrellas estudiadas, también se derivaron sus distancias al Sol y sus enrojecimientos. Ligeras diferencias en los tipos espectrales derivados a partir del parámetro  $Q$  con los listados en SIMBAD, podrían deberse a un valor diferente de 0.72 de la pendiente de la línea de enrojecimiento en el diagrama de dos colores.

*Key Words:* Galaxy: stellar content — open clusters and associations: individual: ADS15184, ADS728, ADS2843, ADS16795 — techniques: photometry

## 1. INTRODUCTION

The stellar trapezia are formed in the interior of emission nebulae, such as the Orion Nebula. They are physical systems formed by three or more approximately equal stars, where the largest separation between its stars is never larger than three times the smallest separation (Ambartsumian 1955). That means the distances between the stars that form a trapezium are of the same order of magnitude. Trapezia are completely different to the hierarchical systems, where there could be a difference of an order of magnitude (10) between the smallest and largest separations.

The best known trapezium system is found in the Orion Nebula. Figure 1 shows this prototypical system. The brightest star in this system is  $\theta^1$  C Orionis, around which we can see the other three stars in the system.

Trapezia are not dynamically stable, the orbits of their stellar components are not closed. This leads very quickly to close encounters which result in the expulsion of one or more members of the system and by this

<sup>1</sup>Based upon observations acquired at the Observatorio Astronómico Nacional on the Sierra San Pedro Mártir (OAN-SPM), Baja California, México.

<sup>2</sup>Instituto de Astronomía, Universidad Nacional Autónoma de México, Ciudad de México, México.

<sup>3</sup>Instituto de Astronomía y Meteorología, Universidad de Guadalajara, Guadalajara, Jal. 44130, México.

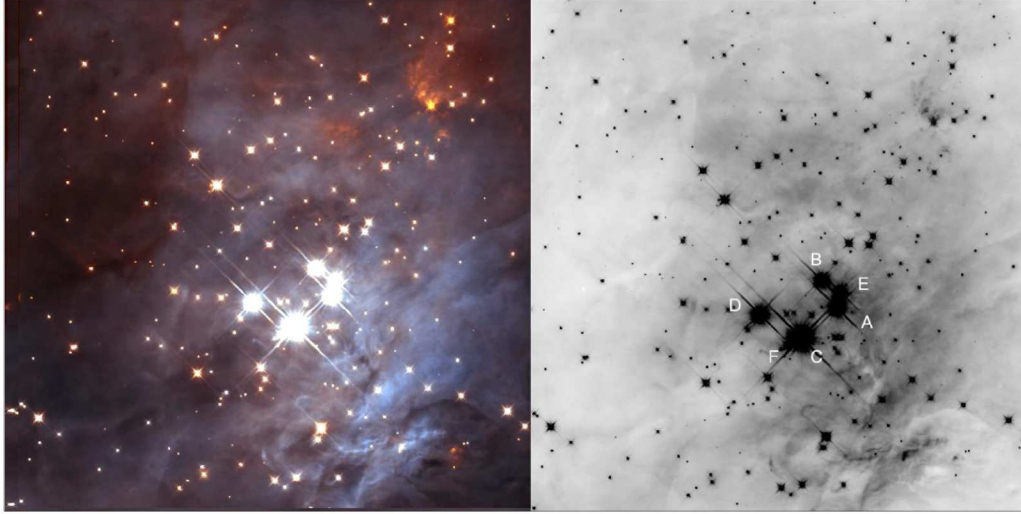


Fig. 1. The prototypical trapezium type system in the Orion Nebula. On the right, the six main components are marked (Taken from Allen et al. 2019). The colour figure can be viewed online.

they turn into hierarchical systems (Abt & Corbally 2000). As a consequence of this fact it is found that the maximum age of stellar trapezia cannot be larger than a few million years.

Using numerical simulation, Allen et al. (2018) showed that stellar trapezia evolve in time in different ways according to their initial configuration; some systems could break up into individual stars, whilst others evolve into binary or more complex stellar systems.

The age and evolution of trapezia also help us understand the evolution of stars. Knowing the distance between their stars and the total size of a trapezium system is fundamental in order to understand its dynamical evolution (Abt 1986).

This paper constitutes the first part of a photometric, spectroscopic and dynamical study of trapezia in our Galaxy. In § 2 we present the observations of the standard stars as well as those of the stars in the trapezia, in § 3 we discuss the slope of the reddening line on the two-colour diagram, and in § 4 we present our conclusions.

## 2. THE OBSERVATIONS

The observations were performed during two observing seasons in June and December 2019, with the 84 cm telescope at the OAN in San Pedro Mártir, Baja California, México. We observed regions of standard stars (Landolt 1992) in the five filters of interest ( $U-I$ ) distributed along the night so as to have measurements at different values of air mass. Interspersed within these observations, we observed the stars in the trapezia of interest. The images have a plate scale of  $0.47 \pm 0.06$  arcsec/pix and a total size of  $8.04 \pm 1.05$  arcmin respectively.

### 2.1. Reduction of Standard Stars

The standard stars are used in general to calibrate other astronomical observations. In this work, we shall refer to the set of equatorial standard stars published by Landolt (1992). We observed several of the Landolt standard regions every night and used them to calibrate our observations of the trapezia stars. Figure 2 shows a comparison of the standard region Rubin 149 observed by Landolt (1992) and by us.

In order to express the magnitude of the stars in the trapezia in a standard system, we performed aperture photometry of stars in some of the Landolt Standard Regions (Landolt 1992). The photometric measurements of the standard stars were carried out using the APT (Aperture Photometry Tool) programme, (see <https://www.aperturephotometry.org/about/>), and Laher et al. (2012).

The APT programme is a software that permits aperture photometry measurements of stellar images on a frame. The programme accepts images in the *fits* format; therefore, no transformation of the images to other formats was necessary. The observed standard regions had already been pre-processed.

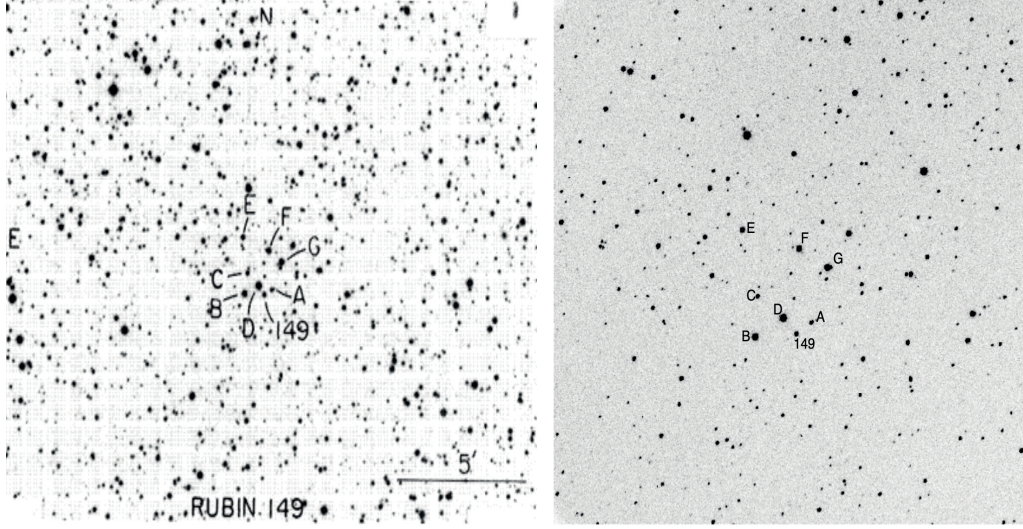


Fig. 2. On the left the Standard region RUBIN 149 Landolt (1992), on the right our observed image.

TABLE 1  
TRANSFORMATION COEFFICIENTS FOR  $U$

Standard Systems	A	K	C
13-14 June 2019	-0.56	0.13	23.51
10-11 December 2019	-0.44	0.18	23.49
12-13 December 2019	-1.20	0.06	24.47
13-14 December 2019	-	-	-
14-15 December 2019	17.07	-85.51	46.00
15-16 December 2019	-0.49	0.14	23.60

The transformation equations between the observed and intrinsic photometric systems are as follows:

$$U_{int} - U_{obs} = A_U * X + K_U * (U - B)_{obs} + C_U , \quad (1)$$

$$B_{int} - B_{obs} = A_B * X + K_B * (B - V)_{obs} + C_B , \quad (2)$$

$$V_{int} - V_{obs} = A_V * X + K_V * (B - V)_{obs} + C_V , \quad (3)$$

$$R_{int} - R_{obs} = A_R * X + K_R * (R - I)_{obs} + C_R , \quad (4)$$

$$I_{int} - I_{obs} = A_I * X + K_I * (R - I)_{obs} + C_I , \quad (5)$$

where the suffixes *int* and *obs* stand for *intrinsic* and *observed*. The coefficients  $A$ ,  $K$  and  $C$  represent the negative of the coefficient of atmospheric absorption, a colour term and a zero point shift term. We intend to calculate these terms using the observed values measured with APT, and the intrinsic values for the magnitudes given in Landolt (1992). The least squares procedure is used to solve the equations, and the coefficients obtained are shown in Tables 1–5.

In Figure 3 we see graphs of the calculated magnitude minus the intrinsic magnitude versus the observed instrumental magnitude ( $-2.5 \log(\# \text{ counts})$ ) for the five filters  $U$ – $I$ , for the set of standard stars we use as calibrators. As can be seen from the figures, the majority of the stars lie confined in the interval  $-0.1 \leq M_{cal} - M_{int} \leq 0.1$ , with a few stars falling outside this interval, except for the  $I$  filter where a substantial number of stars ventures past the  $\pm 0.2$  limit, reaching as far as  $\geq 0.4$ . When we check these values they all come from the observations on the nights 2019, December 12 and 13 and from the Rubin 149 and PG0220 standard regions. The night of December 12 was an excellent photometric observing night, whereas that on the 13 of December was a very poor night, for which, in fact, we have discarded the observations acquired.

TABLE 2  
TRANSFORMATION COEFFICIENTS FOR  $B$

Standard Systems	A	K	C
13-14 June 2019	-0.28	0.04	25.42
10-11 December 2019	-0.26	0.04	25.39
12-13 December 2019	-0.30	0.02	25.40
13-14 December 2019	664.84	3.79	-693.02
14-15 December 2019	-0.14	-0.08	25.14
15-16 December 2019	-0.31	0.04	25.42

TABLE 3  
TRANSFORMATION COEFFICIENTS FOR  $V$

Standard Systems	A	K	C
13-14 June 2019	-0.17	-0.07	25.04
10-11 December 2019	-0.14	-0.07	25.05
12-13 December 2019	-0.10	-0.08	24.97
13-14 December 2019	-39.46	0.75	63.66
14-15 December 2019	-0.14	-0.09	25.04
15-16 December 2019	-0.17	-0.06	25.10

TABLE 4  
TRANSFORMATION COEFFICIENTS FOR  $R$

Standard Systems	A	K	C
13-14 June 2019	-0.14	-0.05	25.09
10-11 December 2019	-0.10	-0.07	25.16
12-13 December 2019	-0.14	-0.03	25.15
13-14 December 2019	19.33	-2.21	5.28
14-15 December 2019	-0.09	-0.07	25.10
15-16 December 2019	-0.19	-0.07	25.22

TABLE 5  
TRANSFORMATION COEFFICIENTS FOR  $I$

Standard Systems	A	K	C
13-14 June 2019	-0.10	0.11	24.95
10-11 December 2019	-0.04	0.11	25.06
12-13 December 2019	-0.34	0.14	25.47
13-14 December 2019	-3.51	-1.37	29.93
14-15 December 2019	-0.06	0.07	25.11
15-16 December 2019	-0.12	0.05	25.17

## 2.2. Photometry of Trapezia Stars

Trapezia are open clusters in which their stars interact gravitationally, and this interaction has very noticeable dynamical consequences. As mentioned in subsection 2.1 the aperture photometry for the standard stars was done using the APT programme. However, the photometry of the trapezia stars must be carried out on a set of more than a thousand images. For this photometric measurements, we used the aperture photometry capabilities of the programme AstroImageJ (see <http://astro.phy.vanderbilt.edu/~vida/aij.htm>, Collins et al. (2017)). As the aperture photometry measurements carried out with AstroImageJ are automatic, we performed a comparison between the results obtained with APT and with AstroImageJ for the stars in

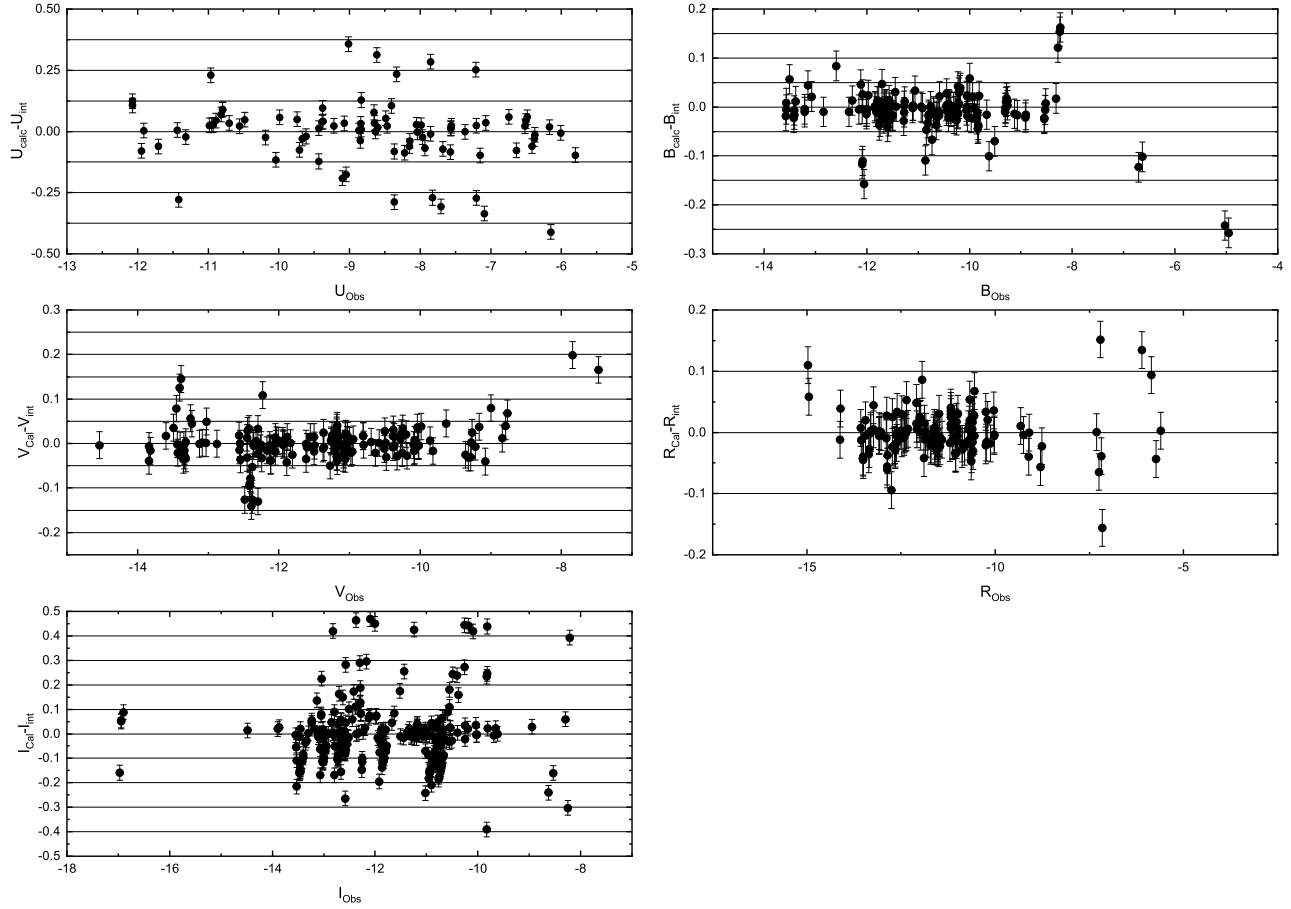

 Fig. 3. Calculated minus intrinsic magnitudes versus observed magnitudes for the  $U-I$  filters.

TABLE 6

 MEASURED COUNTS FOR COMPONENTS A TO F OF ADS 13292, OBTAINED WITH  
 ASTROIMAGEJ AND APT

	Number of Counts (AstroImageJ)	Number of Counts (APT)	Difference (counts)	Difference(%) (Percentage)
A	163657.5663	163640	17.566316	0.01073358012
B	1505427.035	1503700	1727.034662	0.1147205824
C	72591.87383	72488.6	103.273825	0.1422663716
D	58946.5638	59003	56.436205	0.09574129748
E	123743.0788	123762	18.921178	0.015290696
F	1170320.58	1169260	1060.580108	0.09062304176
A	40307.63323	40359.5	51.866766	0.1286772798
B	94842.91829	94752.7	90.218291	0.0951239087
C	871463.4746	870522	941.474566	0.1080337379
D	80068.28323	80192.9	124.616769	0.1556381178
E	150244.2993	150189	55.299313	0.0368062637
F	1175990.939	1175830	160.93914	0.01368540646



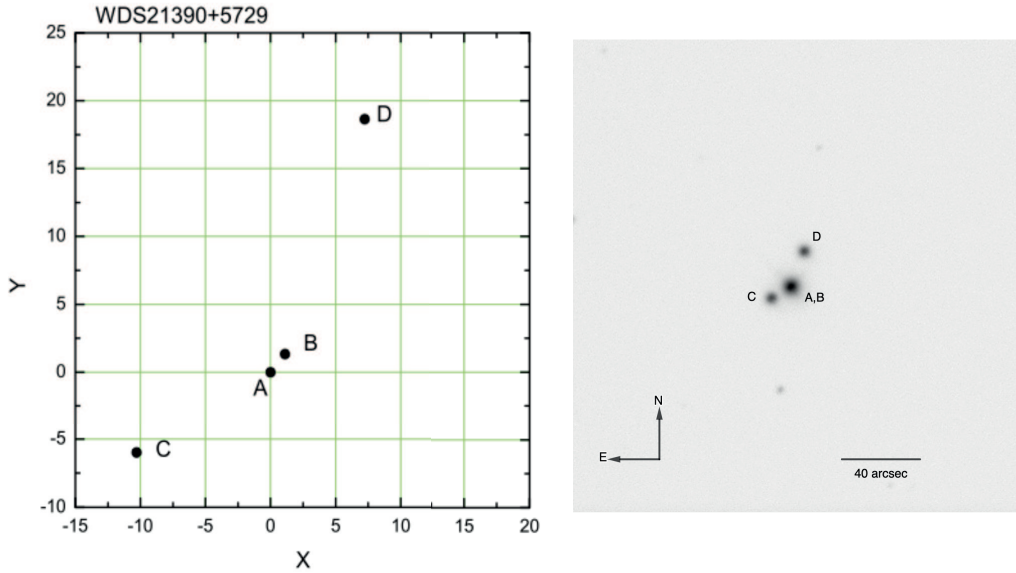


Fig. 4. The left image represents the components of the trapezium ADS 15184. The axes are given in arcsecs. On the right, we show our observed image in the  $V$  filter, with N-E orientation and scale in arcsecs. Exposure time is 0.2 seconds

one trapezium. Table 6 shows a comparison between the number of counts obtained with AstroImageJ and that found with APT. This was done for measurements of the six components (A, B, C, D, E, and F) of the trapezium ADS 13292; the full photometry for this trapezium will be reported elsewhere. As stated in the last column of this table, the difference in the number of counts measured with one programme or the other is at most of the order of 0.1%.

We opted for using the AstroImageJ programme for the measurement of the stellar components of the different trapezia since the measurement of a large number of images may be done in an automatic way.

### 2.2.1. ADS 15184

The trapezium ADS 15184 (also known as WDS 21390+5729) is located at RA=21h 38m, Dec=+57° 29'. It has four bright components denoted as A, B, C, and D. Their distribution is presented on the left of Figure 4. The right panel of this figure shows our image for ADS 15184 in the  $V$  filter. On the figure we have identified the components A, B, C and D. The A and B components are very bright and even on the short time exposure appear melded as shown in Figure 5. Due to this fact, the photometry of both these objects is carried out as if they represented one star only, which we denote as the AB component.

We obtained 70 images of this trapezium in the filters  $U-I$ . Two sets of images were taken with integration times of 0.1 and 8 seconds respectively, so that we could get images where the bright stars were not saturated and also images where the fainter stars could have a substantial number of counts.

To perform photometry on each one of the stars of a trapezium, it is necessary to vary the aperture radius to ensure that the same percentage of the light is included for each stellar image. Table 7 shows the radii for each component, where  $r_1$  is the radius of the central aperture,  $r_2$  is the inner radius of the sky annulus, and  $r_3$  is the outer radius of the sky annulus.

The photometric measurements we obtained are given in number of counts, which is directly proportional to the exposure time. We normalise all our measurements to a standard time of 10 seconds. To achieve this, we use the following equation:

$$I_{10} = \frac{10}{t} I_{obs}. \quad (6)$$

Where  $I_{10}$  represents the intensity of the star at the normalised time (10 seconds),  $t$  is the observation time and  $I_{obs}$  is the observed intensity. The normalised intensity is transformed to magnitude in a standard manner.

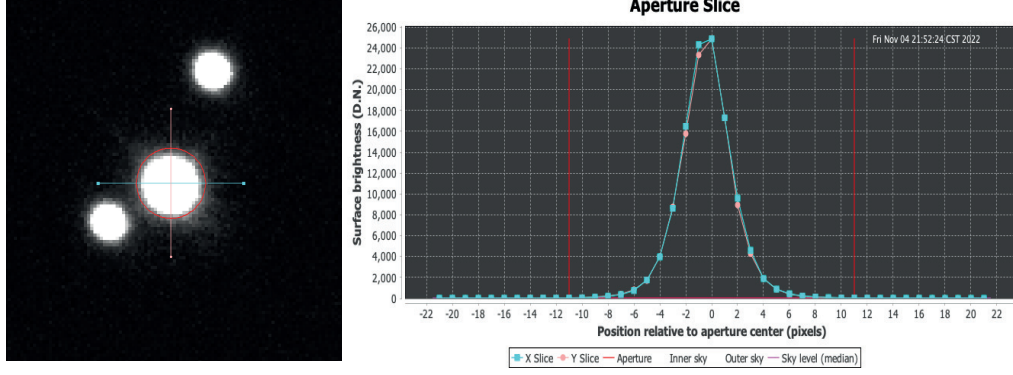


Fig. 5. At the centre of the left image we show the blended  $AB$  components of ADS 15184. On the right panel, vertical and horizontal cuts are performed on the central star component  $AB$ . These cuts show that components  $A$  and  $B$  are not well resolved in our images. The colour figure can be viewed online.

TABLE 7

PHOTOMETRIC APERTURE RADII IN PIXELS FOR THE TRAPEZIUM ADS 15184

	$r_1$ (pix)	$r_2$ (pix)	$r_3$ (pix)
AB	8	12	16
C	8	11	14
D	8	11	14

TABLE 8

OBSERVED MAGNITUDES AND COLOURS FOR THE STARS IN TRAPEZIUM ADS15184

	$U$	$B$	$V$	$R$	$I$	$U - B$	$B - V$	$V - R$	$R - I$	$V - I$
AB	5.29	5.62	5.37	5.28	5.10	-0.33	0.24	0.09	0.18	0.27
C	7.93	8.18	7.87	7.66	7.49	-0.25	0.32	0.20	0.17	0.37
D	7.83	8.05	7.80	7.67	7.52	-0.22	0.25	0.13	0.15	0.28

Using equations 1–5 for each filter and taking the coefficients  $A$ ,  $K$  and  $C$  for the night 10 – 11 December, shown in Tables 1–5, we calculate the values for the magnitudes and colours of the stars in the trapezium. We estimate the magnitude errors to be of the order of  $\pm 0.02$  and  $\pm 0.03$  for the colours.

Using the colour values, we may determine the  $Q$  index (see Johnson & Morgan (1953)), which we know is reddening independent:  $Q = (U - B) - 0.72(B - V)$ .

We can associate a different spectral type to different values of  $Q$  depending on whether we consider stars of Luminosity Class  $I$  (Supergiants) or  $V$  (Dwarfs) (see Table 9). We could also use for this classification the empirical calibration published by Lyubimkov et al. (2002) in which they associate the effective temperature of stars of luminosity classes II–III and IV–V to the value of the  $Q$ -parameter (see their equations 6 and 7 and their Figure 11). We shall try this approach elsewhere.

Table 10 gives the spectral types associated to each star of this trapezium based on the values of  $Q$ . In the case of  $AB$ , the spectral type given is that of a star that results from the union of  $A$  and  $B$ .

From the  $U - B$  and  $B - V$  colours shown in Table 8 we make a two-colour diagram, where the red dots represent the components  $AB$ ,  $C$  and  $D$ . The blue and green lines represent the intrinsic main sequence and the intrinsic supergiant sequence respectively. We also see the reddening line (red colour line, see Figure 6). This line has a slope equal to  $\approx 0.72$  (see Figure 6). This line allows us to deredden the observed colours of a star shifting the points in a direction parallel to this line until we intersect one of the intrinsic sequences (green or blue lines).

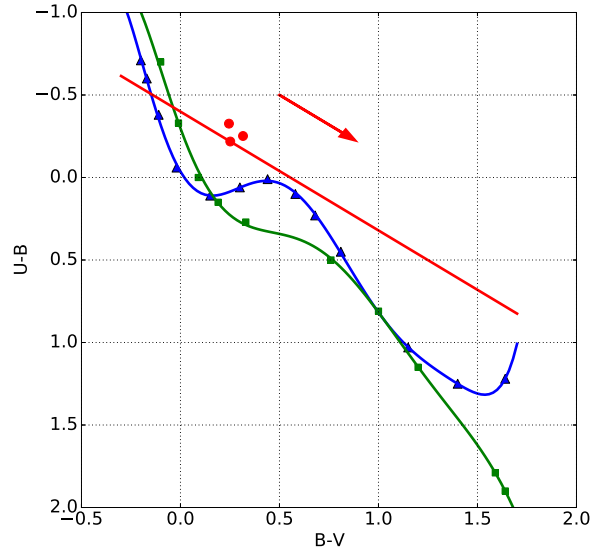


Fig. 6. Two colour diagram ( $U - B$  vs  $B - V$ ) for ADS 15184. The green line is the supergiant intrinsic sequence (SGIS), in blue the main sequence (MSIS) intrinsic sequence and the red dots represent the observed colours of the components of this trapezium. The red line and the red arrow represent the reddening line and direction. The colour figure can be viewed online.

TABLE 9

Q VERSUS SPECTRAL TYPE. TAKEN FROM Johnson & Morgan (1953)

Spectral Type	Q	Spectral Type	Q
O5	-0.93	B3	-0.57
O6	-0.93	B5	-0.44
O8	-0.93	B6	-0.37
O9	-0.9	B7	-0.32
B0	-0.9	B8	-0.27
B0.5	-0.85	B9	-0.13
B1	-0.78	A0	0
B2	-0.7		

TABLE 10

SPECTRAL TYPES FOR STARS IN ADS 15184

	Q	Spectral Type
AB	-0.50	B5
C	-0.48	B5
D	-0.40	B6

Finding the intersection of a line parallel to the reddening line that also passes on the observed points with the intrinsic sequences allows us to find the intrinsic colours of each star, which permits us to calculate the colour excess  $E(B - V)$ , the absorption  $A_V$  and the distance in parsecs to the star in question ( $d(pc) = 10^{(m_v - M_V - A_v + 5)/5}$ ). We have assumed the ratio of total to selective absorption  $\left[\frac{A_V}{E(B - V)}\right]$  to be equal to 3.1.

TABLE 11  
INTRINSIC COLOURS, COLOUR EXCESS, ABSORPTION AND DISTANCE FOR ADS 15184

Assuming Supergiant Stars							
	$(U - B)_0$	$(B - V)_0$	$E_{U-B}$	$E_{B-V}$	$A_V$	Distance (pc)	Parallax (mas)
AB	-0.56	-0.07	0.23	0.32	0.99	1380.43	0.72
C	-0.53	-0.07	0.27	0.38	1.18	3975.93	0.25
D	-0.43	-0.04	0.21	0.29	0.90	4349.30	0.23
Assuming Main Sequence Stars							
	$(U - B)_0$	$(B - V)_0$	$E_{U-B}$	$E_{B-V}$	$A_V$	Distance (pc)	Parallax (mas)
AB	-0.63	-0.18	0.31	0.42	1.31	135.51	7.38
C	-0.60	-0.17	0.35	0.49	1.51	389.58	2.57
D	-0.51	-0.15	0.29	0.40	1.24	355.85	2.81

TABLE 12  
COMPARISON OF OUR MEASUREMENTS OF ADS 15184 WITH SIMBAD (\*)

Magnitude			
	AB	C	D
$U$	5.29	7.93	7.83
$U^*$	-	7.72	7.53
$B$	5.62	8.18	8.05
$B^*$	-	7.63	-
$V$	5.37	7.87	7.80
$V^*$	-	7.46	-
$R$	5.28	7.66	7.67
$R^*$	-	-	8.73
$I$	5.10	7.49	7.52
$I^*$	-	7.67	-
Spectral Type			
	AB	C	D
St	B5	B5	B6
St*	-	B1.5V	B1V
Parallax			
	AB	C	D
$P_{sg}$	0.72	0.25	0.23
$P_{sp}$	7.38	2.57	2.81
$P^*$	-	0.8589	1.1051

Table 11 gives the values for the intrinsic colours, the excesses, the absorption and distances assuming the stars are supergiants (top panel), while in the bottom panel it gives the same information assuming the stars belong to the main sequence.

A comparison of our results with the SIMBAD Astronomical Database (Wenger et al. 2000) is presented in Table 12. The magnitudes of the stars listed in SIMBAD come from the following references: Fabricius et al. (2002), Reed (2003), Mercer et al. (2009), and Zacharias et al. (2012). Table 12 shows that our magnitudes differ in the worst case by one magnitude.

Using Curve 15 of van de Hulst's (Johnson 1968) we can obtain the dereddened values of the magnitudes for each component. The results of this exercise is shown in Table 13, these values coincide with those reported in Table 11.

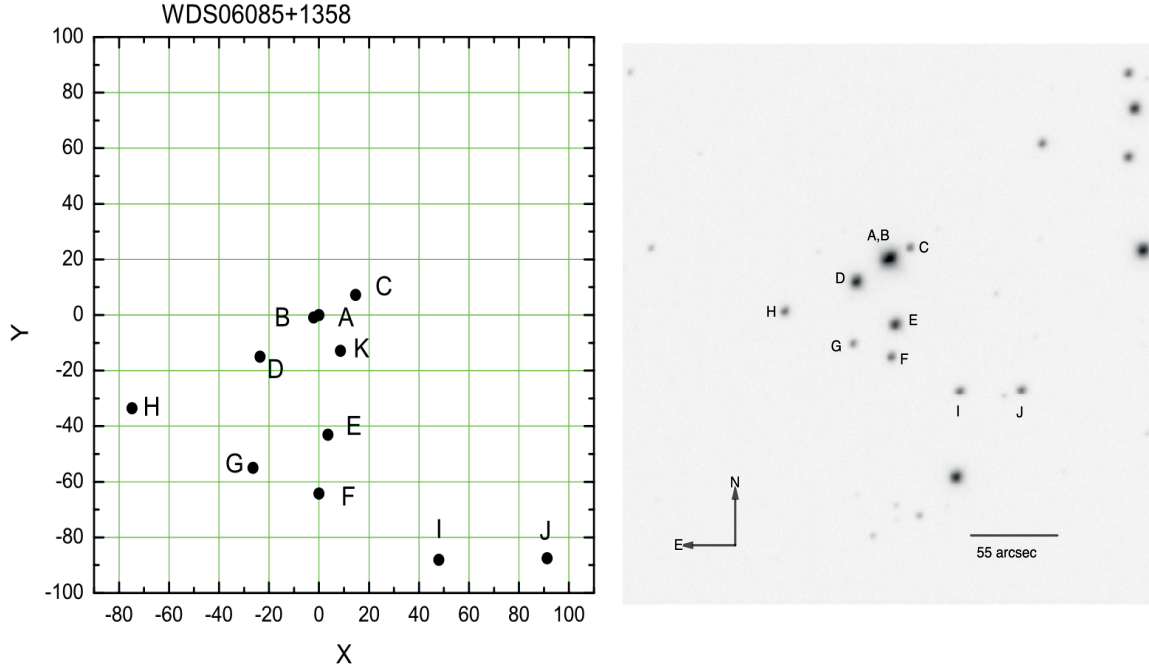


Fig. 7. The left image represents the components of the trapezium ADS 4728. The axes units are seconds of arc. On the right, we show our observed image in the  $V$  filter, with N-E orientation and scale in arcsec. Exposure time is 1 second.

TABLE 13

DEREDDENED MAGNITUDES AND COLOURS FOR STARS IN ADS 15184 USING VAN DE HULST CURVE 15

Assuming Supergiant Stars										
	$U$	$B$	$V$	$R$	$I$	$U - B$	$B - V$	$V - R$	$R - I$	$V - I$
AB	3.76	4.31	4.39	4.55	4.63	-0.55	-0.07	-0.16	-0.08	-0.25
C	6.10	6.62	6.68	6.78	6.93	-0.52	-0.07	-0.10	-0.14	-0.25
D	6.44	6.86	6.90	7.00	7.09	-0.42	-0.04	-0.10	-0.09	-0.19
Assuming Main Sequence Stars										
	$U$	$B$	$V$	$R$	$I$	$U - B$	$B - V$	$V - R$	$R - I$	$V - I$
AB	3.25	3.88	4.06	4.31	4.48	-0.63	-0.18	-0.25	-0.17	-0.42
C	5.58	6.18	6.35	6.54	6.77	-0.60	-0.17	-0.19	-0.23	-0.42
D	5.91	6.41	6.56	6.75	6.93	-0.50	-0.15	-0.19	-0.18	-0.37

### 2.2.2. ADS 4728

Trapezium ADS 4728 (also known as WDS 06085+13358) located at RA=6h 8m, Dec=+13° 58'. It has eleven components: A–K, which are distributed as shown on the left panel of Figure 7.

We observed 110 images for this trapezium in filters  $U-I$ .

The images for this trapezium were obtained with three different integration times 0.5, 1 and 8 seconds.

Figure 7 also shows an image of this trapezium in the  $V$  filter (right panel). The stellar components as well as the orientation and plate scale are indicated on this figure.

Table 14 shows the values of the radii we used for performing the photometry for each component. As done previously, all the measurements are normalised to 10 seconds with Equation 6.

Using the values of  $A$ ,  $K$  and  $C$  we obtain the magnitudes and colours for the stars of trapezium ADS 15184 (see Table 15).

TABLE 14  
PHOTOMETRIC APERTURE RADII FOR ADS 4728

	$r_1$ (pix)	$r_2$ (pix)	$r_3$ (pix)
C	9	11	13
D	10	11	14
E	9	11	14
F	9	11	14
G	11	13	16
H	11	13	16
I	10	12	14
J	10	12	14

TABLE 15  
OBSERVED MAGNITUDES AND COLOURS FOR TRAPEZIUM ADS 4728

	$U$	$B$	$V$	$R$	$I$	$U - B$	$B - V$	$V - R$	$R - I$	$V - I$
C	11.66	11.72	11.51	11.46	11.31	-0.05	0.21	0.04	0.15	0.20
D	7.98	8.60	8.59	8.64	8.62	-0.62	0.01	-0.05	0.02	-0.03
E	8.88	9.22	9.12	9.13	9.04	-0.35	0.10	-0.00	0.08	0.08
F	11.16	11.08	10.87	10.83	10.68	0.08	0.21	0.04	0.15	0.19
G	12.11	11.98	11.76	11.72	11.57	0.13	0.22	0.04	0.15	0.18
H	12.25	11.08	9.88	9.34	8.76	1.17	1.21	0.54	0.58	1.12
I	10.70	10.87	10.75	10.74	10.65	-0.17	0.12	0.01	0.09	0.09
J	10.72	10.95	10.81	10.76	10.64	-0.22	0.13	0.05	0.12	0.17

TABLE 16  
Q DERIVED SPECTRAL TYPES FOR ADS 4728

	Q	Spectral Type
C	-0.20	B8
D	-0.63	B3
E	-0.42	B5
F	-0.08	B9
G	-0.03	A0
H	0.30	A0
I	-0.26	B8
J	-0.32	B7

Table 16 shows the spectral type associated to each star from the  $Q$  parameter calibration

Using the  $U - B$  and  $B - V$  colours from Table 15 we plot the points on the two-colour diagram (see Figure 8) where the same conventions as those followed for the previous trapezium are followed.

The first part of Table 17 presents the values for intrinsic colours, colour excesses, absorption and distances assuming the stars are supergiants, while the second part shows the same results assuming the stars to be in the main sequence.

The magnitudes of the stars listed in SIMBAD come from the following references: Høg et al. (2000), Zacharias et al. (2003), Reed (2003), Zacharias et al. (2009), Krone-Martins et al. (2010), and Gaia Collaboration (2020). Table 18 shows our results compared with those listed in SIMBAD (shown with \*).

Table 19 shows the dereddened values for magnitudes and colours for the stars in ADS 4728.

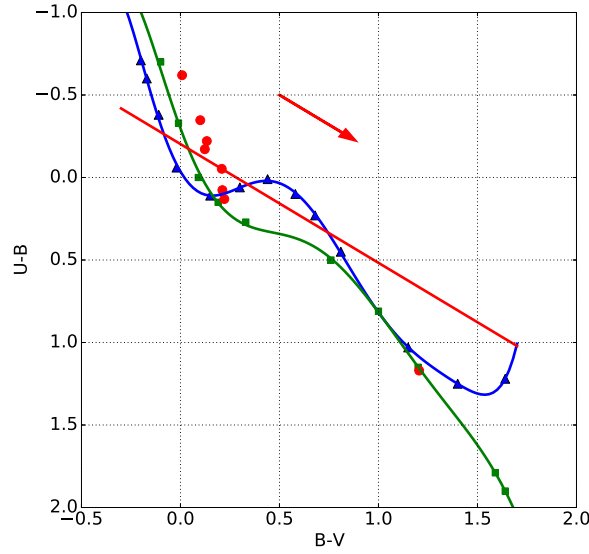


Fig. 8. Two-colour diagram ( $U - B$  vs  $B - V$ ) for ADS 4728. The colour figure can be viewed online.

TABLE 17

INTRINSIC COLOURS, COLOUR EXCESSES, ABSORPTION AND DISTANCES FOR ADS 4728

Assuming Supergiant Stars							
	$(U - B)_0$	$(B - V)_0$	$E_{B-V}$	$E_{U-B}$	$A_V$	Distance (pc)	Parallax (mas)
C	-0.17	0.04	0.17	0.12	0.52	27948.93	0.04
D	-0.71	-0.11	0.12	0.09	0.38	8201.46	0.12
E	-0.45	-0.04	0.14	0.10	0.45	9945.13	0.10
F	0.00	0.11	0.10	0.07	0.32	22636.52	0.04
G	0.07	0.14	0.08	0.06	0.25	34886.01	0.03
H	-	-	-	-	-	-	-
I	-0.25	0.02	0.11	0.08	0.33	21454.01	0.05
J	-0.32	-0.01	0.14	0.10	0.44	21340.38	0.05
Assuming Main Sequence Stars							
	$(U - B)_0$	$(B - V)_0$	$E_{B-V}$	$E_{U-B}$	$A_V$	Distance (pc)	Parallax (mas)
C	-0.26	-0.08	0.29	0.21	0.91	1466.26	0.68
D	-0.78	-0.21	0.22	0.16	0.69	1261.05	0.79
E	-0.53	-0.15	0.25	0.18	0.79	969.79	1.03
F	-0.09	-0.03	0.24	0.17	0.74	931.28	1.07
G	-0.02	0.01	0.22	0.16	0.67	866.56	1.15
H	-	-	-	-	-	-	-
I	-0.34	-0.10	0.23	0.16	0.71	1132.09	0.88
J	-0.41	-0.12	0.26	0.18	0.80	1483.90	0.67

### 2.2.3. ADS 2843

Trapezium ADS 2843 (also known as WDS 03541+3153) is at RA=3h 54m, Dec=+31° 53' and has five components: *A*, *B*, *C*, *D*, and *E*, distributed as seen on the left of Figure 9.

We obtained 148 images for this trapezium in filters  $U-I$ , with exposure times of 0.2 and 0.5 seconds.



TABLE 18  
COMPARISON OF OUR RESULTS FOR ADS 4728 WITH SIMBAD (\*)

Magnitude								
	C	D	E	F	G	H	I	J
<i>U</i>	11.66	7.98	8.88	11.16	12.11	12.25	10.70	10.72
<i>U*</i>	-	7.75	-	-	10.94	-	-	-
<i>B</i>	11.72	8.60	9.22	11.08	11.98	11.08	10.87	10.95
<i>B*</i>	11.51	8.239	9.051	11.02	11.882	11.03	10.82	-
<i>V</i>	11.51	8.59	9.12	10.87	11.76	9.88	10.75	10.81
<i>V*</i>	11.529	8.659	9.265	10.968	11.892	9.905	10.825	-
<i>R</i>	11.46	8.64	9.13	10.83	11.72	9.34	10.74	10.76
<i>R*</i>	11.32	8.89	9.10	10.86	11.69	9.65	-	-
<i>I</i>	11.31	8.63	9.04	10.68	11.57	8.76	10.65	10.64
<i>I*</i>	-	-	-	-	12.40	-	-	-
Spectral Type								
	C	D	E	F	G	H	I	J
St	B8	B3	B5	B9	A0	A0	B8	B7
St*	B9V	B1V	B3V	B9V	-	G8	B5	-
Parallax								
	C	D	E	F	G	H	I	J
<i>P<sub>sg</sub></i>	0.04	0.12	0.10	0.04	0.03	0.24	0.05	0.05
<i>P<sub>sp</sub></i>	0.68	0.79	1.03	1.07	1.15	10.27	0.88	0.67
<i>P*</i>	1.0671	0.96	0.9537	1.0783	1.0151	1.657	1.086	-

TABLE 19  
DEREDDENED MAGNITUDES AND COLOURS FOR ADS 4728 USING VAN DE HULST CURVE 15

Assuming Supergiant Stars										
	<i>U</i>	<i>B</i>	<i>V</i>	<i>R</i>	<i>I</i>	<i>U - B</i>	<i>B - V</i>	<i>V - R</i>	<i>R - I</i>	<i>V - I</i>
C	10.85	11.03	10.99	11.08	11.06	-0.17	0.04	-0.09	0.01	-0.08
D	7.39	8.1	8.21	8.36	8.44	-0.71	-0.11	-0.15	-0.08	-0.23
E	8.18	8.63	8.67	8.79	8.83	-0.45	-0.04	-0.12	-0.04	-0.15
F	10.66	10.66	10.55	10.59	10.53	0	0.11	-0.04	0.07	0.02
G	11.73	11.65	11.51	11.54	11.46	0.07	0.14	-0.03	0.08	0.06
H	7.59	7.11	6.88	7.11	7.33	0.48	0.24	-0.23	-0.22	-0.45
I	10.18	10.43	10.41	10.49	10.49	-0.25	0.02	-0.08	0	-0.08
J	10.05	10.37	10.38	10.44	10.43	-0.32	-0.01	-0.06	0.01	-0.05
Assuming Main Sequence Stars										
	<i>U</i>	<i>B</i>	<i>V</i>	<i>R</i>	<i>I</i>	<i>U - B</i>	<i>B - V</i>	<i>V - R</i>	<i>R - I</i>	<i>V - I</i>
C	10.26	10.52	10.6	10.79	10.88	-0.26	-0.08	-0.19	-0.09	-0.28
D	6.91	7.69	7.9	8.13	8.29	-0.78	-0.21	-0.23	-0.16	-0.39
E	7.65	8.18	8.33	8.54	8.67	-0.53	-0.15	-0.21	-0.13	-0.33
F	10.02	10.11	10.14	10.28	10.33	-0.09	-0.03	-0.15	-0.04	-0.19
G	11.07	11.09	11.09	11.22	11.25	-0.02	0.01	-0.13	-0.03	-0.17
H	6.77	6.41	6.34	6.71	7.07	0.36	0.06	-0.37	-0.36	-0.73
I	9.6	9.93	10.04	10.22	10.31	-0.33	-0.1	-0.18	-0.1	-0.28
J	9.49	9.89	10.02	10.17	10.26	-0.4	-0.12	-0.15	-0.09	-0.24

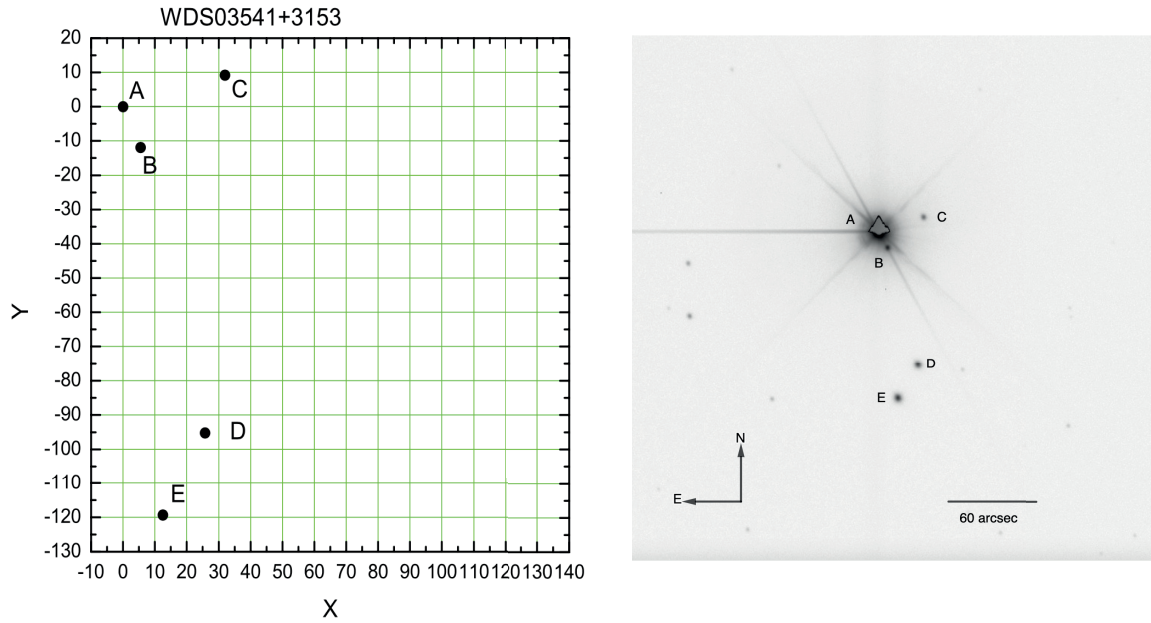


Fig. 9. The left image represents the components of the trapezium ADS 2843. The axes units are arcseconds. On the right, we show our observed image in the  $V$  filter, with N-E orientation and scale in arcsecs. 3 seconds exposure time.

TABLE 20

INTEGRATION TIMES FOR EACH FILTER FOR THE TRAPEZIUM ADS 2843

Filter	Time (sec)
$U$	10
$B$	5
$V$	3
$R$	2
$I$	1

TABLE 21

PHOTOMETRIC APERTURE RADII IN PIXELS FOR TRAPEZIUM ADS 2843

	$r_1$ (pix)	$r_2$ (pix)	$r_3$ (pix)
C	8	10	12
D	12	14	16
E	12	14	16

The right panel of Figure 9 shows the image of this trapezium in the  $V$  filter. Component A is clearly saturated, and its brightness affects component B making it impossible to obtain good photometric measurements.

In Table 21 we show the photometric radius for each component.

In a similar manner as before, we use the transformation coefficients in Tables 1–5 and equations 1–5 to transform the number of counts for each star to intrinsic magnitudes and colours (see Table 22).

Table 23 shows the spectral type associated to each star based on the value of its  $Q$  parameter.

Figure 10 shows the two-colour diagram for ADS 2843, where the red dots represent component C, D and E.

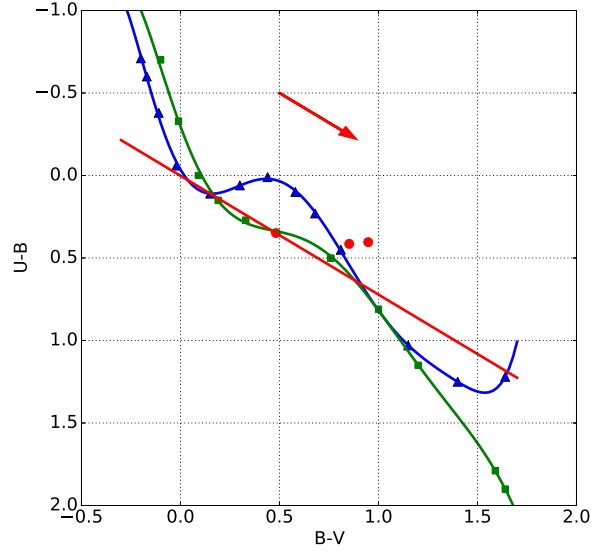


Fig. 10. Two-colour diagram ( $U - B$  vs  $B - V$ ) for ADS 2843. The colour figure can be viewed online.

TABLE 22

OBSERVED MAGNITUDES AND COLOURS FOR ADS 2843

	$U$	$B$	$V$	$R$	$I$	$U - B$	$B - V$	$V - R$	$R - I$	$V - I$
C	12.79	12.39	11.44	11.00	10.69	0.40	0.95	0.44	0.31	0.75
D	11.49	11.07	10.22	9.87	9.67	0.41	0.85	0.35	0.20	0.55
E	10.62	10.27	9.79	9.66	9.61	0.35	0.48	0.13	0.05	0.18

TABLE 23

$Q$  DERIVED SPECTRAL TYPES FOR ADS 2843

	$Q$	Spectral Type
C	-0.28	B8
D	-0.20	B9
E	0.00	A0

From the two-colour diagram we obtain the values for the intrinsic colours, excesses, absorption and distance. However, in this case, the reddening lines for the components cross the intrinsic lines more than once. We have taken the excesses that appear to be more similar. Table 24 show the results for each case.

The magnitudes of the stars listed in SIMBAD come from the following reference: Høg et al. (2000). Table 25 shows the comparison of our results with SIMBAD (\*).

We show the magnitudes dereddened with van de Hulst curve 15 in Table 26. This table assumes respectively supergiant stars and main sequence stars.

#### 2.2.4. ADS 16795

Trapezium ADS 16795 (also known as WDS 23300+5833) is located at RA=23h 30m, Dec=+58° 32' and has six components: AB, C, E, F, G and I, whose location is shown in Figure 11.

TABLE 24  
INTRINSIC COLOURS, EXCESSES, ABSORPTION AND DISTANCES FOR ADS 2843

Assuming Supergiant Stars							
	$(U - B)_0$	$(B - V)_0$	$E_{U-B}$	$E_{B-V}$	$A_V$	Distance (pc)	Parallax (mas)
C	-0.27	0.01	0.68	0.94	2.92	8989.06	0.11
D	-0.17	0.04	0.58	0.81	2.51	6119.40	0.16
E	0.12	0.17	0.22	0.31	0.96	10113.19	0.10
Assuming Main Sequence Stars							
	$(U - B)_0$	$(B - V)_0$	$E_{U-B}$	$E_{B-V}$	$A_V$	Distance (pc)	Parallax (mas)
C	-0.36	-0.11	0.76	1.06	3.28	475.21	2.10
D	-0.26	-0.08	0.67	0.93	2.90	255.21	3.92
E	0.03	0.04	0.32	0.45	1.38	251.98	3.97

TABLE 25  
COMPARISON WITH SIMBAD (\*) FOR ADS 2843

Magnitude			
	C	D	E
$U$	12.79	11.49	10.62
$U^*$	-	-	-
$B$	12.39	11.07	10.27
$B^*$	-	11.05	10.21
$V$	11.44	10.22	9.79
$V^*$	11.24	10.36	9.92
$R$	11.00	9.87	9.66
$R^*$	-	10.21	-
$I$	10.69	9.67	9.61
$I^*$	-	-	-
Spectral Type			
	C	D	E
St	B8	B9	A0
St*	-	-	A2V
Parallax			
	C	D	E
$P_{sg}$	0.11	0.16	0.10
$P_{sp}$	2.10	3.92	3.97
P	3.4918	7.3793	3.5114

For this trapezium we obtained 144 images in filters  $U-I$ . This trapezium was observed on the night 2019, 14-15 December. For this night the transformation coefficients  $A$ ,  $K$  and  $C$  for the filter  $U$  have no physical meaning (see Table 1), so no calculation of the  $U$  magnitude was possible.

Figure 11 shows the image of this trapezium in the  $V$  filter.

It is clear that the component AB is saturated so that the photometric measurements will only be performed on the other components (C, E, F, G and I).

Table 27 shows the photometric aperture radii for each component.

Table 28 gives the observed magnitudes and colours for the components of this trapezium. We obtained only those for the filters  $B$ ,  $V$ ,  $R$  and  $I$  because the results for  $U$  have no physical meaning and have been omitted.

Since we cannot obtain a value of  $U$ , it is impossible to calculate the value of the  $Q$  parameter.

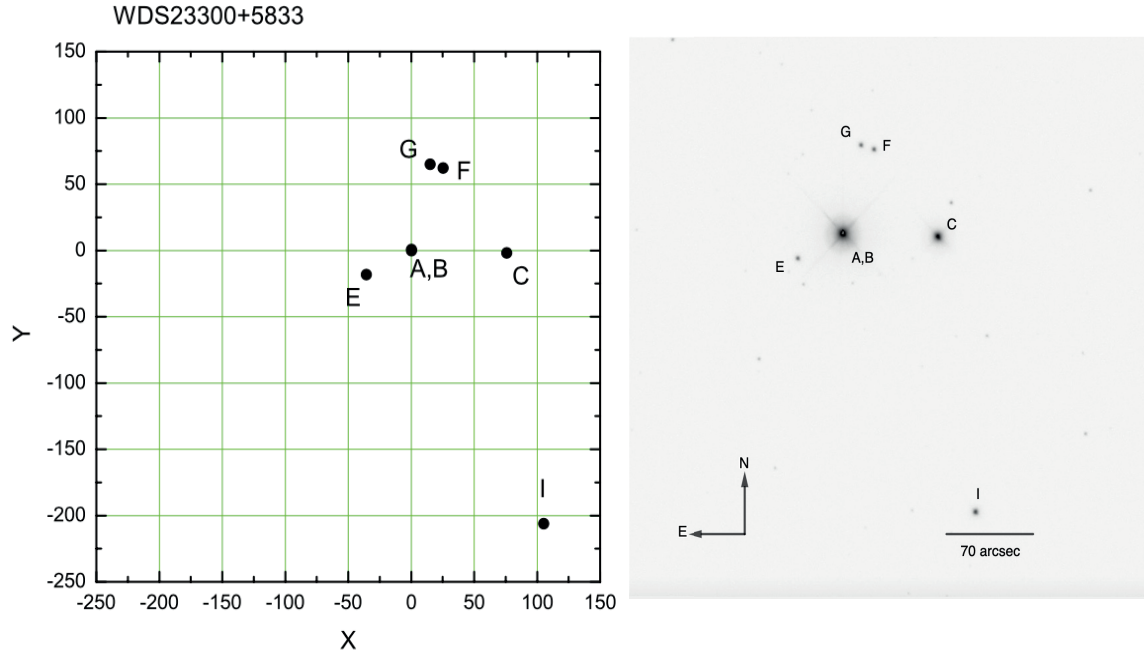


Fig. 11. The left image represents the components of the trapezium ADS 16795. The axes units are arcseconds. On the right, we show our observed image in the  $V$  filter, with N-E orientation and scale in arcsec. Exposure time is 5 seconds.

TABLE 26

DEREDDENED MAGNITUDES AND COLOUR WITH VAN DE HULST CURVE 15 FOR ADS 2843

Assuming Supergiant Stars										
	$U$	$B$	$V$	$R$	$I$	$U - B$	$B - V$	$V - R$	$R - I$	$V - I$
C	8.27	8.53	8.52	8.84	9.3	-0.26	0.01	-0.31	-0.46	-0.78
D	7.59	7.75	7.71	8	8.47	-0.16	0.04	-0.29	-0.46	-0.76
E	9.12	8.99	8.82	8.94	9.15	0.13	0.17	-0.12	-0.21	-0.33
Assuming Main Sequence Stars										
	$U$	$B$	$V$	$R$	$I$	$U - B$	$B - V$	$V - R$	$R - I$	$V - I$
C	7.7	8.04	8.15	8.56	9.12	-0.35	-0.11	-0.41	-0.56	-0.97
D	6.99	7.24	7.32	7.72	8.28	-0.25	-0.08	-0.39	-0.57	-0.96
E	8.48	8.44	8.41	8.63	8.95	0.03	0.04	-0.22	-0.32	-0.54

TABLE 27

PHOTOMETRIC APERTURE RADII FOR ADS 16795

	$r_1$ (pix)	$r_2$ (pix)	$r_3$ (pix)
C	14	16	20
E	10	12	14
F	9	11	13
G	9	11	13
I	11	13	15

TABLE 28  
OBSERVED MAGNITUDES AND COLOURS FOR ADS 16795

	$B$	$V$	$R$	$I$	$B - V$	$V - R$	$R - I$	$V - I$
C	7.81	7.79	8.45	8.26	0.01	0.18	-0.65	-0.47
E	11.83	11.18	10.74	10.34	0.65	0.40	0.44	0.84
F	11.52	10.98	10.59	10.32	0.54	0.27	0.38	0.65
G	11.64	11.08	10.68	10.40	0.56	0.28	0.40	0.67
I	10.19	9.74	9.41	9.20	0.45	0.22	0.33	0.55

TABLE 29  
COMPARISON OF OUR RESULTS FOR ADS 16795 AND THOSE LISTED IN SIMBAD (\*)

	Magnitude				
	C	E	F	G	I
$B$	7.81	11.83	11.52	11.64	10.19
$B^*$	-	11.93	-	-	-
$V$	7.79	11.18	10.98	11.08	9.74
$V^*$	-	11.19	-	-	-
$R$	8.45	10.74	10.59	10.68	9.41
$R^*$	8.15	11.14	10.94	11.03	-
$I$	8.26	10.34	10.32	10.40	9.20
$I^*$	-	-	-	-	-

The magnitudes of the stars listed in SIMBAD come from the following reference: Zacharias et al. (2012). In Table 29 we compare our results with those listed in SIMBAD.

### 3. THE SLOPE OF THE REDDENING LINE

Since the  $Q$ -derived spectral types differ slightly from those listed in SIMBAD, we speculate that these differences might be due to slight differences in the value of the slope of the reddening line on the two-colour diagram from the canonical value (0.72).

The slope of the reddening line corresponds to the ratio of the colour excesses  $E(U - B)$  and  $E(B - V)$ , and its value is clearly dependent on the physical and chemical properties of the interstellar medium through which the light from the stars travels on its way to our observing instruments. Carrying out a full investigation as to whether the slope of the reddening line differs from region to region is not only a rather interesting endeavour, but one that is clearly outside the scope of this paper. Here we shall only speculate that this might be the reason for the slight differences in stellar spectral types, and use the seven points we have to obtain a value for the new slope. Aidelman & Cidale (2023) suggest that the possible difference of the slope of the reddening line from the canonical value may be due to an anomalous colour excess or to variations of the extinction law.

In Table 30 we present the object name, the  $Q$ -derived spectral type, the measured  $Q$  index, the SIMBAD spectral type and the value of the  $Q$  index for the spectral type given in Column 4.

Figure 12 shows the relation we obtain from Table 30 between the observed  $Q$  index ( $Q_{obs}$ ) and the  $Q$  associated to the spectral type reported in SIMBAD ( $Q_{int}$ ). We fitted a least squares straight line that produced the following equation:

$$Q_{int} = (1.40 \pm 0.30) Q_{obs} - (0.02 \pm 0.12). \quad (7)$$

Using this equation we might be able to correct the  $Q$ -derived spectral types. However, the number of points which produce this equation is very small so, at present, we have decided to leave its use and confirmation of usefulness for further investigations.

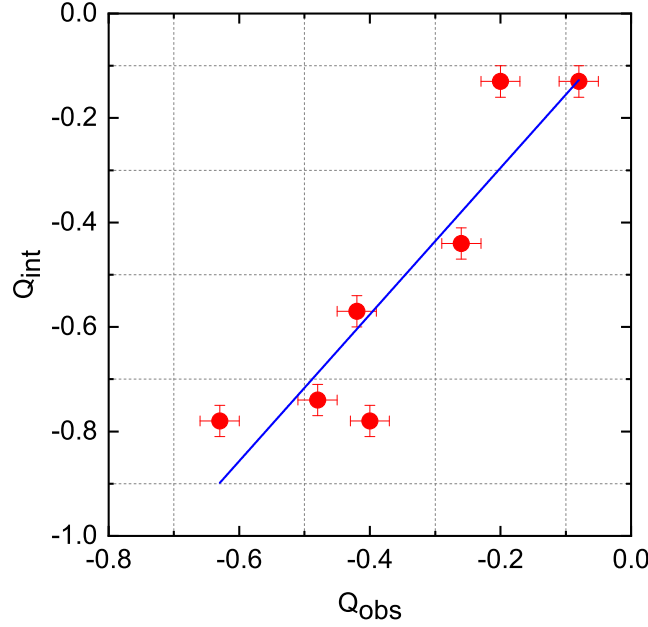


Fig. 12. Graph of the values shown in Table 30. The colour figure can be viewed online.

TABLE 30

$Q$  PARAMETER VALUES ASSOCIATED WITH THE SPECTRAL VALUE DERIVED AND THE TYPES GIVEN IN THE LITERATURE

<i>Object</i>	$ST_{obs}$	$Q_{obs}$	$ST_{int}$	$Q_{int}$
ADS15184C	B5	-0.48	B1.5	-0.74
ADS15184D	B6	-0.40	B1	-0.78
ADS4728C	B8	-0.20	B9	-0.13
ADS4728D	B3	-0.63	B1	-0.78
ADS4728E	B5	-0.42	B3	-0.57
ADS4728F	B9	-0.08	B9	-0.13
ADS4728I	B8	-0.26	B5	-0.44

Algebraic manipulation of equation (7) allows us to express it as follows:

$$1.40 E(B - V) m + 0.40 (U - B)_{int} - 1.01 (B - V)_{Obs} + 0.72 (B - V)_{int} - 0.02 = 0 \quad (8)$$

where  $m$  represents the possible new slope of the reddening line, and the suffixes *int* and *Obs* refer to the intrinsic and observed values. Effecting a least squares solution for  $m$  from this equation would allow us to explain the difference between the  $Q$ -derived spectral types and the spectral types listed in SIMBAD as a difference (from 0.72) of the slope of the reddening line on the two-colour diagram.

In what follows we shall use the information we have for the seven discrepant points and calculate a value for the slope of the reddening line that fits these results. In Table 31 we see in Column 1 the name of the star, in Column 2 the spectral type, in Column 3 the  $(U - B)_{int}$ , in Column 4  $(B - V)_{Obs}$ , in Column 5  $(B - V)_{int}$  and in Column 6  $E(B - V)$  for the stars for which a discrepant  $Q$ -derived spectral type was found.

Effecting a least squares solution for  $m$  in equation (8) using the values listed in Table (31) produces a value for the slope of the reddening line  $m = 1.14^{+0.34}_{-0.61}$ , higher than the accepted one. However, the number of points which we are using for the calculation is rather limited and we could hardly expect the result to have some degree of statistical significance. We would like to leave this fact as a possible explanation for the discrepancy of spectral types and hope that, as more discrepant results are collected with the observations of further trapezia stars, the determination of this new slope for the reddening line acquires a more robust statistical significance.



TABLE 31

DATA FOR STARS WITH DISCREPANT SPECTRAL TYPES BETWEEN THE  $Q$ -DERIVED VALUE AND THE VALUE FOUND IN SIMBAD

<i>Object</i>	<i>Spectral Type</i>	$(U - B)_{int}$	$(B - V)_{obs}$	$(B - V)_{int}$	$E(B - V)$
ADS15184C	B1.5V	-0.88	0.32	-0.25	0.57
ADS15184D	B61V	-0.95	0.25	-0.26	0.51
ADS4728C	B9V	-0.18	0.21	-0.07	0.28
ADS4728D	B1V	-0.95	0.01	-0.26	0.27
ADS4728E	B3V	-0.68	0.10	-0.20	0.30
ADS4728F	B9V	-0.18	0.21	-0.07	0.28
ADS4728I	B8	-0.36	0.12	-0.11	0.23

#### 4. CONCLUSIONS

This paper constitutes a photometric study of some trapezia in the Galaxy. The data were obtained during several observing seasons.

Here we present CCD photometry of the brighter stars in the stellar trapezia ADS 15184, ADS 4728, ADS 2843, and ADS 16795, which we have used to explore the possibility of finding the spectral type of the stars using the  $Q$  parameter, defined as  $Q = (U - B) - 0.72(B - V)$ . This parameter is reddening independent, since the slope of the reddening line on the two-colour diagram is approximately equal to 0.72 (see Johnson & Morgan 1953). This, of course, is a first approach since the calibration we used for the  $Q$  parameter versus the spectral type does not take into consideration peculiar stars and is only based on typical stars of luminosity classes I and V.

The spectral types which we have determined coincide reasonably well with those listed in SIMBAD. However, a different value of the slope of the reddening line on the two-colour diagram might produce a better coincidence between the  $Q$ -derived spectral types and those listed in SIMBAD. Effecting a least squares solution for the slope of the reddening line in equation (8) produces a value of its slope  $m$  of  $1.14^{+0.34}_{-0.61}$ , ascribing the difference in spectral types to a difference in the slope of the reddening line is, at this point, only a speculation which needs a full investigation to be confirmed or discarded. The  $Q$  parameter appears to be useful only for early type stars (earlier than A0), so if it is used for stars whose spectral type is later than A0 the results obtained might be in error.

As part of our study we intend to determine the spectral type of the stars in the trapezia through classification of their spectra and hope to be able to measure their radial velocities which, joined with proper motions from GAIA will allow us to perform a detailed dynamical study of the Galactic trapezia.

We would like to thank the Instituto de Astronomía at Universidad Nacional Autónoma de México (IAUNAM) and the Instituto de Astronomía y Meteorología at Universidad de Guadalajara (IAMUdeG) for providing a congenial and stimulating atmosphere in which to work. We also thank the computing staff at both institutions for being always available and ready to help with random problems with our computing equipment, which arise when one least expects them. We would also like to thank Juan Carlos Yustis for help with the production of the figures in this paper. We also thank Dirección General de Asuntos del Personal Académico, DGAPA at UNAM for financial support under projects PAPIIT IN103813, IN102517 and IN102617. This research has made use of the SIMBAD database, operated at CDS, Strasbourg, France. The help and valuable suggestions provided by an anonymous referee are gratefully acknowledged.

REFERENCES

- Abt, H. A. 1986, *ApJ*, 304, 688, <https://doi.org/10.1086/164207>
- Abt, H. A. & Corbally, C. J. 2000, *ApJ*, 541, 841, <https://doi.org/10.1086/309467>
- Aidelman, Y. & Cidale, L. S. 2023, *Galax*, 11, 31, <https://doi.org/10.3390/galaxies11010031>
- Allen, C., Ruelas-Mayorga, A., Sánchez, L. J., & Costero, R. 2018, *MNRAS*, 481, 3953, <https://doi.org/10.1093/mnras/sty2502>
- Allen, C., Sánchez, L. J., Ruelas-Mayorga, A., & Costero, R. 2019, *JAAH*, 22, 201, <https://doi.org/10.48550/arXiv.1908.11437>
- Ambartsumian, V. A. 1955, *Obs*, 75, 72
- Collins, K. A., Kielkopf, J. F., Stassun, K. G., & Hestman, F. V. 2017, *AJ*, 153, 77, <https://doi.org/10.3847/1538-3881/153/2/77>
- Fabricius, C., Høg, E., Makarov, V. V., et al. 2002, *A&A*, 384, 180, <https://doi.org/10.1051/0004-6361:20011822>
- Gaia Collaboration. 2020, *VizieR Online Data Catalog*, I/350, <https://doi.org/10.26039/cds/vizier.1350>
- Høg, E., Fabricius, C., Makarov, V. V., et al. 2000, *A&A*, 355, 27
- Johnson, H. L. in *Nebulae and Interstellar Matter*, ed. B. M. Middlehurst & L. H. Aller (University of Chicago Press), 167
- Johnson, H. L. & Morgan, W. W. 1953, *ApJ*, 117, 313, <https://doi.org/10.1086/145697>
- Krone-Martins, A., Soubiran, C., Ducourant, C., Teixeira, R., & Le Campion, J. F. 2010, *A&A*, 516, 3, <https://doi.org/10.1051/0004-6361/200913881>
- Laher, R. R., Gorjian, V., Rebull, L. M., et al. 2012, *PASP*, 124, 737, <https://doi.org/10.1086/666883>
- Landolt, A. U. 1992, *AJ*, 104, 340, <https://doi.org/10.1086/116242>
- Lyubimkov, L. S., Rachkovskaya, T. M., Rostopchin, S. I., & Lambert, D. L. 2002, *MNRAS*, 333, 9, <https://doi.org/10.1046/j.1365-8711.2002.05341.x>
- Mercer, E. P., Miller, J. M., Calvet, N., et al. 2009, *AJ*, 138, 7, <https://doi.org/10.1088/0004-6256/138/1/7>
- Reed, B. C. 2003, *AJ*, 125, 2531, <https://doi.org/10.1086/374771>
- Wenger, M., Ochsenbein, F., Egret, D., et al. 2000, *A&AS*, 143, 9, <https://doi.org/10.1051/aas:2000332>
- Zacharias, N., Finch, C., Girard, T., et al. 2009, *VizieR Online Data Catalog*, I/315
- Zacharias, N., Finch, C. T., Girard, T. M., et al. 2012, *VizieR Online Data Catalog*, I/322A
- Zacharias, N., Urban, S. E., Zacharias, M. I., et al. 2003, *VizieR Online Data Catalog*, I/289
- A. Paéz-Amador, A. Ruelas-Mayorga, L. J. Sánchez, and O. Segura-Montero: Instituto de Astronomía, Universidad Nacional Autónoma de México, Apartado Postal 70-264, Cd. Universitaria 04510, Ciudad de México, México (emacias,rarm,leonardo,osegura@astro.unam.mx).
- A. Nigoche-Netro: Instituto de Astronomía y Meteorología, Universidad de Guadalajara, Guadalajara, Jal. 44130, México. (anigoche@gmail.com).



## ERRATUM: A PECULIAR GALAXY NEAR M104 (RMxAA, 2023, 59, 323)

E. Quiroga

Universidad del Atlántico Medio, Facultad de Comunicación, Canary Islands, Spain.

*Received December 22 2023; accepted January 22 2024*

In the article ‘A PECULIAR GALAXY NEAR M104’, the author erroneously linked the X-ray emission of the object. The accurate link can be found in “<https://heasarc.gsfc.nasa.gov/db-perl/W3Browse/w3hdprods.pl?files=P&Target=heasarc%5Fxray%7C%7C%7C%5F%5Frow%3D1412003%7C%7C&Coordinates=Equatorial&Equinox=2000>” Link. Figure 1 contains the correct table in HEASARC.

Parameter Name	Parameter Value	Unit	Description
<a href="#">name</a>	CXOGSG J124006.2-113647		Common Source Designation
<a href="#">ra</a>	12 40 06.24		Right Ascension
<a href="#">dec</a>	-11 36 47.7		Declination
<a href="#">count_rate</a>		ct/s	Count Rate (counts/sec)
<a href="#">count_rate_error</a>		ct/s	Error in Count Rate
<a href="#">flux</a>	2.410e-15	erg/cm^2/s	Flux (erg/cm^2/s)
<a href="#">database_table</a>	CXOGSGSRC		Database Table This Entry Comes From
<a href="#">observatory</a>	CHANDRA		Observatory or Mission Name That Originated the Database Table
<a href="#">bii</a>	51.16102	degree	Galactic Longitude
<a href="#">class</a>			Browse Object Classification
<a href="#">error_radius</a>	1.00	arcsec	Positional Uncertainty (arcsec)
<a href="#">exposure</a>		s	Exposure Time (seconds)
<a href="#">lii</a>	298.50368	degree	Galactic Latitude

Fig. 1. Correct data for the X-ray emission of the object from dadabase table CXOGSGSRC, observatory CHANDRA (from HEASARC database).



La *Revista Mexicana de Astronomía y Astrofísica*, fundada en 1974, publica trabajos originales de investigación en todas las ramas de la astronomía, astrofísica y temas vinculados a éstas. Se publican dos números por año y su distribución es gratuita a las instituciones relacionadas con los campos cubiertos por esta revista. La *RMxAA* no cobra a los autores por publicar sus artículos, ni por el proceso de envío y revisión de los mismos.

La política editorial de la *RMxAA* consiste en enviar a arbitrar los artículos recibidos a especialistas en el campo. Los interesados en publicar en nuestra revista deberán enviar por correo electrónico, a la dirección [rmaa@astro.unam.mx](mailto:rmaa@astro.unam.mx), la versión completa de su artículo en formato PostScript o PDF y el archivo LaTeX. Estos archivos deberán ir acompañados de una carta de presentación. Todos los trabajos deben ser preparados en inglés usando la versión más reciente del macro en LaTeX de la *RMxAA* “*rmaa.cls*” (disponible en <http://www.astroscu.unam.mx/~rmaa>). Se requiere un “Abstract” y un “Resumen” en español (este último podrá ser provisto por los editores de ser necesario). Ambos deberán ser de 12 líneas o menos. También se incluirá de 1 a 6 palabras clave (“Keywords”) de la lista de las revistas astronómicas internacionales. Se requiere que cada tabla incluida en el texto esté numerada y con título; las figuras deberán estar en formato PostScript (.ps) o PostScript encapsulado (.eps), estar numeradas y con leyenda explicativa. Se requiere que cada tabla y figura estén mencionadas en el texto. El estilo de las referencias sigue las normas astronómicas internacionales recientes. Para mayor información sobre el estilo de la *RMxAA* se puede consultar el archivo de ejemplo que viene incluido en los macros.

La revista se publica bajo la modalidad de acceso abierto, por lo que todo su contenido es accesible libremente y sin costo para el usuario o su institución. Los usuarios están autorizados a leer, descargar, copiar, distribuir, imprimir, buscar o enlazar a los textos completos de los artículos de esta revista (o a las figuras y tablas en ellos contenidas) sin permiso previo del editor o del autor, de acuerdo con la definición de las BOAI (Budapest Open Access Initiative) de Open Access. La reutilización de los trabajos puede hacerse con fines no comerciales y siempre con reconocimiento de la autoría e indicando la fuente original.

En 1995 se inició la Serie de Conferencias de la *Revista Mexicana de Astronomía y Astrofísica*, dedicada a la publicación de las memorias de reuniones astronómicas efectuadas en México y en otros países del continente. Hasta 1994 las memorias de reuniones astronómicas de la región se publicaron como volúmenes especiales de la *RMxAA*.

Las condiciones de publicación de cada volumen de las memorias de conferencias serán el resultado de un convenio establecido entre la *RMxAC* y los organizadores de cada evento. Los detalles de la publicación, que incluyen fechas y extensión de los textos, serán anunciados por los editores de cada conferencia. Las contribuciones extensas estarán en inglés con un resumen en español (o portugués en caso de las reuniones regionales). Los resúmenes de las reuniones que no son temáticas tendrán una extensión máxima de 300 palabras incluyendo título, autores y afiliación; serán exclusivamente en inglés. Los macros LaTeX para las memorias se encuentran en <http://www.astroscu.unam.mx/~rmaa>. Todas las contribuciones y resúmenes deberán estar en estos formatos.

The *Revista Mexicana de Astronomía y Astrofísica*, founded in 1974, publishes original research papers in all branches of astronomy, astrophysics and closely related fields. Two issues per year are published and are distributed free of charge to institutions engaged in the fields covered by the *RMxAA*. Authors pay neither page charges nor submission or refereeing fees for publication in *RMxAA*.

All papers received by the *RMxAA* are sent to a specialist in the field for refereeing. Authors interested in publishing in the *RMxAA* should send their papers to the e-mail address [rmaa@astro.unam.mx](mailto:rmaa@astro.unam.mx), in PostScript or PDF format, along with the LaTeX file. A submission letter should also be sent. Papers should be prepared in English, using the most recent version of the *RMxAA* LaTeX document class “*rmaa.cls*” (available from <http://www.astroscu.unam.mx/~rmaa>). An “Abstract” of at most 12 lines is required, as well as a “Resumen” in Spanish. The latter can be provided by the Editors, if necessary. A total of six or fewer “Keywords” should be included, taken from the lists of international astronomical journals. Tables should be numbered and include a title. Figures should be submitted in PostScript (.ps) or Encapsulated PostScript (.eps) format, should be numbered, and should include a caption. Both tables and figures should be mentioned in the text. The style of the references follows recent international astronomical usage. For more information about the style norms of *RMxAA* please consult the example included in the LaTeX package.

*RMxAA* is an open access journal. Its contents are freely accessible both by individuals and institutions. Authors and readers are authorized to read, access, download, copy, distribute, print, search or link complete texts or parts thereof, including figures and tables, without previous permission from editors or authors, in accordance to the BOAI (Budapest) Open Access Initiative definition. Papers may be reutilized for non-commercial purposes, provided the full reference to authors and original source is given.

The Conference Series of *Revista Mexicana de Astronomía y Astrofísica* was founded in 1995 to publish the proceedings of astronomical meetings held in Mexico and other countries throughout the continent. Until 1994 such proceedings had been published as special issues of *Revista Mexicana de Astronomía y Astrofísica*.

Conditions of publication of proceedings of each conference will be the result of a mutual agreement between the *RMxAC* and the organizing committee. Details of publication, including length of papers, will be announced by the editors of each event. The extensive contributions should be in English, and should include an abstract in Spanish (or Portuguese for regional meetings). The abstracts of non-thematic meetings should not exceed 300 words including title, authors, and affiliation; they should be exclusively in English. The LaTeX templates specially prepared for proceedings can be obtained at <http://www.astroscu.unam.mx/~rmaa>; all papers should be submitted in this format.

The *RMxAA* is indexed in Current Contents, Science Citation Index, Astronomy and Astrophysics Abstracts, Physics Briefs, Publicaciones Científicas en América Latina, Astronomy and Astrophysics Monthly Index, PERIODICA, RedALyC, Latindex, and SciELO.





instituto de astronomía

unam.

# revista mexicana de astronomía y astrofísica

volumen 60  
número 1  
abril 2024

COMPUTING POLYTROPIC AND ISOTHERMAL MODELS USING MONTE CARLO METHOD	<i>Mohamed I. Nouh, Essam A. Elkholy, &amp; Samah H. El-Essawy</i>	3
RADIO PROPER MOTIONS OF THE NEARBY ULTRA-COOL DWARF BINARY VHS 1256-1257AB	<i>L. F. Rodríguez, S. A. Dzib, L. A. Zapata, &amp; L. Loinard</i>	13
XookSuut: A BAYESIAN TOOL FOR MODELING CIRCULAR AND NON-CIRCULAR FLOWS ON 2D VELOCITY MAPS	<i>C. López-Cobá, Lihwai Lin, &amp; Sebastián F. Sánchez</i>	19
THE CALAR ALTO LEGACY INTEGRAL FIELD AREA SURVEY: SPATIAL RESOLVED PROPERTIES	<i>S. F. Sánchez, J. K. Barrera-Ballesteros, L. Galbany, R. García-Benito, E. Lacerda, &amp; A. Camps-Fariña</i>	41
INVESTIGATION ON FOUR CONTACT BINARY SYSTEMS AND A SEMIDETACHED ONE AT THE BEGINNING OF THE CONTACT PHASE	<i>F. Acerbi, M. Martignoni, R. Michel, C. Barani, H. Aceves, L. Altamirano-Dévora &amp; F. J. Tamayo</i>	69
CCD PHOTOMETRY OF THE GLOBULAR CLUSTER NGC 5897	<i>A. Ruelas-Mayorga, L. J. Sánchez, E. Macías-Estrada, &amp; A. Nigoche-Netro</i>	83
THE FIRST MULTICOLOUR PHOTOMETRY OF THE V840 LYR CONTACT BINARY STAR	<i>M. Tanriver, R. Michel, A. Bulut, H. Aceves, &amp; A. Keskin</i>	99
COMPACT RADIO SOURCES IN THE FIELD OF TYCHO'S SUPERNOVA REMNANT	<i>Luis F. Rodríguez, Vanessa Yanza, &amp; Sergio A. Dzib</i>	113
ASTRONOMICAL TESTS OF A MEDIUM FORMAT DIGITAL CAMERA ON A LARGE SCHMIDT TELESCOPE	<i>F. Della Prugna</i>	121
SNIa DETECTION ANALYSIS RESULTS FROM REAL AND SIMULATED IMAGES USING SPECIALIZED SOFTWARE	<i>Juan Pablo Reyes, Marcela Hernández Hoyos, &amp; Dominique Fouchez</i>	125
TESTING AN ENTROPY ESTIMATOR RELATED TO THE DYNAMICAL STATE OF GALAXY CLUSTERS	<i>J. M. Zúñiga, C. A. Caretta, A. P. González, &amp; E. García-Manzanárez</i>	141
ASTRONOMICAL SIGNALS IN BRIGHTEST FIREBALLS FALLEN ON EARTH	<i>D. Maravilla, M. Pazos, &amp; G. Cordero</i>	165
CCD PHOTOMETRY OF TRAPEZIA STARS I	<i>A. Ruelas-Mayorga, L. J. Sánchez, A. Páez-Amador, O. Segura-Montero, &amp; A. Nigoche-Netro</i>	177
ERRATUM: A PECULIAR GALAXY NEAR M104 (RMxAA, 2023, 59, 323)	<i>E. Quiroga</i>	199



ISSN: 0185-1101

9 17701851110108